Università degli Studi di Torino
Doctoral School of the University of Torino
PhD Programme in Chemical and Materials Sciences XXXV Cycle

The tight connection between artificial organic fluorescent compounds and naturally occurring biological systems: new perspectives in solid-state lighting and chemical biology

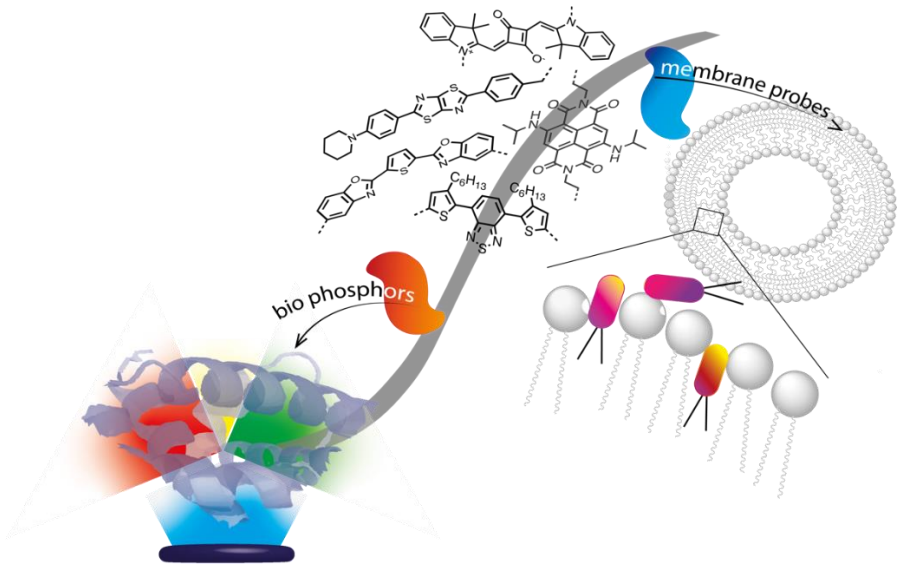

Giacomo Renno

Supervisor:
Prof. Claudia Barolo

Università degli Studi di Torino

Doctoral School of the University of Torino

PhD Programme in Chemical and Materials Sciences YYY cycle

The tight connection between artificial organic fluorescent compounds and natural occurring biological systems: new perspectives in solid-state lighting and chemical biology

Candidate: **Giacomo Renno**

Supervisor: Prof. **Claudia Barolo**

Jury Members:

Prof. **Rubén D. Costa**
Technical University of Munich
Chair of Biogenic Functional Materials

Prof. **Pedro B. Coto**
Material Physics Center (CFM-CSIC)
Theoretical and Computational Chemistry Group

Prof. **Nadia Barbero**
University of Torino
Department of Chemistry

Head of the Doctoral School: Prof. Eleonora Bonifacio
PhD Programme Coordinator: Prof. Bartolomeo Civalleri

Torino, 2023

ACKNOWLEDGMENTS

First, I would like to thank my supervisor, Claudia, for having offered me this great opportunity. For your constant support along all this amazing experience. For having given me all the space I needed to fail, correct me and, maybe, fail again. I can't go on without thanking Andrea, whose advices made me a better scientist and whose teaching allowed me to grow as quick as possible. An additional thank to Prof. Viscardi, for your wise advices and your door always open to listen, discuss and plan.

These three years have passed and I can barely recognize the scientist I was when everything started. I've been through many professional failures and successes along with an unbelievable personal growth. Nothing could have been possible without all the people I met during this journey. I would like to thanks all the guys from the MOF Lab. The Friday's Pizzas we shared together, all the songs we listened to closing the lab door to avoid any complain by the bosses, those opened windows when outside was snowing while someone (I must say, often me) was using some smelly substances. Thanks because the lab has quickly become a bubble able to protect us from everything was happening outside. Thanks to Martina, Francesca, Onur, Daniel, Maks, Mattia, Gabriel. Thanks Vale, for all the apero and chats we had in just few weeks spent together. Thanks Baptiste for your quite useful french lessons and for everything I learned from you. Thanks Pablo and Eisuke for your spanish mood always ready to shine, and for all the paellas, always promised and never prepared. And a special thank for Marco and for Matteo. You two guys have been the most amazing friends I could have ever imagined to meet along this trip. I would not be where I am right now without your constant help and support.

Thanks to the Straubing guys, with you I have spent only few months but you have been able to never let me feel homesick or alone. You have made Straubing my home in few days, and I will always remind that peaceful and exciting time we spent together.

Lastly, a warm thanks to my family, to my parents and my brother. You all always supported me. Thanks to my granma, I am sure you have shared every day of this trip with me.

TABLE OF CONTENT

CHAPTER ONE

INTRODUCTION

1.1. Overview

Light emission from a plethora of molecules and materials upon external stimuli is a powerful tool in several scientific fields. At the crossroad of different disciplines, the research on photoluminescent materials is constantly pushed beyond the existing limits to address all the emerging necessities. The development of novel efficient emitting systems can provide diagnostic and analytical tools, alternative lighting technologies to replace conventional yet not sustainable ones, or smart probes acting as molecular lightbulbs to visualize crucial biochemical pathways *in vivo*.

In this context, Nature represents a great source of inspiration, providing a wide and heterogeneous range of fluorescent systems whose complexity and colors are easily to change. Bright small emissive amino acids (e.g., tryptophan, tyrosine, phenylalanine) have been smartly introduced within the genetic code. At the same time, a brilliant network of hydrogen bonds and electrostatic interactions, along with other interactions (e.g., π–π. dipole induced) resulted in providing naturally occurring proteins with a narrow fluorescence able to cover the whole visible spectrum.

During the previous century, organic synthesis has developed several artificial molecular structures, starting from many brilliant natural examples. The fine tunability of the photophysical features achieved by smart molecular functionalizations and the low cost of organic synthesis

have afforded a wide palette of versatile emitters universally adopted in many fields (e.g., material science, photovoltaics, chemical biology). Additionally, the artificial organic emitters combined with naturally occurring biological systems (e.g., cellular membranes, proteins, nucleic acids) have already proved to represent a powerful tool for developing novel technologies. The fluorophores intercalation within nucleic acids' grooves or their accommodation into the protein pockets have proved to enhance the molecules photo/thermal stability, expanding the applicability range of the organic moieties. Alternatively, the perturbation of their photophysical features upon interaction with biomembranes lipidic bilayers offers the possibility to follow many crucial biochemical pathways *in vivo*, monitoring the cellular health status and the physical forces acting in the organelles. These few mentioned examples highlight how a synergistic approach resulting from combining synthetic organic compounds and different biological scaffolds is powerful to provide novel materials and tools.

1.2. Aim of the thesis

Herein, oligoaromatic emitting compounds have been designed and their interaction with complex biological systems has been evaluated. The fluorophores properties enhancement or perturbation upon interaction with proteins or lipidic bilayers have been carefully investigated, developing smart responsive materials applied in solid-state lighting and chemical biology.

In detail, the synthetic work allowed us to prepare a wide and heterogeneous library of compounds, whose photophysical features have been finely tuned by structural modifications. Then, smart functional groups have been introduced to enhance the interaction and compatibility

with the different biological systems. Small and compact emitters have been decorated with proper functionalizations (*e.g.*, triple bond, maleimide) allowing the bioconjugation with proteins, while polar groups (*e.g.*, carboxylic acids, charged moieties) have been attached to the hydrophobic core when the interaction with cell membranes' phospholipids was required. Lastly, the interaction with the proteins or the lipidic bilayers was evaluated and their key properties were implemented in specific applications, as briefly presented below.

The enhanced thermal-/photo- stabilities achieved by shielding the fluorophore with a protein scaffold allowed us to implement these so-formed artificial fluorescent proteins into a novel generation of bio-hybrid LEDs, assessing one of the energetic issues raised by the European Union (EU) few years ago.[1] The need for more efficient electricity consumption has been clearly stated, still the traditional white inorganic LEDs (WILEDs) cannot represent a sustainable technology in the long-term despite their outstanding performances. WILEDs briefly consist of a blue chip covered by down-converting filters, commonly based on toxic and/or rare-earth materials. The limited availability (< 10/15 years) of the latter, along with their geopolitical control by China and the environmental impact related to their extraction and refining, strongly hamper the sustainability of the current WILED technology. Although several alternatives have been proposed (*e.g.*, perovskites, organic compounds, metal coordination complexes), they have not met customer requirements in terms of cost, stability and performance. Novel materials based on naturally occurring fluorescent proteins (FP) emerged in 2015, although Thompson's and Forrest's groups proposed their use in lighting already in 2000.[2] FPs combine high photoluminescent quantum yield (PLQY), good photostabilities and a highly optimized in-place production, without

the necessity of a high level of purification. Although FPs' stability outside physiological conditions has been improved, their natural chromophores still undergo to prominent photodeactivation processes. In this work, the natural chromophore has been replaced with well-suited synthetic dyes, providing artificial fluorescent proteins able to combine the benefits of the organic synthesis (*i.e.*, narrow bandwidth, easy synthetic tunability, low cost) and the biological peptidic scaffold (*i.e.*, prevention of the dye aggregation-induced quenching, inherent stability of the scaffold). The complementarity of the organic compounds and biological systems allowed us to achieve outstanding results in LED, improving the state-of-the-art and previous data obtained when the organic compounds or the natural FPs had been used separately.

While the fluorophore accommodation into a protein pocket can enhance its inherent stability providing promising materials for optoelectronic devices, the smooth intercalation of similar fluorophores inside phospholipidic bilayers might serve as a cellular diagnostic tool. The probes' emission features can visually highlight the properties of the biological membranes, and the proper functioning of the most crucial biochemical pathways can be monitored *in vivo*. Visualizing physical forces and lipidic phases can provide essential information on cell apoptosis and basic cellular parameters (e.g., membrane tension). During the last decades, the design of fluorescent cell membrane probes afforded a wide range of bright compounds whose photophysical features strongly depend on the membrane composition. They have helped investigating the physical parameters of the membranes' bilayer as viscosity, polarity, hydration, tension and fluidity. In this work, several fluorescent probes have been designed, and their ability to discriminate between different biophysical parameters upon intercalation into the lipidic bilayer has been

assessed. The effect of saturated and unsaturated phospholipids, along with other different components of biomembranes (*e.g.*, cholesterol), have been correlated to the probes' optical traits by using liposomes, *i.e.* model vesicles useful as cellular membranes mimic spontaneously arranged upon the exposure of the single fatty acids molecules to precise external conditions. Herein, solvatochromic probes have been prepared and successfully used to evaluate membrane hydration. Lastly, a particular focus has been directed toward developing bright fluorophores staining in the Near Infra-Red (NIR) region of the electromagnetic spectrum due to many appealing features, such as the deep tissue penetration, negligible autofluorescence and low tissue photodegradation achieved in this spectral window.[3]

CHAPTER TWO

SCIENTIFIC CONTEXT

2.1. General

The ability of molecular systems to emit light upon external stimuli is one of the most extraordinary phenomena ever occurring in Nature and artificially reproduced by human science. Nowadays, the research on photoluminescent materials is constantly pushed beyond the existing limits to address all the emerging necessities. Nature represents the pioneer responsible for emissive systems, providing a heterogeneous class of molecular structures whose complexity can span from small emissive amino acids to the bigger and more elaborated fluorescent proteins able to cover the whole visible spectrum. The possibility of designing and preparing artificial emitting compounds inspired by a plethora of natural references can produce a huge library of artificial systems, labelling intrinsically non-fluorescent biological moieties (e.g., lipid bilayers, nucleic acids) and exporting the versatility of Nature in many different applied scientific fields.

Merging the tunability of organic synthesis with the wide versatility of biological systems paves the way for a family of novel emitting materials with a high potential both in the investigation of crucial biochemical pathways and in the development of emerging technologies in the field of optoelectronics and material science. The most critical challenge in this field remains the ability to prepare emissive compounds able to show remarkable fluorescent properties (*i.e.*, high quantum yield, tunable emission profiles) and, at the same time, to interact with biological systems without perturbating or altering their natural functioning. In the

first part of this chapter, bright examples from Nature are presented, along with some of their artificial analogues. Then, further sophisticated advances are shown toward their exploitation in solid state lighting (**Section 2.4**) and chemical biology (**Section 2.5**).

2.2. Fluorescence spectroscopy

Photoluminescent spectroscopy is one of the most attractive techniques to deeply investigate luminescent systems, due to its high sensitivity and remarkable versatility. In particular, while the absorption spectroscopy (e.g., UV-Vis, infrared) uses a minimum difference in the absorbed photon flux, the fluorescence detects a signal energetically different from the incident one, strongly reducing the interference from the excitation source with a beneficial effect on the signal-to-noise ratio and technique sensitivity. Shortly, proper electromagnetic radiation will promote the fluorophore to the Franck-Condon excited state (10^{-15} s), in a high vibrational state of the S_n. Then, among the others, vibrational relaxation and internal conversion phenomena (10^{-10} – 10^{-12} s) take the excited fluorophore to the lowest emissive S_1 state, creating an energy difference between the photons absorbed and the ones finally emitted. This energy loss ($\upsilon_{abs} - \upsilon_{em}$), usually indicated as Stokes shift, is strictly related to each fluorophore and to a particular set of experimental conditions (e.g., local environamental polarity). The excited state lifetime corresponds to the sum of all the decay rates - both radiative (k_r) and non-radiative (k_{nr}) – that can bring the fluorophore again to the ground state (Equation 1).

$$\tau = \frac{1}{k_r + k_{nr}} \quad (1)$$

The efficiency of the overall process can be related to different factors. While the excitation process is mainly connected with the molar absorption coefficient (ε), the emission efficiency depends on the radiative and non-radiative decay processes. The emission efficiency, usually expressed as PLQY, describes the number of emitted photons normalized per the number of absorbed ones. In terms of decays' rates, PLQY can be defined as in Equation 2:

$$PLQY = \frac{k_r}{k_r + k_{nr}} \quad (2)$$

The combined efficiency of excitation and emission processes can be expressed by the brightness, described as the product of the ε and the PLQY. In this way, fluorophores suffering low PLQY values can still compensate them with higher ε coefficients and, *vice versa*, poorly absorbing compounds can exhibit bright emission thanks to high PLQY values.[4]

The high versatility and straightforwardness of the experiments along with the growing number of robust and sophisticated benchtop fluorimeters justify the wide spread of this technique in several applicative fields (*e.g.*, chemical biology, analytical chemistry, optoelectronics).

2.3. Looking at the Nature

2.3.1. Natural amino acids and emitting artificial analogues

The aromatic amino acids (AA) – tryptophan **1** (Trp), phenylalanine **2** (Phe), tyrosin **3** (Tyr) – are almost ubiquitous in most of the natural

proteins, representing the smallest examples of fluorescent biological compounds. While Phe is less present than the other two AAs and exhibits a lower PLQY, the tryptophan emission in buffer (pH 7.0) is centered around 360 nm in the UV region and responses properly to environment polarity changes, enabling its use as a tool for monitoring protein-protein and protein-substrate interactions.[5–7]

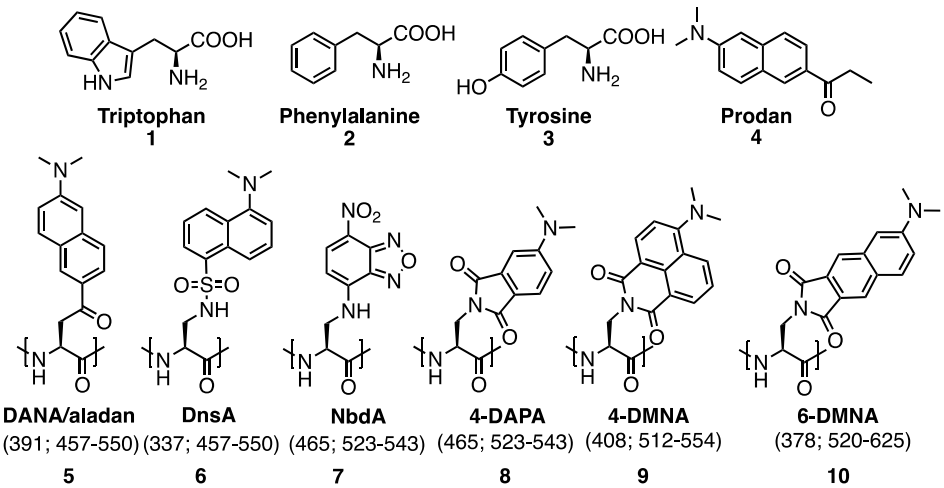

Figure 2.1 Emissive natural (**1**-**3**) and artificial (**5**-**10**) aminoacids. Between brackets, absorption and emission wavelengths are separated by semicolons. Data taken from references.[8,9]

Although the widespread of natural aromatic AAs is an advantage, it may become a disadvantage when the main target is to visualize a specific protein. Moreover, the UV emission meets several issues in term of background noise and autofluorescence upon interaction with other biomolecules in the cell. In this context, several unnatural fluorescent amino acids have been developed within the last decades. They are structurally similar to the natural occurring AAs, resulting in a low perturbation of the natural functioning or the protein folding. Some AAs have been modified through the replacement of the conventional peripheral groups with small solvatochromic dyes, as reported in Figure 2.1. One of the most common solvatochromic emitters is the PRODAN **4**,

a push-pull naphthalene-derivative compound showing a blue-shift of 130 nm moving from water to cyclohexane solutions along with an increase in the PLQY.[10] The functionalization of an AA with this little dye can provide unnatural fluorescent amino acids (e.g., **5**, **6**), used to monitor the interaction of a phosphoserine-containing binding peptide to a target protein. The replacement of a tyrosine residue with **5** led to a 20 nm blue-shift along with a four-fold emission intensity increase upon the binding.[11–13] Then, a further structural refining afforded the analogue **8** (DAPA), closer in size to the natural occurring tyrosine and with a higher emission increase.[14] Finally, analogues **8**-**10** were recently applied to investigate SH2 phosphotyrosine binding domain or the interactions between peptides and calmodulin.[9,15,16]

Lastly, Klimchenko *et al.* used a 3-hydroxychromone mimic of triptophan **11**, exhibiting a dual emission due to an occurring excited-state intramolecular proton transfer (ESIPT) phenomenon at the excited state (**12** → **13**, Figure 2.2A). The strong dependence of the ESIPT on the environment hydration and polarity (Figure 2.2C) allowed to closely monitor the oligonucleotide-peptide interaction by simple color changes in the emitted light (Figure 2.2B).[17]

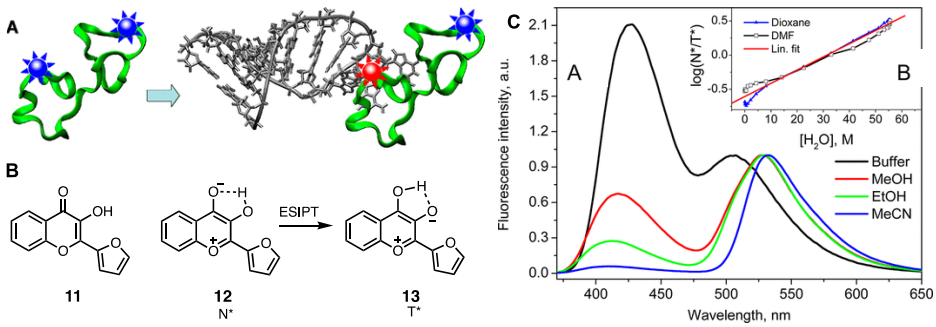

Figure 2.2 a) The interaction of the labelled peptide (green) with the oligonucleotide (gray) changes the color and the intensity of the emitted light. b) ESIPT process between the two tautomeric forms **12** and **13**. c) The response of the emitted light color to the polarity changes. Images from reference.[17]

2.3.2. Enzymatic cofactors

Nicotinamide adenine dinucleotide (NADH), nicotinamide adenine dinucleotide phosphate (NADPH), flavin adenine dinucleotide (FAD), flavin mononucleotide (FMN), and pyridoxal phosphate are enzymatic cofactors, fluorescent and often associated with a protein or an enzyme, enabling its catalytical activity. While NADH and NADPH are non-fluorescent in their oxidized forms, FAD and FMN result emissive only in the oxidized form. Additionally, the NADH and FAD fluorescence is quenched by the adenine present in their chemical structures, but NADH remains emissive upon interaction with proteins. These features are often used to monitor the kinetics of interaction between co-factors and enzymes, but the complexity of their emissive behaviour has limited their widespread use.[18]

2.3.3. Fluorescent proteins

While the amino acids' fluorescence relies on their chemical structures, the strategy adopted in fluorescent proteins (FPs) is completely different, involving a central natural chromophore stabilized into a tight pattern of hydrogen bonds and electrostatic interactions. The green fluorescent protein (GFP) was firstly isolated from the jellyfish *A. Victoria* in 1962, representing the archetype of this brilliant fluorophores class. The wild-type avGFP consist of a rigid 11-stranded β barrel ending with a α-helix running into the center of the can and bearing the chromophore consisting in a 4-(p-hydroxybenzylidene)-5-imidazolinone (*p*-HBI) motif (Figure 2.4**A**). It's noteworthy that the primary amino acid sequence contains all the information for the chromophore maturation, that spontaneously occurs after the protein folding via a series of cyclization/oxidation/dehydration reactions derived from a triplet of amino

acids Ser65-Tyr66-Gly67.[19] Several mechanisms have been proposed and Figure 2.3 shows a widely accepted one affording the *p*-HBI.

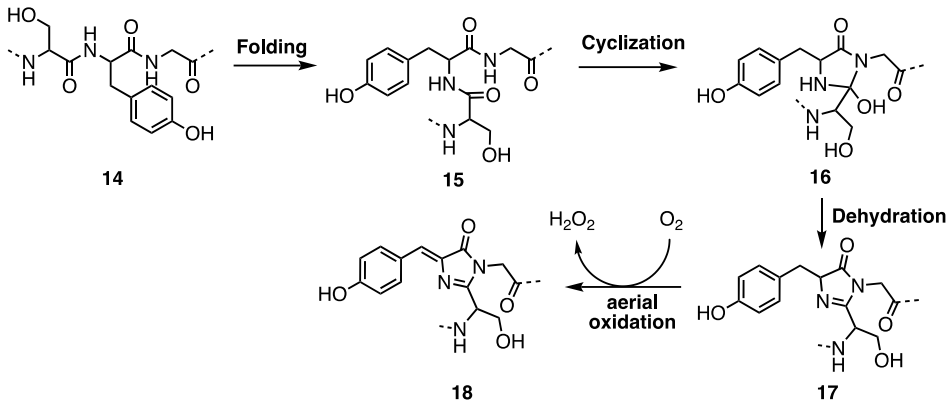

Figure 2.3. Proposed mechanism for the maturation of FPs natural chromophore.

The *p*-HBI chromophore is highly fluorescent due to *i)* the presence of the protein scaffold acting as a shield from the bulk-solvent molecules and *ii)* to the tight network of electrostatic interactions (*e.g.*, induced dipole, π–π interactions, hydrogen-bonds - HB) blocking the chromophore in an almost planar cis-conformation. In solution, the *p*-HBI is not fluorescent because of thermal and vibrational non-radiative decays from the excited states. HBs are then responsible of the two absorption peaks: the one at higher energy (395 nm) is related to the neutral form, while the band at 475 nm corresponds to the anionic form after the loss of the phenolic proton. Although the protonated neutral species is favored at room temperature, the equilibrium slowly shifts to the anionic one upon irradiation. Excitation at either wavelength causes green emission, at 503 nm (excitation at 475 nm) or 508 nm (excitation at 395 nm). The irradiation at 475 nm excites the anionic chromophore B $\rightarrow$ B* that emits at 503 nm. The irradiation at 395 nm excites the neutral species A $\rightarrow$ A*, that converts

into the intermediate I* upon ESIPT process that emits at 508 nm. The I species then slowly converts to B at the ground state (Figure 2.5).[19]

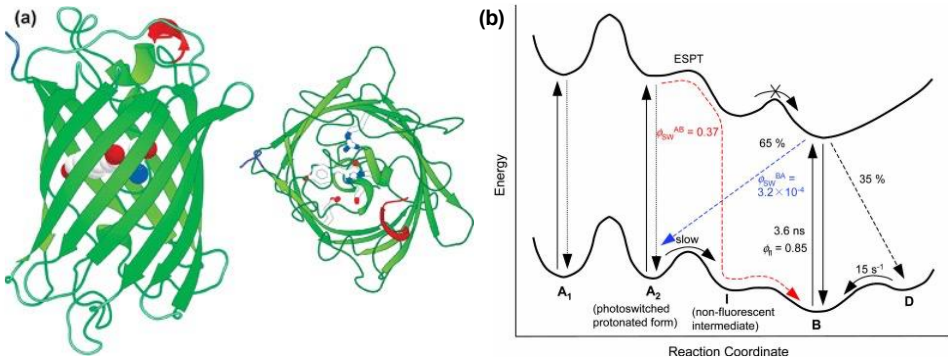

Figure 2.4 a) GFP tertiary structure. b) Energy levels diagram of photoswitiching process involving the chromophore of *Dronpa*, a GFP-like protein. Image from references.[19,20]

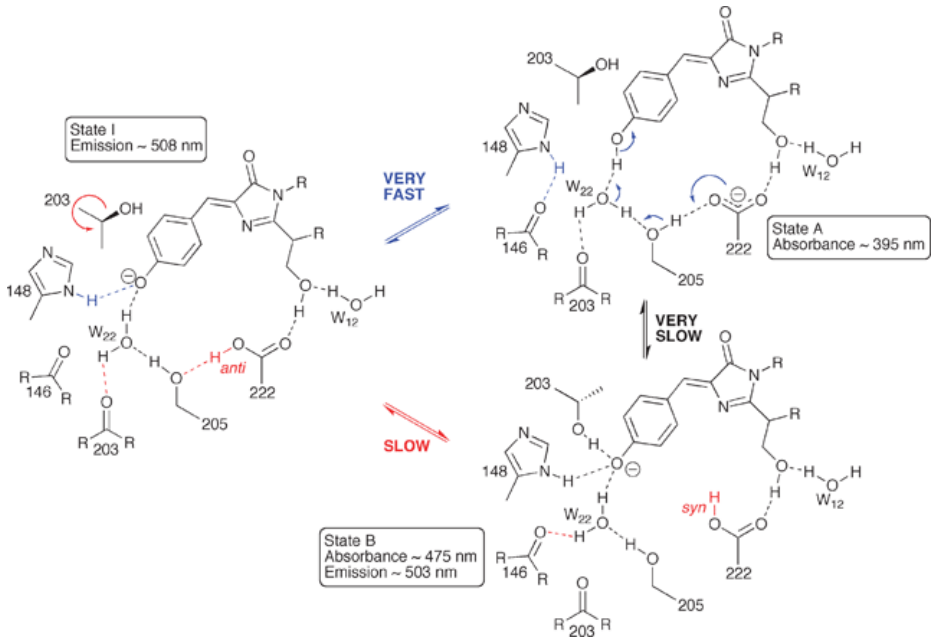

Figure 2.5 Excited proton transfer mechanism. Image from reference.[19]

Lastly, the FPs photophysics is also complicated by the photoisomerization *cis-trans* that leads to a chromophore blinking due to the not-emissive character of the *trans* isomer.

Nowadays, most efforts are focused on the existing FPs improvements and isolation of novel FPs, starting from the wide Nature range of organisms. As an example, red and orange emitting FPs were isolated by the corals or from the marine anemone *Discosoma striata*. The elongation of the conjugated system along with some chemical modifications and mutagenesis in the protein sequence allows to span the whole visible spectrum, providing a huge number of bright FPs (Figure 2.6).[21]

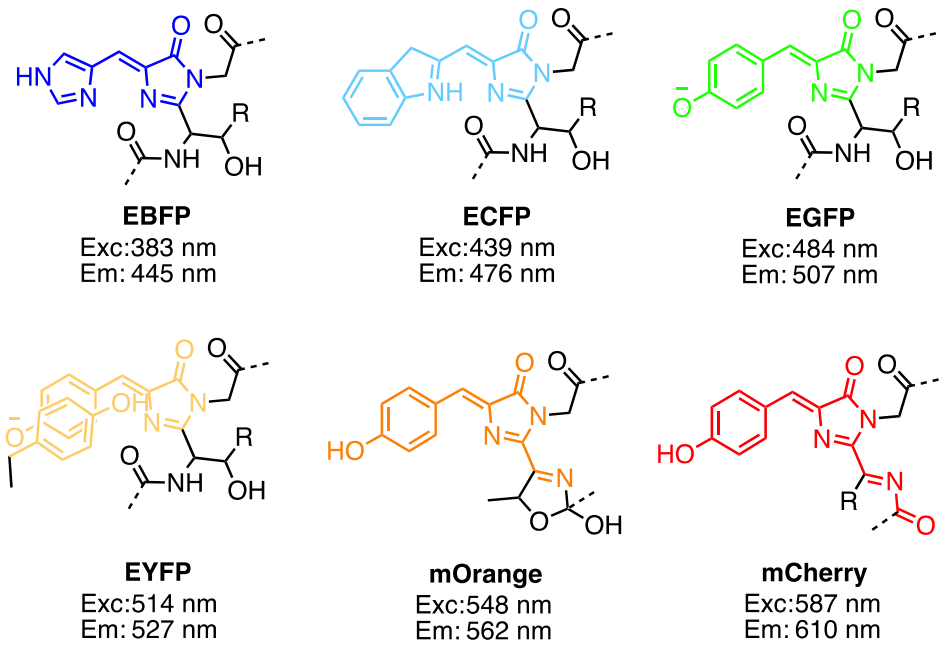

Figure 2.6 Natural FPs able to span the whole visible spectrum.

2.4. Merging fluorescent proteins and solid-state lighting: a sustainable route toward bio-hybrid white LEDs

2.4.1. Biological compounds in optoelectronics

During the last decade, several biological systems have been investigated to increase and broaden the currently available optoelectronic technologies. As an example, lighting devices (e.g., light-emitting diodes, light- emitting electrochemical cells) have already been implemented with versatile biogenic materials. A wide range of highly efficient architectures are currently replacing the conventional, yet highly consuming, lighting systems.

In the early 2000s, the **non-fluorescent DNA** has been implemented in organic light-emitting diodes (OLED) to increase the emission intensity of the active material due to its electron blocking effect. In other words, the DNA allowed to reduce the electron losses and enhanced the electron-hole recombination in the cell, providing devices thirty times brighter and ten times more efficient than their counterparts.[22] Additionally, the insertion of a chromophore within the DNA through intercalation or binding to the grooves has proved to provide remarkable photophysical features. The DNA film can stabilize the organic dyes, enhancing the luminescent features, acting as a better host compared with the conventional polymeric matrixes (*e.g.*, PMMA).[23–25]

In the same period, other natural candidates – **fluorescent proteins** – have appeared on the scenes of LED technology. Their remarkable optical features have been implemented for the realization of visible and white LEDs. First proposed by Thomson and Forrest's groups in 2000s and implemented only in 2015 by Costa's group, a hard work has been

carried out in stabilizing and implementing them in device, providing promising results in terms of sustainability, performances and costs, although some stability issues still limit their spread in the market.

In this section, a brief history of the traditional visible white LEDs is presented (**Sections 2.4.2** and **2.4.3**) along with their figures-of-merit and a critical analysis of their current limitations. The advances concerning the fluorescent proteins implementation into a more sustainable generation of bio-hybrid LEDs are shown along with the main drawbacks still affecting this technology.

2.4.2. History of Visible-spectrum LEDs

LED's history dates back to 1907, when Henry James Round observed the emission of a yellowish light upon application of 10 V between two points on a crystal of silicon carbide (also known as *carborundum*).[26] This was the first report of the **electroluminescence**, a novel phenomenon dealing with the light emission from a solid-state material caused by an electrical power source.

After the silicon carbide, many other semiconductors started to be investigated in this sense during the twentieth century. Several examples quickly came from elements of the second, fourth and sixth periodic table groups due to their natural abundance (*e.g.* ZnS and CdSe or SiGe and SiC as II-VI and IV-IV materials respectively), while the III-V semiconductors class emerged only in 1950 thanks to Heinrich Welker work since they are not naturally occurring anywhere.[27] The commercial upscale production started in 1954, and the realization of visible III-V semiconductors LEDs became feasible in 1955 when Wolff *et al.* published the first electroluminescent phenomenon in a single-crystal

GaP emitting a brilliant orange-red light.[28] In addition to the binary III-V semiconductors (*e.g.*, the above-mentioned GaP), tertiary and quaternary alloys were then prepared, providing materials whose chemical modification allowed to finely tune their luminescent features. As a first example, Folberth proposed tertiary alloy semiconductors by simply mixing GaAs and GaP, affording the $GaAs_yP_{1-y}$ alloy,[29] whose derived red-emitting LEDs were commercialized in 1960s by the General Electric Company.[30] Several other alloys were used to prepare other infrared and red emitting LEDs, like GaAs and AlGaAs[31,32] that constitute nowadays the most used infrared and red LEDs. Then, green LEDs emerged at the end of 1960s, when N impurities were added in the form of GaN to GaP crystals grown from melth (N-doping GaP technique). The so-formed devices were able to emit light in the green region of the visible spectrum and, although the quantum efficiency was lower when compared to the red LEDs, the higher human eye sensitivity to the green light makes the brightness of the two devices comparable.

Having highly efficient green and red LEDs in hand, the blue emitting devices were the only primary color missing. The achievement of a blue-luminescent material took more time than expected, resulting in a difficult task. Although the first blue emitted light occurring from a GaN single crystal has been reported by RCA laboratories in 1971[33], the devices efficiency was so low that RCA scientists gave up. Only ten years later, a Japanese team of scientists – including Asaki and Amano from Nagoya University – came back to the GaN, giving a strong contribution the field. The GaN crystal growth was dramatically improved and a blue LED with an efficiency of 1% was prepared. Then, a further contribution was provided by Shuji Nakamura and Takashi Muhai, who prepared the first blue laser operating at room temperature. Nichia Company sold in the

market the first GaN-based high brightness blue and green LEDs in 1994 and 1995, respectively. The difference between the previous mentioned GaP:N green LEDs was the brightness: the Nichia GaInN LEDs were brighter, enabling the application as green traffic lights signals. The widely recognized pioneers of GaN materials, GaN LEDs and lasers, Isamu Asaki, Hiroshi Amano and Shuji Nakamura, received the 2014 Nobel Prize in Physics *"for the invention of efficient blue light-emitting diodes which has enabled bright and energy-saving white light sources".*[34]

2.4.3. History of White LEDs

While traditional visible LEDs emits monochromatic light, white LEDs (WLEDs) deal with a polychromatic light, evidencing a significant distance between the two kinds of device. Since highly efficient monochromatic devices able to cover the whole visible spectrum were available in the 1990s, WLEDs were at hand by the mid of 1990s. Several strategies can be followed to realize white emitting LEDs and they are summed up below.

Multi-LED-chip approach. According to this approach firstly proposed by Stinson in 1991,[35] the light provided by the three LED chips emitting the three primary colors (blue, green and red) is mixed to generate white light. As described in Figure 2.7A, each chip has its own anode to be injected with the appropriate current. Although this strategy was proposed for the first time by Stinson in 1991, it became really feasible only after the mid 1990s when Nakamura was able to prepare the first highly efficient blue and green LED chips.

UV/Violet LED + White-emitting phosphors. The second approach is based on using a UV or violet LED chip covered by a phosphor able to

absorb the incident light from the chip and emit it as a broad-band white light. In other words, the phosphor is a material acting as a down-converting filter able to emit white light upon photoexcitation by the UV/Violet chip (Figure 2.7B).

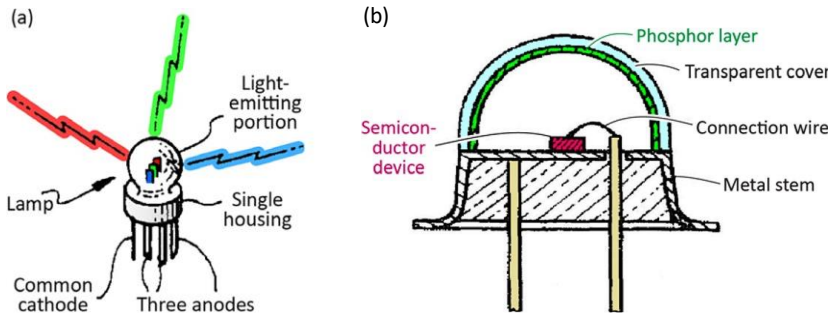

Figure 2.7. a) Multi-LED chip approach for the preparation of a white LED by summing a red, a green and a blue chip. b) LED structure showing a chip whose light is down-converted by a phosphor layer coated on the inside of a transparent cover. Images from reference.[36]

This second strategy reminds the obsolete fluorescent lamp architecture, whose working principle was already based on the down-conversion of the UV light emitted by a Hg-source (254 nm) through a phosphor. The general concept of applying a phosphor to a LED chip can be attributed to Potter who up-converted the infra-red emission to visible light,[37] but the production of white light dates back to 1973 by Tabuchi, years before the advent of the highly efficient blue LED.[38] Since then, it was adopted by several grousp during the last three decades of the twentieth century.[39,40] Both inorganic and organic phosphors were proposed, following the same principle: the UV (or violet) light from the LED chip excites the phosphor that emits light in a wide range from blue to red. The main drawback of this approach is the low efficiency, since the material

requires a high Stokes shift, meaning high non radiative energy dispersion.

Blue LED + Phosphors. Lastly, the third and most successful approach uses a blue-emitting LED chip and a combination of green and red emitting phosphors (Figure 2.8A). The blue light is *partially* absorbed by the phosphor, while the other part can be transmitted through it. The green and red emitted light (from the phosphor) can form the white light when summed to the not-absorbed blue component from the LED chip (Figure 2.8B-C).

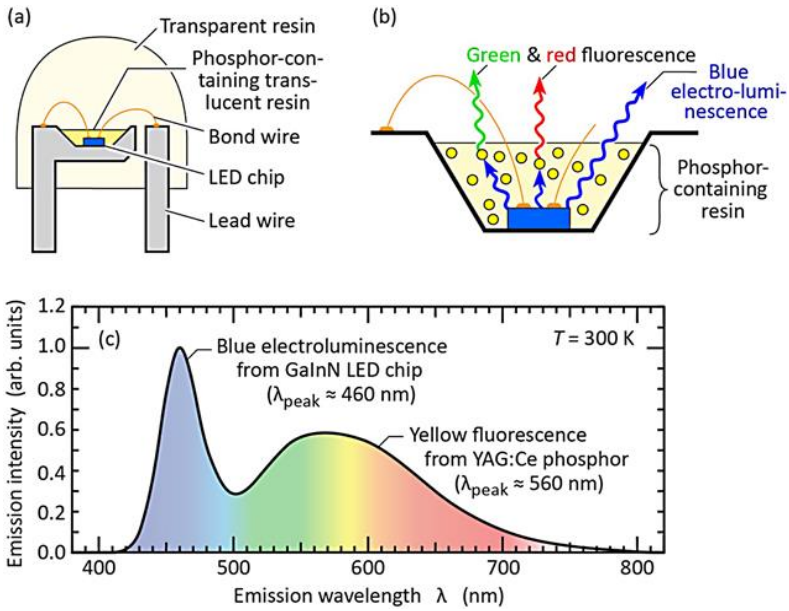

Figure 2.8. a) Structure of a white LED. b) The working principle of a white LED. The LED chip emits a blue electroluminescence, while the phosphor emits green and red fluorescence upon photoexcitation from the blue chip. c) Emission spectrum of a white LED showing a blue electroluminescent peak and a broad fluorescence band from the phosphor. Image taken from reference.[36]

In 1996, several publications and patents emerged, proving that a new era in solid-state lighting was beginning. At first, several organic phosphors were patented since their extremely short radiative lifetime was attractive for the devices, but the lack of intrinsic stability to withstand to the harsh operative conditions undermined their wide application.[41–43] The turning point came when Shimizu and co-workers adopted a yttrium-aluminum-garnet $Y_3Al_5O_{12}$ phosphor doped with optically active cerium atoms (YAG:Ce), that proved higher chemical stability and, although with some modifications, is currently used nowadays.[44] The YAG phosphor is also known as the “yellow phosphor” due to its two emissive bands, green and red, that appear yellow to the human eye. By the end of 1996, WLEDs with efficiency of 12 lm/W were demonstrated, exceeding the values of the low-wattage incandescent lamps.[44] A new era in solid-state lighting had definitively begun.

In 2000, a report by Haitz *et al.* highlighted that the large-scale introduction of LEDs would have saved more than 1000 TWh every year, decreasing the global electrical power of more than 50% along with a carbon dioxide reduction of 20 megatons due to the replacement of traditional electrical power plants based on coil, oil and natural gas.[45]

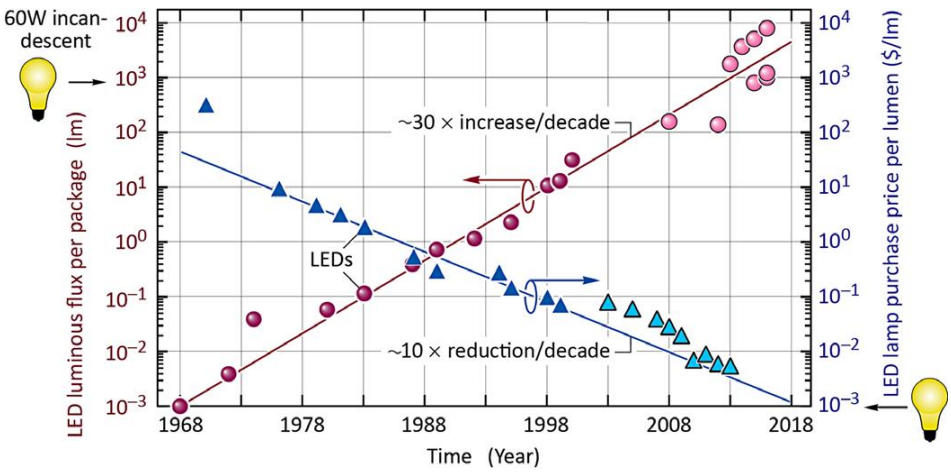

Figure 2.9 LED luminous flux per package and LED lamp purchase price per lumen. Image taken from reference.[36]

Another problem that LED technology had to face at the beginning was the low power produced when compared to other lighting devices, as the incandescent light bulbs. As shown in Figure 2.9, the luminous flux per package increased by almost four orders of magnitude in 30 years, while the cost dropped of a factor 10 per each decade.

Table 2.1 reports the luminous efficacy of other ancient and now obsolete light-sources, evidencing the outstanding performances of the WLEDs.

Table 2.1 Luminous efficacy of different kind of light sources.[36]

Kind of lamp	Luminous efficacy (lm/W)
Incandescent lightbulb with C filament	1.2-2
Incandescent lightbulb with W filament	10-18
Incandescent halogen lightbulb with W filament	16-24
Linear fluorescent lamp (LFL)	65-95
Compact fluorescent lamp (CFL)	50-70
White LED*	100-303

*Cree Company 2014; 303 lm/W; CCT=5150 K; Osram Company 2014; 205 lm/W; CCT = 3000K

Additionally, the development of the luminous efficacy for visible and white LEDs over time is presented in Figure 2.10. The growth of visible and white LEDs is outstanding, showing how the luminous efficacy doubled every four years from 1960 to 2000 and sets stable above the other kind of light sources.

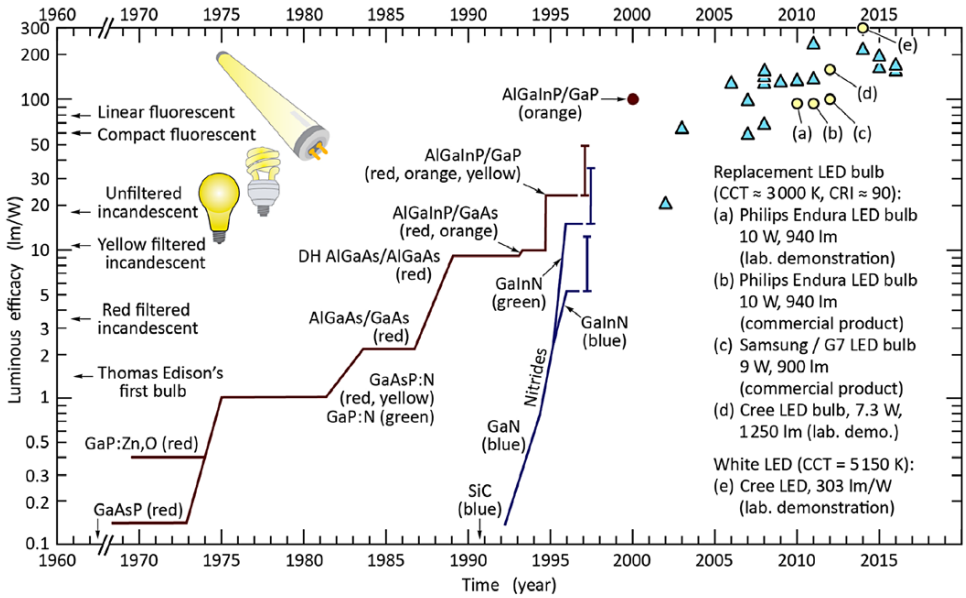

Figure 2.10 Development of luminous efficacy of visible and white LEDs, compared with traditional light sources. Image taken from reference.[36]

2.4.4. Phosphor-converted WLEDs

As mentioned above, phosphor-converted WLEDs consist of a LED chip, whose emission is partially (or fully) converted in white light by means of phosphors, acting as color-converting filters. In particular, there are several methods to produce white light, known as dichromatic, trichromatic or tetrachromatic sources depending on the distinct emission bands number (Figure 2.11). The higher the light source chromaticity the lower is potential luminous efficacy. On the other side, low chromaticity will lead to low color-rendering ability.

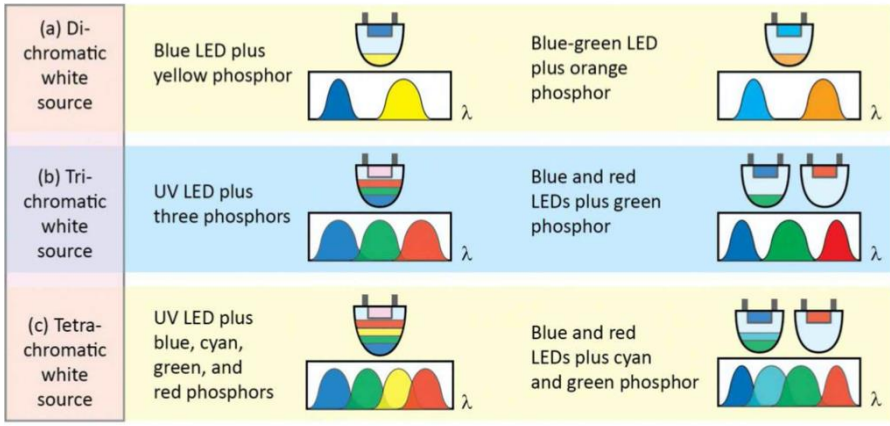

Figure 2.11 White sources using different architectures. Image taken from reference.[46]

When a phosphor is filtering the primary radiation from the LED chip, a full or a partial conversion can occur (Figure 2.12). In the first case, the primary radiation from the LED chip (usually, a UV or violet excitation source) is totally used to excite the phosphor and fully converted into a white secondary radiation. In the second case, the partial conversion allows a part of the blue excitation source to be transmitted through the phosphor and participate directly to the white light, while the resting part to be absorbed and converted into a secondary radiation.

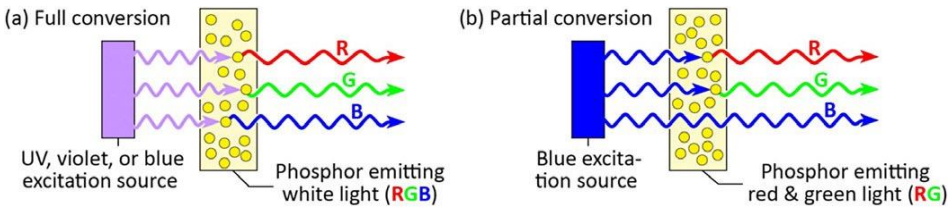

Figure 2.12 Full (a) and partial (b) conversion of primary radiation in a white LED. Image taken from reference.[36]

As previously mentioned, the full conversion of a primary radiation by means of a converting phosphor dates back to the obsolete incandescent Hg-lamp, in which the Hg-vapor light (λ = 254 nm – UV light) was fully converted to a secondary radiation. The partial conversion has an intrinsic higher efficiency compared to the full conversion approach, since it shows a lower Stokes shift, *i.e.* a lower wavelength-conversion losses.

2.4.5. Figures of merit

Several figures of merit can be defined to evaluate the device performances.[46]

Internal Quantum Efficiency (IQE). IQE is defined as follows:

$$IQE = \frac{no.\ of\ photons\ emitted\ from\ active\ region\ per\ second}{no.\ of\ electron\ injected\ into\ LED\ per\ second} = \frac{P_{int.}/_{h\upsilon}}{I/_e} \qquad (3)$$

Where I is the current injected into the LED chip, while the $P_{int.}$ is the optical power emitted from the active region. In the ideal case, an LED should emit one photon per each injected electron affording a 100% of IQE.

External Quantum Efficiency (EQE). EQE is defined as follows:

$$EQE = \frac{number\ of\ photons\ emitted\ into\ free\ space\ per\ second}{number\ of\ electron\ injected\ into\ LED\ per\ second} = \frac{P_{LED.}/_{h\upsilon}}{I/_e} \qquad (4)$$

where P_{LED} is the optical power emitted by the LED into free space.
The EQE is the ratio of the number of useable photons to the number of electron injected into the LED chip.

Power conversion efficiency (PCE). The PCE of a device is defined as the ratio of the optical output power emitted by the LED to the electrical input power (eq X).

$$PCE = \frac{P_{optical}}{P_{electrical}} = \frac{P_{optical}}{IV} \quad (5)$$

where IV is the electrical input power defined as the product of the current I and the voltage V.

Luminous efficacy. Two different kinds of efficacy can be taken into account: the luminous efficacy of the radiation (LER) and the luminous efficacy of the source (LES).

Luminous efficacy of the radiation (LER). When considering lighting applications targeting the human eye, it should be pointed out that the sensitivity of the human eye is not equally distributed along the whole visible spectrum. It follows a distribution ($V(\chi)$) centered on the green emission at $\lambda = 555$ nm. In this context, the luminous flux (Φ_{lum}) can be defined as the power of a light source as perceived by the human eye:

$$\Phi_{lum} = 683 \frac{lm}{W} \int_{\lambda} V(\lambda) * P(\lambda)\, d\lambda. \quad (6)$$

where P(λ) is the power spectral density, *i.e.* the light power emitted per unit wavelength. 683 lm/W is a normalization factor: 1 W of optical power at 555 nm corresponds to 683 lm.

The integration of the power spectral density along the wavelength axes affords the optical power emitted:

$$P_{optical} = \int_{\lambda} P(\lambda)\, d\lambda \quad (7)$$

Finally, the ratio of the luminous flux to the optical power emitted is **the luminous efficacy of the radiation (LER)**:

$$LER = \frac{\Phi_{lum}}{P_{optical}} \quad (8)$$

This quantity only depends on optical features, without involving any electrical components of the device. According to this definition, the LER parameter can be useful to describe which portion of the radiant flux contributes to the luminous flux, i.e., to the light as is perceived by the human eye. In this context, lights with wavelengths out of the visible spectrum show low efficacies since these parts are included in the radiant flux at denominator, without contributing to the numerator. In the visible range, monochromatic green light (555 nm) shows LER = 683 lm/W, while other components in the violet or red regions of the spectrum show just few lm/W as LER values. For white light, the Sun has, as a good approximation, a Planckian spectrum with a LER = 93 lm/W due to the presence of significant controbition in the UV and infrared regions. Trichromatic (blue + green + red bands) and dichromatic (blue + yellow bands) white lights exhibit higher LER values, up to 300 and 450 lm/W, respectively.

Luminous efficacy of the source (LES). The LES parameter is of importance for the white light sources and describes the ability of a device to convert the electrical energy into optical power:

$$LES = \frac{\Phi_{lum}}{P_{electrical}} = \frac{\Phi_{lum}}{IV} \quad (9)$$

The LES parameter depends both on the conversion of the electrical into optical energy and on the efficacy of the radiation emitted on the source (LER contribution). Hence, for a system with an ideal electrical-to-optical conversion efficiency, LER = LES. The luminous efficacy of the source describes not only the power consumption of the source, but also the energy dissipation by heat, operating costs, etc. This is why the LES parameter is a key figure of merit when describing a WLED.

Phosphors power-conversion efficiency (PPCE). The two main factors affecting the efficiency of the primary radiation down-conversion are related to the *i*) quantum efficiency of the phosphor (**PQE**); *ii*) energetic loss during the wavelength conversion **(λCE**). The first contribution is intrinsically related to the phosphors and can be defined as follows:

$$PQE = \frac{n.of\ photons\ the\ phosphor\ emits\ in\ the\ free\ space\ per\ second}{n.photons\ the\ phosphor\ absorbs\ per\ second} \quad (10)$$

The second component is related to the Stokes shift. When converting a primary radiation with a wavelength λ_1 to a secondary one with $\lambda_2 > \lambda_1$, there is an intrinsic energy loss since $E_1 > E_2$. Thus, the wavelength-conversion efficiency λCE can be defined as follows:

$$\lambda CE = \frac{E_2}{E_1} = \frac{h\upsilon_2}{h\upsilon_1} = \frac{\lambda_1}{\lambda_2} \quad (11)$$

This phenomenon explains why a partial conversion is more efficient than a full conversion, when realizing a WLEDs. And, why a multi-chip approach is more convenient than the phosphor-conversion.

Lastly, the PPCE can be defined as:

$$PPCE = PQE * \lambda CE \quad (12)$$

Color-rendering index (CRI). The CRI parameter quantifies the ability of a white light to accurately render the true colors of an object. This information is of importance for the evaluation of a white light source for indoor applications, whereas is neglectable for street lights or traffic signals. In a range between 0 and 100, the sunlight has the maximum

value (i.e., 100). For indoor lights, CRI > 70 is highly recommended. The traditional incandescent lamps show the highest CRI value, but they suffer from a high-power consumption. White LEDs have already reached high CRIs between 55 and 95, depending on the device architecture, highlighting their suitability as indoor lighting sources (Table 2.2).

Table 2.2 General CRI values for several kind of light sources.[46]

Light source	Color Rendering Index
Sunlight	100
W filament incandescent light	100
Fluorescent light	60-95
Phosphor-WLED	55-95
Hg vapor light coated with phosphor	50
Hg vapor light	33
Green monochromatic light	-50

Correlated colour temperature (CCT). To define the CCT, we have to start from the description of the black-body radiation spectrum (also known as Planckian spectrum). As an example, looking at a metal bar heating on the fire at T > 500 K, a electromagnetic radiation will be emitted, whose colour strongly depends on the temperature. The bar will appear dark red at lower temperatures (T ≈ 500 K), then orange, yellowish and, finally, white at T > 2000 K. This phenomenon commonly known as incandescence was accurately described by Max Planck in 1900. Planck could elaborate an equation to describe how the emission spectrum changes upon the temperature increase: as clearly shown in Figure 2.13**A**, the maximum intensity emitted from the black body shifts to shorter wavelengths upon temperature increases.

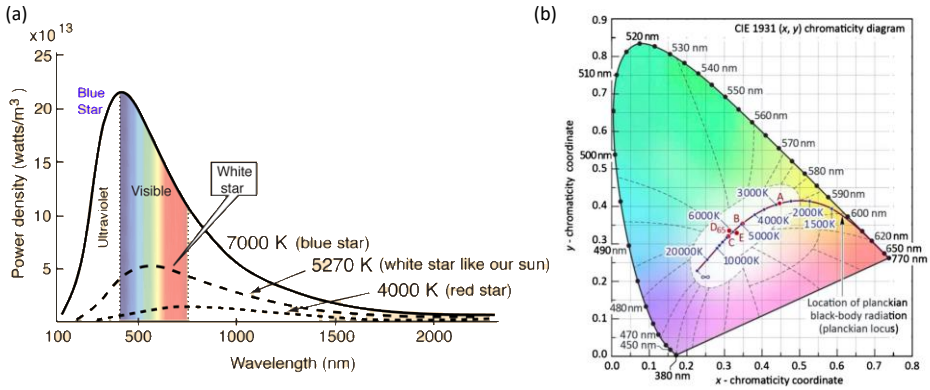

Figure 2.13 a) Dependence of the incandescence light on the temperature. b) Planckian locus in the chromaticity diagram. Images taken from references.[36,47]

In particular, the position of the black-body radiation in the chromaticity diagram will create a curve line, known as *Planckian locus*: the points along the line moves from the red to the white region of the diagram when the temperature increases (Figure 2.13B). The **color temperature** (CT) of a white light source is the temperature of the Planckian black-body emission that shows the same chromaticity coordinates of the considered source. When the chromaticity coordinates of the sources do not fall on the Planckian locus, the **correlated colour temperature** (CCT) is considered. The CCT is defined as the temperature of the black-body radiator whose chromaticity on a *u'v'* uniform chromaticity diagram is closest to the considered white source (Figure 2.14).

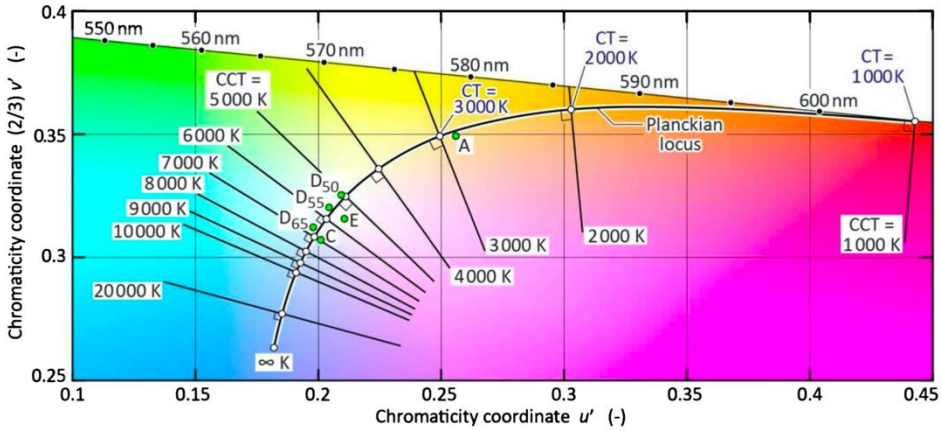

Figure 2.14 Planckian locus and right-angle intersecting lines of CCT in the chromaticity diagram.[36]

2.4.6. Health implications of using WLEDs

When comparing the spectrum of several different lighting devices, it's clear how many differences can be found. In Figure 2.15, a dichromatic WLEDs made up of a blue and a yellow band is shown, along with a tricolor fluorescent lamp and an incandescent bulb. Although these lights may look similar by eye, the blue component contributes differently to the three devices. This aspect influences some health-related considerations due to the blue light involvement in the human photoreceptor damage and in the circadian rhythm alteration.

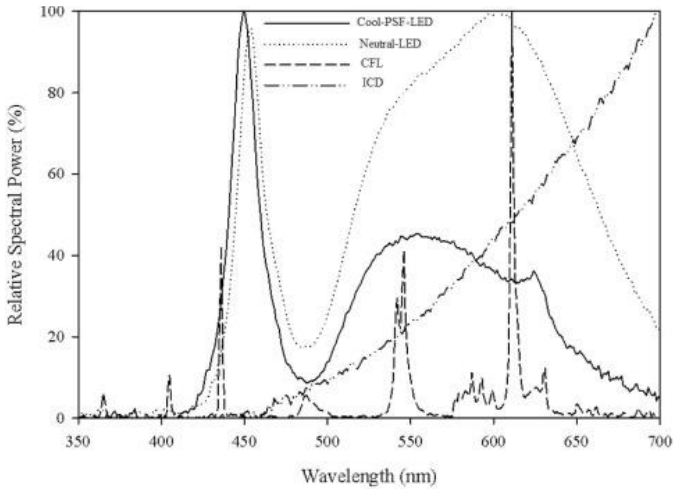

Figure 2.15 Comparison of spectrum of four different light sources: Cool Poultry specific filtered LED (Cool-PSF-LED, 5000 K); Neutral-LED (Neutral-LED, 3500 K); Compact fluorescent lamp (CFL, 2700 K); Incandescent Bulb (ICB, 2010 K). Image taken from reference.[48]

In mammals, photoreception occurs only in retina through different types of photoreceptors: cone, rods and the intrinsically photosensitive retinal ganglion cells (ipRGCs). While the formers are responsible for the visualization and the image formation, the latter – the ipRGCs – are involved in the regulation of the circadian system, pupillary light response and many other biological functions. While cones and rods rely on different opsins and on the rhodopsin respectively, the photopigment expressed in ipRGCs dendrites is the melanopsin. The melanopsin is involved in the regulation of sleep, mood, metabolism and in the pupillary light reflexes.[49] The melanopsin spectral absorption, centered around 479 nm, explains why the blue light exposure affects the human circadian rhythm more significantly than green and yellow wavelengths. An experimental study[50] showed that the melatonin suppression upon exposure to blue light was twice when compared to an equal-photon density green light. Similar studies proved a significant influence of the blue light on the body temperature, heart rate and sleepiness, evidencing

that it is a potent modulation of brain function. While an increase in the blue light during the daytime might be crucial for the vitality of the organisms, an exposure reduction during the night should be suggested to avoid the melatonin suppression and the sleepiness decrease. Many devices (e.g., smartphones, laptops, e-books) offer the possibility of blue-light blocking in the displays (the "*night shift*" mode).

Moreover, long-term exposure to the blue light may cause retinal photodamage. Although the mechanism is not fully understood, the retinal damage probably involves the lipofuscin (absorption peak at 450 nm), a byproduct of the degradation of the rod photoreceptors disks. When the lipofuscin absorbs the blue light, a higher number of reactive-oxygen species (ROS) are produced with the consequent oxidative photodamage of the retinal photoreceptors. Furthermore, the lipofuscin level is low in the young and higher in the elders, making the retinal damage an age-related degradation.

2.4.7. Inorganic LEDs (WILEDs)

Inorganic phosphors (IPs) are widely used as down-converting materials in WLEDs due to their well-known stability. IPs usually consist of a host lattice doped with some optically active species (**activators**). The host lattice has to be transparent in the visible region, with a stable and stiff crystal structure to reduce the non-radiative vibrational relaxation. The only possibility to achieve transparency in the visible region (i.e., to possess a large bandgap) is to include into the lattice anions from elements at the top of the groups of the periodic table. This limits the choice between nitrides, oxides, sulfides and fluorides. Furthermore, the host lattice has to be a stable material, able to withstand the high radiation intensities occurring at the blue LED surface. On the other hand, the **activator** is an atom able to absorb the incident radiation and emit a

photon with a lifetime in the fluorescence range. Activators are usually rare-earth elements, e.g. cerium, europium or erbium, whose optical activity is already widely known and proved.[51–53] Sometimes, a **sensitizer** can be present. It is useful to shift the wavelength emission to a desired value through an energy transfer from the sensitizer to the activator. Both external atoms (e.g., manganese) and neighbouring atoms (e.g., oxygen) can play the sensitizer role. In other cases, the host lattice can act as the sensitiser. The sensitiser can also be avoided when the activator can convert the light directly to the desired wavelength (Figure 2.16).

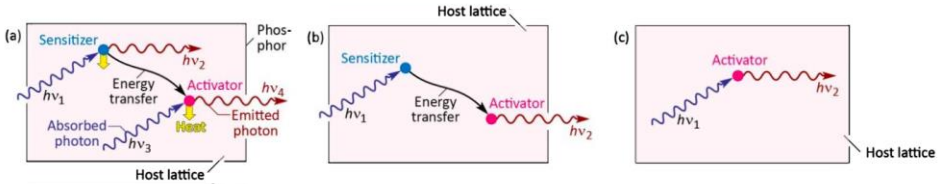

Figure 2.16 (a) A phosphor containing a sensitizer and an activator. Both can absorb and emit radiation, while the sensitizer can also transfer energy to the activator. Both dissipate energy in the form of heat. (b) Desired optical processes occurring in a phosphor presenting both a sensitizer and an activator. (c) Desired optical processes occurring in a phosphor presenting only the activator. Image taken from reference.[46]

One of the most common IP is the $Y_3Al_5O_{12}$ doped with cerium, whose lattice has a garnet crystal structure.[54,55] Garnet structures have the general formula $A_3B_5O_{12}$ where A and B are the cations and O is the oxygen. In particular, the yttrium aluminium garnet (YAG) is widely used in LED devices as host material and doped with several different rare earth elements (REE). Cerium is employed for obtaining WLEDs, neodymium in lasers, erbium in optical amplifiers. The external REE can replace the yttrium cation in the lattice due to their chemical similarity (Y is a REE as well), affording an optically active material. The final emissive features can be finely tuned by modulating the amount of REE doping. In particular, YAG:Ce(III) can cover the visible spectrum from green to red

by simply replacing the Al atoms with different metals (Figure 2.17) or varying the cerium amount in the lattice.

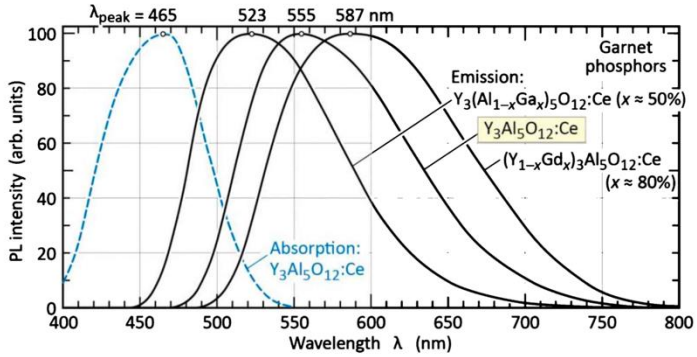

Figure 2.17 Absorption (dashed) spectrum for YAG:Ce and emission (solid) spectra for YAG:Ce-based phosphors replacing part of the Al atoms with Ga and Gd. Image taken from reference.[46]

2.4.8. IPs drawbacks

The ILEDs high performances rely on the use of rare earth elements both as components of the host lattice (e.g., yttrium) and as activators (e.g, cerium, europium), undermining somehow the long-term sustainability of this technology.[56] REE are commonly considered critical materials by the European Commission[57] and the US Department of the Interior[58] due to their economic importance (EI factor) and the risk of supply shortage (SR factor). In particular, Y and Ce SR values are two of the highest ones of the whole periodic table (3.8 and 5.7, respectively, when the critical threshold is 1), even if Ce is the most abundant and the cheapest REE. The high SR values are mainly related to the uneven distribution of these materials all over the world. In particular, China has the monopoly of most REE – 95% of cerium extractions are located there – rising a geopolitical issue responsible of the high costs and the supply risks.[59]

Moreover, the ecological impact of the REE extraction has to be taken into account with care. It is intensive because of the use of polluting chemical additives, the presence of radioactive materials (e.g., uranium, thorium) in the REE ores and from an energetic point of view.[60–62]

Although the amount of Y and Ce for a typical 12 W YAG:Ce WLED is "only" 300 mg and 6 mg respectively,[63] the increasing LEDs share in the lighting market strongly stresses their long-term sustainability concerns. The forecasted 80% LED share in the market by 2025 with 16 billion of LED units shipped per year puts a strong limitation to the current technology.[64] The first signals have already been reported by the McKinsey Global Institute: while the blue LED chips efficiency are increased with beneficial effects on the final device, the overall WILEDs price raised due to the IPs that today contribute to the 15-25% of the overall cost, with a predicted increase up to 40% in the next few years.[65]

The rare-earth resources will finish by the end of the century, after several years of geopolitical and economic tensions. In this context, a rare-earth free scenario is strongly advised.

2.4.9. RE-free IPs

Since 1990s, several rare-earth free inorganic phosphors have been explored, even though satisfactory results have not been fully achieved.

Quantum Dots. Quantum dots (QD) are nanocrystals of luminescent semiconducting material, with a diameter of 2-10 nm and tunable optical features.[66–68] Highly promising white emitting CdSe QDs were developed in the past, although at the beginning their QY was very low (5.7 %). Further studies proved that QY could be enhanced up to 61% upon

treatment with citric acid, exhibiting a bluish white emission (CIE coordinates x = 0.21, y = 0.22).[69] Then, their stability and processability were further improved by the preparation of composite materials where the QDs were encapsulated in polymeric materials. Xinsheng and co-workers prepared blue, green and red emitting $CdSe_xS_{1-x}$/ZnS QDs in ZIF-8 MOFs, proving the encapsulation beneficial effects on QY (> 85%), thermal stability and long-term durability.[70] Unfortunately, the biological toxicity of Cd undermined all these results, limiting their production for the market.[71,72] In 2017, the EU pointed out the "total negative environmental, health and customer safety impacts" of Cd-based QDs, forbidding their use by the end of 2019.[73]

Other Cd-free alternatives were investigated (e.g., InP-QDs) for displays realization and WLEDs, although their costs and performances still need to be improved before achieving practical applications.[74]

Perovskites.[75] Both hybrid organic-inorganic and all-inorganic perovskites exhibit remarkable photophysical properties, with PLQY > 90% and narrow emission profile able to cover the whole visible spectrum.[76,77] The use of perovskite as down-converting filters for the WLEDs realization was pioneered by Snaith and co-workers, in 2015.[78] Since then, several WLEDs were realized with outstanding performances in term of CRI (> 89) and efficiencies (85 lm/W).[79] A CRI of 96 was obtained by using five differently emitting perovskite films onto a blue LED chip.[80] Unfortunately, the great perovskite sensitivity to oxygen and moisture along with low device stabilities strongly limit the perovskite-based WLEDs. Several polymeric encapsulants were investigated, but the highest stability currently reported is 227 h at a driving current of 20 mA, too far from the market requirements.[81]

Mn – fluorides. The idea is to replace the rare-earth activator with some transition metals. Among several possibilities (e.g., vanadates, tungstates), red emitting Mn^{4+}-based fluoride phosphors represent the most promising family in the inorganic rare-earth free scenario. Several host lattices have been tested (Table 2.3), using the Mn^{4+} as activator species.

Table 2.3 The main red emitting Mn-fluorides phosphors.[82]

Activator	Sensitizer	Compound	Excitation	Emission
Mn^{4+}	Non	K_2SiF_6	450	630
	Non	$BaGeF_6$	457	634
	Non	Cs_2TiF_6	474	632
	Non	$BaSiF_6$	470	632
	Non	K_2TiF_6	468	632

The intraconfigurational $3d^3$ transitions of the Mn^{4+} ions are responsible of the luminescence of the material.[83] The narrow emission centered around 630 nm allows the application of K_2SiF_6:Mn^{4+} in displays and warm-light WLEDs for indoor lighting. The luminescence is stable at the application temperatures in WLEDs, with even better results when compared to certain red Eu^{2+}-phosphors.[84] The chemical stability of the phosphor remains an issue due to the sensitivity of the material to moisture and water. In particular, the phosphor darkens in high temperature and high humidity conditions (85% humidity at 85°C) due to the hydrolysis of $[MnF_6]^{2-}$ to the black MnO_2.[85,86] Fortunately, several encapsulants have already been tested with significant benefits in term of stability, and further improvement upon coating screening will still broaden the application field of K_2SiF_6:Mn^{4+} red phosphor.[87,88]

2.4.10. Hybrid WLEDs

Hybrid LEDs (HLED) consist of a LED chip whose emission is partially converted by an organic phosphor. This approach gained more and more attention since: *i)* allows to avoid the use of rare-earth resources; *ii)* photophysical properties of organic compounds can be finely tuned by structural modifications; *iii)* the organic compounds high absorption coefficient allows to reduce the phosphor loading into the device.

There are several possibilities to deposit the organic material. As a first possibility, thin films can be prepared from a solution of the organic compound and a UV- or thermal- curable sealing reagents and then placed on the top of the LED packing.[89–91] This approach showed high degradation of the down-converting material and a phase separation in the coating morphology, limiting the device stability to few hours.[90,91] Another possibility is the use of metal-organic frameworks (MOF) as hosts for the organic material. In this way, the LED chip can excite either the molecule or the MOF that can excite in a second moment the organic compound upon an energy transfer process. The MOF approach resulted to be compatible with small molecules, QDs and coordination complexes.[92,93] A third method relies on a cellulose-based coating embedding the organic compounds, although stability data are still not reported in literature.[94,95]

Lastly, Costa's group developed a way to prepare rubber-like coatings by mixing the emissive material with a mixture of branched and linear polymers. This approach demonstrated to be useful for small molecules, carbon-based nanodots, polymers and coordination complexes.[96]

Small molecules. Some of the many molecules implemented in HLEDs are reported in Figure 2.18. The molecules **18-20** were used by

Costa's group for the realization of a white HLED by preparing a cascade-like coating system.[96] A blue LED chip with a top coating based on **19**/**20**/**21** was prepared and the electroluminescence spectra showed the clearly distinguishable peaks of the three emitters, providing a white light with a CRI of 93 at a driving current of 10 mA. Unfortunately, despite such mild conditions the initial white emission changed toward the blue in few hours, hampering the use of small molecules according to this strategy. Other examples use aromatic amines to produce green light, due to their high photoluminescence efficiency, as the 4-dimethylaminochalcone (DMAC **22**). The combined use of the green-emitting amines with typical red dyes (*e.g*, Nile Red **23**) allows to obtain red light by simply exciting the former with a UV LED chip.[97] Several other attempts were carried out with commercial organic fluorophores (**24-27**), proving the accessibility to LEDs covering the whole visible spectrum by down-converting organic phosphors.[98–100] **24** is worthy of a special mention due to its ability to emit a yellow light, that summed to the blue primary radiation from the LED chip produces a cool white light.[101] The use of one single molecule to emit white light is remarkable when compared to the previous examples, where several organic dyes were required.

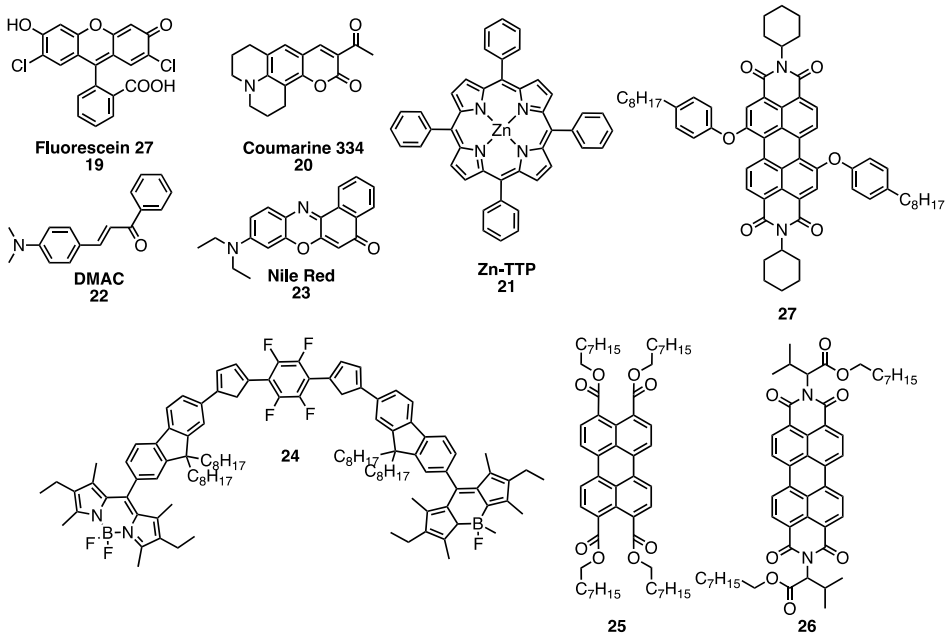

Figure 2.18 Chemical structures of some small molecules implemented in HLEDs.

Lastly, another attempt has been carried out by He and co-workers, who used the perylenes **25-27** with green, yellow and red fluorescence dispersed in a thermoplastic resin at high temperature as down converting phosphors to prepare white and yellow HLEDs.[102] The dispersion of the three emitters in an alyciclic epoxy sealant resin was carried out. The bluish green light of **25**, summed to the yellow and red emissions of **26** and **27** respectively, produces a white light with a CRI of 91.7 and a luminous efficacy over 50 lm/W. The stability of the device (700 h) represents the best result achieved with small molecules based WHLEDs at the best of my knowledge, but it's still far from the market requirements.

Coordination complexes. The best performing white LED devices based on coordination complexes were realized by Costa's group according to a cascade-like coating system.[96] Two rubber-like coatings

were placed on the top of a blue LED chip. A blue chip/**28**/**29** architecture (Figure 2.19) device was prepared, emitting white light with CRI of 85, high luminous efficiency (200 lm/W) and stable color quality. Although the outstanding device stability (> 4000 h), the main limitation to the wide-spread is represented by the high cost of the organo-metallic species.

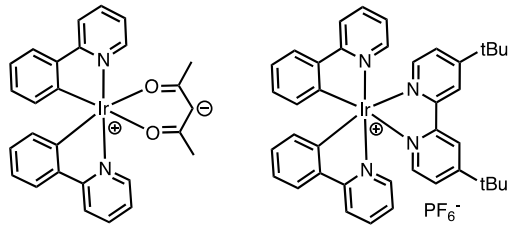

28 **29**

Figure 2.19 Chemical structures of two coordination complexes used in phosphors for HLEDs.

Conjugated polymers. Conjugated fluorescent polymers are an interesting class due to their low cost, processability from solution and tunable optical features. Moreover, they are almost insensitive to the aggregation-induced quenching phenomena, in contrast to the most of small molecules. This allows a high chromophore loading into the coating, with beneficial effects on the device performances.[89] Since 1997, several structural possibilities have been explored toward a wide range of colored WLEDs spanning the whole visible spectrum. A series of polyphenylenvinilene-based polymers were used to prepare blue and green emission upon excitation through a blue chip, by the introduction of different electronic donating group on the aromatic moieties. **30** and **31**, along with a Dow proprietary Red F, films spin coated on two separate glass substrates were placed on the optical path of a blue chip (450 nm), generating a white light (CIE coordinates 0.34, 0.29) - **Figure 2.20**.

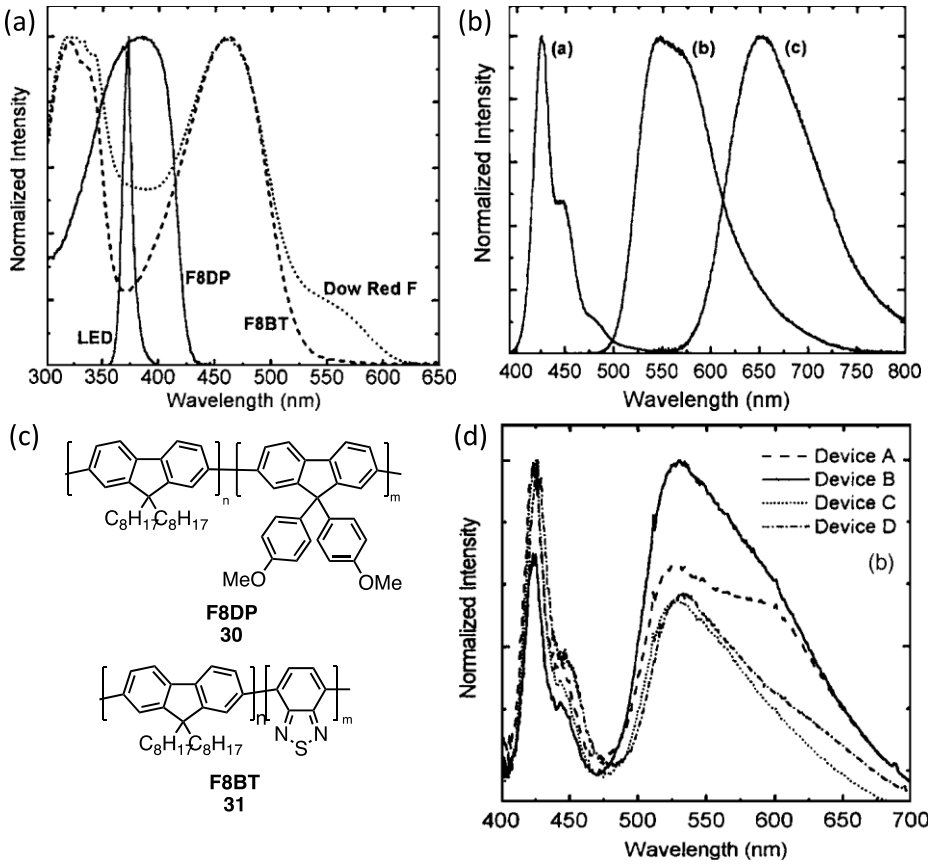

Figure 2.20 (a) The absorption spectra of F8DP, F8BT, Dow Red F and the emission spectrum of InGaN micro LED. (b) Normalized emission spectra of F8DP, F8BT, Dow Red F. (c) Chemical structures of conjugated polymer F8DP and F8BT. The Red F is propriety of Dow. (d) Emission spectra from devices. F8DP (A: 98%; B: 98%; C: 99%; D: 99%), F8DP (A: 0.5%; B: 1%; C: 0.4%; D: 0.6%); RedF (A: 1.5%; B: 1%; C: 0.6%; D: 0.4%). Image adapted from reference.[89]

Additionally, the fluorene has been introduced in the copolymer along with benzothiadiazole, anthracene and bisthienyl-benzothiadiazole providing a red emitting material (em 640 nm) with a full conversion upon excitation via a blue LED chip (exc 455 nm).[103] Lastly, an oligofluorene has been coupled to a BODIPY using either *beta* or *meso* positions of the aromatic fluorophore, providing several red-emitting materials (**32-35**). The light

down-conversion has been proved by depositing a coating on a UV LED chip, under a operating current of 5 mA (Figure 2.21).[104]

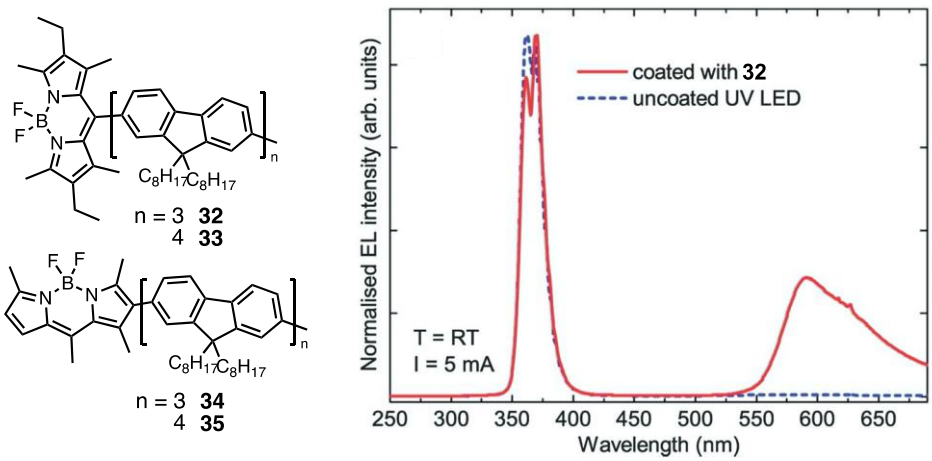

Figure 2.21 Chemical structures and HLEDs prepared with oligofluorene-BODIPY based phosphors. Image adapted from reference.[104]

2.4.11. Bio-hybrid LEDs

2.4.11.1. FPs based bio-HLEDs

The use of FPs for lighting applications as down-converters phosphors represents a breakthrough in the field since 2000, from a Thompson and Forrest groups idea.[2] FPs production is cheap and sustainable. High purification is not required for lighting applications, as demonstrated by Nizamoglu and co-workers since comparable results in term of luminous efficiency emerged whenever purified (by chromatography) or not-purified FPs (lysate without a chromatography step) were used.[105]

The narrow emission, the lack of toxic residues and excellent photon flux saturation make FPs extremely appealing for the implementation in lighting devices.[106,107] The major drawbacks mainly deal with their

stability in a water-free environment, outside from the physiological environment.[108] In particular, temperature and pH are two factors that may play a pivotal role in the FPs degradation. Under the device operative conditions, the temperature increase might unfold the protein with quenching and degradation of the natural chromophore upon exposure to harsh conditions. The pH influences stability as well, since fluorescence increases at moderate alkaline values (pH 8-9), while denaturation occurs at higher values (pH 10-13). Even mild acidic conditions lead to denaturation.[109,110] As a first solution, thermal- and photo- resistant protein mutants can be produced.[109,111] Another approach – the most used in lighting – relies on the design of a matrix able to stabilize the FP (e.g., MOF, cellulose, polymers).[109–111] A satisfactory matrix has to be photostable, cheap, easily preparable without any thermal-/UV-curing method and compatible with FPs aqueous solutions.

In 2015, Costa reported an outstanding method for the preparation of rubber-like FPs coating, able to stabilize the FPs at ambient conditions over years (Figure 2.22).[112] High-weight linear and low-weight branched polyethylene oxide polymers (i.e., trimethylolpropane ethoxylate – TMPE and linear polyethylene oxide – l-PEO, respectively) were mixed to the FP aqueous solution, affording a gel after a night under stirring. The hydroxyl groups of the polymer allow to retain the necessary water amount inside the gel network to stabilize the protein. The first white bio-hybrid LED (Bio-HWLED) has been realized according to a cascade system coating with mTagBGP (blue), eGFP (green) and mCherry (red) proteins. CRI value of 80 and 10% loss of efficiency after 100 h have been achieved, paving the way to a low cost and sustainable strategy toward the preparation of white LEDs.

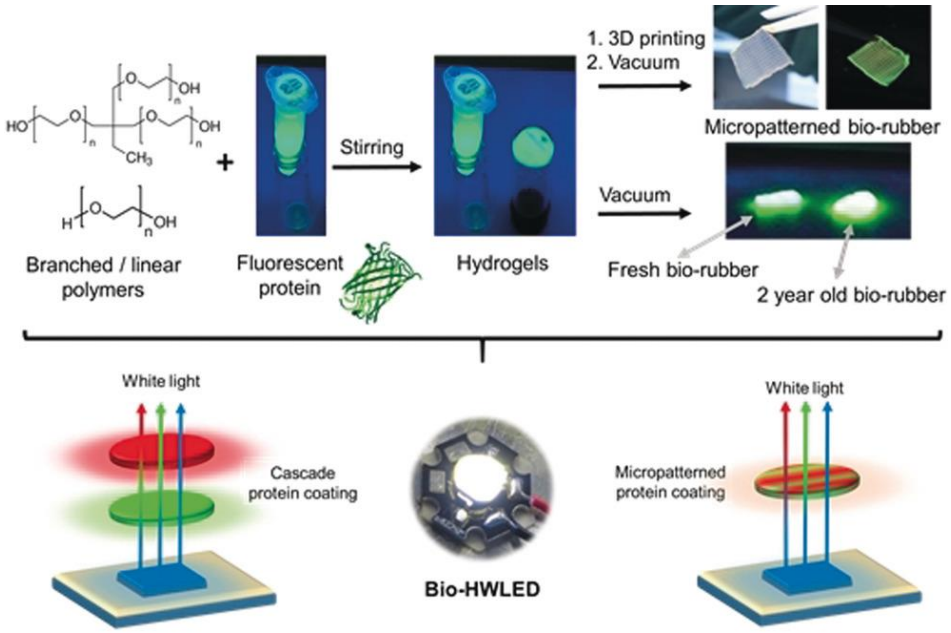

Figure 2.22 Scheme of the bio-rubber fabrication (top) and sketches of Bio-HWLEDs based on a cascade coating (bottom left) and micropatterned coating (bottom right). In the middle, a picture of a running device is shown. Image taken from reference.[110]

Lastly, Figure 2.23 show a comparison of the performances of different HLEDs coated with different kinds of phosphor materials. FPs based bio-HLEDs exhibit outstanding performances. Only coordination complexes can provide comparable results, but their wide use in the market is strongly limited by the high iridium cost.

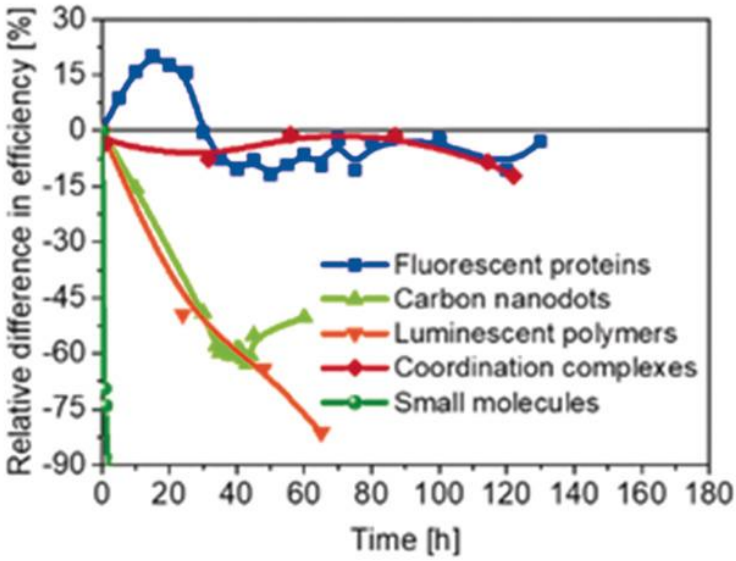

Figure 2.23 Comparison of the performance of blue-emitting (450 nm) HWLEDs coated with different commercial color down-converters. Image taken from reference.[110]

2.4.11.2. Bio-HLEDs stability: an open question

Although the FPs became a feasible option as down-converting phosphor at the beginning of the twenty-first century, their stability under the device operative conditions remains a big issue nowadays. If they can achieve hundred hours of stability at low currents, harsher conditions lead to a dramatic drop with a device lifetime < 1 min.

The degradation mechanism has been deeply investigated by Costa and coworkers in 2019.[108] The first issue is related to the non-radiative energy relaxation of the FPs chromophore. The energy is transmitted to the polymeric matrix and contributes to increase the operating temperature (60°C), with negative effect on the device efficiency (thermal quenching) and on the protein stability. A remote device configuration can be easily realized, overcoming this issue with stabilities > 300 h at the same operating conditions.

At this point, the photodeactivation of the natural chromophore remains the last issue to be solved. Costa explains how two processes occur under device operative conditions. During the first 185 h, a slow reversible dehydration process leads to a small change in the FPs emission band. Then, a quick and irreversible photodeactivation takes place, assisted by a local conformational change in the chromophore environment (Figure 2.24).

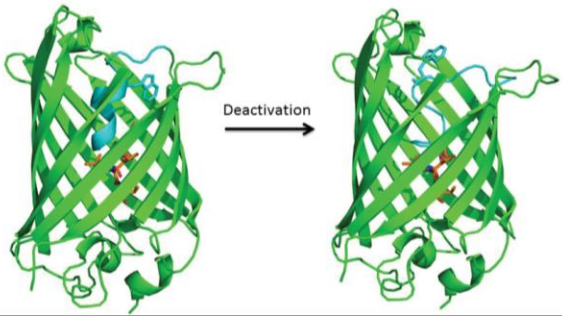

Figure 2.24 Schematic representation of the partial conformational change quenching the Trp57–chromophore FRET mechanism. The crystal structure of eGFP (PDB ID: 2Y0G) featuring the chromophore as orange sticks, the Trp57 as cyan sticks. Image taken from reference.[108]

The modification of the local environment and, consequently, of the overall charge distribution inside the protein pocket leads to an irreversible change of the chromophore excited state: the highly emissive anionic form is not stabilized anymore, leaving the non-emissive neutral species. Additionally, many other factors could be involved, *e.g.,* the possible transformation to the not emitting *trans* form.

While solutions at oxidative and thermal damages have been achieved, the natural chromophore still undergoes prominent photodeactivation, undermining the application of the FPs on the lighting market. Mechanistic more detailed studies and solutions to the occurring photodeactivation remain an open question.

2.5. Organic fluorescent probes as selective stains for cell membrane visualization

2.5.1. Visualization of cellular plasma membrane through small fluorescent probes

The visualization of cellular components has always been of importance to investigate the complex functioning and health status of cells and organelles.[113–116] In particular, the plasma membrane (PM) shows a phospholipidic bilayer decorated with diversified functional proteins,[117] playing a key role in the cell biochemistry and organism functioning.[118] The PM does not act just as an intrinsic barrier, but participates to several activities (e.g., trafficking, signaling, cellular uptake) ensuring the good health status of the cell.[119,120] The investigation of PM lipidic composition and assembly along with its dynamic and cell's morphology can provide further instruments to monitor many physiological and/or pathological conditions related to the entire organism.[121,122] The selective staining of PM along with the ability of visually highlighting the physical forces and discriminating the lipidic compositions is a primary necessity in chemical biology as a quick and powerful cellular diagnostic tool.

In this context, fluorescence is a powerful and non-invasive technique which allows well-defined investigations in space and time of bio-chemical/physical events by using specific probes. The investigations concerning small fluorescent probes are obtaining higher and higher attention for their tunable optical traits and a small size that allows an accurate location within the membrane.[123–126] Many molecular fluorescent probes with different scaffolds have already been reported for chemical fluorescence sensing (ratiometric probes, fluorogenic molecules or energy transfer pairs) involving either the lipid bilayer and the intrinsic

proteins of the PM. They have also resulted useful to investigate the physical parameters of the membranes bilayer as viscosity, polarity, hydration, tension and fluidity. Historically, Weber and Lakowicz have pioneered the design of small probes suitable for the investigation of biological domains such as proteins and membranes by functionalizing a naphthalene core to introduce unique photophysical features in the so called Prodan **1**, Laurdan **36**, and Patman **37** dyes.[10,127] Nowadays many fluorescent probes, specifically designed for the investigation of lipid bilayer membrane, are available on the market and are extensively used by the scientific community. Lipophilic probes, not covalently linked to membrane building blocks, such as DPH **38**, ANS **39**, DCVJ **40**, DPE **41**, have been used to investigate membrane fluidity due to their fluorogenic features.[128–130] More polar fluorophores such as NBD **42**, Texas Red **43**, Dansyl **44**, Cyanines **45** have been reported to label or replace the polar head groups of phospholipids to explore the outer membrane surface Figure 2.25.[131,132] Well-known fluorophores such as pyrene and fluorene have been covalently linked on-chain and in chain-end to investigate the interior of the membrane.[133,134] More recently, bright dyes absorbing and emitting in the near infrared region of the spectra have been proposed to shed light on membrane dynamics.[135]

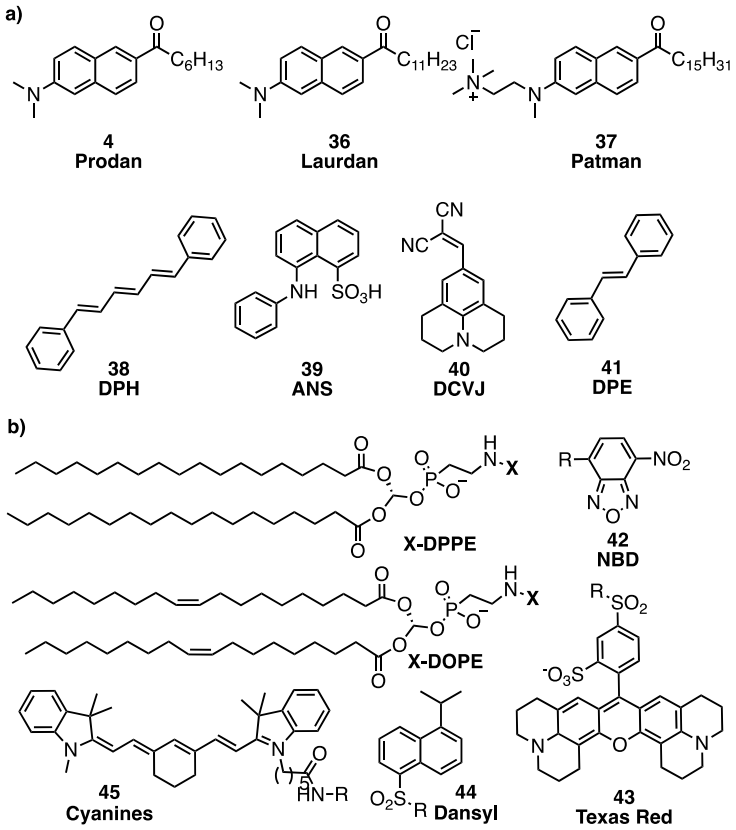

Figure 2.25 a) Examples of fluorescent dyes applied as cellular membrane probes. b) Fluorescent moieties covalently linked to polar phospholipids head group.

Finally polarizable and planarizable oligo-aromatic probes have been developed to visualize membrane hydration and mechanical compression in living cells.[136] The design and investigation of molecules, suitable for application in bioimaging is a dynamic field in which novel probes are constantly prepared and evaluated to provide novel tools for basic and applied science.

2.5.2. Solvatochromic chromophores

Push–pull dyes have a molecular structure in which electron-rich donor (D) and electron-deficient acceptor (A) moieties are connected by a π-conjugated linker. Generally, this class of probes exhibit a larger dipole moment in the excited state then in the ground state due to the formation of an intramolecular charge transfer (ICT) state upon photoexcitation (Figure 2.26**A**). The excited state is stabilized by dipole–dipole interactions between the dye and the surroundings solvent molecules. Both solvent relaxation and environment polarity contribute to the stabilization effect (Figure 2.26**B**). Solvent relaxation is the rate of reorientation of solvent molecules around the dye dipole in the excited state and relies on lifetime of the dye. Increasing environment polarity leads to greater stabilization, resulting in a bathochromic shift in the emission maximum of the dye. This effect is known as fluorescent solvatochromism (Figure 2.26C).

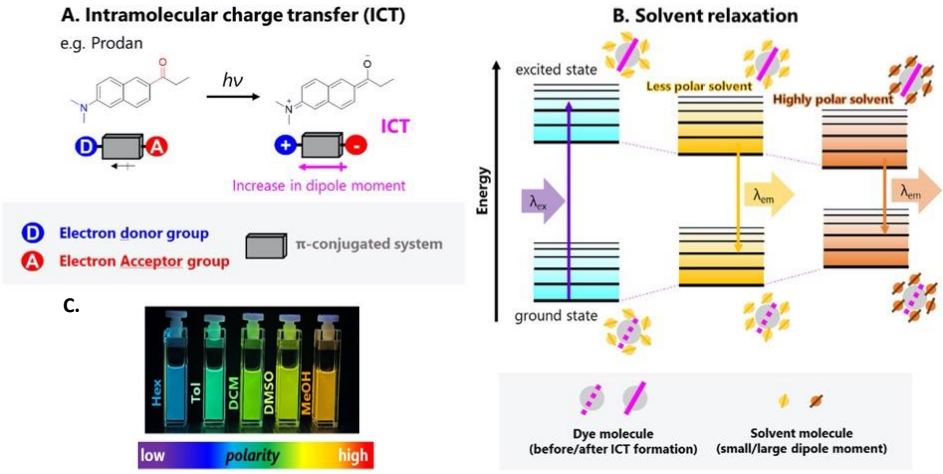

Figure 2.26 a) Intramolecular charge transfer occurring at the excited state, for a push-pull dye. b) Schematic representation of the solvent relaxation

phenomenon. c) Fluorochromic behaviour, typical of push-pull dyes. Images from reference.[126]

Donor-acceptor systems have been extensively adopted for many applications. While the donor groups usually show high HOMO energy levels, accepting moieties exhibit low LUMO energy levels. Thus, the preparation of combined D-π-A systems allows to increase the conductivity and to finely tune the band gap and the frontiers orbital energy levels, providing a heterogeneous range of versatile materials - small molecules and polymers - widely adopted in photovoltaics and organic electronics.

Concerning their role as fluorescent dyes, their sensitivity to the environmental polarity can represent a powerful tool in bioimaging. The evaluation of the local polarity in different cell organelles (e.g., nucleus, endoplasmic reticulus, Golgi apparatus, mitochondria) can be used to monitor the occurring biochemical processes and identify abnormal functioning, serving as early disease markers.[137–140] These informations can be further translated into the lipid order of membranes (e.g., packing degree, lipidic composition), providing key connections to the cellular processes. According to the lipid microdomains raft hypothesis,[141] differently organized phases coexist (Figure 2.27).

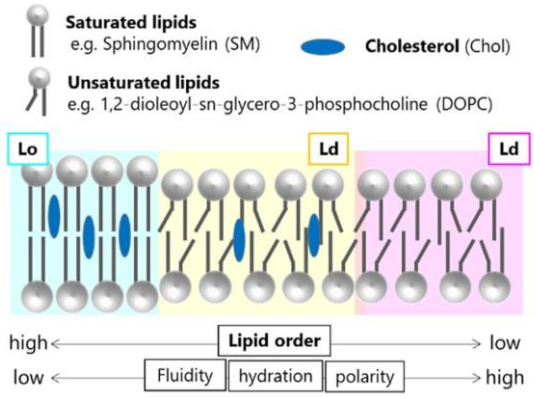

Figure 2.27 Lipidic phases organization in biomembranes. Image from reference.[126]

A liquid ordered phase (L_o) mainly composed by saturated phospholipids and cholesterol is more well-packed, while a liquid disordered phase (L_d) shows a more fluid behaviour due to the presence of unsaturated phospholipids. The rigid L_o acts as “rafts floating in the sea of L_d phase”, and these rafts are involved in many cellular processes (e.g., endocytosis, signal transduction, protein cluster formations).[142,143] In this context, the ability of solvatochromic dyes of changing color depending on the packing degree of the lipid domains has been widely used to discriminate between the different phases and evaluate the correct functioning of the above-mentioned membrane processes (Figure 2.28).

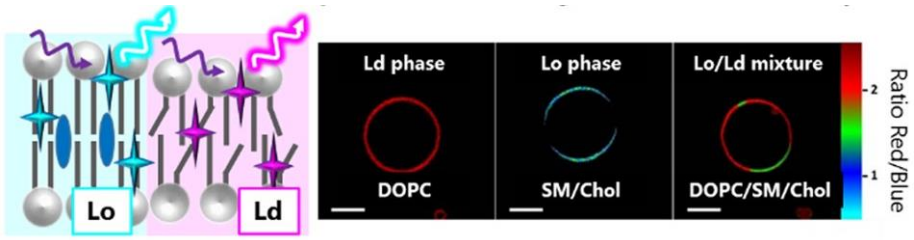

Figure 2.28 The use of solvatochromic dyes to visualize differently packed lipidic phases. Image from reference.[126]

Starting from historically traditional probes (e.g., Prodan, Laurdan, Patman), several novel or better refined structures have been developed throughout the last decade, evidencing the great attention on this topic still nowadays.

2.5.2.1. Prodan and Laurdan analogues

Such need of well performing tools for investigation within model and real membranes has led new design for Prodan **4**. In 2010, Kucherak and colleagues have proposed new fluorophores (**46** and **47**), where the naphthalene core of Prodan has been substituted by fluorene to have push-pull fluorophores with better solvatochromic and photostability properties within probing activities.[144] The polarity increment from toluene to methanol is responsible of a red-shift of emission from 434 nm to 570 nm in case of **46** and from 425 nm to 555 nm for **30**, with PLQY decrease from 98% to 19% and from 83% to 35% respectively due to the large charge separation of their excited state. The small size of **46** and **47**, along with the observed strong charge transfer and the high photostability make these two candidates suitable as cell membrane probe. Then, other push-pull fluorene based asymmetrical systems, designed and synthesized with ICT and H-bonding properties have been furtherly investigated, **48-58** (Figure 2.29).[145,146]

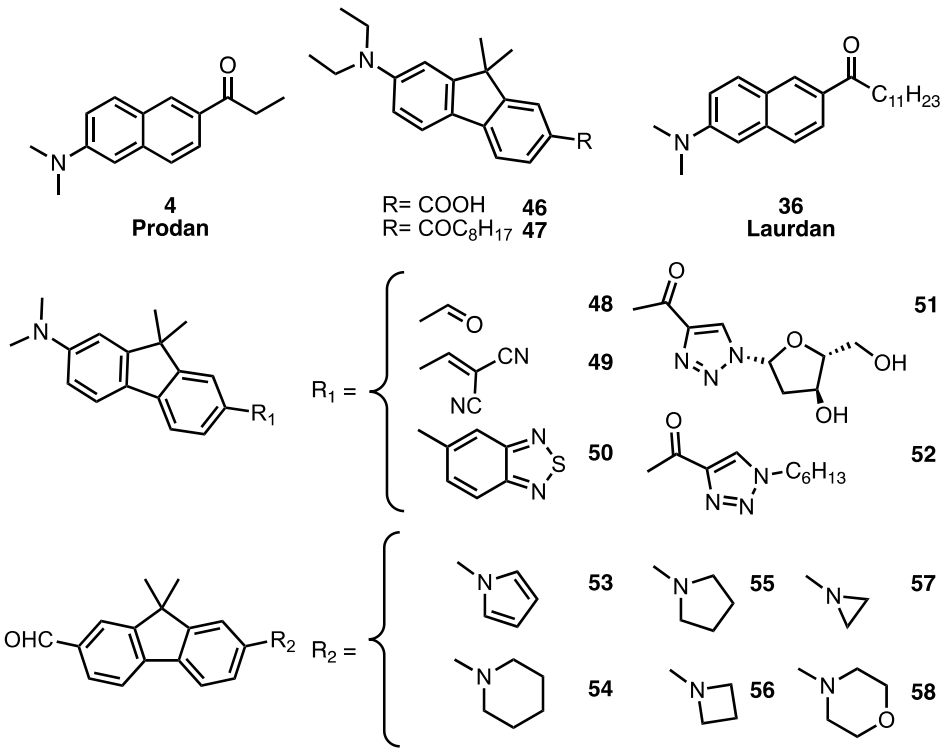

Figure 2.29 Molecular structures of Prodan, Laurdan and fluorene-based analogues. A systematic approach has been reported, by modification of both acceptor and donor groups.

2.5.2.2. Nile Red analogues

Another widely spread solvatochromic dye is the Nile Red (**59**), whose novel analogues have been particularly explored within the recent past. Among the first candidates, **60** has been synthesized in 2010 and resulted to link only to the outer portion of membranes in model vesicles.[147,148] Its absorption properties shift depending on the lipid ordering, allowing a precise discrimination of the two lipid phases. The probe presents different optical properties depending on the cholesterol contribution in *in vitro* experiments representing a promising tool for further optimization. It has been successfully tested for the apoptosis detection,[149] loading in diacetylene amphiphilic micelles used as delivery systems[150] and imaging of hippocampal membranes.[151] Danychuck *et al.* recently better

refined **60** molecular structure, proposing two novel solvatochromic compounds **61** and **62** bearing a sulfonate group as anchoring moiety upon cell surface, and hydrophobic chains of different lengths, responsible for reversible (short chain) or irreversible (long chain) binding.[150,151] Lastly, the same group recently presented a library of solvatochromic Nile Red derivatives **63**-**68** reported in Figure 2.30, showing an emission centered around 640 nm in MeOH (average PLQY 40%) and between 630 and 645 nm in DOPC (PLQY 21-61%) to specifically target plasma membrane, mitochondria, lysosomes, endoplasmic reticulum (ER), Golgi and lipid droplets, successfully evaluating the local lipid order.[152]

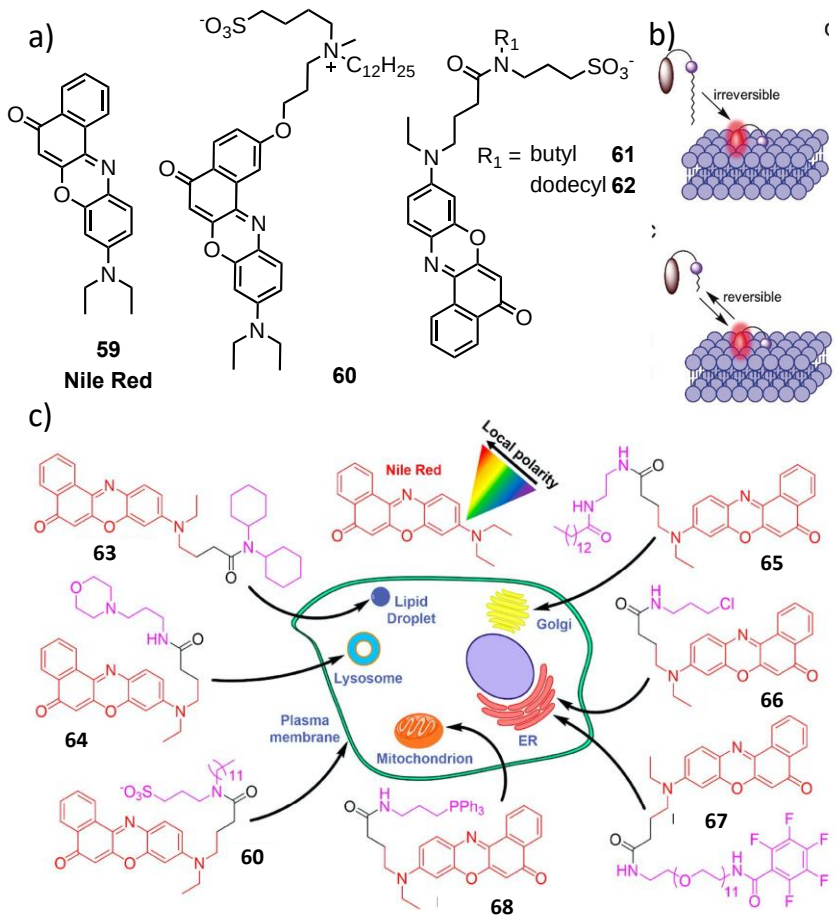

Figure 2.30 a) Nile-Red analogues as fluorescent membrane probes. b) Reversible and irreversible binding of analogues **61** and **62**, respectively. c) Nile-Red analogues selectively staining specific cellular organelles. Images from references.[152,153]

2.5.3. Planarizable chromophores

2.5.3.1. General

While push-pull systems can monitor the local environment polarity, planarizable chromophores help to visualize physical forces and membrane tension.

Planarization can originate from temperature,[154–156] pressure,[157] voltage[158] and self-assembly at the solid state,[159] representing a powerful tool for the development of chemosensors, light emitting systems or nanostructures with enhanced emission and transport.

The effect of the temperature on the chromophore π system planarization is a well-known phenomenon, widely investigated on many scaffolds. The absorption spectrum of the *trans*-stilbene derivative **69** shows a blue shift upon temperature increase due to the deplanarization of the bulky triphenylamine, while smaller amino groups (**70**-**73**) afford a thermal quenching due to the activation of non-radiative decay processes without any significant shift (Figure 2.31).[160]

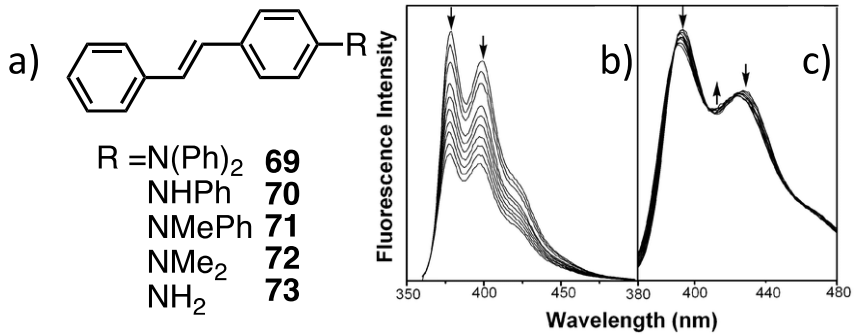

Figure 2.31 a) *trans*-stilbene derivatives molecular structures, bearing different sterically hindered amino groups on one moiety. Effect of the temperature on **69** (b) and **70** (c) absorption spectra. Image adapted from reference.[160]

An opposite trend has been found in the perilene diimide (PDI) derivative **74**, where the temperature activates the fluorescence deplanarizing the system and avoiding quenching *via* ICT (Figure 2.32).[155]

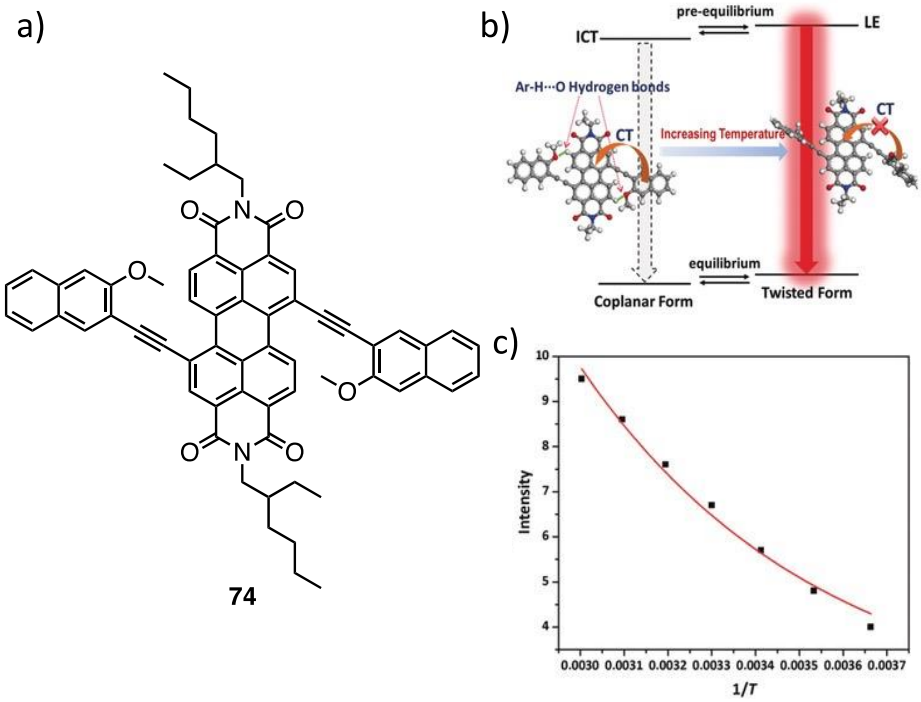

Figure 2.32 a) Structure of PDI **74**. b) The simplified model proposed by reference to explain the fluroescence enhancement upon temperature increase. c) Intensity against the temperature reciprocal. Image from reference.[155]

Similar considerations have been carried out on polymeric systems (**75**, **76**), where low temperatures usually batochromically shift the absorption maxima upon planarization of the π system (Figure 2.33).[156]

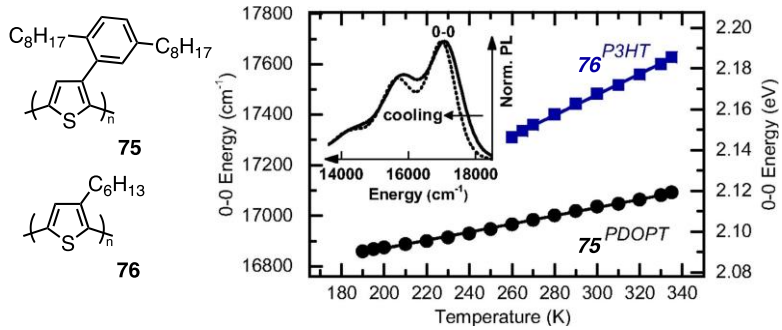

Figure 2.33 The influence of temperature on the planarization of two polimeric systems **75** and **76**. Image from reference.[156]

Several other planarizable chromophores have been proposed, assessing different stimuli. As an example, diketopyrrolopyrrole **77** undergoes planarization induced by applying high bias voltage in a single Au-**77**-Au junction (Figure 2.34).[158]

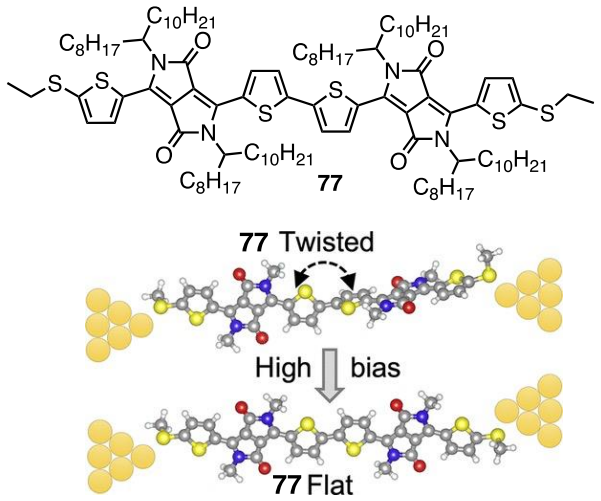

Figure 2.34 Planarization of DPP derivative **77** upon application of high voltage. Image from reference.[158]

2.5.3.2. Using planarizable chromophores to visualize physical forces within biomembranes

While solvatochromic probes report on environmental parameters by changes in emission and PLQY, the planarization occurs at the ground state providing a bathochromic shift in absorption and excitation maxima, along with a color change easily detectable by naked eye.[161–164] These fundamentals have been widely applied in bioimaging for the visualization of physical forces occurring within the phospholipidic membrane. The main idea is that a chromophore, once intercalated into the membrane, can be planarized by lateral (e.g., lateral pressure) or axial forces (e.g., dipole-potential interactions in polarized membranes) while these phenomena are monitored by probes color changes.

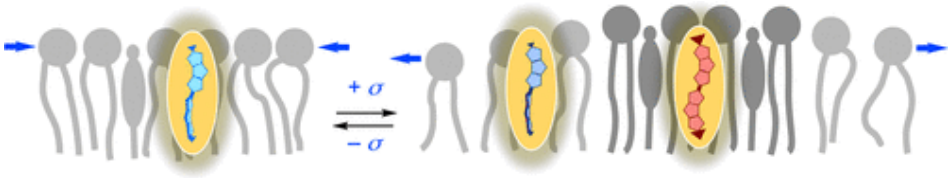

Figure 2.35 The membrane tension increase can planarize the chromophore, increasing the excited state lifetime and red-shfiting the excitation maximum. Image from reference.[165]

The Matile group has worked intensely in the last decade at the development of several push-pull oligothiophene based planarizable systems, universally known as FLIPPERS.[166–168] Starting from pioneering investigations reported by Matile group,[164,167,169] *ter*- and *tetra*-thiophenes (**78-81** and **82-86**) have been prepared bearing a methoxy moiety as donor group, while several accepting groups have been proposed modulating the photophysics and amphiphilicity of the overall probe (Figure 2.36A-B). Although promising results had been obtained in LUVs model systems Figure 2.36C), further structure refining was necessary to still increase the sensitivity in membrane tension detection and lipidic order detection.

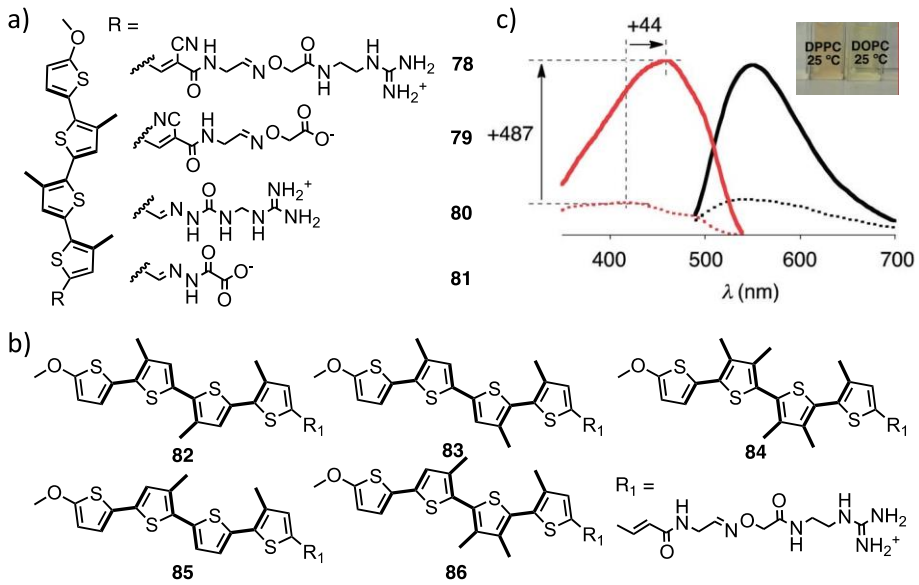

Figure 2.36 *Ter*- (a) and *tetra*- (b) thiophenes used as cell membrane probes. c) Excitation (red) and emission spectra (black) of probe **86** in DPPC (solid) and DOPC (dotted) LUVs at 25°C. Image from reference.[164]

Further investigations better refined the previous oligothiophene base structures with the mechanophore **87** (Figure 2.37), providing in 2015 the first satisfactory responses to planarization occurring in the biomembranes (Figure 2.37B).[170] Since then, many analogues (**88**-**97**) have been proposed and prepared during the last decade, tuning the selection of substituents and the core design (Figure 2.37).[171–173] The strategy has driven to twisted pull stable and highly fluorescent probes, with valuable Stokes Shifts and planarization-regulated mechanosensitive excited-state dynamics, with low solvation interferences. Detailed studies upon the mechanosensitive structure-related activity have been proposed investigating the chalcogen-bond cascade mechanism and the importance of the position and type of substituents for the desired mechanosensitive effect. With deep investigations about the methyl position in the probes scaffolds, concluding with the message that methyl

groups in twist region, are essential while the ones in the switch region aren't affecting the activity.[174] The latest new compound (**98-103**) proposed by Matile *et al.* in the FLIPPER family show an even more tension responsivity and photostability accompanied by red shifted emission in the range between 600 and 700 nm in dependence of the solvent polarity proving once more with studies in GUV the complexity of the supramolecular chemistry of these families of planarizable push-pull probes highlighting the essentiality of the primary structural dipole for their functioning.[175,176]

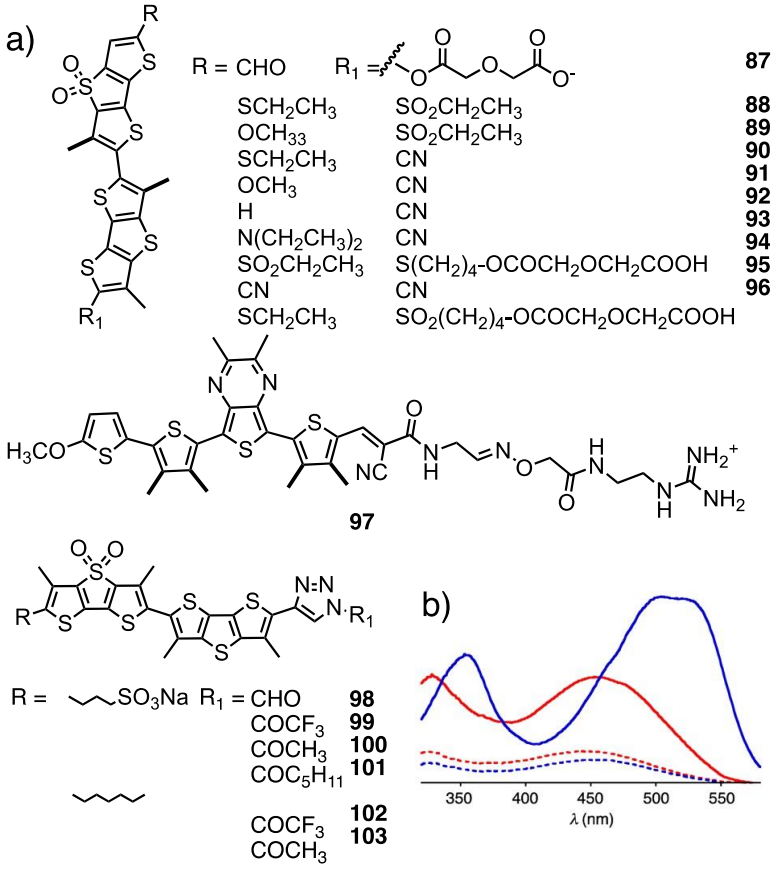

Figure 2.37 a) More recent planarizable FLIPPERS probes. b) Excitation spectra of **87** in DPPC LUVs (solid) and DOPC LUVs (dotted) at 25 °C (blue) and 55 °C (red).[170]

2.5.4. Molecular Rotors

Molecular rotors are a group of fluorescent planarizable molecules highly sensitive to local viscosity and widely applied for probing biomembranes. They undergo an intramolecular twisting motion in the excited state, responsible of their remarkable photophysical features.

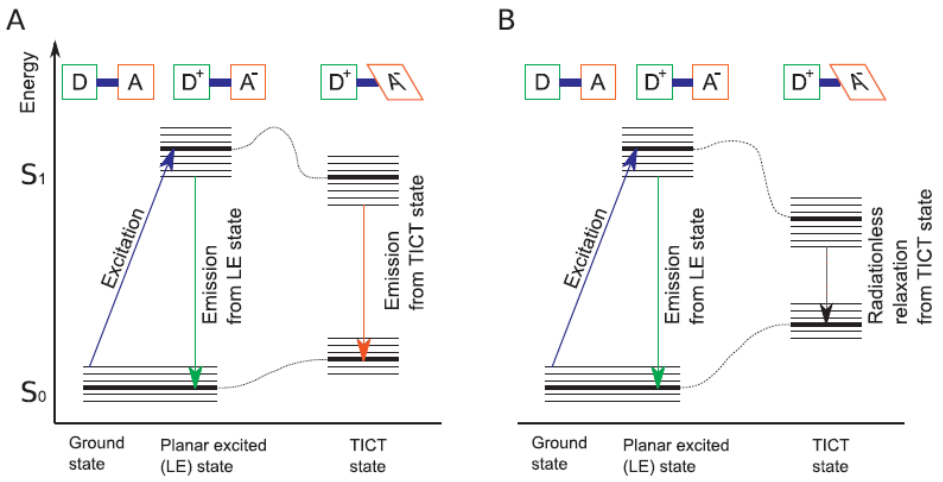

Figure 2.38 Extended Jablonski diagram for two possible molecular rotors. Image from reference.[177]

They generally consist of an electron-donor and an electron-withdrawing moiety linked through an electron-rich spacer unit. As the common fluorophores, they are excited from the ground state to the local excited (LE) state upon photon absorption. Then, an intramolecular twist takes place, originating a second more stable excited state (TICT state) and an analogue S_0 with higher energy. Depending on the specific fluorophore, relaxation from such novel TICT state can *i)* originate a second emission band, batochromically shifted from the LE fluorescence (Figure 2.38**A**) or *ii)* occur through non radiative decays when the energy gap in the twisted state is small compared to the LE energy gap (Figure 2.38**B**).[177]

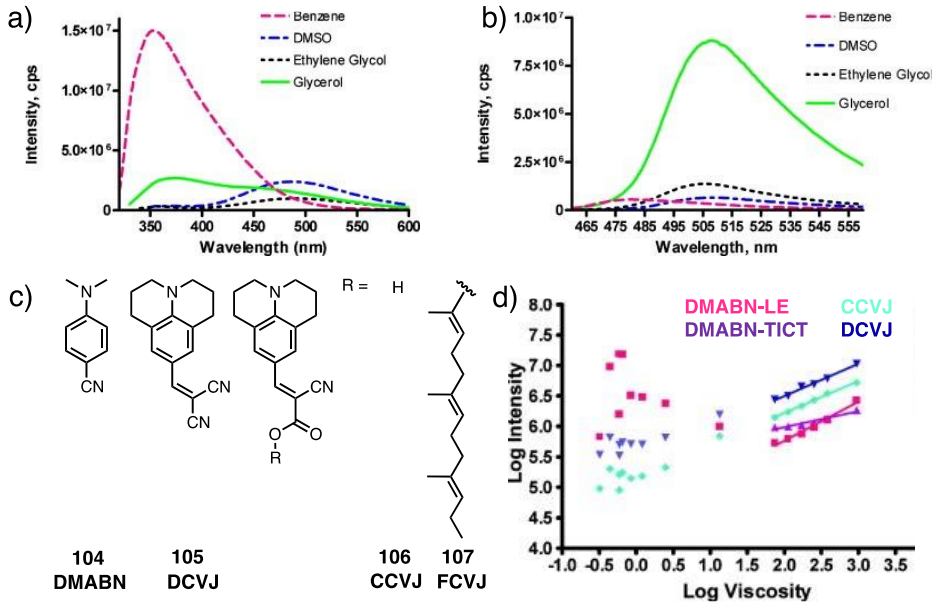

Figure 2.39 a) Emission of **104** in different solvents. A second red-shifted band appears in more polar solvents due to the relaxation from the TICT state, while the highly viscous glycerol suppresses it increasing the LE-TICT barrier. b) Emission of **105** in different solvents. No secondary emission is detected, and the intensity is increased by the glycerol viscosity. c) Chemical structure of the most common julolidine derivative molecular rotors. d) Peak emission intensity and viscosity of the fluorophores displayed in double logarithmic scale. At low viscosities, the intensity is influenced by the solvent polarity. Image from reference.[128]

The TICT state interaction with the local environment is of importance to evaluate the final photophysical traits of the fluorophore. Polar solvent molecules can reorient efficiently along the emitter's dipole, relaxing to the ground state after having consumed part of its excited state energy and bathochromically shifted its emission band (Figure 2.39A). Additionally, highly viscous solvents are known to increase the energetic barrier from the LE to the TICT states (dashed lines in Figure 2.38), influencing the overall PLQY and the relative intensities for dual emissive fluorophores. In this context, the PLQY of single emissive molecular rotors becomes

strongly dependent on the medium viscosity, making such fluorophores suitable as viscosity sensors (Figure 2.39**B**). A power-law relationship (Forster – Hoffmann equation) relates the PLQY with the medium viscosity η, according to the following Equation 3:

$$\log(PLQY) = C + x \log(\eta) \qquad (3)$$

where C and x are dye and solvent-related constants.

This equation proved to be valid for several different molecular rotors (Figure 2.39D).[178,179] They usually show donor and acceptor groups, connected through a π-conjugated bridge, spanning from simple to more complex molecular structures. Some small examples are dimethylaminobenzonitrile or julolidine derivatives (Figure 2.39C), while more articulated rotors show a coumarine (**112**, **113**, **114**, **116**), cyanine (**109**, **110**) or BODIPY (**108**, **115**) core (Figure 2.40).[180–185]

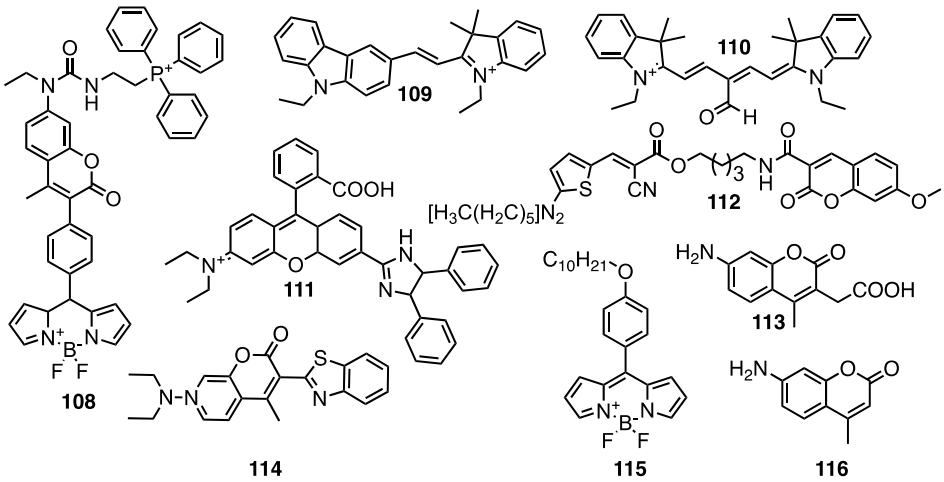

Figure 2.40 Chemical structures of the most common molecular rotors.

CHAPTER THREE

RESULTS AND DISCUSSION

In this work, oligoaromatic emitting compounds have been designed and their interaction with complex biological systems has been evaluated. The fluorophores' properties enhancement or perturbation upon interaction with proteins or lipidic bilayers have been carefully investigated, developing smart responsive materials applied in solid-state lighting and chemical biology. In particular, the approach and the results concerning the development of novel sustainable white HLEDs are presented in the first part of this section (**Section 3.1**), while the design and preparation of fluorophore as cell fluorescent membrane probes is shown at the end (**Section 3.2**).

3.1. Designing artificial fluorescent proteins

As mentioned at the beginning of this thesis, the need for a more efficient electricity consumption has been clearly stated, but traditional white inorganic LEDs cannot represent a sustainable technology in the long-term despite their outstanding performance. WILEDs briefly consist of a blue chip covered by down-converting filters, commonly based on toxic and/or rare-earth materials. The limited availability (< 10/15 years) of the latters, along with their geopolitical control by China and the environmental impact related to their extraction and refining, strongly hamper the sustainability of the current WILED technology. Traditional organic phosphors (OPs) have been adopted since 1995. OPs are essentially based on polymers, carbon nanodots and fluorescent dyes embedded into a matrix, but they have not met the customer requirements

because of limited device efficiencies and stabilities.[92,101] Aggregation-induced quenching, oxidative and photodegradation dramatically affect OPs stability with a dramatic drop of device performances over time. Another approach is represented by natural fluorescent proteins. Although they have been first mentioned by Thomson and Forrest groups in 2000,[2] they have been first implemented in LED by Costa's group in 2015. FPs combine high PLQY, good photostabilities and a highly optimized in-place production, without the necessity of high level of purification. FPs stability out of the cellular environment has been improved by using an innovative stabilization method with a polymer matrix. Unfortunately, natural chromophores of FPs still undergo to prominent photodeactivation processes.[108] It is mandatory to enforce evolution of FPs toward meeting the lighting requirements. The EU project ARTIBLED fits in this context aiming to develop a new generation of white LEDs able to meet health, costs and performances customer requirements. ARTIBLED proposes a radically new approach to enhance Bio-WLEDs, designing new artificial fluorescent proteins (AFPs) in which the natural chromophore is replaced by well-suited small synthetic fluorescent dyes inside the protein cavity. Photodeactivation processes should be overcome without losing the benefits of protein scaffold. The main idea is to combine the advantages of organic emitters (*i.e.*, narrow bandwidth, easy synthetic tunability) with the benefits of proteins scaffold (*i.e.*, prevention of the dye aggregation induced quenching, intrinsic stability of the scaffold). The results concerning this part emerged from a multidisciplinary and heterogeneous consortium, where organic chemistry, biotechnology, computational studies and hybrid optoelectronics co-worked toward one unique goal.

As a proof of concept, a new red-emitting AFP has been obtained combining a Lactococcal multidrug resistance Regulator (LmrR) as protein host with a symmetric squaraine dye (**S**) as guest emitter. The performances of the device bearing the dye embedded into the polymeric matrix have been improved by shielding the dye within the protein scaffold.

Then, a white LED has been targeted looking for several AFPs able to span the visible spectrum from green to red. High PLQY and photostability have been targeted by choosing the most suitable organic dye and designing the most proper protein scaffold.

3.1.1. Squaraine – based AFP: a proof of concept

These results have been published in *Adv. Funct. Mater.* **2022**, 32, 2111381.

As a proof of concept, a new red-emitting AFP has been obtained combining a Lactococcal multidrug resistance Regulator (LmrR) as protein host with a symmetric squaraine dye (**S**) as guest emitter. The device performances dramatically increased when the protein scaffold has been implemented as a dye shield.

More in detail, a red-emitting AFP has been targeted as a starting point since highly efficient and stable red-emitting FPs are restricted to a few options, representing a bottleneck in the development of white bio-hybrid LED.[186] Among them, mCherry has been widely used as a representative candidate, as it combines good photophysical properties (PLQY of 22%), high expression yields, and excellent pH tolerance;[107,187–189] though this still does not comply with standard lighting applications. Thus, new strategies to design highly emissive and stable deep-red AFPs are

needed. It is here where the major thrust of this work sets in with the straightforward realization of a new red-emitting AFP combining a Lactococcal multidrug resistance Regulator as a protein host with a symmetric and not water-soluble archetypal **S** as a guest emitter.

The LmrR is a homodimeric protein with a β-winged helix-turn-helix structure. The two LmrR dimers form a large hydrophobic pocket at the interaction interface, where planar molecules can be bound to form supramolecular assemblies. The interaction between LmrR and the guest molecule is promoted mainly by hydrophobic interactions with the pocket and/or π-π* interactions with the indole rings of the two tryptophan residues in position 96, contributed by each monomer (W96 and W96´). Indeed, LmrR has shown a high versatility to accommodate organic dyes with different structures.[190] The lack of needing a covalent co-factor attachment and the non-specific nature of complexation allow an easy dye screening, being a potential scaffold to generate highly stable AFPs.

Synthesis and S-LmrR complex characterization

S was synthesized under microwave irradiation through the condensation reaction between the squaric acid and an indolenine quaternary compound as reported in **Scheme 3.1** (yield after two steps 43%).[191]

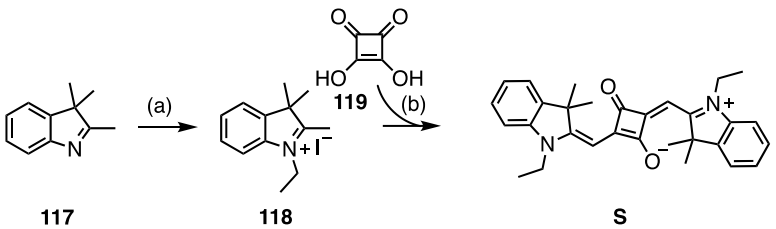

Scheme 3.1 Synthetic procedure toward **S**. a) iodoethane, MW irradiation,130°C, 9 min, (91%). b) Tol/*n*-BuOH, MW irradiation, 160°C,15 min, 55%.

A simple host-guest approach was explored and, through complex formation, the protein scaffold resulted to solubilise lipophilic organic dyes in aqueous solutions, along with protecting them from oxidation. The

optimization of the LmrR-S affinity was investigated by substituting the tryptophan in position 96 (W96) of the protein cavity with histidine (W96H), phenylalanine (W96F), and alanine (W96A), leading to AFPs W96-S, W96H-S, W96F-S, and W96A-S, as shown in Figure 3.1. W96A was used to assess a purely hydrophobic pocket, W96H mutant probed the effects of a hydrogen donor, while W96 and W96F variants allowed us to study the effects of proton donor or non-donor aromatic groups, respectively.

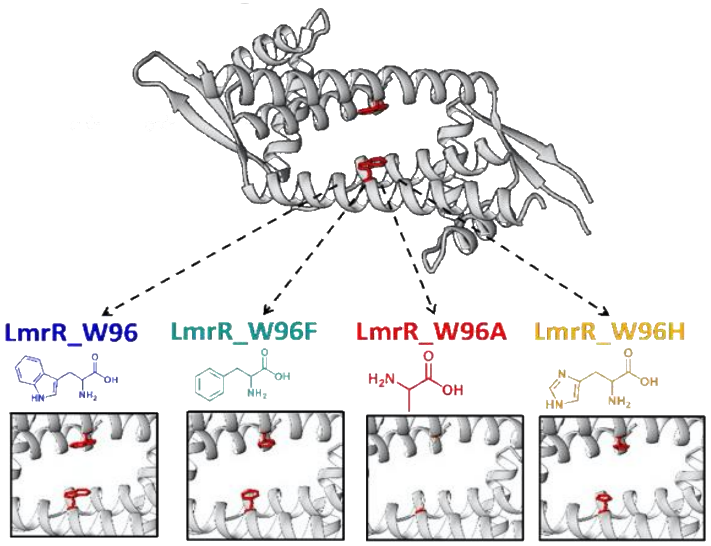

Figure 3.1 Structure of dimeric LmrR, in which the positions 96 and 96´ are highlighted in red for the tryptophan (blue), phenylalanine (green), alanine (red) and histidine (yellow) variants.

The formation of the LmrR-S was monitored *via* steady-state absorption spectroscopy. In water (phosphate buffer pH 8), **S** forms H-type aggregates with the typical broad absorption peak centered at λ_{abs} = 625 nm.[192,193] The interaction of the squaraine with LmrR manifests in two different spectral changes when comparing the absorbance spectrum of the dye in solution and in the presence of LmrR mutants: *i*) a decreased absorption intensity, which is attributed to electrostatic interactions of the negatively charged squaraine ring with positively charged LmrR protein

surface; electrostatic interactions are expected to destabilize the π-conjugation of the squaraine dye causing color bleaching; and *ii*) a red shift in the absorption features, which is consistent with dye being in an hydrophobic environment inside the LmrR pocket. Both spectral changes happen simultaneously and, even though the effects could not be separated, they were used to estimate the affinity of the dyes to the LmrR mutants - Figure 3.2. The apparent dissociation constant of the electrostatic interaction (K_{de}) was obtained by monitoring the absorption bleaching ($\Delta\lambda_{bleach}$) during the titration, whereas the apparent dissociation constant of the hydrophobic interaction (K_{dh}) was obtained by monitoring the spectral shift ($\Delta\lambda_{shift}$), which allowed estimating K_{de} and K_{dh} (Table 3.1).

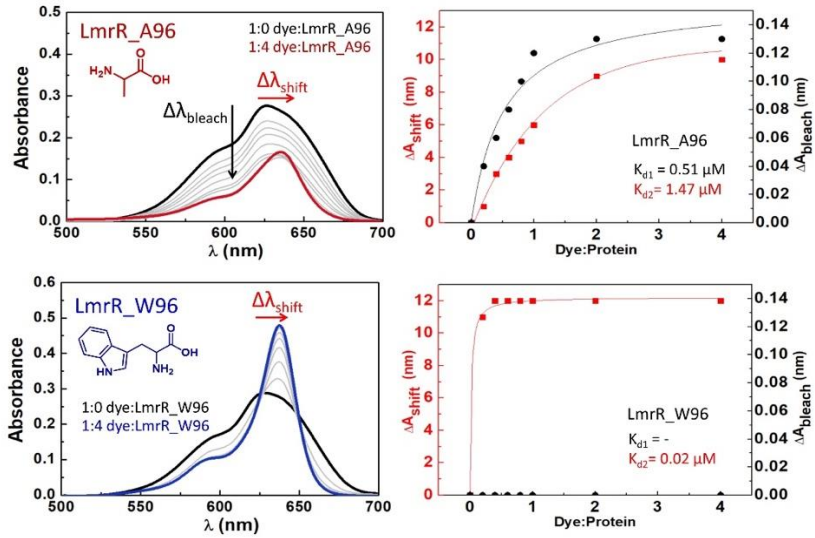

Figure 3.2 Left: absorbance spectra of squaraine in buffer (black solid line) and upon addition of different concentration of LmrR_W96A or LmrR_W96 (indicated in the figure). Right: the red shift (Δλshift) and the absorption bleach (Δλbleach) in absorbance maxima of the squaraine upon serial addition of LmrR_W96A or LmrR_W96 (indicated in the figure). Fitting curves are shown in red and black for electrostatic and hydrophobic interactions, respectively. The dissociation constants k_{de} (for $\Delta\lambda_{bleach}$) and k_{dh} (for $\Delta\lambda_{shift}$) were obtained from the fitting of the curves.

Table 3.1 K_{de}, K_{dh}, $\Delta\lambda_{bleach}$, and $\Delta\lambda_{shift}$ for LmrR/S interaction in solution

Compound	K_{de} (μM)	$\Delta\lambda_{bleach}$ (nm)	K_{dh} (μM)	$\Delta\lambda_{shift}$ (nm)
W96A-**S**	0.52	0.16	1.47	14.8
W96H-**S**	0.41	0.16	1.01	14.5
W96F-**S**	0.1	0.06	0.19	11.4
W96-**S**	-	-	0.02	12.2

The wild-type LmrR_W96 showed the highest affinity towards the **S**, with a K_{dh} of 0.02 μM. No spectral bleaching was observed with this mutant, suggesting very low or non-existent electrostatic interactions. In the case of LmrR_W96F, both spectral shift and bleaching were observed; with K_{de} of 0.10 μM for electrostatic interaction and K_{dh} of 0.19 μM for hydrophobic interaction measured. For LmrR_A96 and LmrR_W96H mutants, hydrophobic interactions with the LmrR pocket were weaker than for the aromatic mutants, with K_{dh} of 1.47 and 1.01 μM, respectively. Thus, at low protein concentrations electrostatic interaction were predominantly observed, with K_{de} of 0.52 and 0.41 M for LmrR_W96A and LmrR_W96H, respectively. Overall, aromatic amino acids increase the affinity of the protein pocket towards the dye - Table 3.1**.**

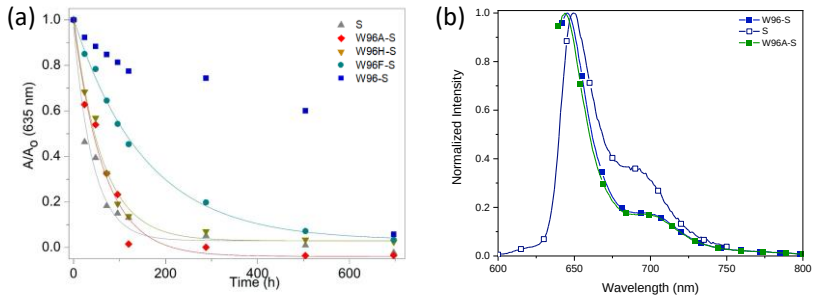

Figure 3.3 (a) Stability of LmrR-**S** in aqueous solution over time. The decrease in absorbance at 635 nm was fit with an exponential decay function. (b) Photoluminescence spectra of W96-S (blue) and W96A-S (green) in aqueous

solution (λ_{exc}= 638 nm; 10^{-5} M) and S (white squares) in acetonitrile solution (λ_{exc}= 590 nm; 10^{-5} M).

The LmrR-**S** stability was studied monitoring the absorption spectrum over time and fitting the absorbance difference using an exponential decay function to obtain the bleaching rate constant (k_b; Figure 3.3**A**). The k_b value of 0.015 h^{-1} for W96A-S was comparable to that of free S (0.024 h^{-1}), while W96-S exhibited a small reduction in the intensity that could not be fit by any exponential decay. Thus, the S could be considered efficiently stabilized into the protein cavity in aqueous solution. Further corroboration came studying the photoluminescence features of W96-S compared to **S** in acetonitrile. While **S** featured only a weak (*i.e.,* PLQY < 5%) emission due to a prominent vibrational non-radiative deactivation rate (Figure 3.3B), the W96-S showed emission bands centered at 645 and 705 nm associated to PLQY ~ 50% and an excited state lifetime (of ~ 3.8 ns (Figure 2; Table 1). Remarkably, W96-S was found to be stable under ambient conditions for a week, suggesting that **S** is efficiently locked and shielded into the protein cavity. In addition, W96A-**S** also exhibited a similar emission spectrum with PLQY <1% and low stability in aqueous solution, confirming that the stabilization of **S** *via* electrostatic interactions at the protein surface is not effective to maintain its emission features.

The X-ray crystallographic analysis of the protein-dye complex showed that the dye was not rigidly held in the binding pocket, but instead had significant mobility within the protein cavity, and the binding pocket was not sufficiently deep to fully shield the dye from oxygen (Figure 3.4).

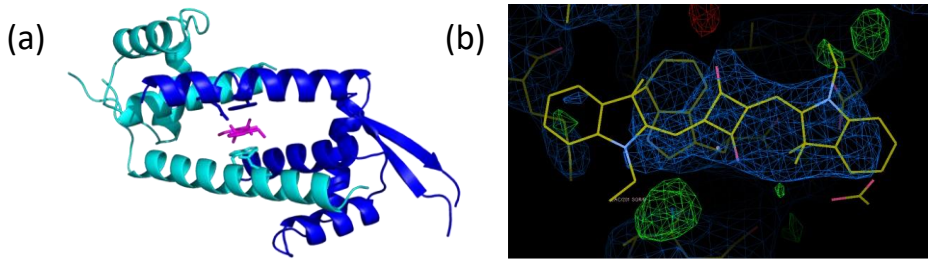

Figure 3.4 The crystal structure of LmrR-**S**, diffracting to 2.6 Å. (a) molecular structure of the complex in cartoon depiction; the constituent LmrR monomers are coloured blue and cyan, the squaraine dye is in magenta; the tryptophan residues involved in π–π stacking interactions with the dye are depicted as sticks. (b) Electron density map of the squaraine dye in the LmrR binding pocket, with the dye modelled; the lack of clear features in the electron density suggests dye flexibility.

The two tryptophan sidechains are likely sufficient to maintain tight contacts with a guest molecule (LmrR-**S**), even if lack of clear features in the electron density still suggests dye flexibility. These findings have been further supported by computational studies, that showed that **S** exhibits large conformational flexibility within the W96 binding pocket. Additionally, a larger freedom of movement has been noticed in the case of W96A-**S**, where **S** displaces to the edges of the protein cavity and towards the protein surface. This type of arrangement makes **S** in W96A-S more exposed to the external aqueous environment than in W96-S. This is in line with the photophysical findings. namely *i*) the absorption spectral changes between variants (Figure 3.2) and *ii*) the low PLQY in W96A-S, as both electrostatic interactions and conformational distortions of **S** may affect the emission efficiency and promote non-radiative deactivation processes.

Characterization of S-LmrR AFP

Lastly, both the only **S** and the W96-S have been implemented in two deep-red Bio-hybrid LEDs. The former has been prepared as a reference

to evaluate the effect of the protein shielding on the photophysical properties and performances under operating conditions. The improved solubilization and the hydrophobic local environment of the protein pocket enhanced the PLQY of the squaraine **S** from an almost quenched form to 50% in solution. Similarly, within the rubber coating, the emission of the W96-S phosphor corresponds to a well-defined emission shape centered at 665 and 705 nm with PLQY ~ 65% and τ ~ 5 ns (Table 3.2), remaining constant over months under ambient conditions (Figure 3.5). Likewise, the **S**-based phosphor featured a similar emission band centered at 650 and 705 nm with PLQY ~ 50% and τ ~ 3.9 ns (Table 3.2).

Table 3.2 Photophysical features of **S** and W96-**S** in aqueous solution and polymer coatings (bio-phosphor).

Cpd	Solution					Bio-phosphor				
	λ_{em} (nm)	PLQY (%)	τ (ns)	k_r [a] (s^{-1})	k_{nr} [a] (s^{-1})	λ_{em} (nm)	PLQY (%)	τ (ns)	k_r [a] (s^{-1})	k_{nr} [a] (s^{-1})
S	650 -705	<5 %	-	-	-	650 - 705	50	3.9	1.28	1.28
W96-S	645 - 705	50	3.8	1.32	1.32	665 - 705	65	5	1.30	0.7

[a] $\times 10^8$

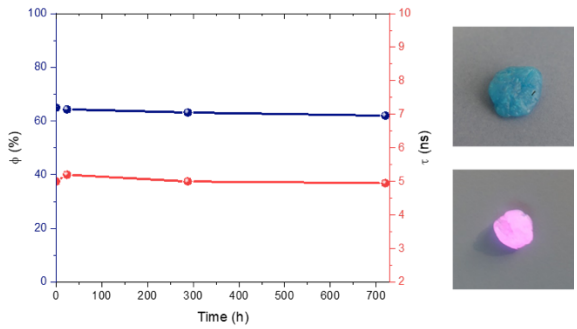

Figure 3.5 Left: Changes in PLQY (blue) and τ (red) of W96-S based phoshor over time under ambient storage conditions. Right: Picture of 1 under room light (top) and UV-irradiation (bottom).

Characterization of deep-red Bio-hybrid-LEDs

The on-chip device stability was investigated using an applied current of 50 mA, corresponding to the maximum EQE (7%) for both, LmrR-**S** and **S** devices. L_{50} values of around 35 h and 20 h were noted for each device, respectively. To further enhance the device stability, LmrR-**S** Bio-HLEDs were fabricated using a remote configuration. Figure 3.6 depicts an increase of the L_{50} value up to 780 and 320 h for LmrR-**S** and **S** devices, respectively.

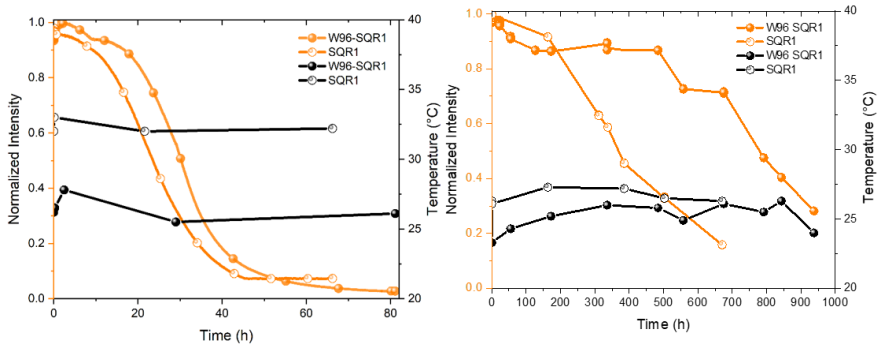

Figure 3.6 Emission intensity decay/phosphor temperature over time of on chip (left) and remote (right) configurations of W96-S and S-devices at 50 mA at ambient operating conditions.

Additionally, the emission spectra of W96-S and S have been monitored over time, showing strong vibrational changes under operating conditions (Figure 3.7). In detail, the emission band centered at 705 nm holds constant over the first 5 and 15 h for **S** and LmrR-**S** based Bio-HLEDs, respectively. Afterwards, the vibrational progression of the emission changed toward a dominant vibrational peak centered at 675 nm. At this point, **S** exhibited the same quick photobleaching with a slight blue shift in the emission band shape. The first process is much faster for reference **S**-devices, highlighting the effective shielding effect of the protein cavity. In line with the previously mentioned theoretical simulations, the changes

in the vibronic progression might be caused by the rearrangement of **S**, which is stabilized inside the protein binding pocket mainly by weak (non-covalent) interactions. Under operating conditions, the LmrR-**S** system can acquire a sufficient excess of energy to induce the conformational transition of **S** from a more locked conformation inside the protein binding pocket to a more labile structure exposed to the external and more polar matrix environment, ultimately leading to a blue-shifted emission and its final photobleaching (Figure 3.7).

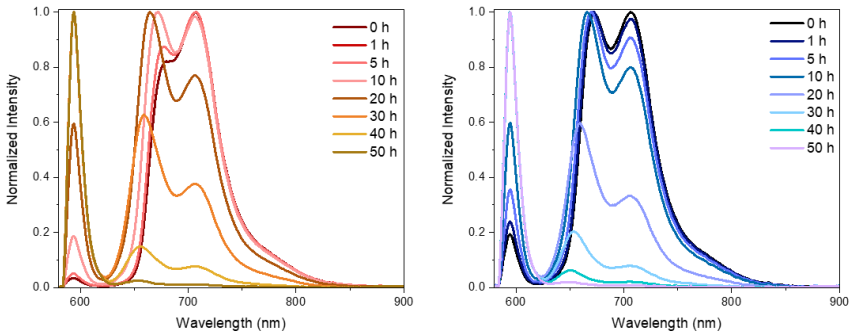

Figure 3.7 Emission intensity decay profile over time of W96-S (left) and S- (right) on chip devices at 50 mA and operating under ambient conditions.

3.1.2. The need of a covalent bioconjugation

The results provided by the Squaraine-LmrR AFPs in device clearly confirmed our hypothesis: the protein scaffold can effectively shield the dye, enhancing the stability and improving the device performances up to the 140%. However, the squaraine high conformational flexibility along with the high energy acquired by the W96 system under operating conditions induced the transition from a more locked conformation inside the binding pocket to more labile structures, where the **S** is more exposed to the external environment and resulting in an ultimate photobleaching (Figure 3.7). Thus, the large degree of freedom of the dye may result in

issues concerning its stabilization on a mid and long-term. These considerations convinced us to better refine the previous approach either by designing a suitable peptidic scaffold aiming at maximizing the dye stabiliziation into the pocket or by covalently bind the fluorophore to the protein scaffold. The emitter flexibility should still be reduced with a beneficial effect on the complex stability. The next structures investigated within this work bear a suitable functional group (*e.g.*, terminal triple bond, maleimide rings) to prepare emitters already suitable for the bioconjugation whereas the flexibility and the freedom within the binding pocket will make it necessary.

In detail, terminal triple bonds and maleimide rings have been introduced to use well-known reactions in chemical biology. The formers can undergo the copper-catalyzed Huisgen cycloaddition with azide moieties properly introduced during the protein production. The absence of natural occurring azide moieties makes this reaction extremely biorthogonal. Similarly to many other famous organic reactions (e.g. Diels Alder, thiol-Michael addition, Staudinger ligation), azide-alkyne addition represents, indeed, one of the widest applied examples of click reactions due to its high yields and remarkable feasibility.[194],[195] It should be pointed out that the triple bond can react with natural occurring cysteines according to the UV light-mediated thiol-yne chemistry, yet in a not-selective manner. As an alternative bioconjugation strategy, maleimide groups have been introduced to undergo the Michael addition with natural cysteines. Maleimide represents a powerful tool for bioconjugation due to its versatility and high yields.[196]

3.1.3. Naphthalene diimides as rainbow-coloured emitters

Naphthalene diimides (NDI) are made up of an aromatic central core fused with two electron-withdrawing imide moieties. The resulting strong electron deficiency makes naphthalene rings extremely reactive toward the nucleophilic substitution. Thus, electron donating groups can be easily inserted to increase the push-pull character, creating a wide library of fluorescent dyes along the whole visible spectrum. These peculiar features made NDIs appealing for our purposes, since one single class may provide in few synthetic steps all the required emitters to realize a white HLED. Additionally, computational studies and genetic engineering supported us in the production of a suitable peptidic scaffold, able to accommodate the prepared NDIs fluorophores.

3.1.3.1. General

Although a pioneering work by Vollmann *et al.*[197] had proposed the first synthetic approach in 1937, only in 2000s NDIs became protagonists, thanks to more accessible synthetic routes and to the discovery of their modulable fluorescence. The possibility of dramatically influence their optical properties upon small structural variations (Figure 3.8)[198] induced scientists to test several synthetic modifications, producing huge libraries of NDIs. The broad interdisciplinarity of applicative fields reflects such surprising versatility: supramolecular analysis, organic synthesis, medicinal and biological chemistry are just few examples of the numerous scientific fields involved into NDIs research. Core-substitution is able to remarkably modulate optical and electrochemical properties, while imide substituents have just negligible effects on them.[199] The creation of a push-pull system makes NDIs extremely colorful[200] candidates for biomimics, photoinduced electron transport[201] or molecular recognition.[202],[203] On the contrary, electron-withdrawing groups contribute to a higher π acidity of the aromatic core: these aspects are

appealing for their application in organic electronics,[204] catalysis[205] and anion transport.[206]

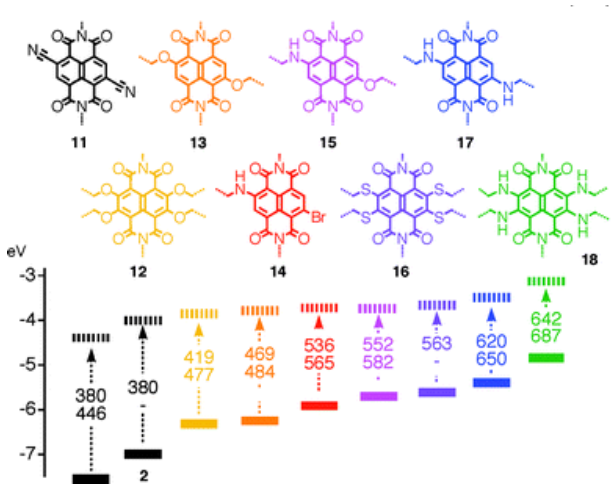

Figure 3.8 A rainbow collection of NDIs with indication of HOMO (bold) and LUMO (dashed) energies in eV against vacuum and maximal absorption (top) and emission wavelength (bottom) in nm. Picture from reference.[207]

3.1.3.2. Molecular design and synthetic considerations

As mentioned above, NDIs can be modified by inserting various functional groups on the aromatic rings or at the two imide sites (Figure 1A). Decorations on the aromatic core allow a tuning of the optical properties (λ_{abs}, λ_{em}, PLQY), while modification on the imides addresses supramolecular assembly, bioconjugation properties and solubility. These orthogonal positions allow to improve NDI photophysical properties (e.g. wavelengths, Stokes shift, PLQY) without affecting their solubility, and *vice versa*. In particular, electron-donating groups on the naphthalene core raise HOMO energy, providing a rainbow-colored range of compounds whose emission covers the whole visible spectrum.[199,208] On the other side, many different moieties (e.g. amino acids, alkynes, thiols, maleimide derivatives) can be introduced on the imides for the bioconjugation.

A synthetic scheme has been designed based on the above considerations to achieve the desired targets in a straightforward manner. A key intermediate for the exploration of a wide library of NDIs can be obtained in three steps from commercially available materials. A first approach relies on the preparation of symmetrical NDIs bearing the same functional groups at the imide sites, while having different functionalities on the core to tune their optical properties. This first approach is of importance to easily screen for the photophysical and photostability requirements for the dyes. Upon a first screening, the NDI structures have been better refined by asymmetrization to differentiate the substituents on the imide sites, finely tuning bioconjugation as well as solubility.

At first, three combinations have been prepared, showing on the core ethoxy-ethoxy, ethoxy-isopropyl amino and isopropyl amino-isopropyl amino substitutions respectively with green, orange and red fluorescence. On the imide sites, a propargyl linker has been inserted to enable the alkyne reactivity (e.g., thiol-yne chemistry, Huisgen cycloaddition), providing a first generation of highly hydrophobic NDIs - namely **NDI-01**, **NDI-02** and **NDI-03** (Figure 3.9). Additionally, modifications of bioconjugation strategies have been investigated and a green-emitting NDI bearing a maleimide functionality (**NDI-05**) has been obtained. One further core-substitution has been prepared, introducing two hydroxylic groups on the core, since literature data report a strong emission shift upon deprotonation. The possibility of interaction with basic and acidic groups into the protein may produce a material with different emission bands. In this context, **NDI-07** was prepared introducing two octyl chains on the imide sites, aiming at first to evaluate the photophysics in polymeric coatings and the LED conversion ability.

Although a first preliminary screening carried out at Costa's Lab at TUM on the three core-combinations (**NDI-01**, **NDI-02** and **NDI-03**) evidenced a more significant stability of the red-emitting **NDI-03**, the highly hydrophobic character conferred to the whole system by the two short propargyl groups has strongly affected the **NDI-03** solubility in aqueous and DMSO solutions, hampering the bioconjugation step. Furthermore, the promising results concerning the **NDI-05** achieved by Cortajarena's Lab in San Sebastian showed a successful covalent binding between the fluorophore and the protein scaffold upon the thiol-maleimide Michael addition, suggesting the potentiality of this kind of functionality on the dye. Lastly, **NDI-07** showed poor conversion and, thus, discarded.

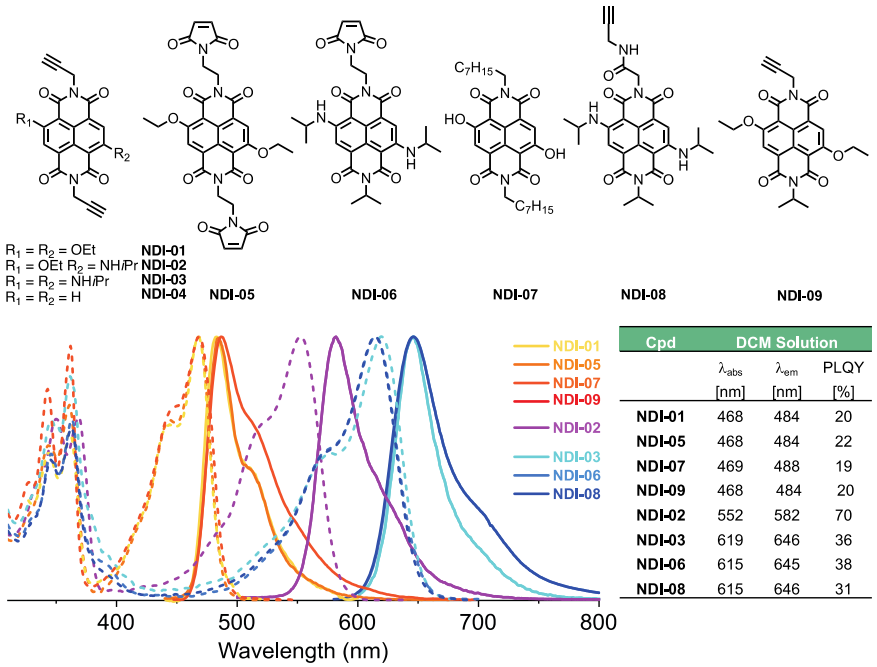

Cpd	DCM Solution		
	λ_{abs} [nm]	λ_{em} [nm]	PLQY [%]
NDI-01	468	484	20
NDI-05	468	484	22
NDI-07	469	488	19
NDI-09	468	484	20
NDI-02	552	582	70
NDI-03	619	646	36
NDI-06	615	645	38
NDI-08	615	646	31

Figure 3.9 The prepared NDIs within this work. Their absorption (dashed) and emission (solid) spectra in DCM solution, along with their photophysical parameters.

Then, a second generation of NDIs has been prepared. The **NDI-03** (*i.e.*, the most stable according to preliminary photostability data in HLEDs) has been better refined and two analogs have been designed aiming to

increase the solubility by either keeping the alkyne functionality (**NDI-08**) or exploring an alternative bio-conjugation strategy through a pending maleimide group (**NDI-06**). In both cases, two isopropyl amino groups were used as core-substituents to preserve the **NDI-03** promising optical features.

During the device characterization, as already described for the LmrR/S biophosphor, a reference device based on the simple dye embedded into the polymeric matrix has been prepared. In this case, an additional reference has been prepared post-functionalizing an azide-derivative low-molecular weight TMPE with **NDI-01** and **NDI-09**. The covalently bounded fluorescent polymer might be used as an additional reference to better evaluate the protein shielding effect once the dye will be covalently bounded into the AFP.

3.1.3.3. Synthesis

Two alternative procedures were followed whether symmetrical or unsymmetrical structures were targeted. The diethoxytetraester **123** (Scheme 3.1) has been easily prepared in a gram-scale according to reported procedures[209] and used as a key intermediate.

First NDIs generation

As shown in Scheme 3.2, a one-pot approach allowed to prepare **NDI-01** from **123** upon basic hydrolysis of the four esters and the subsequent imidization reaction with propargyl amine in acidic conditions to prevent the core substitution. Then, treatment of **NDI-01** with isopropyl amine afforded both **NDI-02** and **NDI-03** in one single reaction. Furthermore, the use of microwave-assisted heating allowed to lower the time from 24 h to 2 h, with good reaction yields for both the products (52% for **NDI-02** and 35% for **NDI-03)**.

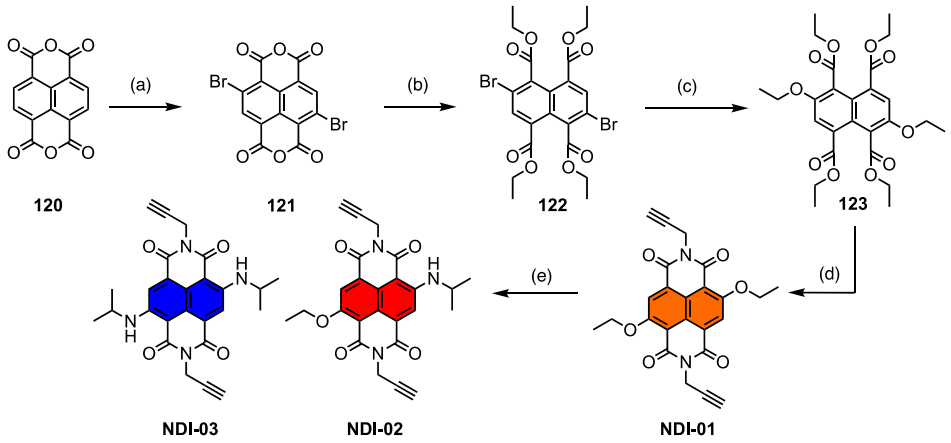

Scheme 3.2 Synthetic strategy toward the first alkyne derivatives **NDI-01, NDI-02** and **NDI-03**. (a) DBI, H_2SO_4, 130°C, 12 h; b) ethyl iodide, K_2CO_3, ethanol, reflux, 12 h (24%); c) EtONa, DMF, 50°C, 12 h (51%); d) 1. KOH, iPrOH, 80°C, 12 h; 2. propargyl amine, AcOH, 80°C, 12h (56%) e) isopropyl amine, 120 °C, 1 h, MW (65% for **NDI-02**, 35% for **NDI-03**).

The preparation of the maleimide derivative **NDI-05** has been trickier than expected, as reported in Scheme 3.3. In a first attempt, Mitsunobu reaction was carried out between the intermediate **125** and maleimide affording unreacted starting material probably due to the low solubility of **125** in the conventional organic solvents. The same solubility limitation along with undesired intramolecular nucleophilic substitution hampered the final product synthesis starting from amine functionalized scaffold **128**. Lastly, a further alternative pathway has been explored. A furan-protected maleimide bearing reactive exocyclic amine **131** has been prepared and reacted with the tetra-ester scaffold **123** to afford the desired NDI bearing protected maleimide groups **132**. Final **NDI-05** was obtained by a retro-Diels Alder reaction in good yields.

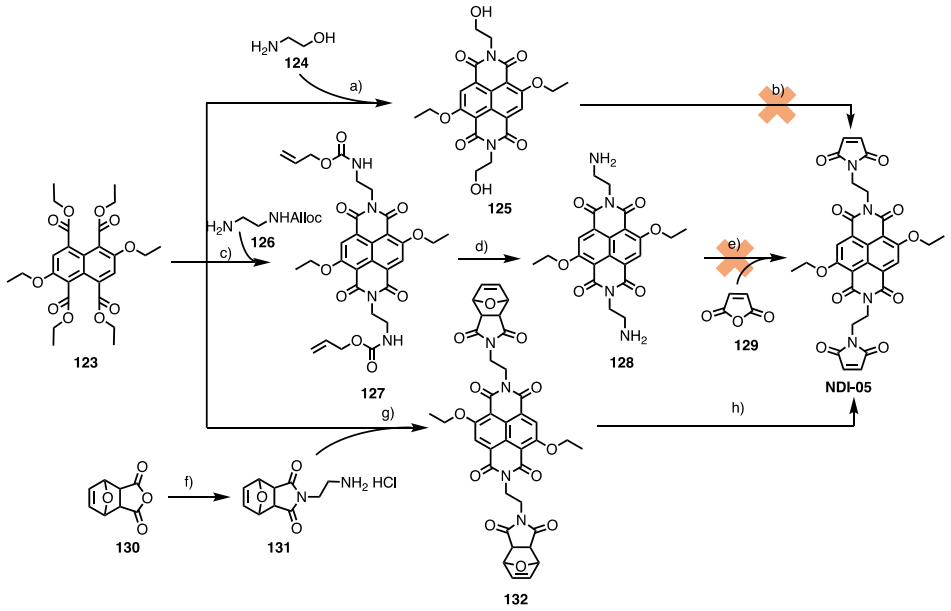

Scheme 3.3 Explored synthetic strategies for maleimide-derivative **NDI-05**. a) **124**, AcOH, 80°C, 12 h (yield) b) PPh_3, DIAD, dry THF, reflux, 8 h (failed) c) **126**, AcOH, 80°C, 12 h (72%) d) phenylsilane, $Pd(PPh_3)_4$, DCM, rt, 3 h (-%) e) 1. **128**, acetone, rt, 6 h 2. Ac_2O, reflux, 10 h (failed) f) 1. Mono-Boc-ethylendiamine, MeOH, reflux, 10 h (54%) 2. HCl (4 M), EtOAc (98%) g) **131**, AcOH, 70°C, 7 h (16%) h) toluene, 120°C, 10 h (33%).

Lastly, the synthetic preparation of the **NDI-07** is very straightforward and adapted from a reported procedure (Scheme 3.4).[210] The symmetrical NDI has been prepared by reaction with octyl amine in refluxing acetic acid to suppress the core-substitution. Then, an allyloxy group has been introduced in the core and, lastly, cleaved in a Pd-mediated reaction providing the **NDI-07** in moderate yield.

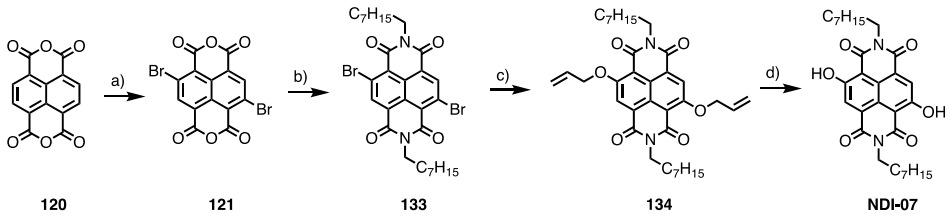

Scheme 3.4 Synthetic procedure toward **NDI-07**. (a) DBI, H_2SO_4, 130°C, 13 h (quantitative). b) 1-octylamine, AcOH, 100°C, 12 h (55%). c) AllylONa, DCM, rt, 12 h (28%). d) Ph_3SiH, $Pd(PPh_3)_4$, DCM, rt, 10 h (56%).

Second NDIs generation

After the first symmetrical generation of NDIs was completed, the **NDI-03** emerged as the most stable candidate according to preliminary photostability data in HLEDs and, thus, better refined. Two analogs have been designed aiming to increase the solubility by either keeping the alkyne functionality (**NDI-08**) or exploring an alternative bio-conjugation strategy through a pending maleimide group (**NDI-06**). In both cases, two isopropyl amino groups were used as core-substituents to preserve the **NDI-03** promising optical features. A divergent synthetic plan has been designed, adapting from a protocol recently reported by Bonifazi's group.[211] Starting from **123** - already key-player within the first NDIs generation - a common intermediate (compound **137**) toward both **NDI-06** and **NDI-08** has been identified - Scheme 3.5.

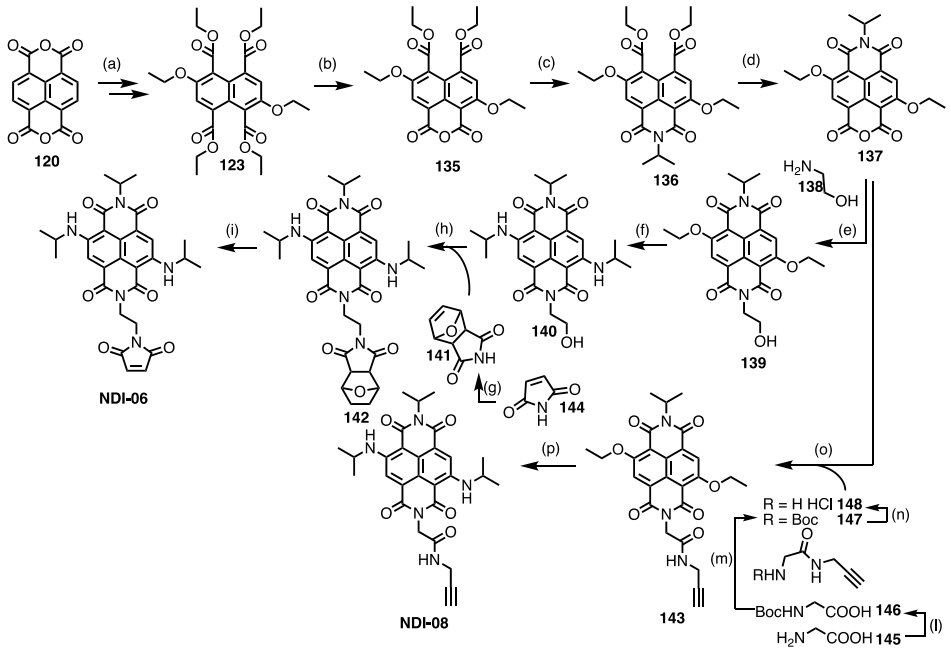

Scheme 3.5 Synthetic strategy for the second NDIs generation **NDI-06** and **NDI-08**. a) several reported steps; b) AcOH/HCl, 101°C, 24 h (quantitative); c) *i*PrNH$_2$,

DIPEA, 1,4-dioxane, 101°C, 24 h (18%); d) TFA, 73°C, 24 h (63%); e) ethanolamine, DIPEA, 1,4-dioxane, 101°C, 6 h (81%). f) *i*PrNH$_2$, 50°C, 2d (27%); g) furan, Et$_2$O, 2d, rt (67%); h) 141, DIAD, PPh$_3$, THF, rt, 12 h (-%). i) toluene, 110°C, 12 h (41% over the last two steps); l) Boc$_2$O, 1,4-dioxane/H$_2$O, rt, 10 h (98%); m) EDC HCl, HOBt, methylmorpholine, DCM, rt, 12 h (quant.): n) HCl (4.0 M in Dioxane), rt, 4 h (40%); o) 148, DIPEA, 1,4-dioxane, 101°C, 6 h (73%); p) *i*PrNH$_2$, 50°C, 2d (24%).

In detail, boiling **123** in a mixture 5:1 of acetic and hydrochloric acids afforded **135** in quantitative yield without any purification after the removal of the volatiles from the reaction mixture. Then, one equivalent of isopropyl amine was used to prepare **136** in basic conditions, while heating at reflux in trifluoroacetic acid provided the napthalenemonoimide **137** in moderate yield (63%) without any degradation. From the intermediate **137**, **NDI-06** and **NDI-08** have been obtained in still four and two steps, respectively. Toward **NDI-06**, the intermediate **137** has been treated with the ethanolamine, providing the unsymmetric **139**, then converted into the red-emitting **140** by heating with an excess of isopropyl amine. The hydroxylic group then underwent a standard Mitsunobu reaction with the furan-protected maleimide (**142**), affording **NDI-06** as a blue powder after the last thermal cleavage step. *En route* to **NDI-08,** the green-emitting **143** was prepared by reacting **137** and **148** with two-fold molar amount of DIPEA and finally converted into the desired **NDI-08** by microwave-mediated heating in neat isopropyl amine.

TMPE post-functionalization

As an additional reference, **NDI-01** has been conjugated to an azide derivative low molecular weight TMPE prepared at Costa's Lab at TUM. TMPE tosylation followed by a further treatment with sodium azide provided the azide-derivative **151** affording the fluorescent **NDI-01@TMPE** upon reaction with **NDI-01** under conventional click conditions (Scheme 3.6).

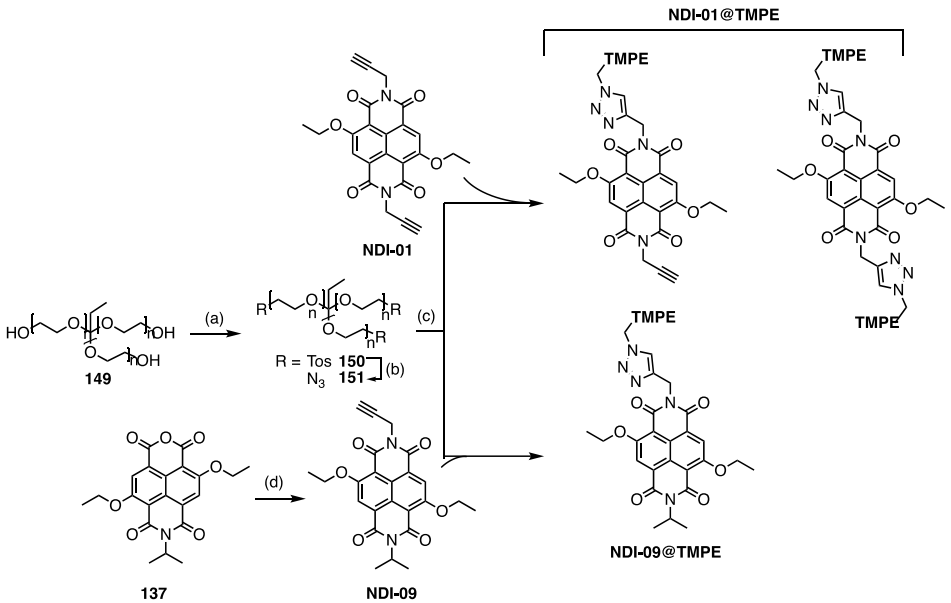

Scheme 3.6 Synthetic approach for TMPE-post functionalization. a) TsCl, NaOH, THF/water, 0°C to rt, 24 h (86%) b) NaN_3, DMF, rt, 12 h (91%); c) CuOAc, sodium ascorbate, DCM/ACN (1:1), 40°C, 24 h; d) propargyl amine, DIPEA, Dioxane, 101°C, 24 h (64%).

The successful covalent functionalization of the polymer with the NDI has been proven by NMR (Figure 3.10). Triazole signals can be detected around 7.8 ppm, while the protons H_b in the free **NDI-01** (4.9 ppm) shift to lower fields (5.4 ppm) upon formation of the triazole ring. Moreover, the polymeric methylene groups in α-position to the azide shift to higher ppm values after the click reaction, affording a new band centered at 3.80 ppm. The structure reported in Figure 3.10 is intended as a model structure to present all the possible H-signals detectable at the ^{1}H-NMR. A more complex situation occurs in the experimental system, where both bistriazole and monotriazole-derivatives have been formed.

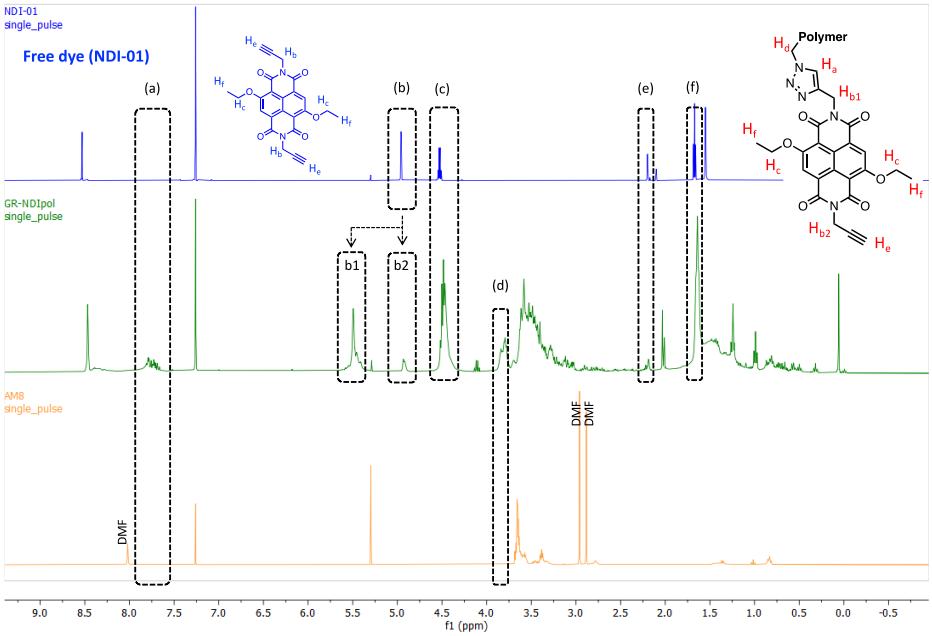

Figure 3.10 ^{1}H-NMR characterization for TMPE-NDI conjugates. Top: **NDI-01** as a free dye. Middle: TMPE conjugated with NDI-01. The free dye has been removed through filtration on silica pad. Bottom: Azide-derivative TMPE **151**. All NMRs have been performed in $CDCl_3$.

To avoid any cross-linking phenomena that may distort the fluorophore scaffold and quench the emission, the unsymmetrical analogue **NDI-09** has been prepared by reacting the intermediate **137** already prepared in Scheme 3.5 with one equivalent of propargyl amine and further bounded to the TMPE **151**. The optical characterization of both fluorescent TMPEs is reported below.

3.1.3.4. Photophysical characterization

In solution

The UV-Vis spectra (Figure 3.9) show the first typical π-π* transition with a characteristic vibronic structure centered around 360 nm not sensitive to the core-substitution, and the second charge-transfer band able to

move along the visible spectrum upon modification of the push-pull system. The replacement of ethoxy substituents with the alkyl amino groups leads to a bathocromic shift of the optical features due to the increased donating ability of the latter when compared to the formers. In particular, the emission moves from 480 nm in **NDI-01** to 580 nm in **NDI-02** and to 645 nm in **NDI-03**. As mentioned before, the imide-substitution does not affect the photophysics in solution as confirmed by the perfect match between the **NDI-03**, **NDI-08** and **NDI-06** features listed in Table 3.3. All the dyes show excited state lifetime τ in the fluorescence range, oscillating from 2 ns for **NDI-01**, to 13 ns and 10 ns for **NDI-02** and **NDI-03/06/08**, respectively (Table 3.3).

Table 3.3 Photophysical parameters of all NDI candidates in DCM solution.

Compound	DCM Solution					
	λ_{abs} [nm]	λ_{em} [nm]	PLQY [%]	τ [ns]	k_r [a)] [s^{-1}]	k_{nr} [a)] [s^{-1}]
NDI-01	470	480	20	2	10.00	40.00
NDI-02	550	580	55	13	4.23	3.46
NDI-03	615	645	28	10	2.80	7.20
NDI-05	464	488	22	-	-	-
NDI-06	615	645	38	-	-	-
NDI-07	469	488	19	-	-	-
NDI-08	615	645	28	10	2.80	7.20

[a)] x 10^7; Emission wavelength - λ_{em} [nm]; absorption wavelength - λ_{exc} [nm]; photoluminescence quantum yield - PLQY [%], excited state lifetime τ - [ns] with λ_{exc} = 375 nm; radiative constant - k_r [s^{-1}]; non-radiative constant - k_{nr} [s^{-1}].

In polymer coating

(The results shown herein have been achieved by ARTIBLED consortium at Costa's Lab, TUM, Straubing)

The preparation of the polymeric coating has been realized by using a combination of branched (TMPE) and linear (PEO) polyethylene oxide. All the NDI candidates were implemented in a TMPE:PEO matrix at low amounts (10^{-3} mg). Compared to the photoluminescence in solution (Table 3.3), the photoluminescence features of the polymer coatings are similar (similar emission/excitation spectra shape), nicely covering the whole visible range between 490 to 655 nm associated to PLQY spanning from *ca*. 20 to 60 %.

The photophysical properties are mainly maintained in terms of λ_{ex}, λ_{em}, and PLQY, highlighting a good compatibility of the dyes with the polymeric matrix. The τ values undergo a small increase in the case of **NDI-01** passing from solution to coating ($\tau \approx 2$ ns vs $\tau \approx 2.5$ ns), and a slight decrease in the case of the others NDI dyes. **NDI-03**, **NDI-06**, and **NDI-08** showed analogue photophysical features with an emission band centred at *ca.* 650 nm and associated to PLQYs of 30-35 %. These figures and trends hold changing to other hydrophobic polymer coatings, such as PMMA:TMPE - Table 3.4.

Table 3.4 Photophysical characterization of NDI polymer coatings.

LED emitter	Matrix	Solvent	λ_{exc} [nm]	λ_{em} [nm]	PLQY [%]	τ [ns]
NDI-01	TMPE:PEO	DCM	470	490	22	2.32
NDI-02	TMPE:PEO	DCM	548	589	59	11.29
NDI-03	TMPE:PEO	DCM	615	655	34	7.6
	HPC	DCM	623	655	40	10.83
NDI-06	TMPE:PEO	DCM	613	655	34	7.31
	HPC	DCM	616	650	45	10.67

NDI-07	TMPE:PEO	DCM	545	615	n.m.	n.m.
NDI-08	TMPE:PEO	DCM	615	655	35	8.91
	PMMA:TMPE	DCM	613	645	30	11.76
	HPC	DCM	615	652	46	11.01

Additionally, the photophysical evaluation of the references **NDI-01@TMPE** and **NDI-09@TMPE** has been carried out. A dramatic PLQY drop both in solution and polymeric coating can be observed compared to the free dyes **NDI-01** and **NDI-09**. Since the preparation of **NDI-09** allowed to exclude that the occurring crosslinking with **NDI-01** might be the quenching responsible, the drop should be ascribed to a distorted conformation of the fluorophore upon binding to the TMPE. Eventual free azide grups have been discarded by IR spectroscopy and some negative controls in liquid state claim that eventual N_3 traces have not any effects on the PLQY drop. Having these data in hand, these two references have been discarded and not implemented in the HLEDs.

Additional studies increasing the concentration of fluorophore inside the coating have been carried out on **NDI-03** and **NDI-08** to evaluate the effect of the novel groups introduced in the second NDI generation. For this purpose, several coatings were prepared following the same procedure and increasing the amount of dye, namely 5×10^{-9} mol (**a**), 1×10^{-8} mol (**b**), 6×10^{-8} mol (**d**) and 1.2×10^{-7} mol (**e**). Figure 3.11 shows the excitation and emission spectra of **NDI-03** and **NDI-08** coatings upon increasing concentration of the dye, while Table 3.5 provides a comparative overview on PLQY and τ values.

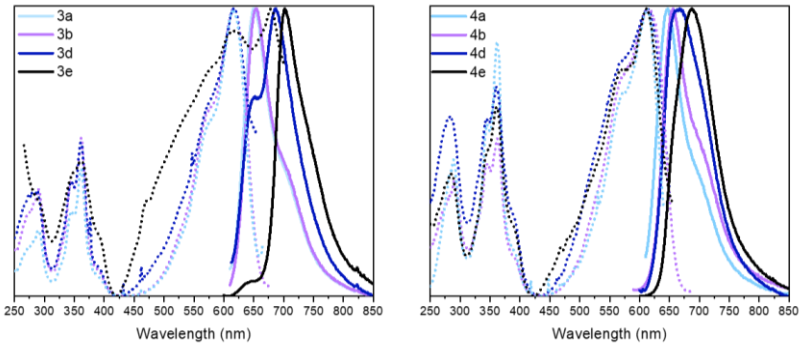

Figure 3.11 Excitation and emission of **NDI-03** (left) and **NDI-08** (right) polymer coatings upon dyes amount increase.

Table 3.5 Photophysical features of **NDI-03** and **NDI-08** polymer coatings upon dyes amount increasing.

	Polymeric coating							
	***a**: 5 E-9 mol*		***b**: 1 E-8 mol*		***d**: 6 E-8 mol*		***e**: 1.2 E-7 mol*	
	PLQY	*τ*	*PLQY*	*τ*	*PLQY*	*τ*	*PLQY*	*τ*
NDI-03	0.31	8.51	0.34	8.61	0.19	1.25-9.26	0.09	1.62-5.16
NDI-08	0.34	9.21	0.35	8.91	0.37	9.8	0.28	0.7-8

PLQY [%], excited state lifetime τ - [ns] with λ_{exc} = 375 nm.

NDI-03a and **NDI-03b** (Table 3.5) coatings do not show significant photophysical differences. **NDI-03d** coating starts facing a decrease of the emission band centered at λ_{em} = 650 nm, showing a more prominent emission maximum at λ_{em} = 687 nm, which appears as a variation at the vibronic structure level, confirmed by the unchanged excitation spectrum. Anyway, this leads to an increase of the competing vibrational relaxations and to a quench of the PLQY to 19%. A further shift to λ_{em} = 700 nm is appreciable in sample **NDI-03e** (PLQY = 9%), where an excitation peak centered at λ_{em} = 687 nm is now visible beside a strong deformation of the previous excitation band centered at λ_{ex} = 615 nm. As expected, such

strong aggregation tendency shown by **NDI-03** resulted improved by the structural modifications introduced in **NDI-08**. The small branched isopropyl group allowed to lower the $\pi-\pi$ stacking, reducing the aggregation-induced quenching as confirmed by coatings data. In this case, the initial emission centered at λ_{em} = 645 nm (**a**) gradually shifts to λ_{em} = 670 nm (**d**) and to λ_{em} = 688 nm (**e**) upon dye concentration increase, while PLQY is retained ~ 35% for all the coating **NDI-08a** – **NDI-08d**, with a not significant decrease (PLQY = 30%) starting for sample **NDI-08e**. We suggest the presence of a combination of J- and H-aggregates upon increasing concentration, in agreement with previous report on the perylene dyes aggregates.[212–214]

3.1.3.5. Photostability of NDI-based phosphors in HLEDs

(The results shown herein have been achieved by ARTIBLED consortium at Costa's Lab, TUM, Straubing)

As a next step, the photostability of the NDI polymer coatings was studied using different photon flux excitations, monitoring the photo-induced heat generation in the polymer coatings and the NDIs emission intensity. Table 3.6 summarizes the most relevant conditions as well as lifetimes (L_{50}; time to reach half of the initial emission intensity). As already mentioned, **NDI-01** and **NDI-02** do not satisfy the stability requirements (L_{50} < 20 min for **NDI-01** and **NDI-02**, regardless of the conditions and polymer coatings), probably due to a photo-induced radical formation mechanism.[215] In contrast, **NDI-03** shows a promising stability when embedded into the polymeric matrix (L_{50} > 1 h).

In detail, several HLEDs implementing **NDI-01**, **NDI-02** and **NDI-03** coatings have been prepared using a 365 nm LED chip, under 200 mA of applied current. Seen the very low concentration of dye in **a** samples, series **b-** and **e-** were selected to prepare LEDs.

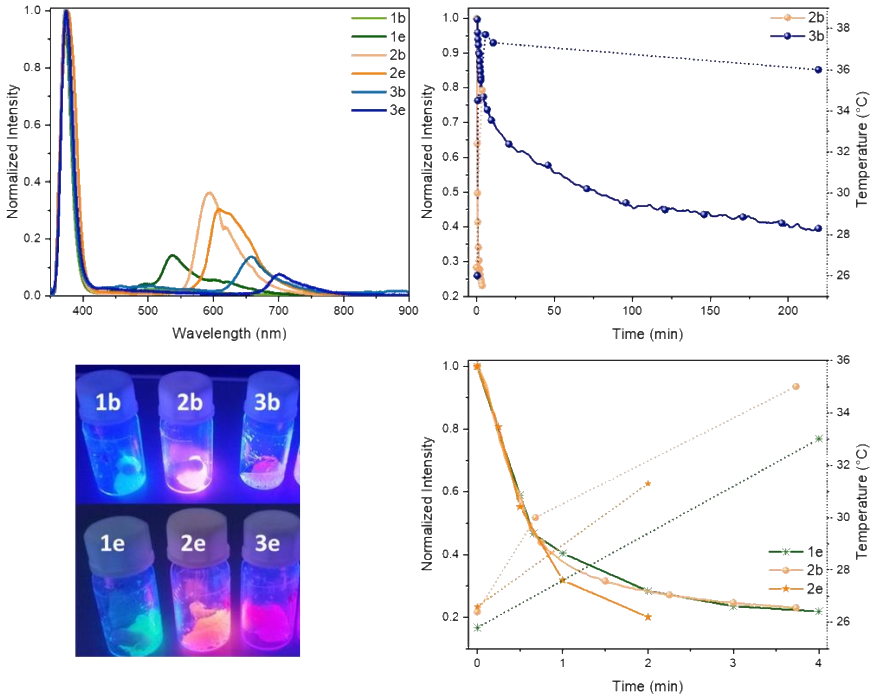

Figure 3.12 Top: fresh spectra of 1b, 1e, 2b, 2e, 3b, 3e coatings under 365 nm irradiation in ambient conditions (left) and photostability decay profile of 2b and 3b coatings under 365 nm irradiation in ambient conditions, 200 mA of applied current (right). Bottom: 1b, 2b, 3b, 4b and 1e, 2e, 3e, 4e coatings under UV irradiation (left); photostability decay profile of 1e, 2b, 2e coatings under 365 nm irradiation, ambient conditions, 200 mA.

In the case of **NDI-01** phosphors, the conversion of the UV incident light into green light resulted too poor in the case of **NDI-01b** – Figure 3.12. Sample **NDI-01e**, although an improvement in the down-converting properties was observed, does not lead to a significant stability (< 2 min, on chip configuration). The low stability is not accompanied by a temperature increase in operando, and therefore might be related to an intrinsic low stability of the molecule upon irradiation. As expected, yellow emitting **NDI-02e** leads to a red shifted emission compared to **NDI-02b** coating. Anyway, both the HLEDs show a L_{50} < 2 min, not sufficient for a

further optimization of the device – Figure 3.12. Surprisingly, the red emitting **3b** coating leads to a stability of ~ 1 h (200 mA, on chip), despite a slightly higher increase in temperature up to 38 °C. Seen the poor stability of **1** and **2** coatings and the more promising performance of **3** phosphor, we proceeded with the optimization of red emitting HLEDs.

Its analogues prepared within the second NDIs generation - namely **NDI-06** and **NDI-08** - featured excellent stabilities, respectively > 200 h and ~900 h (TMPE:PEO, 590 nm irradiation, 130 mW/cm^2, 200 mA, on-chip). These outstanding results might be related to the improved compatibility of the organic dyes with the hydrophilic polymeric coating. Compared to the highly hydrophobic **NDI-03**, the **NDI-08** linker and the **NDI-06** maleimide ring increase the hydrophilicity of the whole system, with a beneficial effect on the dye stabilization inside the polymeric coating (**Figure 3.13**). Additionally, PLQY of both **NDI-06** and **NDI-08** increased in HPC coatings (Table 3.4), while the L50 slightly decreases, still evidencing an important contribution of the polymer on the dye's performances.

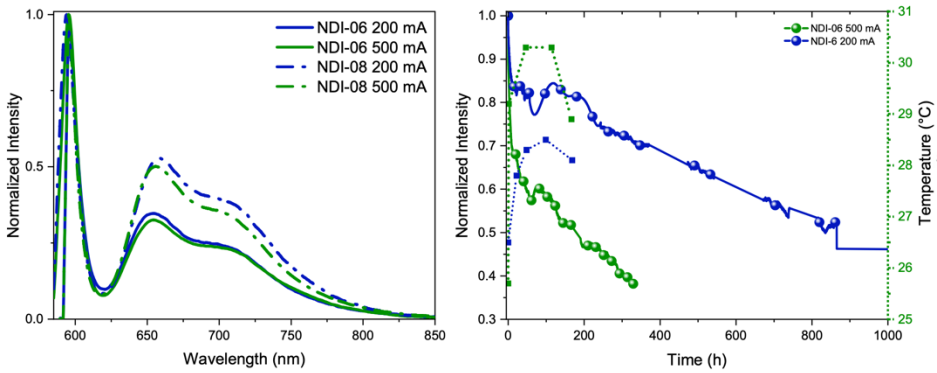

Figure 3.13 Left: emission spectra profile for **NDI-06** and **NDI-08** based HLEDs under ambient operating conditions. Right: Emission intensity decay over time for **NDI-06** based HLED under different applied currents.

Table 3.6 NDI-molecules performances in HLEDs under ambient operating conditions, 200 mA of applied current.

Cpd	Matrix	Conditions	Amounts	Temp.	L_{50}
NDI-01	TMPE:PEO	Blue 450 nm[a]	10^{-3} mg	40/45 °C	< 5 min
	PMMA:TMPE			40°C	< 5min, < 1h
NDI-02	TMPE:PEO	Blue 450 nm[a]	10^{-3} mg	40°C	< 20 min
	PMMA:TMPE				1 h
NDI-03	TMPE:PEO	590 nm[b]	10^{-3} mg	40 °C	1 h
NDI-06	TMPE:PEO	590 nm[b]	10^{-3} mg	28 C	> 800 h
NDI-07	TMPE:PEO	Blue 450 nm[a]	10^{-3} mg	/	no conversion
NDI-08	TMPE:PEO	590 nm	10^{-3} mg	28 °C	1800 h[b]/900 h[c]
	PMMA:TMPE				1800 h
	HPC			35 °C	665 h[c]

[a] 150 mW/cm^2 [b] 55 mW/cm^2 [c] 130 mW/cm^2

These preliminary results highlight the isopropyl amino-isopropyl amino groups as the most suitable and stable core-combination for the implementation in Bio-HLEDs. If **NDI-03** was already able to show higher stabilities compared to the analogues **NDI-01** and **NDI-02**, a better refining provided outstanding results for **NDI-06** and **NDI-08**.

3.1.3.6. Conclusion and future perspectives

The first preliminary screening carried out on the NDI candidates elected among green, orange and red fluorescent compounds the red-emitting isopropyl amino-isopropyl amino substituted **NDI-03** as the most stable candidate. Since his highly hydrophobic character strongly hampered the bioconjugation step, the molecular structure has been better refined in **NDI-06** and **NDI-08** by introducing hydrophilic linkers and short branched

aliphatic chains on the imides increasing the solubility and lowering the π–π stacking.

The achieved results within the NDI family provided a long-living red phosphor, while the low photostability of the green and orange candidates hampers the preparation of a white HLED. In this context, suitable compounds able to cover the mid- and high-energy parts of the spectrum are necessary toward the realization of a white light emitting device. Alternative oligoaromatic fluorophores have been explored and presented in the next sections.

3.1.4. Covering the high-energy part of the spectrum: TTZ derivatives

The thiazolo[5,4]thiazole (TTZ) derivatives are widely explored candidates in several scientific disciplines, *i.e.* organic electronics, photovoltaics,[216,217] photocatalysis,[218] white organic LEDs[219] and fluorescent ion sensing.[220,221] They usually consist of a thiazolothiazole fused scaffold as a part of a symmetrically functionalized π-system. Their intrinsic resistance to oxidation due to the core π-electronic deficiency, along with remarkable photophysical features (e.g., high PLQY and excellent extinction molar coefficients) point out the high versatility and applicability of TTZ system. Although TTZs are usually symmetrical, the simultaneous introduction of electron-donor and electron-withdrawing moieties on the two opposite sides of the conjugated system contributes to increase the push-pull character of the fluorophore. The occurring charge-transfer transitions along with high dipole moments able to generate large Stokes shifts and limited reabsorption processes provide

remarkable photophysical features deeply investigated by a pioneering work of Sayresmith and co-workers.[222]

Herein, the piperidine has been chosen as electron-donor group due to the structural rigidity of the ring, limiting the dispersion of the absorbed energy *via* non-radiative phenomena. At first, a cyano moiety has been introduced on the opposite side as a withdrawing group but the low solubility hampered the purification and further compound reactivity. Then, synthetic modifications have been investigated and a pending triple bond has been inserted through an ether linkage in **TTZ-02**. Although **TTZ-02** has not been implemented in any protein scaffold yet, preliminary encouraging results in HLEDs have been reported. The strong thermal quenching occurring in the on-chip configuration has been overcome in the remote architecture, providing remarkable photostability results able to justify their further implementation in *ad-hoc* prepared AFPs. Additionally, the high versatility of TTZ derivatives has been proven by exploring their ability to stain the cell membrane hydration in **Section 3.2.1**.

Synthesis

Starting from the data reported by Sayresmith and co-workers,[222] unsymmetrical TTZs were targeted, aiming to prepare a push-pull fluorophore with a high dipole moment. The piperidine has been chosen as electron-donor group due to the structural rigidity of the ring, limiting the dispersion of the absorbed energy *via* non-radiative phenomena. Although at first a strong push-pull system had been targeted (namely, **TTZ-01** in Scheme 3.7) by the introduction of an accepting group (*i.e.*, cyano moiety), the extremely low solubility of these candidates

undermined their feasibility. Hence, a pending triple bond has been introduced through an ether linkage - **TTZ-02**.

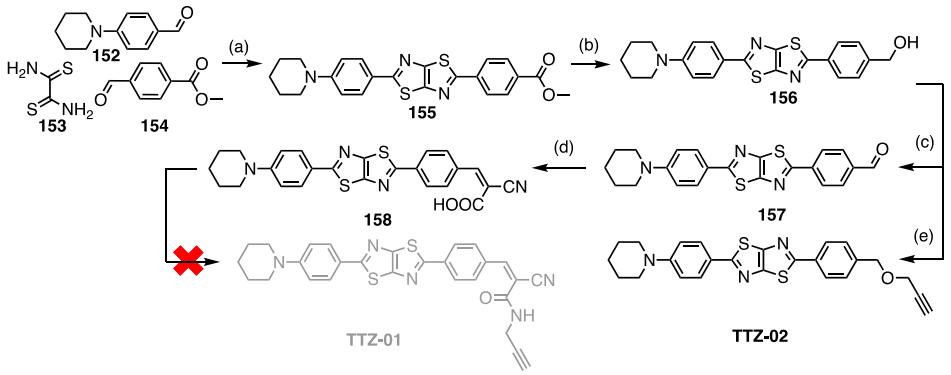

Scheme 3.7 a) DMF, 120°C, 6h (12%). b) DIBAL-H, DCM, -78 °C, 3h (37%) c) MnO_2, DCM, rt, 2 h (45%) d) cyanoacetic acid, DCM/EtOH (2:1), 40°C, 12 h e) THF, NaH 60%, propargyl bromide, 0°C, overnight (9%).

At first, a methyl ester was introduced in **155**, due to the possibility to be converted in several other motifs (*e.g.,* alcohol, ethers, aldehydes, amides), representing an optimal starting point for the preparation of a wide and heterogeneous TTZ library. The asymmetric synthesis of **155** was performed through a one-pot condensation reaction between the dithiooxamide **153** and two aromatic aldehydes (**152** and **154**). The three starting materials (**152**-**154**) were heated in DMF at 120°C for 6 hours under vigorous stirring, following Sayresmith and co-authors work.[222] Then, the dark mixture was poured in water and the precipitate recovered by a slow filtration. The desired product **155** was then separated by several side-products (*e.g.,* the two symmetric TTZs and other reddish intermediates) *via* a series of difficult and solvent-consuming flash chromatographic columns. The high solvent consumption along with the long time required to prepare just few milligrams of **155** strongly limited the scalability of this approach, highlighting the need of an alternative and

more straightforward strategy – Table 3.7. In this context, the nitrobenzene replaced the DMF to avoid any solvent degradation (DMF frees dimethylamine in the system at high temperatures) along with the possibility to reach higher temperatures. Additionally, the use of nitrobenzene allowed to dramatically reduce the solvent consumption: while 1 g of **153** requires 60 mL of DMF, only 10 mL of nitrobenzene are necessary. Then, after having stirred the reaction crude at 150°C in nitrobenzene for 6 h, an additional treatment with DDQ allowed to enhance product aromatization and the reaction yield.[223] A final precipitation in methanol allowed to isolate the product without the need of any further purification before the next reaction step. This synthetic approach was then optimized by performing a microwave-assisted synthesis, resulting in a remarkable reduction in the reaction time (30 min) without affecting the reaction yield.

Table 3.7 The optimization of first one-pot approach for preparation of **155**.

	Method A	Method B	Method C
Heating	Conventional	Conventional	MW
Solvent	DMF	Nitrobenzene	Nitrobenzene
Temperature	120°C	150°C	150°C
Time (h)	6	5 + 1[a]	0.5 + 1[b]
Additive	-	DDQ[c]	DDQ[c]
Yield (%)	12	15	17
Purification technique	Chromatography	Precipitation	Precipitation

[a] 5 h in nitrobenzene at 150°C + 1 h in THF at reflux. [b] 0.5 h in nitrobenzene at 150°C + 1 h in THF at reflux. [c] The addition of DDQ is reported to enhance the aromatization of reactive intermediates.[223]

Lastly, further modifications of the push pull system were explored, reducing the methyl ester **155** to alcohol **156** by treatment with DIBAL-H. Then, the alcohol oxidation in mild conditions afforded the aldehyde **157**, but the further push-pull character enhancement by introduction of a

cyano group has been hampered by the low solubility of the compound. In the end, a smart alkyne functionalization has been introduced by reaction with sodium hydride and propargylic bromide affording **TTZ-02**.

Photophysical study

In solution

TTZ-02 optical features were explored in several organic solvents, showing a strong solvatochromic behaviour - Figure 3.14. Emission maxima shift from 466 nm in Toluene to 531 nm in DMSO. PLQYs remain extremely good regardless of the solvent, leading to large Stokes shifts (*e.g.,* DMSO, ACN, DMF, and MeOH).

a)

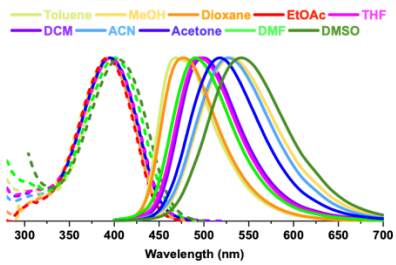

b)

Solvent	λ_{abs} (nm)	ε ($M^{-1}cm^{-1}$)	λ_{em} (nm)	Stokes Shift (cm^{-1})	PLQY -
DCM	396	42016	499	5212	0.76
Toluene	397	39866	468	3821	0.70
MeOH	393	40027	530	6577	0.59
THF	396	40121	495	5051	0.77
ACN	394	41914	527	6405	0.68
Dioxane	395	42805	476	4308	0.77
EtOAc	393	39623	491	5079	0.76
DMF	401	37284	532	6141	0.72
Acetone	395	41711	518	6011	0.84
DMSO	405	38511	542	6241	0.72

Figure 3.14 a) Absorption (dashed) and emission (solid) spectra of **TTZ-02** in several organic solvents. b) Photophysical parameters of **TTZ-02** measured in several organic solvents. PLQY was measured referring to Rhodamine 101 as standard.

In polymer coating

(The results shown herein have been achieved by ARTIBLED consortium at Costa's lab, TUM, Straubing)

TTZ-02 was characterized in TMPE:PEO and HPC matrices at low amounts (0.1 mg). Likewise photoluminescence in solution, the polymer coatings show a similar green emission band shape at 520 nm with PLQY

of around 80 % - Table 3.8. Unfortunately, their photostability at blue excitation (450 nm; 200 mW/cm^2) was poor (L_{50} < 20 min) due to the significant photo-induced heat generation, reaching values of 65 °C. Thus, the low stability is related to a prominent temperature induced emission quenching. If the temperature is reduced at 30 °C using a remote configuration, the stability is, indeed, increased up to ~ 150 h (Figure 3.15).

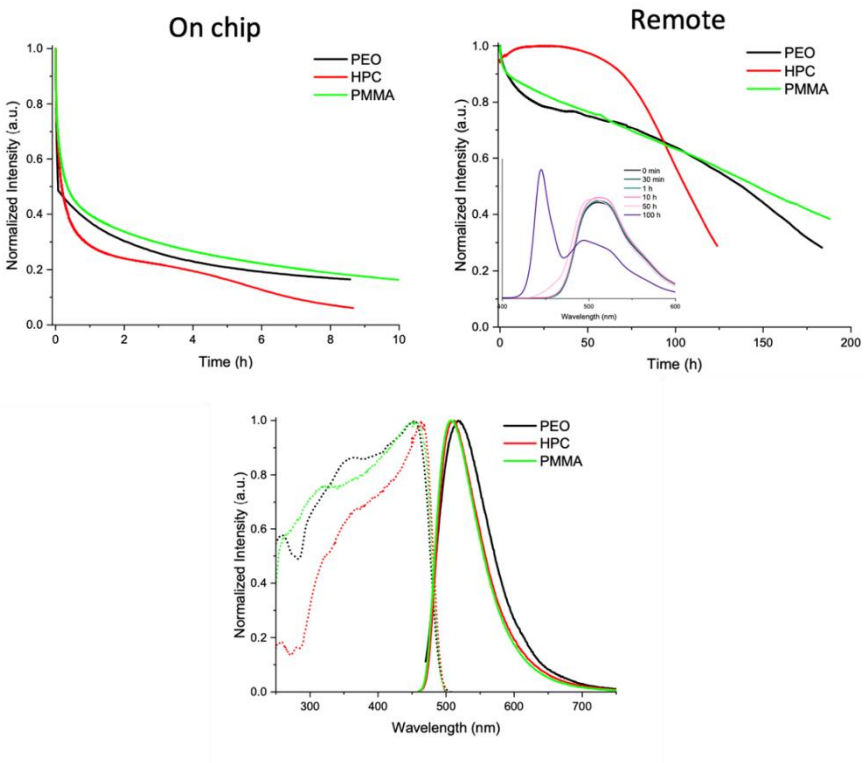

Figure 3.15 Top: Emission intensity decay over time for **TTZ-02** based devices under ambient operating conditions (130 mW/cm^2) both on chip (left) and remote (right) configurations. Bottom: Emission (solid) and excitation (dashed) spectra of **TTZ-02** polymer coatings.

Table 3.8 Photophysical characterization of TTZ-based polymer coatings.

LED emitter	Matrix	λ_{exc} [nm]	λ_{em} [nm]	PLQY [%]	τ [ns]	Conditions	L50[a]	L50[b]
TTZ-02	TMPE:PEO	452	518	78	2.11	450 nm	<5 min	135 h
	PMMA:TMPE	450	507	91	2.26		20 min	145 h
	HPC	451	510	82	2.13		< 5min	105 h

[a] 150 mW/cm^2 on-chip b 5 mW/cm^2 remote (2 cm).

Conclusions and perspectives

Despite preliminary solubility issues related to the introduction of strong with-drawing groups (e.g., cyano moiety), the preparation of **TTZ-02** provided a good candidate for the high-energy part of the spectrum. A high stability up to 145 h in HLEDs should be still improved due to the shielding protein, in line with the previous data on squaraine. Furthermore, the remarkable solvatochromic behaviour highlights the importance of a proper protein scaffold design due to the strong influence of the binding pocket local polarity on the fluorophore optical features. Although the previous mentioned solubility issues limited the introduction of bioconjugation groups, the outstanding optical traits of the solvatochromic intermediates (**156**, **157**) have been used to stain the cellular membrane hydration and fluidity, as reported in **Section 3.2.1**.

3.1.5. The mid-energy part of the spectrum: benzothiadiazole derivatives

The 2,1,3-benzothiadiazole core is a renowned scaffold in the fields of organic electronics,[224,225] photovoltaics,[226] and fluorescent imaging.[227] Once the core is bounded to two thiophene rings, the fluorescent properties of the whole system (namely, BTD) turn on providing remarkable PLQYs and large Stokes shifts in the yellow region of the visible spectrum. The strong electron-withdrawing character and the charge-carrier ability of the benzothiadiazole core merged to the electron-rich thiophene groups provide a powerful fluorescent scaffold, widely applied both in small molecules and polymers. Additionally, many BTD-based materials have already been implemented in optoelectronic devices (e.g., organic LEDs).[228–231] Herein, two aliphatic chains have been introduced on the thiophenes aiming at increasing the solubility and reducing the π–π stacking. Two hexyl chains have been selected due to the commercial reagents low cost, while their positions into the scaffold have been modified to finely tune the photophysical features (Figure 3.16).

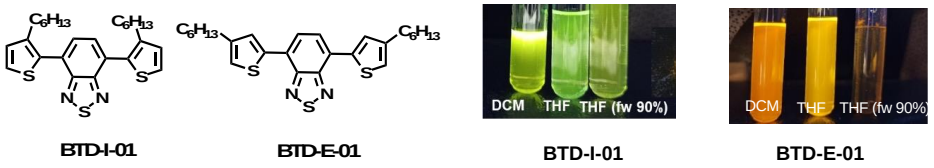

Figure 3.16 Left: Different location of the hexyl chains on the thiophenes position. Right: The hypsochromic shift upon system deplanarization is clearly visible under UV lamp.

The chains location on the two thiophene β-positions induces different deplanarization degree (**BTD-I** and **BTD-E**), with different optical

hypsochromic shifts. Additionally, the introduction of triple bond and maleimide in a symmetrical and unsymmetrical manner has been achieved, affording a clear relationship between the number/type of linkers and the photostability under operating conditions.

Synthesis

The synthesis of the BTD core has been carried out according to reported procedures. As shown in Scheme 3.8, a first bromination of commercial 2,1,3-benzothiadiazole **159** has been followed by Suzuki coupling with the suitable 2-thienylboronic acid pinacol ester **161**, providing **BTD-E-01** and **BTD-I-01**, with alkyl chain in the "external" or "internal" position respectively.[232]

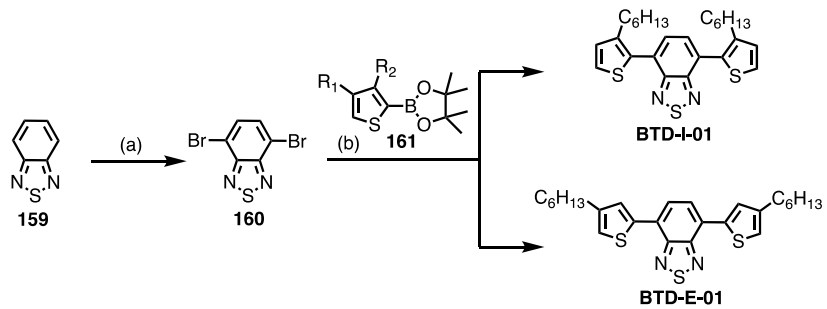

Scheme 3.8 Synthesis of **BTD-I-01** and **BTD-E-01**. (a) NBS, H_2SO_4, 40°C, 4 h (91%). b) 161, $Pd(PPh_3)_4$, K_2CO_3 (aq.), toluene, reflux, 12 h (94%).

The assembly of the dye with the linker for bioconjugation was carried out starting first by **BTD-I-01**, due to its higher solubility in DMSO. First, the 5-position of the thiophene ring was functionalized with an aldehyde moiety through Vilsmeier-Haack formylation. By modulating the equivalents of the two reagents, $POCl_3$ and DMF, it was possible to orient the reactivity towards a single functionalization, obtaining the unsymmetrical aldehyde **162**, or towards a double formylation, affording

the symmetrical aldehyde **164** - Scheme 3.9. Oxidation of the aldehyde group to carboxylic acid, *en route* to the amide bond, was performed with $NaClO_2/H_2O_2$, since the more common $KOH/AgNO_3$ system failed to give reproducible and satisfying yields. Finally, the sequential conversion of the acid into acyl chloride and reaction with propargylamine or 1-(2-aminoethyl)maleimide trifluoroacetic acid salt afforded the desired BTD derivatives with linkers for bioconjugation.

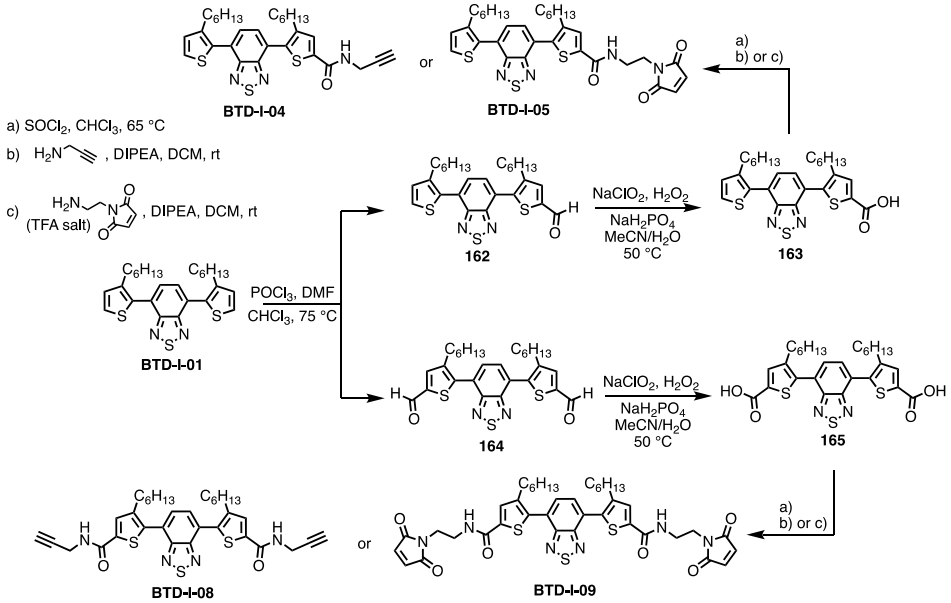

Scheme 3.9 Synthetic pathways towards BTD dyes with linkers for bioconjugation.

Photophysical characterization

In solution

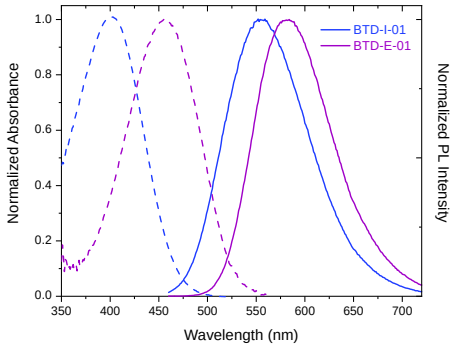

BTD-I-01 **BTD-E-01**

Solvent	λ_{abs}	λ_{em}	PLQY
BTD-I-01	401	555	88
BTD-E-01	458	603	98

Photophysics in DCM solution

Figure 3.17 Left: Absorption (dashed) and emission (solid) spectra of **BTD-I-01** and **BTD-E-01** in DCM solution. Right: Solutions in DCM, THF and THF/H_2O (9:1) under UV lamp.

Figure 3.17 compares the photophysical features of **BTD-I-01** and **BTD-E-01**. As already well-known in literature, the hexyl chains distort the fluorophore structure if introduced in the most internal thiophene β-positions, resulting in a blue shift of both emission and absorption profiles. The excellent PLQY values and the large Stokes shifts (6900 cm^{-1}) make this emitters family an extremely powerful candidate. Furthermore, the reduced π–π stacking upon deplanarization increases the "internal" series (BTD-I) solubility. Thus, the first explored BTD compounds bear the aliphatic chains internally and their optical data in DCM solution are reported in Figure 3.18. All the intermediates and the final compounds emit in the yellow region of the visible spectrum, with remarkable PLQY (Table 3.9). The introduction of electron-withdrawing groups (e.g., aldehydes, carboxylic acids) at the edges slightly hypsochromically shifts the optical traits compared to the archetype BTD-I-01. This trend can be appreciated even when weak electron-withdrawing groups (as the amide

in **BTD-I-04**, **-05**, **-08** and **-09**) are introduced in the final compounds. Additionally, the presence of two symmetric linkers (**164, 165**) increases this trend when compared to the unsymmetrical derivatives. Two electron-withdrawing groups blue-shift the emission maximum 13 nm, while the presence of only one provides a shift of 4 nm. The high PLQY and good molar extinction coefficient provide extremely bright fluorophores, worthy to be implemented into polymeric coatings.

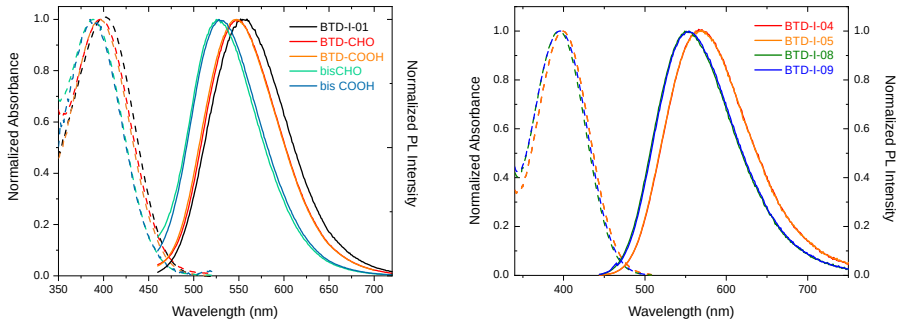

Figure 3.18 Absorption (dashed) and emission (solid) spectra of all BTD-I dyes, both intermediates (left) and final (right) compounds.

Table 3.9 Photophysical parameters all BTD-I dyes, intermediated and final compounds. All data are in DCM solution.

Compound	λ_{abs} (nm)	λ_{em} (nm)	Stokes shift (cm^{-1})	PLQY -	log(ε) (cm^{-1} M^{-1})
BTD-I-01	401	555	6920	0.88	-
162	400	547	6718	0.69	-
163	397	548	6941	0.88	-
164	388	525	6726	0.30	-
165	388	528	6834	0.72	-
BTD-I-04	399	563	7301	0.94	3.89
BTD-I-05	399	562	7269	0.89	3.88
BTD-I-08	396	549	7038	0.97	4.15
BTD-I-09	396	554	7202	0.98	4.15

In polymeric coating

(The results shown herein have been achieved by ARTIBLED consortium at Costa's lab, TUM, Straubing)

All the BTD final candidates were implemented in TMPE:PEO, PMMA:TMPE, and HPC matrices at low and high amounts. Though the PLQY remains high, spanning from 60 to 80 % as expected from those values in solution – Table 3.10, the emission spectrum changes upon using different polymer matrices, suggesting a strong interaction with different polymers. In short, the use of PMMA matrix red-shifts the emission (*ca*. 40 nm), while HPC blue-shifts the emission (*ca*. 25 nm). These trends are also noted regardless of the amount of dye, suggesting a lack of aggregation/agglomeration effect.

Table 3.10 Photophysical characterization of BTD-based polymer coatings.

Compound	Matrix	Amounts	λ_{exc} [nm]	λ_{em} [nm]	PLQY [%]	τ [ns]
BTD-E-01	TMPE:PEO	10^{-3} mg	465	600	60	11.92
	PMMA:TMPE		460	575	60	11.92
	TMPE:PEO	0.1 mg	465	600	60	n.m.
	PMMA:TMPE		460	575	60	n.m.
BTD-I-01	TMPE:PEO	10^{-3} mg	410	575	60	13.2
	PMMA:TMPE		410	535	60	11.59
	TMPE:PEO	0.1 mg	425	575	60	n.m.
	PMMA:TMPE		420	535	60	n.m.
	HPC		n.m.	555	85	11.9
BTD-04	TMPE:PEO	0.1 mg	410	565	80	8.73
	PMMA:TMPE		425	535	80	10.38
BTD-05	TMPE:PEO	0.1 mg	n.m.	570	81	n.m.
	PMMA:TMPE		n.m.	535	82	n.m.
BTD-08	TMPE:PEO	0.1 mg	425	565	80	8.73
	PMMA:TMPE		425	535	80	8.12
	HPC		n.m.	532	75	6.89

BTD-09	TMPE:PEO	0.1 mg	n.m.	560	80	n.m.
	PMMA:TMPE		n.m.	540	75	n.m.

Photostability evaluation in HLEDs

(The results shown herein have been achieved by ARTIBLED consortium at Costa's lab, TUM, Straubing)

Concerning photostability, BTD candidates were tested in all the polymer matrices using high amounts (0.1 mg) with a blue (450 nm) photon flux excitation of 150 mW/cm^2 – Table 3.11.

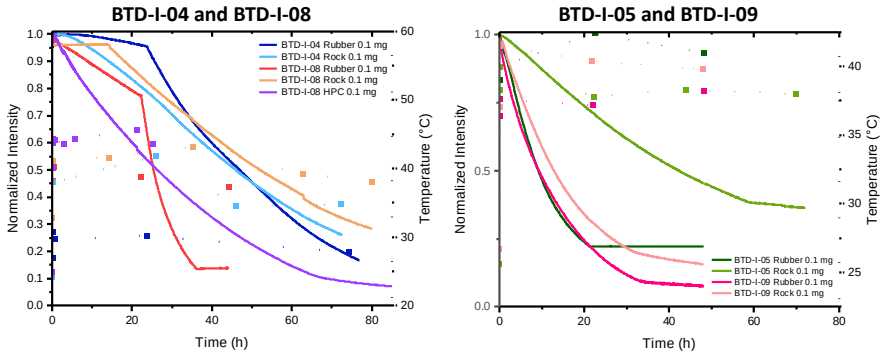

Figure 3.19 Emission intensity decay over time for triple bond-based BTDs (left) and maleimide-based BTDs (right). (200 mA, on chip architecture)

In general, these polymer coatings did not show an increase of working temperature, reaching a maximum temperature < 35 °C. **BTD-I-04**, **BTD-I-05**, **BTD-I-08,** and **BTD-I-09** comparison (Figure 3.19) confirms that the presence of one linker leads to higher stability than two linkers (symmetric *vs*. asymmetric). This finding can be easily rationalized thinking about the functional group (e.g., triple bond and maleimide) as a weakness reactive point. The lower is the number of reactive groups present on the molecule, the higher is the compound stability. According to this explanation, after bioconjugation, both maleimide and triple bond will be reacted and, thus, the fluorophores intrinsic stability is expected to increase.

Table 3.11 Photostability of BTD-based polymer coatings.

LED emitter	Matrix	Conditions	Amounts	Temperature [°C]	L_{50} [h]
BTD-E-01	TMPE:PEO	450 nm (150 mW/cm^2)	10^{-3} mg	32	16
	PMMA:TMPE			32	9
	TMPE:PEO		0.1 mg	34	85
	PMMA:TMPE			32	85
BTD-I-01	TMPE:PEO		10^{-3} mg	33	10
	PMMA:TMPE			34	10
	TMPE:PEO		0.1 mg	37	30
	PMMA:TMPE			34	70
	HPC			40	13
BTD-I-04	TMPE:PEO			30	45
	PMMA:TMPE		0.1 mg	40	40
BTD-I-05	TMPE:PEO			40	10
	PMMA:TMPE		0.1 mg	38	40
BTD-I-08	TMPE:PEO			40	25
	PMMA:TMPE		0.1 mg	45	50
	HPC			48	27
BTD-I-09	TMPE:PEO		0.1 mg	37	10
	PMMA:TMPE			39	12

Conclusions and perspectives

The wide versatility of BTD-based fluorophores is well-proven by several literature reports in different applicative fields. Their remarkable photophysical properties suggested us to implement them in polymeric coating for stability evaluation. After a preliminary screening (i.e., **BTD-I-01** and **BTD-E-01**) confirming their suitability for the implementation in HLED, a smart synthetic work afforded BTDs derivatives properly functionalized with either triple bond and maleimide moieties in a symmetrical and unsymmetrical manner. Preliminary studies carried out by our partners at Costa's Lab confirmed interesting stabilities of all candidates, with a particular mention for the unsymmetrical BTDs. This

finding might be attributed by the presence of only one reactive site able to start a chain-degradation. This issue should be solved upon bioconjugation of the dye with the protein. The interaction of the dyes with the protein scaffold is currently ongoing at Cortajarena's Lab in San Sebastiàn. The preparation of BTD-based AFPs is expected to further increase the emitters' stability, affording an idoneous yellow candidate for the preparation of a white bio-HLED.

3.1.6. Benzoxazole derivatives as highly emissive fluorophores covering the high and mid-energy part of the visible spectrum

2,5-bis(benzoxazol-2-yl)thiophene (BBT) shows a hybrid structure composed by a thiophene central moiety and two benzoxazole rings. They present strong emission and high photostability along with a suitable spatial orientation as supported by recent investigations. The insertion of different functional groups might improve the fluorophores optical properties, stability and photochemical-photophysical character for biological purposes.

They are usually functionalized at the benzoxazoles edges through short aliphatic carbon chains to improve their solubility and processability. The introduction of amino groups on the benzoxazole rings confers a highly solvatochromic character to the fluorophore with excellent PLQY (up to 0.99 in toluene),[233] while an ESIPT process occurs when hydroxyl moieties are inserted on the thiophene β positions.[234] The BBT photophysical behaviour has already been partially described by theoretical calculations[235] and highly promising experimental results, but further alternative functionalizations of the π system remains un-explored.

Herein, electron-donor and electron-withdrawing groups have been introduced on the benzoxazoles' edges, aiming at creating push-pull systems and highly solvatochromic compounds. Additionally, the effects of a methyl group on the thiophene β-position have been evaluated in relation with the photophysical features of the whole system. After a first BBTs generation (namely, **BBT-01** and **BBT-02**) with remarkable optical traits and extremely low solubility, the molecular structure has been better refined by introduction of solubilizing groups and different electronic effects on the benzoxazoles moieties. Methoxy and N-ethylamino groups have been introduced as donor moieties, while methyl ester, aldehyde or cyano groups have been candidate as acceptors to bathochromic shift the emission. Several synthetic strategies have been proposed until a Pd-free up-scalable procedure able to provide a series of highly soluble BBTs spanning the whole visible spectrum with excellent optical traits.

Further studies to implement the most bathochromic compounds within the AFPs have already been planned at our partners' laboratories, while the blue emitting BBTs (**BBT-00**, **BBT-03**) have been already tested in LEC (light-emitting electrochemical cells) devices. Although their filming properties should be improved by introduction of longer aliphatic chains, preliminary results have been achieved and summarized below.

Synthesis

Two synthetic approaches can be pursued to prepare symmetric and asymmetric compounds: *i*) modification of the core (**166**) *ii*) *ex novo* synthesis of **166** from modified thiophenes and substituted benzoxazole moieties. As proof of concept, the investigations started with the former strategy.

First BBTs generation

Synthesis of compounds **167-168** and **169-170** has been performed accordingly with a literature procedure with slight modifications for the purification of the latter (Scheme 3.10). At first, two NO_2 groups have been introduced with HNO_3 in sulphonitric mixture and further reduced to amino moieties upon treatment with $SnCl_2$ in ethanol. Purification of **169** and **170** has consisted of a basic treatment followed by filtration and soxhlet extraction of the crude allowing its purification by flash column chromatography to prepare the amino substituted intermediates. Although the low solubility of intermediates **169** and **170** strongly hampered the removal of tin byproducts along with good recovering of the desired compounds, the N-alkylation in basic conditions afforded **BBT-01** and **BBT-02**, showing a slightly improved solubility and bearing a triple bond for the further bioconjugation.

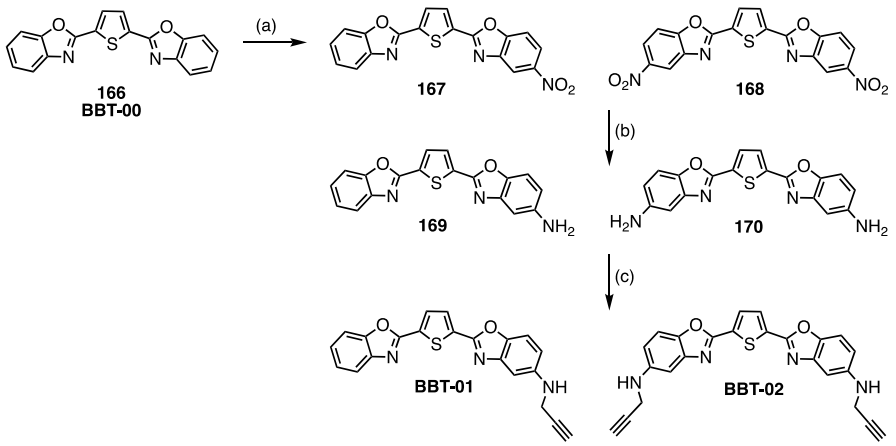

Scheme 3.10 Synthetic path for **BBT-01** and **BBT-02**. a) 1. HNO_3, H_2SO_4, 0°C, 1 h 2. H_2O, 0° C to rt, 12 h b) $SnCl_2$*$2H_2O$, EtOH, 80° C, 5 h c) Propargyl bromide, K_2CO_3, dry DMF, rt, 72-96 h.

Despite the presence of the alkyl chains, the two candidates still exhibit severe solubility issues, hampering their purification and large-scale production. The second BBT generation aims at improving the solubility by preparing the core according to a modular approach.

Second BBTs generation

To overcome these limitations an alternative synthetic strategy was implemented by following a modular approach (Scheme 3.11A). A second BBT generation was prepared (**BBT-03**, **BBT-04**, and **BBT-05**) introducing a methyl group on the thiophene β-position to deplanarize the system with a beneficial effect on the system solubility, along with a blue shift of the photophysical features. Benzoxazole moieties **172** can be linked to iodinated β-methylthiophene **171** through a Pd-catalyzed direct C-arylation. The methyl group on the thiophene leads to an improved solubility, while substituents on benzoxazoles lead to a fine tuning of optical features. Both symmetric (**BBT-03** and **BBT-04**) and unsymmetric (**BBT-05**) derivatives have been obtained (Scheme 3.11**A**). Since one-pot procedure for unsymmetric BBTs yielded only the two symmetric compounds, a synthesis *via emi*-BBT **173** has been developed. Different decorations at the two benzoxazoles moieties should allow to increase the dipole moment and to create a push-pull character along the conjugated system.

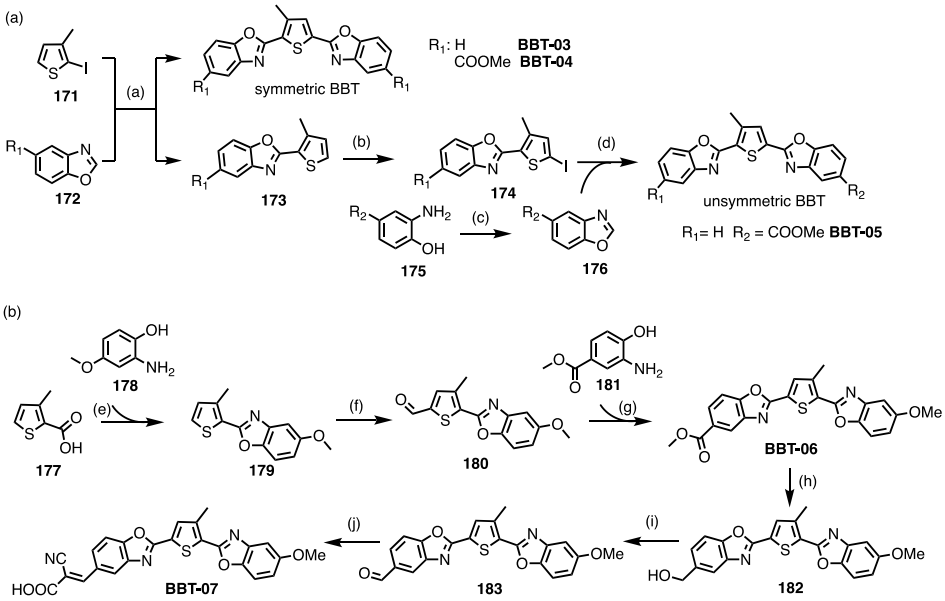

Scheme 3.11 a) $[Pd(phen)_2](PF_6)_2$, Cs_2CO_3, DMA, 150°C, 8 h (15-20%) b) 1. BuLi, THF, -78°C to 0°C, 1 h 2. NIS, THF c) triethylortoformiate, 155°C, 12 h d) 19, $[Pd(phen)_2](PF_6)_2$, Cs_2CO_3, DMA, 150°C, 8 h (30 %). e) 1. $SOCl_2$, DCM, 6 h 2. 24, NMP, 200°C, 6 h (30%). f) 1. BuLi, THF, -78°C 2. DMF, -78 °C to rt, overnight (13%). g) 1. 27, MeOH, 60°C, 6 h 2. PIDA, MeOH, rt, 2 h (44%). h) DIBAL-H, DCM -78 °C, 4 h (40 %) i) MnO_2, DCM, rt, 3 h (28 %) j) cyanoacetic acid, piperidine, DCM/EtOH (2:1), reflux, 9 h (24%).

Steps *a)* and *d)* of Scheme 3.11A represent the bottleneck of the synthetic pathway, since their yield dramatically decreases (3-5%) during reaction scale up (0.5 g scale). An alternative Pd-free synthetic strategy has been developed (Scheme 3.11B). The semi-BBT **179** has been prepared by a cyclization reaction between differently substituted 2-aminophenols and the 2-carboxy-3-methylthiophene **177** and then converted into the formylated derivative **180** upon treatment with one equivalent of butyl lithium (BuLi) and DMF. The aldehyde was then coupled with **181** and a cyclization mediated by diacetoxyiodobenzene provided the BBT core (**BBT-06**). The methyl ester was then converted into the more strongly

withdrawing cyano group *via* a series of reduction (**182**), oxidation (**183**) and Knoevenagel condensation affording **BBT-07**.

The **179** formylation has been performed in two manners. At first, treatment of **179** with butyl lithium and DMF has been investigated, but the tricky purification along with the very low yield encouraged us to find an alternative way. As a second approach, the Vilsmeyer-Haack reaction has been performed, but it afforded the regioisomer shown in Figure 3.20, almost selectively.

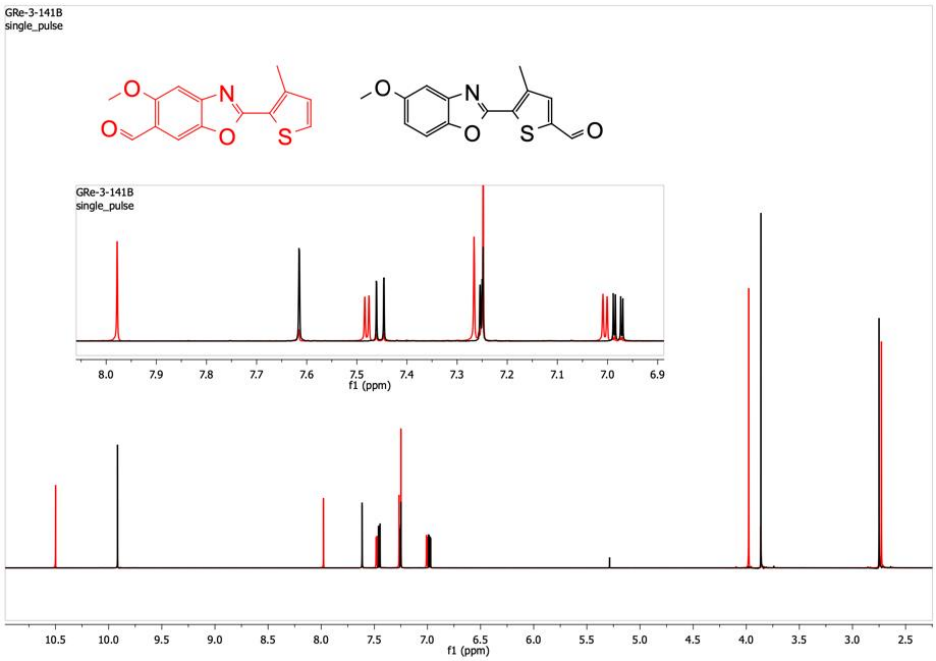

Figure 3.20 ^{1}H-NMR ($CDCl_3$, 600 MHz, 25°C) of the two regioisomers afforded by **179** formylation. The red product is formed through the Vilsmeyer-Haack procedure, while treatment with BuLi and DMF provides the black one.

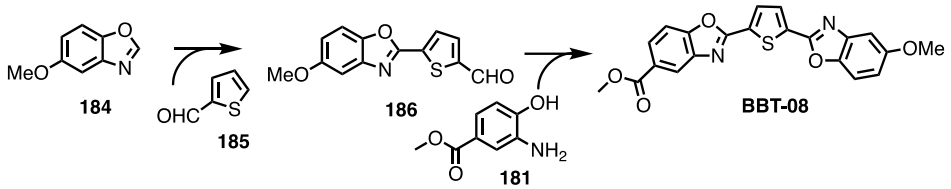

Scheme 3.12 Synthetic scheme for BBT-08 in small scale (60 mg of 184). a) $Pd(OAc)_2$, CuCl, $Cu(OAc)_2$, 185, DMA, 120°C, 20h (33%). b) 1. 181, MeOH, 60°C to rt, 6 h. 2. PIDA, rt, 4 h (38%).

Additionally, a C-H activation has been explored in a small scale (55 mg of starting material) aiming at preparing the off-methyl analogue of **28** and clearly evaluate the methyl contribution on the photophysics (Scheme 3.12). The **BBT-08** good solubility in organic solvents along with the challenging **179** formylation encouraged us to design a further synthetic plan removing the methyl group and introducing an amino functionalization to bathochromically shift the optical properties. The presented approach showed to be highly versatile and robust, resulting in the successful preparation of all already previous-mentioned BBTs. It provides an up-scalable and straightforward method to prepare push-pull BBTs.

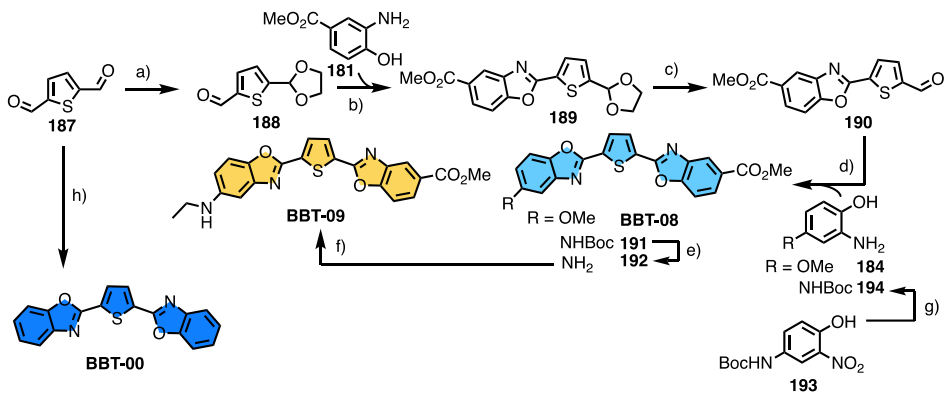

Scheme 3.13. a) Ethylene glycol, TsOH, toluene, 100°C, overnight (50%). b) 1. **181**, MeOH, 60°C, 6 h. 2. PIDA, MeOH, 4 h, rt (42%). c) TsOH, acetone, 70°C, overnight (92%). d) 1. **184**/**194**, MeOH, 60°C, 6 h. 2. PIDA, MeOH, 4 h, rt (BBT-08: 38%, 191: 37%). e) HCl (4 M) in dioxane, 6 h, rt (quant.). f) Acetaldehyde, $NaCN(BH_3)$, DCE, 40°C, overnight (28%). g) 1. $SnCl_2H_2O$, EtOH, 60°C, 1 h. 2.

$NaBH_4$, EtOH, rt, 2 h (24%). h) 1. 2-aminophenol, MeOH, 60°C, 6 h. 2. PIDA, MeOH, 4 h, rt (65%).

Since the **179** formylation resulted highly challenging in terms of purification, yield and regioselectivity, the last explored approach moves from a commercial thiophene already bearing two aldehyde groups on its two α-positions (**187**) – Scheme 3.13. The methyl group has been removed due to the low cost of the intermediate when compared to methyl-bearing one. The functionalized *semi*BBT **189** has been prepared by cyclization of the mono-protected carboxylaldheyde thiophene **188** with **181**. Then, a further acetal cleavage in acidic conditions provided the key intermediate **190** toward a wide range of BBTs. A robust reaction with differently substituted aminophenols (**195, 196, 197**) provided naked, methoxy and amino derivatives in moderate yields (43%). While **196** and **197** are commercially available, the amino derivative **195** has been prepared starting from the nitrophenol **193** that achieved the boc-protected BBT **191** upon further structural modifications. Lastly, one ethyl chain has been introduced in the system (**BBT-09**) to increase the solubility by reductive amination of acetaldehyde in presence of $NaCNBH_3$. **Error! Reference source not found.**clearly shows the high v ersatility of the reported cyclization of aminophenols with aromatic aldehydes to afford benzoxazoles. The reaction performs well when both accepting (e.g., methyl ester in step *a)*) and donor groups (e.g., methoxy in step *b)*) are involved into the aminophenol π-system. In addition, after the cyclization, the BBT precipitates pure from the reaction mixture avoiding any critical and solvent-consuming chromatographic steps.

The methyl ester has been introduced as electron-withdrawing moiety since it can be easily converted into a high number of accepting motifs (e.g., aldehydes, cyano). In the future, analogously to what reported in Scheme 3.11, a series of reduction and oxidation reactions might be

useful to insert a cyanoacetic group able to still increase the dipole moment providing, at the same time, a reactive carboxylic group to further introduce a smart bioconjugation moiety.

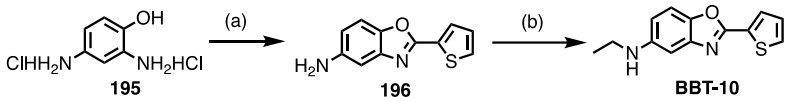

Scheme 3.14. a) Thiophene-2-carboxylic acid, PPA, 180°C, 5 h (18%). b) Acetaldehyde, $NaCNBH_3$, DCE, rt, overnight (56%).

In addition, one small dye (namely, **BBT-10**) has been prepared during this last investigation (**Scheme 3.14**). The aminoderivative **196** was prepared by cyclization between **195** and the thiophene-2-carboxylic acid in strong dehydrating conditions affording in low yield the desired product. The introduction of an ethyl chain by reductive amination of the acetaldehyde improved the solubility of the scaffold, affording the **BBT-10** in moderate yields.

Photophysical properties

The first BBT generation shows a bright green emission, with excellent PLQYs making them interesting candidates for the high-energy part of the spectrum in bio-HLEDs (Figure 3.21**A**). The low solubility along with the high aggregation prominence undermined their up-scaling and led us to prepare a new generation of more soluble BBTs.

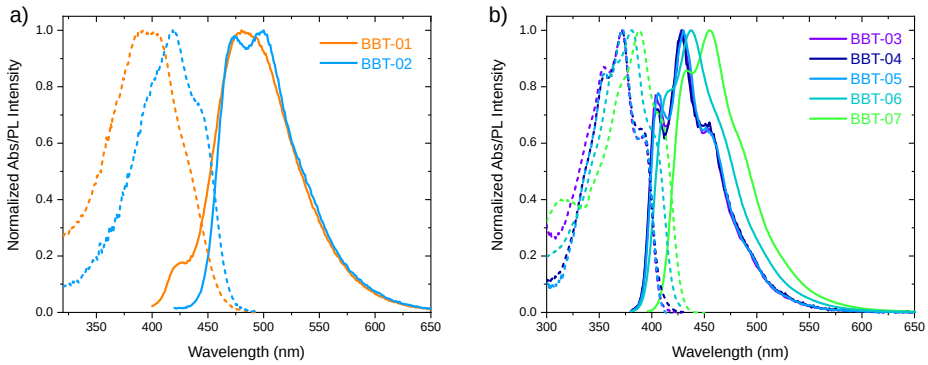

Figure 3.21 Emission (solid) and absorption (dashed) spectra of BBT first (a) and second (b) generation in toluene solution. Data are normalized at the maximum intensity.

BBT-03, **BBT-04** and **BBT-05** exhibit a remarkable blue emission centered at 428 nm with outstanding PLQY values (Table 3.12). The aggregation reduction and the solubility enhancement lead to a fine vibronic structure appearance both in absorption and emission spectra (Figure 3.21B). Additionally, any solvent dependence has been detected, preserving the blue emission in all the investigated systems.

Table 3.12 Photophysical parameters of BBTs in toluene solution.

Compound	λ_{abs} (nm)	λ_{em} (nm)	Stokes shift (cm^{-1})	PLQY -
BBT-01	390	480	4808	0.80
BBT-02	415	500	4096	0.90
BBT-03	371	428	3590	0.86
BBT-04	371	428	3590	0.95
BBT-05	372	430	3626	0.95
BBT-06	380	446	3894	0.95
BBT-07	389	455	3729	0.95

Since the blue component in a white HLED is provided by the chip primary radiation, further structural modifications have been explored to further bathochromically shift the BBTs photophysics. In particular, electron donor and withdrawing groups have been placed on the two benzoxazoles edges aiming at increasing the dipole moment and red-shifting the emission profile. Although a shift has been clearly observed comparing **BBT-03** and **BBT-07** as a result of our expectations, this red-shift is not necessary to reproduce the remarkable optical features of **BBT-01** (Figure 3.22**A**). The two-electron donor and withdrawing moieties do not contribute enough to increase the dipole moment, suggesting that the lack of π-conjugation along the emitters axis might not allow the creation of a push-pull system.

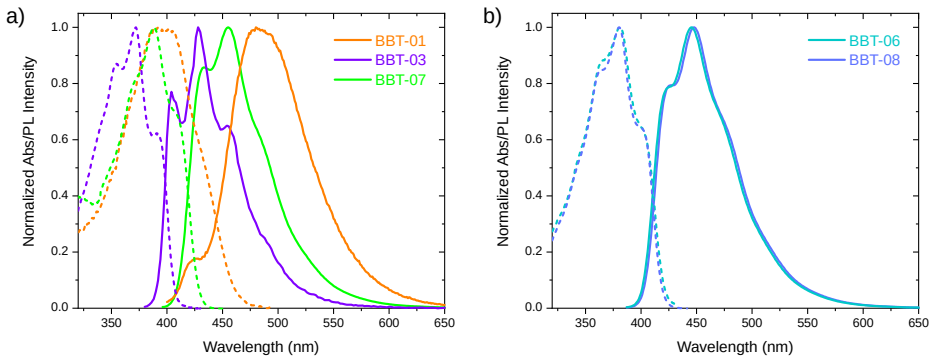

Figure 3.22 Absorption (dashed) and emission (solid) spectra in toluene solution of different BBTs. (a) The dipole moment increase in **BBT-07** allows to batochromically shift the **BBT-03** emissive properties, but still in the blue region. (b) The methyl group has not influence on the BBTs photophysics and solubility.

As a proof of the methyl effect on the fluorophore planarization, **BBT-06** and **BBT-08** photophysics have been compared (Figure 3.22**B**). The spectroscopic results surprisingly evidenced the same optical features for both emitters, along with a remarkable solubility in several organic

solvents even in the **BBT-08**, suggesting a marginal role of the methyl group on the photophysics and supramolecular properties. All these properties when compared to the previous **BBT-02** allowed us to claim that a major role is played by the electronic effects of the benzoxazoles electron-donor substituents rather than by the planarization degree induced by the groups on the thiophene β-position. These considerations have been proved by the photophysical investigation on the free-NH_2 bearing **192**. When an amino group serves as a donor moiety and a methyl ester as the electronic acceptor, the emission profile dramatically shifts in the yellow region of the spectra displaying a strong solvatochromic behaviour (Figure 3.23A). Additionally, dual emission strongly dependent on the local environmental polarity has been observed. A first transition is centered around 430 nm, not sensitive to the solvent and showing a well-defined vibronic structure, similar to the observed one for the previous BBTs (excluding **BBT-01** and **BBT-02**). Then, a second charge-transfer (CT) band has been observed, highly influenced by the local polarity. The CT band strongly moves from 520 nm in toluene up to 632 nm in acetonitrile, while its relative intensity drops significantly upon increasing the solvent polarity. A figure-of-merit (I_{blue}/I_{CT}) has been defined as the ratio between the blue-band and the CT intensities and plotted against the solvent polarity (Figure 3.23B) The plot highlights how the CT band intensity strongly decreases upon solvent polarity increase.

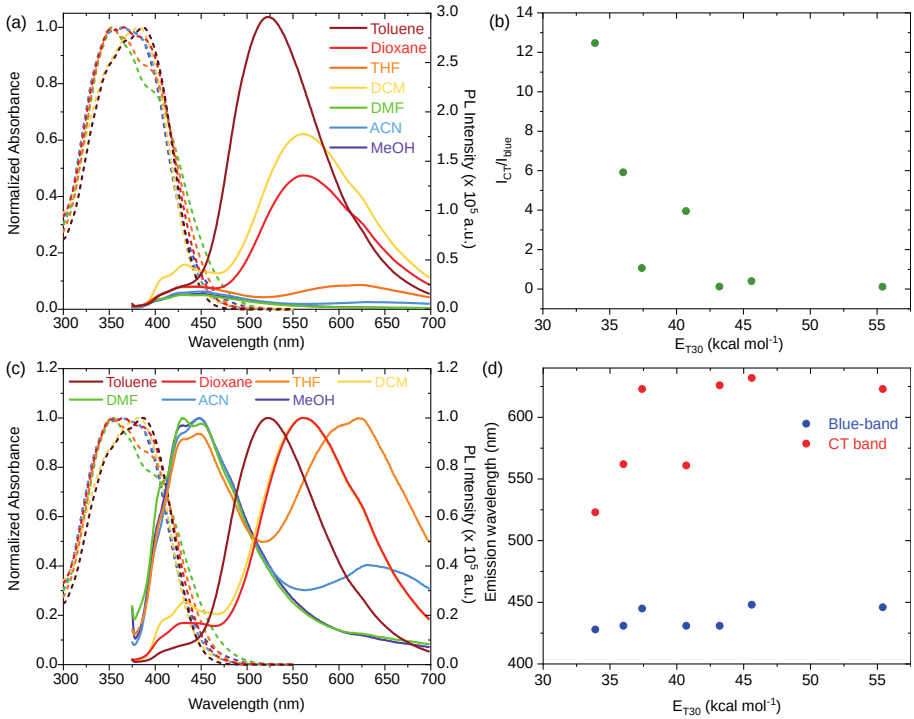

Figure 3.23 a) Absorption (dashed) and emission (solid) spectra of **192** in several organic solvents. Absorption spectra have been normalized at maximum absorption wavelength, while the emission spectra have been normalized at 0.1 absorbance at the excitation wavelength. b) Plot of the ratio of the intensities of blue-shifted band and the charge transfer band against the solvent polarity. (c) Absorption (dashed) and emission (solid) spectra of **192** in several organic solvents. All spectra have been normalized at their maximum. (d) Emission wavelength dependance on the solvent polarity for both the observed bands. The blue band results to be almost unsensitive to the polarity, while the CT band is strongly dependent on the solvent at lower polarity, while reaches a plateau value upon polarity increasing.

This drop is accompanied by quenched PLQY values in case of polar solvents, e.g. DMF, acetonitrile, MeOH (Table 3.13)**.** The anomalous DCM behaviour may be rationalized by the high contribution of the polarizability, peculiar of this particular solvent.[236]

Table 3.13 Solvatochromic properties of the free-NH_2 intermediate **192**.

Solvent	λ_{abs}	λ_{blue}[a]	λ_{CT}[b]	I_{CT}/I_{blue}[c]	Stokes shift	PLQY
	nm	*nm*	*nm*	-	*cm^{-1}*	-
Toluene	387	428	523	12.47	6719	0.75
Dioxane	365	431	562	5.92	9604	0.37
THF	366	445	623	1.07	11271	0.10
DCM	382	431	561	3.95	8353	0.51
DMF	355	431	626	0.13	4967	0.04
ACN	365	448	632	0.40	5076	0.05
MeOH	366	446	623	0.12	4901	0.03

[a] Emission wavelength of the most blue-shifted band. [b] Emission wavelength of the red-shifted charge transfer band. [c] Ratio of the intensities of blue-shifted band and the charge transfer band.

Additionally, the introduction of an ethyl chain (**BBT-09**) increased the solubility of the system, without significantly affecting the photophysical properties (Figure 3.24). A dual emission is still clearly visible, while the ratio I_{blue}/I_{CT} is reduced compared to **192**, although the same trend is reproduced. The ratio decreases along with the PLQY upon increasing the solvent polarity.

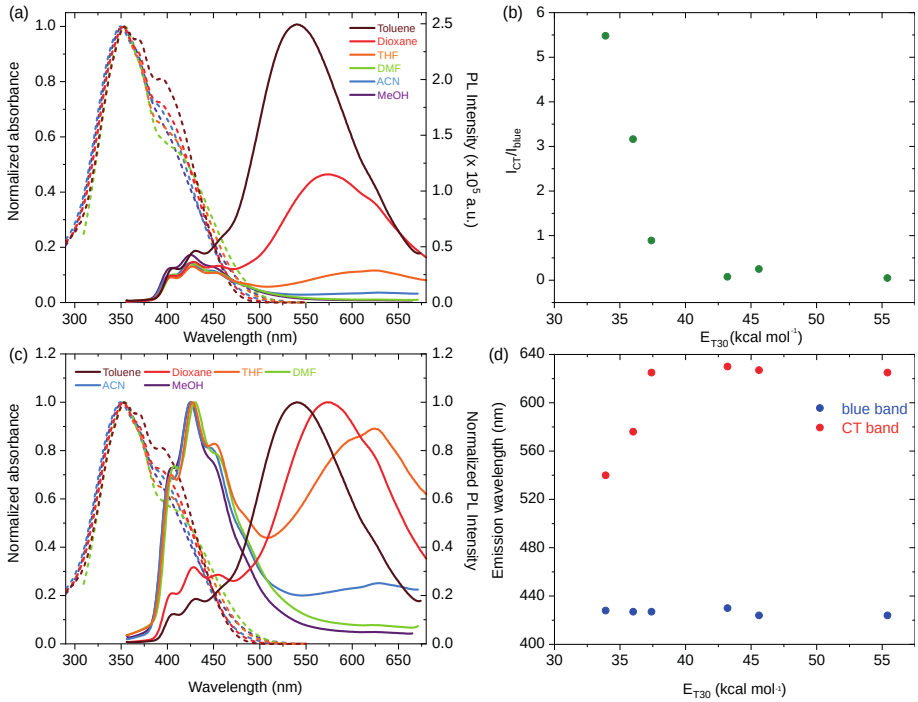

Figure 3.24 a) Absorption (dashed) and emission (solid) spectra of **BBT-09** in several organic solvents. Absorption spectra have been normalized at maximum absorption wavelength, while the emission spectra have been normalized at 0.1 absorbance at the excitation wavelength. b) Plot of the ratio of the intensities of blue-shifted band and the charge transfer band against the solvent polarity. (c) Absorption (dashed) and emission (solid) spectra of **BBT-09** in several organic solvents. All spectra have been normalized at their maximum. (d) Emission wavelength dependance on the solvent polarity for both the observed bands. The blue band results to be almost unsensitive to the polarity, while the CT band is strongly dependent on the solvent at lower polarity, while reaches a plateau value upon polarity increasing.

This fluorogenic behaviour makes the BBTs remarkable as fluorescent probes, while, at the same time, their implementation in artificial fluorescent protein will allow to observe a bright yellow emission due to the hydrophobic environment of the binding pocket. Further modifications of the push-pull character should still increase the dipole moment of the system. The replacement of the methyl ester with aldehydes or cyano

moieties may further red-shift the CT band and increase the solvatochromic behaviour.

Table 3.14 Solvatochromic properties of **BBT-09**.

Solvent	λ_{abs}	λ_{blue}[a]	λ_{CT}[b]	I_{CT}/I_{blue}[c]	Stokes shift	PLQY
	nm	*nm*	*nm*	-	*cm^{-1}*	-
Toluene	354	428	540	5.48	9730	0.70
Dioxane	353	427	576	3.16	10968	0.34
THF	352	427	625	0.89	12409	0.07
DMF	354	430	630	0.08	4993	0.08
ACN	350	424	627	0.25	4987	0.08
MeOH	351	424	625	0.05	4905	0.06

[a] Emission wavelength of the most blue-shifted band. [b] Emission wavelength of the red-shifted charge transfer band. [c] Ratio of the intensities of blue-shifted band and the charge transfer band.

Lastly, once clearly stated the primary role of the amino functionality on the BBTs bathochromic shift, a small **BBT-10** has been prepared and characterized. A strong solvatochromic behaviour has been observed. The Stokes shift increases with the environment polarity, providing an emission able to span from blue, in hexane, to yellow, in acetonitrile or methanol (Figure 3.25). The small and compact shape makes **BBT-10** suitable for his accommodation into a small protein pocket.

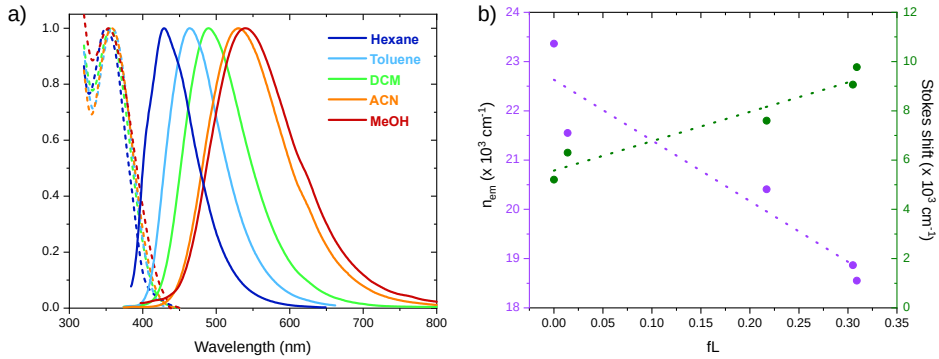

Figure 3.25 a) Absorption (dashed) and emission (solid) spectra of **BBT-10** in several organic solvents. b) Emission wavenumber and Stokes shift against the Lippert polarity parameters.

Implementation in LEC devices

(The results shown herein have been achieved during my abroad period spent at Costa's lab, TUM, Straubing)

During an abroad period spent at Costa's Lab in TUM – Campus Straubing, the use of two blue emitting BBTs – namely, **BBT-00** and **BBT-03** – has been investigated for the realization of light-emitting electrochemical cells (LECs). LECs represent a sustainable solid-state lighting technology, based on electroluminescent compounds. The organic materials have to be highly photo- and thermal- stable, electrochemically active and processable from solution. They are usually deposited on a PEDOT:PSS layer by spin coating, thus the ability of affording films with good morphologies represent a key-parameters in the development of efficient compounds for LECs. The **BBT-00** and **BBT-03** film morphologies have been deeply investigated in the presence of several electrolytes aiming at increasing the layer ion conductivity keeping the high PLQY. Despite the wide number of different conditions (Table 3.15), all the prepared films suffered of high tendency to crystallization.

As soon as the spin coating process ended, the BBTs showed to afford eye-visible crystals hampering the formation of a proper film.

Table 3.15 Screened electrolytes and solvents for the preparation of **BBT-00** and **BBT-03** films.

Electrolytes	Mass ratio	Solvents
Dye: PS: PEO: LiOTf	10: 0.2: 2.6: 0.78	THF, Anisole
Dye: CA: $THABF_4$	1: 0.2: 0.2	THF, Anisole, Toluene
Dye: $THABF_4$	1: 0.2	THF, Anisole, Toluene
Dye: TMPE: LiOTf	1: 0.15: 0.06	THF, Anisole
Dye: PEO: TMPE: LiOTf	1: 0.43: 0.15: 0.06	THF, Anisole
Dye:BMIM PF_6	4:1 (molar ratio)	THF, Anisole, Toluene

PS: polystyrene, PEO: polyethyleneoxide, CA: cellulose acetate, $THABF_4$: tetrahexylammonium hexafluoroborate, BMIM PF_6: butylmetyl imidaziolium hexafluorophosphate.

Thus, a different approach has been pursued by dispersing the dye in a PVK:PBD-based polymeric matrix. An energy transfer occurring from the polymeric PVK:PBD exciplex to the BBTs may activate their photoluminescent under device operating conditions. **BBT-00** displays an emission centered around 460 nm (Figure 3.26A), while the **BBT-03** aggregates shift the emission to 525 nm (Figure 3.26B) showing the typical fine vibronic structure already noticed in toluene solution (Figure 3.21B). Then, the two emitters have been dispersed in a PVK:PBD polymeric matrix in different percentages in weight. Three samples per each BBT have been prepared and optically characterized. The overlap between the **BBT-00** containing samples' excitation spectra and the only PVK:PBD's emission profile becomes significant above the 5% in weight, as clearly shown in Figure 3.26**C**. Although the same phenomenon is less pronounced probably due to a lower aggregation degree, the trend is still

confirmed in **BBT-03** samples (Figure 3.26D). Preliminary devices are reported implementing amount of BBTs > 5% to maximize the energy transfer between the organic emitters and the PVK:PBD exciplex.

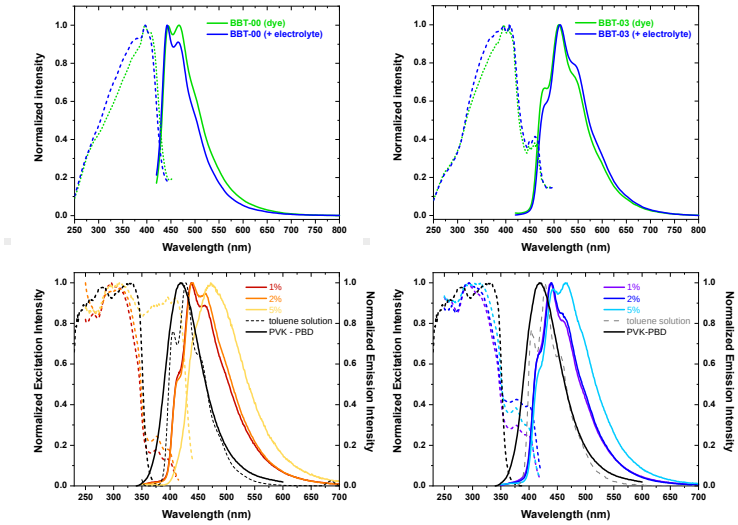

Figure 3.26 Top: Excitation (dashed) and emission (solid) spectra of **BBT-00** (left) and **BBT-03** (right) films. Bottom: Excitation (dashed) and emission (solid) spectra of **BBT-00** (left) and **BBT-03** (right) containing PVK-PBD samples. The percentages of emitters are expressed as weight ratio.

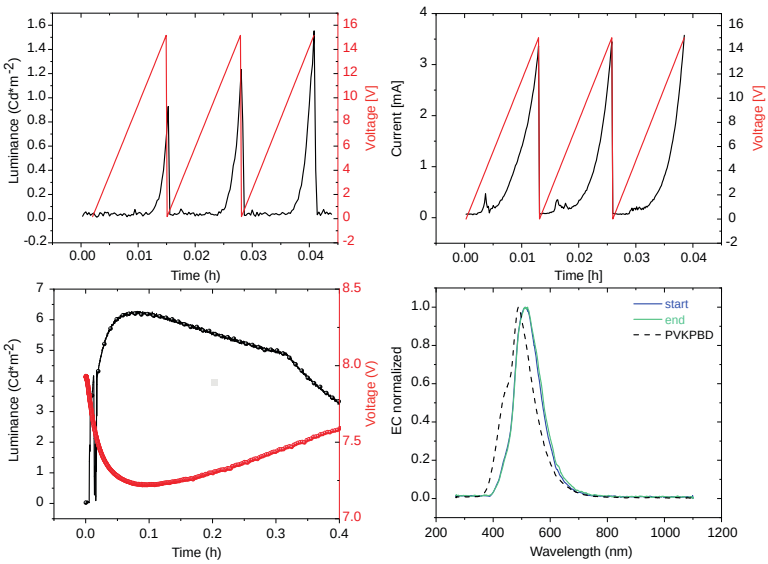

Figure 3.27 Implementation of the **BBT-00** in a PVK:PBD matrix (20% wt). Top: L-I-V- experiment. Bottom left: luminance decay and voltage over time, under 5 mA. Bottom right: electroluminescence (EC) profiles of the PVK:PBD matrix without **BBT-00** (dashed black line) and profiles of the matrix implemented with the **BBT-00** at the beginning at the device lifetime.

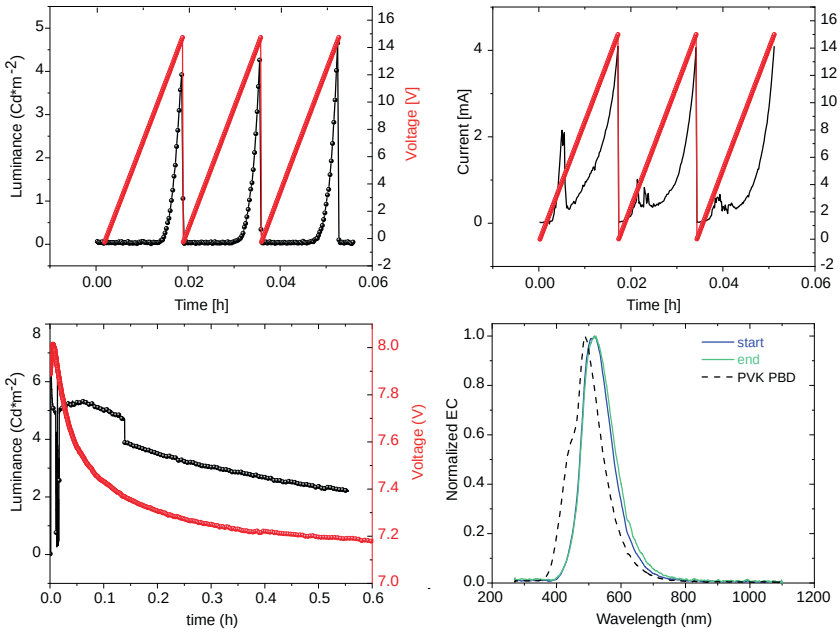

Figure 3.28 Implementation of the **BBT-03** in a PVK:PBD matrix (20% wt). Top: L-I-V- Experiment. Bottom left: luminance decay and voltage over time with a applied current of 5 mA. Bottom right: electroluminescence (EC) profiles of the PVK:PBD matrix without **BBT-03** (dashed black line) and profiles of the matrix implemented with the **BBT-03** at the beginning at the device lifetime.

Both devices (**BBT-00** and **BBT-03** based) show similar stabilities (LT_{50} *ca.* 0.5 h under 5 mA operating conditions) and both electroluminescence profiles are not affected by the compound degradation. As noticeable by the current profile during the LIV experiment, both devices suffer from bad film morphology negatively influencing the device lifetimes. In this sense, any conclusion can be claimed with respect to the two emitters structures. Further structural refining is required to improve the BBTs filming properties: the replacement of the **BBT-03** methyl group with longer aliphatic chains (e.g., hexyl, octyl) may help in this sense.

Implementation of BBTs in HLED devices

(The results shown herein have been achieved by ARTIBLED consortium at Costa's lab, TUM, Straubing)

BBT-01 polymer coatings (TMPE:PEO) showed a red-shifted emission (540 nm) with PLQYs of 70 % compared to those in solution. The photostability was studied under UV irradiation/ambient conditions, reaching a lifetime of *ca*. 25 h. Concerning **BBT-01** and **BBT-03,** they show interesting photophysical properties ranging from blue to yellow emission with high PLQYs of *ca*. 75% in polymer coating, but their photostability is not suitable yet for LED application (<1 h upon UV irradiation, 200 mA, on chip). Thus, further structural modifications are needed. The **BBT-09** implementation will be carried out aiming at improving the photostability and LED performances.

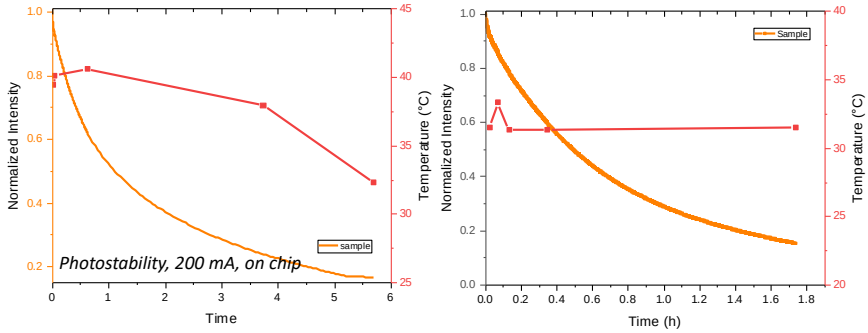

Figure 3.29 Photostability (200 mA, on chip architecture) of **BBT-01** (left) and **BBT-03** (right) in HLED.

After several synthesis trials, **BBT-10** was embedded in TMPE:PEO and PMMA:TMPE matrices in low and high amounts **–** Figure 3.30. Although the emission is tunable in a range 480-550 nm according to the hosting matrix, the photostability under 380 nm irradiation at 200 mA of applied current was found to be ~1 h at its best (Table 3.16).

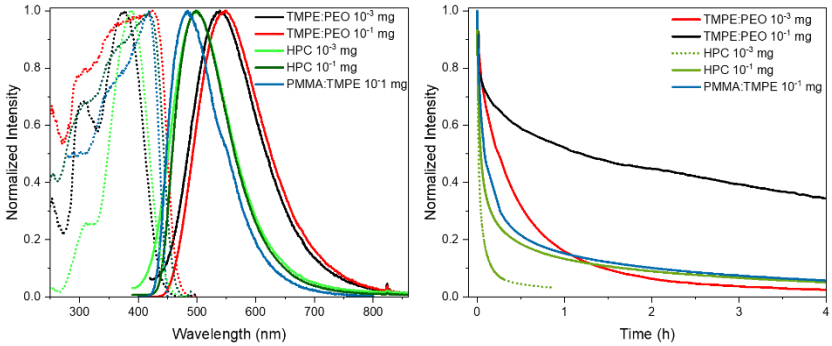

Figure 3.30 Left: excitation and emission spectra of **BBT-10** in low and high amount hosted in TMPE:PEO, HPC and PMMA:TMPE matrices. Right: photostability decay profile of **BBT-10** coatings (low and high amount) based on TMPE:PEO, HPC and PMMA:TMPE matrices (380 nm irradiation, 200 mA).

Table 3.16 Characterization and stability data of **BBT-10** in polymeric coating.

Matrix	Amounts	PLQY [%]	τ [ns]	L_{50}[a]
PEO	10^{-3} mg	27	6.37	12 min
	10^{-1} mg	38	6	1h10 min
PMMA	10^{-1} mg	75	8.27	5 min

a Irradiation with 380 nm LED at 200 mA, on chip.

BBTs: conclusions and future perspectives

The work presented herein has been mainly focused on the design, synthesis and photophysical characterization of a novel class of emitters. The few reported data in literature lack a precise correlation between the molecular structure and the photophysical features. The large discussion provided during this section allowed to shed light on this key-relationship, enabling the preparation of fluorophores able to span from the blue to the yellow region of the visible spectrum with excellent PLQYs values (Figure 3.31). Although the few reports on BBTs analogues show mainly blue and green emission, the effects of the substituents on both β-thiophene positions and benzoxazoles edges have been extensively studied,

identifying in the creation of a push-pull system the only proper way to red-shift the optical features.

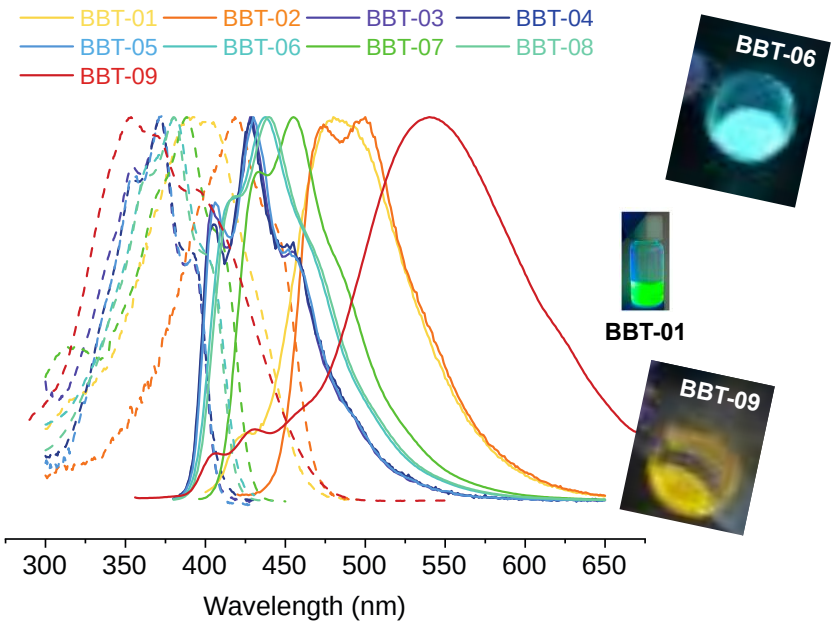

Figure 3.31 Absorption (dashed) and emission (solid) spectra of several BBTs prepared within this work. All data are shown in toluene solution.

Additionally, only preliminary studies have been carried out to identify the BBTs possible applicative fields. While some blue emitting candidates (**BBT-00**, **BBT-03**) have already been preliminary implemented in LECs, they still require further structural refining to improve the filming properties. The green/yellow BBTs (**BBT-09**, **BBT-10**) are currently being investigated for the realization of AFPs and bio-HLEDs.

3.1.7. Conclusions

The work carried out in this first part allowed to combine the tailored organic synthesis with the beneficial effect of a properly designed protein scaffold. In this way, the low-cost and fine optical tunability of the LED emitters have been supported by an enhanced photo/thermal stability and

reduced aggregation-induced emission quenching phenomenon through the action of the protein shield. As first exploitable results, we have demonstrated that **LmrR/S** is a nice candidate to fabricate white Bio-HLEDs featuring luminous efficiency of 55 lm/W and stabilities of < 500 h using 10 mW/cm^2 excitation.

Additionally, other blue-green and yellow candidates have already been identified (TTZ and BTD, respectively) due to their moderate photostability and excellent photophysical properties. Based on LmrR-s results, their implementation in AFPs will pave the way for the realization of a long-living and efficient white bio-HLED.

3.2. Bright organic dyes as fluorescent membrane probes

The organic fluorophores accommodation inside a properly designed protein pocket proved to enhance the dyes photostability features, enabling their implementation in optoelectronic devices. Additionally, the interaction of similar fluorophores with bilayer membranes has been investigated. The photophysical traits perturbation upon intercalation within the membranes along with the dependence of the ground and excited states features on the membrane characteristics make the fluorescent probes a powerful diagnostic tool. Several crucial biochemical pathways (e.g., apoptosis) are usually accompanied by changing in membrane lipidic composition and in membrane tension. The use of smart fluorescent organic dyes allows to visually highlight these phenomena, monitoring the cellular health status and important biophysical parameters (e.g., hydration, membrane tension, fluidity).

Artificial unilamellar vesicles (also known as liposomes) have been used for studying *in vitro* membrane dynamics since they can act as membrane mimics. They are usually assembled by spontaneous self-organization from pure lipids or lipid mixtures in aqueous media upon several heating-cooling cycles. In this work, DOPC and DPPC have been used due to their ability of creating two differently packed lipidic phases. While the DOPC create a fluid and hydrated phase, the DPPC-based liposomes are more ordered and tightly packed, providing a more hydrophobic local environment inside the vesicle.

First, TTZ-based solvatochromic compounds have been tested to monitor the local membrane polarity, resulting in a remarkable emission profile shift upon variation of hydration and fluidity. Then, a focus on deep-red and NIR squaraine dyes is presented due to the paramount importance of having red-emitting stains for biological purposes. A fine structure-activity relationship has been clearly evidenced starting from the already

mentioned **S** squaraine, while novel perimidine-based squaraine dyes are reported along with a detailed investigation as membrane probes.

3.2.1. Solvatochromic thiazolothiazoles as polarizable fluorescent probes

The remarkable solvatochromic behaviour of **TTZ-02** presented in **Section 3.1.4** suggest the TTZ derivatives' ability to act as cell membrane probes. The fluorescence dependence on the local environmental polarity might allow to discriminate between the different lipidic phases and evaluate the correct functioning of many crucial biochemical pathways (e.g., apoptosis, lipid rafts). Some intermediates (**156**, **157**) already prepared for the TTZ-based phosphors in bio-HLEDs have been tested. In contrast, a not-substituted TTZ (**197** – Figure 3.32) has been designed as a negative control due to the lack of electron-withdrawing and donor groups on the edges. The four compounds shown in Figure 3.32 have been optically characterized and tested in LUVs vesicles, resulting in a powerful tool for the different lipidic phases discrimination.

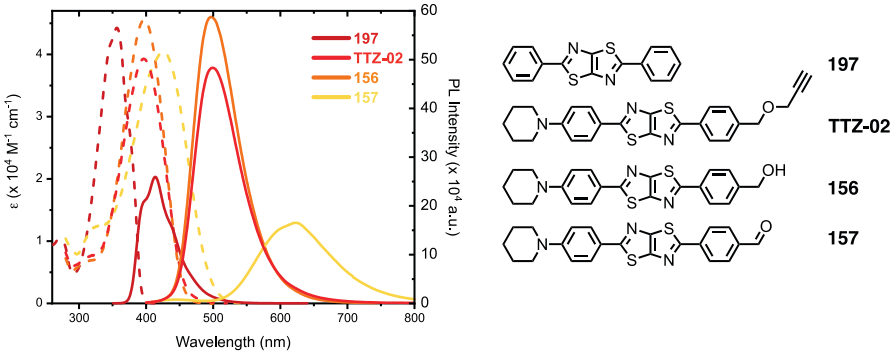

Figure 3.32 Chemical structures along with their absorption (dashed) and emission (solid) spectra in DCM solution. The emission spectra were normalized to 0.1 intensity at the excitation wavelength.

Photophysical characterization

As shown in Figure 3.33, **197** is the less solvatochromic probe as expected by the lack of electron-withdrawing and donating groups on the two sides of the conjugated system. Blue emission of **197** is centered around 410 nm with a PLQY value of ~ 0.30 for almost all the investigated solvents.

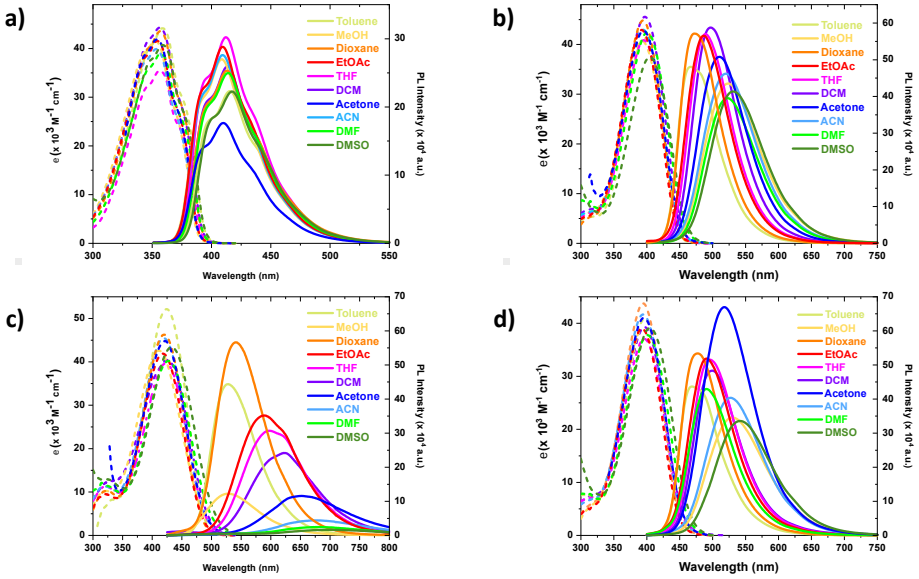

Figure 3.33 Absorption (dashed) and emission (solid) spectra of probes a) **197**, b) **156**, c) **157**, d) **TTZ-02** in different solvents. Emission spectra are normalized to 0.1 intensity at excitation wavelength.

Photophysical features batochromically shift due to the electronic effects of the substituents introduced for probes **TTZ-02**, **156, 157**. In particular, **156** exhibits high PLQY values (> 0.70 for all the investigated solvents) and an increased solvatochromic behaviour when compared to **197**. The green emission in THF or toluene becomes yellowish when the probe is dissolved in DMSO or in ACN, highlighting an increased dipole moment and the presence of a push-pull character even despite the lack of a

strong accepting group on one side. Emission maximum shifts from 466 nm in toluene (polarity of 0.014 according to the Lippert scale) to 531 nm in DMSO (polarity of 0.264 according to the Lippert polarity scale). Photoluminescent quantum yields remain extremely good even with solvents leading to large Stokes shifts (e.g., DMSO, ACN, DMF, MeOH) - Table 3.17.

When the aldehyde is introduced as an electron-withdrawing group in **157**, the emission profile red-shifts when compared to **156,** and the push-pull character dramatically increases, affording the most solvatochromic compound within the prepared probes library. Emission maxima shift from 527 nm in toluene up to 697 nm in the polar DMSO, causing a naked-eye visible change in emission colour from yellow to red. PLQY is moderate in aprotic apolar – or slightly polar - solvents (e.g., toluene, DCM, THF, dioxane), while rapidly lowers upon solvent polarity increase (DMSO, DMF, ACN). Finally, the optical features of **TTZ-02** are similar to **156** ones, as expected. The terminal alkyne is not conjugated with the fluorophore π-system, not affecting the photophysical parameters of the core. Slight changes might be attributed to the lack of the hydroxyl group that could interact with solvents by hydrogen bonding and non-covalent interactions different from those exhibited by the ether **TTZ-02**. Thus, remarkable photophysical features are successfully maintained, and this probe can be used as a covalently bound fluorescent tag.

Table 3.17 Photophysical parameters of TTZ-based probes in several organic solvents

Solvent	λ_{abs} (nm)	ε ($M^{-1}cm^{-1}$)	λ_{em} (nm)	Stokes shift (cm^{-1})	PLQY -	Brightness ($M^{-1}cm^{-1}$)
			197			
DCM	357	44973	414	3857	0.29	12862

Toluene	359	44144	415	3759	0.17	7472
MeOH	353	41424	409	3879	0.23	9437
THF	357	36616	412	3739	0.31	11482
ACN	353	39832	409	3879	0.26	10541
Dioxane	356	40611	413	3877	0.38	15308
EtOAc	354	41009	409	3799	0.29	11970
DMF	357	38628	414	3857	0.27	10523
Acetone	354	41959	410	3858	0.19	7983
DMSO	359	38413	417	3874	0.27	10234
			156			
DCM	398	48195	497	5005	0.88	42242
Toluene	396	40766	466	3793	0.76	30864
MeOH	393	41536	524	6361	0.73	30361
THF	395	43576	489	4867	0.80	34841
ACN	396	43198	520	6022	0.72	30935
Dioxane	394	44121	472	4194	0.75	32956
EtOAc	393	43393	487	4911	0.79	34372
DMF	401	42069	523	5817	0.72	30244
Acetone	395	45299	510	5709	0.77	34926
DMSO	406	36953	531	5798	0.84	31151
			157			
DCM	425	40433	622	7452	0.39	15951
Toluene	425	51874	527	4554	0.68	35235
MeOH	411	42591	528	5392	0.14	5778
THF	423	41562	598	6918	0.52	21524
ACN	419	45496	677	9095	0.08	3492
Dioxane	421	45996	540	5234	0.67	30590
EtOAc	418	42638	590	6974	0.52	22183
DMF	428	39556	679	8637	0.06	2481
Acetone	422	46553	652	8359	0.19	9048
DMSO	433	41980	697	8747	0.05	1997
			TTZ-02			
DCM	396	42016	499	5212	0.76	31803
Toluene	397	39866	468	3821	0.70	27988
MeOH	393	40027	530	6577	0.59	23778
THF	396	40121	495	5051	0.77	30873

ACN	394	41914	527	6405	0.68	28305
Dioxane	395	42805	476	4308	0.77	32842
EtOAc	393	39623	491	5079	0.76	29991
DMF	401	37284	532	6141	0.72	26726
Acetone	395	41711	518	6011	0.84	35072
DMSO	405	38511	542	6241	0.72	27852

[a]PLQY was calculated referring to Coumarine153 (φ = 0.38 in EtOH, λ_{ex} 420 nm). All photophysical values reflect the average of three independent measurements.

The Stokes shift dependence on the solvent polarity was investigated and Lippert, Bakhshiev and Kawsky-Chamma-Viallet plots are shown in Figure 3.34. As stressed by the normalized emission spectra (Figure 2.8), the Stokes shift strongly depends on the solvent polarity. The three plots report a linear fit of the Stokes shift (or the semisum of the absorption and emission wavenumber) with the polarity of the solvents defined as Lippert, $\boldsymbol{f_L}$, or Bakhshiev, $\boldsymbol{f_B}$, parameters (or the Kawsky parameter, $\boldsymbol{f_K}$). All parameters used and their calculation is reported in the Experimental Section.

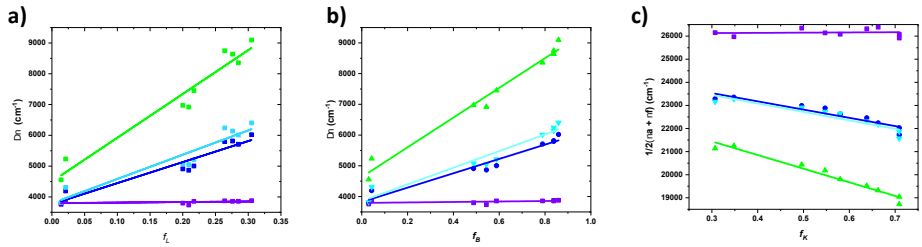

Figure 3.34 Lippert (a), Bakhshiev (b) and Kawski-Chamma-Viallet (c) for **197** (purple), **156** (blue), **157** (green), **TTZ-02** (light blue).

The linearity observed for **197, 156, 157** and **TTZ-02** highlights the fluorophores' ability to respond to the surrounding polarity changes, making them suitable candidates as cell membrane probes.

LUV experiments

Polarity-sensitive dyes present a shift in the emission maximum in response to changes in membrane hydration and solvent relaxation, thus, are widely used for probing lipid rafts. The behaviour of TTZ-based compounds **197, 156, 157** and **TTZ-02** was studied in two different model lipid vesicles to assess their ability to explore lipidic organization. The excitation and emission spectra of TTZ-based compounds were recorded in two large unilamellar vesicles (LUVs), 1,2-dioleoyl-*sn*-glycero-3-phosphocholine (DOPC) and 1,2-dipalmitoyl-*sn*-glycero-3-phosphocholine (DPPC). To evaluate the incorporation of the compounds in the bilayer, kinetics studies were carried out by monitoring the emission at different times. As shown in Figure 3.35 and Figure 3.36, the emission maximum of each compound increases over time. At t_0 the probes experience an aqueous environment, thus molecular aggregation occurs and no emission is recorded. Fluorescence intensity incrementally increases towards the equilibration time, suggesting the incorporation of all of them in both LUV

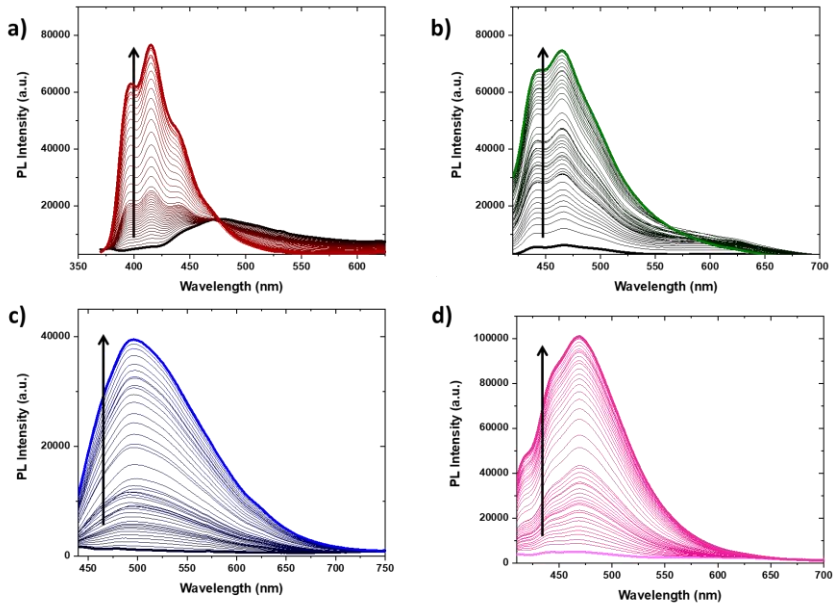

Figure 3.35 Kinetics studies in DPPC for probes a) **197**, b) **156**, c) **157** and d) **TTZ-02.**

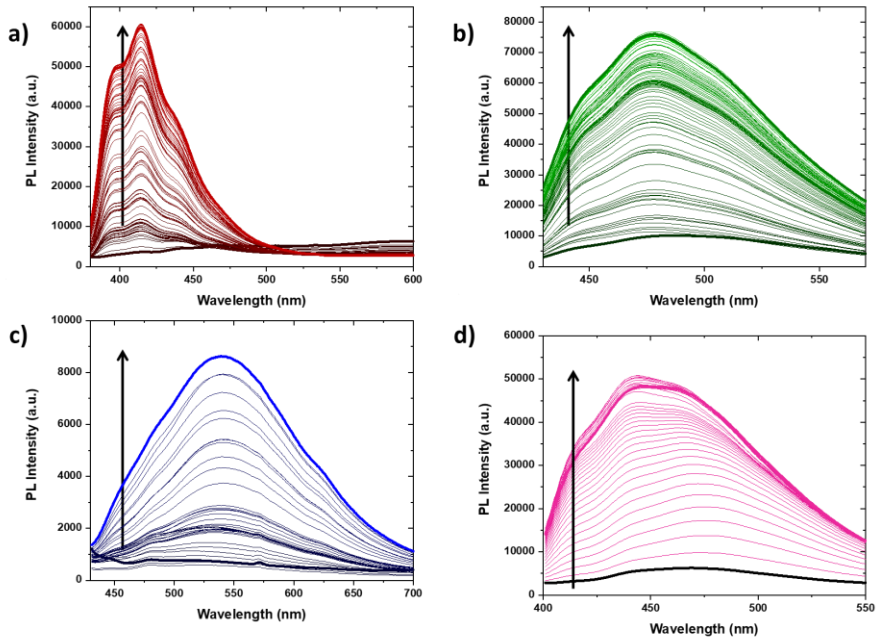

Figure 3.36 Kinetics studies in DOPC for probes a) **197**, b) **156**, c) **157** and d) **TTZ-02**.

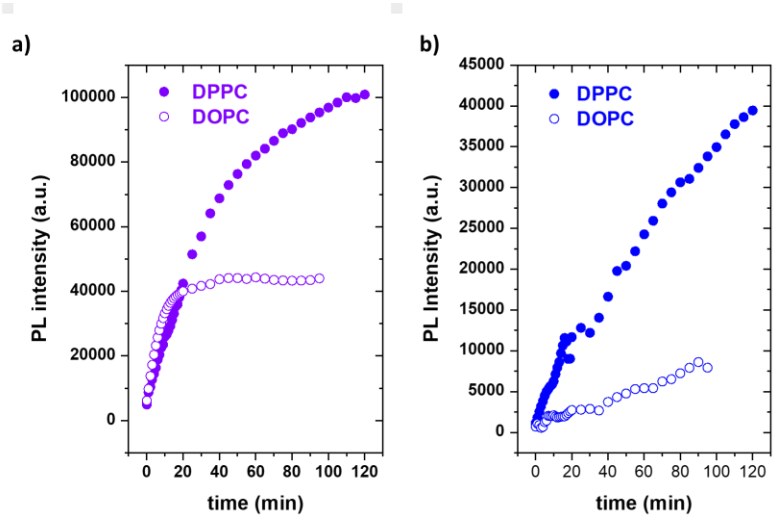

Figure 3.37 Plot of emission versus time for **TTZ-02** a) and **157** b) in DPPC and DOPC.

As, shown in Figure 3.37, both probes **157** and **TTZ-02** exhibit a faster incorporation in DOPC vesicles, while in DPPC a slower signal increase is shown. On the other side, DPPC reaches a higher intensity value at the equilibration time for both compounds. This phenomenon may be attributed either to a higher PLQY value in the DPPC system or to a higher number of probe molecules internalized into the vesicles. Further analyses are necessary to investigate both the hypotheses.

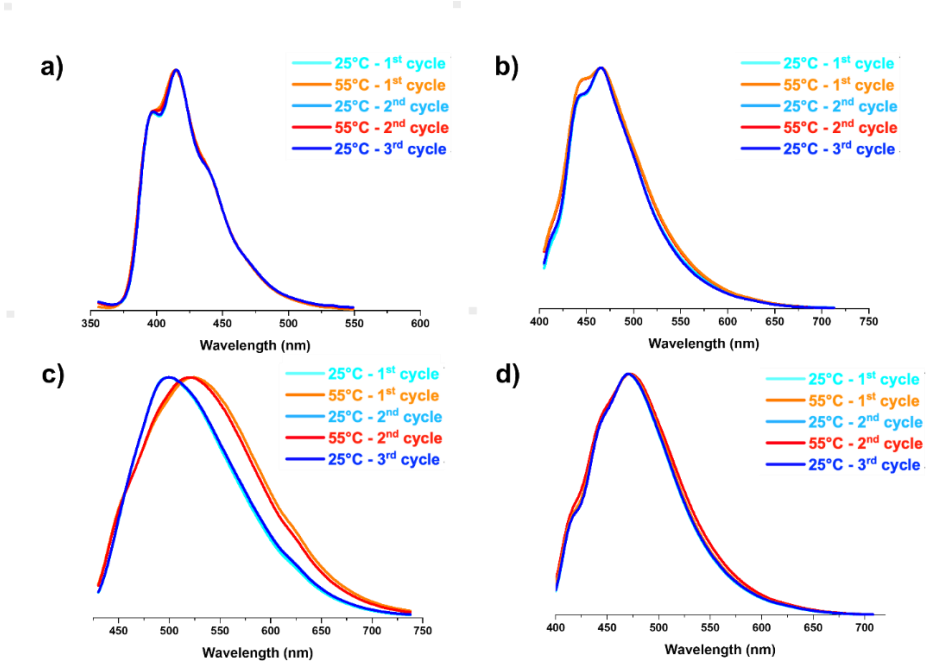

Figure 3.38 Normalized emission spectra of probes a) **197**, b) **156**, c) **157** and d) **TTZ-02** in DPPC vesicles at 25°C and 55°C for several heating–cooling cycles.

Then, after having determined the equilibration time for all the prepared compounds, they were added to DPPC-based large unilamellar vesicles (LUVs) and temperature-dependence experiments were carried out. DPPC LUVs undergo to phase transition from gel to fluid phase $L_\beta \rightarrow L_\alpha$ at 41°C. Thus, the samples were subjected to heating–cooling cycles (from 25°C to 55°C) and the emission was acquired. As shown in Figure

3.38, no significant shifts were recorded for compounds **197**, **156** or **TTZ-02**.

On the other hand, when **157** is incorporated in DPPC membranes, an important redshift in emission is recorded during $L_\beta \rightarrow L_\alpha$ phase transition, which means substantial hydration increases in DPPC bilayers. At 25°C, the emission maximum of **157** was located at 474 nm. The temperature increase led to phase transition, causing the shift to λ_{max}= 498 nm, with a $\Delta\lambda$ = 24 nm, which suggests that **157** molecules experienced a more polar environment. The solvation relaxation explains this redshift. Part of the excited-state energy of 157 is utilized to reorientate the surrounding water dipoles, reducing the singlet excited state (S1) energy of the probe and resulting in the redshifting of the emission spectrum. As temperature decreases, the maximum emission shifts to shorter wavelengths (λ_{max} = 474 nm), indicating that **157** molecules experienced a hydrophobic environment (Figure 3.38**C**). More tightly packed lipid environments such as DPPC in the Lβ phase (25°C) accommodate a lower number of water molecules, which means a lower polarity than a disordered environment. In L_β phase (25°C), the excitation spectrum of **157** is redshifted, with a maximum of around 415 nm and displays a second excitation band with a maximum of about 388 nm. This second blueshifted band increases its intensity along with temperature, resulting really intense in L_α phases. The presence of different isosbestic points could be tentatively explained by the presence of two species, a planar and a twisted conformation of the probe, which undergoes reversible interconversion. Both the species are present in L_β and L_α phases. However, the contribution of the twisted one is higher in L_α, causing the enhanced blueshifted pick in the excitation spectrum. Viscosity increases from L_α to L_β. In L_β, the probe is in a more packed environment; thus, the molecule's rotation is more obstructed, resulting in the planarization of the molecule in lipid bilayers. In the Lα

phase, the probe can experience a more relaxed environment due to the system's hydration, allowing rotation to occur.

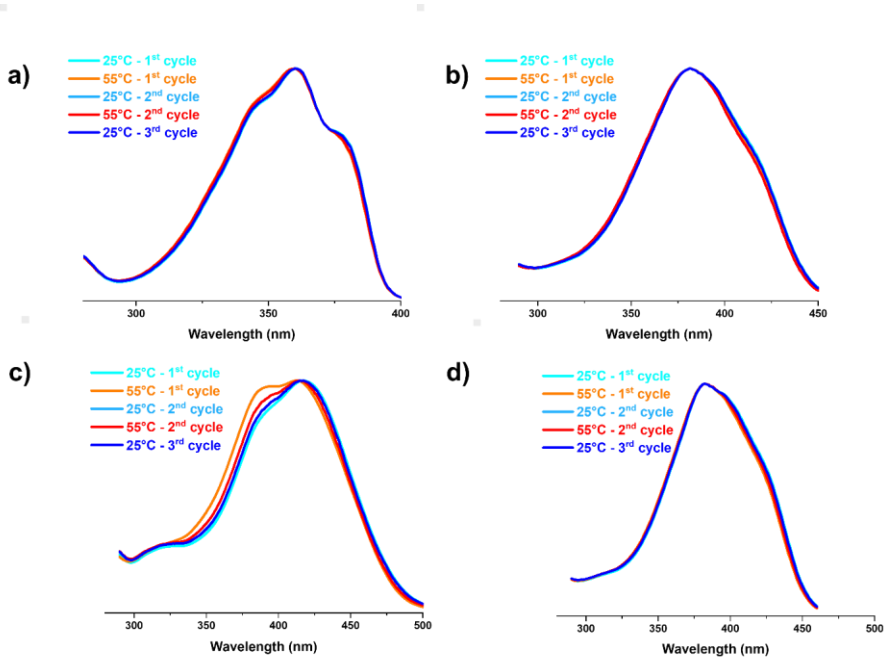

Figure 3.39 Normalized excitation spectra of probes a) **197**, b) **156**, c) **157** and d) **TTZ-02** in DPPC vesicles at 25°C and 55°C for several heating–cooling cycles.

Then the four TTZ-based compound behaviour in DOPC was studied. The solutions were undergone to the same heating–cooling cycles (from 25°C to 55°C) and the emission was acquired. Unlike DPPC, DOPC membranes remain in the fluid phase also at 25°C, therefore the emission spectrum is not affected by changing temperature. For this reason DOPC vesicles have been used as negative control (Figure 3.40).

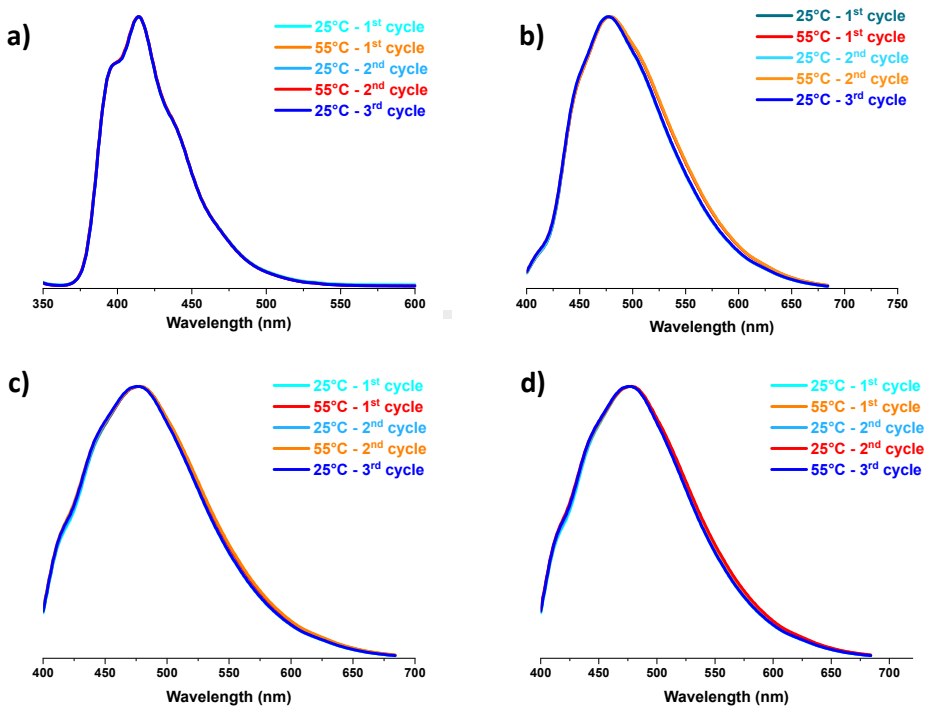

Figure 3.40 Normalized emission spectra of probes a) **197**, b) **156**, c) **157** and d) **TTZ-02** in DOPC vesicles at 25°C and 55°C for several heating–cooling cycles.

The difference in the lipid order (L_β or L_α) could be distinguished by using **156, 157** or **TTZ-02** as membrane probes. Unlike **197,** they present a shift in the emission spectra between DOPC and DPPC vesicles, as shown in **Figure 3.41**. The main change in λ_{max} is recorded for compound **157,** where emission maxima are located at 540 nm, 474 nm and 498 nm in DOPC, DPPC in the fluid phase and DPPC in the gel phase, respectively. These results conform to expectations; λ_{max} emission from L_β DPPC LUVs at 25°C is indeed similar to λ_{max} recorded in a hydrophobic environment during solvatochromic experiments, while the emission in L_α and DOPC results more redshifted due to the surrounding more polar environment. This property leads to a visible change of colour from green to yellow based on the lipidic order.

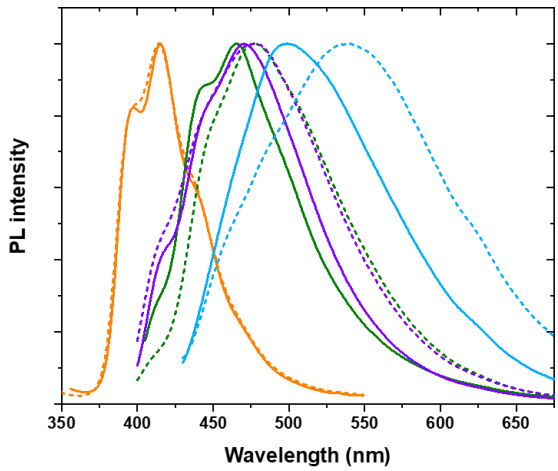

Figure 3.41 Emission spectra of compound **197**, **156**, **157** and **TTZ-02** in DPPC (solid) and DOPC (dashed) at 25°C.

Table 3.18 Emission maxima (in nm) of different probes upon interaction with DOPC and DPPC.

$\lambda_{em\ max}$ (nm) at 25°C				
Cpd	**197**	**156**	**157**	**TTZ-02**
DOPC	414	478	540	478
DPPC	415	465	474	475

Conclusion

As a proof of concept, this work provides the first example of solvatochromic TTZ derivatives as fluorescent cell membrane probes. The remarkable photophysical features (e.g., high Stokes shift and PLQY), along with the proper intercalation into the lipidic vesicles, highlight the suitability of these compounds to stain the cellular membrane visually. In particular, while hydroxyl and ether groups only slightly discriminate between DOPC and DPPC phases, the accepting aldehyde moiety strongly improves the solvatochromic behaviour, showing a bathochromic $\Delta\lambda$ *ca.* 66 nm when moving from the L_O to the L_d phases. A

further increase of the push-pull dipole moment (*e.g.,* replacement of the aldehyde with cyano groups) might still improve the staining abilities. Additionally, experiments in more complex liposomal models should be carried out before moving to living cell lines.

3.2.2. Imidazo[1,5*a*]pyridine-based fluorescent membrane probes

The results reported herein have been published in *Molecules* **2022**, *27*, 3856.

Imidazo[1,5-*a*]pyridine is a well-known and widely tested scaffold for the development of innovative compounds in several fields. It gained an increased attention during the last decades[237,238] as versatile moiety able to fulfill different requirements such as a compact shape, emissive properties, and photo/thermal stability among others.[239] The synthesis is straightforward and can be achieved by different approaches in an easily up-scalable manner.[240–243] Imidazo[1,5-*a*]pyridine compounds can be used as (i) candidates in medicinal chemistry;[244,245] (ii) ligands for a plethora of coordination complexes;[246,247] (iii) chemical sensors;[248,249] (iv) smart materials in optoelectronics;[239,250] and (v) fluorophores for bioimaging.[251,252]

To the best of our knowledge, any imidazo[1,5-*a*]pyridine had ever been tested in biological applications so far. The straightforward synthesis, the easily functionalization of the core with various groups (e.g electron donating or withdrawing moieties, hydrophilic or lipophilic groups) suggests broad range of applicability of this family of probes in the domain of chemical biology. Therefore, the present work aims to provide a preliminary evaluation of the biocompatibility and potential as membrane

fluorophores of a first generation of imidazo[1,5-*a*]pyridine probes rather than proposing novel dyes with feature comparable with commercially available probes. In this context, five emissive probes were prepared from the imidazo[1,5-a]pyridine scaffold: two monomeric units, **198** and **202**, and three dimeric products **199**–**201**, as reported in

Figure 3.42. The synthesis of the asymmetric bis-imidazo[1,5-*a*]pyridine **200** is herein reported for the first time along with the photophysical analyses in comparison with the corresponding symmetric analogs **199** and **201**. All of the prepared compounds were optically evaluated and the dimeric species were tested as fluorescent membrane probes using two different liposomal model systems as cell membrane mimics.

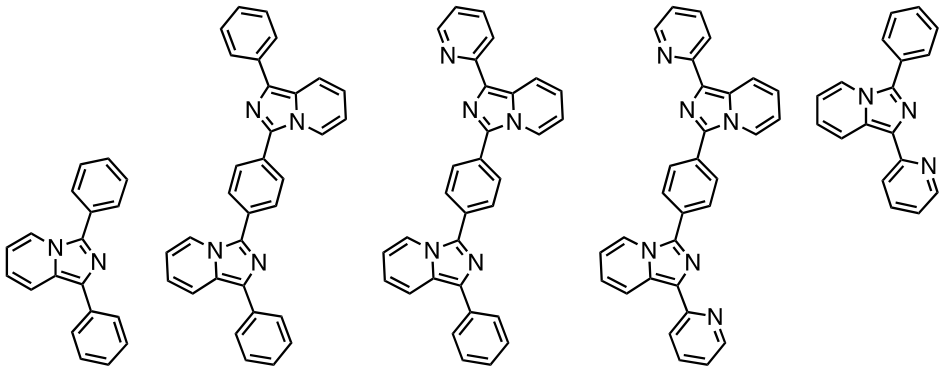

Figure 3.42 Chemical structures of compounds **198-202** explored within this work.

Synthesis

Products **198**, **199**, **201**, and **202** were synthesized by a direct cyclization of phenyl(pyridin-2-yl)methanone (**198** and **199**) or 2,2′-dipyridylketone (**201** and **202**) with different aromatic aldehydes in the presence of

ammonium acetate.[242,253–255] The heterocyclization was pursued in acidic conditions using the ammonium acetate as nitrogen source for the final ring closure as previously reported.[242] Varying the aromatic aldehydes in refluxing acetic acids provides easy access to a large number of both imidazo[1,5-*a*]pyridine and bis-imidazo[1,5-*a*]pyridine. Benzaldehyde reaction with diaryl ketones gives access to the mono-imidazo[1,5-*a*]pyridine products **198** and **202**. The replacement of the benzaldehyde with a bifunctional analogs as the terephthalaldehyde allows the preparation of the symmetic, **199** and **201**, and the asymmetric **200** bis-imidazo[1,5-*a*]pyridine derivatives. The symmetrical bis-imidazo[1,5-*a*]pyridines **199** and **201** were obtained by reacting either the phenyl(pyridin-2-yl)methanone or the 2,2′-dipyridylketone with terephthalaldehyde in stoichiometric ratio 2:1 (Scheme 3.15). To the best of our knowledge only the preparation of symmetrical bis-imidazo[1,5-*a*]pyridine compounds have been reported, following the above mentioned strategy or by varying the acidic environment (e.g., succinic, maleic, phthalic or trimesic acids)[256] for the dialdehydes (e.g., terephthalaldehyde and isophthalaldehyde).[257] The so obtained products could be considered alternative to polypyridine, polypyrrole, and polyimidazole behaving as promising multidentate scaffolds or ligands for organometallic and supramolecular design.

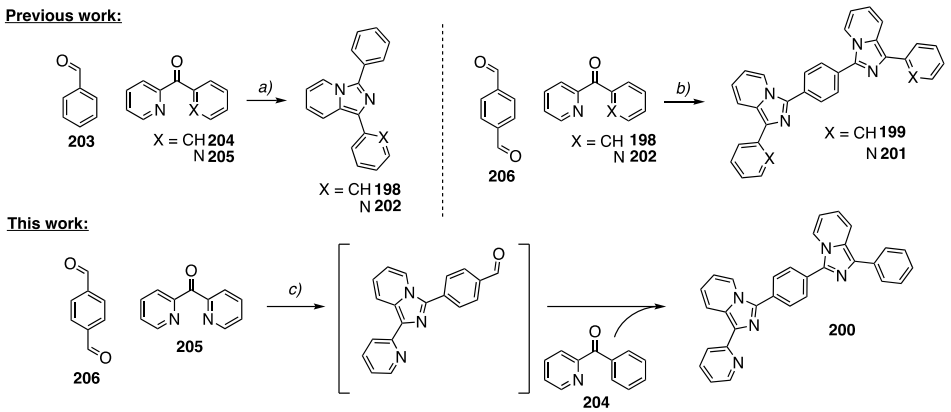

Scheme 3.15 Synthetic approach toward the prepared compounds. *a*) ammonium acetate, acetic acid, 110°C, 5 h (**198**: 78%, **202**: 80%); *b)* ammonium acetate, acetic acid, 118°C, 12 h (**199**: 96%, **201**: 96%); *c) 1.* ammonium acetate, acetic acid, 118°C, 6 h*; 2.* (phenyl(pyridin-2-yl)methanone, 118°C, 12 h (78%).

Herein, for the first time, the synthesis of the asymmetric bis-imidazo[1,5-*a*]pyridine product **200** is reported, by coupling the terephthalaldehyde with two different aryl ketones in a stoichiometric ratio 1:1:1. The present single step coupling of three components allows the introduction of different chemical groups to modulate the π-system features and the functionalization with electron rich or electron poor moieties by straigforward employment of di-aldehydes and substituted aryl ketones. More in detail, the unsymmetric scaffold **200** was obtained in a straighforward manner by promoting a first reaction over 6 hours in acetic media between the di(2-pyridyl)ketone and terephthalaldehyde followed by the addition of the phenyl(pyridin-2-yl)methanone, providing after 12 hours the final product as a yellow powder.

Optical features

The absorption and emission spectra of the whole series of probes were acquired in toluene and depicted in Figure 3.43**A**. While the emission spectra of all the compounds are centered around 480 nm, the absorption

maximum results batochromically shifted when moving from the monomeric species **198** and **202** to the dimeric ones **199**, **200**, and **201** due to an increased conjugation. The absorption band of the former is centered around 305–325 nm, while the latter one moves to 380 nm, gaining a more significant contribution in the visible range. As noticed by Volpi et al.,[256,257] the substitution of the benzene ring of **199** with a pyridinil group in **201** increases the quantum yield along with a bare blue-shift of the emission spectra. The preparation of the asymmetrical compound **200** confirmed the above considerations and highlights the possibility to tune the quantum yield value by modulating the number of the pyridine rings introduced in the scaffold. The solvatochromic features of all the reported probes were evaluated (Figure 3.43**B-E**) and are listed in Table 3.19. The highest PLQY for the dimeric compounds **199**–**201** were observed in apolar environments, such as toluene. The symmetric dipyridil analog **201** was characterized by a good PLQY of 0.38, which was three times more emissive than the dyphenyl analog **199** showing a PLQY of 0.12. The asymmetrical scaffold **200** shows an intermediate behaviour, with a PLQY of 0.18, in agreement with the above hypoteses. All the probes exhibited a wide Stokes shift, higher than 5000 cm^{-1}. In general, imidazo[1,5-*a*]pyridine derivatives are well known in the literature for a wide Stokes shift useful for different application such as down-shifting conversion.[258]

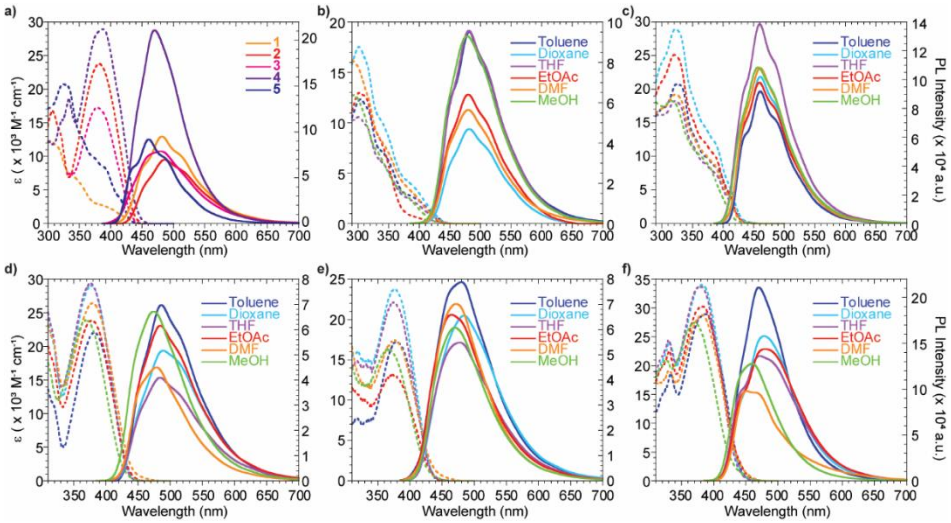

Figure 3.43 Photophysical properties of the reported probes **198–202**. (a) Absorption (dashed) and emission (solid) spectra of compounds 198–202 in toluene. (b–f) Absorption (dashed) and emission (solid) spectra in different solvents for compounds **198** (b), **202** (c), **199** (d), **200** (e), **201** (f). The emission spectra were normalized to 0.1 intensity at the excitation wavelengths.

Table 3.19 Photophysical properties of probes **198-202**.

Cpd	Solvent	λ_{abs} [nm]	ε [M^{-1} cm^{-1}]	λ_{em} [nm]	Stokes shift [cm^{-1} (nm)]	PLQY[a] -
198	Dioxane	300	17430	482	12586 (182)	0.10
	DMF	288	16280	480	13889 (192)	0.13
	Ethyl Acetate	302	12980	480	12279 (178)	0.14
	Methanol	293	12770	481	13340 (188)	0.13
	THF	301	10580	479	12346 (178)	0.17
	Toluene	305	12315	482	12040 (177)	0.20
199	Dioxane	377	29066	488	6033 (111)	0.11
	DMF	379	26470	479	5508 (100)	0.08
	Ethyl Acetate	375	30205	484	6006 (109)	0.08
	Methanol	370	23960	474	5930 (104)	0.10
	THF	379	23910	484	5724 (105)	0.11
	Toluene	382	23810	486	5602 (104)	0.12
200	Dioxane	376	23760	483	5892 (107)	0.13
	DMF	377	17430	471	5294 (94)	0.12

	Ethyl Acetate	375	22130	478	5746 (103)	0.11
	Methanol	368	16305	464	5622 (96)	0.08
	THF	374	13180	470	5461 (96)	0.09
	Toluene	378	16820	480	5622 (102)	0.18
201	Dioxane	380	33950	478	5395 (98)	0.29
	DMF	384	28660	451	3869 (67)	0.17
	Ethyl Acetate	379	33795	472	5199 (93)	0.24
	Methanol	369	27475	460	5361 (93)	0.15
	THF	384	30248	482	5295 (98)	0.26
	Toluene	383	28922	470	4833 (87)	0.38
202	Dioxane	322	28980	460	9317 (138)	0.13
	DMF	322	19240	461	9364 (139)	0.18
	Ethyl Acetate	326	24707	459	8888 (133)	0.16
	Methanol	313	18270	457	10067 (144)	0.16
	THF	319	18138	460	9609 (141)	0.19
	Toluene	325	20745	461	9077 (136)	0.17

All photophysical values reflect the average of three independent measurements. [a] Φ_F was measured referring to quinine sulphate as standard (φ_F = 0.546 in H_2SO_4 0.5 M, λ_{ex} 366 nm).

The monomeric species **198** and **202** showed negligible solvent effects on their optical features, due to the low charge-transfer character of the ground state.[256] The probes **199**, **200** and **201** highlighted a higher solvatochromic behaviour, as evidenced by the linear fit of the emission maximum wavenumbers against the E_{T30} polarity scale (Figure 3.44).

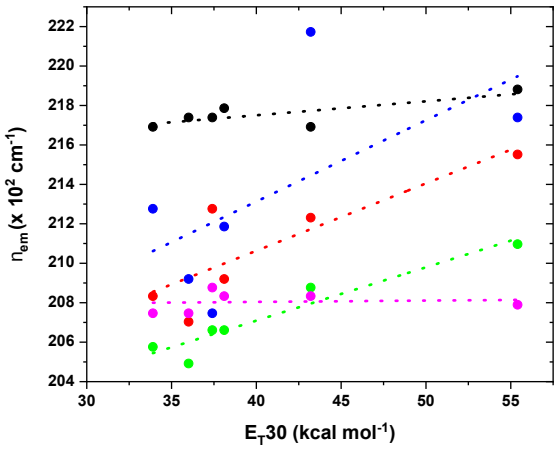

Figure 3.44 Emission wavenumber vs E_{T30} polarity scale for probe **198** (pink), **199** (green), **200** (red), **201** (blue), **202** (black).

Moreover, in a polar protic solvent as methanol, a clear hypsochromic shift of the emission maxima was present for all the bis-imidazo[1,5-*a*]pyridine derivatives. This effect was more remarkable in presence of one or two pyridine rings in **200** and **201**, most likely due to hydrogen bond interaction of the solvent with the aromatic pyridil nitrogen. These considerations highlight again the notable tunability of the optical features by simple modifications of the number of pyridine rings in the system.

Previously reported data on the imidazo[1,5-*a*]pyridines' lifetime shows uniformity with values spanning from 2 to 8 ns.[254] Compounds **198** and **202** have been previously investigated, revealing lifetime values of 5.8 and 4.6 nm, respectively. Similarly, eight multiple imidazo[1,5-*a*]pyridine derivatives have been previously reported showing similar values in a range of 2–7 ns, thus demonstrating a stringent uniformity in the lifetime data.[256] Additionally, the possible aggregation in water was evaluated for the dimeric compounds **199**–**201**, aiming to investigate the effects on the photophysical features. In this context, several measurements were carried out in THF with different amount of

water (Figure 3.45). The absorption spectra show a hypochromic effect when increasing the amount of water, along with a peak broadening that becomes more significant in pure water and with the 20% of THF. All the probes still exhibit a clear absorption peak in pure water, suggesting the presence of stable aggregates, while the emission of **199** and **200** is almost completely quenched. Moreover, the shape and position of the emission peaks are characterized by a bathochromic trend while increasing the amount of THF in water for all the investigated probes. This phenomenon highlights the fluorogenic character of these compounds, making them suitable candidates for applications as probes in biological systems. The fluorogenic behavior of a membrane probe can ensure low background noise with beneficial effects on the signal/noise ratio.

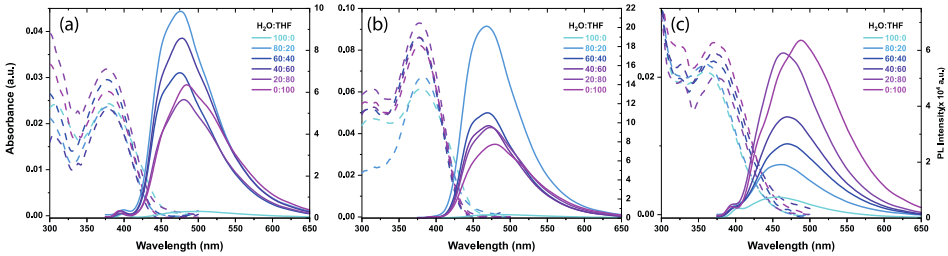

Figure 3.45 Absorption (dashed) and emission (solid) spectra of probes **199** (a), **200** (b) and **201** (c) in water and THF/water mixtures.

LUV experiment

Dimeric species **199-201** have been investigated as suitable candidates as fluorescent membrane probes due to their distinguished solvatochromic behavior and good PLQY in apolar environment compared to **198** and **202**. Several experiments were carried out on **199**, **200** and **201** to verify this hypothesis, evaluating their emissive features upon the interaction with a lipidic model membrane. 1,2-dioleoyl-*sn*-glycero-3-phosphocholine (DOPC) and 1,2-dipalmitoyl-*sn*-glycero-3-phosphocholine (DPPC) large unilamellar vesicles (LUVs) were used to

simulate two differently ordered lipid phases at 25 °C, a liquid disordered (L_d) and a solid ordered (S_o) one, respectively. Intercalation kinetic experiments were run, at first to evaluate the probes fluorescence upon interaction with the liposome bilayer membrane over time (Figure 3.46).

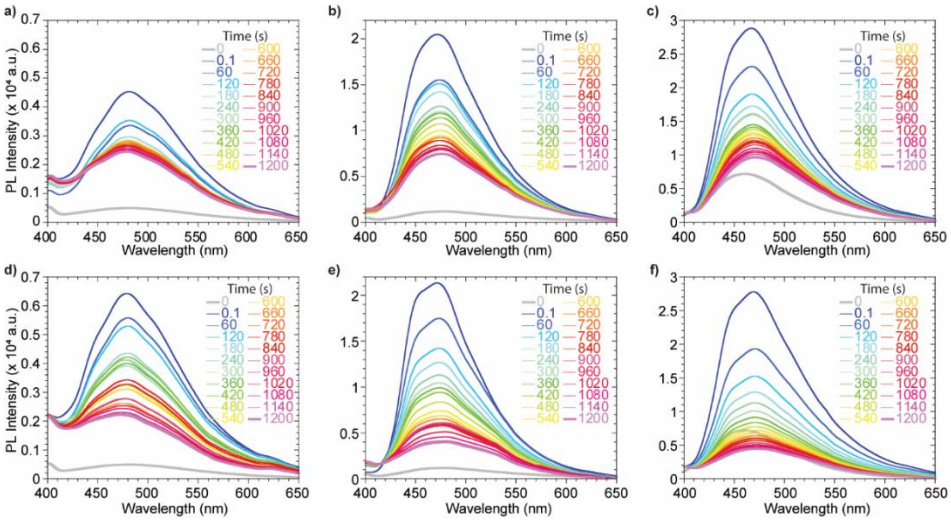

Figure 3.46 Kinetic experiments in DOPC (a–c) and DPPC (d–f) for compounds **199** (a,d), **200** (b,e), **201** (c,f). Probes concentration during the measurement: 7.28×10^{-7} M for 199, 3.7×10^{-6} M for 200 and 3.4×10^{-6} M for 201.

The quenched fluorescence signal in buffer media rapidly increases as soon as the probe intercalates in the lipidic bilayer, highlighting a successful and immediate response to the environmental change. Upon an initial remarkable increase of the emission signal due to the probe intercalation, the system equilibrates displaying a lower emission intensity for all probes (**Figure 3.47D-E**). This might be due to the lack of a polar or charged anchoring group on the probes able to stabilize the fluorophores inside the membrane by additional electrostatic or hydrogen bond interactions with the hydrophilic head of the outer layer. The interaction of each probe with the vesicles is almost immediate, allowing a strong fluorescence turn-on. The maximum emission wavelength is not

affected by the lipid phase for probes **200** and **201**, while a bathochromic shift can be observed comparing the emission of probe **199** in DOPC with the one in DPPC (Figure 3.47**A-C**). The tightly packed organization of the lipid molecules in the DPPC S_o phase allows the probe to experience a more hydrophobic environment when compared to the interaction with DOPC LUVs. The L_d mobility of DOPC makes the probes surrounding more polar, bathochromically shifting the emission spectrum. Upon the initial incorporation in the bilayer membrane, driven by hydrophobic interaction, the decrease in the fluorescence signal, observed in the initial 20 min, suggested a slow partial release of the probes from the bilayer membrane. This might be explained considering a destabilization of the supramolecular lipidic environment by the deplanarized molecular conformation of the dimeric probes **198**–**200** (**Figure 3.47D-E**). Nevertheless, after 20 min, stable fluorescence signals were present for all the probes, indicating a positive staining of the membranes. It is worth noting that among the three investigated molecules, the asymmetric scaffold of **200** was the best performing since it had higher intensity, compared to the poorly soluble **199**, and higher signal to noise (I/I_0) when compared to the brighter **201**.

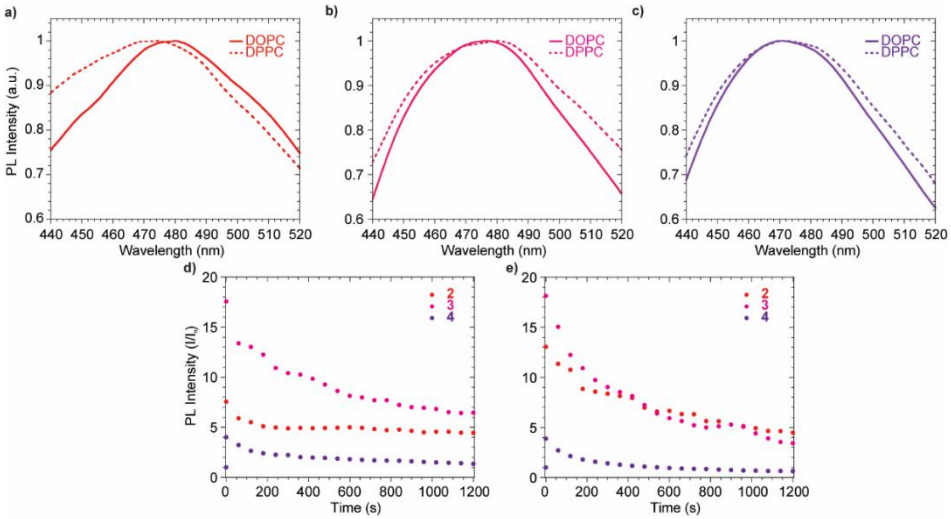

Figure 3.47 (a-c) Normalized emission profile in DOPC (solid line) and DPPC (dashed line) for compounds **199** (a), **200** (b), **201** (c). (d) Emission intensity *vs* time in DOPC for **199** (red), **200** (magenta), **201** (purple). (e) (e) Emission intensity *vs* time DPPC for **199** (red), **200** (magenta), **201** (purple).

Upon the equilibration, the intercalated probes into the liposome membranes were subjected to several heating-cooling cycles, since DPPC undergo to a phase transition at 41 °C.[259] The probes were warmed up to 55 °C and then cooled down to 25 °C several times to assess their response to the change of membrane fluidity. DOPC liposomes were also tested as negative control, since they exhibit no transition phase in the explored temperature range. Probe **199** was showing the most promising results to monitor the membrane phases (Figure 3.48). The DPPC phase transition, driven by temperature, is characterized by higher system fluidity and higher hydration of the membrane which led to a more polar micro-environment reflected in a bathochromic shift of the emission signal. The complete reversibility of this phenomenon allows to exclude any chemical transformations driven by the higher thermal energy given to the probe. The emission profile of **199** was not affected by any heating-cooling cycle in DOPC since no

phase transition occurs between 25 °C and 55 °C confirming the central role of the lipidic phase in the probe emissive response. The lack of changes in the emission profiles of probes **200** and **201** during the warm-cool cycles might be related to the presence of the pyridyl substituents on the imidazopyridine core. As known by literature, the pyridine group might reduce the degree of deplanarization via a hydrogen-bonds based pattern, while the presence of two pending phenyl rings might confer to **199** higher sensitivity to the variation of a lateral pressure inside the membrane which should drive the probe planarization.[260]

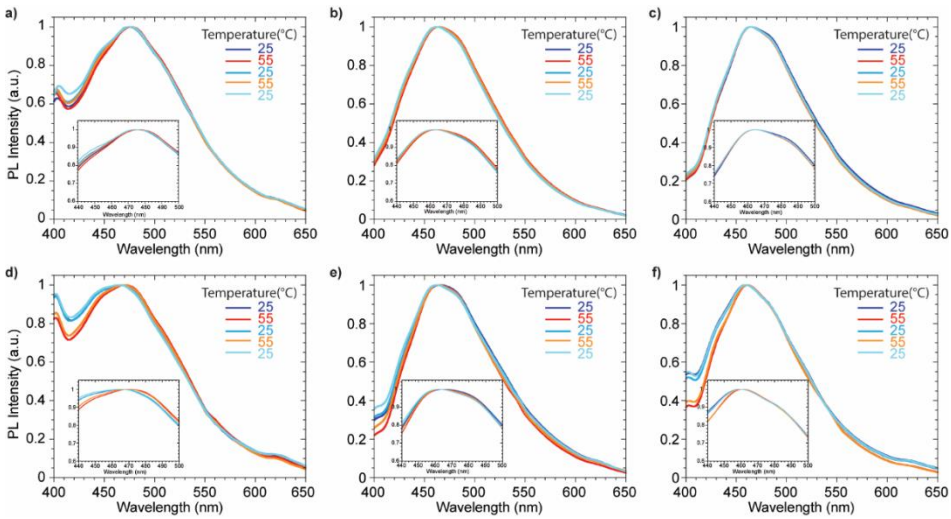

Figure 3.48 Normalized emission spectra of compounds **199** (a,d), **200** (b,e), **201** (c,f) in DOPC (a–c) and DPPC (d–f) over the heating cycles.

Further support for this explanation can be found observing the normalized excitation spectra (Figure 3.49). While no significant differences occurred for probes **200** and **201**, **199** showed a variation in the relative intensities of two main contributions upon the temperature change. The blue-shifted band became more intense at 55°C and decreased at 25 °C due to a greater contribution of the red-shifted

planarized band in the S_o phase. The reduced Stokes shift of **199** in DPPC at low temperature, originating from a more conjugated ground-state and a blue-shifted emission might be explained considering the presence, at the same time, of the planarization effect induced by the membrane lateral pressure and less polar microenvironment arising from a lower hydration of the membrane bilayer. On the other hand, **199** did not highlight any variation either on the emission or on the excitation spectra recorded in DOPC where no significant variation of the fluidity or the hydration was expected.

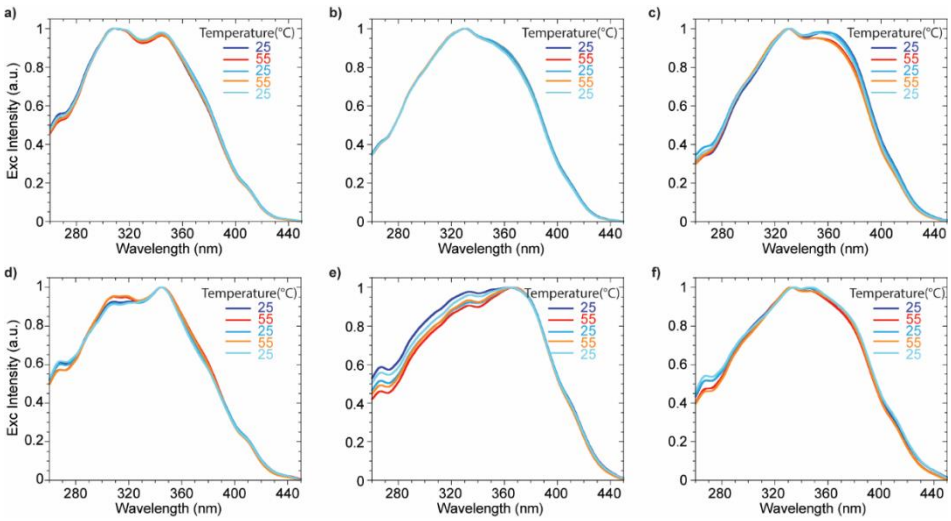

Figure 3.49 Normalized excitation spectra of compounds **199** (a,d), **200** (b,e), **201** (c,f) in DOPC (a–c), and DPPC (d–f) over the heating cycles.

Additionally, the partition coefficient between the two explored lipid phases (DOPC and DPPC at rt) and water was evaluated for the unsymmetrical probe **200**. The fluorescence enhancement by titration with increasing amounts of liposomes was monitored (Figure 3.50 and Figure 3.51) and elaborated providing the partition coefficient value according to a procedure reported in literature for commercial fluorescent

membrane probes.[261] In particular, the intensities of the emission spectra maxima were fitted versus the liposome's concentration (Figure 3.51) according to Equation S11 reported in the Experimental Section. Finally, the partition coefficient K_R was obtained as the slope of the linear fit according to Equation S12 of the double reciprocal plot of the fluorescence intensity versus the liposome concentration (Figure 3.50 inset). The partition coefficient K_R in DOPC (9.6×10^5) resulted to be slightly higher than the one in DPPC (6.0×10^5). The tightly packed organization of phospholipids in DPPC makes less favorable the **200** partition in lipid phase compared to the liquid disordered DOPC phase. A comparison with partition coefficient of commercial probes (1,6–Diphenyl-1,3,5–hexatrien-DPH, 4-(4-didecylaminostyryl)-N-methylpyridiniuimodide–4-di-10-ASP) exhibiting K_R in DPPC around 1–3 $\times$ 10^6 values[261] highlights the remarkable partitioning effect of the imidazo[1,5-*a*]pyridine in the lipidic bilayer, strongly encouraging further studies on these family of fluorophores.

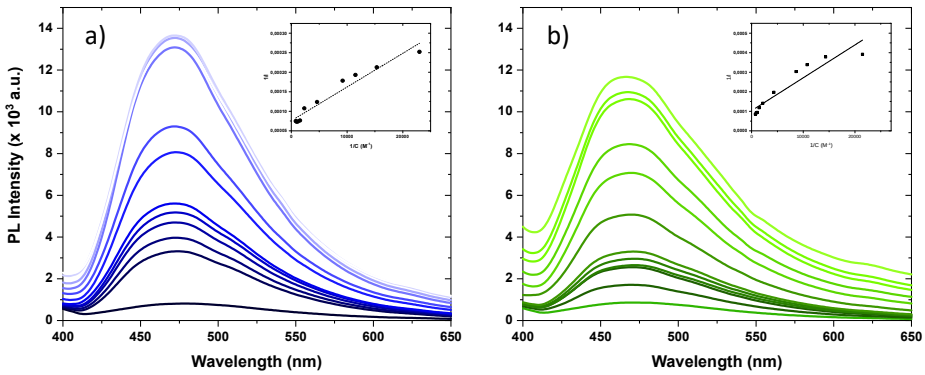

Figure 3.50 Emission spectra of probe **200** at increasing concentrations of (a) DOPC and (b) DPPC. Inset: titration linearization plot.

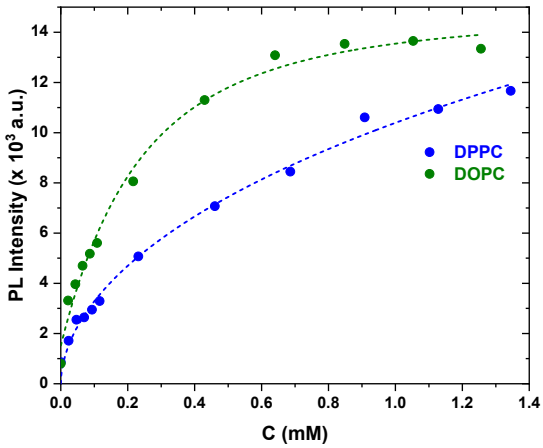

Figure 3.51 Emission maximum of probe **200** as a function of DOPC (green) and DPPC (blue) concentration.

Conclusions

In this work, we described the synthesis of a series of fluorescent probes based on the imidazo[1,5-*a*]pyridine core. Both monomeric **198** and **202** and extended structures **199-201** were prepared and an asymmetric version, **200**, was herein reported for the first time. The obtained probes were optically characterized in several organic solvents highlighting the wide Stokes shift and the peculiar features of the imidazo[1,5-*a*]pyridine based compounds. The presence of a pyridinil substituent in **199-201** enhances the PLQY from 0.12 of **199** up to 0.38 of **201**, passing through 0.18 for **200** in apolar environment. The solvatochromic response of the most extended probes made them suitable candidates for the application as membrane bilayer probes. DOPC and DPPC LUVs were used to simulate the biological membrane: although all the tested compounds successfully interact with liposomes, probe **199** can discriminate between different lipid phases according to an emission profile shift. Nevertheless, the reported preliminary investigation

in liposomes have suggested that the probe scaffolds require molecular modifications such as the introduction of polar or charge moieties to enhance the interaction and stabilization inside the membrane layers. Moreover, stronger push-pull character along the probe scaffold might be suitable to improve the membrane phases discrimination considering the different polarity and hydration degree among the membrane phases. This preliminary study encourages further detailed investigation of these class of compounds as fluorescent membrane probes, evaluating the electronic effects of functional groups on the core and exploring several heterogeneous liposomal model systems.

3.2.3. NIR squaraine-based fluorescent probes

The importance to have the possibility of a staining into the NIR region of the electromagnetic spectrum is of fundamental importance due to the deep tissue penetration, negligible autofluorescence and low tissue degradation of light in this spectral area.[3] Several families of NIR dyes have been designed, synthesized and also proposed to the market for selective staining of PM along with a plethora of biological structures[124,262] but proper modernization in the study of cutting-edge probes for PM is still a current challenge. Klymchenko *et al.*[263–267] have recently presented outstanding designs and application as membranes' fluorophores for both squaraine, merocyanine and cyanine dyes highlighting their potentialities and relevance due to singular lightness, specificity, and synthetic design. Among the families of NIR fluorophores, squaraine dyes[268,269] are a well-known class of 1,3-disubstituted derivatives of squaric acid with excellent photochemical properties characterized by significant and sharp absorption and emission in the visible or NIR.[268,270] They usually show two electron-rich heterocyclic

donor groups (D) on the two opposite sides of the central electron-deficient squaric acid (A) core in a D-A-D structure. Their excellent optical and electrochemical properties and their consolidated one or two steps synthesis involving the condensation of squaric acid/squarate derivatives with electron donating aromatic or heteroaromatic moieties have strength their application from material science to the biological field.[268,270]

3.2.3.1. A structure-activity relationship

The results reported herein have been published in Renno, G. *et al. Eur. J. Org. Chem.* **2022**, e202200833.

Squaraines have already been proposed to stain cell membranes,[263,264] but detailed investigations on the fluorophores' design and a preliminary structure to function study for novel bilayer membrane probes are missing. However, the investigation of these parameters could represent the starting point to precisely direct further investigations and improve the development of novel biomembranes selective NIR fluorophores. Herein we report the synthesis and the fundamental photophysical investigation in liposomes of six squaraine dyes. The synthetic efforts have been addressed to prepare both symmetrical and unsymmetrical derivatives of the common probe scaffold. Moreover, the degree of hydrophilicity and lipophilicity of the probes have been addressed either by the presence of polar carboxylic moieties on the scaffold or by the elongation of the hydrocarbon chain used to quaternarize the nitrogen of the indolenine core. The former decorations should facilitate indeed the solubilization in biological media and lock the probes on the outer side of the amphiphilic bilayer, while the latter portions have been varied to investigate the respective interactions with the hydrophobic portion of the membranes.

The presented probes have been synthesized with a straightforward approach involving few synthetic steps, microwave technology and low-cost commercial building blocks. The photophysical properties, the insertion kinetics into LUVs bilayer membranes along with the effects of different lipid phases on the optical features have been analysed with regards to the probe molecular structures, providing key data to optimize the design of new generations of NIR probes for bioimaging purposes.

Synthesis

The synthesis of compounds **214**-**219** have been performed as presented in Scheme 3.16 starting from 2,3,3-trimethylindolenines commercially available substrates (**117**, **207**) by mainly MW assisted synthesis.

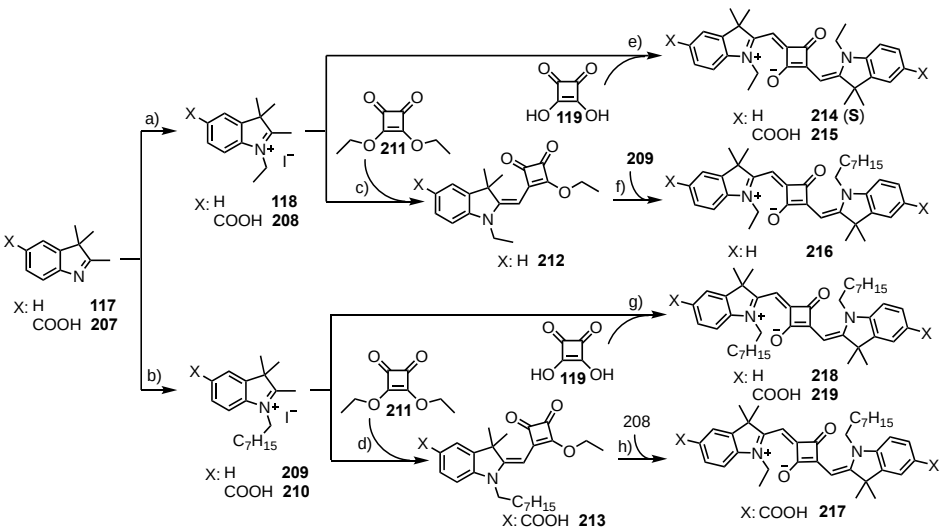

Scheme 3.16 a) iodoethane, MW irradiation. **118**: neat conditions, 130°C, 9 min, 91%. **208**: MeCN, 155°C, 20 min, 73%. b) **119**, Tol/*n*-BuOH, MW irradiation, 160°C. 214 (S): 15 min, 55%. **215**: 20 min, 25%. c) **211**, TEA, EtOH, reflux, 30 min, 60%. d) **209**, Tol/*n*-BuOH, MW irradiation, 160°C, 25 min, **216**: 25%. e) 1-iodooctane, MeCN, MW irradiation. **209**: 130°C, 10 min, 60%. **210**: 155°C, 25 min, 66%. f) **209**, TEA, EtOH, MW irradiation, 90°C, 45 min, 51%. g) Tol/*n*-BuOH, MW irradiation, 160°C, 25 min, **217**: 20%. h) **208**, Tol/*n*-BuOH, MW irradiation, 160°C. **218**: 20 min, 55%. **219**: 25 min, 40%.

The preparation of heterocyclic ammonium salts **118**, **208**-**210** has been performed treating the corresponding electron-rich aromatic base, **117** or **207**, with an excess of the appropriate iodoalkane. High yields were obtained ranging from 60 to 91%, and the pure compounds were isolated by filtration after a simple precipitation in diethyl ether from the reaction mixture. The formation of a formal positive charge on the nitrogen atom activates the methylene base in the indolenine 2-position, allowing the further condensation reaction with the squaric acid **119** or the diethyl squarate **211** toward the desired compounds. In detail, the squaraine formation belongs to the nucleophilic additions family. While Treibs and Jacob used to carry out the reaction in acetic acid,[271] nowadays the addition is usually performed in *n*-butanol with an equal volume of benzene (or, better, the less toxic toluene) to azeotropically remove the water formed during the reaction.[271] Two slightly different procedures have been explored whether symmetrical or unsymmetrical products were targeted. The former **214**, **215** and **218**, **219** were prepared by one-step reaction of the indolenine quaternary ammonium salts, **118**, **208** and **209**, **210** respectively, with the squaric acid **119**. Law and Bailey identified the formation of the *n*-butylsquarate as reactive intermediate, that at first undergoes to a nucleophilic attack by the methylene bases **118**, **208**-**210**.[271] Then, the loss of an alcohol molecule affords the semisquaraine species, able to react with another equivalent of the methylene base, finally providing the symmetrical squaraine after the loss of one further water molecule.[270] On the other side, the preparation of the unsymmetrical dyes **216** and **217** requires the isolation of the semisquaraine intermediates **212** and **213** after the reaction of activated indolenines **118** and **210** with **211** in presence of triethyl amine, according to a 1,4-addition to the squarate double bond and a subsequent elimination of one ethanol molecule. [272] The key intermediates **212** and

213 can be finally treated with one equivalent of the different activated heterocycles **208** or **209** affording the unsymmetrical desired squaraines **216** and **217** in moderate yields (20-25% on the last step). The reactions were carried out under microwave irradiation, since our previous work demonstrated satisfying results in terms of reaction times and afforded yields[191] when compared to the canonical procedure.[268,270,273] Furthermore, microwave-assisted synthesis allows a strong regioselectivity toward the 1,3-condensation products, avoiding the formation of the undesired 1,2 tipically recovered during the traditional procedures.[273,274] Additionally, while the hydrolysis of **212** and **213** to the monosubstituted squaric acid is usually required for the final condensation reaction,[272] the use of MW heating allowed to carry **213** and **213** toward the last step without further modifications, improving the overall yield. Finally, the carboxylated compounds **215**, **217** and **219** were purified by crystallization in alcohols (ethanol or *n*-butanol), providing an up-scalable and solvent-saving purification method, alternative to the usual flash chromatography.

Photophysical properties

The optical properties of all the synthetized probes have been evaluated in ethanol (Figure 3.52 and Table 3.20), and additionally their solvent-dependent behaviours have been qualitatively tested in ten different solvents (Table 3.21, Figure 3.53, Figure 3.54).

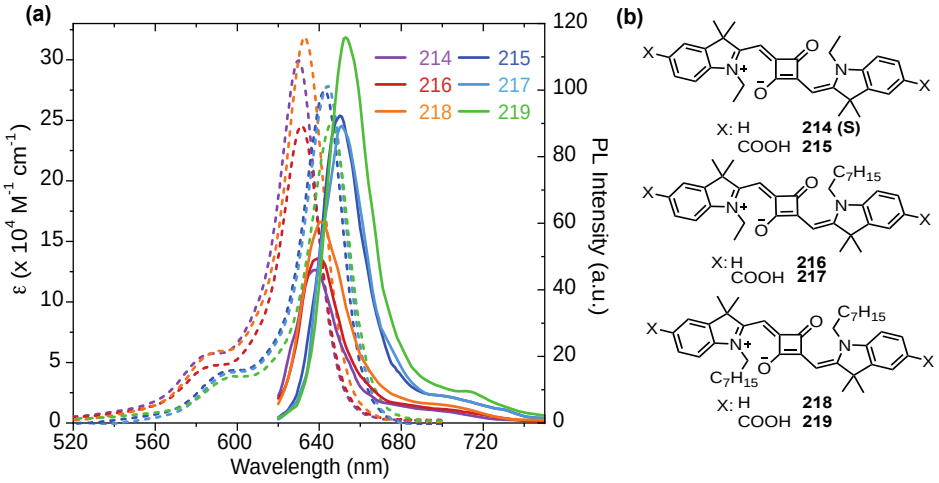

Figure 3.52 a) Absorption (dashed) and emission (solid) spectra of probes **214-219** in ethanol. The emission spectra were normalized at 0.1 intensity at the excitation wavelength. b) Structures of the probes **214-219**.

All the probes absorb and emit in the NIR region of the electromagnetic spectrum. The absorption profiles show a narrow peak with a weak vibronic band, centered respectively around 630 and 580 nm for probes 1,3 and 5. The main band can be attributed to a π-π* charge-transfer transition of the conjugated system.[274] The introduction of the carboxylic moiety in species 2,4 and 6 batochromically shifts their UV-Vis spectrum of 10 nm due to the participation of the COOH to the resonance and resulting in an increased π conjugation.

Table 3.20 Photophysical parameters of the probes 214-219 in ethanol.

	λ_{abs}[a]	ε[a]	λ_{em}[a]	PLQY[b]	Brightness[a]	Stokes shift[a]
214	630	2.92	638	0.16	46.7	199.0
215	642	2.74	649	0.27	78.6	168.0
216	632	2.47	638	0.13	32.1	148.8
217	644	2.81	650	0.23	64.4	143.3
218	633	3.19	641	0.16	51.8	197.2
219	647	2.46	653	0.30	68.7	142.0

[a] λ_{abs}, λ_{em} are reported in nm. ε, brightness and Stokes shift are reported in 10^5 $M^{-1}cm^{-1}$, 10^3 $M^{-1}cm^{-1}$ and cm^{-1}, respectively. [b] QY was measured referring to Rhodamine 101 in MeOH as standard.

The emission profiles show the same trend and the PLQY was evaluated in ethanol for all the probes, highlighting moderate values (0.15) for **214**, **216** and **218**, while an increase (up to 0.30) has been found for the analogues bearing the carboxylic moiety. The introduction of a functional group on the indolenines may reduce their rotational ability with a beneficial effect on the PLQY.[274] The small Stokes shift is typical of the squaraine dyes, describing a similar electronic configuration for both the ground and the excited states. Then, the probes response to environments with different polarity was assessed, evaluating their optical features in ten organic solvents (Table 3.21, Figure 3.53).

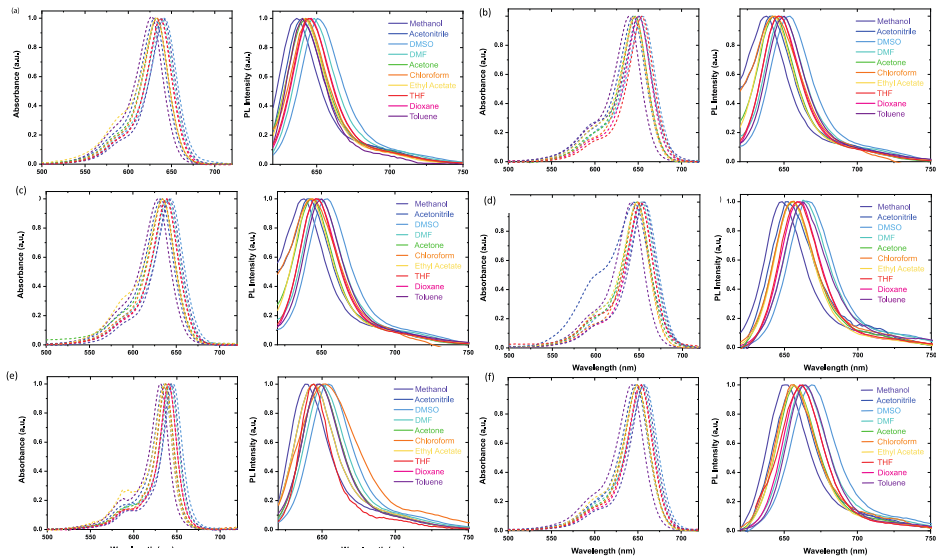

Figure 3.53 Absorption (dashed) and emission (solid) spectra of probes **214-219** (a-f) in several solvents, normalized to 1 in intensity at the maximum value.

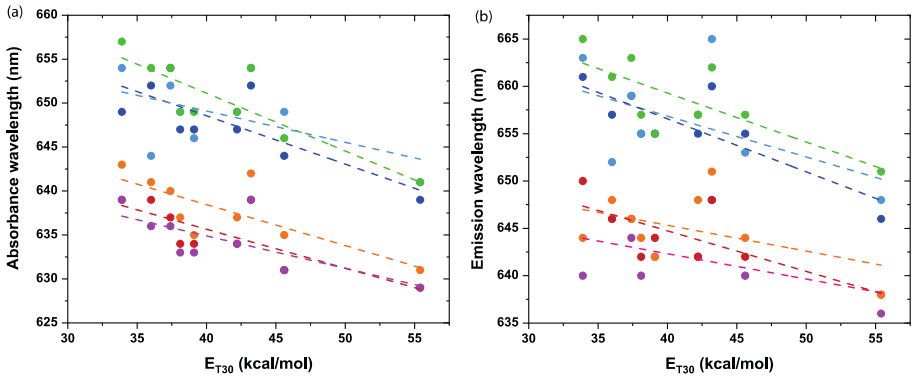

Figure 3.54 Absorbance (a) and emission (b) wavelengths plotted against the ET30 polarity scale for the probes **214** (purple), **215** (blue), **216** (red), **217** (light blue), **218** (orange), **219** (green).

Table 3.21 Solvatochromic properties of probes **214-219** in several organic solvents.

	λ_{Abs}[a]	λ_{em}[a]	Stokes shift[b]		λ_{Abs}[a]	λ_{em}[a]	Stokes shift[b]
Methanol				**Dimethyl sulfoxide**			
214	629	636	174.98	**214**	641	651	239.64
215	639	646	169.58	**215**	654	664	230.28
216	629	638	224.27	**216**	644	654	237.43
217	641	648	168.52	**217**	657	667	228.2
218	631	638	173.88	**218**	645	655	236.7
219	641	651	239.64	**219**	657	669	273.02
Dimethylformamide				**1,4-Dioxane**			
214	639	648	217.35	**214**	636	646	243.39
215	652	660	185.91	**215**	652	657	116.72
216	639	648	217.35	**216**	639	646	169.58
217	654	665	252.93	**217**	644	652	190.53
218	642	651	215.34	**218**	641	648	168.53
219	654	662	184.78	**219**	654	661	161.93
Acetonitrile				**Acetone**			
214	631	640	222.86	**214**	634	642	196.55
215	644	655	260.78	**215**	647	655	188.78
216	631	642	271.54	**216**	634	642	196.55
217	649	653	94.38	**217**	649	657	187.62

218	635	644	220.08	**218**	637	648	266.49
219	646	657	259.18	**219**	649	657	187.62
Ethyl acetate				**Chloroform**			
214	633	640	172.79	**214**	633	642	221.46
215	647	655	188.78	**215**	647	655	188.78
216	634	642	196.55	**216**	634	644	244.92
217	649	655	141.15	**217**	646	655	212.7
218	637	644	170.64	**218**	635	642	171.71
219	649	657	187.62	**219**	649	655	141.15
Toluene				**Tetrahydrofuran**			
214	639	640	24.45	**214**	636	644	195.32
215	649	661	279.72	**215**	654	659	116.01
216	639	650	264.84	**216**	637	646	218.71
217	654	663	207.56	**217**	652	659	162.92
218	643	644	24.15	**218**	640	646	145.12
219	657	665	183.11	**219**	654	663	207.56

[a] Absorption and emission maxima are reported in nm, [b] Stokes Shift values are reported in cm^{-1}.

A hypsochromic shift of both absorption and emission profiles upon environmental polarity increase was observed (Figure 3.54). This negative solvatochromic behaviour highlights a more significantly polar character of the ground state compared to the excited state, in agreement with data already reported for cyanines chromophores.[274] Apolar systems (e.g., toluene, tetrahydrofuran, 1,4-dioxane) stabilize better the LUMO than the HOMO, red-shifting the absorption maxima. The opposite trend can be described looking at more polar solvents (e.g., acetone, acetonitrile, methanol). Furthermore, as already noticed by Salice *et al.*,[274] the weak optical features dependence from the solvent polarity also suggests either that the initially populated excited states do not differ much from the emissive excited states in terms of charge transfer character or that the charge transfer character of the excited state is very similar to the one of the ground state. Finally, the outstanding high molar

coefficient spanning from 2.46 to 3.19×10^5 $M^{-1}cm^{-1}$ (data in ethanol) along with moderate QY values in the NIR region provide extremely bright fluorophores, highly promising as emissive membrane probes.

LUV experiment

All the prepared fluorophores have been tested as cell membrane probes using LUVs of different compositions as models. DOPC, DPPC and a mixture of DPPC and cholesterol (CL) have been used to simulate liquid disorder, solid ordered and liquid ordered phases respectively at room temperature. The interaction between the probes and the liposomes has been monitored by steady-state fluorescence experiments. While the probes emissive properties result partially (or even fully) quenched in buffer, a strong fluorescence turn-on occurs upon the interaction with the lipid bilayers hydrophobic environment, highlighting the successful intercalation of the probes (**Figure 3.55**). The hydrophobic probe **214**, the smallest probe among the series bearing two short ethyl chains on the indolenine nitrogen positions, highlighted similar results in DOPC and DPPC systems while a weak yet detectable emissive signal was observed upon interaction with DPPC/CL membranes. The replacement of one ethyl chain with a longer octyl moiety in **216** increases the probe affinity for the mixed DPPC/CL and lowers the intercalation in DOPC, while the result in DPPC is comparable as for **214**. The additional replacement of the N-ethyl moiety with another highly hydrophobic octyl chain in **218** confers poor solubility in aqueous media also affecting the partition and the affinity to liposome membranes, depicted by an overall ten times lower intensity signal in all the liposome systems.

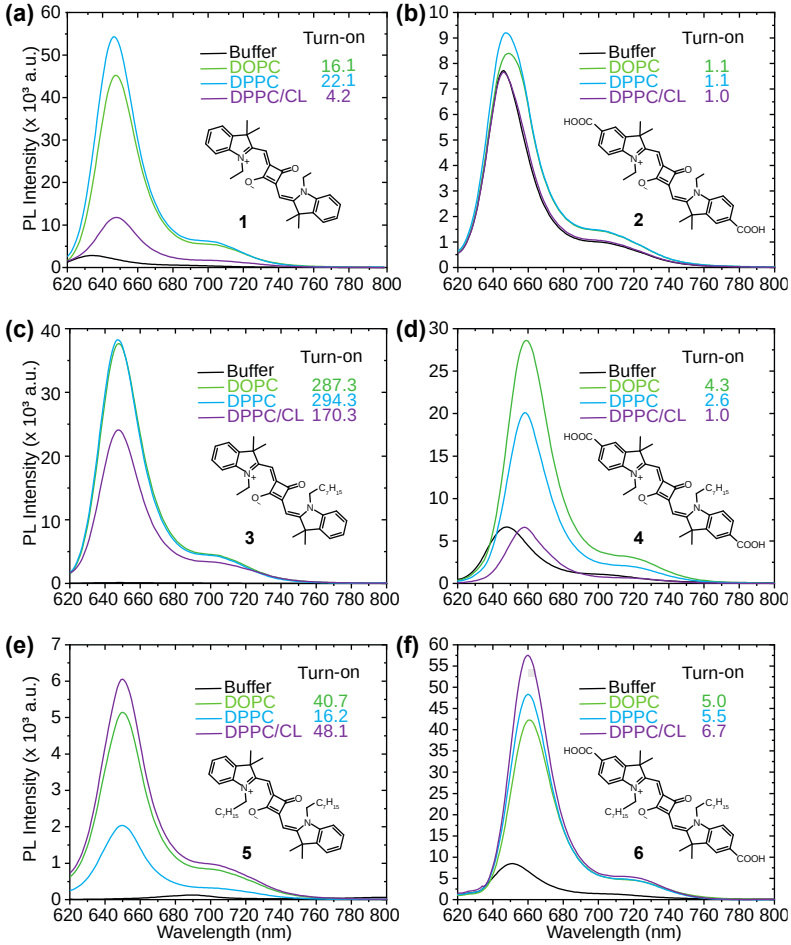

Figure 3.55 Emission spectra of probes **214** (a), **215** (b), **216** (c), **217** (d), **218** (e), **219** (f) in buffer (black), DOPC (green), DPPC (blue) and DPPC/CL (purple) LUVs after their equilibration time.

The decoration of the squaraine core with two carboxylic functions on the indolenine rings remarkably improves the solubility in water which must be compensated by the presence of at least one octyl chain to confer hydrophobicity and successful incorporation into the bilayer membranes. Therefore, the small hydrophilic candidate **215** shows poor emissive fingerprint in different liposome systems most likely due to the remarkable solubility in water which hampers the partition into the lipophilic bilayer.

The presence of one octyl chain in **217** rises the fluorescence signal in both DOPC and DPPC membranes with the former one that is a more suitable environment for the amphiphilic probe scaffold. It is worth noting that the comparison between **216** and **217** - both bearing one ethyl and one octyl chain – highlights two different behaviors. While **216** equally stains both DOPC and DPPC, the more hydrated DOPC are preferred by **218**, thanks to the higher hydrophilic character due to the presence of two carboxylic functional groups. The addition of one further octyl chain in **219** increases the response in all the liposomal systems, with a particular beneficial interaction with the mixed DPPC/CL, in agreement with the response of **218**. Finally, it is worth noting that the higher molecular similarity of **219** to the phospholipids structures prompt remarkable affinity of the probes to all the different membrane systems due to the more balanced and defined amphiphilic character. The polar head characterized by the carboxylic moieties provides high solubility in aqueous media allowing good diffusion towards the liposomes, while hindered hydrocarbon chains drive the hydrophobic interaction leading to an efficient partition inside the membrane bilayer.

To better quantify the results observed in different liposomes, the partition coefficients K_R between the water and the three lipid phases have been evaluated for **214**. The fluorescence enhancement upon the addition of increasing aliquots of liposomes was monitored (**Figure 3.56**) and fitted according to the equation S11 reported in the Experimental Section. The K_R was then calculated from the linear fit slope (Equation S12) of the double reciprocal plot (**Figure 3.57**) of the fluorescence intensity versus the liposome concentration, according to a well-established protocol.[261] The partition coefficients in DOPC (2.6×10^5) and mixed DPPC/CL (1.9×10^5) resulted to be slightly lower than the value in DPPC (7.8×10^5),

in agreement with the trend for the probe **214** observed in the different kind of LUVs (**Figure 3.55A**). Furthermore, the DPPC value is only slightly lower than commercial fluorescent probes (e.g., (1,6–Diphenyl-1,3,5–hexatrien - DPH, 4-(4-didecylaminostyryl)-N-methylpyridiniumimodide – 4-di-10-ASP) that exhibit partition coefficients around 1-3×10^6 in the same vesicles.[261]

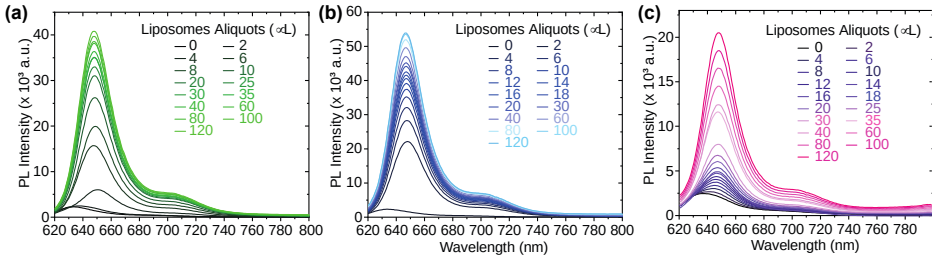

Figure 3.56 Emission spectra of probe **214** at increasing concentrations of (a) DOPC and (b) DPPC and (c) DPPC/CL (aliquots from 32 mM, 31 mM and 34 mM stock solutions, respectively).

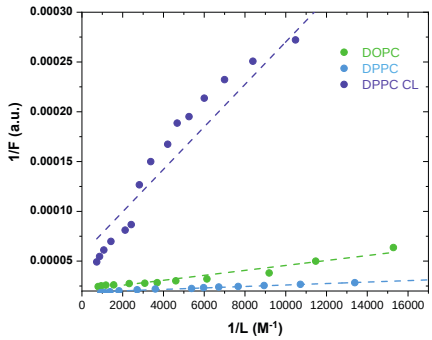

Figure 3.57 Double reciprocal plot of fluorescence intensity F against the liposome concentration L for probe **214**.

In a complementary manner, the fluorogenic character of the investigated probes allows the evaluation of their incorporation kinetics in the lipid bilayers, providing a comprehensive study on the properties of compounds **214-219**. The full spectra for all the probes are reported in

Figure 3.59, monitoring the fluorescent increasing over time after the vesicles addition to the probes' buffer solutions. Additionally, the I/I_{buffer} increase over time of **216** is reported in **Figure 3.58** for the different LUVs. **215**, **217** and **219** bearing a carboxylic moiety exhibit an instantaneous response to the LUVs presence, while the kinetics of **214**, **216** and **219** significantly depends on the steric hinderance of the overall structure (**Figure 3.58**). The two small ethyl groups of **214** allow a fast and immediate accommodation of the probe into the vesicle membranes. The introduction of one or two octyl chains in **216** and **218** lowers the intercalation rate, with slower kinetic for **218** when compared to **216**.

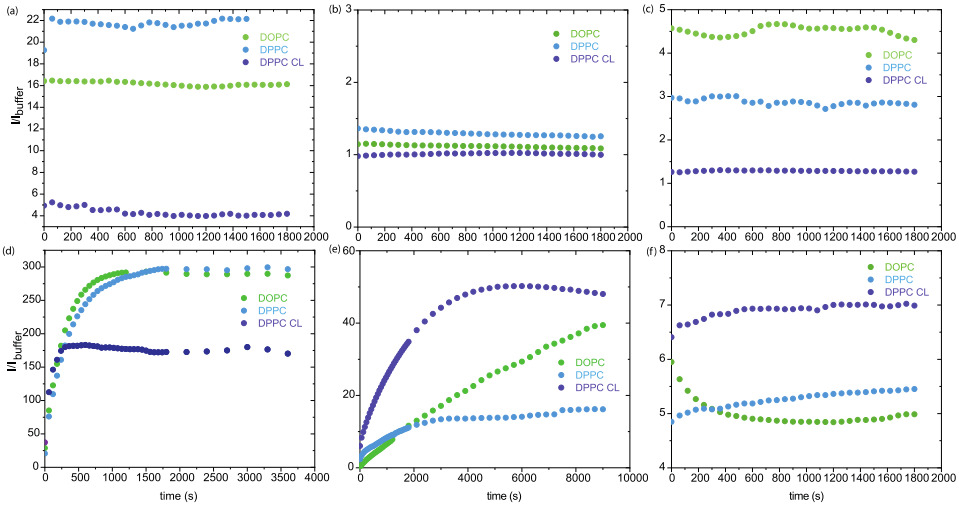

Figure 3.58 I/I_{buffer} against time for probes **214** (a), **215** (b), **216** (c), **217** (d), **218** (e). **219** (f) in DOPC (green), DPPC (blue) and DPPC:CL (purple) LUVs.

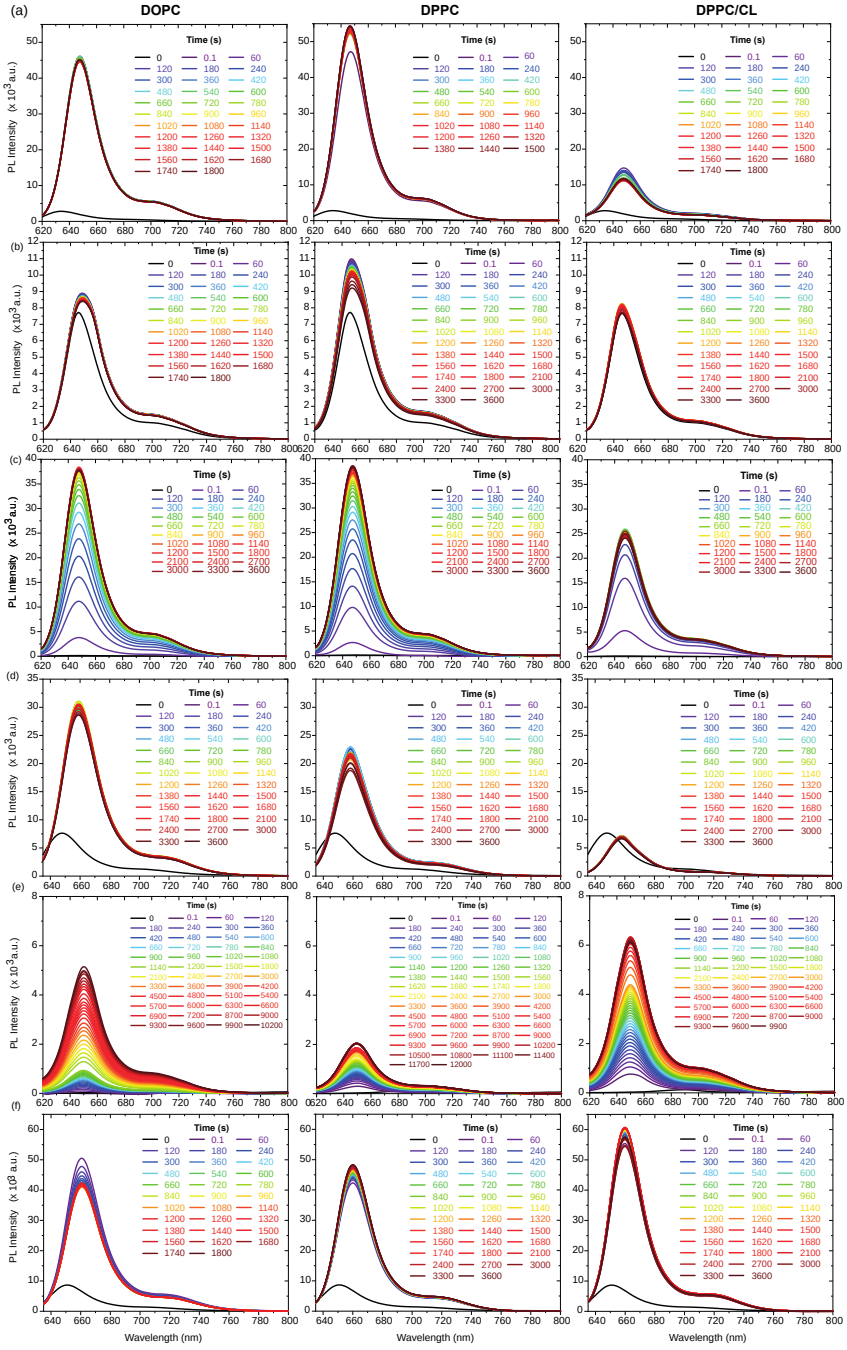

Figure 3.59 Kinetic experiments of probe **214-219** (a-f) in DOPC, DPPC and DPPC:CL LUVs.

Lastly, an additional parameter – the "turn-on effect" – can be defined as the ratio between the fluorescence intensity reached at the equilibration time and the probe emission intensity in buffer. The turn-on effect represents a key figure of merit to evaluate the suitability of probes **1**-**6** as lipid membrane stains (**Table 3.22**). It is even of more importance than the simple photoluminescence intensity since a high turn-on effect can provide a low background noise and a high signal/noise ratio.

Table 3.22 I/I_{buffer} ratio calculated for the six probes **214-219** in different kinds of LUVs.

LUVs	214	215	216	217	218	219
DOPC	16.1	1.1	287.3	4.3	40.7	5.0
DPPC	22.1	1.1	294.3	2.6	16.2	5.5
DPPC/CL	4.2	1.0	170.3	1.0	48.1	6.7

The three probes **215**, **217** and **219** bearing the carboxylic moieties show an emission signal already detectable in buffer (**Figure 3.55**) and lower I/I_{buffer} values when compared to the more hydrophobic analogs **214**, **216** and **218** without the COOH groups. In particular, the turn-on effect of **2** is very low (1-1.1), complicating the evaluation of the probe interaction with liposomes due to the strong background noise. Then, the ratio barely increases when one or two octyl chains in **217** and **219** are introduced into the system, highlighting the importance to balance the hydrophilic character given by the carboxylic moieties with the lipophilic contribution of the alkyl chains. Finally, the turn-on effect dramatically increases moving to the other series (**214**, **216** and **218**). While **214** and **218** show only moderate values in DOPC and DPPC, probe **216** displays a remarkable turn-on effect (I/I_{buffer} ~ 170-294) in all the kinds of LUVs. The structure of **216**, bearing a small ethyl group and a longer octyl chain, may

represent the right molecular trade-off between its two symmetric versions, **214** and **218**. The two-carbon atoms chain may contribute to create a more hydrophilic part able to interact with the polar phospholipids heads, while the longer hydrophobic residue should better fit with the apolar environment within the lipid bilayer. At the best of our knowledge, **216** shows the highest turn-on effect ever reported for a squaraine-based cell membrane probe in liposomal model systems.[267] These additional considerations highlight once again the suitability of the designed squaraine dyes as NIR bright membrane probes, strongly encouraging further investigation both in more complex liposomal models and in cell lines.

Conclusion

In the present work, the synthesis of three novel squaraines - both symmetric and unsymmetric - is reported for the first time along with the synthesis of three already-known squaraines to provide a complete panel of six probe-candidates with precise structural variation on two key scaffold's position.

A carboxylic moiety has been introduced to increase the hydrophilicity of the molecular systems, while two different alkyl chains (*i.e.*, ethyl and octyl residues) were used to tune the probe lipophilic character. The six compounds were optically characterized highlighting their use as cell membrane probes thanks to their high extinction coefficients and moderate quantum yields in the NIR region of the electromagnetic spectrum. Their ability to interact with artificial membrane models has been successfully tested with different key experiments in three kinds of LUVs. Our studies show how all the six probes successfully interact with the membrane, but the absence of the carboxylic moiety strongly increases the turn on effect, lowering the background noise and improving

the signal/noise ratio. In particular, the unsymmetric **216** resulted to be the best performing compound with a turn on effect of 287 in DOPC LUVs: one ethyl and one octyl chains result to be the most convenient balance between the hydrophobic-hydrophilic character of the probes presented in this study. This preliminary study has been focused on understanding basic but fundamental structural dependent functional properties, to strongly encourages further investigation on new bright NIR dyes for bioimaging outcomes.

3.2.3.2. Perimidine-based squaraine dyes

The results shown in the previous section confirmed the suitability of the squaraine scaffold as promising NIR probes, providing key informations for a better refining at the molecular design stage. The low dipole moment did not allow the dyes to discriminate between the differently packed lipidic phases, resulting in overlapping emission profiles not depending on the lipidic composition. Herein, the chromophore π-system has been strongly modified by replacing one indolenine moiety with a perimidine-based unit, aiming at breaking the π-system symmetry, increasing the dipole moment and improving the sensitivity to phase-changes. Additionnally, a carboxyindolenine (**CI**, **227-230**) or a carboxybenzoindolenine (**CBI**, **231**-**234**) moieties have been placed on one side, while on the opposite one the perimidine derivative has been decorated with alkyl chains of different length (**C1**, **C2**, **C4** or **C8**). The COOH group improves the water solubility of the whole system, while the alkyl chains tuned the interaction of the probe with the lipophilic components of the cell membrane.

Synthesis

Two series of novel unsymmetrical squaraine dyes were prepared as following reported. A CI or a CBI moiety has been placed on one side, while on the opposite one a perimidine derivative has been decorated with alkyl chains of different length (C1, C2, C4 or C8). The squaraine dyes were synthetized by direct condensation between an emisquaraine (3 or 6) and a perimidine derivative (8a-d) in a microwave reactor. The emisquaraine partners were obtained following published procedures, while perimidines 8a-d were prepared according to a novel acid catalyzed grams-scale method. The 1,8-diaminonaphthalene 7 was refluxed in toluene with the relative ketone in presence of few drops of p-toluenesulfonic acid.

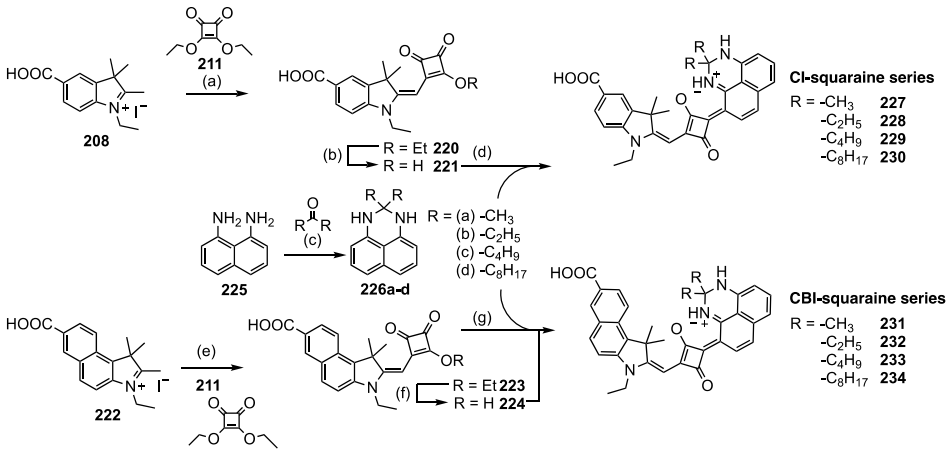

Photophysical studies

The optical properties of all the synthetized probes have been evaluated in ethanol (Figure 3.60), and additionally their solvent-dependent behaviours have been qualitatively tested in several different organic solvents (Figure 3.61). The CI squaraines exhibit a shoulder and a main band attributable to a $\pi-\pi^*$ transition centered at 680 nm and 745 nm,

respectively. The introduction of one more fused phenyl ring (**234-237**) extend the conjugation, bathochromically shifting the UV-Vis profiles of *ca.* 5 nm.

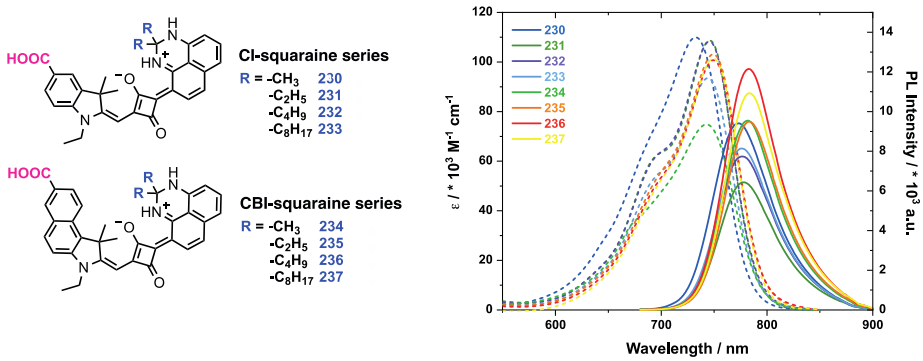

Figure 3.60 Molecular structures for probes **230-244**. Absorption (dashed) and emission (solid) spectra in ethanol Emission spectra have been normalized to 0.1 intensity at the excitation wavelength.

Cpd	λ_{abs}[a]	λ_{em}[a]	ε[a]	PLQY[a]	Brightness[a]	Stokes shift[a]
230	733	773	109423	0.015	1593	706
231	746	778	109635	0.010	1066	551
232	745	777	107712	0.011	1225	553
233	744	777	94504	0.013	1189	571
234	744	782	75086	0.015	1090	653
235	749	783	103029	0.014	1472	580
236	749	783	103793	0.017	1724	580
237	750	783	100755	0.017	1663	562

[a] λ_{abs}, λ_{em} are reported in nm. ε, brightness and Stokes shift are reported in $M^{-1}cm^{-1}$, $M^{-1}cm^{-1}$ and cm^{-1}, respectively. [b] PLQY was measured referring to Rhodamine 101 in MeOH as standard.

The emission spectra follow the same trend, with generally low PLQY values for the CI series (*ca.* 1.2 %). These values barely increase upon the addition of one further fused phenyl ring in the CBI series (*ca.* 1.6%) due to the limited rotation of the more hindered π-system. Then, the

behaviour of all the probes have been evaluated in several organic solvents, aiming at assessing their response to polarity changes and supramolecular interactions (e.g., hydrogen bonding). A positive solvatochromic effect evidences a higher polarity for the excited state compared to the ground state. The highly polar solvent can better stabilize the excited state, red shifting the emission maxima and increasing the Stokes shift. This behaviour is in contrast with the negative solvatochromism reported for the previous squaraines set and, in general, for other polymethine dyes (e.g., cyanines). The protic solvent quenches the PLQY involving N-H non-radiative relaxation decays, while the emission is turned-on in non-protic solvents (e.g., toluene, dioxane, ethyl acetate) according to a fluorogenic character. Additionally, the remarkable dependence of the optical parameters on the local environmental polarity makes these candidates suitable as cell membrane probes.

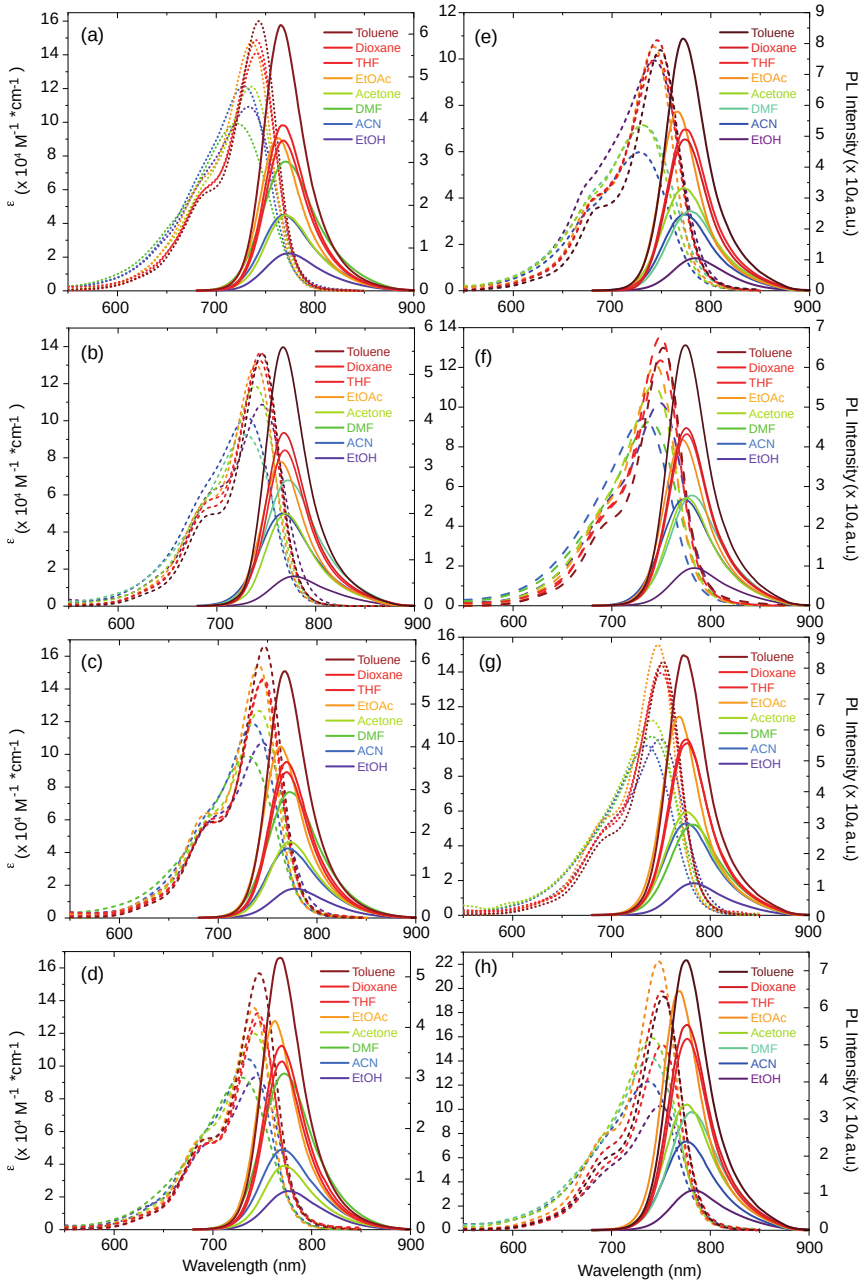

Figure 3.61 Absorption (dashed) and emission (solid) spectra for CI-series squaraines **227-230** (a-d), and for CBI-series **231-234** (e-h). The emission spectra have been normalized to 0.1 intensity at the excitation wavelength.

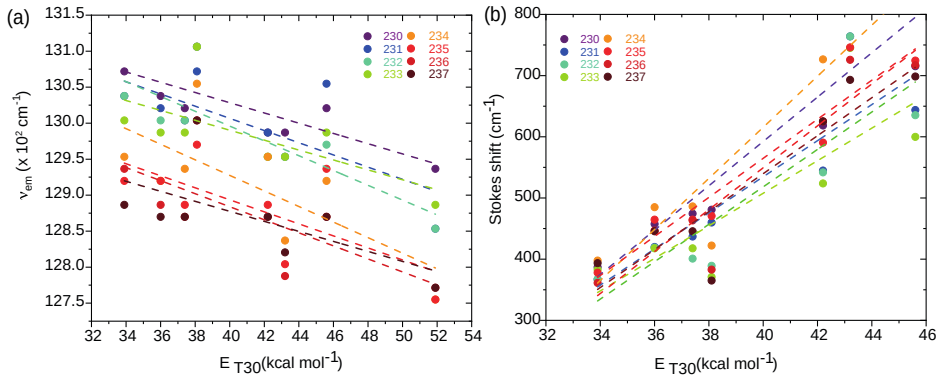

Figure 3.62 Emission wavenumber (a) and Stokes shift values (b) against the solvent polarity for probes **230-237**.

LUV experiments

The prepared probes behaviour in DOPC and DPPC LUVs vesicles has been monitored by steady-state fluorescence spectroscopy. As already described in the previous section, the probes' emission in aqueous buffer (black line in Figure 3.63) is quenched, while a strong turn-on occurs upon the interaction with vesicles. The chains length and the presence of CI/CBI moieties affect the probes ability for DOPC and DPPC stain (Figure 3.63). Concerning the carboxyindolenine series, short chains allow the probe to equally stain DPPC and DOPC L_o and L_d phases while chains elongation provides a better response to the DPPC system. The **232** and **233** hydrophobic character makes the probe better fitting with the DPPC tighter packing, reducing the affinity with the more polar and hydrated DOPC. An additional phenyl fused ring in the carboxybenzoindolenine series increases the overall probes hydrophobicity, resulting in a different phase staining compared to the CI analogues. While two methyl groups in **234** provide similar results to **230**, longer chains seem to favor the affinity in the more fluid and disordered DOPC phase. This trend might be related to the higher steric hinderance

upon the additional fused phenyl ring, evidencing the importance of a proper probe molecular design and a fine structure-activity study. Additionally, longer aliphatic chains are necessary to increase the CI-series probes response in all the vesicles. In particular, the higher molecular similarity of **233** to the phospholipids structures prompt remarkable affinity of the probes to all the different membrane systems due to the more balanced and defined amphiphilic character. The polar head characterized by the carboxylic group provides moderate solubility in aqueous media allowing good diffusion towards the liposomes, while hindered hydrocarbon chains drive the hydrophobic interaction leading to an efficient partition inside the membrane bilayer. It is also worth noting that CI-series exhibit an increasing response moving from small methyl groups to the octyl chains, while the hindering CBI shape follows the same trend only until the butyl derivatives. The introduction of octyl chains dramatically reduces the solubility and the probe's diffusion into the aqueous medium, with a consequent drop in the detected fluorescence.

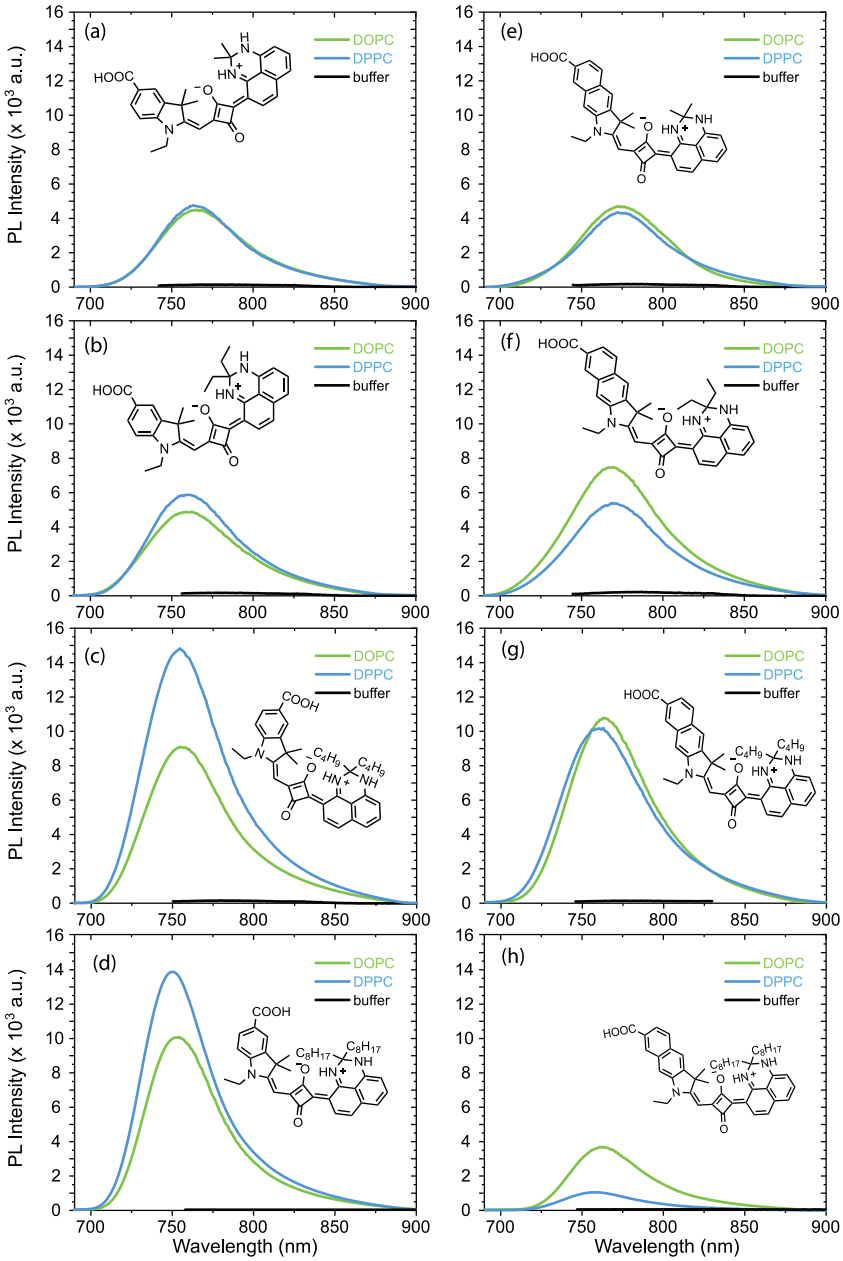

Figure 3.63 Emission spectra of probes **230** (a), **231** (b), **232** (c), **233** (d), **234** (e), **235** (f), **236** (g), **237** (h) in buffer (black), DOPC (green), DPPC (blue) after their equilibration time.

Then, the incorporation kinetics have been evaluated for all the probes in both kinds of vesicles. The full spectra are reported in Figure 3.64 and Figure 3.65, while Figure 3.66 reports the turn-on effects variation over time, providing a smart overview on all the probes. As already defined in the previous section,

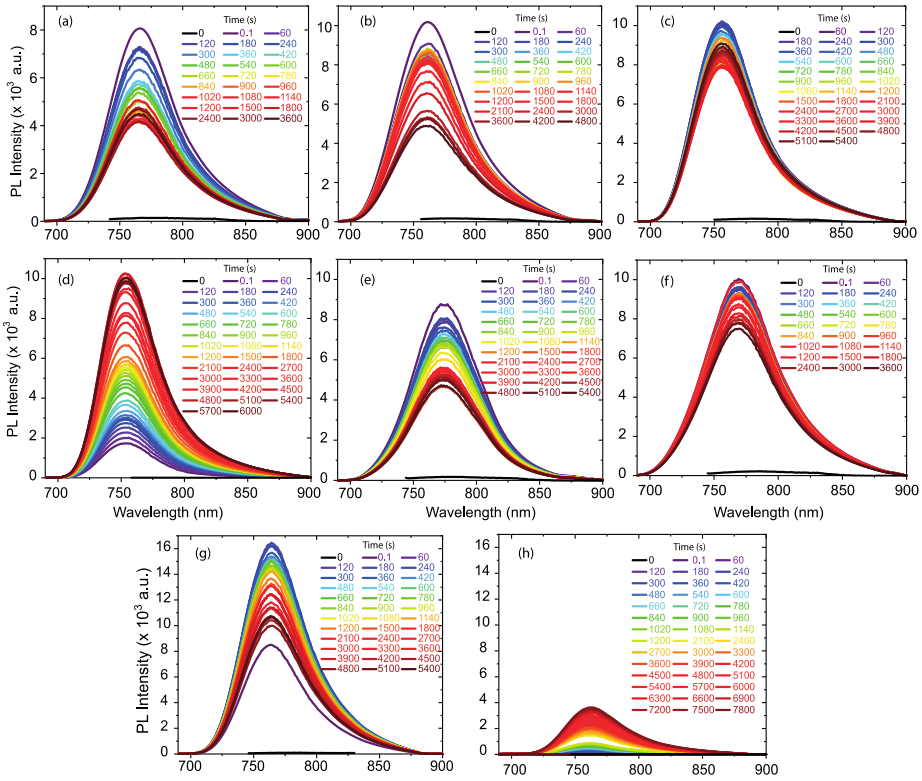

Figure 3.64 Intercalation of probes **230** (a), **231** (b), **232** (c), **233** (d), **234** (e), **235** (f), **236** (g), **237** (h) into DOPC LUV vesicles.

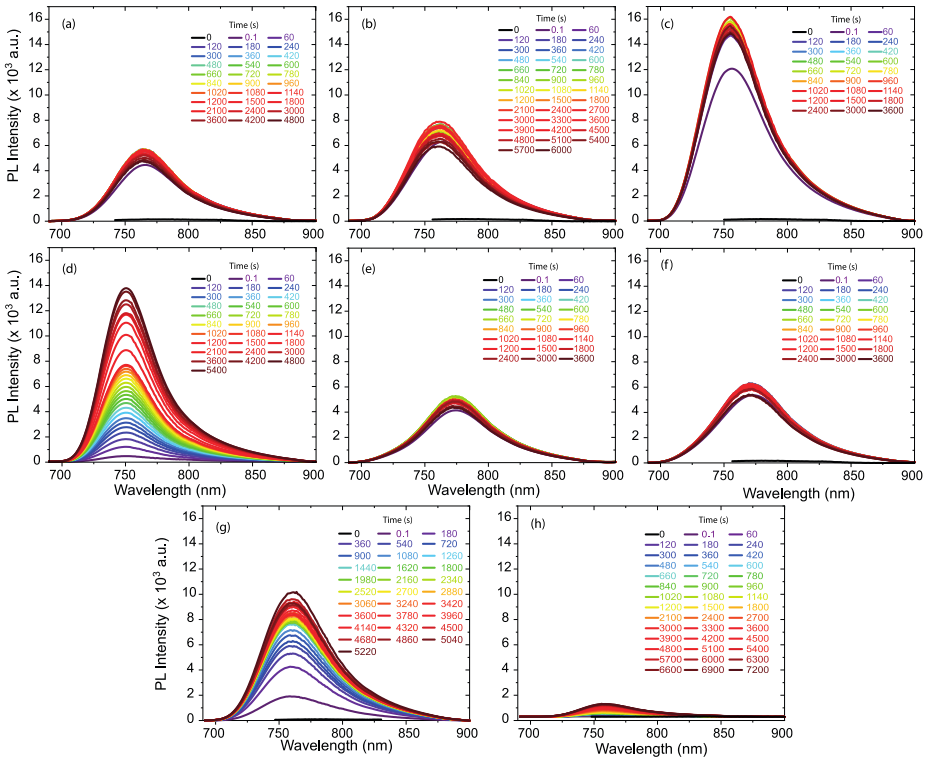

Figure 3.65 Intercalation of probes **230** (a), **231** (b), **232** (c), **233** (d), **234** (e), **235** (f), **236** (g), **237** (h) into DPPC LUV vesicles.

Although the short aliphatic chains (**a-c**; **e-g**) allow an immediate response to the intercalation, they avoid the probe to accurately interact with the phospholipids hydrophobic tails. This reflects in a quick yet not stable fluorescence signal, since the system equilibrates over time displaying a lower emission intensity. Both DOPC and DPPC show this same issue, but the latter can better lock the fluorophore reducing the emission drop due to a higher packing degree. Although butyl chains can lower the trend and reduce the signal drop over time, longer octyl hydrophobic chains (**d-h**) are necessary to better stabilize the fluorophores within the lipidic bilayer. Additionally, the **233** quenched emission in aqueous buffer along with the remarkable detected

fluorescence signal provide an outstanding turn-on effect (≈ 3500 in DPPC).

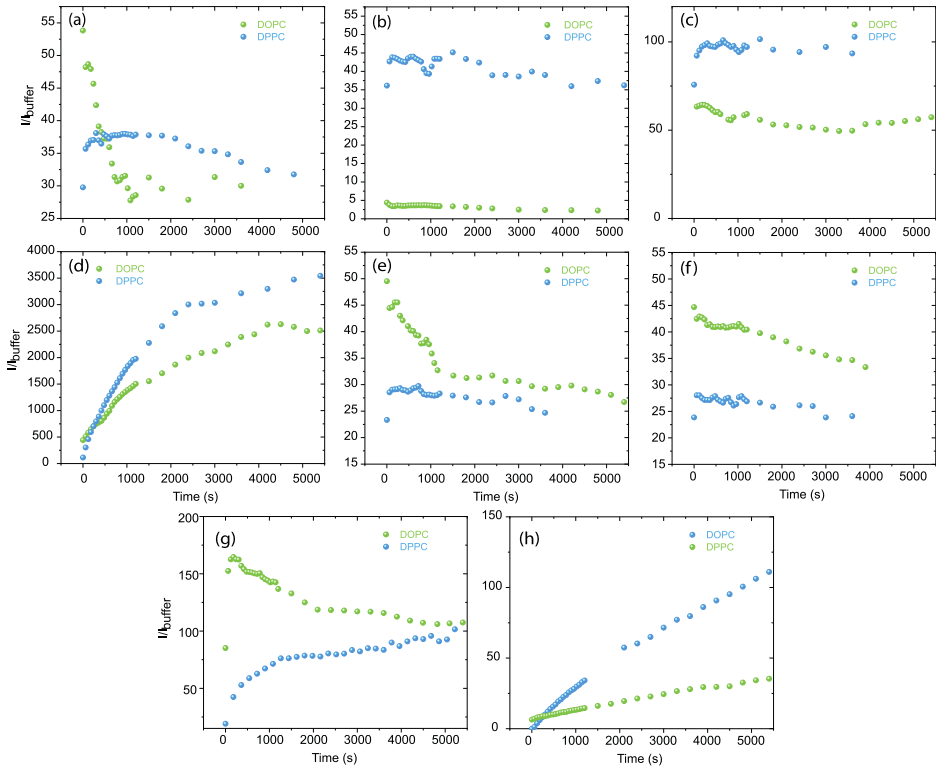

Figure 3.66 I/I_{buffer} ratio plotted against time for all the probes.

Upon equilibration, the intercalated probes into the liposome membranes were subjected to several heating-cooling cycles, since DPPC undergo to a phase transition at 41 °C.[259] The probes were warmed up to 55 °C and then cooled down to 25 °C several times to assess their response to the change of membrane fluidity. DOPC liposomes were also tested as negative control, since they exhibit no transition phase in the explored temperature range. While no differences are detected for butyl and octyl chains bearing fluorophores, the resting probes' emission hypsochromically shifts upon warming the loaded DPPC vesicles at 55°C

in a reversible manner, as confirmed by the occurring red shift upon cooling down to 25°C (Figure 3.67). This shift can be rationalized by the π-system planarization occurring at room temperature, where the DPPC show a packed solid-ordered (S_o) phase. At 55°C, a phase transition creates a more fluid L_d phase, reducing the S_o planarization and resulting in a hypsochromically shifted emission. DOPCs have been tested as a negative control since any phase transition above room temperature (Figure 3.68). Further support to this theory can be found looking at the excitation spectra recorded in DPPC (Figure 3.69). $\Delta\lambda_{exc} > \Delta\lambda_{em}$ since the planarization is a phenomenon highly appreciable at the ground state (*i.e.*, with the excitation spectra) and less at the excited state (*i.e.*, with the emission spectra). The not-occurring planarization for compounds **232**, **233** and **236**, **237** might be related to the bulkier emitters scaffold, whose planarization would require a higher membrane tension than the one provided by the DPPC S_o phase.

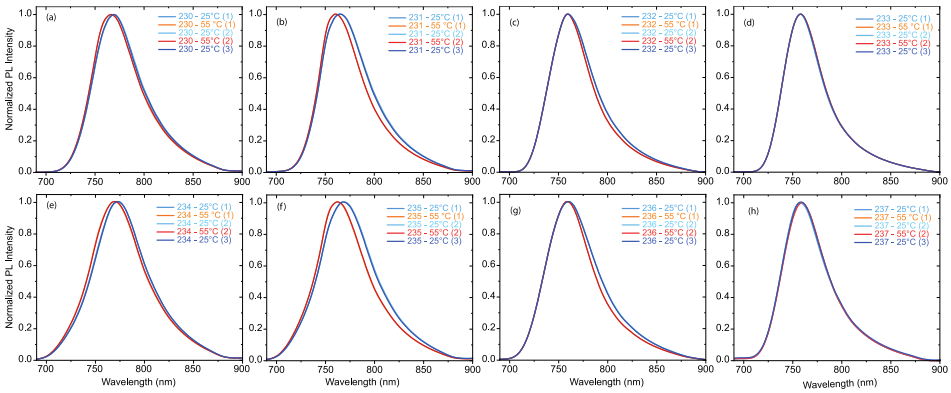

Figure 3.67 Normalized emission spectra upon several heating-cooling cycles in DPPC vesicles for the probes **230-237** (a-h).

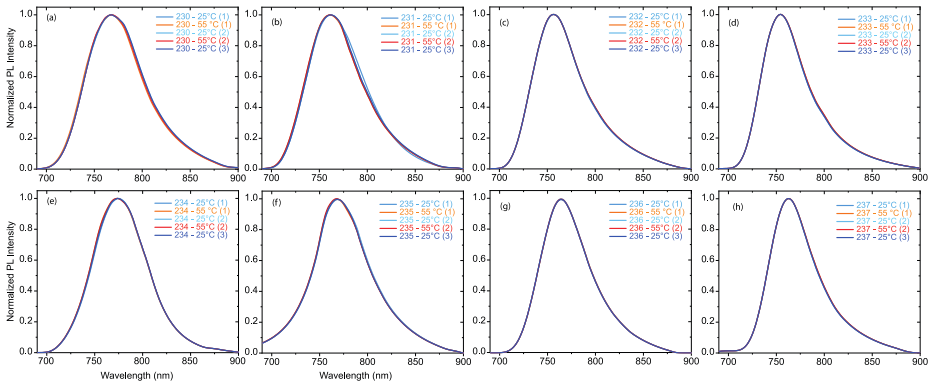

Figure 3.68 Normalized emission spectra upon several heating-cooling cycles in DOPC vesicles for the probes **230-237** (a-h).

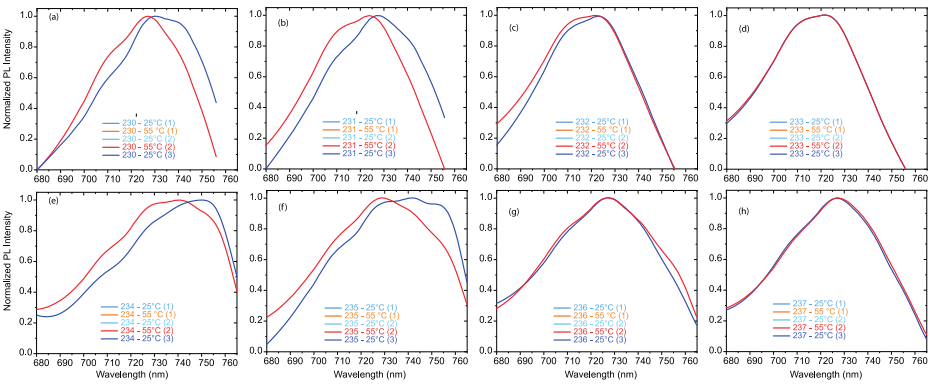

Figure 3.69 Normalized excitation spectra upon several heating-cooling cycles in DPPC vesicles for the probes **230-237** (a-h).

Conclusion

In this section, novel squaraine dyes have been presented, bearing indolenine-based moieties on one side of the centered squaric ring and perimidine groups on the other one. The unsymmetric π-conjugated system emitting at *ca.* 750 nm has shown a positive solvatochromism in contrast with the previously presented squaraine based probes and with many other similar cyanine fluorophores. Additionally, their weak fluorescence is fully quenched in protic solvents (e.g., water, ethanol) and

turned on in apolar environments (e.g., toluene). Their implementation into LUVs vesicles proved their intercalation into the lipid bilayer with particular outstanding results for octyl chain-bearing probes **233** and **237**. Their accentuated fluorogenic behaviour and stability inside the bilayer make them promising candidates to stain the cell membranes in a powerful spectral window. Additionally, the fluorophores bearing shorter alkyl chains proved to be sensitive to the membrane tension, undergoing π-system planarization upon viscosity increase. This finding suggests their use as a promising cellular tool to monitor many cellular pathways (e.g., endocytosis, apoptosis) where the membrane tension plays a key-role.

FUTURE PERSPECTIVES

In this work, the synergistic combination of organic synthesis with naturally occurring biological systems has been deeply explored. The tailoring capability of the former has been smartly implemented to provide novel and powerful tools in optoelectronics and chemical biology upon interaction with natural macromolecules. In detail, the optical properties enhancement by using a protein shield along with the photophysical perturbation upon interaction with phospholipid bilayers have been the two main key players of this work.

The enhanced thermal and photo stability achieved by shielding the fluorophore through a protein scaffold allowed us to implement these so-formed artificial fluorescent proteins into a novel generation of bio-hybrid LEDs, assessing one of the energetic issues raised by the European Union (EU) few years ago. Although white LEDs allow to reduce the energy consumption, increasing the efficiency when compared to the traditional lighting devices, the current technology does not represent a sustainable option due to the geopolitical and ecological impact of rare earth-based components. In this work, the organic small molecules advantages have been combined with the benefits derived from the use of a protein scaffold. The organic synthesis ability of tailoring the photophysical properties along with its low cost has been merged with the shielding effect of a peptide scaffold, able to reduce the aggregation-induced quenching and increasing the photo and thermal stability. The implementation of a squaraine emitter into a LmrR scaffold proved the validity of this approach improving the device performances from few hours up to 150 h in remote device configuration. Then, the synthesis of properly designed NDI-based fluorophores has been deeply explored,

preparing three differently emitting dyes covering the green, orange and red parts of the visible spectrum. Upon a first screening, the red emitting candidate resulted to be the best performing under device operative conditions and its molecular structure refining afforded **NDI-08** and **NDI-06**, whose implementation in device provided the longest living red-emitting HLEDs at the best of our knowledge. The realization of a white LED pushed us toward the preparation of green and yellow candidates to merge with the red NDI one. In particular, the synthetic investigation on a TTZ-based scaffold provided a remarkable green candidate (**TTZ-02**), while a well-known benzothiadiazole BTD emitter has been properly functionalized to provide promising yellow phosphors. Soon, their accommodation into suitable protein binding pockets will be carried out, affording additional artificial fluorescent proteins toward the realization of a white bio-HLED. Lastly, the investigation carried out on the BBT scaffold provided a novel fluorophore able to span along the visible spectrum still keeping excellent PLQY values. The preparation of blue emitters has been implemented in LEC devices, although structural modifications (*i.e.*, longer alkyl chains, bulkier groups) to improve filming morphologies are necessary. The green and yellow BBT candidates will be implemented soon in HLEDs devices to test their photostability.

In the second part of this work, the implementation of organic emitters in phospholipidic bilayers has provided novel fluorescent membrane probes. Solvatochromic TTZ-derivatives probes have been developed, able to discriminate between differently hydrated lipid phases ($\Delta\lambda$ = 70 nm between DOPC and DPPC at rt) and exhibiting a remarkable fluorogenic behaviour. Then, a particular focus on NIR probes was presented. Although squaraine dyes have already been proposed for cell membrane staining, a detailed structure-activity relationship is still missing. The

hydrophilicity/hydrophobicity balance have been finely tuned either by the presence of polar carboxylic moieties on the scaffold or by the elongation of the hydrocarbon chain used to quaternarize the nitrogen of the indolenine core. The former decorations should facilitate indeed the solubilization in biological media and lock the probes on the outer side of the amphiphilic bilayer, while the latter portions have been varied to investigate the respective interactions with the hydrophobic portion of the membranes. At first, the unsymmetric **216** resulted to be the best performing compound with a turn on effect of 287 in DOPC LUVs: one ethyl and one octyl chains result to be the most convenient balance between the hydrophobic-hydrophilic character of the probes presented in this study. The two-carbon atoms chain may contribute to create a more hydrophilic part able to interact with the polar phospholipids' heads, while the longer hydrophobic residue should better fit with the apolar environment within the lipid bilayer. Additional structural modifications have been lastly investigated by introducing a perimidine moiety from one side of the centered squaric acid ring. In this context, additional experiments in living cells should be carried out to better investigate the probes' performances in terms of cytotoxicity, stability and organelle-selectivity.

EXPERIMENTAL SECTION

5.1. Materials and methods

Reagents were purchased from Sigma-Aldrich, TCI, Intatrade Chemicals GmbH and Carlo Erba and used without further purification. 1,2-dioleoyl-sn-glycero-3-phosphocholine (DOPC) and 1,2-dipalmitoyl-sn-glycero-3-phosphocholine (DPPC) were purchased from Avanti Polar Lipids. Solvents were purchased from VWR, Carlo Erba and Sigma-Aldrich and used as received. NMR solvents were purchased from Sigma-Aldrich and Euriso-top. H_2O was purified with a Millipore RiOs 3 Water System. The reactions performed under microwave irradiation were conducted with a Biotage Initiator 2.5. All reactions were monitored with analytical TLC (Merck Kieselgel 60 F254). Column chromatography was carried out with Biotage Isolera and Buchi Pure C-850 FlashPrep with silica gel particle size 60 μm. NMR spectra were obtained on Bruker 200 MHz or 600 MHz and are reported as chemical shifts (δ) in ppm relative to TMS (δ= 0). Spin multiplicities are reported as a singlet (*s*), broad singlet (*bs*), doublet (*d*), doublet of triplets (*dt)*, triplet (*t*), triplet of doublets (*td*), quartet (*q*) and quintet (*quint*) with coupling constants (*J*) given in Hz, or multiplet (*m*). Mass spectra (ESI-MS) were obtained on a Thermo Scientific LCQ Advantage Max. HRMS spectra were recorded on a Bruker maXis 4G instrument. Lipid Vesicles (DOPC-DPPC) were prepared with a Mini-Extruder from Avanti Polar Lipids (pore size 100 nm).

5.2. Synthetic procedures

Compounds 118 has been prepared according to the literature procedures.[191]

Compounds 121, **122** and **123** have been prepared according to the literature procedures.[209]

NDI-01. **123** (0.05 g, 0,099 mmol, 1 eq.) was added to a solution of 1 M of KOH in iPrOH (10 mL) and heated at reflux under stirring for 12h. Then, the mixture was evaporated to dryness and redissolved in acetic acid (5 mL). To the obtained clear yellow solution, propargyl amine (19 μL, 0.297 mmol, 3 eq.) was added, and the reaction mixture was heated at 80°C for 12h. Then, ethyl acetate was added, and the organic phase was washed with an aqueous solution of 1 M $KHSO_4$, dried with Na_2SO_4 and the solvent was removed in vacuo. Purification by chromatography (CH_2Cl_2) afforded **NDI-01** as an orange solid. Yield: 56%. M_p > 220°C. ^{1}H-NMR (600 MHz, $CDCl_3$): δ 8.53 (s, 2H), 4.96 (d, 4H, ^{4}J (H,H) = 2.5 Hz), 4.53 (q, 4H, ^{3}J (H,H) = 7.09 Hz), 2.21 (t, 2H, ^{4}J (H,H) = 2.44 Hz), 1.67 (t, 6H, ^{3}J (H,H) = 7.32 Hz). ESI-MS (+ve): 883 [2M + Na^+], 845 [M + (M-OEt)]$^+$, 415 [M-OEt]$^+$. ^{13}C-NMR wasn't recorded due to solubility issues.

NDI-02 and **NDI-03**. **NDI-01** (20 mg, 0.046 mmol, 1 eq.) was suspended in dichloromethane (8.75 mL), and monoisopropyl amine (8.75 mL, 101,2 mmol, 2200 eq.) was added. The reaction mixture was stirred and heated under MW irradiation at 120°C for 1h. Then, the mixture was cooled, and the organic layer was washed with aqueous HCl 1 M, dried with Na_2SO_4 and the solvent removed in vacuo. The mixture of NDI-02 and NDI-03 was purified by chromatographic column (Hexane/ CH_2Cl_2 1:1), affording the two products as red (**NDI-02**, 65%) and blue (**NDI-03**, 35%) powders. ^{13}C-NMRs weren't recorded due to solubility issues. M_p > 220°C. **NDI-02**: ^{1}H-NMR (600 MHz, $CDCl_3$): δ 9.75 (d, 1H), 8.38 (s, 1H), 8.32 (s, 1H), 4.98 (d, 2H, ^{4}J (H,H) = 2.42 Hz), 4.94 (d, 2H, ^{4}J (H,H) = 2.45 Hz) 4.44 (q, 4H, ^{3}J (H,H) = 6.93 Hz), 4.16 (qt, 1H, ^{3}J (H,H) = 6.50 Hz), 2.23 (t, 1H, ^{4}J (H,H)

= 2.1 Hz), 2.20 (t, 1H, ^{4}J (H,H) = 2.09 Hz), 1.65 (t, 3H, ^{3}J (H,H) = 6.9 Hz), 1.43 (d, 6H, ^{3}J (H,H) = 6.60 Hz). ESI-MS (+ve): 909 [2M + Na^+]. **NDI-03**: ^{1}H-NMR (600 MHz, $CDCl_3$): δ 9.30 (d, 2H), 8.21 (s, 2H), 4.97 (d, 4H, ^{4}J (H,H) = 2.6 Hz), 4.10 (qt, 2H, ^{3}J (H,H) = 6.54 Hz), 2.23 (t, 2H, ^{4}J (H,H) = 2.40 Hz), 1.40 (d, 12H, ^{3}J (H,H) = 6.13 Hz). ESI-MS (+ve): 935 [2M + Na^+], 912 $[2M]^+$, 456 $[M]^+$.

Compound 125. **123** (0.05 g, 0.099 mmol, 1 eq.) was added to a solution of 1 M of KOH in iPrOH (10 mL) and heated at reflux under stirring for 12h. The mixture was evaporated to dryness, and the residue was then dissolved in acetic acid (5 mL). To the obtained clear yellow solution, ethanolamine (0.018 g, 0.297 mmol, 3 eq.) was added, and the reaction mixture was heated at 80°C for 12h. Then, ethyl acetate was added, and the organic phase was washed with an aqueous solution 1 M $KHSO_4$, dried over Na_2SO_4, and the solvent was removed in vacuo. Purification by chromatography (CH_2Cl_2/MeOH 95:5) afforded the product as an orange solid. Yield: 43%. R_f: 0.8 (eluent CH_2Cl_2:MeOH 90:10) ^{1}H-NMR (600 MHz, $CDCl_3$/CD_3OD): δ 8.43 (s, 2H), 4.47 (q, 4H, ^{3}J (H,H) = 6 Hz), 4.33 (t, 4H, ^{3}J (H,H) = 6.1 Hz), 3.85 (t, 2H, ^{3}J (H,H) = 6 Hz), 1.57 (t, 6H, ^{3}J(H,H) = 6.4 Hz). ESI-MS (+ve): 907 [2M + Na^+].

Compound 131 was prepared according to the literature procedure.[275]

Compound 132. KOH (1.12 g) was suspended in *i*PrOH (20 mL) and heated at 80°C. Then, **123** (0.1 g, 0.198 mmol, 1 eq.) was added, and the reaction was heated under stirring overnight. Then, the reaction was cooled down and the volatiles were removed in vacuo. The yellowish residue was redissolved in acetic acid (10 mL) and **131** (0.12 g, 0.792 mmol, 4 eq.) was added. The reaction mixture was heated at 70°C for 7

h. Then, the orange precipitate was collected by filtration and dried under vacuo. Then, the solid was purified by flash chromatography (from DCM to DCM/MeOH 90:10) affording **132** (0.023 g, yield 16%) as a yellow solid. ^{1}H-NMR (600 MHz, $CDCl_3$) δ: 8.40 (s, 2H), 6.44 (s, 4H), 5.15 (s, 4H), 4.46 (q, 4H, J = 7.02 Hz), 4.41 (m, 4H), 3.93 (m, 4H), 2.77 (s, 4H), 1.60 (t, 6H, 7.01 Hz). ^{13}C NMR (150 MHz, $CDCl_3$) δ: 176.78, 163.86, 160.44, 136.18, 134.11, 126.01, 124.03, 121.08, 80.50, 65.74, 54.29, 45.55, 39.74, 37.03, 15.04.

NDI-05. 132 (23 mg) was suspended in toluene and heated at 110°C overnight. Then, volatiles were removed in vacuo and the crude mixture was purified by flash chromatography (DCM/EtOAc 1:1) affording pure **NDI-05** (9 mg, yield 61%) as an orange powder. ^{1}H-NMR (600 MHz, $CDCl_3$) δ: 8.40 (s, 2H), 6.64 (s, 4H), 4.49 (q, 4H, J = 7.02 Hz), 4.42 (t, 4H, J = 5.10 Hz), 3.99 (t, 4H, J = 5.16 Hz), 1.62 (t, 6H, J = 6.98 Hz). ^{13}C NMR (150 MHz, $CDCl_3$) δ: 171.58, 164.18, 160.19, 134.01, 128.15, 125.37, 124.21, 121.65, 69.16, 40.28, 35.78, 31.55, 15.12.

Compound 133 has been prepared according to the literature procedure. [276]

Compound 134. A freshly prepared solution of AllylONa in allyl alcohol (240 uL of a solution of 1 M of NaH in allyl alcohol) was added dropwise to a solution of **133** (50 mg, 0.08 mmol) in dry DCM (8 mL). The mixture was stirred at rt for 7 h. Then, DCM was added, and the organic layer was washed with brine and water, dried over Na_2SO_4 and concentrated *in vacuo*. The crude was purified by flash chromatography (DCM/Hexane 3:2), affording **134** as a yellow solid (13 mg, 28%). ^{1}H-NMR (600 MHz, $CDCl_3$): 8.47 (s, 2H), 6.18 (ddt, J = 17.2, 10.6, 5.2 Hz, 2H), 5.72 (dq, J =

17.2 Hz, ^{2}J(H,H) = 1.2 Hz, J = 1.4 Hz, 2H), 5.45 (dq, , J = 10.6 Hz, ^{2}J(H,H) = 1.2 Hz, J = 1.4 Hz, 2H), 5.02 (dt, , J = 5 Hz, J = 1.5 Hz, 4H), 4.15 (t, J = 7.8 Hz, 4H), 1.73 (qt, J = 7.8 Hz, 4H), 1.42 (qt, J = 7.7 Hz, 4H), 1.36 (qt, J = 7.6 Hz, 4 H), 1.32-1.25 (m, 12 H), 0.87 (t, J = 6.8 Hz, 6H). ^{13}C-NMR (150 MHz, $CDCl_3$): δ 162.53, 161.27, 159.80, 131.60, 127.80, 123.88, 120.12, 119.47, 111.36, 71.61, 43.44, 31.96, 29.46, 29.36, 28.14, 27.31, 22.79, 14.79. MS (ESI, DCM/MeOH): 603 ($[M+H]^+$), 1204 ($[2M]^+$), 1227 ($[2M + Na^+]$).

NDI-07. To a solution of **134** (13 mg, 0.02 mmol, 1 eq.) and $Pd(PPh_3)_4$ (1.3 mg, 0.001 mmol, 0.005 eq.) in dry DCM (3 mL), phenylsylane (17.3 mg, 0.16 mmol, 8 eq.) was added. The mixture was stirred under Argon at rt for 12 h. Volatiles were removed *in vacuo,* and the reaction crude was purified by flash chromatography (DCM/Hexane 1:1), affording **NDI-07** as a yellow solid (6 mg, 53%).^{1}H-NMR (600 MHz, $CDCl_3$): 12.38 (s, 2H), 8.30 (s, 2H), 4.17 (t, J = 7.7 Hz, 4H), 1.73 (qt, J = 7.6 Hz, 4H), 1.42 (qt, J = 7.6 Hz, 4H), 1.36 (qt, J = 7.4 Hz, 4 H), 1.32-1.25 (m, 12 H), 0.87 (t, J = 6.9 Hz, 6H). ^{13}C-NMR (150 MHz, $CDCl_3$): δ 168.55, 166.42, 161.92, 160.68, 127.25, 123.94, 106.96, 40.75, 31.93, 29.38, 29.32, 28.09, 27.19, 22.77, 14.24.

Compound 135 has been prepared according to the literature procedure.[211]

Compound 136. To a solution of 3 (0.45 g, 1.04 mmol, 1 eq.) in dry 1,4-Dioxane (16 mL), *i*$PrNH_2$ (0.20 g, 3.38 mmol, 3.25 eq.) and DIPEA (0.44 g, 3.38 mmol, 3.25 eq,) were added. The reaction is stirred at 100°C for 48 h. Then, the solvent is removed *in vacuo*, and the crude mixture is diluted with DCM and washed with water. The organic layer was dried

over Na_2SO_4, and volatiles were removed in vacuo. Flash chromatography (Petroleum Ether/Ethyl Acetate 9/1) afforded the pure **136** (0.12 g, 24% yield) as a yellow powder. ^{1}H-NMR ($CDCl_3$, 600 MHz): δ 8.40 (s, 1H), 7.72 (s, 1H), 5.42 (sept, 1H, J= 7.1 Hz), 4.41 (m, 6H), 4.30 (q, 2H, J= 7.0 Hz), 1.62 (t, 3H, J= 6.96 Hz), 1.57 (d, 6H, J= 6.96 Hz), 1.47 (t, 3H, J= 6.97 Hz), 1.42 (t, 6H, J= 7.1 Hz). ^{13}C-NMR ($CDCl_3$, 150 MHz): δ 167.47, 166.86, 163.32, 162.11, 159.49, 154.54, 136.14, 126.31, 125.38, 122.74, 122.12, 119.48, 119.40, 109.87, 66.20, 66.03, 62.42, 61.78, 45.48, 19.83, 15.00, 14.96, 14.26, 14.22.

Compound 137. 136 (0.87 g, 1.85 mmol) was dissolved in TFA (14 mL) and heated at 70°C for 24 h. Then, volatiles were removed *in vacuo* and the crude was purified by flash chromatography (DCM), affording **137** (0.46 g, yield 63%) as an orange solid. ^{1}H-NMR ($CDCl_3$, 600 MHz): δ 8.46 (s, 1H), 8.43 (s, 1H), 5.41 (sept, 6H, J= 6.90 Hz), 4.54 (q, 2H, J= 6.96 Hz), 4.50 (q, 2H, J= 6.96 Hz), 1.66 (t, 3H, J= 6.90 Hz), 1.64 (t, 2H, J= 6.96 Hz), 1.58 (d, 6H, J= 6.96 Hz). ^{13}C-NMR ($CDCl_3$, 150 MHz): δ 162.28, 161.47, 161.27, 160.04, 159.89, 155.47, 129.38, 125.82, 123.77, 123.15, 121.57, 119.55, 112.84, 106.65, 66.75, 66.71, 46.13, 19.77, 14.87, 14.81.

Compound 139. To a solution of **137** (0.2 g, 0.504 mmol, 1 eq.) in dry Dioxane (10 mL), **138** (34 mg, 0.562 mmol, 1.1 eq.) and DIPEA (73 mg, 0.562 mmol 1.1 eq.) were added. The orange solution was heated at 101°C for 5 h. Then, the solvent was removed in vacuo and the crude was purified by a flash chromatography (from DCM to DCM/MeOH 95:5) affording **139** (0.18 g, yield 81%) as an orange solid. ^{1}H-NMR (600 MHz, $CDCl_3$) δ: 8.45 (s, 1H), 8.43 (s, 1H), 5.44 (sept, 1H, J = 6.84 Hz), 4.52 (q, 2H, J = 6.96 Hz), 4.50 (q, 2H, J = 6.96 Hz), 4.00 (q, 2H, J = 5.16 Hz), 2.24 (t, 1H, 5.3 Hz), 1.66 (m, 6H), 1.60 (d, 6H, J = 6.96 Hz). ^{13}C NMR (150

MHz, $CDCl_3$) δ: 163.56, 162.68, 162.21, 161.73, 160.46, 159.95, 128.34, 126.75, 123.72, 123.67, 120.04, 119.55, 111.75, 110.41, 77.16, 66.44, 61.68, 45.91, 43.11, 19.83, 14.93.

Compound 140. 139 (20 mg) was suspended in 2 mL of DMA and 15 mL of *i*$PrNH_2$. The mixture was heated under MW irradiation (130°C, 2h30). Volatiles were removed in vacuo and the crude was dissolved in DCM and washed with HCl 1M and brine. The organic layer was dried over Na_2SO_4 and concentrated in vacuo. Pure **140** (9 mg, yield 42%) was obtained after flash chromatography (DCM/EtOAc 95/5 to 90/10). ^{1}H-NMR (600 MHz, $CDCl_3$) δ: 9.33 (d, 1H, J = 7.38 Hz), 9.28 (d, 1H, J = 7.40 Hz), 8.15 (s, 1H), 8.14 (s, 1H), 5.46 (sept, 1H, J = 6.12 Hz), 4.47 (t, 2H, J = 5.10 Hz), 4.10 (sept, 1H, J = 6.2 Hz), 3.99 (q, 2H, J = 5.1 Hz), 2.46 (t, 1H, J = 5.4 Hz), 1.60 (d, 6H, J = 6.96 Hz), 1.40 (m, 12H). ^{13}C NMR was not recorded due to solubility issues.

Compound 141. Maleimide (0.5 g, 0.005 mol) was added to a round-bottom flask and suspended in diethyl ether (10 mL). Furan (0.7 g, 0.01 mol) was added and the reaction was stirred at rt for 5 days. Then, **141** (0.75 g, yield 89%) was collected as a white solid by filtration and dried under vacuum. **141** was obtained as a mixture of *exo* and *endo* isomers and used without further purifications.

Compound 142. 140 (20 mg, 0.04 mmol, 1 eq.) was dissolved in dry THF (5 mL) under Ar atmosphere. Then, **141** (8.9 mg, 1.3 eq.) and DIAD (13 uL, 1.6 eq.) are added and mixture is stirred at rt overnight. The day after, no conversion is detected by TLC and few drops of DIAD and a spatula of **141** are added. After 3 h, no **140** was detected. The solvent was removed *in vacuo* and the new blue spot was isolated by flash

chromatography (from 100% DCM to 95:5 DCM/MeOH). Product **142** was a sticky oil (probably due to the high quantity of triphenylphosphine oxide) and carried forward the next step without further purification.

NDI-06. 142 was dissolved in toluene (20 mL) and heated at 110°C overnight. Then, the volatiles were removed *in vacuo* and the crude was passed through a flash chromatography (from DCM to DCM/EtOAc 85:15). The product was then suspended in methanol (5 mL) and filtered to remove the triphenylphosphine oxide from the previous step. **NDI-06** was obtained as a blue solid (yield 34% from **11** over two steps). ^{1}H-NMR (600 MHz, $CDCl_3$) δ: 9.33 (d, 1H, J = 7.56 Hz), 9.22 (d, 1H, 7.56 Hz), 8.12 (s, 1H), 8.08 (s, 1H), 6.62 (s, 2H), 5.45 (sept, 1H, J = 6.86 Hz), 4.42 (t, 2H, J = 5.16 Hz), 4.07 (sept, 1H, J = 6.72 Hz), 3.97 (t, 2H, 5.28 Hz), 1.59 (d, 6H, J = 6.96 Hz), 1.39 (m, 12H). ^{13}C NMR (150 MHz, $CDCl_3$) δ: 170.80, 166.80, 166.62, 166.31, 163.57, 163.43, 148.64, 148.35, 134.15, 125.25, 121.46, 121.24, 118.68, 118.60, 101.11, 45.19, 44.21, 44.12, 38.74, 36.30, 23.26, 23.20, 19.83.

Compound 143. To a solution of **137** (0.02 g, 0.05 mmol, 1 eq.) in dry 1,4-Dioxane (2 mL), **148** (8.4 mg, 0.056 mmol, 1.1 eq.) and DIPEA (15 mg, 0.12 mmol, 2.2 eq.) were added. The orange solution was heated at 101°C overnight. Then, solvent was removed in vacuo and the residue was dissolved in acetic acid (4 mL) and heated at 100°C for 1 h. Then, volatiles were removed in vacuo and the crude was purified by flash chromatography (from 98/2 DCM/EtOAc to 90/10 DCM/EtOAc), affording **143** (18 mg, yield 73%) as an orange solid. ^{1}H-NMR ($CDCl_3$, 600 MHz): δ 8.44 (s, 1H), 8.42 (s, 1H), 6.06 (t, 1H, J= 4.5 Hz), 5.41 (sept, 1H, J= 6.92 Hz), 4.87 (s, 2H), 4.50 (q, 4H, J= 7.02 Hz), 4.08 (2H, dd, ^{J}= 4.70 Hz, J= 1.45 Hz), 2.24 (t, 1H, J= 1.38 Hz), 1.65 (t, 3H, J= 6.96 Hz), 1.63 (t, 3H,

J= 7.02 Hz), 1.59 (d, 6H, J= 6.96 Hz). ^{13}C-NMR ($CDCl_3$, 150 MHz): δ 166.51, 162.57, 162.51, 161.62, 161.05, 160.46, 159.82, 128.33, 126.44, 123.67, 123.63, 120.10, 119.40, 111.71, 110.04, 79.23, 72.12, 66.42, 66.39, 45.93, 42.98, 29.63, 19.80, 14.90.

NDI-08. 143 (95 mg, 0.19 mmol) is dissolved in *i*PrNH$_2$ (15 mL) and DMA (1 mL). Reaction was stirred at 50°C for 48 h and then at 100°C for 2h under MW irradiation. Volatiles were removed *in vacuo* and the crude was redissolved in DCM, washed with HCl 1M, brine and finally dried over Na_2SO_4. The residue was purified by flash chromatography (DCM/MeOH 98/2) affording **NDI-08** (40 mg, yield 40%) as a blue solid. ^{1}H-NMR (600 MHz, $CDCl_3$): δ 9.31 (d, 1H, J= 7.38 Hz), 9.21 (d, 1H, J= 7.41 Hz), 8.14 (s, 1H), 8.13 (s, 1H), 5.97 (t, 1H, J= 4.65 Hz), 5.45 (sept, 1H, J= 7.00 Hz), 4.86 (s, 2H), 4.11 (dd, 2H J= 4.7 Hz, J= 1.45 Hz), 4.05 (sept, 2H, J= 6.97 Hz), 2.25 (t, 1H, J= 1.42 Hz), 1.59 (d, 6H, J= 6.96 Hz), 1.39 (d, 6H, J= 7.01 Hz), 1.37 (d, 6H, J= 7.04 Hz).

Compound 146. Glycine (11.1 g, 148.12 mmol) was dissolved into 1,4-dioxane (150mL). Then, NaOH aqueous solution (2N, 88.88 ml, 178 mmol) and Boc-anhydride (48.5 g, 222mmol) was added and the mixture was stirred at rt overnight. Then, the reaction solution is transferred to a rotary evaporator and concentrated. The aqueous phase have been washed with ether (3 x 50 mL). The aqueous phase was adjusted to pH=4 by adding 1 mol/L hydrochloric acid. And finally extracted with ethyl acetate (150 ml×5). The organic phases were combined, and the organic phase was dried over anhydrous sodium sulfate. Removal of volatile under reduced pressure afforded pure **146** quantitatively.

Compound 147, 148 have been prepared according to literature procedure.[277]

NDI-09. To a solution of **5** (0.02 g, 0.05 mmol, 1 eq.) in dry 1,4-Dioxane (2 mL), propargyl amine (3.1 mg, 0.056 mmol, 1.1 eq.) and DIPEA (7.5 mg, 0.12 mmol, 1.1 eq.) were added. The orange solution was heated at 101°C overnight. Then, solvent was removed in vacuo and the residue was dissolved in acetic acid (4 mL) and heated at 100°C for 1 h. Then, volatiles were removed in vacuo and the crude was purified by flash chromatography (9:1 DCM/EtOAc), affording **NDI-09** (12 mg, yield 55%) as an orange solid. M_p > 220°C. ^{1}H-NMR ($CDCl_3$, 600 MHz): 8.47 (s, 1H), 8.43 (s, 1H), 5.42 (qt, 1H, J = 6.9 Hz), 4.94 (d, 2H, J = 2.3 Hz), 4.50 (q, 4H, 6.9 Hz), 2.19 (t, 1H, J = 2.4 Hz), 1.66 (t, 6H, J = 6.9 Hz), 1.59 (d, 6H, J = 7.0 Hz). ^{13}C-NMR ($CDCl_3$, 150 MHz): δ 162.57, 161.95, 161.59, 160.51, 160.36, 159.84, 128.37, 126.56, 123.71, 123.58, 120.06, 119.46, 111.84, 110.21, 78.39, 70.82, 66.38, 45.85, 29.70, 19.75, 14.86.

Compound 150. To a cooled solution of NaOH (1.92 g, 4.58 mmol) in water was added **149** (2 g, 4.4 mmol) in THF drop-wise over a period of 30 min. To this mixture was added p-toluenesulfonyl chloride (3.05 g, 26 mmol) in THF (150 mL), drop-wise over 10 min. The reaction mixture was stirred vigorously 24 h, allowing it to come to ambient temperature. The reaction mixture was again cooled in an ice bath before the addition of concentrated HCl (37% w/w, ~45 mL) until the pH was 7. The THF was then removed under reduce pressure, taking care to maintain a bath temperature of no more than 30 ˚C. The product was extracted into DCM. The combined DCM extracts were then washed with aqueous Na2CO3 (10% w/w) and MilliQ water until the pH of the aqueous wash was neutral. The DCM layer was dried over MgSO4, filtered, and concentrated under

reduced pressure. (yield: 3.49 g, 86 %) H NMR (400 MHz, CDCl3): δ 7.79 (d, J = 8.3 Hz, 6H, -S-C=CH-CH), 7.34 (d, J = 8.0 Hz, 6H, -S-C=CH-CH), 4.17 – 4.11 (t, 6H, -CH2-CH2-O-Ts), 3.70 – 3.65 (t, 6H, , -CH2-CH2-O-Ts), 3.65 – 3.18 (series of m, 33H, actual number may vary batch to batch based on oligomers represented in the material), 2.44 (s, 9H), 1.39 – 1.26 (m, 2H, -O-CH2-CH3), 0.85 – 0.71 (m, 3H, -O-CH2-CH3) ppm.

Compound 151. This method has been modified from a reported procedure.[278] A round bottom flask was charged with **150** (2.71, 2.97 mmol) and DMF (40 ml) under N_2. To this mixture, NaN_3 (5.78 g, 89.1 mmol) and TBAI (55 mg, 0.1485 mmol) was added. The reaction mixture was heated at 100°C overnight and then cooled to room temperature. The reaction mixture was diluted with water and extracted with DCM. The organic layer was washed with water and dried over MgSO4, and evaporated under vacuum to afford compound **151** as a yellow liquid (1.39 g, 90 %). H NMR (400 MHz, CDCl3) δ 3.67 – 3.45 (series of m, 28H actual number may vary batch to batch based on oligomers represented in the material), 3.43 – 3.20 (m, 8H), 1.42 – 1.22 (m, 2H, -O-CH2-CH3), 0.77 (t, J = 8.0 Hz, 3H, -O-CH2-CH3) ppm.

NDI-01@TMPE. To a solution of **NDI-01** (100 mg) in DCM/ACN (2:1), CuOAc (catalytic amount) and sodium ascorbate (catalytic amount) were added. Then, the reaxtion was heated at 40°C under stirring overnight. Then, the volatiles were removed under reduced pressure, DCM (100 mL) was added and filtered to remove the inorganic salts. A filtration on silica pad allowed to remove the free dye (DCM 100%), while the desired **NDI-01@TMPE** has been eluted with a mixture DCM/MeOH (9:1).

NDI-09@TMPE. To a solution of **NDI-09** (100 mg) in DCM/ACN (2:1), CuOAc (catalytic amount) and sodium ascorbate (catalytic amount) were added. Then, the reaxtion was heated at 40°C under stirring overnight. Then, the volatiles were removed under reduced pressure, DCM (100 mL) was added and filtered to remove the inorganic salts. A filtration on silica pad allowed to remove the free dye (DCM 100%), while the desired **NDI-09@TMPE** has been eluted with a mixture DCM/MeOH (9:1).

Compound 155.

Method A: **154** (1.5 g, 12.5 mmol, 1 eq.), **152** (3.07 g, 18.7 mol, 1.5 eq), **153** (3.52 g, 18.7 mol, 1.5 eq.) were dissolved in dry DMF (18 mL). The mixture was stirred and heated at 120°C for 6 h. The reaction mixture was cooled overnight at room temperature. The precipitate was collected by filtration, rinsed with water and purified by chromatography (Hexane/DCM 8:2), giving compound **155** as an orange powder.

Method B: **154** (3.39 g, 28.2 mmol, 1 eq.), **152** (1.5 eq., 8 g, 42.3 mmol, 1.5 eq.), **153** (6.91 g, 18.7 mmol, 1.5 eq.) were dissolved in nitrobenzene (34 mL). The mixture was stirred and heated at 150°C for 6 h. Then THF (270 mL) and DDQ (3.2 g, 14.1 mmol, 0.5 eq.) were added. The reaction mixture was stirred for 10 minutes at reflux temperature, then MeOH (150 mL) was added. The mixture was cooled to 0°C and the precipitate was collected by filtration, then washed by MeOH. The product **155** is carried forward the next step without further purification.

Method C: To a 10 mL reaction vial was added **154** (1 g, 8.32 mmol, 1 eq.), **152** (2.36 g, 12.48 mmol, 1.5 eq.) and **153** (2.04 g, 12.48 mmol, 1.5 eq.) followed by nitrobenzene (10 mL). The reaction mixture was stirred and heated in microwave reactor for 30 min at 150°C. After cooling to room temperature, the resulting mixture was collected in a flask and THF (100 ml) and DDQ (4.15 mmol, 0.94 g, 0.5 eq.) were added. The reaction

mixture was stirred for additional 10 minutes at reflux temperature, then MeOH (50 mL) was added and the mixture was cooled to 0°C. The precipitate was collected by filtration and washed by MeOH. Compound **155** was obtained as a brown powder (0.64 g, 17%). ^{1}H-NMR:(600 MHz, $CDCl_3$, ppm) δ: 8.11 (d, 2H, J= 8.7 Hz), 8.03 (d, 2H, J = 8.6 Hz), 7.84 (d, 2H, J= 8.9 Hz), 6.93 (d, 2H, J= 8.2 Hz), 3.31 (t, 4H, J= 5.3 Hz), 1.74-1.66 (m, 4H, J= 4.1 Hz), 1.65-1.60 (m, 2H, J= 5.9 Hz). ^{13}C-NMR (150 MHz, $CDCl_3$): 177.84, 166.58, 165.90. 151.76, 150.31, 138.07, 131.32, 130.49, 127.96, 126.13, 114.98, 52.47, 49.27, 25.57, 24.44, 14.27. Mass (ESI+): 436.09 uma

Compound 156. 155 (320 mg, 0.73 mmol, 1 eq.) was dissolved in dry DCM (50 mL) and the solution was cooled to -78°C. DIBAL-H (1.46 mL of a solution 1M in Hexane, 1.46 mmol, 2 eq.) was added and the mixture was stirred for 3 hours. The reaction was warmed up to room temperature, then methanol was added dropwise to quench the reaction. The organic layer was washed with brine and dried over Na_2SO_4. The solvent was removed by rotary evaporation and the residue was purified by flash chromatography (DCM/EtOAc 5:1) giving **156** (110 mg, yield 37%) as a yellow powder. ^{1}H-NMR (600MHz, $CDCl_3$, ppm) δ: 7.96 (d, 2H, J= 8.3 Hz), 7.84 (d, 2H, J= 9 Hz), 7.45 (d, 2H, J= 8.6 Hz), 4,75 (d, 2H, J=5.1 Hz), 3.31 (t, 2H, J= 5.4 Hz), 1.75-1.77 (t, 1OH, J= 5.7), 1.67-1.71 (m, 4H, J= 5.6), 1.61-1.64 (m, 2H, J= 6.2). ^{13}C-NMR (150 MHz, $CDCl_3$/MeOD): 170.41, 167.86, 150.50, 149.53, 143.80, 135.90, 133.03, 127.69, 127.43, 126.33, 125.50, 115.02, 64.13, 34.26, 25.37, 24.31.

TTZ-02. 156 (150 mg, 0.368 mmol, 1 eq.) was added to a suspension of NaH (20 mg of a suspension at 60% in paraffin) in THF (30 mL) at 0°C. The mixture was stirred for 30 minutes at 0°C. Propargyl bromide (0.5 mL,

6.6 mmol, 130 eq.) was added and the resulting mixture was stirred at room temperature for two days. The reaction was quenched by addition of few drops of methanol, then EtOAc was added. The organic layer was washed with HCl 1N and dried over sodium sulphate anhydrous. Solvent was removed *in vacuo* and the crude residue was purified by flash chromatography (DCM/EtOAc 99/1) giving **TTZ-02** (40 mg, 24 %) as a yellow powder**.** ^{1}H-NMR: (600MHz, $CDCl_3$, ppm) δ: 7.95 (d, 2H, J= 8.3 Hz), 7.84 (d, 2H, J= 8.9 Hz), 7.44 (d, 2H, J= 8.4 Hz), 6.92 (d, 2H, J= 8.9 Hz), 4.65 (s, 2H), 4.21 (d, 2H, J= 2.3 Hz), 3.30 (t, 4H, J= 5.3 Hz), 2.48 (t, 1H, J= 2.3 Hz), 1.67-1.71 (m, 4H, ^{3}J (H,H)= 5.6 Hz), 1.61-1.64 (m, 2H, J= 5.8 Hz). ^{13}C-NMR (150 MHz, $CDCl_3$): 170.23, 167.33, 153.34, 150.87, 149.82, 139.81, 133.85, 128.64, 127.75, 126.39, 123.68, 115.01, 79.50, 74.98, 71.08, 57.43, 49.25, 25.54, 24.40.

Compound 157. To a solution of compound **156** (43 mg) in DCM, MnO_2 (8 eq.) was added. After stirring at room temperature for 2 h, the mixture was filtered to remove MnO_2. The solvent was removed *in vacuo* and the crude was purified by chromatography (DCM) giving **157** as an orange solid (19 mg, 45%).^{1}H-NMR (600MHz, $CDCl_3$, ppm) δ: 10.05 (s, 1H), 8.14 (d, 2H, ^{3}J (H,H) = 8.3 Hz), 7.96 (d, 2H, ^{3}J (H,H) = 8.3 Hz), 7.85 (d, 2H, ^{3}J (H,H) = 8.9 Hz), 6.93 (d, 2H, ^{3}J (H,H) = 8.9 Hz), 3.33 (t, 4H, ^{3}J (H,H) = 5.2 Hz), 1.68-1.71 (m, 4H, ^{3}J (H,H) = 5.6 Hz), 1.62-1.65 (m, 2H, ^{3}J (H,H) = 5.6 Hz). ^{13}C-NMR (150 MHz, $CDCl_3$): 191.48, 165.27, 163.64, 153.17, 149.08, 142.34, 139.39, 131.71, 130.52, 127.95, 126.63, 114.88, 49.14, 25.52, 24.41. Mass (ESI+): 406.06 uma.

Compound 158. To a well stirred solution of compound **157** in DCM/EtOH (2:1) cyanoacetic acid and piperidine were added. The mixture was stirred at room temperature overnight. Solvent was removed by rotary

evaporation. the product was dissolved in DCM and the organic layer was washed by HCl 1 N, then neutralized with a saturated solution of NaHCO3. In order to improve the phase separation few drops of TEA were added. The organic layer was dried over Na_2SO_4 and concentrated *in vacuo*. Silica gel column chromatography (DCM/TEA 99:1) of the residue gave **158** as a red oil. The presence of TEA excess was detected by ^{1}H-NMR and did not allow the yield calculation. ^{1}H-NMR: (600MHz, $CDCl_3$, ppm) δ: 8.16 (s, 1H), 8.04 (d, 2H, ^{3}J (H,H) = 8.7 Hz), 8.02 (d, 2H, ^{3}J (H,H) = 8.8 Hz), 7.82 (d, 2H, ^{3}J (H,H) = 8.9 Hz), 6.91 (d, 2H, ^{3}J (H,H) = 8.8 Hz), 3.29 (t, 4H, ^{3}J (H,H) = 9.42 Hz), 1.65-1.69 (m, 4H, ^{3}J (H,H) = 5.8 Hz), 1.59-1.62 (m, 2H, ^{3}J (H,H)= 5.6 Hz). Mass (ESI+): 473.04 uma.

Compound 160 and **BTD-I-01** have been prepared according literature procedures. [232]

Compound 162. This is a modified literature procedure.[279,280] Into a vial under N_2 atmosphere, a solution of **BTD-I-01** (1.0 equiv, 1.0–2.0 mmol) in $CHCl_3$ (0.2 M) was prepared. The solution was cooled down to 0 °C, and $POCl_3$ (2.2 equiv) and anhydrous *N*,*N*-dimethylformamide (2.2 equiv) were added. The mixture was stirred at 75 °C until all starting material disappeared (TLC control, approximately 48 h). Then, the mixture was cooled down to 0 °C and a saturated Na_2CO_3 solution was slowly added. The mixture was extracted three times with DCM; the combined organic layers were dried over anhydrous Na_2SO_4, filtered and the volatiles were removed under reduced pressure. The crude product was purified by flash column chromatography to afford pure **162** as an orange oil (58% yield). Some di-substituted product **164** was also obtained (11% yield). R_f 0.56 (9/1 PE/EtOAc). ^{1}H NMR (600 MHz, $CDCl_3$) δ (ppm): 9.95 (s, 1H), 7.78 (s, 1H), 7.70 (d, 1H, *J* = 7.1 Hz), 7.68 (d, 1H, *J* = 7.2 Hz), 7.46 (d, 1H, *J* = 5.2

Hz), 7.12 (d, 1H, *J* = 5.3 Hz), 2.70–2.65 (m, 4H), 1.66–1.60 (m, 4H), 1.27–1.16 (m, 12H), 0.82 (t, 3H, *J* = 7.0 Hz) superimposed to 0.81 (t, 3H, *J* = 7.0 Hz). ^{13}C NMR (150 MHz, $CDCl_3$) δ (ppm): 183.1 (CH), 154.3 (Cq), 153.7 (Cq), 143.3 (Cq), 143.1 (Cq), 142.7 (Cq), 142.1 (Cq), 137.9 (CH), 131.9 (Cq), 130.5 (CH), 129.7 (CH), 129.5 (CH), 129.2 (Cq), 126.5 (CH), 126.1 (Cq), 31.7 (CH_2), 31.6 (CH_2), 30.8 (CH_2), 30.5 (CH_2), 29.5 (CH_2), 29.5 (CH_2), 29.2 (CH_2), 29.1 (CH_2), 22.7 (CH_2), 22.6 (CH_2), 14.2 (CH_3), 14.1 (CH_3).

Compound 163. This is a modified literature procedure.[281] A solution of **162** (1.0 equiv, 0.1–0.5 mmol) in acetonitrile (0.1 M) was cooled down with an ice bath. A 30% w/w H_2O_2 solution in H_2O (5.0 equiv) was added, followed by the addition of NaH_2PO_4 (0.3 equiv). Finally, $NaClO_2$ was added as a 1.0 M solution in H_2O (2.0 equiv) and the mixture was stirred at 50 °C for 3–4 h. Then, a 1.0 M aqueous solution of HCl was added, and the mixture was extracted three times with EtOAc; the combined organic layers were dried over anhydrous Na_2SO_4, filtered and the volatiles were removed under reduced pressure. The crude products were purified by flash column chromatography to afford pure **163** as a yellow oil. 70% yield. R_f 0.37 (8/2 PE/EtOAc). ^{1}H NMR (600 MHz, $CDCl_3$) δ (ppm): 7.89 (s, 1H), 7.70 (d, 1H, *J* = 7.2 Hz), 7.67 (d, 1H, *J* = 7.2 Hz), 7.46 (d, 1H, *J* = 5.2 Hz), 7.12 (d, 1H, *J* = 5.3 Hz), 2.70–2.63 (m, 4H), 1.67–1.60 (m, 4H), 1.29–1.17 (m, 12H), 0.82 (t, 3H, *J* = 7.0 Hz) superimposed to 0.82 (t, 3H, *J* = 7.0 Hz). ^{13}C NMR (150 MHz, $CDCl_3$) δ (ppm): 166.8 (Cq), 154.3 (Cq), 153.9 (Cq), 143.0 (Cq), 142.2 (Cq), 141.3 (Cq), 136.7 (CH), 132.0 (Cq), 130.5 (CH), 129.8 (CH), 129.5 (CH), 128.9 (Cq), 126.4 (CH), 126.1 (Cq), 31.7 (CH_2), 31.6 (CH_2), 30.8 (CH_2), 30.5 (CH_2), 29.5 (CH_2), 29.5 (CH_2), 29.1 (CH_2), 22.7 (CH_2), 22.6 (CH_2), 14.2 (CH_3), 14.2 (CH_3).

Compound 164. The same procedure as for **162** was followed, using 4.4 equiv of $POCl_3$ and DMF. Flash column chromatography afforded pure **164** as an orange oil (56% yield). Some mono-substituted product **162** was also obtained (10% yield). R_f 0.31 (9/1 PE/EtOAc). ^{1}H NMR (600 MHz, $CDCl_3$) δ (ppm): 9.96 (s, 2H), 7.78 (s, 2H), 7.74 (s, 2H), 2.69–2.66 (m, 4H), 1.67–1.62 (m, 4H), 1.27–1.17 (m, 12H), 0.82 (t, 6H, J = 7.0 Hz). ^{13}C NMR (150 MHz, $CDCl_3$) δ (ppm): 183.1 (CH), 153.6 (Cq), 143.5 (Cq), 143.3 (Cq), 142.0 (Cq), 137.9 (CH), 130.2 (CH), 127.6 (Cq), 31.6 (CH_2), 30.5 (CH_2), 29.5 (CH_2), 29.1 (CH_2), 22.6 (CH_2), 14.1 (CH_3).

Compound 165. The same procedure as for **163** was followed, starting from **164** and using 10 equiv of H_2O_2, 0.6 equiv of NaH_2PO_4, and 4.0 equiv of $NaClO_2$. Flash column chromatography afforded pure **165** as a yellow solid. 76% yield. R_f 0.14 (7/3 PE/EtOAc). ^{1}H NMR (600 MHz, CD_3OD) δ (ppm): 7.82 (s, 2H), 7.78 (s, 2H), 2.70–2.67 (m, 4H), 1.60 (quin, 4H, J = 7.5 Hz), 1.24–1.11 (m, 12H), 0.80 (t, 6H, J = 7.1 Hz). ^{13}C NMR (150 MHz, CD_3OD) δ (ppm): 166.2 (Cq), 155.8 (Cq), 144.9 (Cq), 141.5 (Cq), 137.1 (CH), 136.1 (Cq), 132.5 (CH), 129.5 (Cq), 33.4 (CH_2), 32.2 (CH_2), 31.0 (CH_2), 30.7 (CH_2), 24.4 (CH_2), 15.2 (CH_3).

BTD-I-04. This is a modified literature procedure.[282] To a solution of **162** (1.0 equiv, 0.1–0.5 mmol) in $CHCl_3$ (0.1 M), $SOCl_2$ (3.5 equiv) was added and the mixture was stirred at 65 °C for 3 h. Then, the volatiles were removed under reduced pressure and the mixture was dissolved into DCM (0.1 M). Propargylamine (1.5 equiv) and *N*,*N*-diisopropylethylamine (3.5 equiv) were added and the mixture was stirred at rt overnight. Then, the volatiles were removed under reduced pressure and the crude product was purified by flash column chromatography, affording pure **BTD-I-04** as an orange oil. 84% yield. R_f 0.29 (8/2 PE/EtOAc). ^{1}H NMR (600 MHz,

$CDCl_3$) δ (ppm): 7.67 (d, 1H, *J* = 7.2 Hz), 7.66 (d, 1H, *J* = 7.2 Hz), 7.57 (s, 1H), 7.45 (d, 1H, *J* = 5.2 Hz), 7.11 (d, 1H, *J* = 5,2 Hz), 6.18 (t, 1H, *J* = 5.3 Hz), 4.27 (dd, 2H, *J* = 5.3, 2.6 Hz), 2.69–2.65 (m, 2H), 2.65–2.61 (m, 2H), 2.30 (t, 1H, *J* = 2.5 Hz), 1.65–1.59 (m, 4H), 1.29–1.15 (m, 12H), 0.81 (t, 6H, *J* = 7.0 Hz). ^{13}C NMR (150 MHz, $CDCl_3$) δ (ppm): 161.6 (Cq), 154.3 (Cq), 154.0 (Cq), 142.6 (Cq), 142.1 (Cq), 137.3 (Cq), 137.1 (Cq), 132.0 (Cq), 131.1 (CH), 130.4 (CH), 129.8 (CH), 129.5 (CH), 128.6 (Cq), 126.3 (CH), 126.2 (Cq), 79.4 (Cq), 72.2 (CH), 31.7 (CH_2), 31.6 (CH_2), 30.8 (CH_2), 30.6 (CH_2), 29.9 (CH_2), 29.6 (CH_2), 29.5 (CH_2), 29.2 (CH_2), 29.1 (CH_2), 22.7 (CH_2), 22.6 (CH_2), 14.2 (CH_3), 14.2 (CH_3).

BTD-I-08. The same procedure as for **BTD-I-04** was followed, starting from **163** and using 7.0 equiv of $SOCl_2$, 3.0 equiv of propargylamine and 7.0 equiv of *N*,*N*-diisopropylethylamine. Flash column chromatography afforded pure **BTD-I-08** as a yellow solid. 91% yield. R_f 0.16 (7/3 PE/EtOAc). ^{1}H NMR (600 MHz, $CDCl_3$) δ (ppm): 7.69 (d, 2H, *J* = 0.9 Hz), 7.56 (s, 2H), 6.17 (t, 2H, *J* = 5.3 Hz), 4.27 (dd, 4H, *J* = 5.3, 2.6 Hz), 2.66–2.62 (m, 4H), 2.31 (t, 2H, *J* = 2.6 Hz), 1.65–1.58 (m, 4H), 1.27–1.16 (m, 12H), 0.81 (t, 6H, *J* = 6.8 Hz). ^{13}C NMR (150 MHz, $CDCl_3$) δ (ppm): 161.6 (Cq), 153.9 (Cq), 142.9 (Cq), 137.4 (Cq), 137.0 (Cq), 131.0 (CH), 130.2 (CH), 127.3 (Cq), 79.4 (Cq), 72.2 (CH), 31.6 (CH_2), 30.6 (CH_2), 29.9 (CH_2), 29.6 (CH_2), 29.2(CH_2), 22.6 (CH_2), 14.2 (CH_3).

BTD-I-05. The same procedure as for **BTD-I-04** was followed, using 3.5 equiv of $SOCl_2$, 1.5 equiv of *N*-(2-aminoethyl)maleimide trifluoroacetate salt and 3.5 equiv of *N*,*N*-diisopropylethylamine. Flash column chromatography afforded pure **BTD-I-05** as a dark yellow oil. 44% yield. R_f 0.24 (99/1 DCM/MeOH). ^{1}H NMR (600 MHz, $CDCl_3$) δ (ppm): 7.66 (d, 1H, *J* = 7.2 Hz), 7.65 (d, 1H, *J* = 7.2 Hz), 7.51 (s, 1H), 7.45 (d, 1H, *J* = 5.2

Hz), 7.11 (d, 1H, *J* = 5.2 Hz), 6.75 (s, 2H), 6.59 (t, 1H, *J* = 5.2 Hz), 3.86–3.82 (m, 2H), 3.69–3.65 (m, 2H), 2.68–2.65 (m, 2H), 2.63–2.60 (m, 2H), 1.65–1.57 (m, 4H), 1.27–1.14 (m, 12H), 0.81 (t, 6H, *J* = 7.0 Hz). ^{13}C NMR (150 MHz, $CDCl_3$) δ (ppm): 171.2 (Cq), 162.3 (Cq), 154.3 (Cq), 154.0 (Cq), 142.6 (Cq), 142.1 (Cq), 137.7 (Cq), 137.1 (Cq), 134.5 (CH), 132.1 (Cq), 130.6 (CH), 130.4 (CH), 129.9 (CH), 129.4 (CH), 128.5 (Cq), 126.4 (Cq), 126.3 (CH), 39.9 (CH_2), 37.6 (CH_2), 31.7 (CH_2), 31.6 (CH_2), 30.8 (CH_2), 30.6 (CH_2), 29.6 (CH_2), 29.5 (CH_2), 29.2 (CH_2), 29.1 (CH_2), 22.7 (CH_2), 22.6 (CH_2), 14.2 (CH_3).

BTD-I-09. The same procedure as for **BTD-I-04** was followed, using 7.0 equiv of $SOCl_2$, 2.2 equiv of *N*-(2-aminoethyl)maleimide trifluoroacetate salt and 7.0 equiv of *N*,*N*-diisopropylethylamine. Flash column chromatography afforded pure **BTD-I-09** as a yellow solid. 74% yield. R_f 0.25 (98/2 DCM/MeOH). ^{1}H NMR (600 MHz, $CDCl_3$) δ (ppm): 7.66 (s, 2H), 7.51 (s, 2H), 6.76 (s, 4H), 6.60 (t, 2H, *J* = 5.3 Hz), 3.86–3.83 (m, 4H), 3.68–3.65 (m, 4H), 2.63–2.60 (m, 4H), 1.64–1.58 (m, 4H), 1.26–1.15 (m, 12H), 0.81 (t, 6H, *J* = 7.0 Hz). ^{13}C NMR (150 MHz, $CDCl_3$) δ (ppm): 171.2 (Cq), 162.2 (Cq), 153.9 (Cq), 142.8 (Cq), 138.0 (Cq), 136.8 (Cq), 134.5 (CH), 130.6 (CH), 130.2 (CH), 127.3 (Cq), 40.0 (CH_2), 37.6 (CH_2), 31.6 (CH_2), 30.6 (CH_2), 29.6 (CH_2), 29.2 (CH_2), 22.6 (CH_2), 14.2 (CH_3).

Compound 167 and **168** have been prepared as a mixture according literature procedure.[233]

Compounds 169 and 170 have been prepared according literature procedure[233], while modification during the work-up. The reaction was heated at 80° C under stirring for 5 h. and then cooled to r.t., The obtained orangish precipitate is poured into H_2O (100 mL). The pH of the aqueous

suspension is increased to basic values (8-9) with the addition of a saturated $NaHCO_3$ solution (400 mL). The obtained orangish precipitate was filtered and the limpid aqueous phases were discarded. The precipitate was rinsed with Et_2O (50 mL) and dried. A soxhlet extraction with EtOAc was performed on the obtained solid for 96h. The organic solvent is then evaporated and the crude product was purified by flash column chromatography (EtOAc:Hex 90:10 to 100%) (TLC: 0.8-0.65) to afford **169** as an orange solid in 6.2% yield ^{1}H NMR (600 MHz,DMSO-d6): δ 8.03 (d, J = 4.0 Hz, 1H), 7.90 (t, J = 4.1 Hz, 1H), 7.85 – 7.78 (m, 2H), 7.48 – 7.42 (m, 3H), 6.81 (dd, J = 6.8, 1.9 Hz, 1H), 6.70 – 6.65 (m, 1H), 5.62 (d, J = 13.5 Hz, 2H). ESI-MS:(+ve) 334.08 $[M]^+$ and **170** as an orange solid in 1.2% yield ^{1}H NMR (600 MHz, DMSO-d6): δ 7.80 (s, 2H), 7.38 (d, J = 15.6 Hz, 2H), 6.77 (s, 2H), 6.64 (d, J = 8.4 Hz, 2H), 5.56 (m, 4H). ESI-MS(+ve) 349.07 $[M]^+$.

BBT-01 and **BBT-02**. **169** (80mg, 0.24mmol, 1eq) and **170** (50mg, 0.14mmol, 1eq) were dissolved respectively in 4 and 2.5 mL of degassed dry DMF under argon atmosphere. K_2CO_3 (96mg, 1.08mmol, 3 eq- 40mg, 0.18mmol, 2eq) was added to the mixture followed by the addition, after 10 min, of Propargyl bromide (36 µL, 0.48mmol, 2eq-18 µL, 0.22mmol, 1.5eq). The reaction is stirred at r.t. for 72-96h. The mixture was extracted with EtOAc and washed with H_2O and brine. The organic phases were dried over Na_2SO_4 and the solvent removed in vacuo. The residue was purified by flash column chromatography (EtOAc:Hex 50:50) (TLC: 0.9-0.7) to afford **BBT-01** as a pale orange solid in 16.8% yield _purity level 95%^{1}H NMR (600 MHz,DMSO-d6): 8.03 (d, J = 4.0 Hz, 1H), 7.92 (d, J = 4.0 Hz, 2H), 7.86 – 7.78 (m, 2H), 7.51 (dd, J = 19.8, 9.0 Hz, 1H), 7.49 – 7.40 (m, 2H), 6.92 (dd, J = 13.6, 1.9 Hz, 1H), 6.78 (dd, J = 8.7, 2.0 Hz, 1H), 6.56 (t, J = 6.0 Hz, 1H), 3.98 (dd, J = 2.4 Hz, 2H), 3.13 (t, J = 2.3 Hz,

1H). . ESI-MS:(+ve) 372.01 $[M]^+$ and **BBT-02** as an orange solid (yield not determined) ^{1}H NMR (600 MHz, DMSO-d6): δ 7.88 (s, 1H), 7.52 (dd, J = 8.6, 5.3 Hz, 2H), 6.93 (dd, J = 10.2, 2.2 Hz, 2H), 6.80 – 6.73 (m, 2H), 6.53 (t, J = 6.0 Hz, 2H), 3.95 (dd, J = 2.4 Hz, 4H), 3.10 (t, 2H, J =6.5 Hz).

Compound 171. To a solution of 3-methylthiophene (1.3 g, 1 eq., 15.59 mmol) in toluene (5 mL), HgO (3.14 g, 0.93 eq., 14.96 mmol) and I_2 (4.07 g, 1.03 eq., 16.05 mmol) were added in small portions at 0°C. Then, the mixture is allowed to warm-up to room temperature and stirred for 0.5 h. Then, the reddish precipitate is filtered and washed with diethyl ether. The organic phase was washed with water, brine and thiosulphate aqueous solution, dried over Na_2SO_4 and the solvent removed in vacuo. The NMR shows the presence of 15% of the bis-iodinated product.

General procedure for differently substituted benzoxazoles. The aminophenol (1 eq.) is heated at 150°C under stirring in triethyl orthoformate (13 eq.) for 5 h. Then, the reaction is cooled down and volatiles are removed in vacuo. The crude was then purified by flash chromatography (Hexane/Ethyl Acetate 95/5) affording the pure benzoxazole.

R_1 = OMe (Compound 184). Yield 67%. ^{1}H-NMR (600 MHz, $CDCl_3$) δ: 8.05 (s, 1H), 7.45 (d, 2H, J = 8.94 Hz), 7.24 (d, 1H, J = 1.90 Hz), 6.98 (dd, 1H, J = 8.88 Hz, J = 2.04 Hz), 3.83 (s, 3H).
R_1 = COOMe (Compound 176). Yield 60%. ^{1}H-NMR (600 MHz, $CDCl_3$) δ: 8.51 (s, 1H), 8.16 (d, 1H, J = 2.94 Hz), 8.15 (dd, J = 8.64 Hz, J = 1.82 Hz), 7.63 (d, 1H, J = 8.64 Hz), 3.96 (s, 3H).

General procedure for BBT-03 and BBT-04. To a clear solution of the substituted benzoxazole (2 eq.) in degassed DMA, Cs_2CO_3 (2.2 eq.), 2,5-diiodothiophene (1.1 eq.) and $[Pd(phen)_2](PF_6)_2$ (5% mol) were added in one portion. The reaction was left stirring at 150°C under Ar atmosphere. After completion detected by TLC (Hexane/Ethyl Acetate 10/1), the reaction was cooled down to room temperature, rinsed with hexane and filtered over a celite pad. The volatiles were removed in vacuo. Then, the crude was redissolved in ethyl acetate and the organic phase was washed with brine and water, dried over Na_2SO_4 and the solvent removed in vacuo. Purification via flash chromatography (from 91:9 to 0:100 in hexane/ethyl acetate) afforded the pure product.

BBT-03. Yield 17%. ^{1}H-NMR (600 MHz, $CDCl_3$) δ: 7.79 (m, 2H), 7.60 (m, 2H), 7.38 (m, 4H), 2.81 (s, 3H).
BBT-04. Yield 35%. ^{1}H-NMR (600 MHz, $CDCl_3$) δ: 8.47 (d, 1H, J = 1.26 Hz), 8.45 (d, 1H, J = 1.26), 8.14 (t, 1H, J = 1.46 Hz), 8.12 (t, 1H, J = 1.46 Hz), 7.82 (s, 1H), 7.61 (d, 1H, J = 8.82 Hz), 7.60 (d, 1H, J = 8.82 Hz), 3.97 (s, 3H), 2.81 (s, 3H).

Compound 173. To a clear solution of benzoxazole (59 mg, 0.5 mmol, 1 eq.) in degassed DMA (1 mL), Cs_2CO_3 (179 mg, 0.55 mmol, 1.1 eq.), **171** (123 mg, 0.55 mmol, 1.1 eq.) and $[Pd(phen)_2](PF_6)_2$ (5% mol) were added in one portion. The reaction was left stirring at 150°C under Ar atmosphere. After completion detected by TLC (Hexane/Ethyl Acetate 10/1), the reaction was cooled down to room temperature, rinsed with hexane and filtered over a celite pad. The volatiles were removed in vacuo. Then, the crude was redissolved in ethyl acetate and the organic phase was washed with brine and water, dried over Na_2SO_4 and the solvent removed in vacuo. Purification via flash chromatography (from

93:7 to 80:20 in hexane/ethyl acetate) afforded the pure **173** as a yellow solid (60 mg, 56%). ^{1}H-NMR (600 MHz, $CDCl_3$) δ: 7.74 (d, 1H, J = 6.84 Hz), 7.53 (d, 1H, J = 7.20 Hz), 7.40 (d, 1H, J = 4.98 Hz), 7.31 (m, 2H), 6.98 (d, 1H, J = 5.04), 2.73 (s, 3H).

Compound 174. To a solution of **173** (30 mg, 0.14 mmol, 1 eq.) in dry THF under Ar, butyl lithium (2.5 M in hexane, 112 uL, 0.28 mmol, 2 eq.) is added dropwise at -78°C. The reaction is left to warm-up at room temperature after 45 minutes, when NIS (125 mg, 0.55 mmol, 4 eq.) is added in one portion. The reaction is left stirring at room temperature for 2h. Reaction is then quenched with few drops of NH_4Cl saturated aqueous solution and then diluted with Et_2O. Organic phase is dried over Na_2SO_4 and the solvent removed in vacuo. The crude residue is carried forward the next step without further purification.

BBT-05. To a clear solution of **176** (13 mg, 0.07 mmol, 1.3 eq.) in degassed DMA (1 mL), Cs_2CO_3 (25 mg, 0.07 mmol, 1.3 eq.), **174** (20 mg, 0.055 mmol, 1 eq.) and $[Pd(phen)_2](PF_6)_2$ (5% mol) were added in one portion. The reaction was left stirring at 150°C under Ar atmosphere. After completion detected by TLC (Hexane/Ethyl Acetate 10/1), the reaction was cooled down to room temperature, rinsed with hexane and filtered over a celite pad. The volatiles were removed in vacuo. Then, the crude was redissolved in ethyl acetate and the organic phase was washed with brine and water, dried over Na_2SO_4 and the solvent removed in vacuo. Purification via flash chromatography (from 91:9 to 0:100 in hexane/ethyl acetate) afforded the pure **BBT-05** (8 mg, yield 36%) as a yellow powder. ^{1}H-NMR (600 MHz, $CDCl_3$) δ: 8.47 (s, 1H), 8.15 (d, 1H, J = 8.78 Hz), 7.84 (s, 1H), 7.82 (d, 1H, J = 8.65 Hz), 7.63 (m, 2H), 7.42 (m, 2H), 4.00 (s, 3H), 2.83 (s, 3H).

Compound 179. 177 (4 g, 0.028 mol, 1 eq.) is suspended in DCM (21 mL) and $SOCl_2$ (20.3 mL, 0.28 mol, 10 eq.) is added dropwise. The mixture is stirred at rt for 6 h. Then, volatiles ($SOCl_2$ in excess and DCM) are removed in vacuo and NMP is added. The aminophenol **178** (4 g, 0.029 mol, 1 eq.) is added and the reaction mixture is heated to 200°C for 7 h. Then, the reaction mixture is cooled down, diluted with water and washed with petroleum ether. The organic layers are dried over Na_2SO_4, concentrated in vacuo. The crude mixture is purified by flash chromatography (Petroleum Ether/Ethyl Acetate 9:1), affording the pure **179** (1.2 g, yield 17%) as a white solid. ^{1}H-NMR (600 MHz, $CDCl_3$) δ: 7.43 (m, 2H), 7.23 (d, 1H, J = 2.46 Hz), 6.98 (d, 1H, J = 4.98 Hz), 6.92 (dd, 1H, J= 8.82 Hz, J 2.52 Hz), 3.85 (s, 3H), 2.72 (s, 3H). ^{13}C-NMR (150 MHz, $CDCl_3$) δ: 160.72, 157.58, 144.84, 142.84, 142.19, 132.03, 128.61, 123.80, 113.37, 110.57, 102.77, 77.16, 56.61, 16.29.

Compound 180. To a solution of **179** (0.28 g, 1.14 mmol, 1 eq.) in dry THF (25 mL), butyl lithium (1.5 eq., 0.67 mL of a solution 2.5 M in hexane) is added dropwise at -78°C. The reaction mixture is left stirring at -78°C for 45 min and, then, DMF (4.6 mmol, 0.35 mL, 4 eq.) is added. The reaction is warmed up to rt and left under stirring overnight. The day after, the mixture was poured in HCl (5% wt, 400 mL) and stirred 1 h. Then, the aqueous phase was washed with DCM. The organic layer was dried over Na_2SO_4 and concentrated in vacuo. A flash chromatography (Petroleum Ether/Ethyl Acetate 8:2) provided the pure **180** (40 mg, yield 13%) as a yellow solid. ^{1}H-NMR (600 MHz, $CDCl_3$) δ: 9.91 (s, 1H), 7.61 (s, 1H), 7.45 (d, 1H, J= 8.70 Hz), 7.25 (d, 1H, J = 2.52 Hz), 6.98 (dd, 1H, J= 8.91 Hz, , J = 2.52 Hz), 3.86 (s, 3H), 2.75 (s, 3H). ^{13}C-NMR (150 MHz, $CDCl_3$) δ:

182.97, 159.20, 157.85, 144.93, 143.73, 142.90, 142.05, 139.40, 132.25, 114.97, 110.99, 102.87, 55.90, 16.52.

BBT-06. 181 (0.24 g, 1.44 mmol, 4 eq.) is added in one portion to a suspension of **180** (0.1 g, 0.37 mmol, 1 eq.) in dry methanol (40 mL). The reaction is heated at 60°C for 6 h and then cooled down. The precipitate is recovered by filtration and then suspended in MeOH. (Diacetoxyiodo)benzene (0.595 g, 1.85 mmol, 5 eq.) is added and the reaction is stirred at rt for 4 h. Then, the reaction volume is reduced to one third and the yellow precipitate is recovered by filtration, washed with petroleum ether and methanol affording the pure **BBT-06** (65 mg, yield 42%)**.** ^{1}H-NMR (600 MHz, $CDCl_3$) δ: 8.44 (s, 1H), 8.11 (d, 1H, J = 7.08 Hz), 7.79 (s, 1H), 7.59 (d, 1H, J = 8.46 Hz), 7.45 (d, 1H, J = 8.81 Hz), 7.26 (d, 1H, J = 2.34 Hz), 6.97 (dd, J = 8.82 Hz, J = 2.40 Hz), 3.96 (s, 3H), 3.87 (s, 3H), 2.78 (s, 3H). ^{13}C-NMR (150 MHz, $CDCl_3$) δ: 166.66, 159.44, 159.33, 157.73, 153.49, 144.87, 142.85, 142.46, 142.22, 134.44, 130.18, 128.47, 127.54, 127.51, 122.07, 114.40, 110.80, 110.43, 102.84, 56.02, 52.51, 16.38.

Compound 182. BBT-06 (20 mg, 0.047 mmol, 1 eq.) was dissolved in dry DCM (10 mL) and the solution was cooled to -78°C. DIBAL-H (0.071 mL of a solution 1M in Hexane, 0.0705 mmol, 1.5 eq.) was added and the mixture was stirred for 3 hours. The reaction was warmed up to room temperature, then methanol was added dropwise to quench the reaction. The organic layer was washed with brine and dried over Na_2SO_4. The solvent was removed by rotary evaporation and the residue was purified by flash chromatography (from DCM to DCM/EtOAc 8:2) giving **182** (7.6 mg, yield 41%) as a yellow powder. ^{1}H-NMR (600 MHz, $CDCl_3$) δ: 7.72 (s, 1H), 7.68 (s, 1H), 7.50 (d, 1H, J = 8.34 Hz), 7.42 (d, 1H, J = 8.88 Hz),

7.34 (d, 1H, J = 8.94 Hz), 7.22 (d, 1H, J = 2.46 Hz), 4.73 (s, 2H), 3.84 (s, 3H), 2.73 (s, 3H). ^{13}C-NMR (150 MHz, $CDCl_3$) δ: 159.43, 158.61, 157.70, 149.89, 144.86, 142.63, 142.58, 141.88, 138.76, 134.02, 130.71, 127.81, 124.96, 118.22, 114.39, 110.78, 110.49, 102.77, 64.68, 56.00, 16.37.

Compound 183. To a solution of compound **182** (20 mg, 0.051 mmol, 1 eq.) in DCM, MnO_2 (35 mg, 0.408 mmol, 8 eq.) was added. After stirring at room temperature for 2 h, the mixture was filtered to remove MnO_2. The solvent was removed *in vacuo* and the crude was purified by chromatography (from DCM/EtOAc 9:1 to DCM/EtOAc 6:4) giving **183** (5.6 mg, yield 28%) as a yellow solid. ^{1}H-NMR (600 MHz, $CDCl_3$) δ: 10.08 (s, 1H), 8.23 (s, 1H), 7.94 (d, 8.34 Hz), 7.79 (s, 1H), 7.68 (d, 1H, J = 8.40 Hz), 7.44 (d, 1H, J = 8.82 Hz), 7.27 (d, 1H, J = 2.65 Hz), 6.97 (dd, J = 8.82 Hz, J = 2.52 Hz), 3.87 (s, 3H), 2.78 (s, 3H). ^{13}C-NMR (150 MHz, $CDCl_3$) δ: 191.13, 159.90, 159.29, 157.79, 154.48, 144.89, 142.83, 142.80, 142.50, 134.71, 134.18, 129.86, 128.83, 127.18, 122.51, 114.45, 111.30, 110.88, 102.87, 56.00, 16.50.

BBT-07. To a well stirred solution of compound **183** (4 mg, 0.010 mmol, 1 eq.) in DCM/EtOH (2:1) cyanoacetic acid (1.28 mg, 0.015 mmol, 1.5 eq.) and few drops of piperidine were added. The mixture was stirred at room temperature overnight. The precipitate was recovered by filtration and then washed with few drops of aqueous HCl 1M, affording the pure **BBT-CN** (1.37 mg, yield 30%). ^{1}H-NMR (600 MHz, $CDCl_3$/TFA) δ: 8.53 (s, 1H), 8.27 (d, 1H, J = 8.52 Hz), 7.98 (s, 1H), 7.84 (d, 2H, J = 8.52 Hz), 7.61 (d, 8.91 Hz), 7.37 (s, 1H), 7.15 (d, 2H, J = 8.93 Hz), 3.95 (s, 3H), 2.81 (s, 3H). Some aromatic signals are not detectable since under the TFA signal. ^{13}C-NMR was not recorded due to solubility issues.

Compound 186. $Pd(OAc)_2$ (2.8 mg, 0.0125 mmol, 0.025 eq.), CuCl (5.1 mg, 0.05mmol, 0.1 eq.), $Cu(OAc)_2 \cdot H_2O$ (150 mg, 0.75 mmol, 1.5 eq.), **184** (59.6 mg, 0.5 mmol, 1 eq.), **195** (168.2 mg, 1.5 mmol, 3 eq.), pyridine (39.6 mg, 0.5 mmol), 1 eq. and DMA (0.6 mL) at 120 ^oC for 20 h. Then, the reaction crude was diluted with DCM and filtered over a celite pad. The volatiles were removed in vacuo and the crude was purified by flash chromatography (Petroleum Ether/Ethyl Acetate 9:1) affording **186** (43 mg, yield 33%) as a yellow solid. ^{1}H-NMR (600 MHz, $CDCl_3$) δ: 9.99 (s, 1H), 7.93 (d, 1H, J = 3.96 Hz), 7.81 (d, 1H, J = 3.96 Hz), 7.47 (d, 1H, J = 8.88 Hz), 7.25 (s, 1H), 7.00 (dd, 1H, J = 8.94 Hz, J = 2.58 Hz), 3.87 (s, 3H).

BBT-08. **181** (100.2 mg, 0.60 mmol, 4 eq.) is added in one portion to a suspension of **186** (40 mg, 0.15 mmol, 1 eq.) in dry methanol (5 mL). The reaction is heated at 60°C for 6 h and then cooled down. The precipitate is recovered by filtration and then suspended in MeOH. (Diacetoxyiodo)benzene (241.5 mg, 0.75 mmol, 5 eq.) is added and the reaction is stirred at rt for 4 h. Then, the reaction volume is reduced to one-third and the yellow precipitate is recovered by filtration, washed with petroleum ether and methanol affording the pure **BBT-08** (23 mg, yield 38%)**.** ^{1}H-NMR (600 MHz, $CDCl_3$) δ: 8.45 (s, 1H), 8.11 (dd, 1H, J = 8.78 Hz, J =1.62 Hz), 7.96 (d, 1H, J = 3.96 Hz), 7.92 (d, 1H, J = 3.96 Hz), 7.62 (d, 1H, J = 8.88 Hz), 7.46 (d, 1H, J = 8.88 Hz), 7.25 (s, 1H), 6.99 (dd, 1H, J = 8.88 Hz, J = 2.52 Hz), 3.97 (s, 3H), 3.88 (s, 3H).

Compound 188. To a suspension of **187** (0.6 g, 1 eq.) in toluene (30 mL), ethylene glycol (0.25 mL, 1.05 eq.) and TsOH (0.03 g, 0.05 eq.) were added and the reaction mixture was stirred at 100°C overnight. Then, toluene was removed in vacuo and the reaction crude was purified by

flash chromatography (Petroleum Ether/Ethyl Acetate 9:1), affording **188** as a pale yellow oil (0.4 g, yield: 50%). ^{1}H-NMR (600 MHz, $CDCl_3$) δ: 9.89 (s, 1H), 7.67 (d, 1H, J = 3.84 Hz), 7.24 (dd, 1H, J_1 = 3.84 HZ, J_2 = 0.66 Hz), 6.14 (s, 1H), 4.12 (m, 2H), 4.06 (m, 2H).

Compound 189. 181 (4 eq.) is added in one portion to a solution of **188** (2 g) in dry methanol (35 mL). The orangish reaction is heated at 60°C for 6 h and then cooled down. The reaction volume is reduced to one-third, and the yellow precipitate is recovered by filtration and then suspended in MeOH. (Diacetoxyiodo)benzene is added, and the reaction is stirred at rt for 4 h. Then, volatiles were removed in vacuo, and the crude was purified by flash chromatography (Petroleum Ether/Ethyl Acetate 85:15), affording **189** (1.2 g, yield ..%). ^{1}H-NMR (600 MHz, $CDCl_3$) δ: 8.39 (d, 1H, J = 1.7 Hz), 8.08 (dd, 1H, J_1 = 8.52 Hz, J_2 = 1.7 Hz), 7.81 (d, 1H, J = 3.8 Hz), 7.56 (d, 1H, J = 8.5 Hz), 7.22 (d, 1H, J = 3.8 Hz), 6.17 (s, 1H), 4.16 (m, 2H), 4.07 (m, 2H), 3.95 (s, 3H). ^{13}C-NMR (150 MHz, $CDCl_3$) δ: 166.79, 160.13, 153.49, 148.24, 142.25, 130.42, 129.41, 127.35, 127.25, 127.04, 121.88, 110.37, 99.86, 65.52, 52.49.

Compound 190. To a solution of **189** (1 g, 0.003 mol, 1 eq.) in acetone (15 mL), TsOH (0.1 eq.) was added and the mixture was heated at reflux overnight. Then, the mixture was cooled down, volatiles were removed in vacuo and **190** (0.8 g, 92% yield) was obtained after flash chromatography (from 85/15 Petroleum Ether/Ethyl Acetate to 75/25 Petroleum Ether/Ethyl Acetate). ^{1}H-NMR (600 MHz, $CDCl_3$) δ: 10.02 (s, 1H), 8.47 (d, 1H, J = 1.62 Hz), 8.17 (dd, 1H, J = 8.58 Hz, J = 1.68 Hz), 8.00 (d, 1H, J = 3.90 Hz), 7.85 (d, 1H, J = 3.89 Hz), 7.63 (d, 1H, J = 8.58 Hz), 3.98 (s, 3H). ^{13}C-NMR (150 MHz, $CDCl_3$) δ: 182.93, 166.54, 159.02,

153.57, 146.87, 142.05, 136.91, 136.11, 130.62, 128.11, 127.84, 122.49, 110.70, 77.32, 77.11, 76.90, 52.56.

Compound 191. 194 (0.234 g, 1.04 mmol, 3 eq.) is added in one portion to a solution of **190** (0.1 g, 0.35 mmol, 1 eq.) in dry methanol (10 mL). The reddish suspension is heated at 60°C for 14 h and then cooled down. Then, the red precipitate is recovered by filtration and suspended again in MeOH. (Diacetoxyiodo)benzene (0.450 g, 1.4 mmol, 4 eq.) is added and the reaction is stirred at rt for 4 h. The yellow solid is recovered by filtration and washed with MeOH affording the pure **191** (65 mg, yield 38%). ^{1}H-NMR (600 MHz, $CDCl_3$) δ: 8.45 (s, 1H), 8.13 (dd, 1H, J = 8.52 Hz, J = 1.62 Hz), 7.96 (d, 1H, J = 4.02 Hz), 7.94 (d, 1H, J = 4.02 Hz), 7.72 (s, 1H), 7.61 (d, 1H, J = 8.52 Hz), 7.47 (m, 2H), 6.53 (bs, 1H), 3.96 (s, 3H), 1.54 (s, 9H). ^{13}C-NMR was not recorded due to solubility issues in $CDCl_3$ and DMSO-*d*$_6$.

Compound 192. 191 (60 mg, 0.12 mmol) is stirred in HCl 4M in dioxane (9 mL) at rt for 6 h. Then, the volatiles were removed in vacuo. The solid crude is washed with $NaHCO_{3\,(aq.\ sat.)}$ (20 mL). and brown crystals of pure **192** are collected by filtration (quantitative yield). ^{1}H-NMR (600 MHz, $CDCl_3$) δ: 8.45 (s, 1H), 8.13 (d, 1H, J = 8.6 Hz), 7.95 (d, 1H, J = 3.96 Hz), 7.90 (d, 1H, J = 3.96 Hz), 7.61 (d, 1H, J = 8.52 Hz), 7.35 (d, 1H, J = 8.64 Hz), 7.03 (d, 1H, J = 2.22 Hz), 6.75 (dd, 1H, J_1 = 8.6 Hz, J_2 = 2.28 Hz), 3.97 (s, 3H). ^{13}C-NMR was not recorded due to solubility issues in $CDCl_3$ and DMSO-*d*$_6$.

Compound 193. 4-amino-2-nitrophenol (3 g, 0.019 mol, 1 eq.) and Boc-anhydride (7 g, 0.032 mol, 1.7 eq.) were dissolved in THF (20 mL) and then stirred at 50°C for 10 h. Then, the volatiles were removed in vacuo.

The crude was then suspended in cyclohexane (100 mL) and filtered affording the pure **193** (4.4 g, yield 90%) as a brownish solid. ^{1}H-NMR (600 MHz, $CDCl_3$) δ: 10.35 (s, 1H), 8.18 (s, 1H), 7.57 (bs, 1H), 7.10 (d, 1H, J = 9.06 Hz), 6.50 (bs, 1H), 1.52 (s, 9H). ^{13}C-NMR (150 MHz, $CDCl_3$) δ: 187.92, 152.72, 151.12, 133.21, 131.33, 129.26, 120.34, 28.34.

Compound 194. 193 (1 g, 3.93 mmol, 1 eq.) was suspended in ethanol with $SnCl_2$ $2H_2O$ (3.74 g, 0.019 mol, 5 eq.). The mixture was heated at 60°C for 1 h, then the mixture was cooled down and $NaBH_4$ (0.075 g, 1.95 mmol, 0.5 eq.) was added portionwise. After 2h, the volatiles were removed in vacuo affording a pinkish residue. After having added water, an aqueous solution $NaHCO_3$ was used to reach neutral pH. Then, the aqueous phase was washed with Ethyl Acetate (2 x 100 mL). The organic layers have been collected, dried over Na_2SO_4 and dry under reduced pressure, affording **194** as a pale brownish solid (0.3 g, 24%). ^{1}H-NMR (600 MHz, DMSO-d_6) δ: 8.82 (bs) partially superimposed to 8.77 (bs) (3H total), 6.87 (bs, 2H), 6.51-6.49 (m, 3H), 1.44 (s, 9H).

BBT-09. 192 (35 mg, 0.089 mmol, 1 eq.) was suspended in 1,2-dichloroethane (5 mL). Acetaldehyde (10 uL, 0.018 mmol, 2 eq.) was added, and the mixture was left stirring for 10 min at rt. Then, $NaCN(BH_3)$ (6 mg, 0.009, 1 eq.) was added in one portion, and the mixture was left stirring overnight. The solvent was then removed in vacuo, and the crude mixture was purified by flash chromatography (95/5 DCM/Ethyl Acetate), affording **BBT-09** (13 mg, yield 28%) as a yellow solid. ^{1}H-NMR (600 MHz, $CDCl_3$) δ: 8.45 (d, 1H, J = 1.56 Hz), 8.12 (dd, 1H, J_1 = 8.52 Hz, J_2 = 1.62 Hz), 7.94 (d, 1H, J = 3.96 Hz), 7.88 (d, 1H, J = 3.96 Hz), 7.60 (d, 1H, J = 8.04 Hz), 7.35 (d, 1H, J = 8.62 Hz), 6.93 (d, 1H, J = 2.22 Hz), 6.69 (dd,

1H, J_1 = 8.6 Hz, J_2 = 2.28 Hz), 3.97 (s, 3H), 3.21 (q, 2H, J = 7.14 Hz), 1.31 (t, 3H, J = 7.12 Hz).

Compound 196. PPA (12 g) was transferred into a flask and heated to 110°C. Then, **195** (0.5 g, 2.53 mmol, 1 eq.) and thiophene-2-carboxylic acid (0.32 g, 2.51 mmol, 1 eq.) are added. The green mixture is heated at 180°C under stirring for 5 h. Then, the dark mixture is cooled down and poured into cold water (250 mL). The dark brown precipitate is recovered by filtration and washed with saturated $NaHCO_3$ aqueous solution. Then, the solid is suspended in boiling EtOH (150 mL) and washed. Ethanol was concentrated under vacuum, affording the pure **196** (98 mg, yield 18%) after further crystallization from boiling ethanol. ^{1}H-NMR (600 MHz, DMSO-d_6) δ: 7.89 (d, 1H, J= 1.2 Hz), 7.85 (d, 1H, J= 1.2 Hz), 7.37 (d, 1H, J= 8.58 Hz), 7.27 (dd, 1H, J= 4.98 Hz, J= 3.66 Hz), 6.82 (d, 1H, J= 1.8 Hz), 6.64 (dd, 1H, J= 8.64 Hz, J= 2.22 Hz), 5.12 (s, 2H). ^{13}C-NMR (150 MHz, DMSO-d_6) δ: 158.04, 146.77, 142.38, 142.25, 131.09, 129.59, 129.14, 128.75, 112.96, 110.35, 102.35.

BBT-10. 195 (40 mg, 0.185 mmol, 1 eq.) is suspended in 1,2-dichloroethane (20 mL). Acetaldehyde (12 mg, 0.37 mmol, 2 eq.) is added, and the mixture is left, stirring for 10 min at rt. Then, $NaCN(BH_3)$ (8 mg, 0.185 mmol, 1 eq.) s added in one portion, and the mixture is left stirring overnight. The solvent is removed in vacuo, and the crude mixture was purified by flash chromatography (95/5 Petroleum Ether/Ethyl Acetate), affording **BBT-10** (25 mg, yield 56%) as yellow crystals. ^{1}H-NMR (600 MHz, $CDCl_3$) δ: 7.85 (d, 1H, J = 3.72 Hz), 7.52 (d, 1H, J = 3.72 Hz), 7.31 (d, 1H, J = 8.70 Hz), 7.16 (d, 1H, J = 3.72 Hz), 6.90 (d, 1H, J = 2.28 Hz), 6.61 (dd, 1H, J = 8.70 Hz, J = 2.34 Hz), 3.61 (bs, 1H), 3.19 (q, 2H, J = 7.14 Hz), 1.29 (t, 3H, J = 7.08 Hz). ^{13}C-NMR (150 MHz, $CDCl_3$) δ:

159.35, 146.67, 143.77, 143.31, 130.26, 129.80, 129.44, 128.29, 112.50, 110.59, 101.60, 39.37, 14.92.

Compound 197. has been prepared according to the literature procedure.[223]

Compound 198 has been prepared according to the literature procedure.[123]

Compounds 199, **201** and **202** have been prepared according to the literature procedures.[254]

Compound 200. A mixture consisting of di(2-pyridyl)ketone **205** (0.73 mmol, 1 eq.), terephthalaldehyde **206** (1.46 mmol, 2 eq.), and ammonium acetate (21.85 mmol) in 25 mL of glacial acetic acid was stirred at 118 °C. After 6 h, the reaction mixture was added with (phenyl(pyridin-2-yl)methanone **204** (0.73 mmol, 1 eq.). After 12 h, the reaction mixture was cooled to room temperature and the acetic acid was removed by evaporation under vacuum. The solid was dissolved in a saturated aqueous solution of Na_2CO_3 (40 mL) and the mixture was extracted with CH_2Cl_2 (3 × 30 mL). The organic layer was separated and the solvent evaporated under vacuum. The yellow formed solid was washed several times with diethyl ether (3 × 30 mL) and dried under vacuum. The obtained crude product was purified via column chromatography on silica gel (CH_2Cl_2-CH_3OH 98:2) to get **200** as a yellow solid (0.51 g, 78%). ^{1}H-NMR (600 MHz, $CDCl_3$): δ = 8.78 (1H, d, ^{3}J(H,H) = 9.2 Hz), 8.67 (1H, d, ^{4}J(H,H) = 4.9 Hz), 8.34 (2H, dd, ^{3}J(H,H) = 7.1 Hz, J(H,H) = 10.98 Hz), 8.30 (1H, d, ^{3}J(H,H) = 6.9 Hz), 8.06 (m, 4H), 7.96 (2H, d, ^{3}J(H,H) = 6.9 Hz), 7.89 (1H, d, ^{3}J(H,H) = 9.3 Hz), 7.77 (1H, t, ^{3}J(H,H) =

7.6 Hz), 7.49 (2H, t, ^{3}J(H,H) = 7.5 Hz), 7.33 (1H, ^{3}J(H,H) = 7.8 Hz), 7.15 (1H, dd, ^{3}J(H,H) = 6.6 Hz, ^{4}J(H,H) = 4.2 Hz), 7.00 (1H, dd, ^{3}J(H,H) = 9.3 Hz, ^{4}J(H,H) = 6.3 Hz), 6.85 (1H, dd, 3J(H,H) = 9.3 Hz, 4J(H,H) = 5.3 Hz), 6.74 (1H, t, 3J(H,H) = 6.7 Hz), 6.67 (1H, t, 3J(H,H) = 6.0 Hz) ppm; ^{13}C NMR (150 MHz, $CDCl_3$) δ 149.03, 149.02, 149.00, 137.51, 137.50, 136.47, 134.91, 132.59, 130.65, 130.56, 130.33, 128.87, 128.84, 128.80, 128.15, 126.96, 126.79, 122.06, 121.84, 121.71, 121.44, 120.69, 120.12, 120.06, 119.40, 114.43, 113.76. HRMS (ESI): *m/z* calculated for $C_{31}H_{22}N_5$ [(M + H^+)] 464.1877; found 464.1870. Decomposition at 300 °C before melting.

Compounds 118, 208, 210, 214, 215 and 219 have been prepared according to the literature procedures.[191]

Compound 212 has been prepared according to the literature procedures.[272]

Compound 209. To a solution of **117** (1.00 mL, 6.280 mmol) in ACN (8 mL), 1-iodooctane (3.10 mL, 25.12 mmol) was added, and the mixture was heated and stirred under microwave irradiation at 130°C for 10 min. The solvent was evaporated under reduced pressure to get a brown oil which was then dissolved in the minimum amount of dichloromethane and poured into petroleum ether (150 mL), under stirring. The obtained suspension was rested until complete precipitation, the solvent was gently removed, and the resulting brown oil dried *in vacuo* at room temperature. The product (1.02 g, 60%) was carried forward to the next step without further purification.^{1}H NMR (200 MHz, Chloroform-d) δ 7.68 – 7.54 (m, 4H), 4.71 – 4.58 (m, 2H), 3.09 (s, 3H), 2.00 – 1.81 (m, 2H), 1.64 (s, 6H),

1.49 – 1.16 (m, 10H), 0.89 – 0.78 (m, 3H). MS (ESI, +ve): 272.13 (84, [M]), 670.47 (100, [2M·I^-]).

Compound 213. To a solution of **210** (0.490 g, 1.105 mmol) and **211** (0.3 mL, 2.210 mmol) in EtOH (10 mL), triethyl amine (0.4 mL) was added. The mixture was heated and stirred under microwave irradiation at 90 °C for 45 min. The mixture was cooled to rt, 5 mL of diethyl ether were added, then cooled at 0-4 °C and left warming up to rt overnight. A white precipitate was removed by filtration and the obtained solution evaporated under reduced pressure. The resulting brown oil was purified by flash chromatography ($CHCl_3$: MeOH = 97:3). The pure fractions were dissolved in $CHCl_3$, washed with a saturated aqueous solution of citric acid, then with brine and finally dried over Na_2SO_4. The solvent was evaporated, affording **213** (0.25 g, 51%) as a brown solid. ^{1}H NMR (200 MHz, Chloroform-d) δ 8.02 (dd, J = 8.4, 1.7 Hz, 1H), 7.91 (d, J = 1.6 Hz, 1H), 6.83 (d, J = 8.5 Hz, 1H), 5.43 (s, 1H), 4.85 (q, J = 7.1 Hz, 2H), 3.83 – 3.70 (m, 2H), 1.76 – 1.63 (m, 2H), 1.59 (s, 6H), 1.26 (dt, J = 20.6, 3.9 Hz, 11H), 0.87 – 0.77 (m, 3H).

Compound 216. **209** (0.200 g, 0.501 mmol) and **212** (0.156 g, 0.501 mmol) were added to a mixture 1:1 of Tol/*n*-BuOH (10 mL). The mixture was heated and stirred under microwave irradiation for 25 min at 160 °C. After cooling, the solvents were removed under reduced pressure. The crude was purified by flash chromatography (petroleum-ether:EtOAc = 70:30) affording **216** (67 mg, 25%) as a blue solid. ^{1}H NMR (600 MHz, Chloroform-d) δ 7.36 (d, J = 7.2 Hz, 2H), 7.31 (td, J = 7.8 Hz, J = 2.5 Hz, 2H), 7.14 (t, 7.3 Hz, 2H), 6.98 (t, J = 7.1 Hz, 2H), 5.97 (bs, 2H), 4.06 (bs, 2H), 3.98 (bs, 2H), 1.81 (m, 2H), 1.42 (m, 2H), 1.39 (t, J = 7.2 Hz, 3H), 1.35 (m, 2H), 1.30 (m, 6H), 0.87 (t, J = 6.7 Hz, 3H). ^{13}C NMR (150 MHz,

Chloroform-d) δ 182.78, 182.43, 179.36, 170.28, 169.88, 142.55, 142.40, 142.10, 127.89, 127.84, 123.79, 123.78, 122.45, 122.39, 109.49, 109.20, 104.99, 87.29, 86.35, 49.41, 49.38, 43.86, 38.49, 31.83, 29.42, 29.25, 27.17, 27.15, 27.09, 27.07, 22.69, 14.17, 12.11. HRMS (ESI): m/z calcd for $C_{36}H_{45}N_2O_2$ [(M + H^+)] 537.3436; found 537.3476.

Compound 218. **209** (0.300 g, 0.751 mmol) and **119** (0.039 g, 0.342 mmol) were added to a mixture 1:1 of Tol/*n*-BuOH (15 mL). The mixture was heated and stirred under microwave irradiation at 160 °C for 20 min. After cooling, the solvents were removed under reduced pressure and the crude product was crystallized by EtOH to give the pure **218** (0.11 g, 55%) as blue crystals. ^{1}H NMR (600 MHz, Chloroform-d) δ 7.35 (d, J = 7.4 Hz, 2H), 7.30 (td, J = 7.8 Hz, J = 1.2 Hz, 2H), 7.14 (t, J = 7.4 Hz, 2H), 6.97 (d, J = 7.8 Hz, 2H), 5.97 (bs, 2H), 3.98 (bs, 4H), 1.78 (m, 4H), 1.42 (quint, J = 5.3 Hz, 4H), 1.34 (quint, J = 6.2 Hz, 4H), 1.24 (m, 12H), 0.87 (t, J = 6.8 Hz, 6H). ^{13}C NMR (150 MHz, Chloroform-d) δ 182.38, 179.57, 170.14, 142.61, 142.40, 128.44, 124.20, 122.42, 110.78, 87.41, 49.41, 43.89, 31.08, 29.47, 29.29, 27.22, 27.19, 27.16, 22.73, 14.21. HRMS (ESI): m/z calcd for $C_{42}H_{57}N_2O_2$ [(M + H^+)] 621.4375; found 621.4415.

Compound 217. 208 (0.163 g, 0.4550 mmol) and **213** (0.200 g, 0.4550 mmol) were added to a mixture 1:1 of Tol/*n*-BuOH (10 mL). The mixture was heated and stirred under microwave irradiation at 160 °C for 25 min. After cooling, the solvents were evaporated under reduced pressure. The dark green mixture was crystallized by *n*-BuOH and washed with Et_2O to give the pure **217** (57 mg, 20%) as blue crystals. ^{1}H NMR (600 MHz, Chloroform-d/Methanol-d4) δ 8.05 (m, 2H), 7.99 (s, 2H), 7.01 (t, J = 6.6 Hz, 2H), 6.05 (bs, 2H), 4.09 (bs, 2H), 4.02 (bs, 2H), 1.75 (m, 2H), 1.39 (m, 5H), 1.31 (m, 2H), 1.23 (m, 6H), 0.83 (m, 3H). ^{13}C NMR (150 MHz, Chloroform-d/Methanol-d4): 181.11, 180.24, 180.20, 171.21, 170.79, 168.55, 148.48, 146.67, 146.38, 145.71, 142.24, 134.58, 131.05, 130.98,

126.07, 122.99, 109.50, 108.67, 88.31, 87.89, 49.17, 44.45, 39.26, 31.79, 29.37, 29.20, 27.21, 27.04, 26.99, 26.96, 22.20, 14.10, 12.07. HRMS (ESI): *m/z* calcd for $C_{38}H_{45}N_2O_6$ [(M + H^+)] 625.3233; found 625.3272.

Compound 122 has been prepared according to the literature procedure.[283]

Compound 220 has been prepared according to the literature procedure.[191]

Compound 221 has been prepared according to the literature procedure.[284]

Compound 223. A mixture of **222** (2.0 g, 1.0 eq.), 3,4-diethoxy-3-cyclobutene-1,2-dione **211** (1.0 eq.) and 50 ml a solution ethanol/triethylamine (93:7) was refluxed for 12 h. After cooling the reaction to room temperature, the solvent was removed by evaporation under vacuum. The resulting solid was treated with saturated aqueous solution of citric acid and the mixture was extracted with dichloromethane. The organic layer was separated, dried over sodium sulphate and the solvent evaporated under vacuum. The desired product was purified by flash chromatography on silica gel using dichloromethane/methanol (99:1) as eluent. The product was isolated as a dark orange powder (1.62 g, 82%). R_f (silica gel): 0.20 (98:2 dichloromethane/methanol). M_p: > 200 °C. ^{1}H-NMR (600 MHz, DMSO-d6, RT): δ 8.63 (d, *J* = 1.4 Hz, 1H, Ar-H), 8.23-8.25 (d, *J* = 8.9 Hz, 1H, Ar-H), 8.17-8.18 (d, *J* = 8.9 Hz, 1H, Ar-H), 8.00-8.01 (dd, *J* = 8,9 Hz, *J* = 1.6 Hz, 1H, Ar-H), 7.66-7.68 (d, *J* = 8.9 Hz, 1H, Ar-H), 5.44 (s, 1H, -CH=), 4.83-4.87 (q, *J* = 7.1 Hz, 2H, -CH_2-), 4.07-4.11 (q, J = 7.1 Hz, 2H, -CH_2-), 1.81 (s, 6H, -CH_3), 1.46-1.49 (t, *J* = 7.1 Hz, 3H, -CH_3), 1.24-1.27 (t, J = 7.2 Hz, 3H, -CH_3) ppm.^{13}C-NMR (151

MHz, DMSO-d6, RT): δ 192.20, 187.91, 186.59, 172.23, 168.62, 167.33, 141.56, 132.44, 131.53, 131.47, 129.79, 129.34, 126.50, 125.30, 122.22, 114.44, 80.76, 69.88, 48.96, 37.39, 26.13, 15.71, 11.50 ppm. MS (ESI^-, MeOH + ammonium hydroxide): m/z 404.21 $[M]^-$; calculated for $C_{24}H_{23}NO_5$: 405.16. UV-Vis (EtOH): λ_{max} (*ε*) = 315 (*19057*), 371 (*9691*), 445 (*76326*) nm. Fluorescence (EtOH, λ_{exc} 425 nm): 486 nm. φ: < 1%. IR-Spectrum (cm^{-1}, ATR): 2970 *v*(C–H aliphatic), 2935 *v*(C–H aliphatic), 1785 *v*(C=O), 1680 *v*(C=O), 1550, 1510, 1460, 1365, 1335, 1295, 1250 *δ*(O–H), 1200, 1090, 1020, 975, 905, 875, 815, 750.

Compound 224. A mixture of **223** (1.0 g, 1.0 eq.), 60 ml of acetone and 5 ml of 2 N HCl aqueous solution was refluxed for 8 h. After cooling the reaction to room temperature, the solvent was removed by distillation and the product was obtained without any other purification. The product was isolated as a dark-brown powder (0.84 g, 90%). R_f (silica gel): 0.20 (9:1 dichloromethane/methanol). M_p: > 200 °C. ^{1}H-NMR (600 MHz, DMSO-d6, RT): δ 8.60 (d, *J* = 1.1 Hz, 1H, Ar-H), 8.21-8.22 (d, *J* = 8.9 Hz, 1H, Ar-H), 8.13-8.14 (d, *J* = 8.8 Hz, 1H, Ar-H), 7.96-7.98 (dd, *J* = 8.8 Hz, *J* = 1.5 Hz, 1H, Ar-H), 7.60-7.61 (d, *J* = 8.8 Hz, 1H, Ar-H), 5.62 (s, 1H, -CH=), 4.02-4.06 (q, *J* = 7.1 Hz, 2H, $-CH_2-$), 1.82 (s, 6H, $-CH_3$), 1.24-1.27 (t, J = 7.2 Hz, 3H, $-CH_3$) ppm. ^{13}C-NMR (151 MHz, DMSO-d6, RT): δ 192.10, 191.55, 173.63, 167.39, 166.38, 141.99, 132.48, 131.45, 130.86, 130.00, 129.02, 126.40, 124.89, 122.10, 111.21, 81.66, 48.55, 37.18, 30.69, 26.27, 11.39 ppm. MS (ESI^-, MeOH + ammonium hydroxide): m/z 376.21 $[M]^-$; calculated for $C_{22}H_{19}NO_5$: 377.13 UV-Vis (EtOH): λ_{max} (*ε*) = 296 (*12479*), 386 (*15387*), 448 (*53427*) nm. Fluorescence (EtOH, λ_{exc} 430 nm): 484 nm. φ: < 1%. IR-Spectrum (cm^{-1}, ATR): 2970 *v*(C–H aliphatic), 2860 *v*(C–H aliphatic), 1765 *v*(C=O), 1675 *v*(C=O), 1615, 1530, 1505, 1445, 1295, 1250, 1200 *δ*(O–H), 1130, 910, 785, 755.

General synthesis of *di*-substituted 2,3-dihydro-1*H*-perimidines (226a-d).

A mixture of 1,8-diamminonaphtalene **225** (3.0 g, 18.96 mmol), ketone or aldehyde (19.90 mmol), *p*-toluene sulfonic acid (0.16 g, 0.57 mmol) in 30 ml of toluene was refluxed in a Dean-Stark apparatus for 16 hours. After cooling the reaction to room temperature, the solvent was removed and the crude material was purified by flash chromatography.

Compound 226a. The crude was purified by flash chromatography on silica gel using dichloromethane/hexane (8:2) as eluent. The product was isolated as a pale pink powder (2.79 g, 74%). R_f (silica gel): 0.40 (dichloromethane). M_p: 115-117 °C. ^{1}H-NMR (600 MHz, $CDCl_3$, RT): δ 7.23-7.25 (t, *J* = 8.2 Hz, 2H, Ar-H), 7.15-7.17 (d, *J* = 8.3 Hz, 2H, Ar-H), 6.47-6.48 (dd, *J* = 7.3 Hz, *J* = 0.8 Hz, 2H, Ar-H), 4.17 (br, 2H, -NH), 1.50 (s, 6H, $-CH_3$) ppm. ^{13}C-NMR (151 MHz, $CDCl_3$, RT): δ 140.57, 134.95, 127.35, 117.45, 113.29, 106.29, 64.90, 29.17 ppm. MS (ESI^+, MeOH): m/z 199.53 $[M-H]^+$; calculated for $C_{13}H_{14}N_2$: 198.12. UV-Vis (CH_2Cl_2): λ_{max} (ε) = 336 (*14847*), 349 (*15912*) nm. Fluorescence (CH_2Cl_2, λ_{exc} 330 nm): 402 nm. φ: 7%. IR-Spectrum (cm^{-1}, ATR): 3355 *v*(N–H), 3275 *v*(N–H), 3040 *v*(C–H aromatic), 2970 *v*(C–H aliphatic), 1735, 1590 *δ*(N–H), 1495, 1420, 1400, 1375, 1360, 1215, 1200, 1160, 1065, 1030, 855, 810 *δ*(N–H), 760, 745, 705.

Compound 226b. The crude was purified by flash chromatography on silica gel using dichloromethane/hexane (1:1) as eluent. The product was isolated as a pale pink powder (3.12 g, 73%). R_f (silica gel): 0.75 (dichloromethane). M_p: 93-95 °C. ^{1}H-NMR (600 MHz, $CDCl_3$, RT): δ 7.20-7.23 (t, *J* = 7.4 Hz, 2H, Ar-H), 7.10-7.11 (dd, *J* = 8.3 Hz, *J* = 0.6 Hz, 2H,

Ar-H), 6.45-6.47 (dd, *J* = 7.4 Hz, *J* = 0.7 Hz, 2H, Ar-H), 4.24 (br, 2H, -NH), 1.72-1.76 (q, *J* = 7.4 Hz, 4H, -CH_2-), 0.95-0.97 (t, *J* = 7.5 Hz, 6H, -CH_3) ppm.^{13}C-NMR (151 MHz, $CDCl_3$, RT): δ 140.41, 134.75, 127.20, 116.76, 113.01, 105.69, 69.06, 30.56, 7.90 ppm. MS (ESI^+, MeOH): m/z 227.21 $[M-H]^+$; calculated for $C_{15}H_{18}N_2$: 226.15. UV-Vis (CH_2Cl_2): λ_{max} (ε) = 337 (*13806*), 350 (*14848*) nm. Fluorescence (CH_2Cl_2, λ_{exc} 330 nm): 418 nm. φ: 9%. IR-Spectrum (cm^{-1}, ATR): 3370 *ν*(N–H), 3360 *ν*(N–H), 3040 *ν*(C–H aromatic), 2965 *ν*(C–H aliphatic), 2930 *ν*(C–H aliphatic), 1740, 1595 *δ*(N–H), 1455, 1425, 1370, 1160, 1120, 1035, 955, 805 *δ*(N–H), 755.

Compound 226c. The crude was purified by flash chromatography on silica gel using hexane/dichloromethane (8:2) as eluent. The product was isolated as a dark purple sticky oil (4.68 g, 87%). R_f (silica gel): 0.85 (dichloromethane). M_p: < 20 °C. ^{1}H-NMR (600 MHz, $CDCl_3$, RT): δ 7.20-7.23 (t, *J* = 7.4 Hz, 2H, Ar-H), 7.10-7.11 (d, *J* = 8.2 Hz, 2H, Ar-H), 6.44-6.45 (d, *J* = 7.3 Hz, 2H, Ar-H), 4.25 (br, 2H, -NH), 1.69-1.72 (m, 4H, -CH_2-), 1.36-1.41 (m, 4H, -CH_2-), 1.25-1.32 (m, 4H, -CH_2-), 0.88-0.90 (t, J = 7.3 Hz, 6H, -CH_3) ppm.^{13}C-NMR (151 MHz, $CDCl_3$, RT): δ 140.45, 134.77, 127.21, 116.70, 112.94, 105.55, 68.66, 38.39, 25.85, 23.08, 14.24 ppm. MS (ESI^+, MeOH): m/z 283.09 $[M-H]^+$; calculated for $C_{19}H_{26}N_2$: 282.21. UV-Vis (CH_2Cl_2): λ_{max} (ε) = 338 (*14131*), 350 (*15275*) nm. Fluorescence (CH_2Cl_2, λ_{exc} 330 nm): 415 nm. φ: < 9%. IR-Spectrum (cm^{-1}, ATR): 3385 *ν*(N–H), 3040 *ν*(C–H aromatic), 2950 *ν*(C–H aliphatic), 2855 *ν*(C–H aliphatic), 1735, 1595 *δ*(N–H), 1490, 1410, 1375, 1160, 1085, 1040, 810 *δ*(N–H), 755, 730.

Compound 226d. The crude was purified by flash chromatography on silica gel using hexane/dichloromethane (9:1) as eluent. The product was isolated as a dark purple sticky oil (6.75 g, 90%). R_f (silica gel): 0.95

(dichloromethane). M_p: < 20 °C ^{1}H-NMR (600 MHz, $CDCl_3$, RT): δ 7.21-7.23 (t, *J* = 7.4 Hz, 2H, Ar-H), 7.11-7.13 (d, *J* = 8.2 Hz, 2H, Ar-H), 6.45-6.47 (d, *J* = 7.3 Hz, 2H, Ar-H), 4.28 (br, 2H, -NH), 1.68-1.71 (m, 4H, -CH_2-), 1.38-1.41 (m, 4H, -CH_2-), 1.25-1.30 (m, 20H, -CH_2-), 0.86-0.89 (t, *J* = 7.2 Hz, 6H, -CH_3) ppm. ^{13}C-NMR (151 MHz, $CDCl_3$, RT): δ 140.49, 134.79, 127.21, 116.69, 112.97, 105.55, 68.70, 38.65, 31.98, 29.97, 29.68, 29.35, 23.65, 22.78, 14.23 ppm. MS (ESI^+, MeOH): m/z 395.42 $[M-H]^+$; calculated for $C_{27}H_{42}N_2$: 394.33. UV-Vis (CH_2Cl_2): λ_{max} (*ε*) = 339 (*12903*), 351 (*13961*) nm. Fluorescence (CH_2Cl_2, λ_{exc} 330 nm): 417 nm. φ: 8%. IR-Spectrum (cm^{-1}, ATR): 3375 *v*(N–H), 3030 *v*(C–H aromatic), 2920 *v*(C–H aliphatic), 2850 *v*(C–H aliphatic), 1735, 1600 *δ*(N–H), 1465, 1410, 1375, 1215, 1165, 1090, 810 *δ*(N–H), 755.

General synthesis of carboxyindoline-based squaraine dyes with *di*-substituted DHP (227-230). A mixture of carboxyindolenine emisquaraine **221** (150 mg, 0.46 mmol), *di*-substituted DHP derivatives **226a-d** (0.69 mmol) and 12 mL of a solution toluene/n-butanol (1:1) was introduced in a sealed 20 ml reaction vial and heated in a microwave reactor at 160 °C for 30 min. After cooling to room temperature, the reaction mixture was washed out of the reaction vessel with methanol and all the solvent was removed by evaporation under vacuum. The crude was purified by flash chromatography on silica gel using dichloromethane/methanol/acetic acid (94:5.5:0.5) as eluent.

Compound 227. The product was isolated as a dark-blue powder (75 mg, 32%). R_f (silica gel): 0.60 (9:1 dichloromethane/methanol). M_p: > 200 °C. ^{1}H-NMR (600 MHz, DMSO-d6, RT): δ 10.54 (s, 1H, -NH^+), 8.10 (d, *J* = 1.3 Hz, 1H, Ar-H), 8.00-8.01 (dd, *J* = 8.3 Hz, *J* = 1.5 Hz, 1H, Ar-H), 7.98-8.00

(d, *J* = 9.0 Hz, 1H, Ar-H), 7.53-7.55 (d, *J* = 8.4 Hz, 1H, Ar-H), 7.29-7.32 (t, *J* = 7.8 Hz, 1H, Ar-H), 7.20 (s, 1H, -NH), 6.81-6.83 (d, *J* = 7.6 Hz, 1H, Ar-H), 6.79-6.80 (d, *J* = 9.1 Hz, 1H, Ar-H), 6.48-6.50 (d, *J* = 7.7 Hz, 1H, Ar-H), 5.93 (s, 1H, -CH=), 4.23-4.26 (q, J = 7.3 Hz, 2H, $-CH_2-$), 1.73 (s, 6H, $-CH_3$), 1.52 (s, 6H, $-CH_3$), 1.30-1.33 (t, *J* = 7.3 Hz, 3H, $-CH_3$) ppm. ^{13}C-NMR (151 MHz, DMSO-d6, RT): δ 178.55, 174.00, 171.79, 167.02, 147.68, 145.02, 144.28, 142.05, 136.34, 132.82, 130.33, 126.92, 124.33, 123.38, 116.77, 115.09, 110.84, 109.07, 108.92, 107.86, 88.34, 64.79, 49.21, 38.87, 28.29, 26.02, 11.97 ppm. HRMS (ESI$^+$, MeOH): m/z 508.2231 $[M-H]^+$; calculated for $C_{31}H_{29}N_3O_4$: 508.2231 (+1). UV-Vis (EtOH): λ_{max} (*ε*) = 277 (*22396*), 397 (*15698*), 463 (*12314*), 733 (*109343*) nm. Fluorescence (EtOH, λ_{exc} 720 nm): 773 nm. φ: 1%. IR-Spectrum (cm^{-1}, ATR): 2965 *v*(C–H aliphatic), 2925 *v*(C–H aliphatic), 1720 *v*(C=O), 1685 *v*(C=O), 1620, 1605, 1550, 1540, 1510, 1450, 1430, 1390, 1355, 1290, 1180, 1120, 1090, 1050, 940, 815, 770, 745.

Compound 228. The product was isolated as a dark-blue powder (142 mg, 58%). R_f (silica gel): 0.30 (95:5 dichloromethane/methanol). M_p: > 200 °C. ^{1}H-NMR (600 MHz, DMSO-d6, RT): δ 10.52 (s, 1H, $-NH^+$), 8.09 (s, 1H, Ar-H), 7.99-8.00 (d, *J* = 8.4 Hz, 1H, Ar-H), 7.96-7.97 (d, *J* = 8.9 Hz, 1H, Ar-H), 7.50-7.52 (d, *J* = 8.4 Hz, Ar-H), 7.27-7.29 (t, *J* = 7.8 Hz, 1H, Ar-H), 7.11 (s, 1H, -NH), 6.74-6.76 (m, 2H, Ar-H), 6.51-6.52 (d, *J* = 7.9 Hz, 1H, Ar-H), 5.90 (s, 1H, -CH=), 4.21-4.24 (q, *J* = 7.3 Hz, 2H, $-CH_2-$), 1.74-1.82 (m, 4H, $-CH_2-$), 1.72 (s, 6H, $-CH_3$), 1.29-1.32 (t, *J* = 7.3 Hz, 3H, $-CH_3$), 0.94-0.96 (t, *J* = 7.4 Hz, 6H, $-CH_3$) ppm. ^{13}C-NMR (151 MHz, DMSO-d6, RT): δ 177.56, 174.11, 171.11, 167.02, 148.70, 145.15, 144.86, 141.97, 136.29, 133.13, 130.35, 126.60, 124.29, 123.37, 116.65, 114.51, 110.63, 108.65, 108.41, 107.71, 88.22, 70.11, 49.04, 38.72, 31.56, 26.07, 11.96, 7.66 ppm. HRMS (ESI$^+$, MeOH): m/z 536.2528 $[M-H]^+$; calculated for

$C_{33}H_{33}N_3O_4$: 536.2544 (+1). UV-Vis (EtOH): λ_{max} (ε) = 276 (*32969*), 398 (*17172*), 467 (*12703*), 746 (*108086*) nm. Fluorescence (EtOH, λ_{exc} 730 nm): 778 nm. φ: 1%. IR-Spectrum (cm^{-1}, ATR): 2915 *v*(C–H aliphatic), 2850 *v*(C–H aliphatic), 1700 *v*(C=O), 1580, 1535, 1510, 1450, 1390, 1355, 1280, 1235, 1190, 1085, 1045, 935, 815, 770.

Compound 229. The product was isolated as a dark-blue powder (127 mg, 47%). R_f (silica gel): 0.65 (9:1 dichloromethane/methanol). M_p: > 200 °C.^{1}H-NMR (600 MHz, DMSO-d6, RT): δ 10-54 (s, 1H, -NH^+), 8.09 (s, 1H, Ar-H), 7.99-8.00 (dd, *J* = 8.2 Hz, *J* = 1.1 Hz, 1H, Ar-H), 7.96-7.97 (d, J = 8.9 Hz, 1H, Ar-H), 7.50-7.51 (d, *J* = 8.5 Hz, 1H, Ar-H), 7.26-7.29 (t, *J* = 7.7 Hz, 1H, Ar-H), 7.13 (s, 1H, -NH), 6.73-6.75 (m, 2H, Ar-H), 6.49-6.50 (d, *J* = 7.9 Hz, 1H, Ar-H), 5.90 (s, 1H, -CH=), 4.21-4.25 (q, *J* = 7.1 Hz, 2H, -CH_2-), 1.73-1.79 (m, 4H, -CH_2-), 1.72 (s, 6H, -CH_3), 1-42-1.48 (m, 2H, -CH_2-), 1.34-1.41 (m, 2H, -CH_2-), 1.26-1.31 (m, 7H, -CH_2- and -CH_3), 0.84-0.86 (t, J = 7.3 Hz, 6H, -CH_3) ppm. ^{13}C-NMR (151 MHz, DMSO-d6, RT): δ 177.38, 174.08, 171.00, 167.02, 148.51, 145.13, 144.73, 141.97, 136.26, 133.15, 130.33, 126.60, 124.27, 123.33, 116.63, 114.47, 110.58, 108.57, 108.21, 107.65, 88.24, 69.60, 49.02, 38.69, 26.06, 25.07, 22.37, 14.00, 11.97 ppm. HRMS (ESI^+, MeOH): m/z 592.3148 $[M-H]^+$; calculated for $C_{37}H_{41}N_3O_4$: 592.3170 (+1). UV-Vis (EtOH): λ_{max} (ε) = 277 (*24966*), 398 (*16066*), 466 (*11666*), 745 (*107612*) nm. Fluorescence (EtOH, λ_{exc} 730 nm): 778 nm. φ: 1%. IR-Spectrum (cm^{-1}, ATR): 2970 *v*(C–H aliphatic), 2925 *v*(C–H aliphatic), 2855 *v*(C–H aliphatic), 1705 *v*(C=O), 1540, 1505, 1445, 1390, 1350, 1280, 1230, 1185, 1120, 1085, 1040, 935, 815, 765.

Compound 230. The product was isolated as a dark-blue powder (80 mg, 25%). R_f (silica gel): 0.70 (9:1 dichloromethane/methanol). M_p: 170-172 °C. ^{1}H-NMR (600 MHz, DMSO-d6, RT): δ 10.56 (s, 1H, -NH^+), 8.08 (d, *J*

= 1.4 Hz, 1H, Ar-H), 7.98-8.00 (dd, *J* = 8.3 Hz, *J* = 1.6 Hz, 1H, Ar-H), 7.95-7.97 (d, *J* = 9.0 Hz, 1H, Ar-H), 7.49-7.51 (d, *J* = 8.5 Hz, 1H, Ar-H), 7.25-7.28 (t, *J* = 7.8 Hz, 1H, Ar-H), 7,10 (s, 1H, -NH), 6.72-6.74 (m, 2H, Ar-H), 6.48-6.50 (d, *J* = 7.8 Hz, 1H, Ar-H), 5.89 (s, 1H, -CH=), 4.20-4.23 (q, *J* = 6.5 Hz, 2H, $-CH_2-$), 1.71-1.78 (m, 10H, $-CH_2-$ and $-CH_3$), 1.44-1.49 (m, 2H, $-CH_2-$), 1.35-1.42 (m, 2H, $-CH_2-$), 1.28-1.30 (t, *J* = 7.2 Hz, 3H, $-CH_3$), 1.12-1.24 (m, 20H, $-CH_2-$), 0.79-0.81 (t, *J* = 7.1 Hz, 6H, $-CH_3$) ppm. ^{13}C-NMR (151 MHz, DMSO-d6, RT): δ 177.40, 174.29, 170.86, 166.99, 148.59, 145.13, 144.73, 141.92, 136.27, 133.13, 130.34, 126.53, 124.28, 123.29, 116.65, 114.48, 110.56, 108.67, 108.28, 107.69, 88.17, 69.66, 48.96, 38.65, 31.26, 29.08, 28.82, 28.51, 26.08, 22.62, 22.09, 13.93, 11.91 ppm. HRMS (ESI$^+$, MeOH): m/z 704.4391 $[M-H]^+$; calculated for $C_{45}H_{57}N_3O_4$: 704.4422 (+1). UV-Vis (EtOH): λ_{max} (***ε***) = 398 (*13633*), 466 (*9748*), 744 (*93359*) nm. Fluorescence (EtOH, λ_{exc} 730 nm): 776 nm. φ: 1%. IR-Spectrum (cm^{-1}, ATR): 2920 *v*(C–H aliphatic), 2850 *v*(C–H aliphatic), 1710 *v*(C=O), 1575, 1535, 1510, 1450, 1395, 1355, 1285, 1235, 1180, 1120, 1085, 1045, 940, 815, 770.

General synthesis of carboxy-benzoindoline based squaraine dyes with *di*-substituted DHP (231-234). A mixture of carboxy-benzoindoline emisquaraine **227** (150 mg, 1.0 eq.), *di*-substituted DHP derivative **226a-d** (1.5 eq.) and 12 mL of a solution toluene/n-butanol (1:1) was introduced in a sealed 20 ml reaction vial and heated in a microwave reactor at 160 °C for 40 min. After cooling to room temperature, the reaction mixture was washed out of the reaction vessel with methanol and all the solvent was removed by evaporation under vacuum. The crude was purified by flash chromatography on silica gel using dichloromethane/methanol/acetic acid (94:5.7:0.3) as eluent.

Compound 231. The product was isolated as a dark-blue powder (75 mg, 32%). R_f (silica gel): 0.50 (9:1 dichloromethane/methanol). M_p: > 200 °C. ^{1}H-NMR (600 MHz, DMSO-d6, RT): δ 10.33 (s, 1H, -NH$^+$), 8.73 (d, *J* = 0.7 Hz, 1H, Ar-H), 8.39-8.41 (d, *J* = 8.6 Hz, 1H, Ar-H), 8.30-8.31 (d, *J* = 8.9 Hz, 1H, Ar-H), 8.10-8.11 (dd, *J* = 8.7 Hz, *J* = 1.4 Hz, 1H, Ar-H), 8.03-8.05 (d, *J* = 8.8 Hz, 1H, Ar-H), 7.91-7.93 (d, *J* = 8.9 Hz, 1H, Ar-H), 7.27-7.30 (t, *J* = 7.7 Hz, 1H, Ar-H), 7.12 (s, 1H, -NH), 6.80-6.84 (m, 2H, Ar-H), 6.47-6.49 (d, *J* = 7.7 Hz, 1H, Ar-H), 6.01 (s, 1H, -CH=), 4.39-4.42 (q, *J* = 7.1 Hz, 2H, -CH_2-), 1.98 (s, 6H, -CH_3), 1.52 (s, 6H, -CH_3), 1.37-1.39 (t, *J* = 7.3 Hz, 3H, -CH_3) ppm. ^{13}C-NMR (151 MHz, DMSO-d6, RT): δ 183.29, 178.70, 173.71, 172.04, 167.25, 146.60, 144.02, 140.74, 136.10, 134.68, 132.35, 132.12, 131.89, 130.63, 129.55, 126.94, 126.80, 124.52, 122.97, 116.34, 114.98, 112.53, 109.39, 108.79, 107.40, 87.99, 64.58, 51.39, 40.06, 28.32, 25.68, 12.41 ppm. HRMS (ESI$^+$, MeOH): m/z 558.2367 [M-H]$^+$; calculated for $C_{35}H_{31}N_3O_4$: 558.2367 (+1). UV-Vis (EtOH): λ_{max} (ε) = 360 (*11555*), 404 (*11186*), 463 (*8359*), 743 (*99344*) nm. Fluorescence (EtOH, λ_{exc} 730 nm): 784 nm. φ: 1%. IR-Spectrum (cm^{-1}, ATR): 2965 *v*(C–H aliphatic), 2915 *v*(C–H aliphatic), 1705 *v*(C=O), 1540, 1505, 1445, 1415, 1385, 1285, 1235, 1180, 1125, 1035, 965, 935, 815, 800, 750.

Compound 232. The product was isolated as a dark-blue powder (103 mg, 35%). R_f (silica gel): 0.50 (9:1 dichloromethane/methanol). M_p: 169-171 °C. ^{1}H-NMR (600 MHz, DMSO-d6, RT): δ 10.35 (s, 1H, -NH$^+$), 8.72 (d, *J* = 1.0 Hz, 1H, Ar-H), 8.35-8.36 (d, *J* = 8.9 Hz, 1H, Ar-H), 8.28-8.30 (d, *J* = 8.9 Hz, 1H, Ar-H), 8.08-8.10 (dd, *J* = 8.8 Hz, *J* = 1.0 Hz, 1H, Ar-H), 8.01-8.03 (d, *J* = 9.2 Hz, 1H, Ar-H), 7.88-7.90 (d, *J* = 9.0 Hz, 1H, Ar-H), 7.24-7.26 (t, *J* = 7.7 Hz, 1H, Ar-H), 7.02 (s, 1H, -NH), 6.74-6.75 (m, 2H, Ar-H), 6.48-6.49 (d, *J* = 7.7 Hz, 1H, Ar-H), 5.98 (s, 1H, -CH=), 4.36-4.40 (q, *J* = 6.9 Hz, 2H, -CH_2-), 1.96 (s, 6H, -CH_3), 1.69-1.78 (m, 4H, -CH_2-), 1.35-1.51 (m, 7H, -CH_2- and -CH_3), 1.14-1.29 (m, 20H, -CH_2-), 0.79-0.81

(t, *J* = 7.1 Hz, 1H, -CH_3) ppm. ^{13}C-NMR (151 MHz, DMSO-d6, RT): δ 177.77, 172.92, 172.07, 167.27, 147.46, 144.43, 140.80, 136.05, 134.37, 132.40, 131.85, 130.51, 129.56, 128.90, 128.21, 126.89, 124.50, 122.76, 116.51, 114.36, 112.41, 108.65, 108.49, 107.20, 87.78, 69.38, 51.17, 38.97, 31.26, 29.13, 28.85, 28.52, 25.70, 22.65, 22.10, 13.93, 12.34 ppm. HRMS (ESI$^+$, MeOH): m/z 754.4556 [M-H]$^+$; calculated for $C_{49}H_{59}N_3O_4$: 754.4578 (+1). UV-Vis (EtOH): λ_{max} (*ε*) = 362 (*8778*), 406 (*8663*), 449 (*8778*), 749 (*102695*) nm. Fluorescence (EtOH, λ_{exc} 735 nm): 783 nm. φ: 1%. IR-Spectrum (cm^{-1}, ATR): 2920 *ν*(C–H aliphatic), 2845 *ν*(C–H aliphatic), 1720 *ν*(C=O), 1535, 1505, 1445, 1420, 1390, 1325, 1290, 1230, 1185, 1125, 1095, 1035, 1015, 965, 930, 795, 750.

Compound 233. The product was isolated as a dark-blue powder (127 mg, 50%). R_f (silica gel): 0.45 (9:1 dichloromethane/methanol). M_p: > 200 °C. ^{1}H-NMR (600 MHz, DMSO-d6, RT): δ 10.31 (s, 1H, -NH$^+$), 8.70 (d, *J* = 1.0 Hz, 1H, Ar-H), 8.34-8.36 (d, *J* = 8.9 Hz, 1H, Ar-H), 8.28-8.29 (d, *J* = 8.9 Hz, 1H, Ar-H), 8.10-8.12 (dd, *J* = 8.7 Hz, *J* = 1.1 Hz, 1H, Ar-H), 8.02-8.03 (d, *J* = 8.5 Hz, 1H, Ar-H), 7.89-7.90 (d, *J* = 8.9 Hz, 1H, Ar-H), 7.24-7.27 (t, *J* = 7.7 Hz, 1H, Ar-H), 7.04 (s, 1H, -NH), 6.74-6.76 (m, 2H, Ar-H), 6.48-6.49 (d, *J* = 7.7 Hz, 1H, Ar-H), 5.98 (s, 1H, -CH=), 4.38-4.41 (q, *J* = 7.1 Hz, 2H, -CH_2-), 1.97 (s, 6H, -CH_3), 1.71-1.79 (m, 4H, -CH_2-), 1.36-1.48 (m, 7H, -CH_2- and -CH_3), 1.25-1.32 (m, 4H, -CH_2-), 0.85-0.87 (t, *J* = 7.3 Hz, 6H, -CH_3) ppm. ^{13}C-NMR (151 MHz, DMSO-d6, RT): δ 177.75, 173.06, 172.04, 167.32, 147.36, 144.43, 140.79, 136.05, 134.45, 132.42, 132.34, 131.84, 130.53, 129.56, 126.94, 126.80, 124.46, 122.82, 116.13, 114.35, 112.43, 108.57, 108.40, 107.15, 87.86, 69.32, 51.23, 40.05, 25.68, 25.11, 22.42, 14.03, 12.41 ppm. HRMS (ESI$^+$, MeOH): m/z 642.3326 [M-H]$^+$; calculated for $C_{41}H_{43}N_3O_4$: 642.3326 (+1). UV-Vis (EtOH): λ_{max} (*ε*) = 359 (*7500*), 404 (*7500*), 472 (*6119*), 749 (*101239*) nm.

Fluorescence (EtOH, λ_{exc} 735 nm): 783 nm. φ: 1%. IR-Spectrum (cm^{-1}, ATR): 2950 *v*(C–H aliphatic), 2925 *v*(C–H aliphatic), 2855 *v*(C–H aliphatic), 1710 *v*(C=O), 1540, 1505, 1450, 1420, 1390, 1290, 1230, 1190, 1125, 1035, 1015, 965, 935, 815, 800, 750.

Compound 234. The product was isolated as a dark-blue powder (103 mg, 35%). R_f (silica gel): 0.50 (9:1 dichloromethane/methanol). M_p: 169-171 °C. ^{1}H-NMR (600 MHz, DMSO-d6, RT): δ 10.35 (s, 1H, -NH^+), 8.72 (d, *J* = 1.0 Hz, 1H, Ar-H), 8.35-8.36 (d, *J* = 8.9 Hz, 1H, Ar-H), 8.28-8.30 (d, *J* = 8.9 Hz, 1H, Ar-H), 8.08-8.10 (dd, *J* = 8.8 Hz, *J* = 1.0 Hz, 1H, Ar-H), 8.01-8.03 (d, *J* = 9.2 Hz, 1H, Ar-H), 7.88-7.90 (d, *J* = 9.0 Hz, 1H, Ar-H), 7.24-7.26 (t, *J* = 7.7 Hz, 1H, Ar-H), 7.02 (s, 1H, -NH), 6.74-6.75 (m, 2H, Ar-H), 6.48-6.49 (d, *J* = 7.7 Hz, 1H, Ar-H), 5.98 (s, 1H, -CH=), 4.36-4.40 (q, *J* = 6.9 Hz, 2H, -CH_2-), 1.96 (s, 6H, -CH_3), 1.69-1.78 (m, 4H, -CH_2-), 1.35-1.51 (m, 7H, -CH_2- and -CH_3), 1.14-1.29 (m, 20H, -CH_2-), 0.79-0.81 (t, *J* = 7.1 Hz, 1H, -CH_3) ppm. ^{13}C-NMR (151 MHz, DMSO-d6, RT): δ 177.77, 172.92, 172.07, 167.27, 147.46, 144.43, 140.80, 136.05, 134.37, 132.40, 131.85, 130.51, 129.56, 128.90, 128.21, 126.89, 124.50, 122.76, 116.51, 114.36, 112.41, 108.65, 108.49, 107.20, 87.78, 69.38, 51.17, 38.97, 31.26, 29.13, 28.85, 28.52, 25.70, 22.65, 22.10, 13.93, 12.34 ppm. HRMS (ESI^+, MeOH): m/z 754.4556 $[M-H]^+$; calculated for $C_{49}H_{59}N_3O_4$: 754.4578 (+1). UV-Vis (EtOH): λ_{max} (*ε*) = 362 (*8778*), 406 (*8663*), 449 (*8778*), 749 (*102695*) nm. Fluorescence (EtOH, λ_{exc} 735 nm): 783 nm. φ: 1%. IR-Spectrum (cm^{-1}, ATR): 2920 *v*(C–H aliphatic), 2845 *v*(C–H aliphatic), 1720 *v*(C=O), 1535, 1505, 1445, 1420, 1390, 1325, 1290, 1230, 1185, 1125, 1095, 1035, 1015, 965, 930, 795, 750.

5.3. Photophysical studies

All the measurements were carried out in a 1 cm four-sided quartz cuvette from Hellma Analitics. Absorption spectra were measured on a Shimadzu UV-1900i UV-Vis Spectrophotometer, using a resolution of 0.5 nm. Steady state emission spectra were measured on a Shimadzu RF-6000. The excitation and the emission slits were set at 5 and 10 nm respectively, while the resolution at 1 nm. All the photophysical studies have been performed in anhydrous solvents, purchased from Sigma Aldrich, VWR and Carlo Erba. Aqueous buffer solutions were prepared with de-ionized water (Millipore RiOs 3 Water System), sodium phosphate monobasic monohydrate, di-sodium hydrogen phosphate dihydrate and sodium chloride (Biological grade) properly adjusted to have a final buffer with composition: 10 mM phosphate, 100 mM NaCl, pH 7.4. The probes were excited 5 nm before the absorbance maxima for the general photophysical measurements and 15 nm before the absorbance maxima for the studies in Lipid Bilayer Membranes to provide enough energy to excite all the fluorophore population and maximize the recorded signal in relation with the samples properties and the instrument performance and parameters. All the absorption and steady state emission spectra were corrected for their respective blank.

5.3.1. Fluorescence quantum yield (PLQY) evaluation

The sample concentrations were adapted to have an absorbance lower than 0.1 at the excitation wavelength (λ_{ex}).. The fluorescence quantum yield (PLQY) were evaluated compared on an external standard (e.g., Coumarnne 101, Quinine emisulhate, Rhodamine 6G and Rhodamine 101 depending on the fluorophore) by applying the following equation:

$$PLQY = PLQY_{STD}\frac{I}{I_{STD}}\frac{Abs_{STD}}{Abs}\frac{n^2}{n_{STD}^2} \quad \textbf{(S1)}$$

Where φ_{STD} is the fluorescence quantum yield of the standard, I and I_{STD} are the integrated area of the emission band of the sample and the standard respectively. Abs and Abs_{STD} are the absorbance at the excitation wavelength for the sample and the standard respectively. n and n_{STD} are the solvent refractive index of the sample and the standard solutions respectively.

5.3.2. Lippert equation

Lippert parameters (f_L) were calculated for each solvent with Equation S2. The experimental Stokes shifts were plotted as a function of f_L and then fit with a linear Equation S3 in which Equation S4 defines the slope parameter (mL), and qL is the intercept with the y-axis.

$$f_L = \frac{\epsilon_r - 1}{2\epsilon_r + 1} - \frac{n^2 - 1}{2n^2 + 1} \qquad \textbf{(S2)}$$

$$v_a - v_f = m_L \cdot f_L + q_L \qquad \textbf{(S3)}$$

$$m_L = \frac{2(\mu_e - \mu_g)^2}{hca^3} \qquad \textbf{(S4)}$$

Where v_a is the maximum absorption wavenumber (cm^{-1}), v_f is the maximum emission wavenumber (cm^{-1}), μ_e (statC·cm) is the excited state dipole moment, μ_g (statC·cm) is the ground state dipole moment, h (erg) is the Planck constant, c ($cm \cdot s^{-1}$) is the light speed, a (cm) is the push-pull group distance.

5.3.3. Bakhshiev Equation

Bakhshiev parameters (f_B) were calculated for each solvent using Equation S5. The experimental Stokes shifts were plotted as a function of f_B and then fit with a linear Equation S6 in which the slope parameter (m_B) is defined by Equation S7 and q_B is the intercept with the y-axis**.**

$$f_B = \frac{2n^2+1}{n^2+2}\left(\frac{\varepsilon_r-1}{\varepsilon_r+2} - \frac{n^2-1}{n^2+}\right) \quad \textbf{(S5)}$$

$$v_a - v_f = m_B \cdot f_B + q_B \quad \textbf{(S6)}$$

$$m_B = \frac{2(\mu_e-\mu_g)^2}{hca^3} \quad \textbf{(S7)}$$

Where v_a is the maximum absorption wavenumber (cm^{-1}), v_f is the maximum emission wavenumber (cm^{-1}), μ_e (statC·cm) is the excited state dipole moment, μ_g (statC·cm) is the ground state dipole moment, h (erg) is the Planck constant, c ($cm \cdot s^{-1}$) is the light speed, a (cm) is the push-pull group distance.

5.3.4. Kawski-Chamma-Viallet Equation

Kawski-Chamma-Viallet parameters (f_K) were calculated for each solvent using Equation S8. The experimental semi-sum of the absorption and emission maxima were plotted as a function of f_K and then fit with a linear Equation S9 in which Equation S10 defines the slope parameter (mK), and q_K is the intercept with the y-axis.

$$f_K = \frac{2n^2+1}{2(n^2+2)}\left(\frac{\varepsilon-1}{\varepsilon+2} - \frac{n^2-1}{n^2+2}\right) + \frac{3(n^4-1)}{2(n^2+2)^2} \quad \textbf{(S8)}$$

$$\frac{v_a+v_f}{2} = -\frac{2(\mu_e^2-\mu_g^2)}{hca^3} \cdot f_K + q_K \quad \textbf{(S9)}$$

$$m_k = \frac{2(\mu_e^2-\mu_g^2)}{hca^3} \quad \textbf{(S10)}$$

Where v_a is the maximum absorption wavenumber (cm^{-1}), v_f is the maximum emission wavenumber (cm^{-1}), μ_e (statC·cm) is the excited state dipole moment, μ_g (statC·cm) is the ground state dipole moment, h (erg) is the Planck constant, c ($cm \cdot s^{-1}$) is the light speed, a (cm) is the push-pull group distance parameter.

5.4. Studies in LUVs

5.4.1. DOPC LUVs preparation

A fine lipid film was prepared by slow rotary evaporation (30°C) of a DOPC (25.0 mg, 0.03 mmol) solution in MeOH/$CHCl_3$ 1:1 (2.0 mL), followed by a final draining (5h) *in vacuo*. The prepared film was hydrated with 1.0 mL buffer (10 mM phosphate, 100 mM NaCl, pH 7.4) for 30 min at rt, subjected to freeze-melt cycles (7×, liquid N_2, 40 °C water bath) and extrusions (17×) through a polycarbonate membrane (pore size, 100 nm) at rt. Final conditions: ~32 mM DOPC; 10 mM phosphate, 100 mM NaCl, pH 7.4. The vesicles were used by 7 days after the extrusion.

5.4.2. DPPC LUVs preparation

A fine lipid film was prepared by slow rotary evaporation (50°C) of a DPPC (22.5 mg, 0.03 mmol) solution in MeOH/$CHCl_3$ 1:1 (2.0 mL), followed by a final draining (5h) in vacuo. The prepared film was hydrated with 1.0 mL buffer (10 mM phosphate, 100 mM NaCl, pH 7.4) for 30 min at 55°C, subjected to freeze-melt cycles (7×, liquid N_2, 55°C °C water bath) and extrusions (21×) through a polycarbonate membrane (pore size, 100 nm) at 55° C. Final conditions: ~31 mM DPPC; 10 mM phosphate, 100 mM NaCl, pH 7.4. The vesicles were used by 7 days after the extrusion.

5.4.3. DPPC/CL LUVs preparation

A fine lipid film was prepared by slow rotary evaporation (50°C) of a solution of 17 mg DPPC and 4.5 mg CL in MeOH/$CHCl_3$ 1:1 (2.0 mL), followed by a final draining (5h) in vacuo. The prepared film was hydrated with 1.0 mL buffer (10 mM phosphate, 100 mM NaCl, pH 7.4) for 30 min at 55°C, subjected to freeze-melt cycles (7×, liquid N_2, 55°C °C water

bath) and extrusions (15×) through a polycarbonate membrane (pore size, 100 nm) at 55° C. Final conditions: ~23 mM DPPC; ~11 mM CL (~34 mM total lipid) 10 mM phosphate, 100 mM NaCl, pH 7.4. The vesicles were used by 7 days after the extrusion.

5.4.4. Kinetic measurements

In a typical procedure, to a 2900 µL buffer (10 mM phosphate, 100 mM NaCl, pH 7.4 at rt) in a quartz cuvette, DOPC LUVs (100 µL, 1.1 mM DOPC final), DPPC LUVs (100 µL, 1.02 mM DPPC final) or DPPC CL LUVs (100 µL, 0.77 mM DPPC final, 0.37 mM CL final) all the six tested probes (10 µL, ~0.11 mM in DMSO, ~ 0.35µM final) were added in separated experiments. Each solution was mixed at rt and monitored acquiring the emission spectra every 1 minute during the first 20 minutes, then after 5 minutes up to 1 h. Depending on the specific kinetic of each probe and on the experiment itself, the monitoring is adjusted and continued for a longer time as reported in the main text.

5.4.5. Temperature-dependent measurements

In a typical procedure, to a 2900 µL buffer (10 mM phosphate, 100 mM NaCl, pH 7.4 at rt) in a quartz cuvette, DOPC LUVs (100 µL, 1.1 mM DOPC final) or DPPC LUVs (100 µL, 1.02 mM DPPC final) and aliquotes of the tested probes' DMSO solutions (10 µL, ~0.11 mM in DMSO, ~ 0.35µM final) were added in separated experiments. The solution was mixed at rt, and the emission/excitation spectra were acquired after the respective equilibration time at rt calculated by the time dependence measurements. The solution was kept at 25 ± 1 °C for 15 minutes before the spectra acquisition, the cuvette was then warmed to 55 ± 1 °C using a hot plate and a sand bath, and the solution was kept at this temperature for 15 minutes before the spectra acquisition. Then the temperature was

lowered to 25 ± 1 °C, and the spectra were acquired after 15 minutes. The described temperature cycle was repeated a second time, collecting five measurements for each probe.

5.4.6. Partition coefficient

In a typical procedure, different DOPC, DPPC or DPPC/CL LUVs (32 mM, 31 mM or 34 mM, respectively) aliquots were added to a solution of the desired probe in buffer (10 mM phosphate, 100 mM NaCl, pH 7.4 at rt). The fluorescence spectra were recorded at equilibrium after adding lipids (20 min for all the vesicles). Then, the maximum intensity (F) was plotted against the lipid concentration (L) for each prepared solution, according to the equation (2), reported in literature[261]:

$$F = \frac{F_0 L}{\frac{55.6}{K_{rip}} + L} \qquad (\boldsymbol{S11})$$

where F_0 is the maximum fluorescence resulting from the total probe incorporation into membrane and K_{rip} is the partition coefficient. The double reciprocal plot of the fluorescence (F) and the lipid concentration (L) should give a linear fit according to the following equation (3):

$$\frac{1}{F} = \left(\frac{55.6}{K_{rip} F_0}\right)\frac{1}{L} + \frac{1}{F_0} \qquad (\boldsymbol{S12})$$

Finally, K_{rip} can be calculated from the slope of the linear fit reported in equation (2) using the F_0 value calculated from the intercept of the fit.

SUPPORTING FIGURES

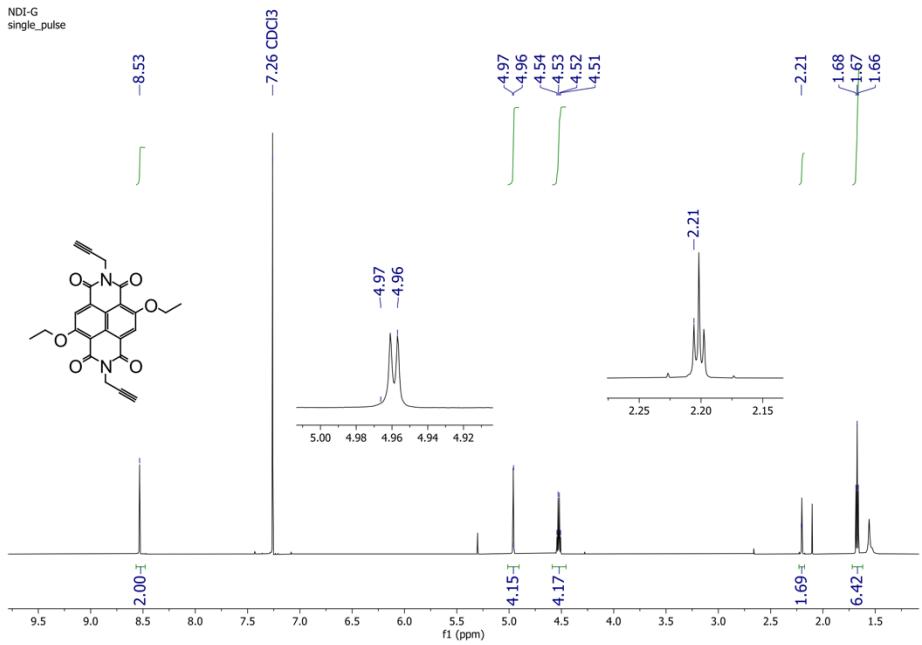

Figure S1. ^{1}H-NMR spectrum of NDI-01 in $CDCl_3$.

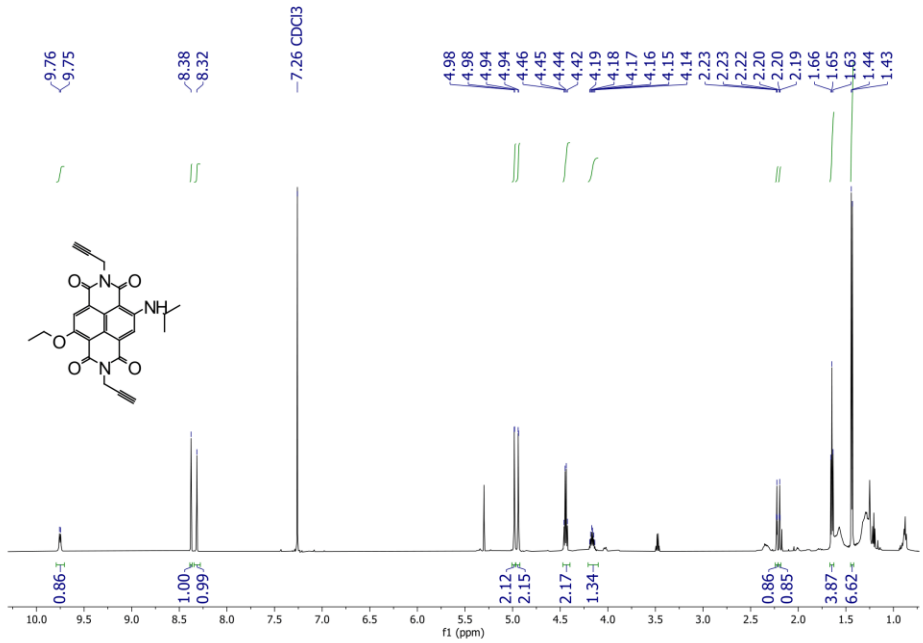

Figure S2. ^{1}H-NMR spectrum of NDI-02 in $CDCl_3$.

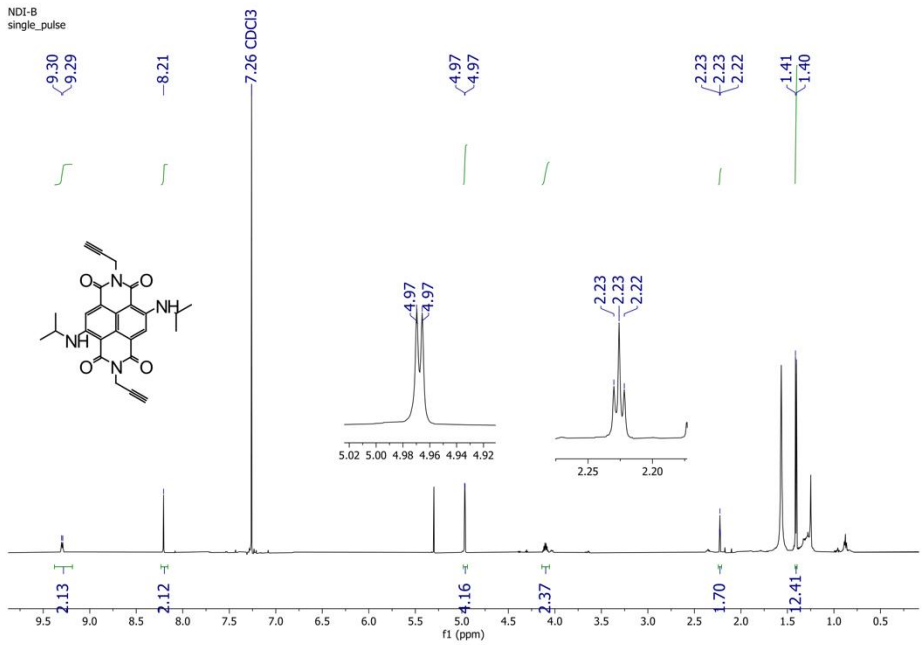

Figure S3. ^{1}H-NMR spectrum of NDI-03 in $CDCl_3$.

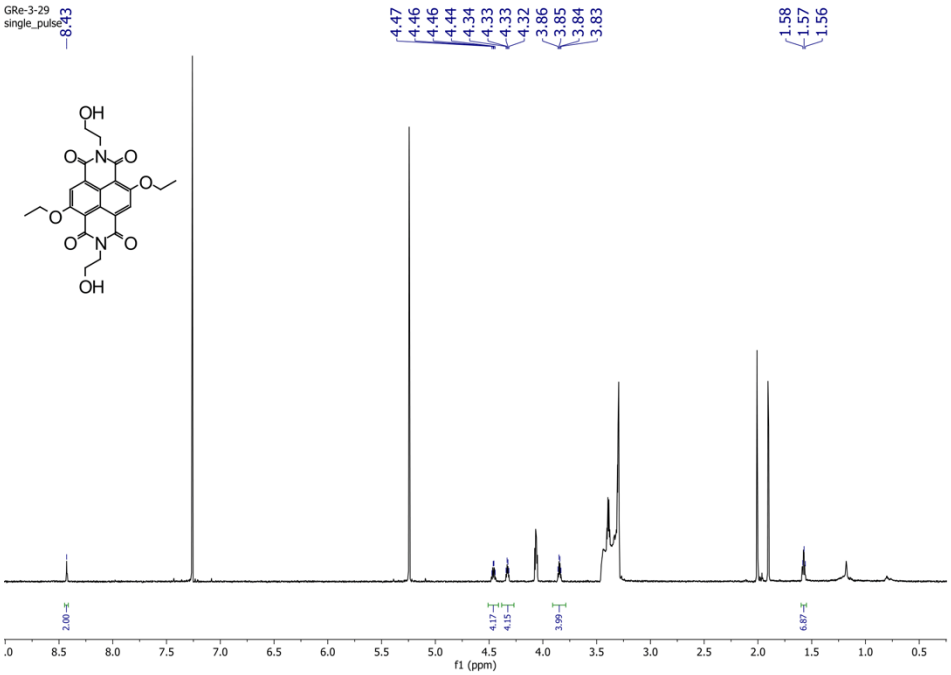

Figure S4. ^{1}H-NMR spectrum of 125 in $CDCl_3$.

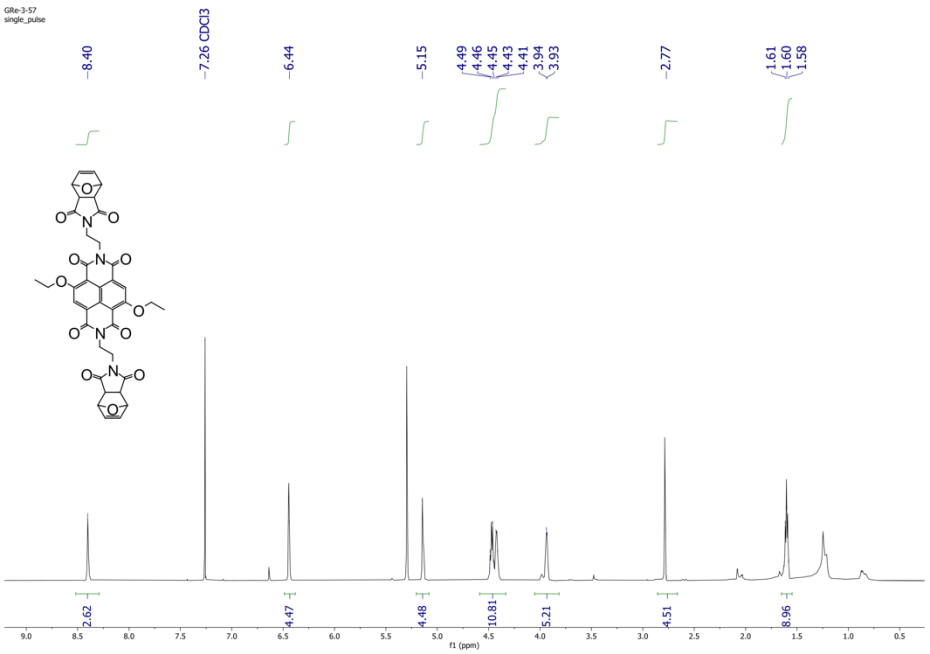

Figure S5. ^{1}H-NMR spectrum of 132 in $CDCl_3$.

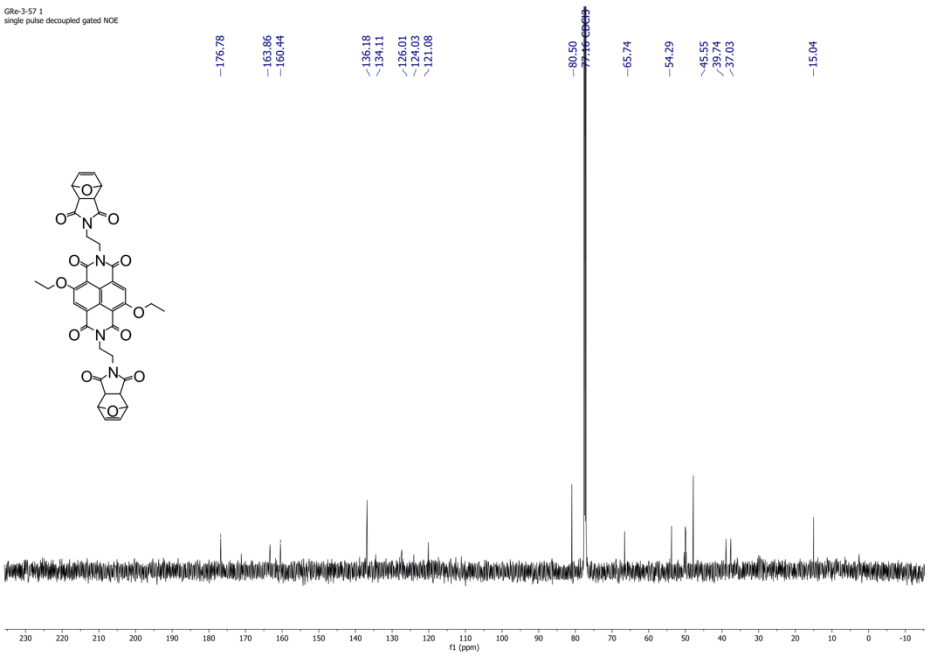

Figure S6. ^{13}C-NMR spectrum of 132 in $CDCl_3$.

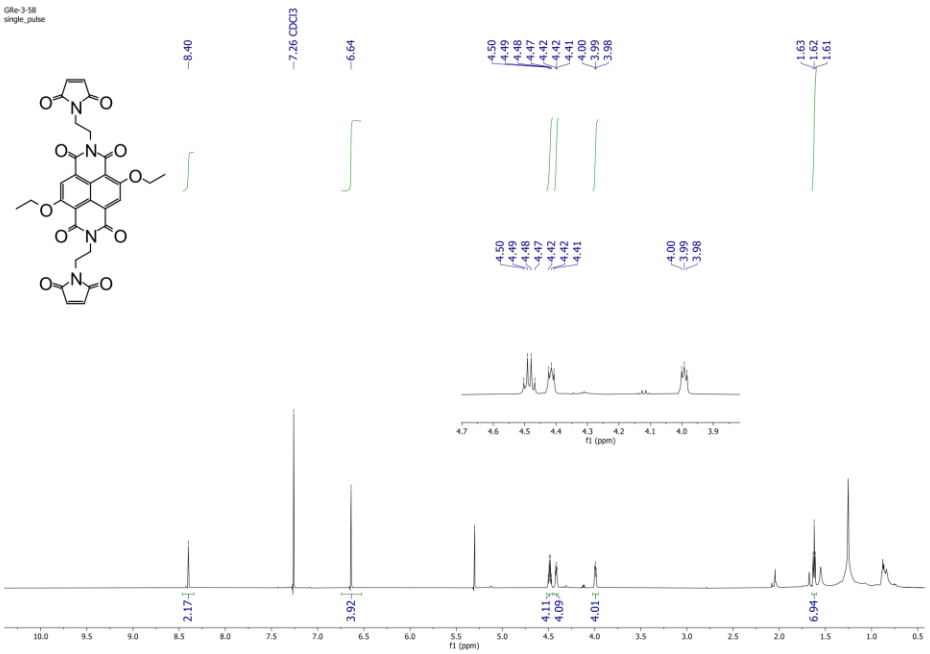

Figure S7. ^{1}H-NMR spectrum of NDI-05 in $CDCl_3$.

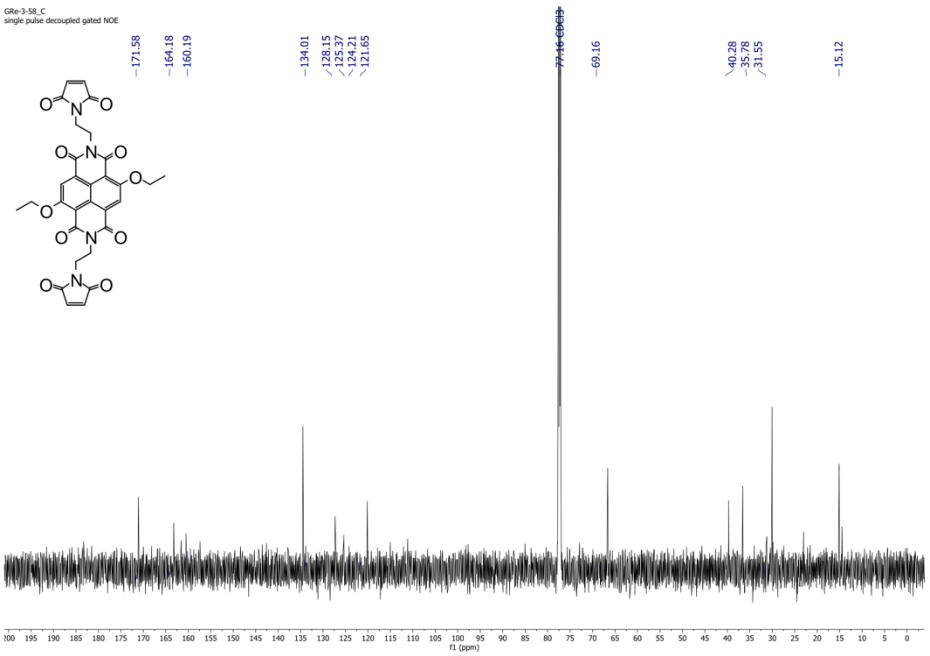

Figure S8. ^{13}C-NMR spectrum of NDI-05 in $CDCl_3$.

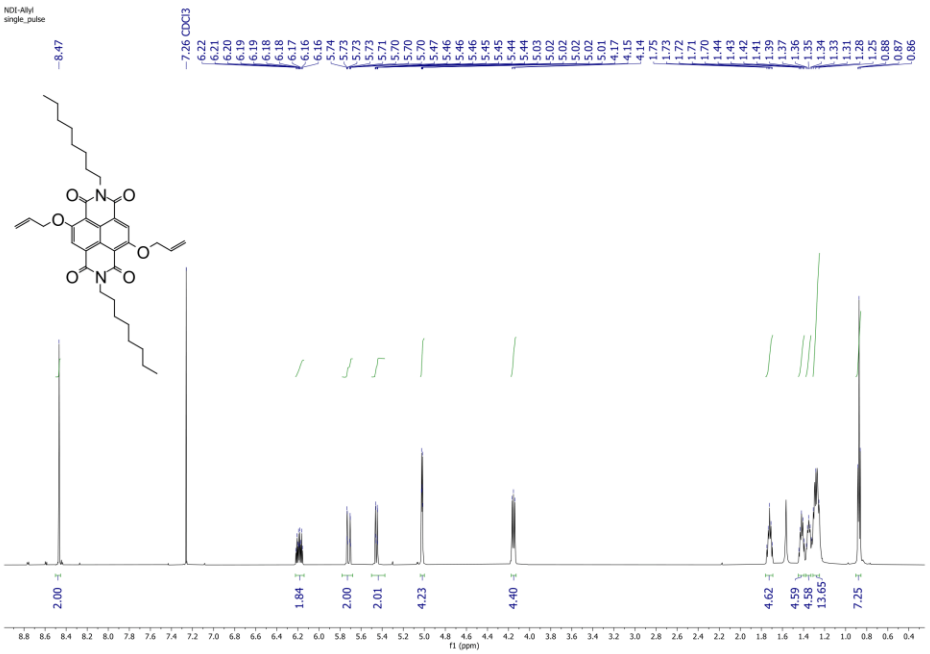

Figure S9. ^{1}H-NMR spectrum of 134 in $CDCl_3$.

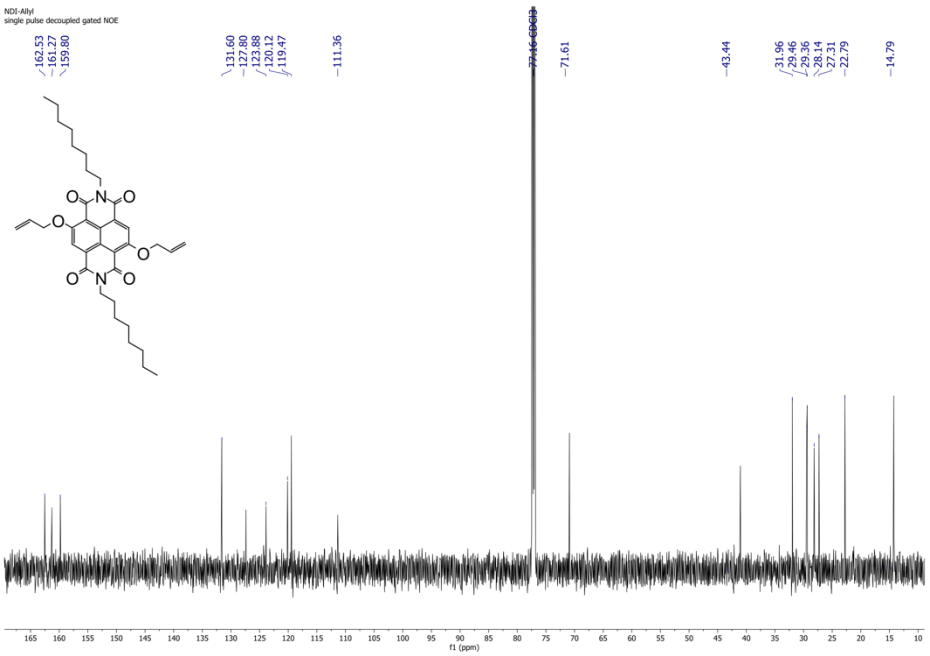

Figure S10. ^{13}C -NMR spectrum of 134 in $CDCl_3$.

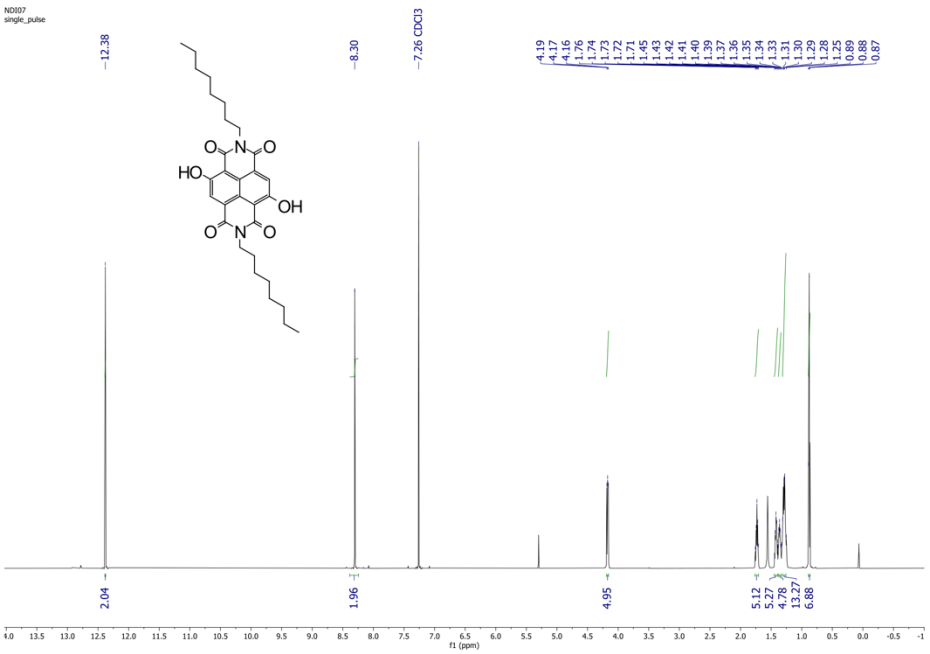

Figure S11. ^{1}H-NMR spectrum of NDI-07 in $CDCl_3$.

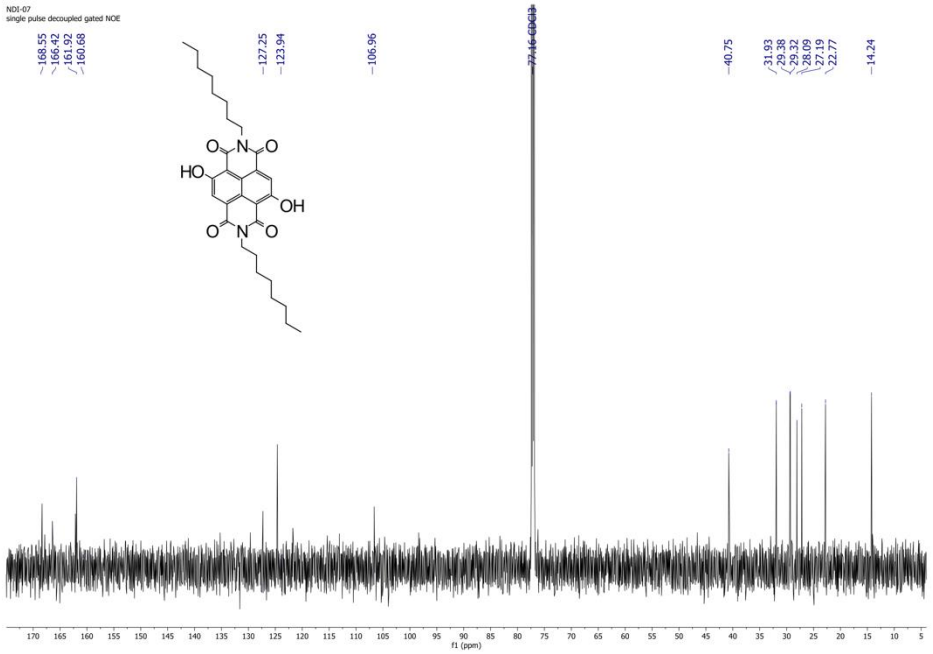

Figure S12. ^{13}C -NMR spectrum of NDI-07 in $CDCl_3$.

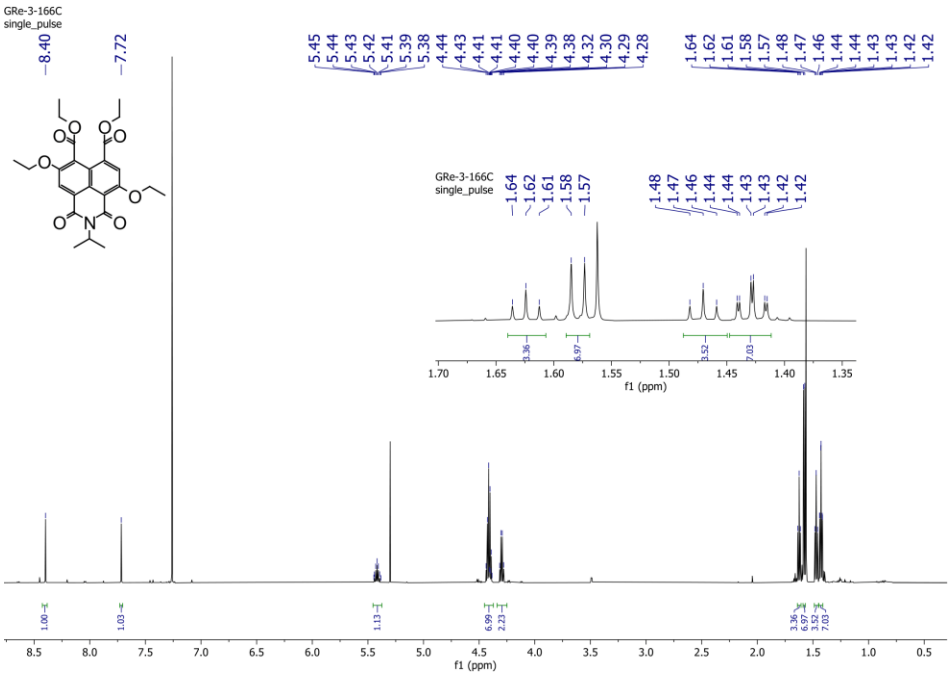

Figure S13. ^{1}H-NMR spectrum of 136 in $CDCl_3$.

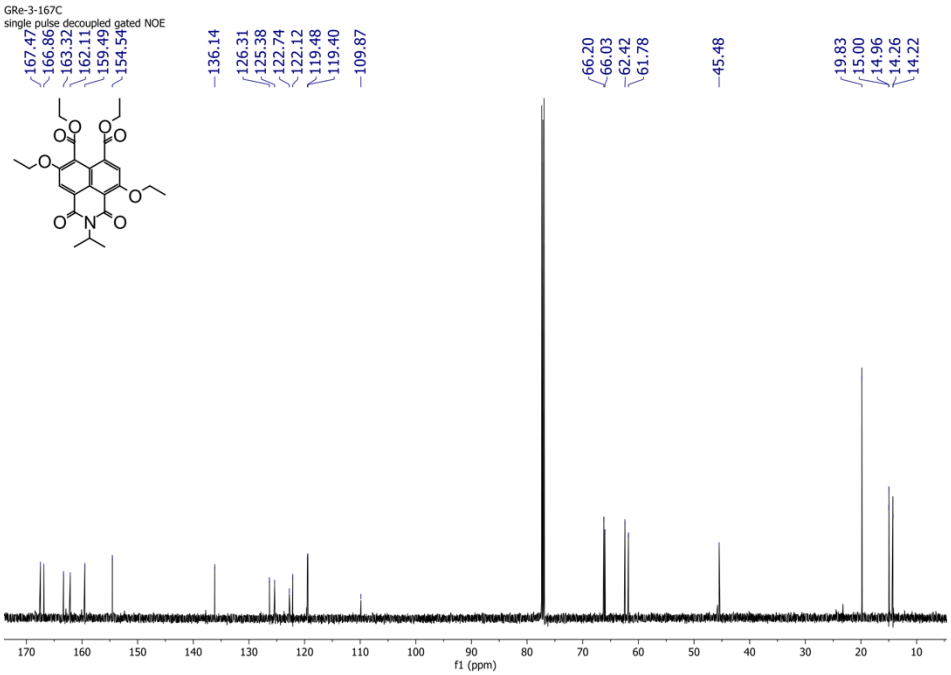

Figure S14. ^{13}C -NMR spectrum of 136 in $CDCl_3$.

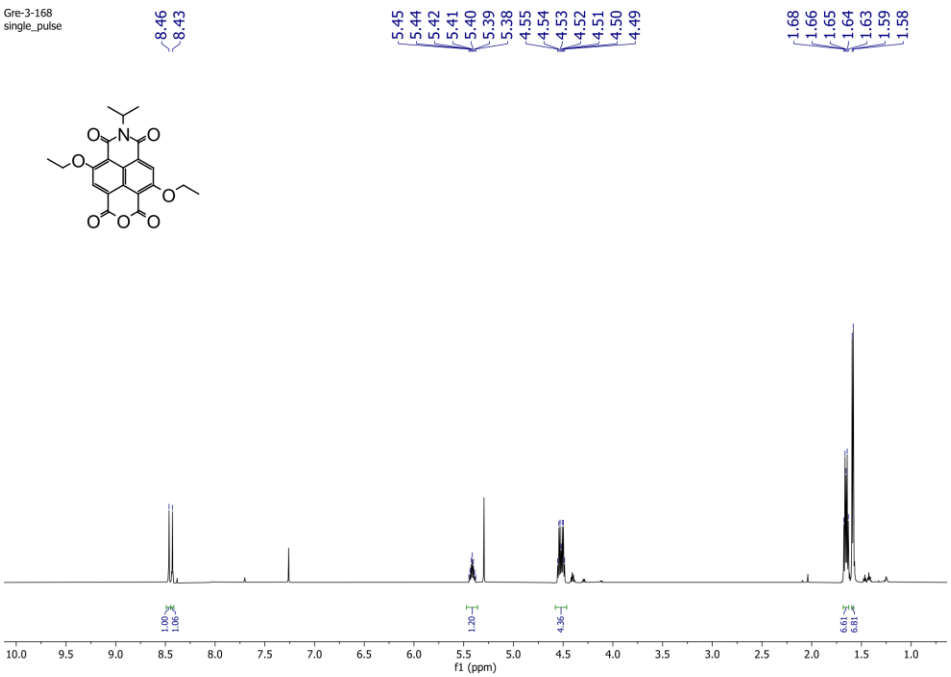

Figure S15. ^{1}H-NMR spectrum of 137 in $CDCl_3$.

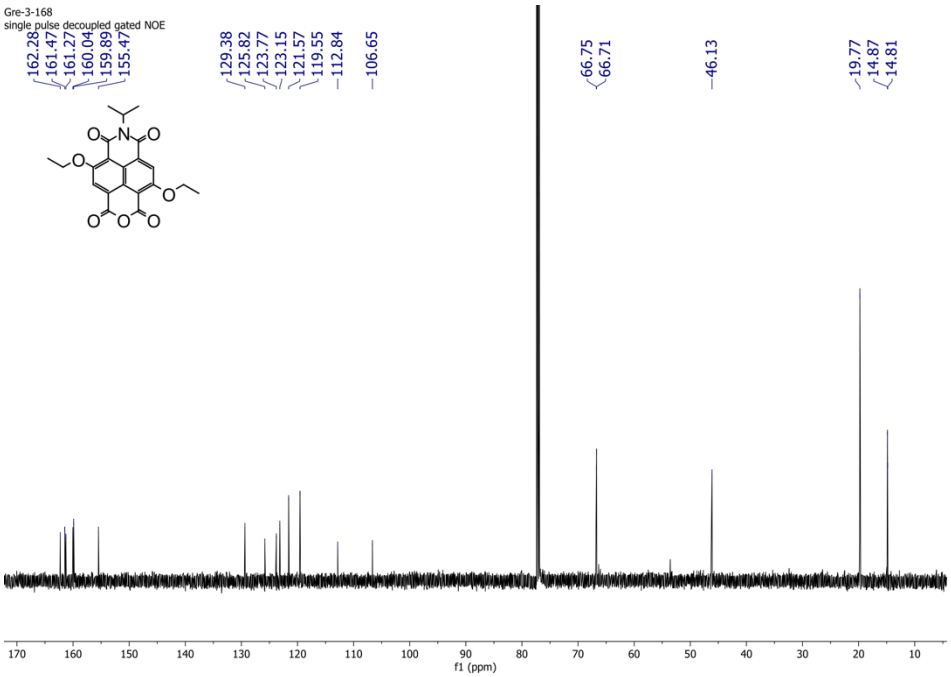

Figure S16. ^{13}C -NMR spectrum of 137 in $CDCl_3$.

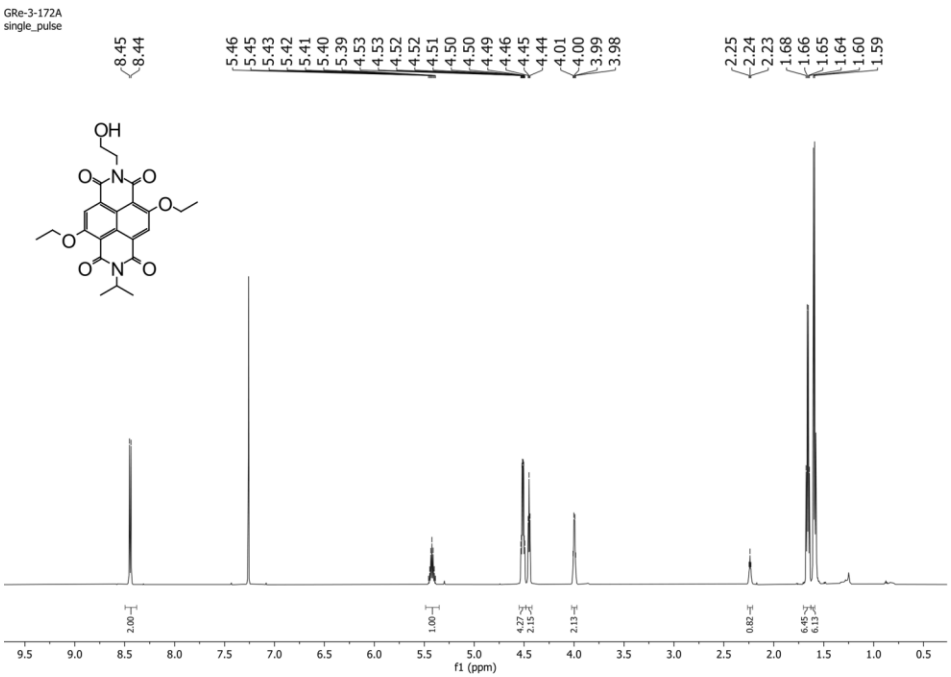

Figure S17. ^{1}H-NMR spectrum of 139 in $CDCl_3$.

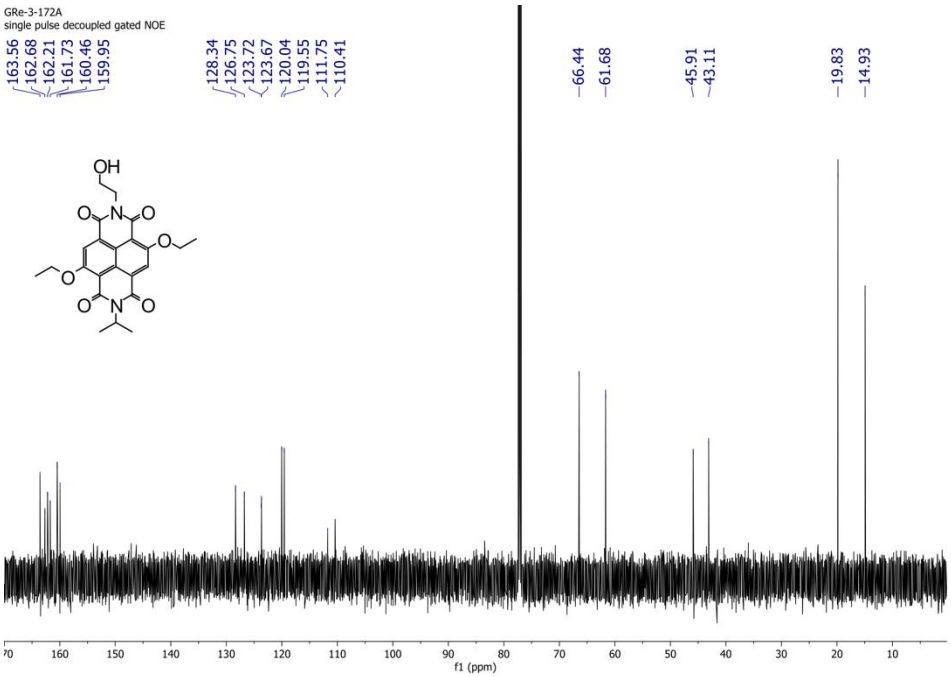

Figure S18. ^{13}C -NMR spectrum of 139 in $CDCl_3$.

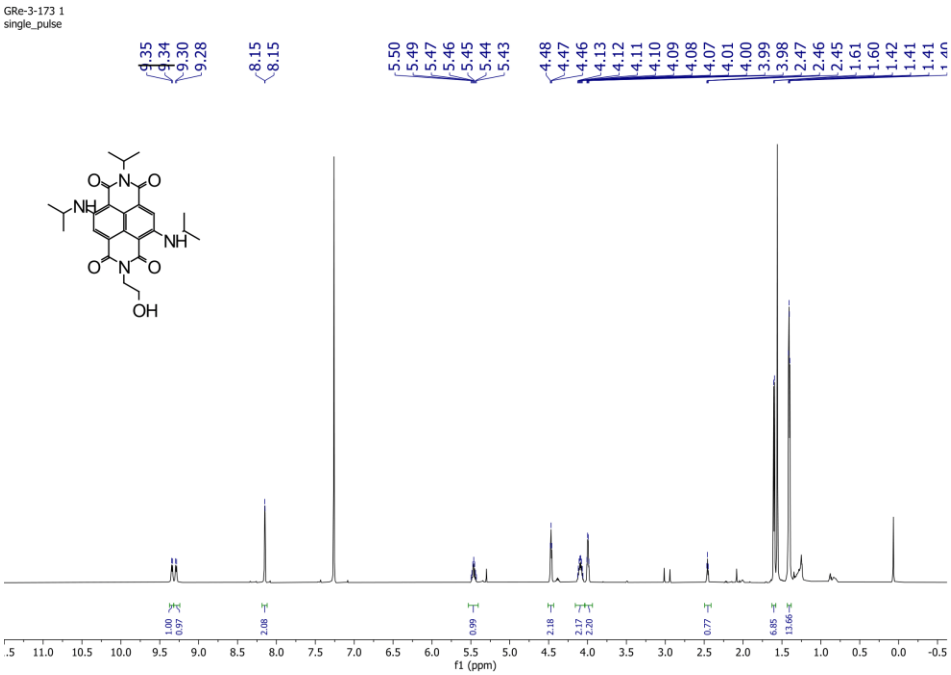

Figure S19. ^{1}H-NMR spectrum of 140 in $CDCl_3$.

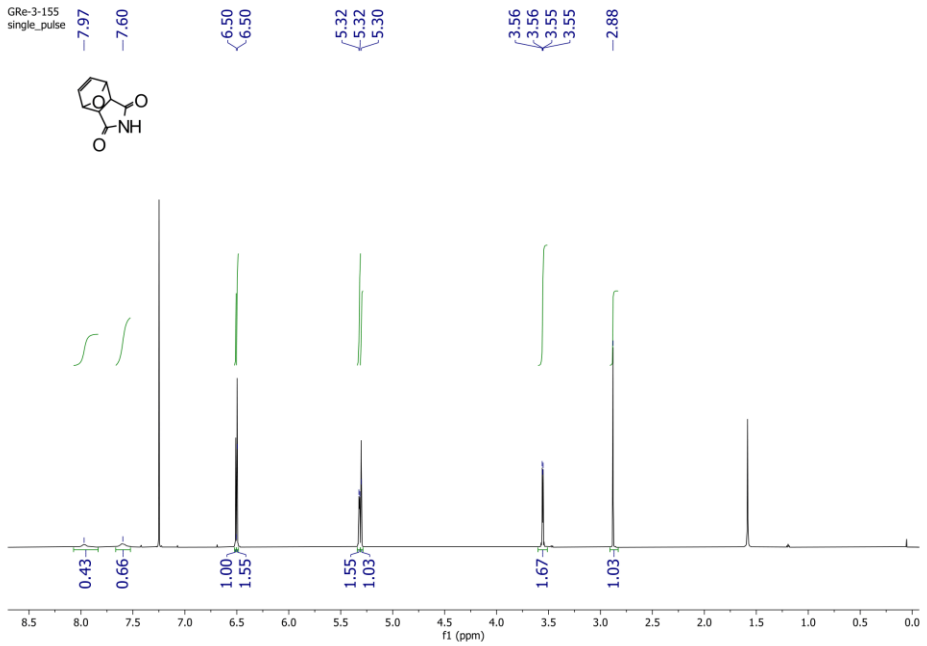

Figure S20. ^{13}C-NMR spectrum of 141 in $CDCl_3$.

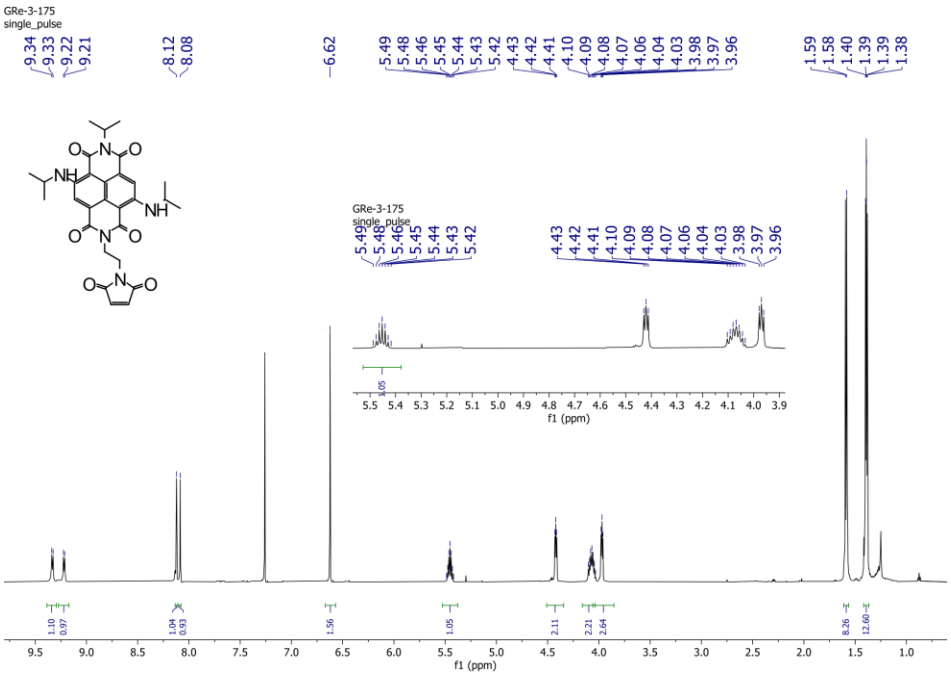

Figure S21. ^{1}H-NMR spectrum of NDI-06 in $CDCl_3$.

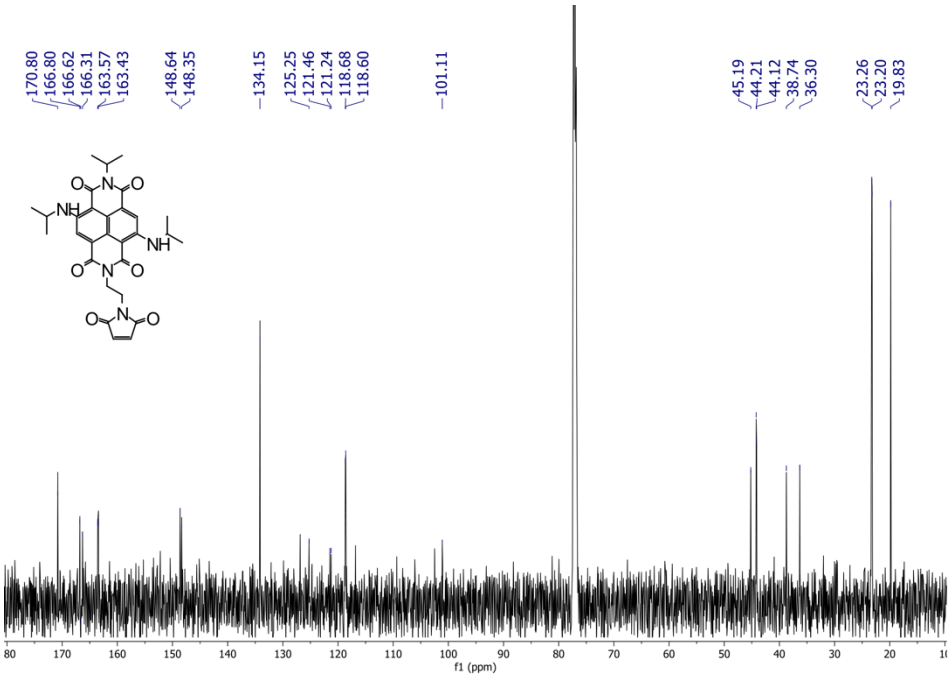

Figure S22. ^{13}C-NMR spectrum of NDI-06 in $CDCl_3$.

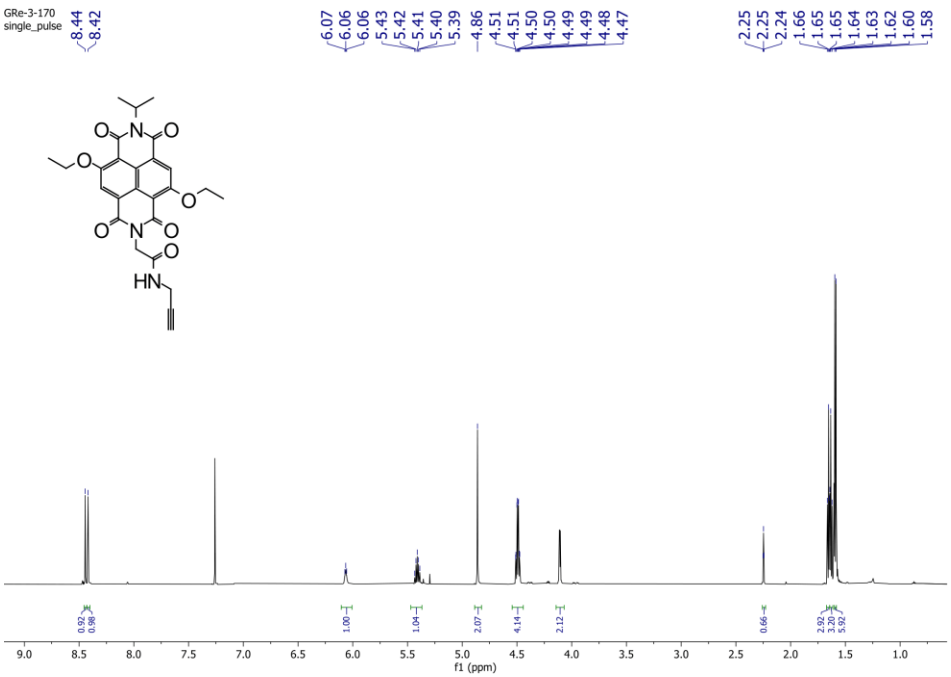

Figure S23. ^{1}H-NMR spectrum of 143 in $CDCl_3$.

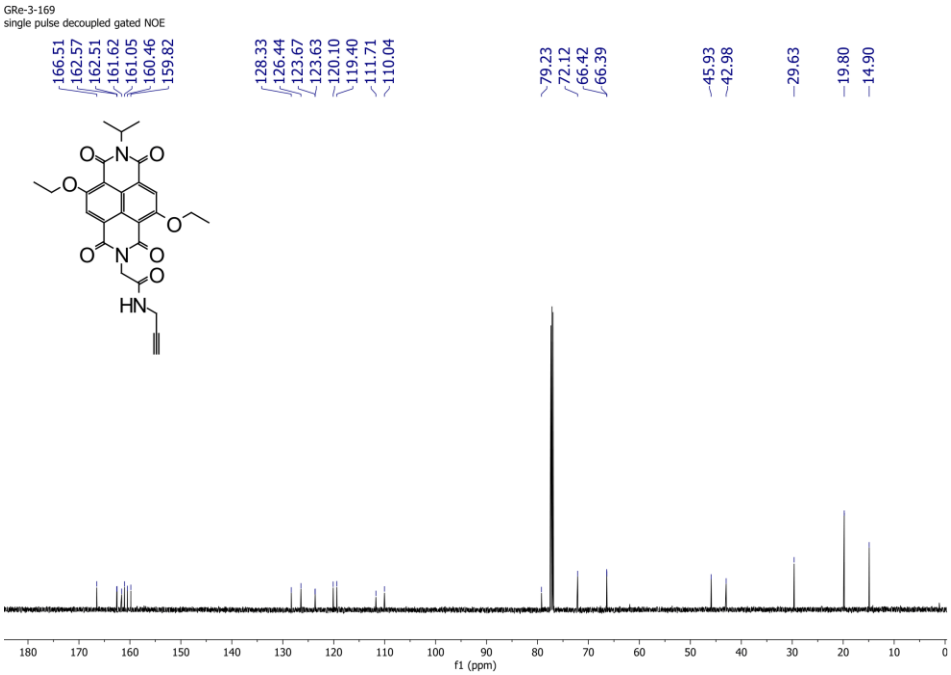

Figure S24. ^{13}C-NMR spectrum of 143 in $CDCl_3$.

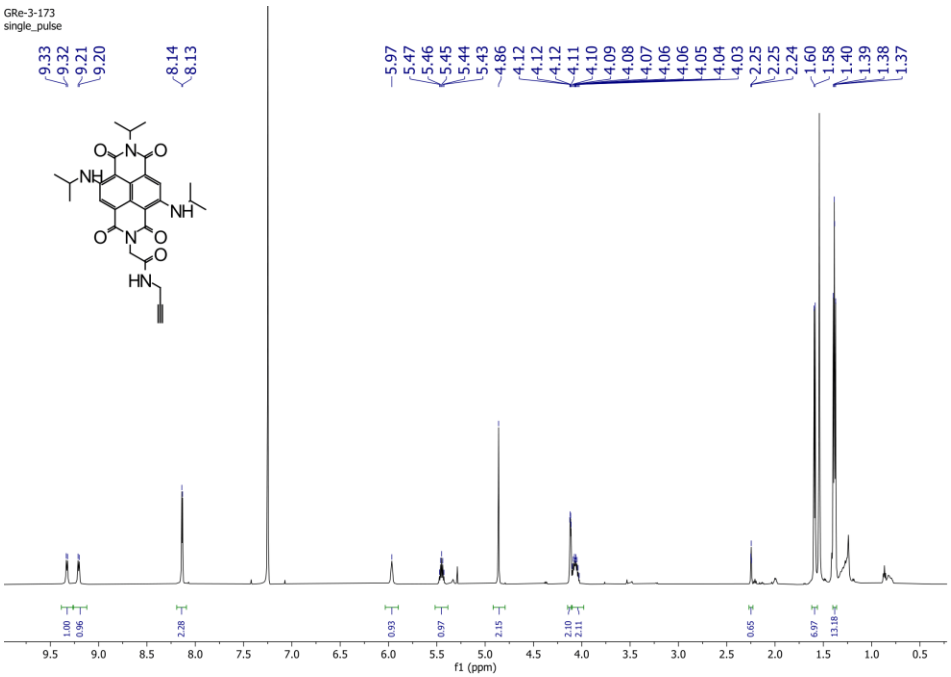

Figure S25. ^{1}H-NMR spectrum of NDI-08 in $CDCl_3$.

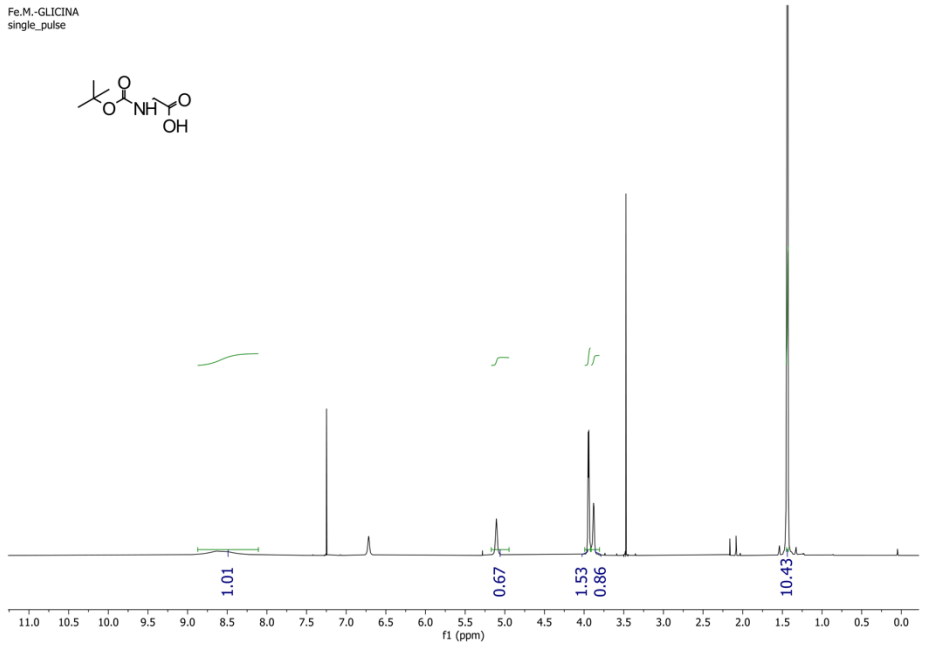

Figure S26. ^{1}H-NMR spectrum of 146 in $CDCl_3$.

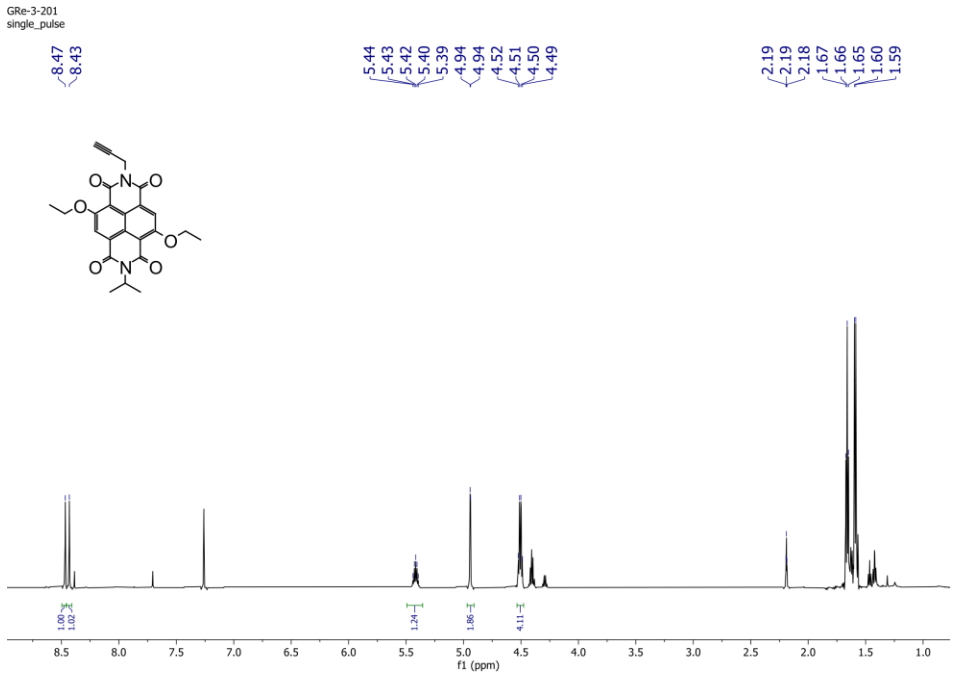

Figure S27. ^{1}H-NMR spectrum of NDI-09 in $CDCl_3$.

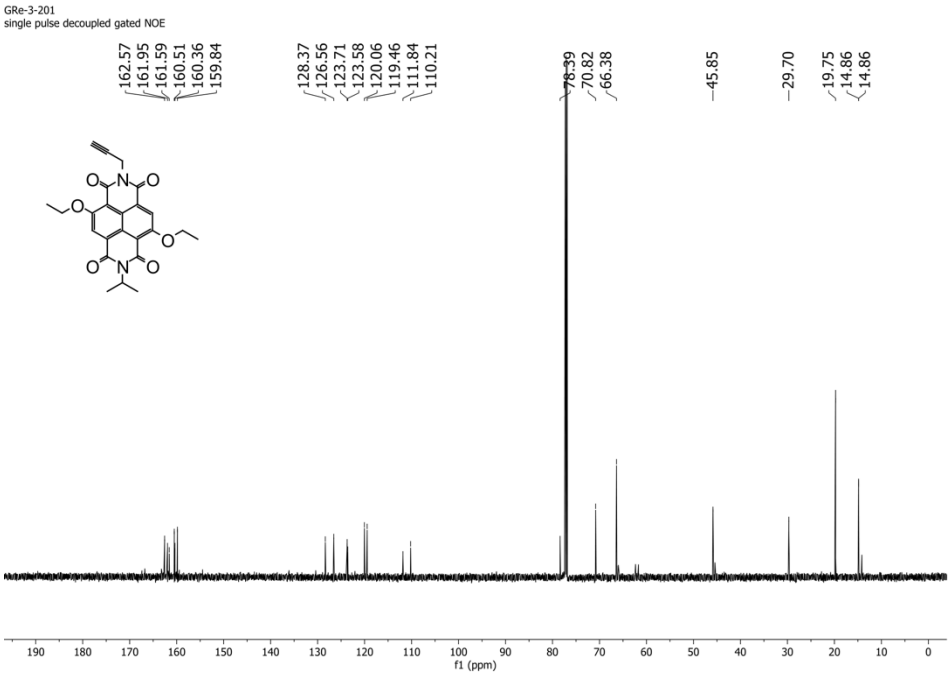

Figure S28. ^{13}C-NMR spectrum of NDI-09 in $CDCl_3$.

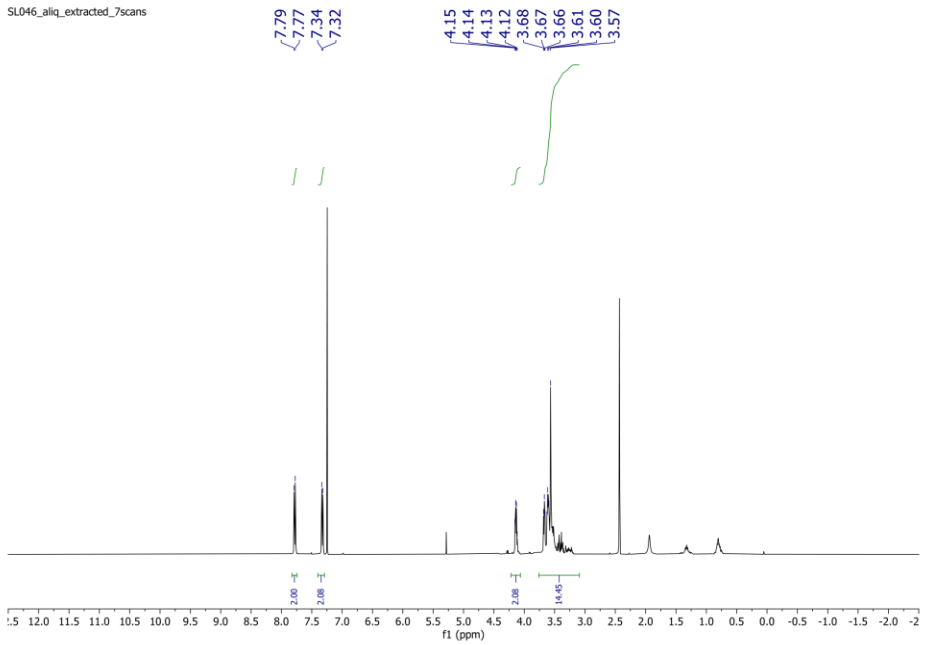

Figure S29. ^{1}H-NMR spectrum of 150 in $CDCl_3$.

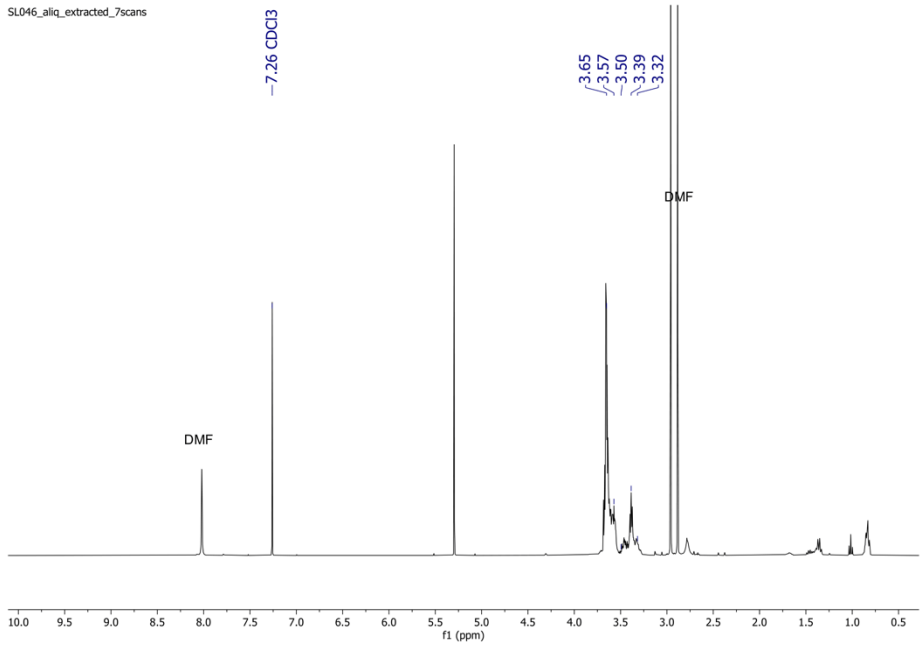

Figure S30. ^{1}H-NMR spectrum of 151 in $CDCl_3$.

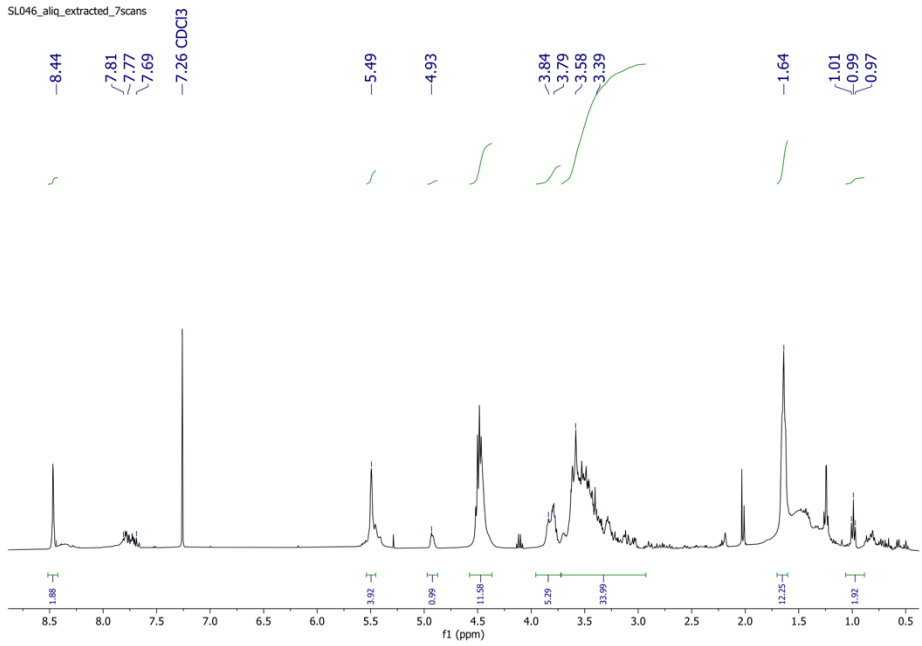

Figure S31. ^{1}H-NMR spectrum of NDI-01@TMPE in $CDCl_3$.

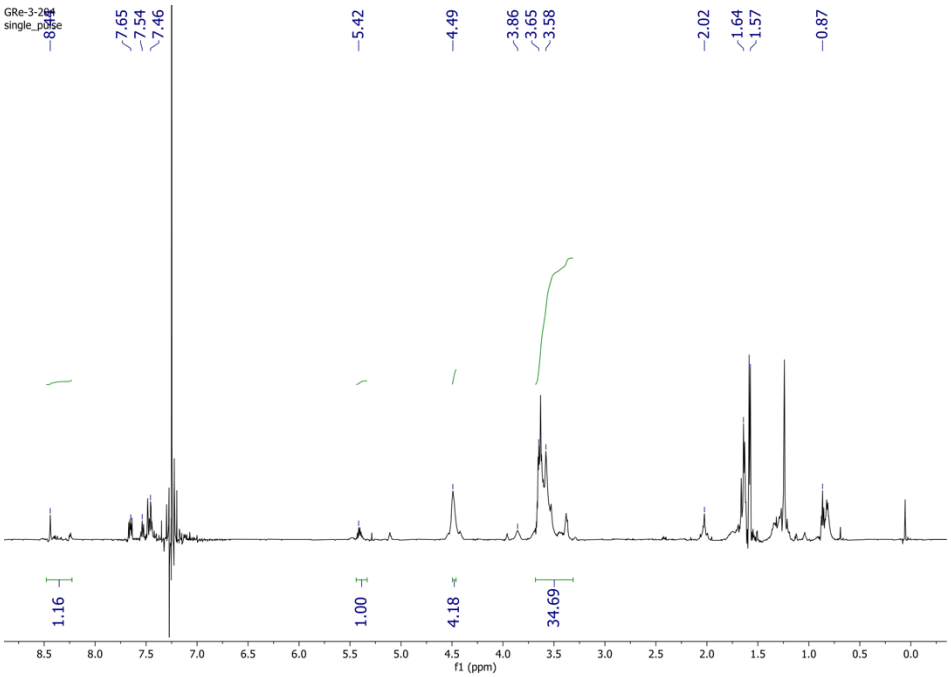

Figure S32. ^{1}H-NMR spectrum of NDI-09@TMPE in $CDCl_3$.

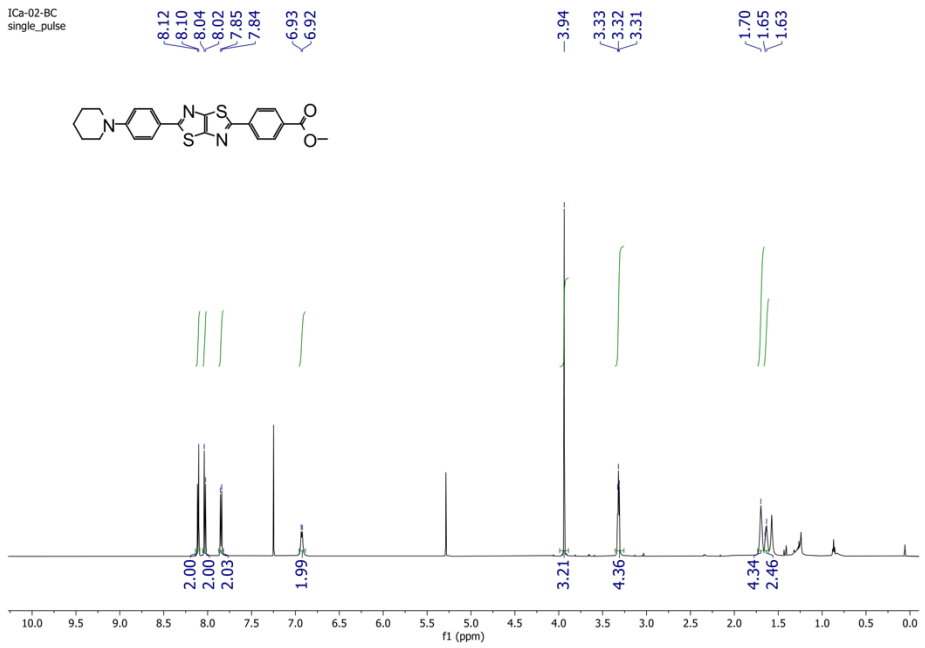

Figure S33. ^{1}H-NMR spectrum of 155 in $CDCl_3$.

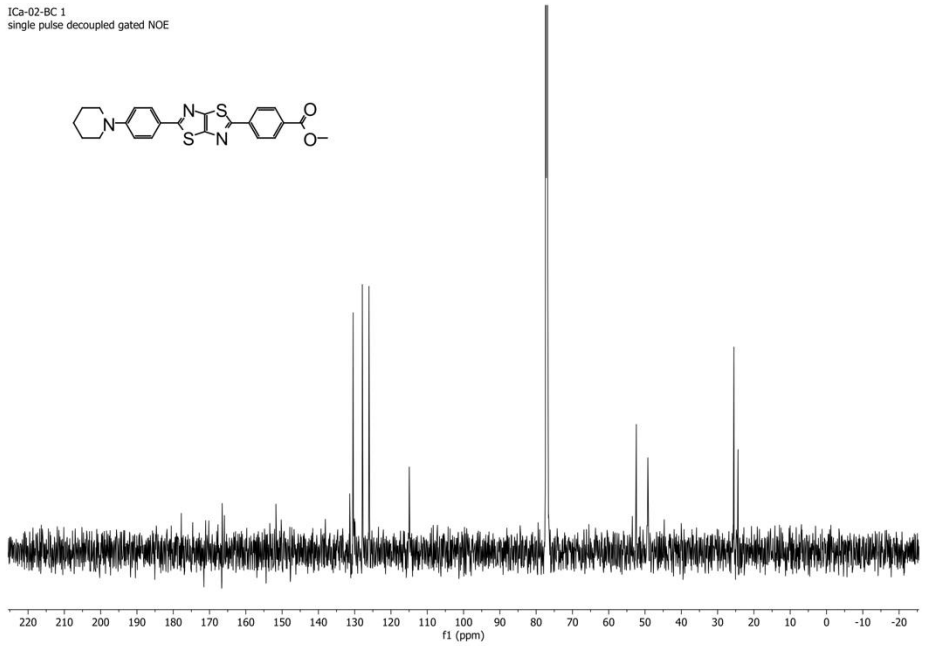

Figure S34. ^{13}C-NMR spectrum of 155 in $CDCl_3$.

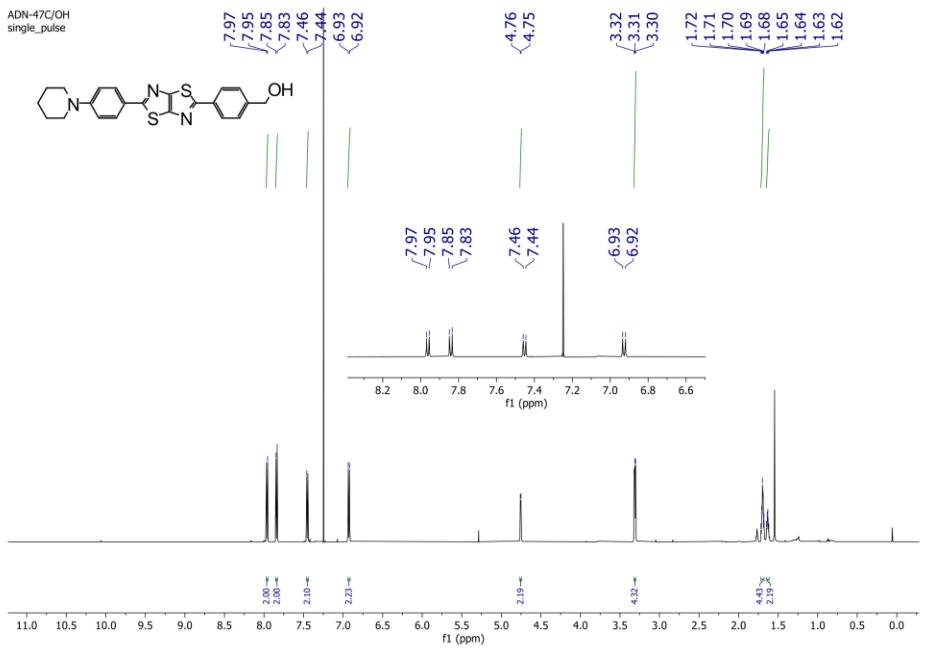

Figure S35. ^{1}H-NMR spectrum of 156 in $CDCl_3$.

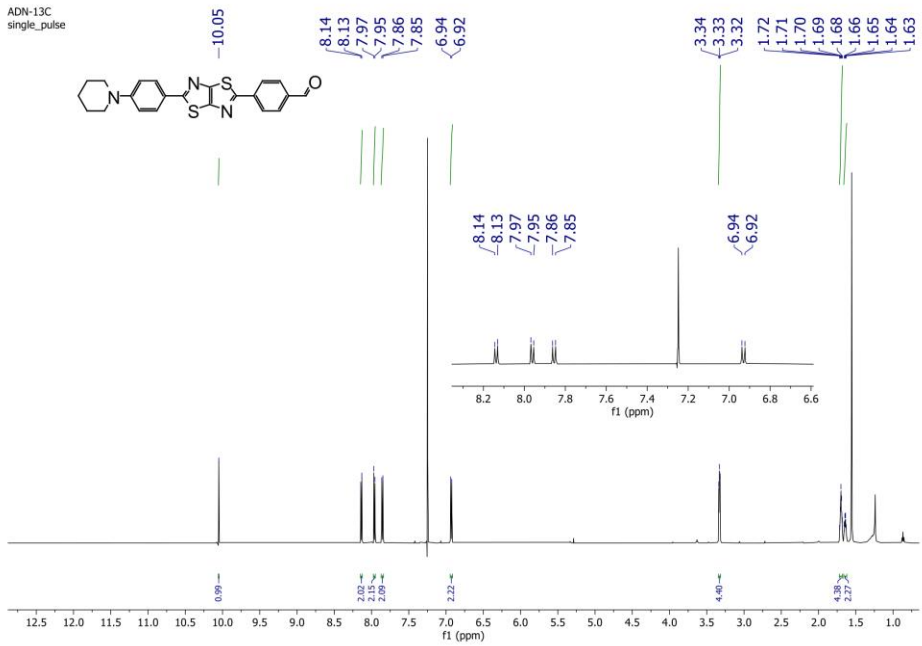

Figure S36. ^{1}H-NMR spectrum of 157 in $CDCl_3$.

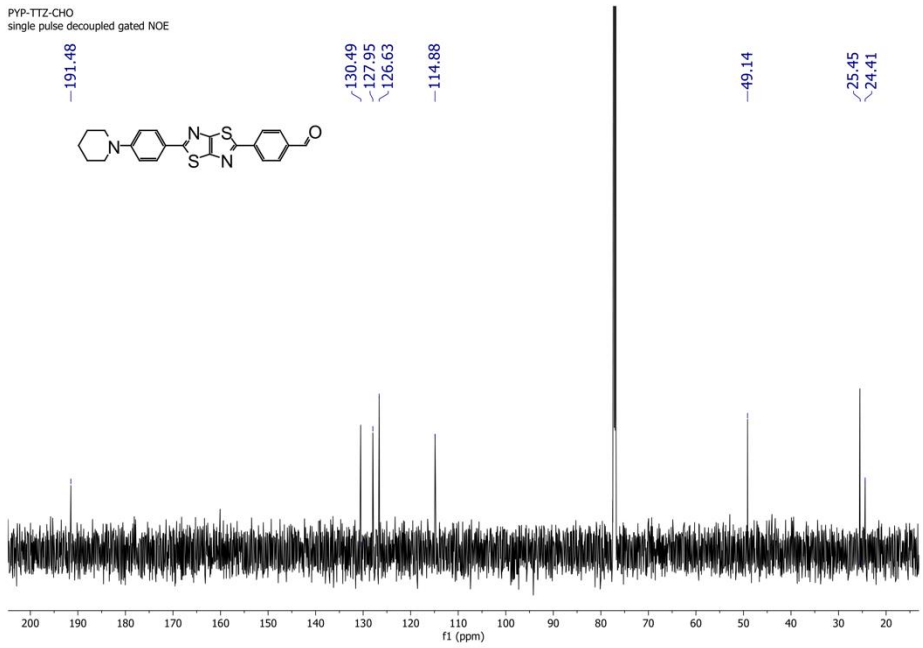

Figure S37. ^{13}C-NMR spectrum of 157 in $CDCl_3$.

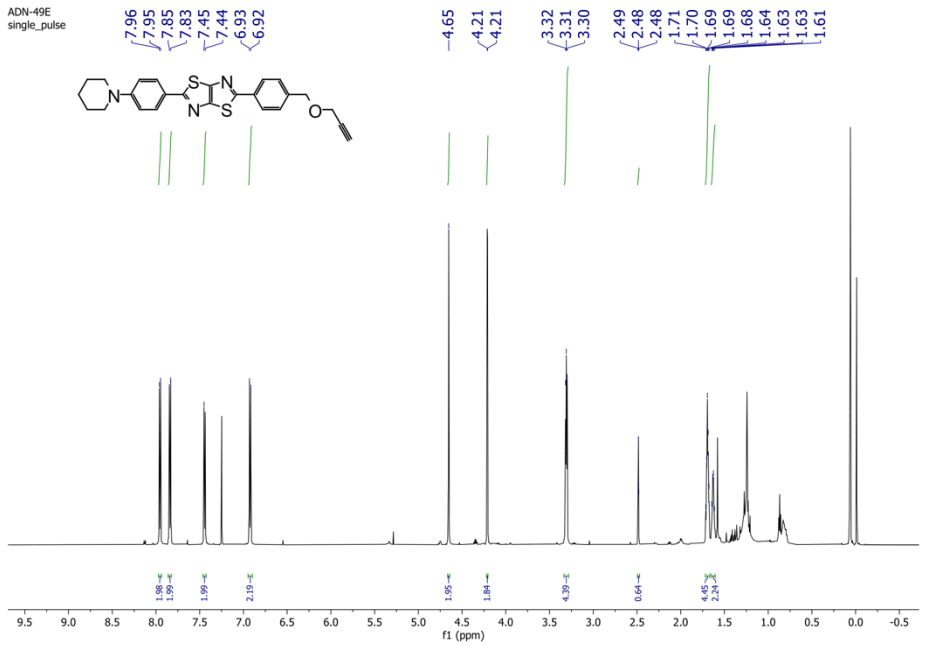

Figure S38. ^{1}H-NMR spectrum of TTZ-02 in $CDCl_3$.

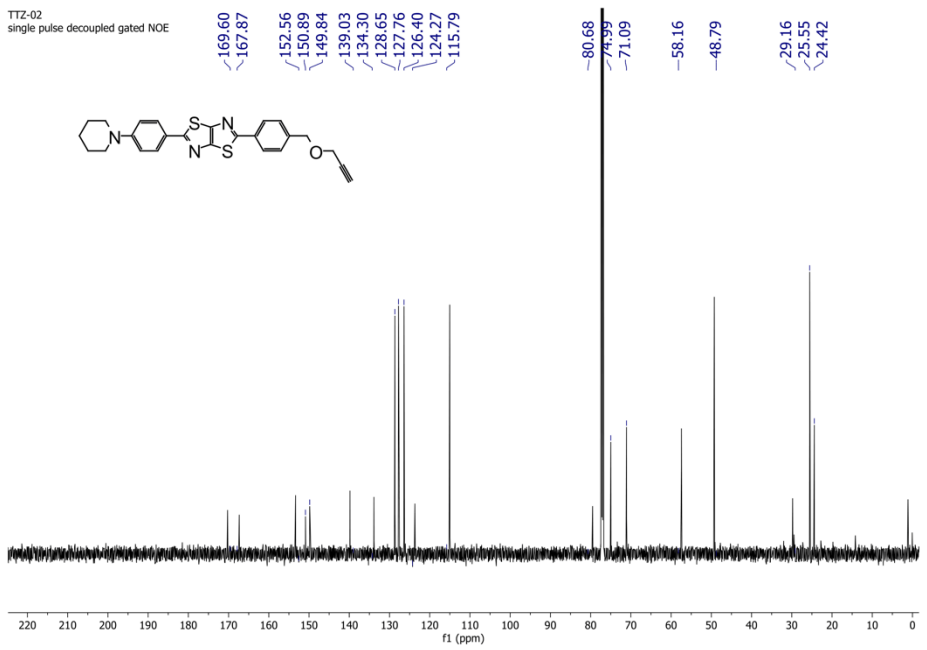

Figure S39. ^{13}C-NMR spectrum of TTZ-02 in $CDCl_3$.

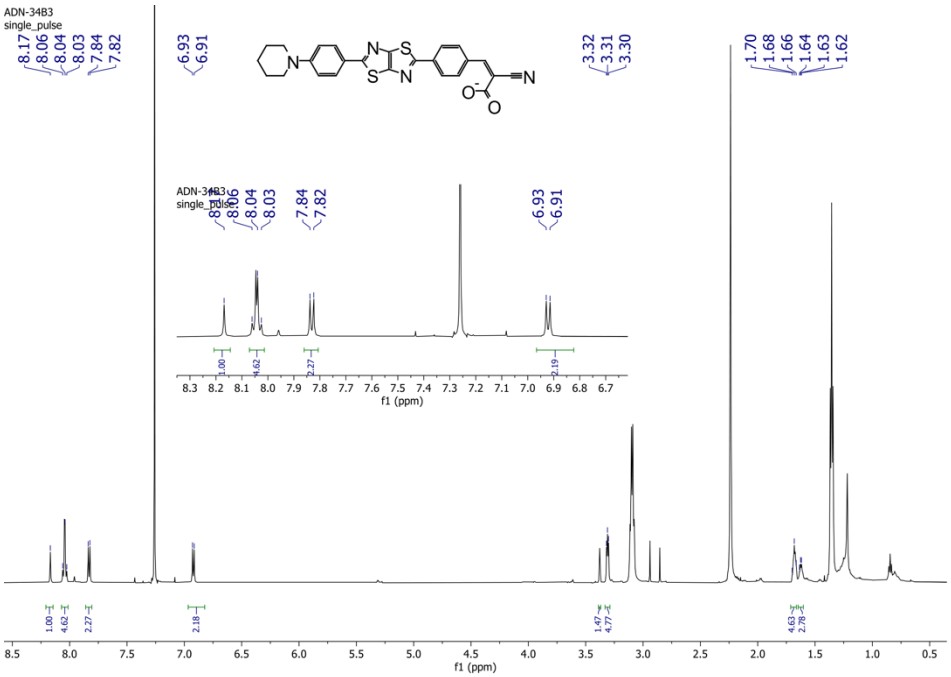

Figure S40. ^{1}H-NMR spectrum of 158 in $CDCl_3$.

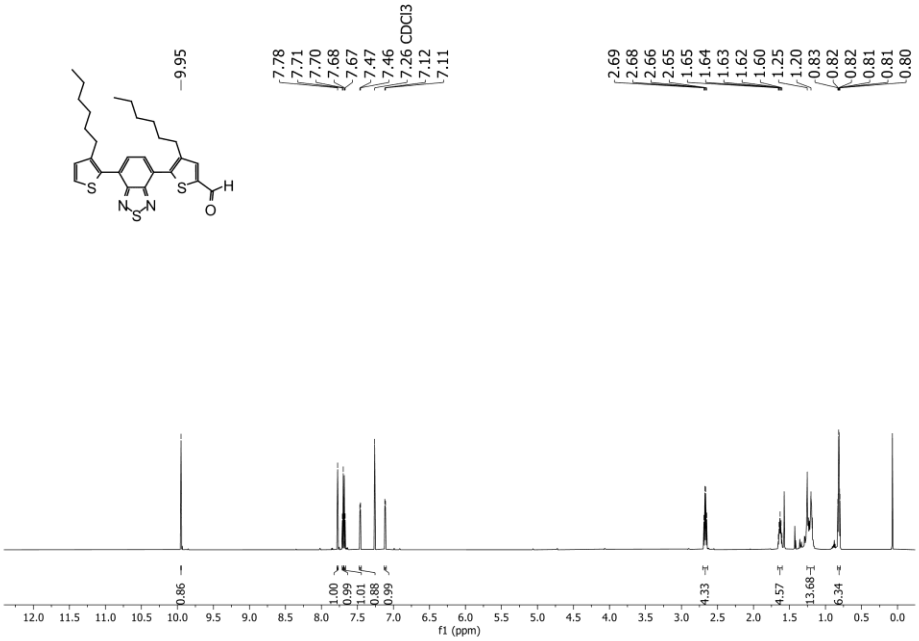

Figure S41. ^{1}H-NMR spectrum of 162 in $CDCl_3$.

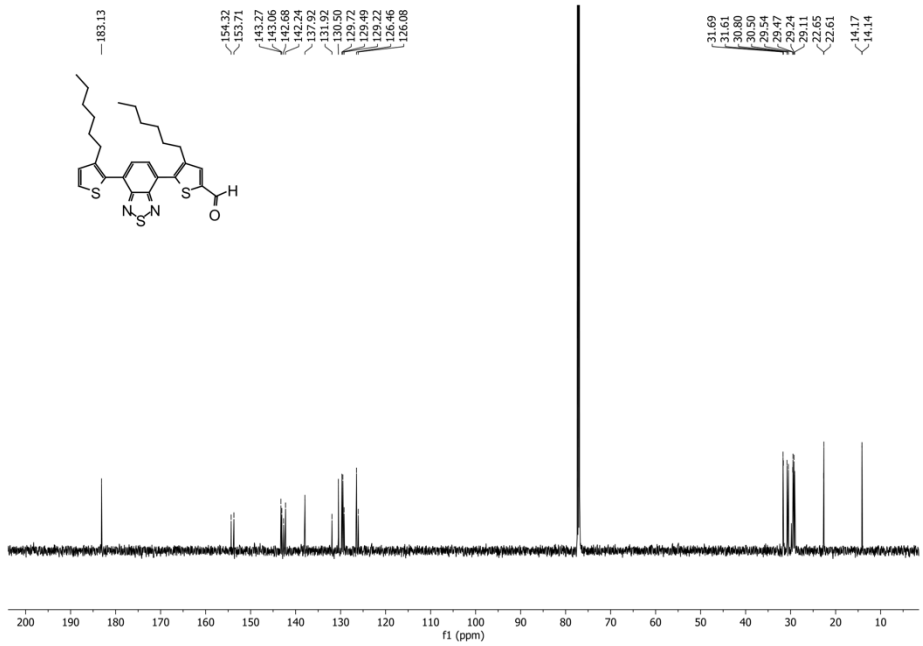

Figure S42. ^{13}C-NMR spectrum of 162 in $CDCl_3$.

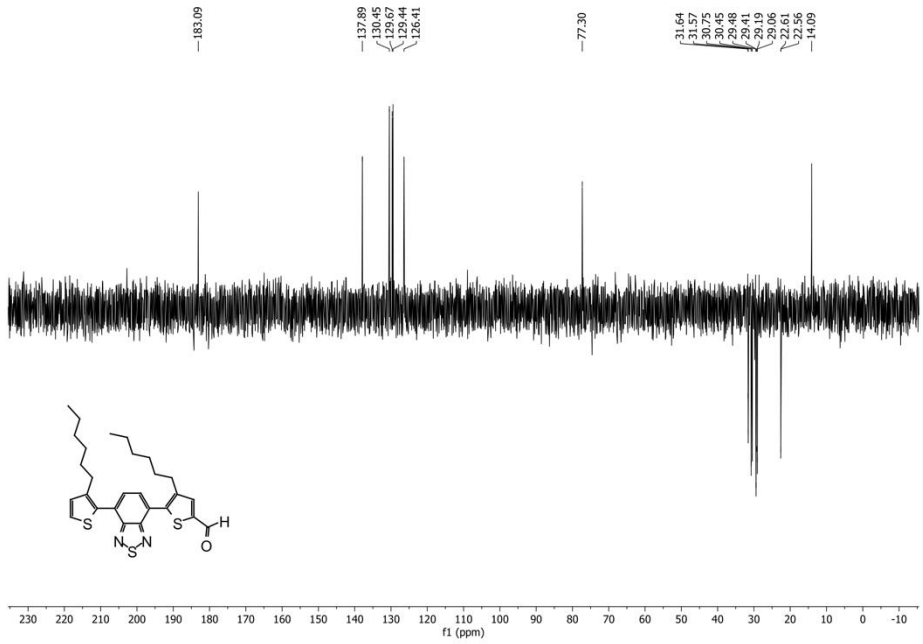

Figure S43. DEPT-135 spectrum of 162 in $CDCl_3$.

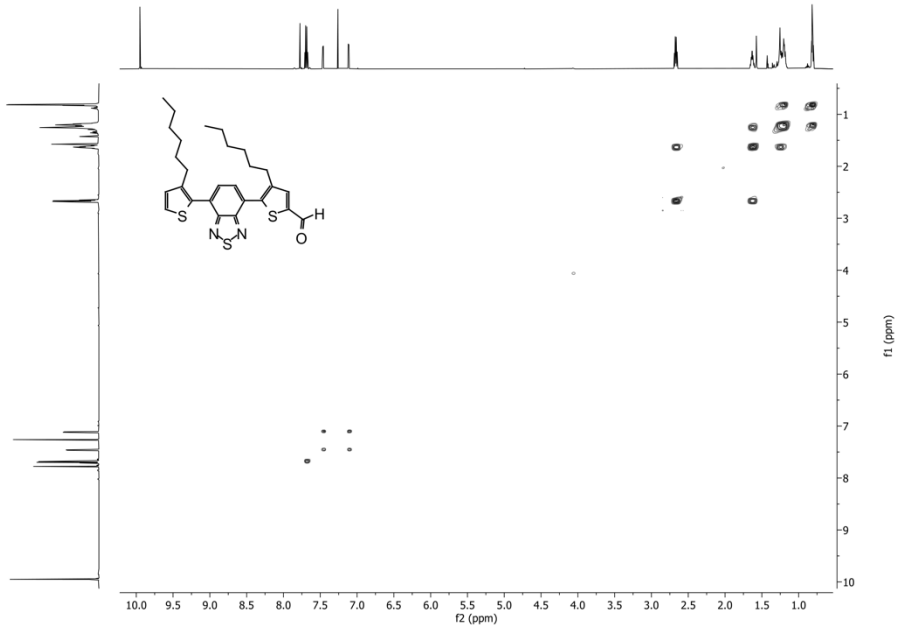

Figure S44. H-H COSY-NMR spectrum of 162 in $CDCl_3$.

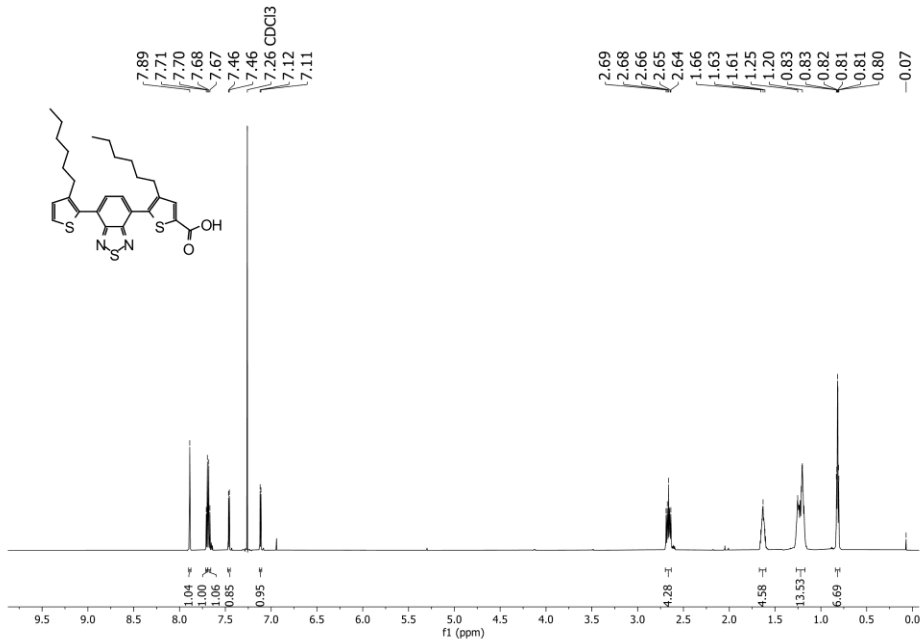

Figure S45. ^{1}H-NMR spectrum of 163 in $CDCl_3$.

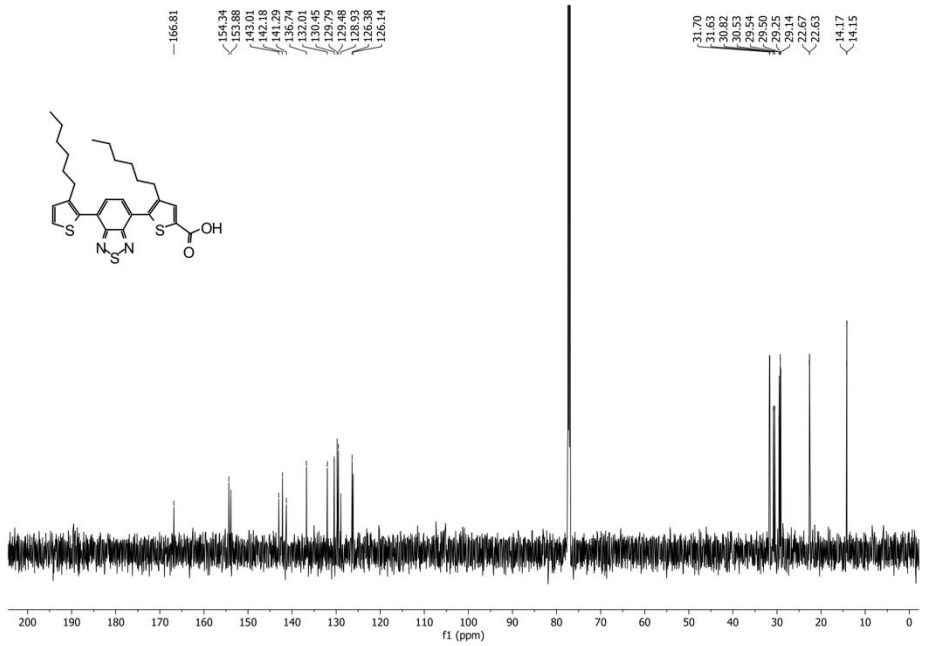

Figure S46. ^{13}C-NMR spectrum of 163 in $CDCl_3$.

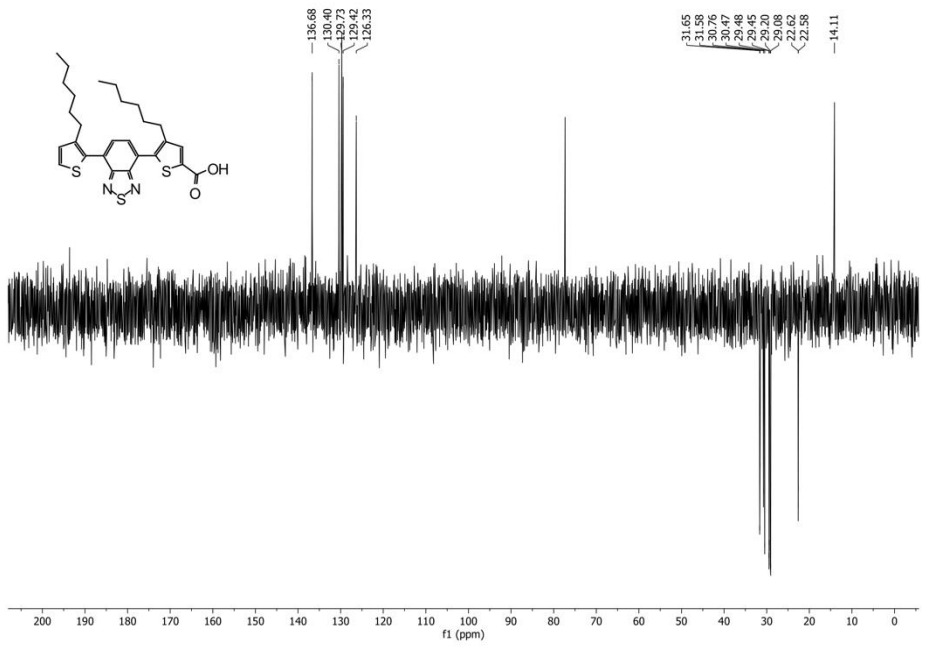

Figure S47. DEPT-135 NMR spectrum of 163 in $CDCl_3$.

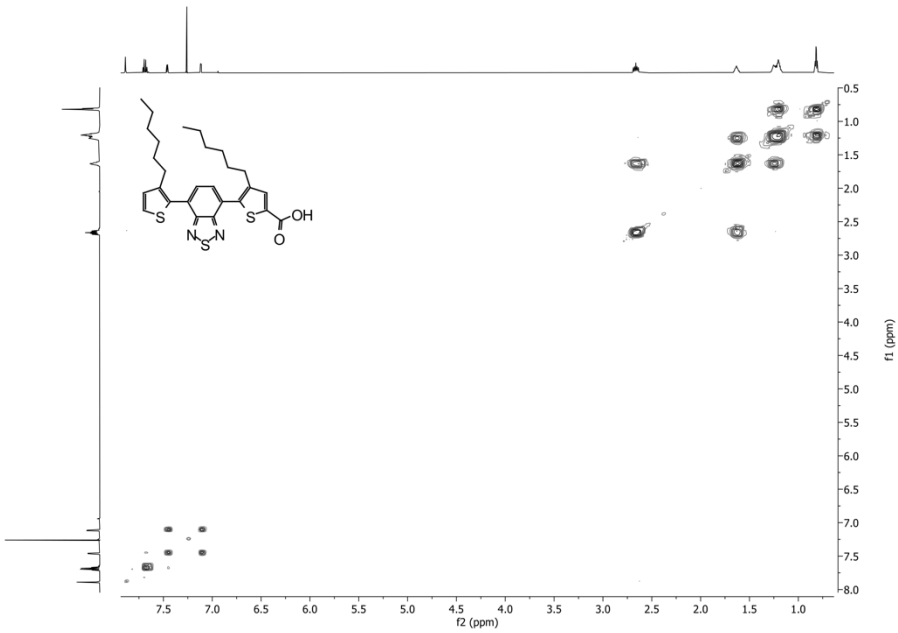

Figure S48. H,H COSY-NMR spectrum of 163 in $CDCl_3$.

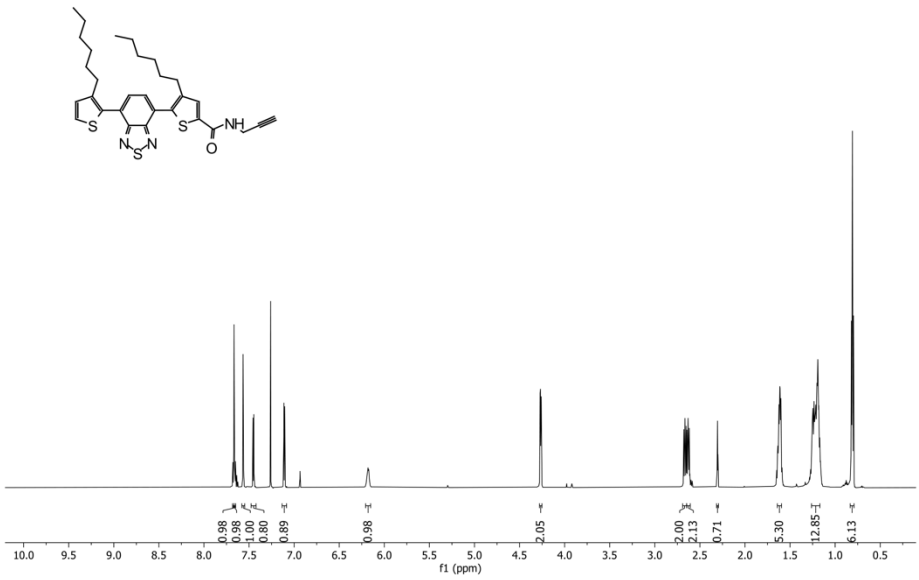

Figure S49. ^{1}H-NMR spectrum of BTD-I-04 in $CDCl_3$.

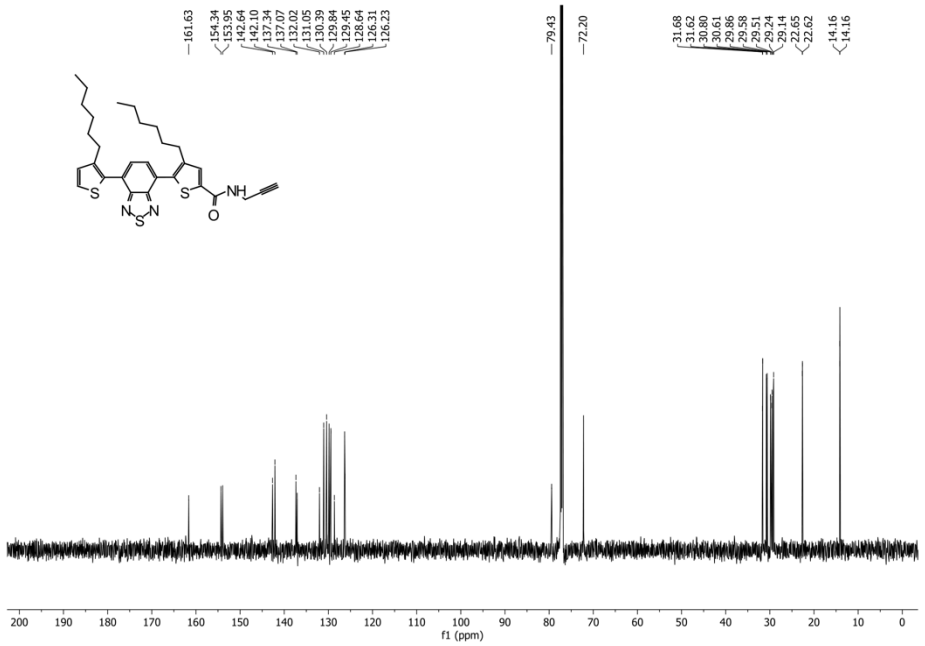

Figure S50. ^{13}C-NMR spectrum of BTD-I-04 in $CDCl_3$.

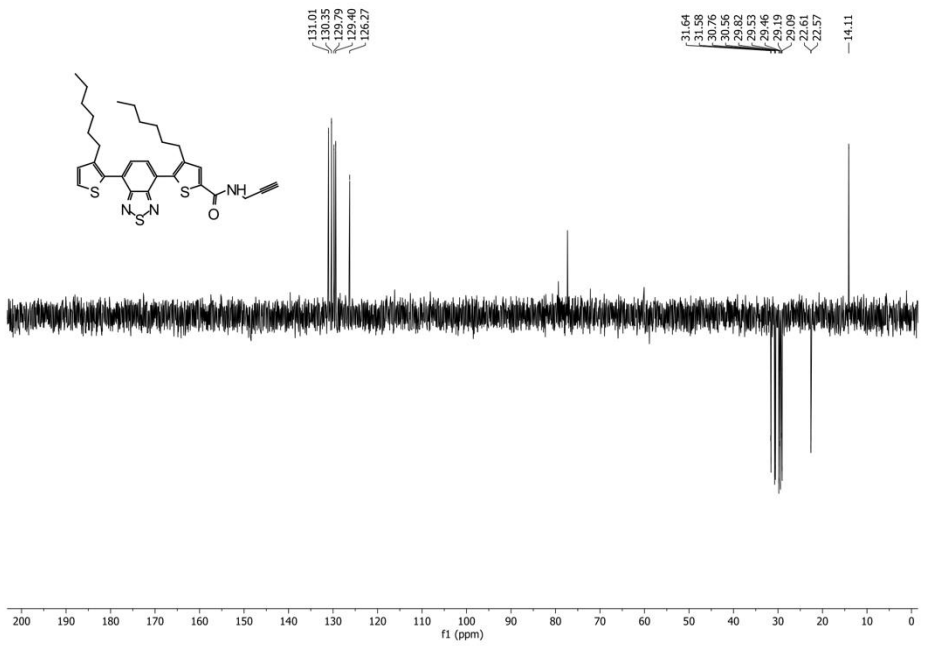

Figure S51. DEPT 135-NMR spectrum of BTD-I-04 in $CDCl_3$.

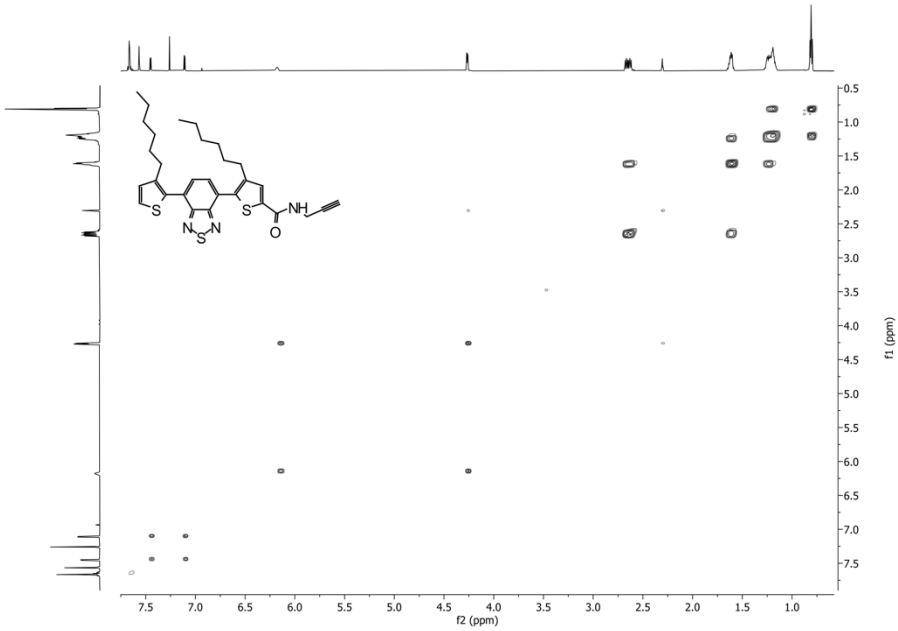

Figure S52. H,H COSY-NMR spectrum of BTD-I-04 in $CDCl_3$.

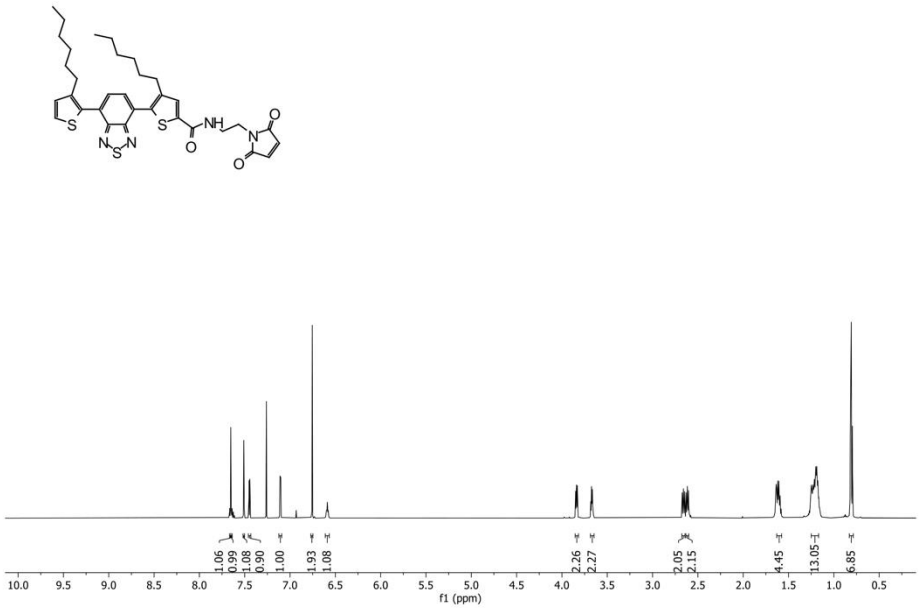

Figure S53. ^{1}H-NMR spectrum of BTD-I-05 in $CDCl_3$.

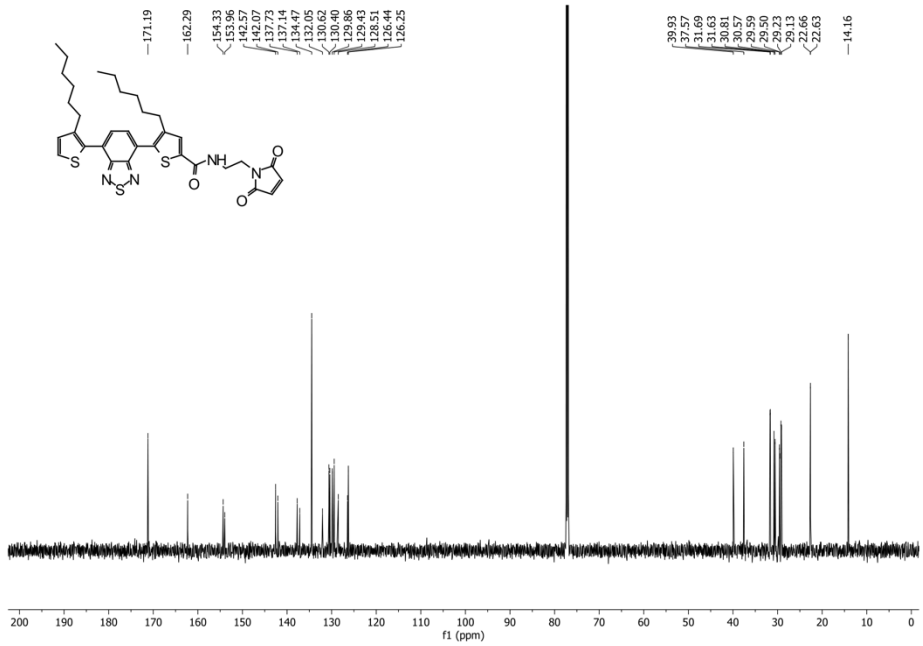

Figure S54. ^{13}C-NMR spectrum of BTD-I-05 in $CDCl_3$.

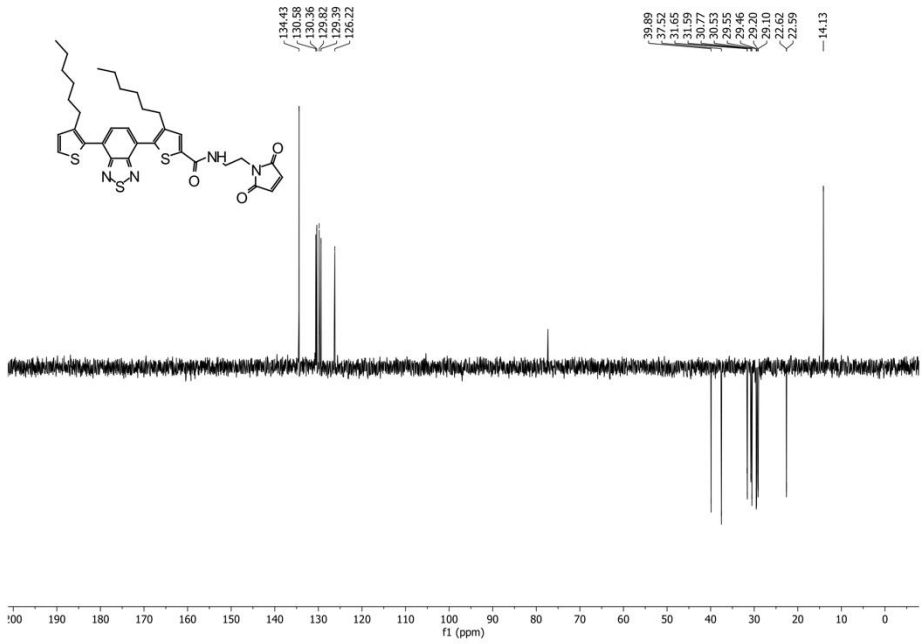

Figure S55. DEPT 135-NMR spectrum of BTD-I-05 in $CDCl_3$.

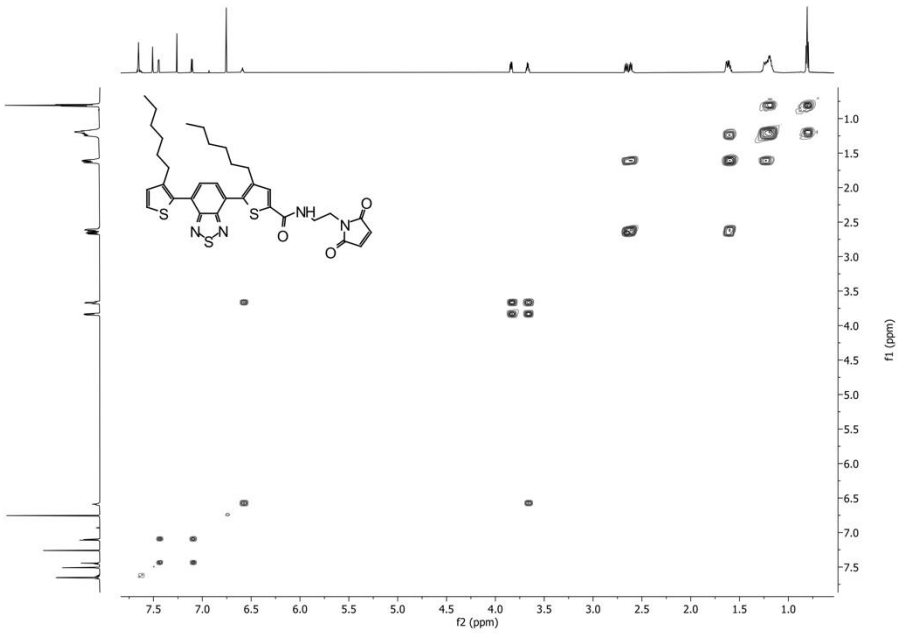

Figure S56. H,H COSY-NMR spectrum of BTD-I-05 in $CDCl_3$.

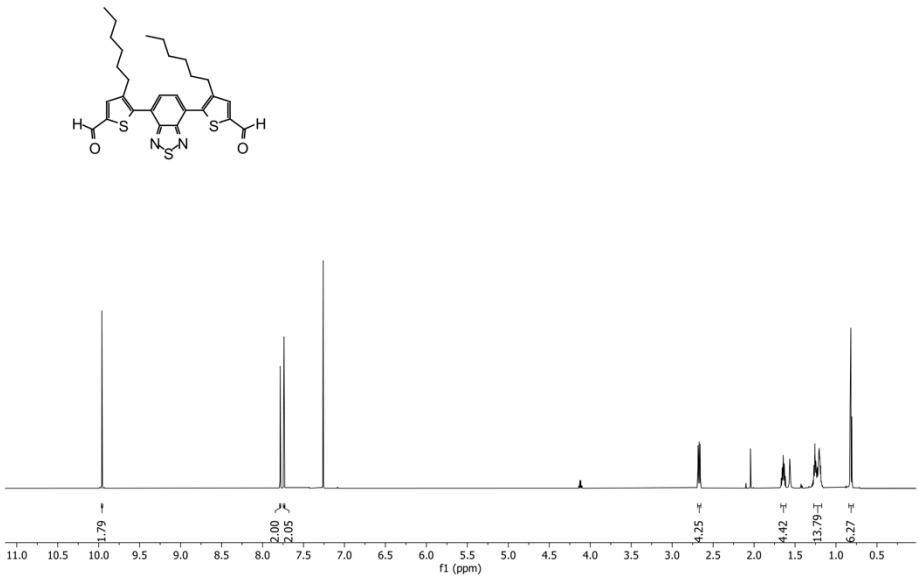

Figure S57. ^{1}H-NMR spectrum of 164 in $CDCl_3$.

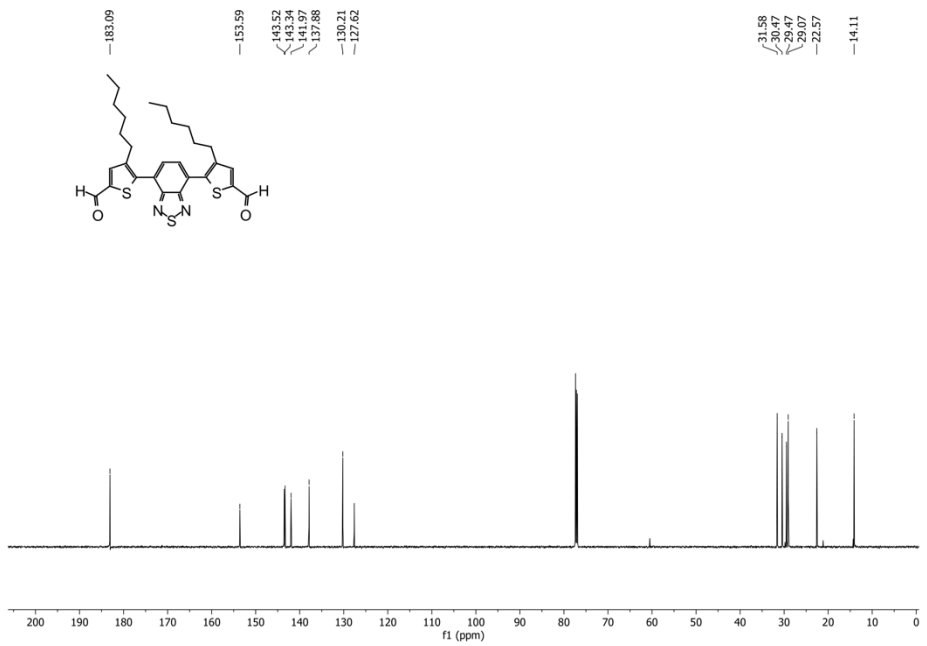

Figure S58. ^{13}C-NMR spectrum of 164 in $CDCl_3$.

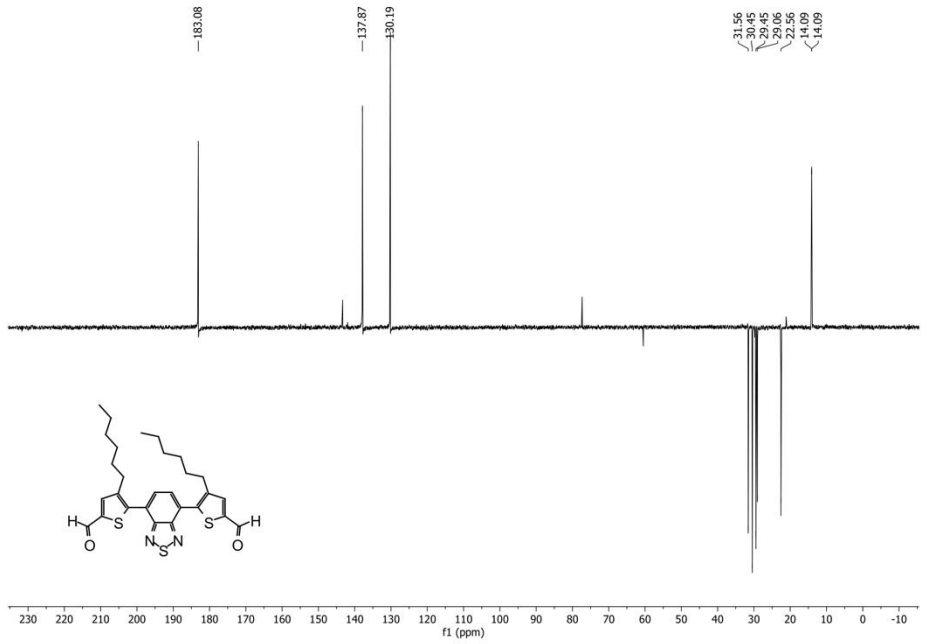

Figure S59. DEPT 135-NMR spectrum of 164 in $CDCl_3$.

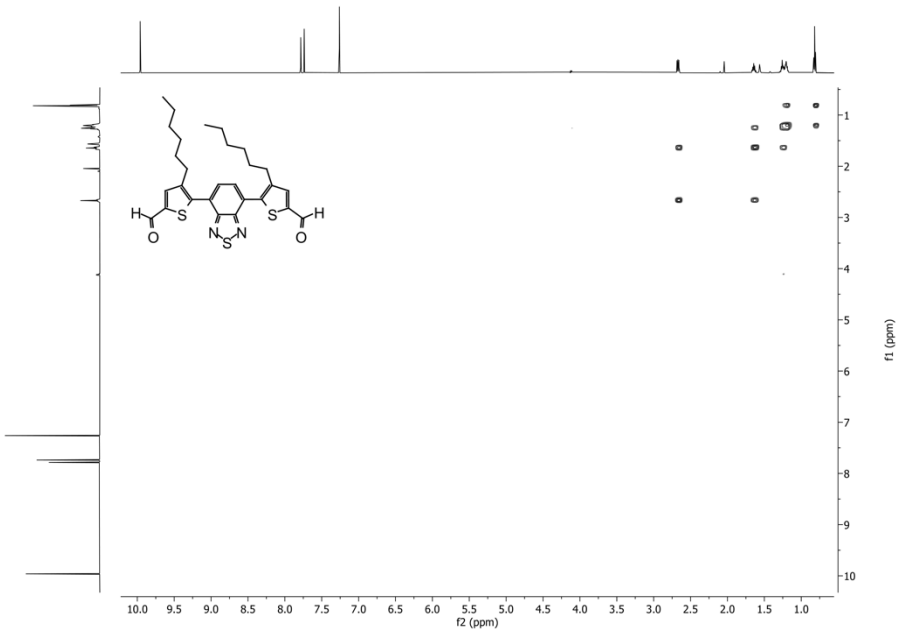

Figure S60. H,H COSY-NMR spectrum of 164 in $CDCl_3$.

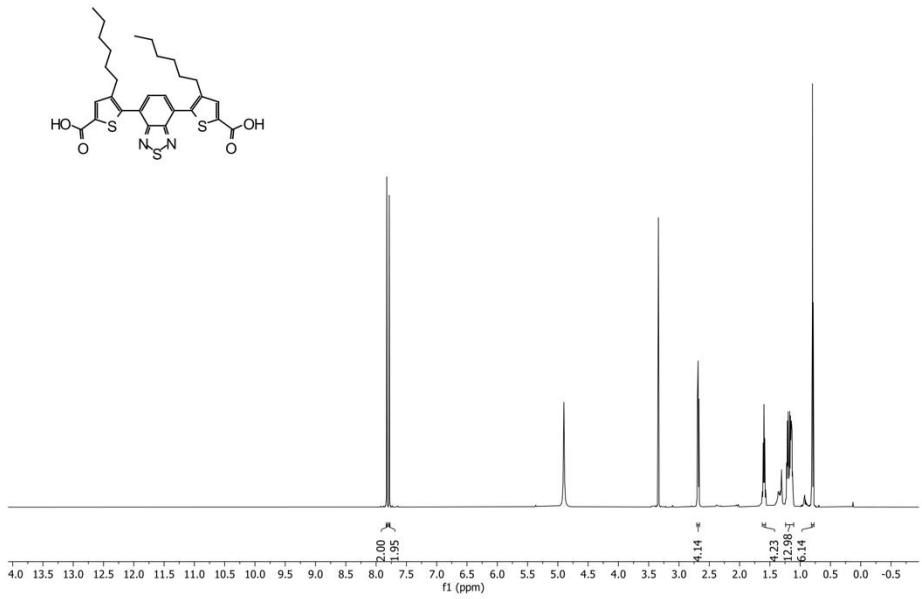

Figure S61. ^{1}H-NMR spectrum of 165 in $CDCl_3$.

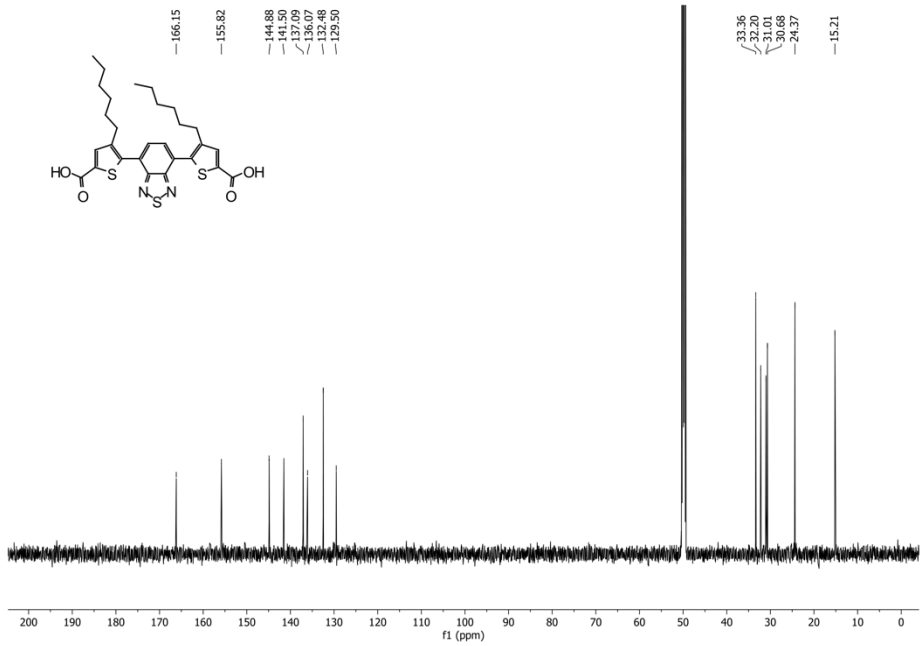

Figure S62. ^{13}C-NMR spectrum of 165 in $CDCl_3$.

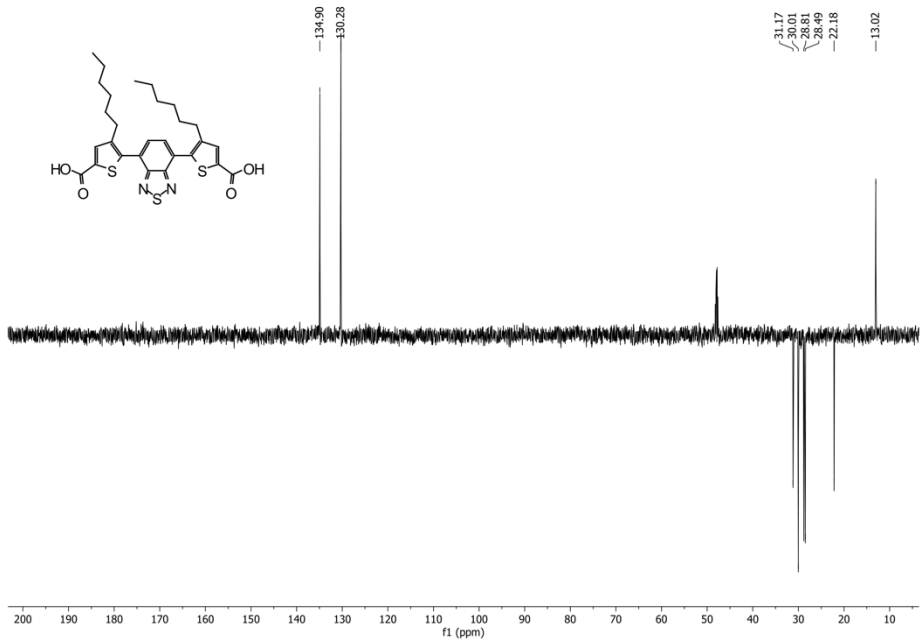

Figure S63. DEPT 135-NMR spectrum of 165 in $CDCl_3$.

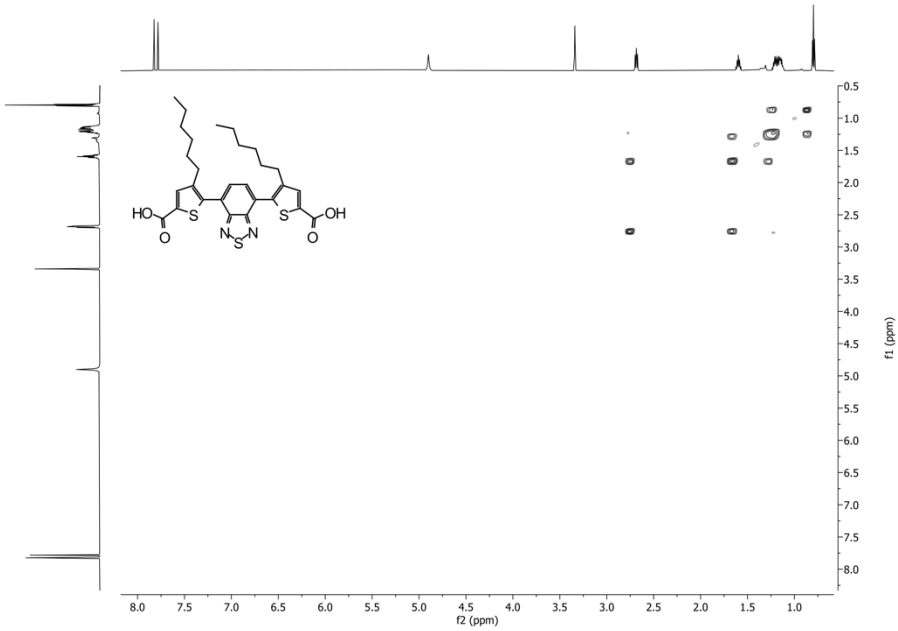

Figure S64. H,H COSY-NMR spectrum of 165 in $CDCl_3$.

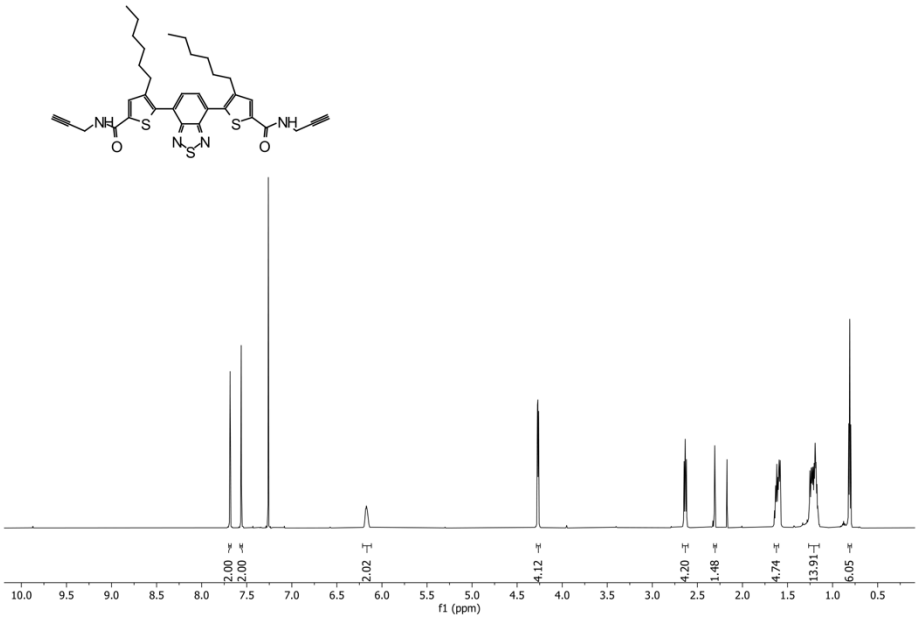

Figure S65. ^{1}H-NMR spectrum of BTD-I-08 in $CDCl_3$.

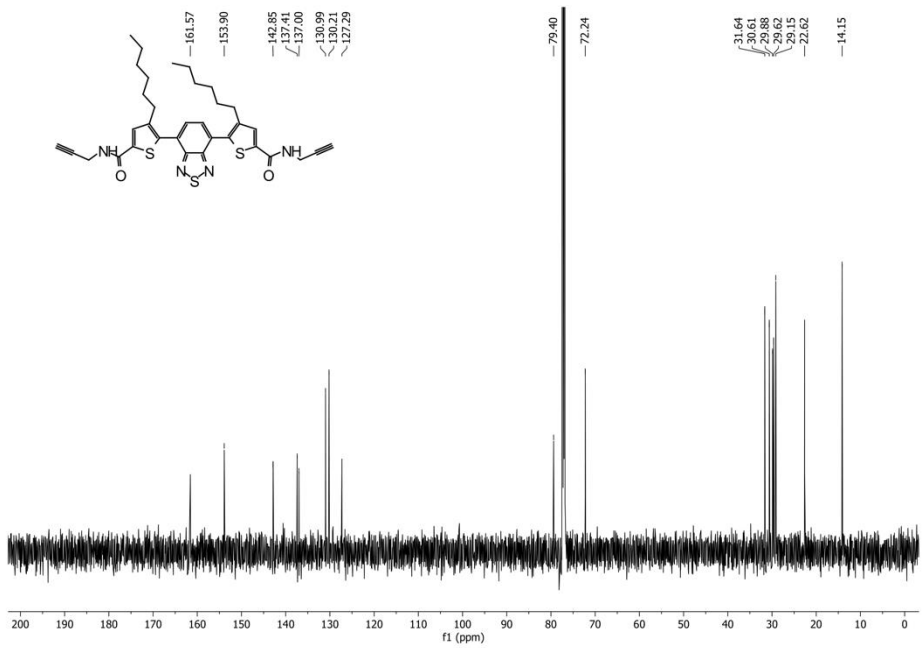

Figure S66. ^{13}C-NMR spectrum of BTD-I-08 in $CDCl_3$.

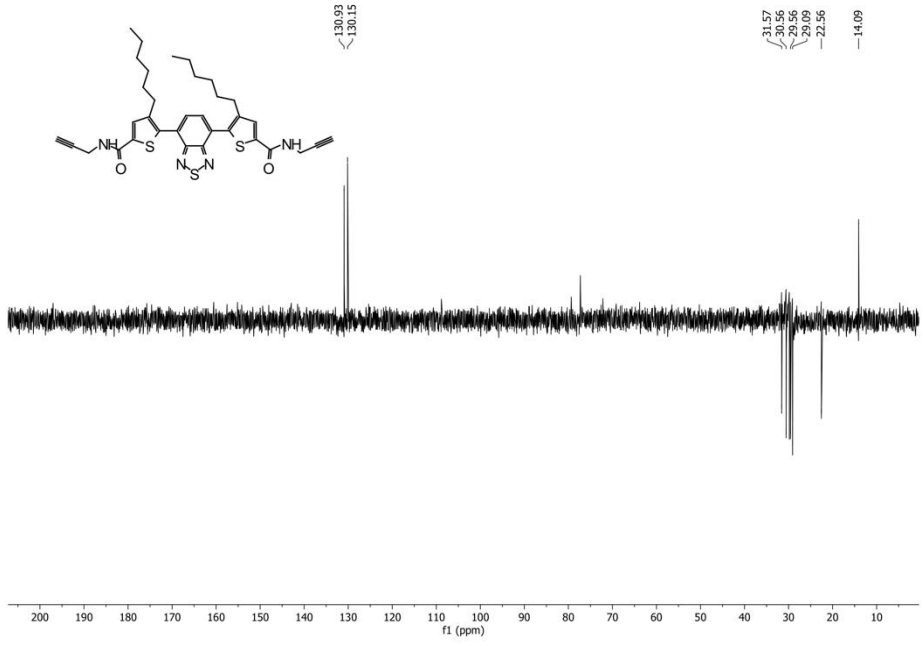

Figure S67. DEPT 135-NMR spectrum of BTD-I-08 in $CDCl_3$.

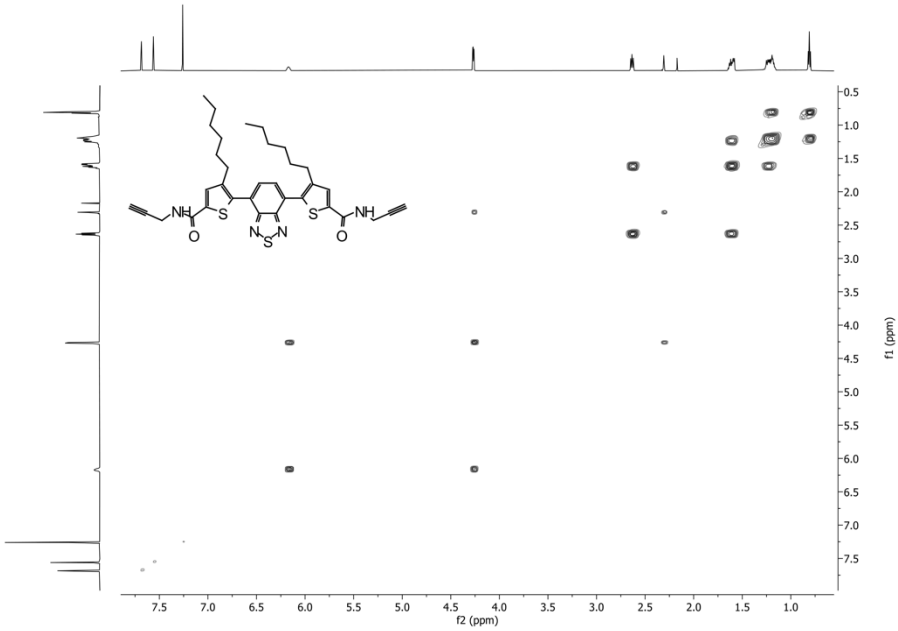

Figure S68. H,H COSY-NMR spectrum of BTD-I-08 in $CDCl_3$.

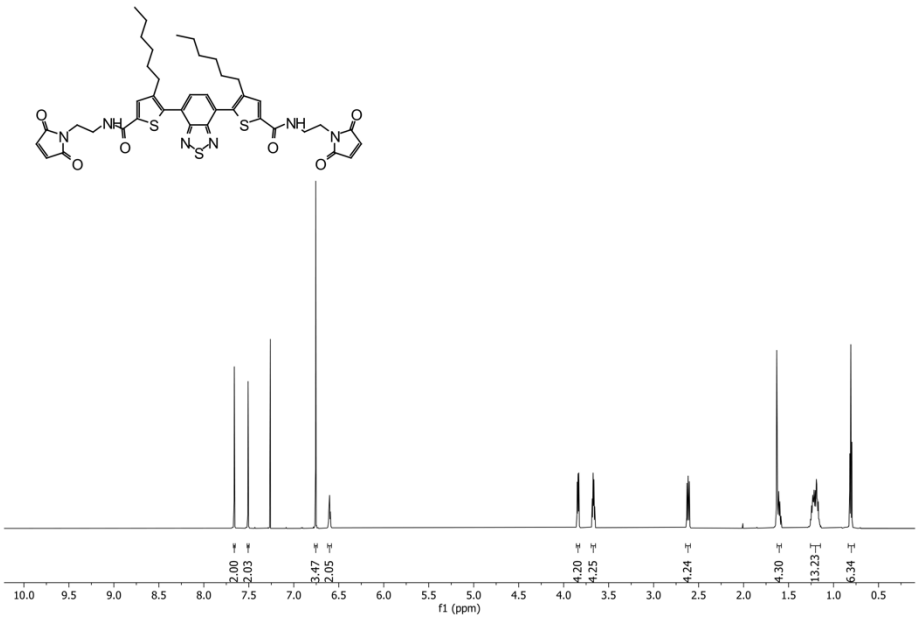

Figure S69. ^{1}H-NMR spectrum of BTD-I-09 in $CDCl_3$.

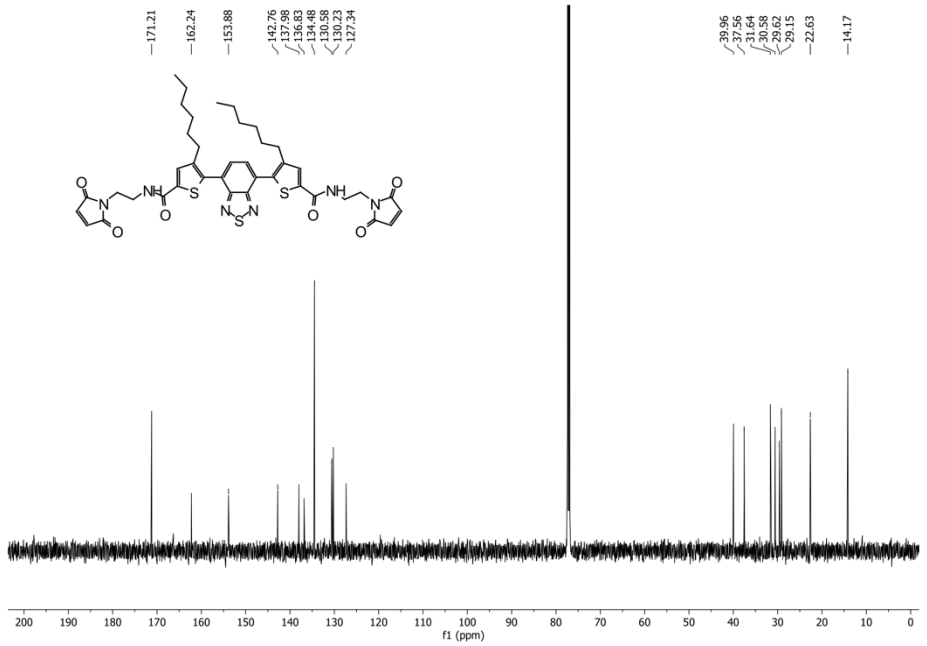

Figure S70. ^{13}C-NMR spectrum of BTD-I-09 in $CDCl_3$.

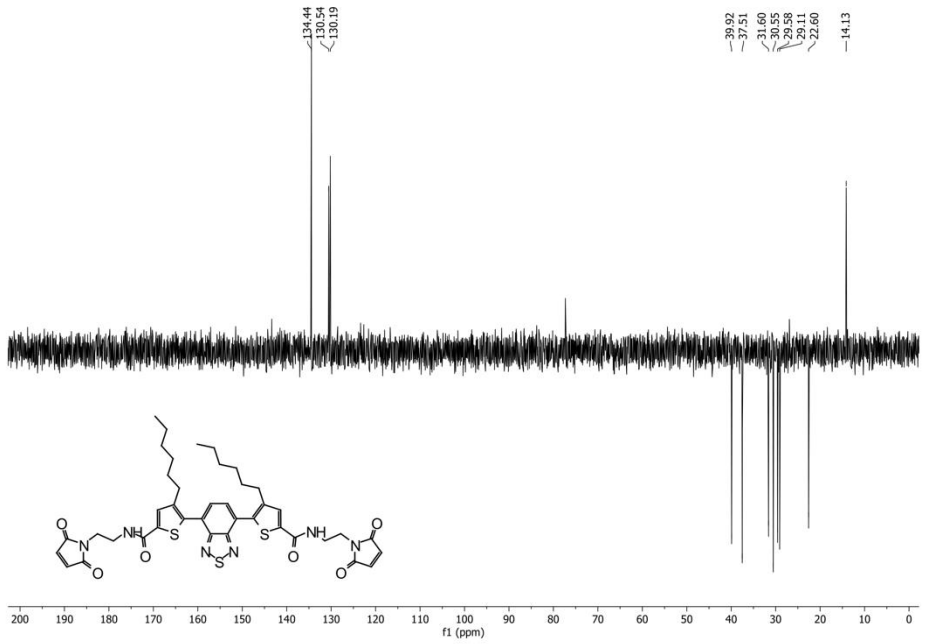

Figure S71. DEPT 135-NMR spectrum of BTD-I-09 in $CDCl_3$.

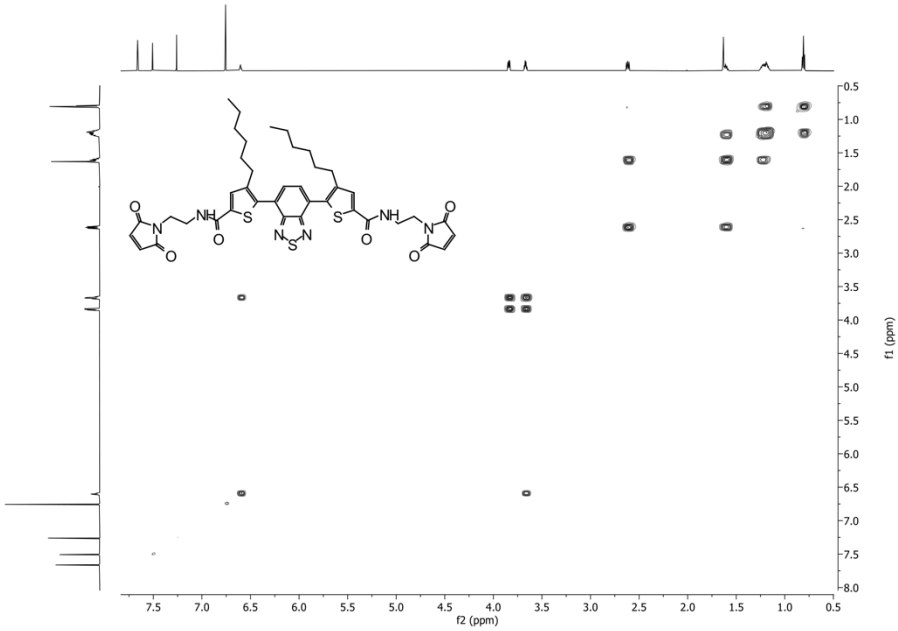

Figure S72. H,H COSY-NMR spectrum of BTD-I-09 in $CDCl_3$.

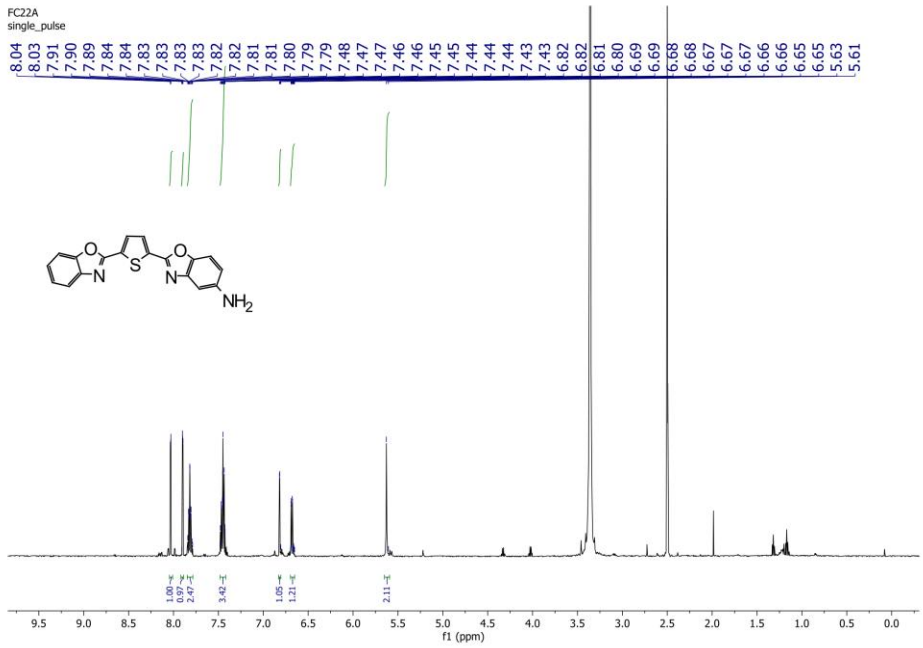

Figure S73. ^{1}H-NMR spectrum of 169 in $CDCl_3$.

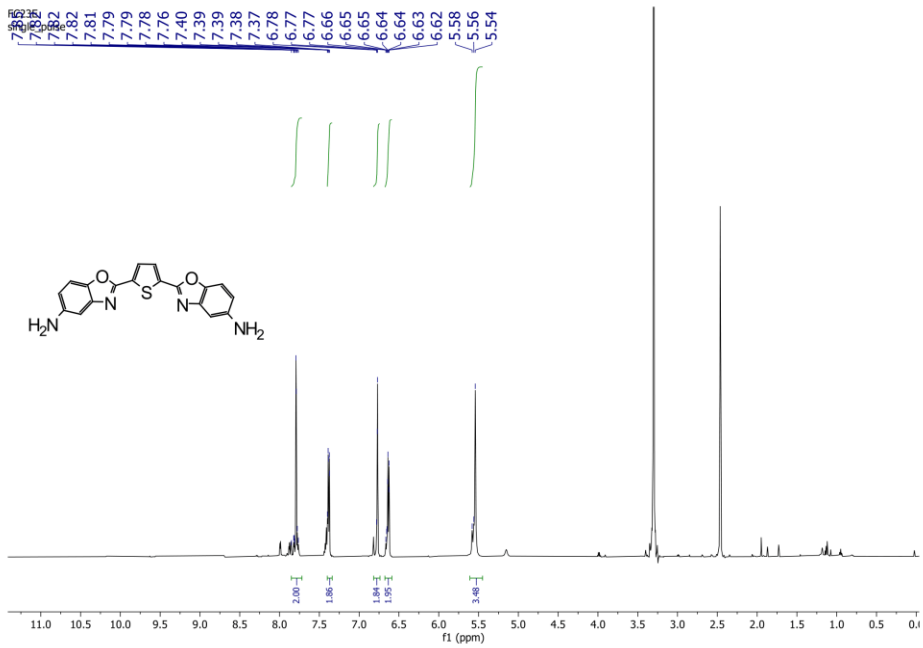

Figure S74. ^{1}H-NMR spectrum of 170 in $CDCl_3$.

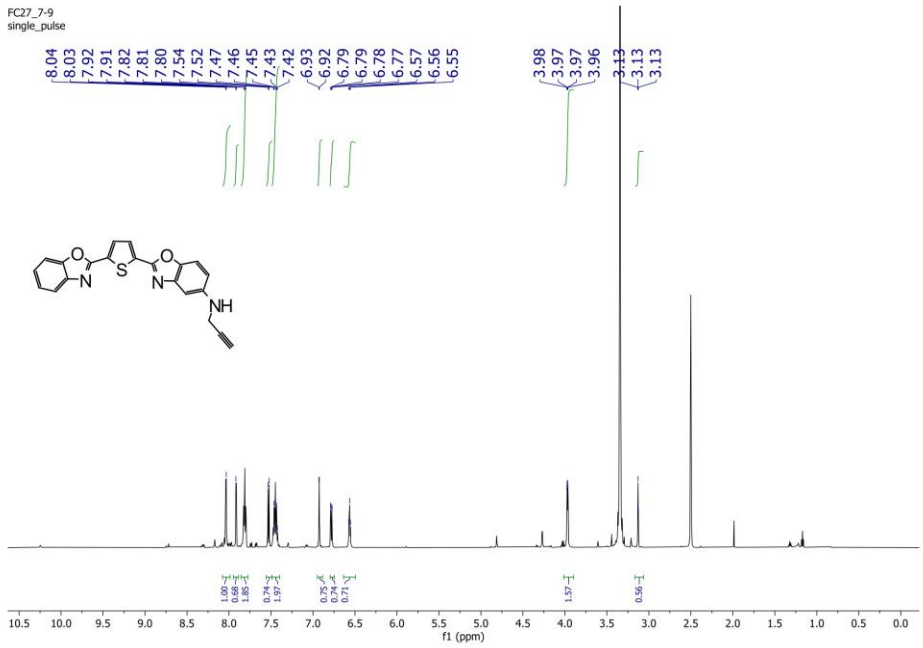

Figure S75. ^{1}H-NMR spectrum of BBT-01 in $CDCl_3$.

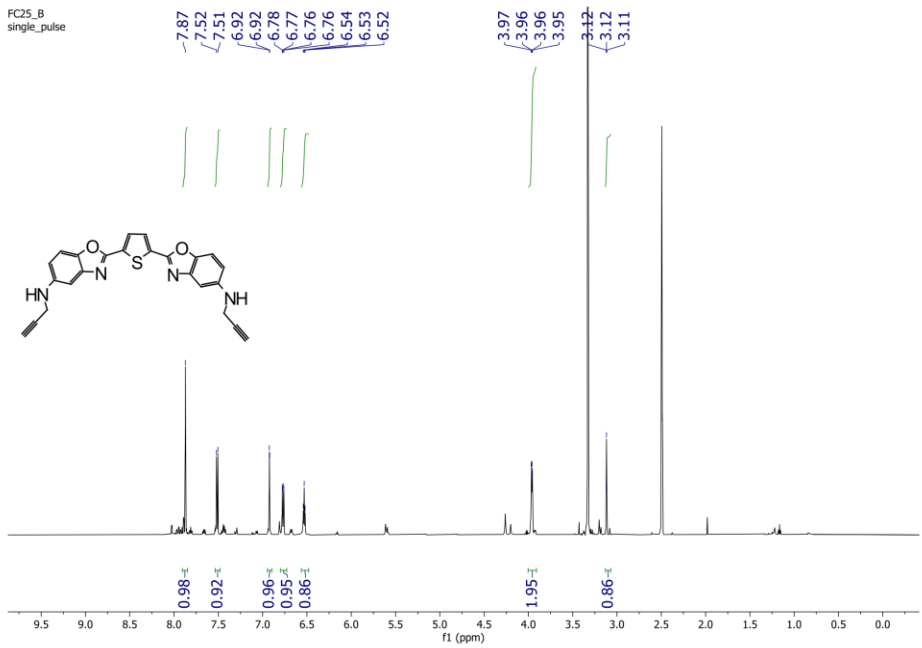

Figure S76. ^{1}H-NMR spectrum of BBT-02 in $CDCl_3$.

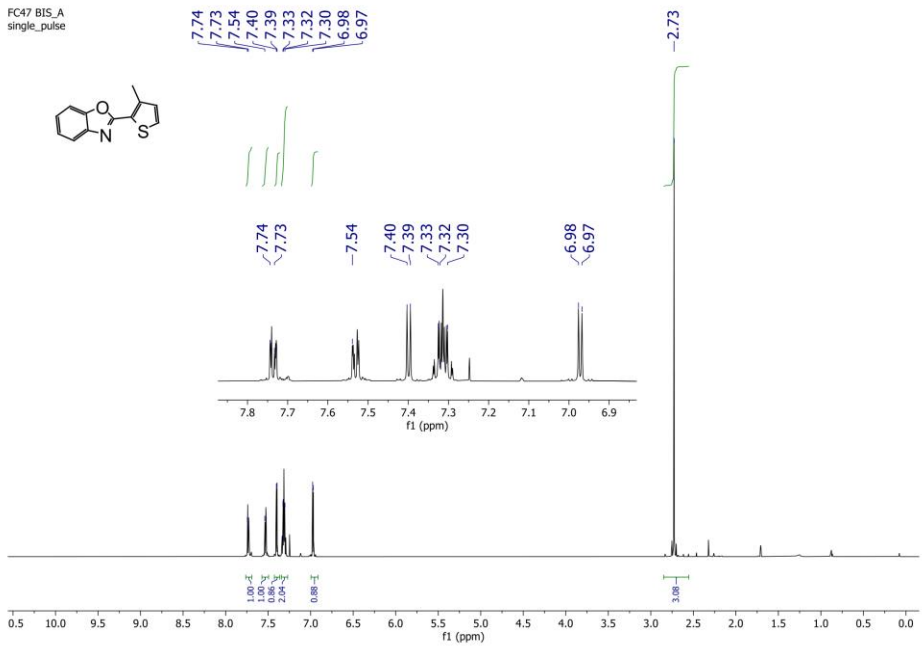

Figure S77. ^{1}H-NMR spectrum of 173 in $CDCl_3$.

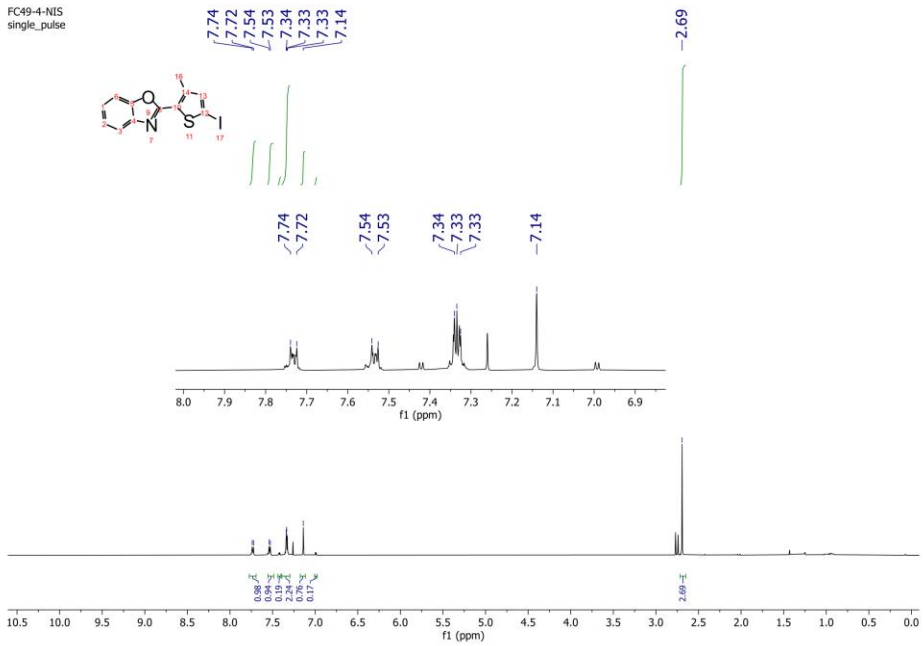

Figure S78. ^{1}H-NMR spectrum of 174 in $CDCl_3$.

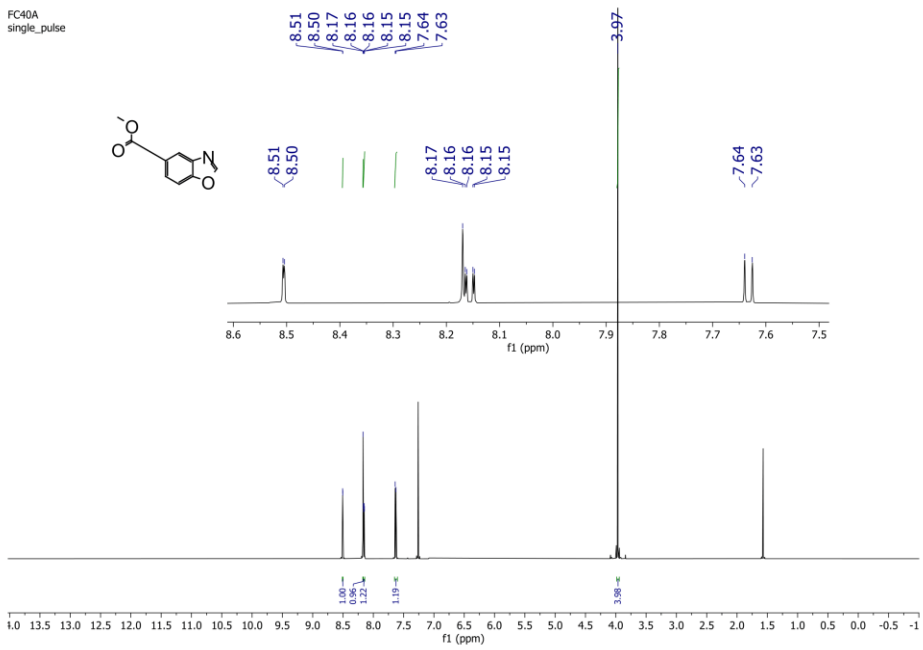

Figure S79. ^{1}H-NMR spectrum of 176 in $CDCl_3$.

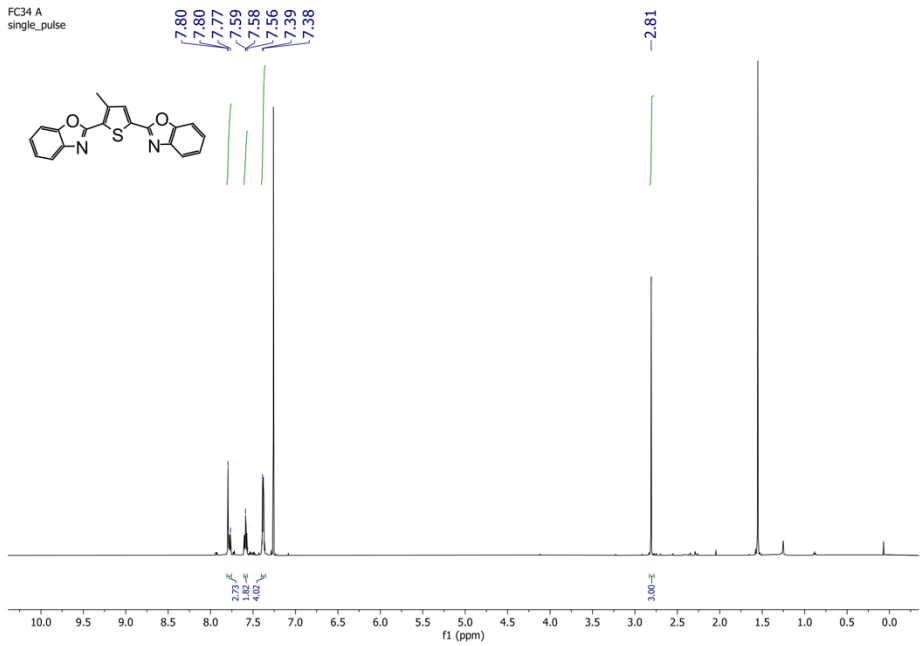

Figure S80. ^{1}H-NMR spectrum of BBT-03 in $CDCl_3$.

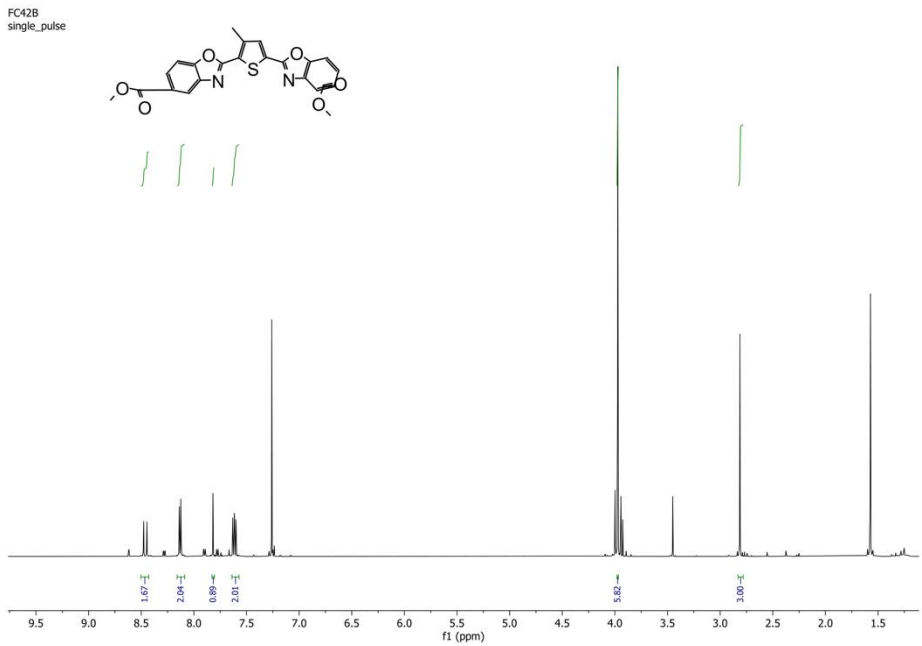

Figure S81. ^{1}H-NMR spectrum of BBT-04 in $CDCl_3$.

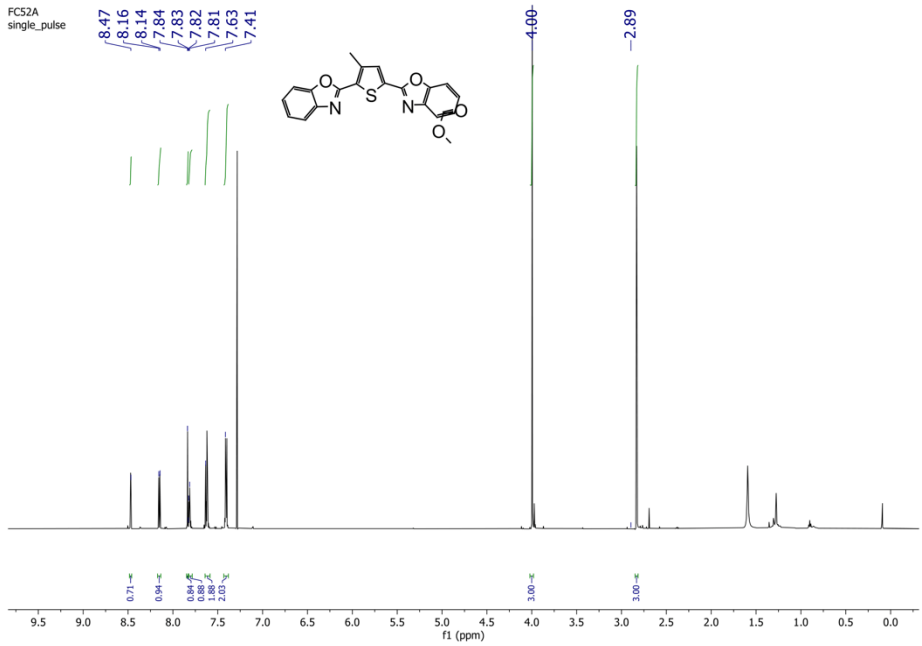

Figure S82. ^{1}H-NMR spectrum of BBT-05 in $CDCl_3$.

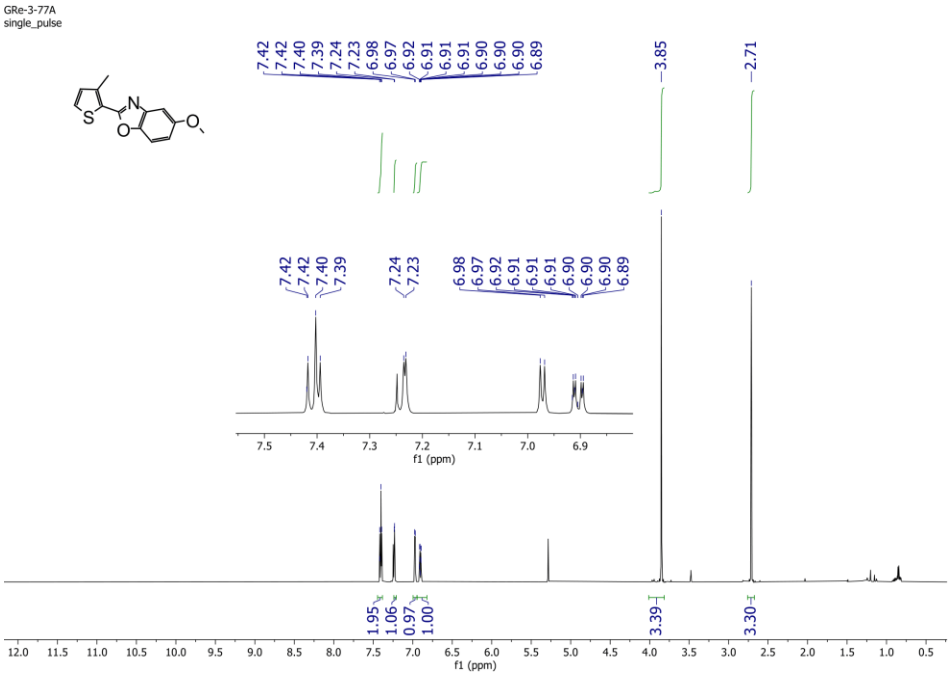

Figure S83. ^{1}H-NMR spectrum of 179 in $CDCl_3$.

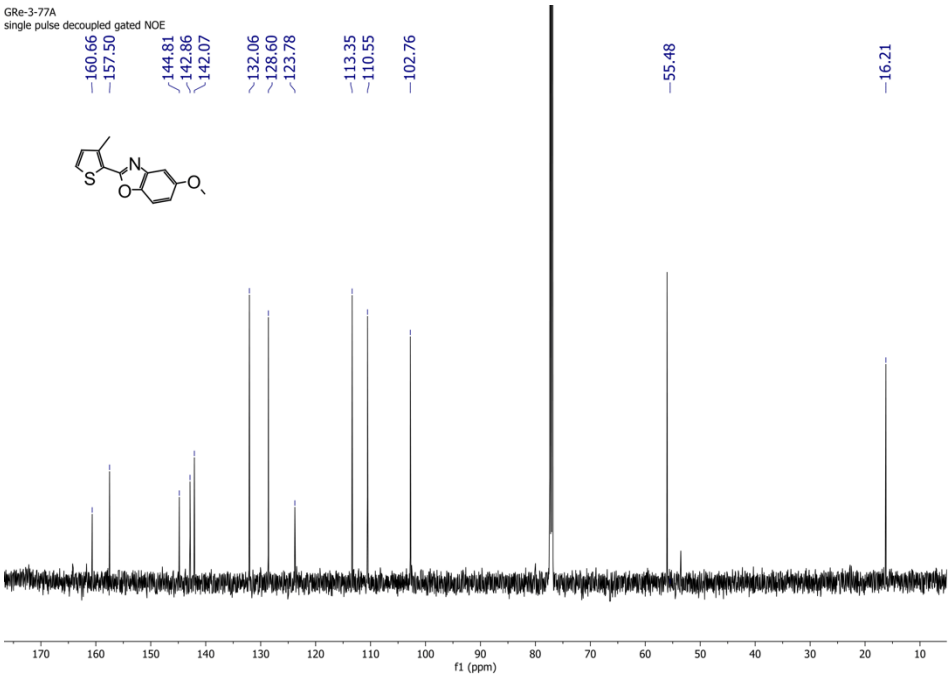

Figure S84. ^{13}C-NMR spectrum of 179 in $CDCl_3$.

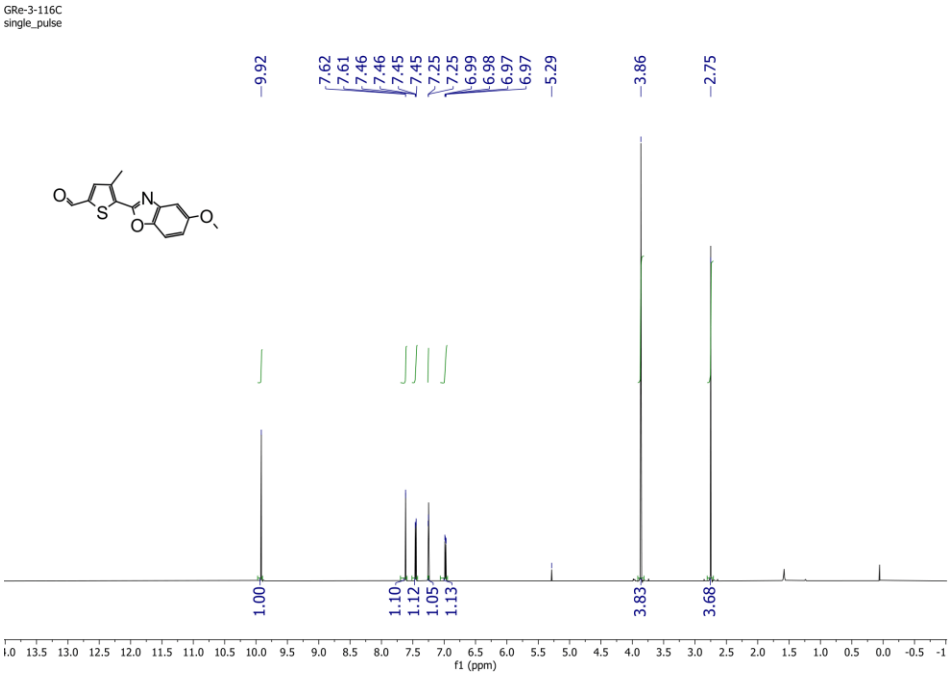

Figure S85. ^{1}H-NMR spectrum of 180 in $CDCl_3$.

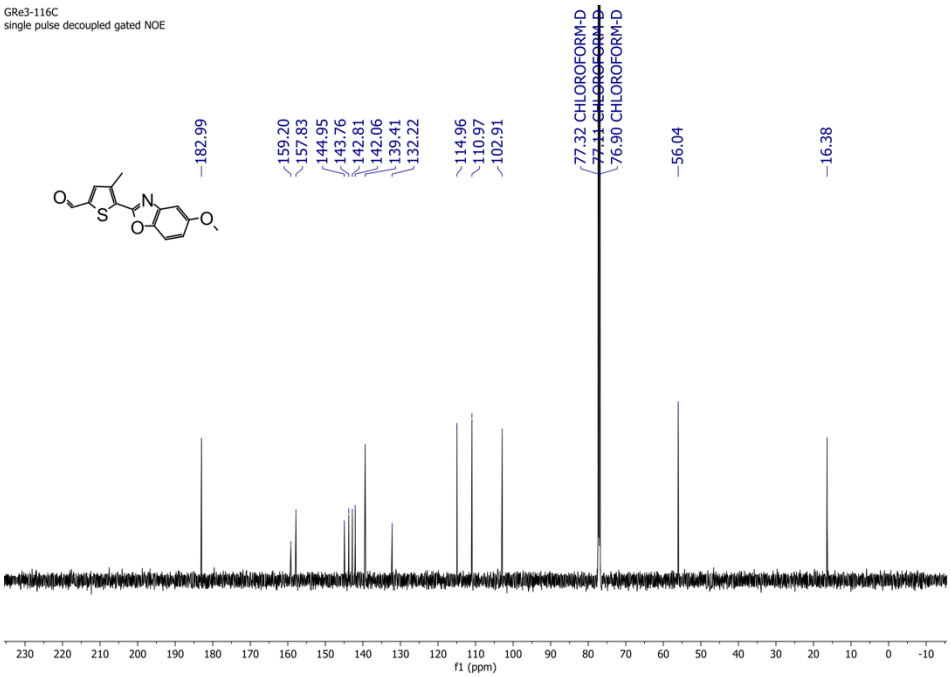

Figure S86. ^{13}C-NMR spectrum of 180 in $CDCl_3$.

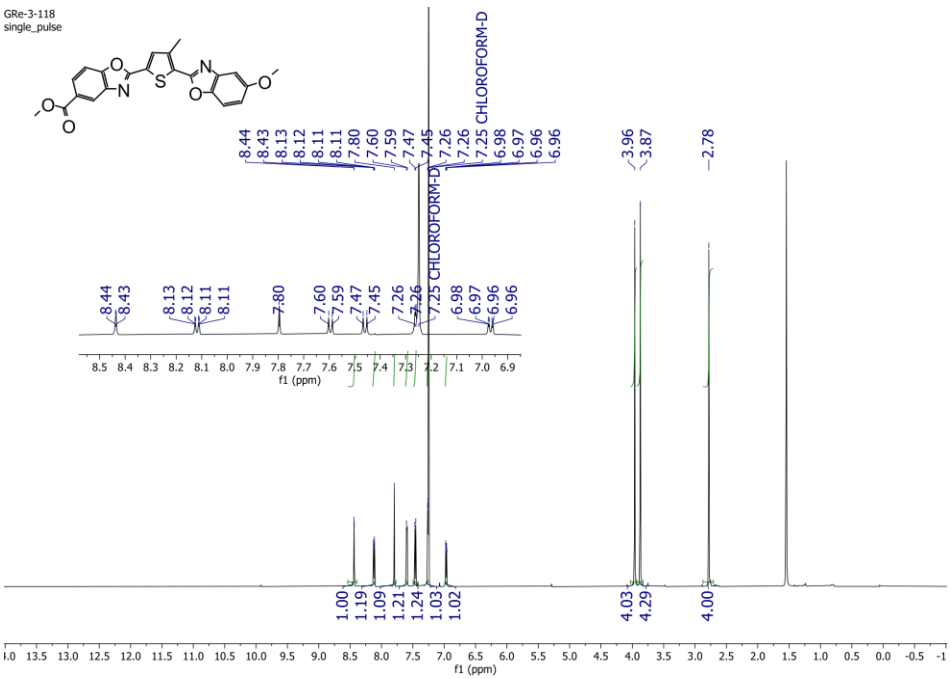

Figure S87. ^{1}H-NMR spectrum of BBT-06 in $CDCl_3$.

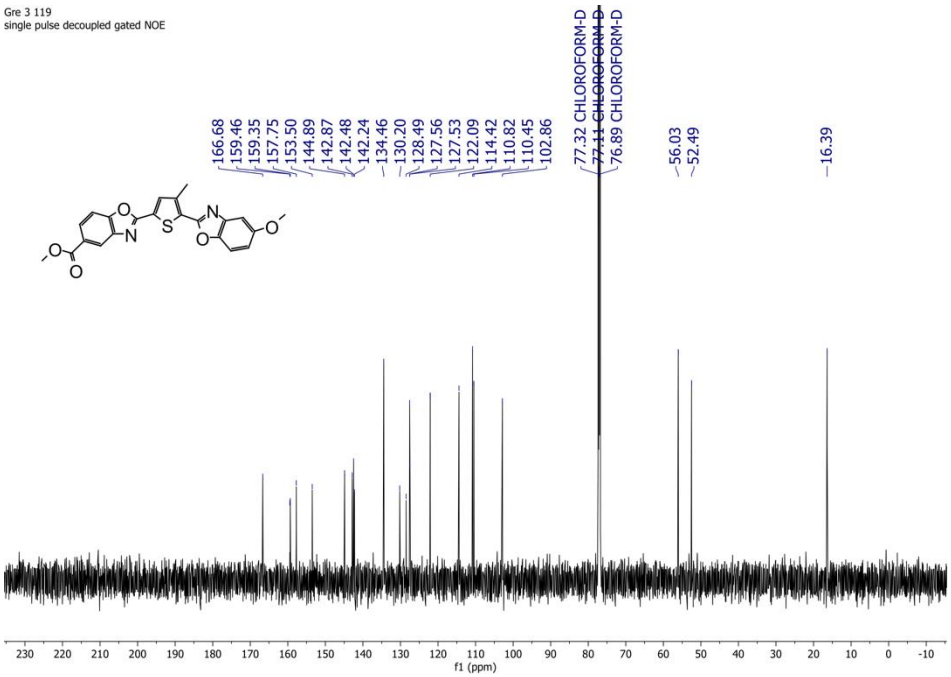

Figure S88. ^{13}C-NMR spectrum of BBT-06 in $CDCl_3$.

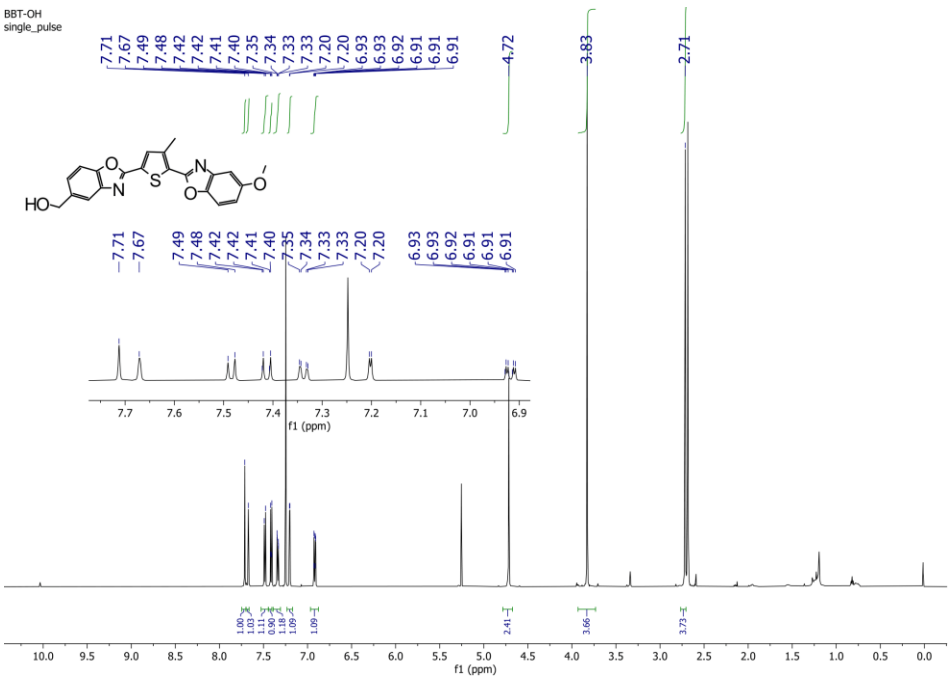

Figure S89. ^{1}H-NMR spectrum of 182 in $CDCl_3$.

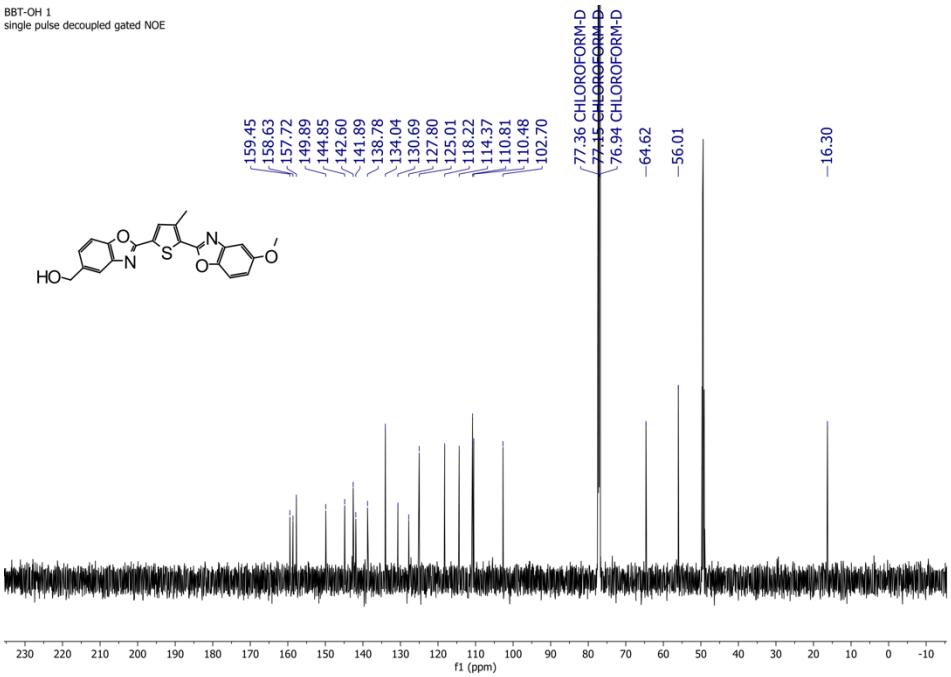

Figure S90. ^{13}C-NMR spectrum of 182 in $CDCl_3$.

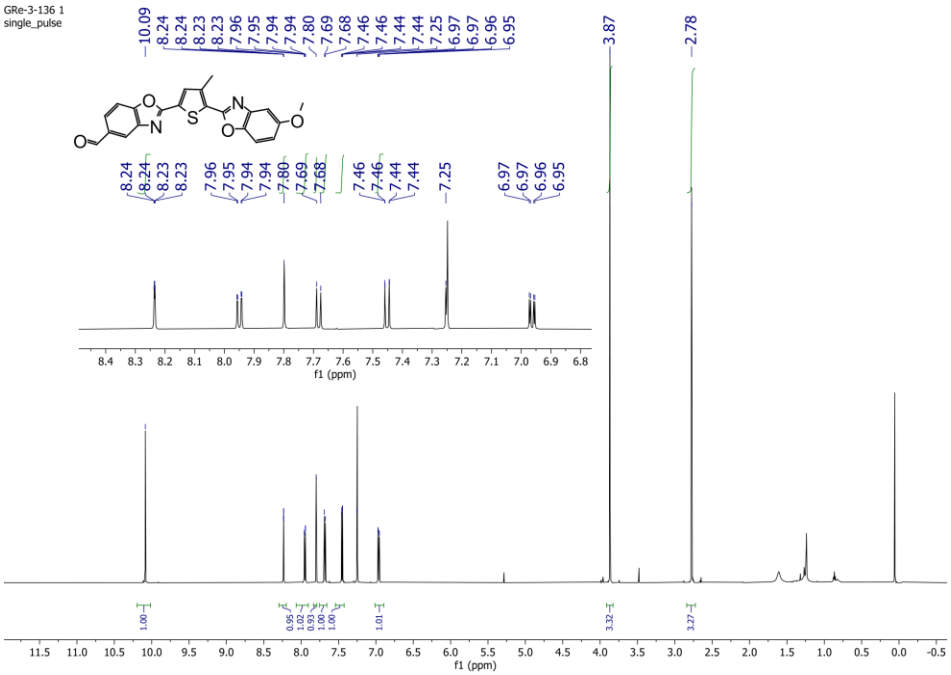

Figure S91. ^{1}H-NMR spectrum of 183 in $CDCl_3$.

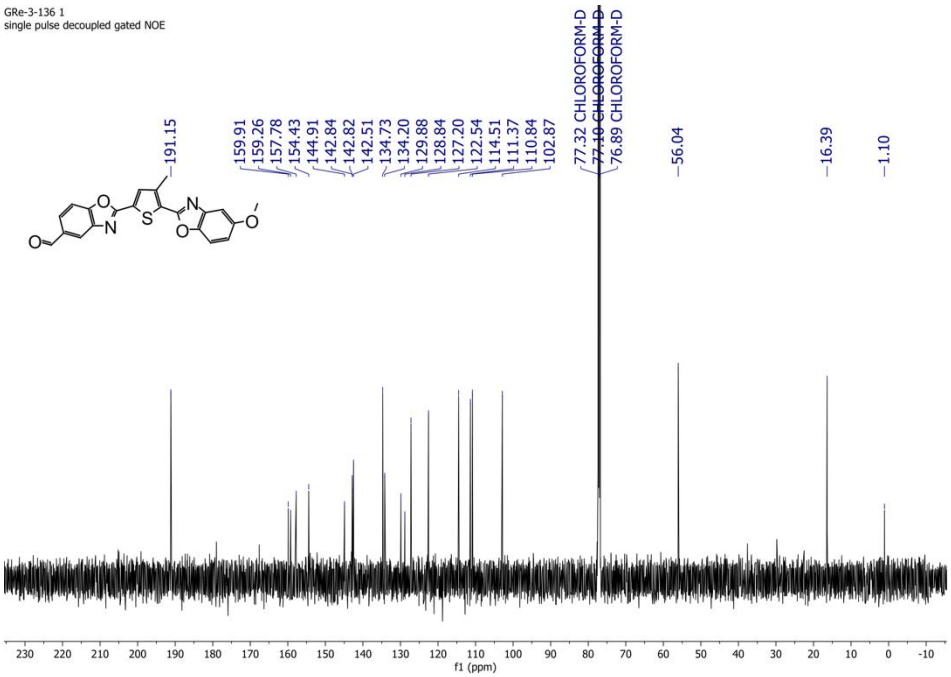

Figure S92. ^{13}C-NMR spectrum of 183 in $CDCl_3$.

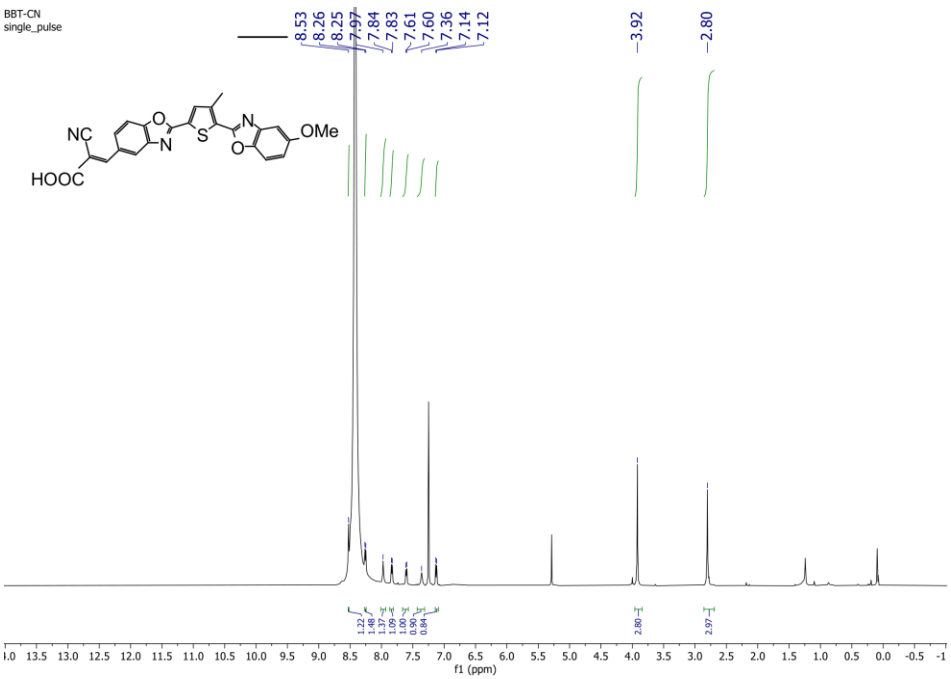

Figure S93. ^{1}H-NMR spectrum of BBT-07 in $CDCl_3$.

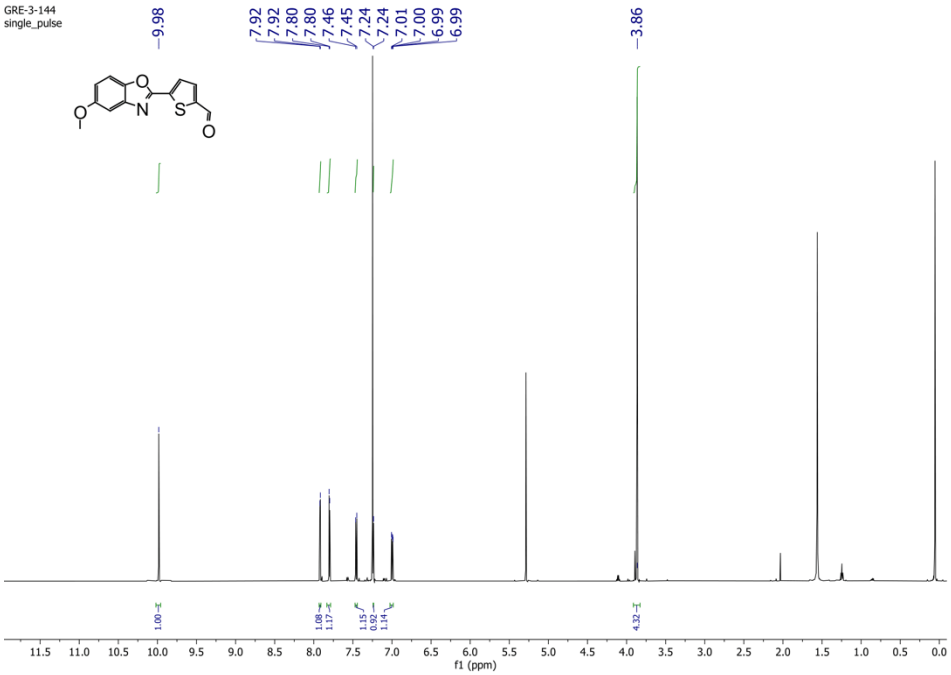

Figure S94. ^{1}H-NMR spectrum of 186 in $CDCl_3$.

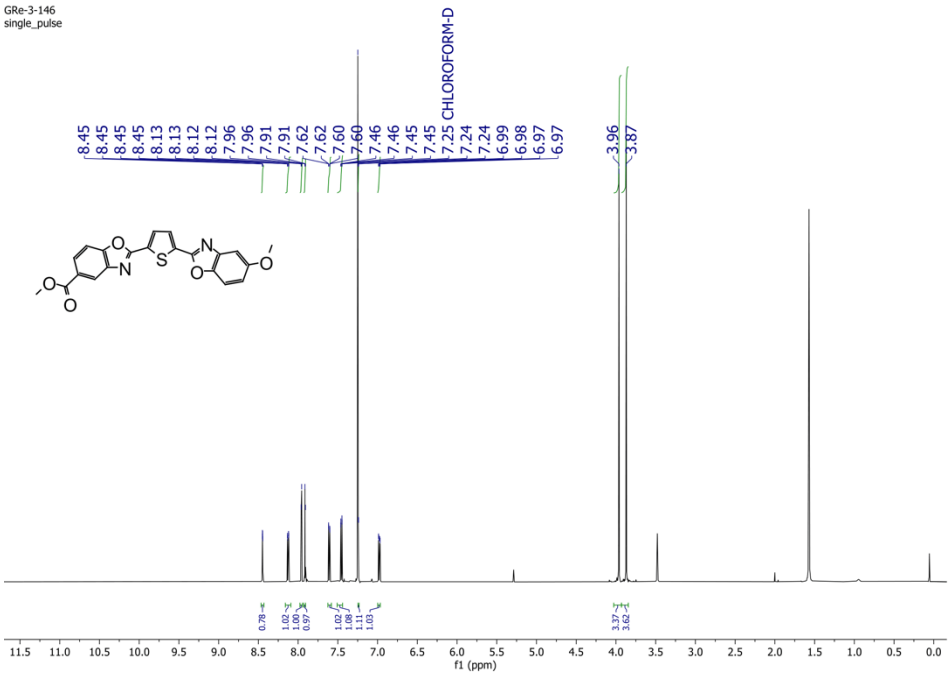

Figure S95. ^{1}H-NMR spectrum of BBT-08 in $CDCl_3$.

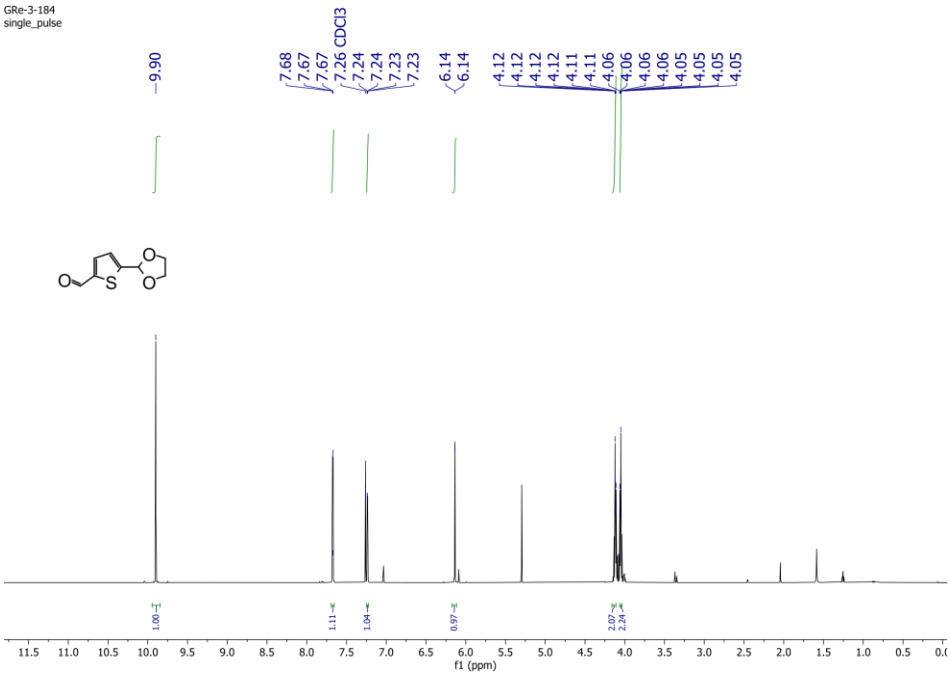

Figure S96. ^{1}H-NMR spectrum of 188 in $CDCl_3$.

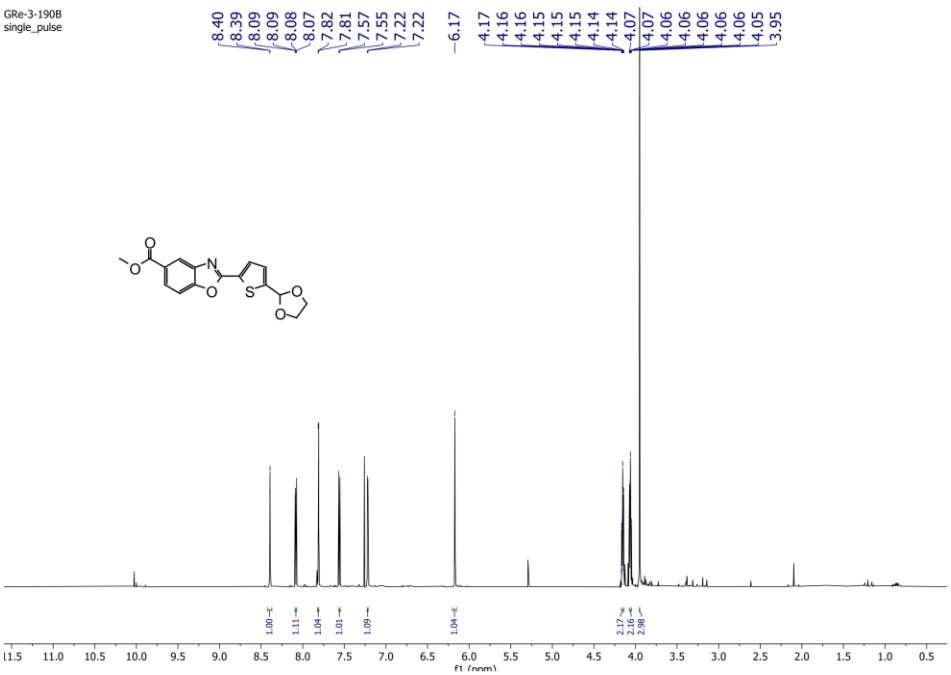

Figure S97. ^{1}H-NMR spectrum of 189 in $CDCl_3$.

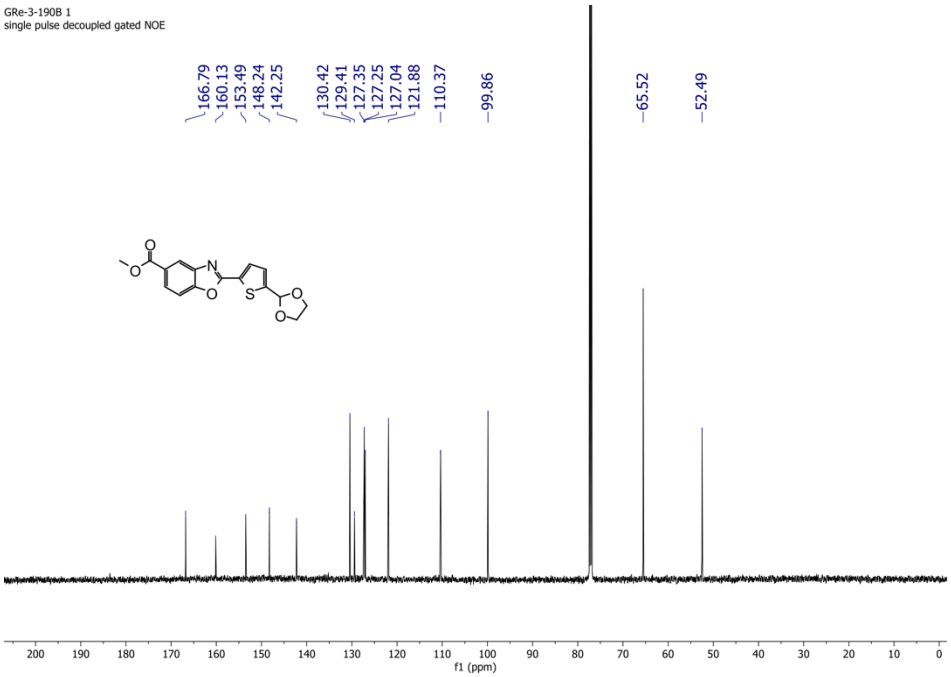

Figure S98. ^{13}C-NMR spectrum of 189 in $CDCl_3$.

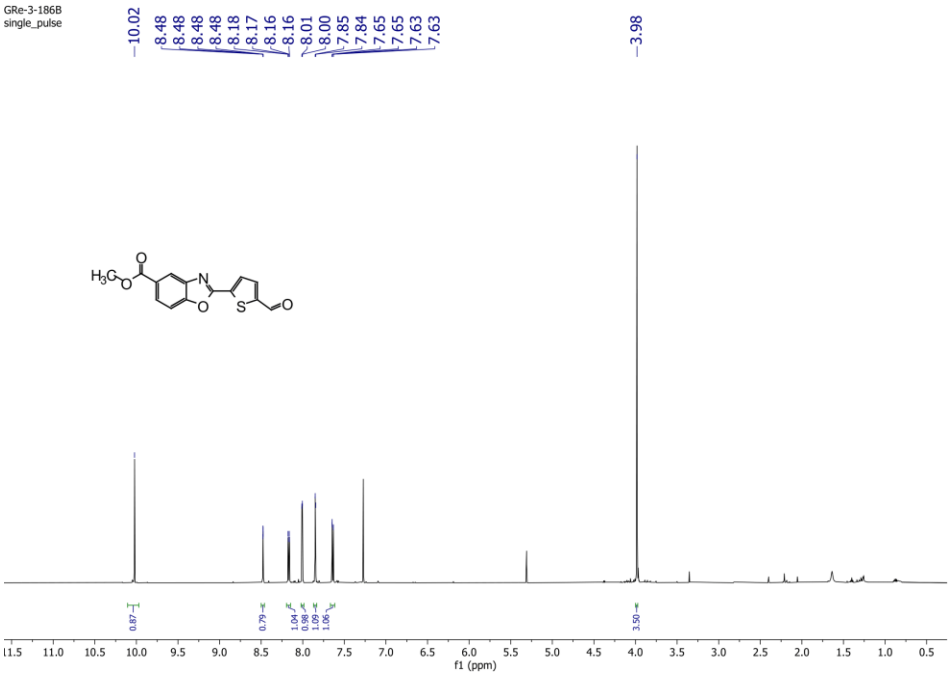

Figure S99. ^{1}H-NMR spectrum of 190 in $CDCl_3$.

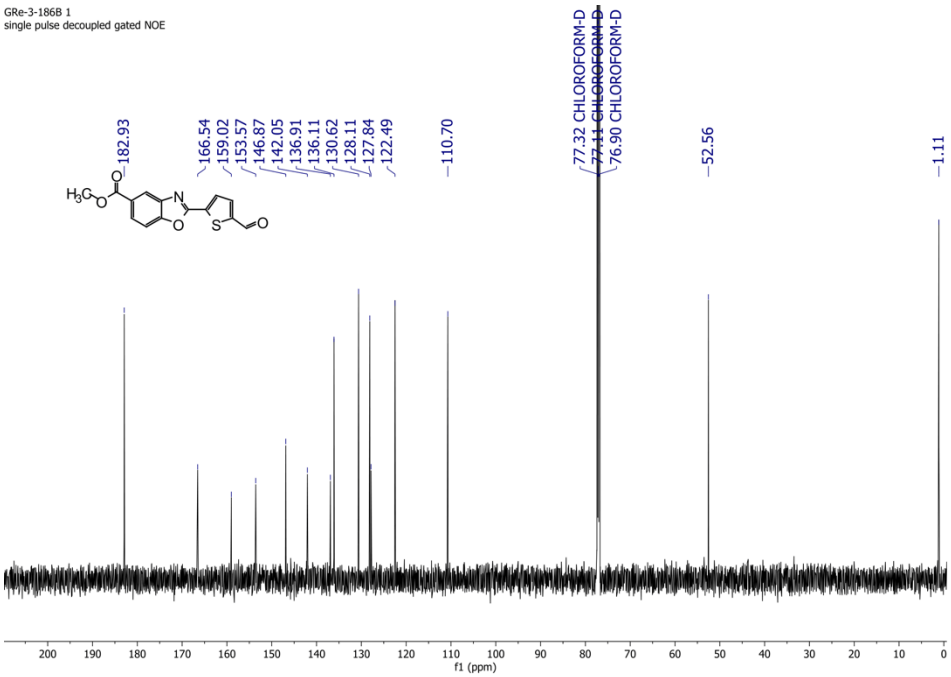

Figure S100. ^{13}C-NMR spectrum of 190 in $CDCl_3$.

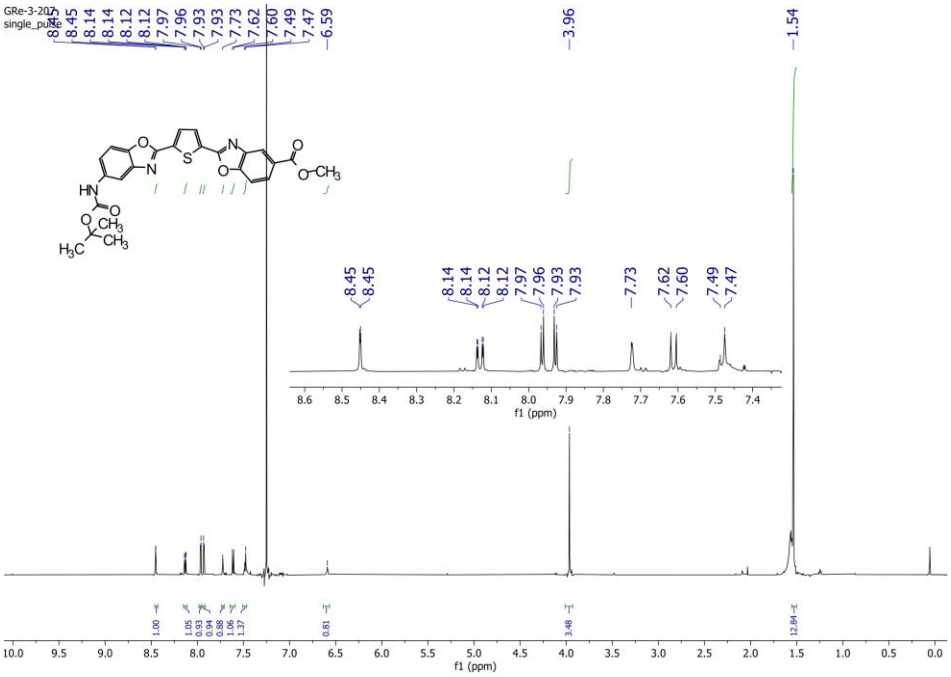

Figure S101. ^{1}H-NMR spectrum of 191 in $CDCl_3$.

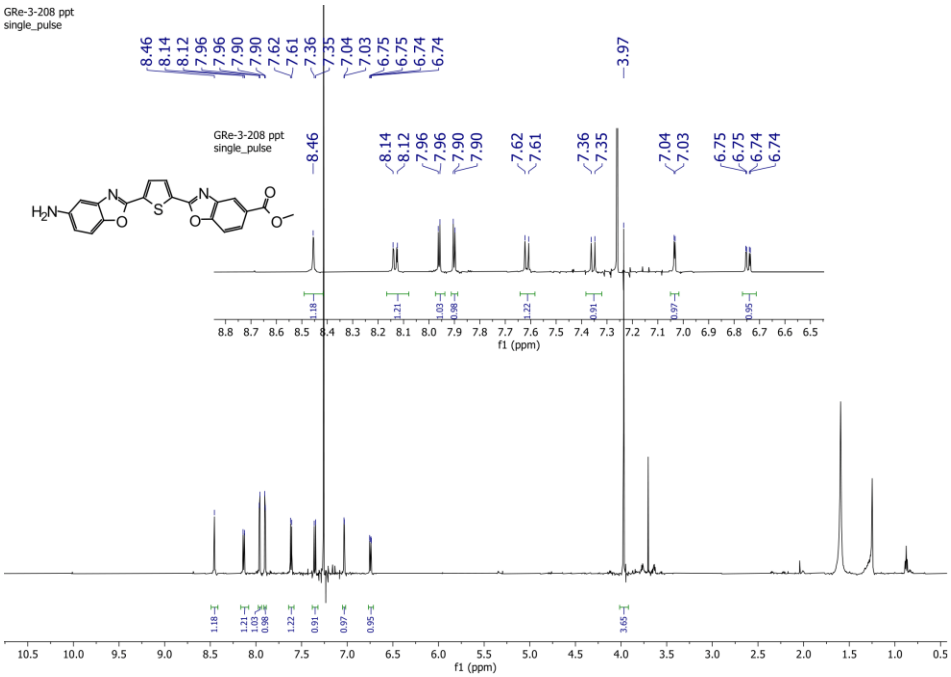

Figure S102. ^{1}H-NMR spectrum of 192 in $CDCl_3$.

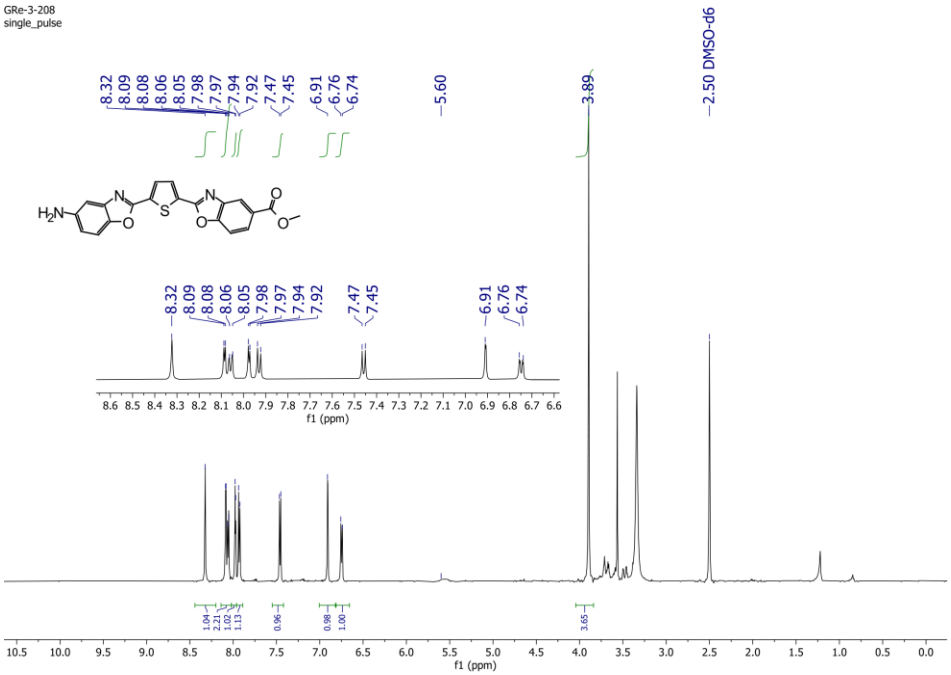

Figure S103. ^{1}H-NMR spectrum of 192 in DMSO.

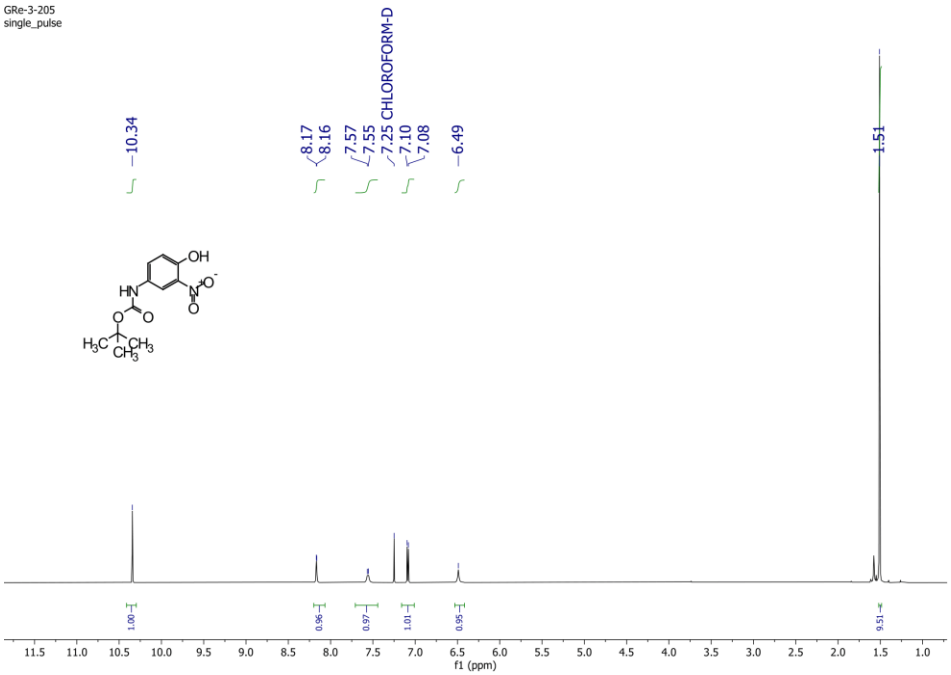

Figure S104. ^{1}H-NMR spectrum of 193 in $CDCl_3$.

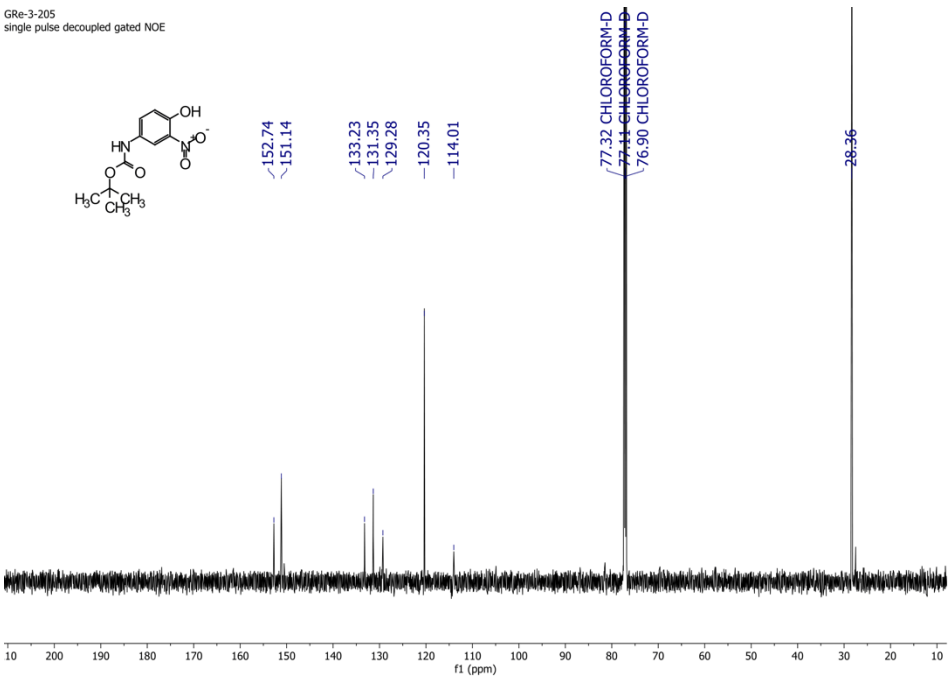

Figure S105. ^{13}C-NMR spectrum of 193 in $CDCl_3$.

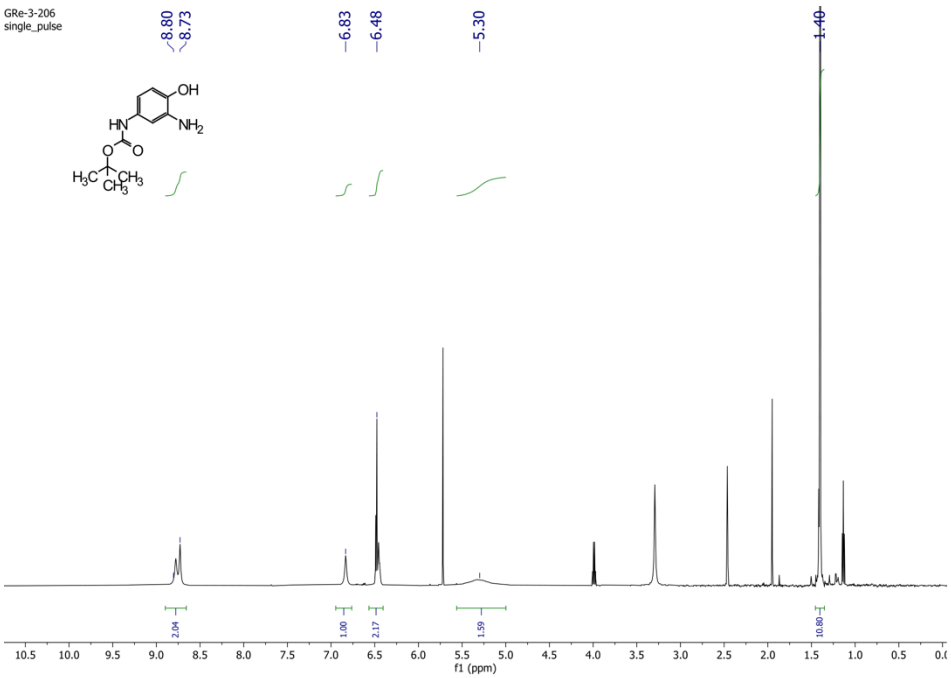

Figure S106. ^{1}H-NMR spectrum of 194 in MeOD.

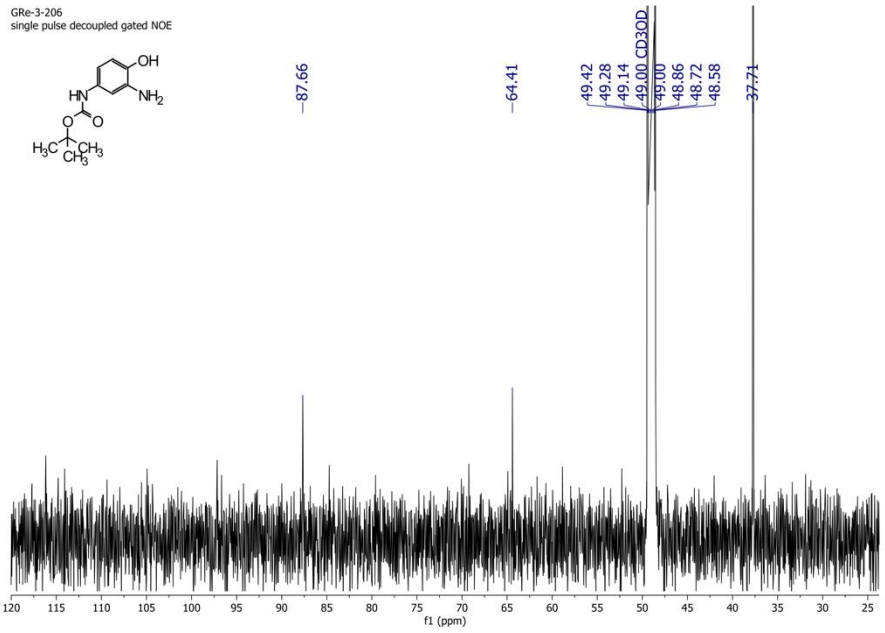

Figure S107. ^{13}C-NMR spectrum of 194 in MeOD.

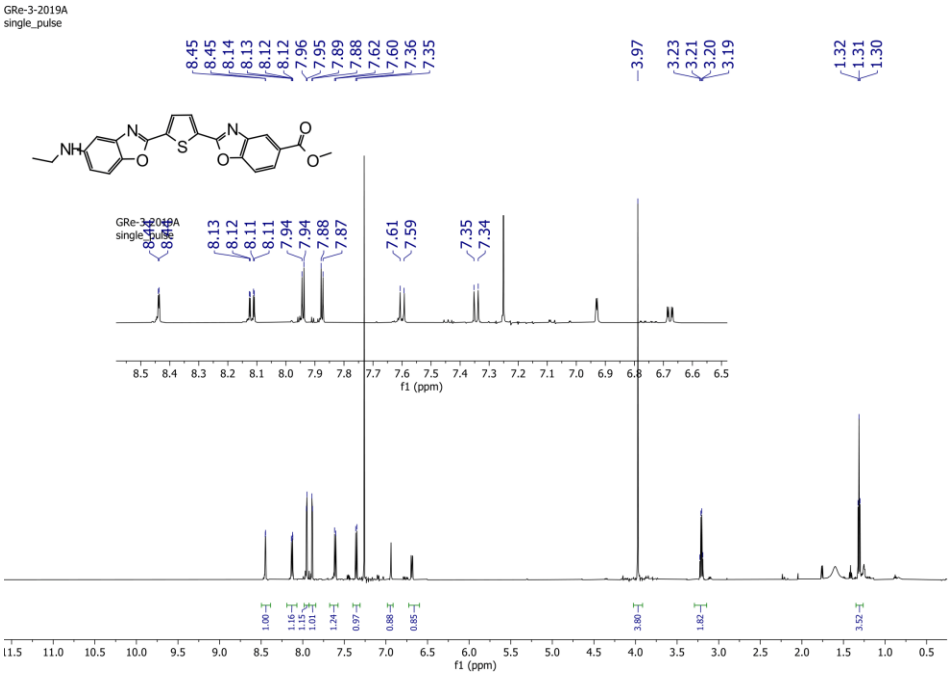

Figure S108. ^{1}H-NMR spectrum of BBT-09 in $CDCl_3$.

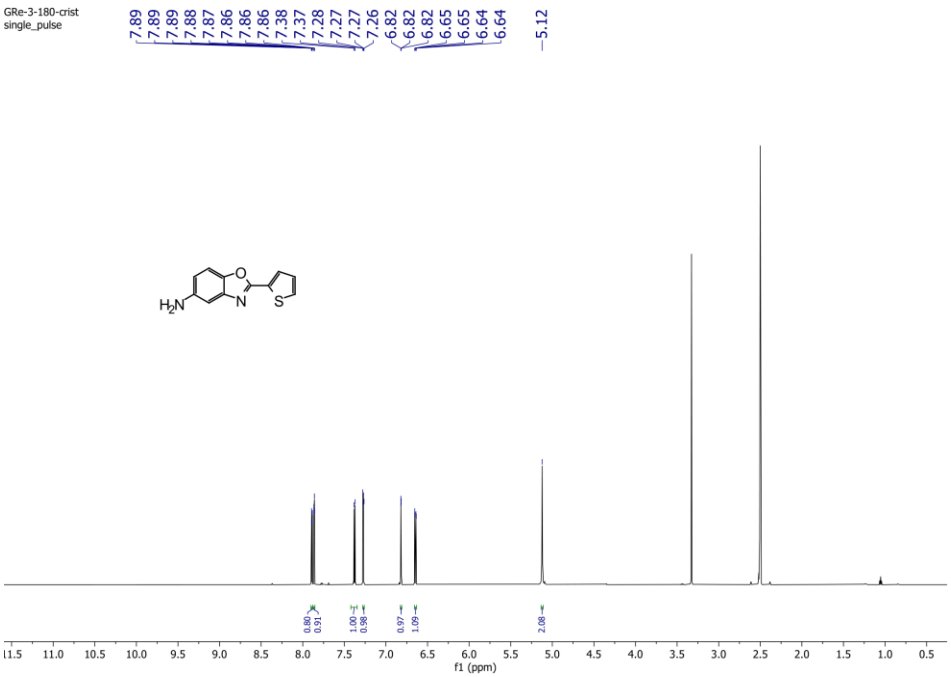

Figure S109. ^{1}H-NMR spectrum of 196 in $CDCl_3$.

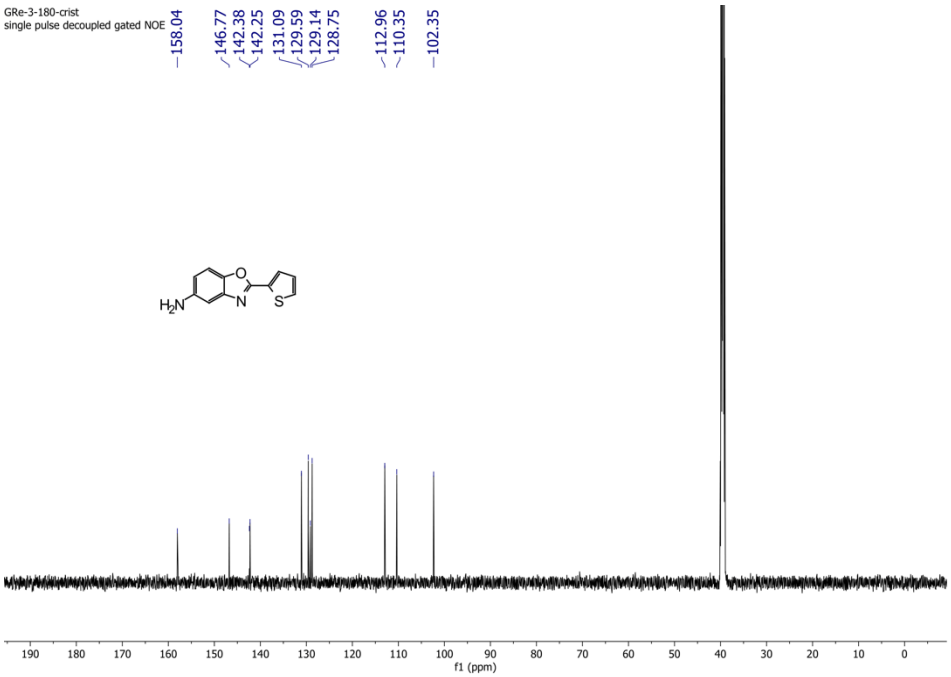

Figure S110. ^{13}C-NMR spectrum of 196 in $CDCl_3$.

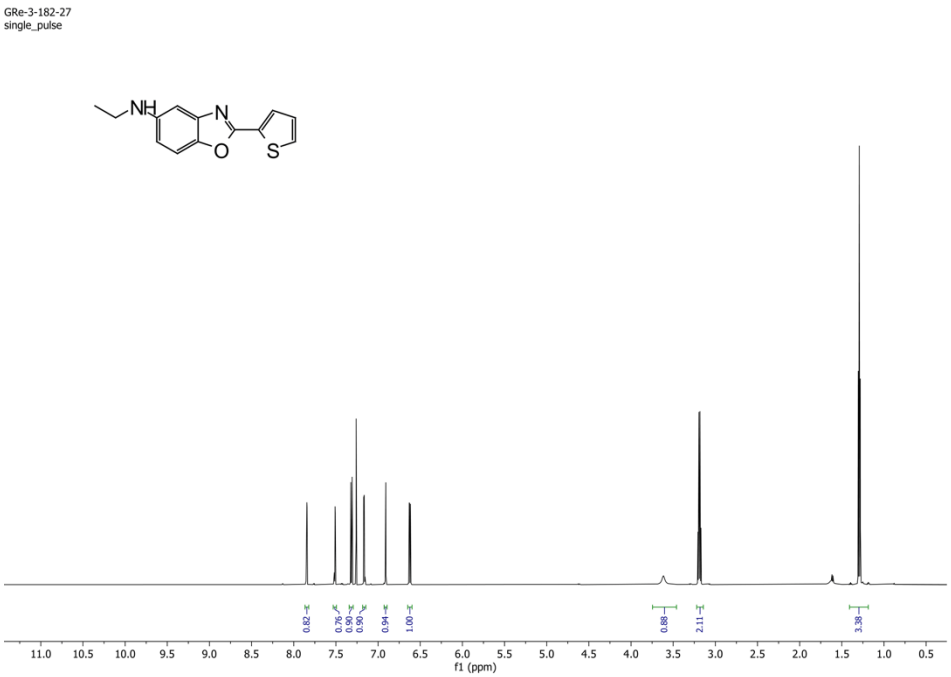

Figure S111. ^{1}H-NMR spectrum of BBT-10 in $CDCl_3$.

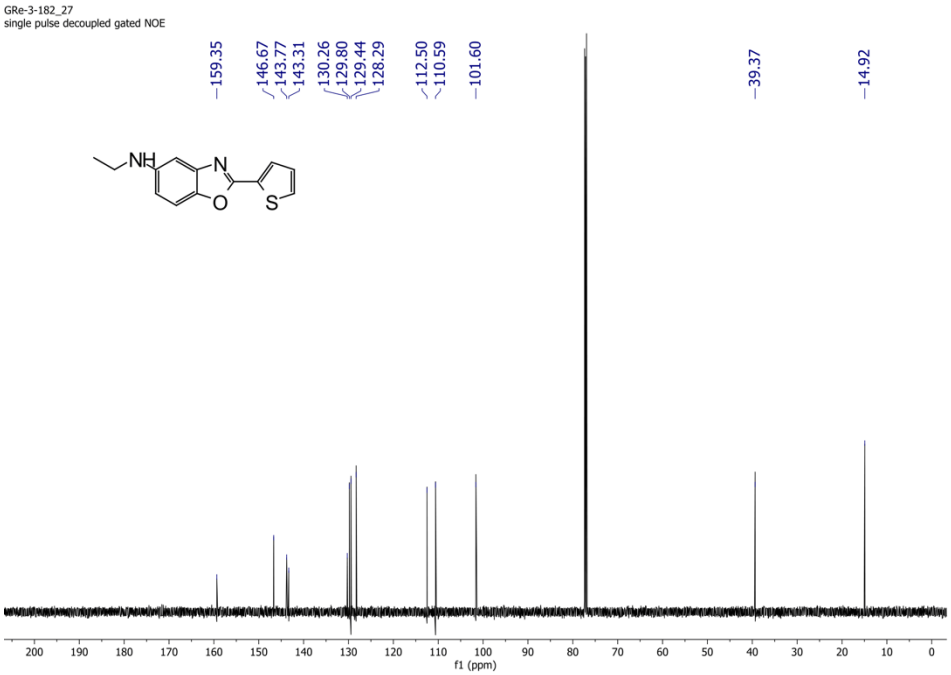

Figure S112. ^{13}C-NMR spectrum of NDI-01 in $CDCl_3$.

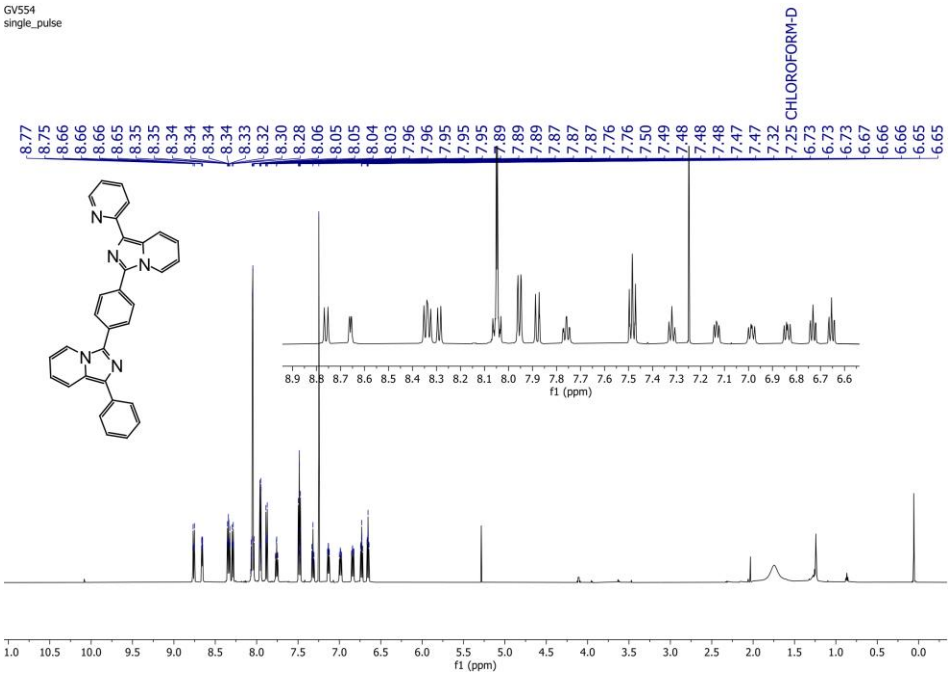

Figure S113. ^{1}H-NMR spectrum of 200 in $CDCl_3$.

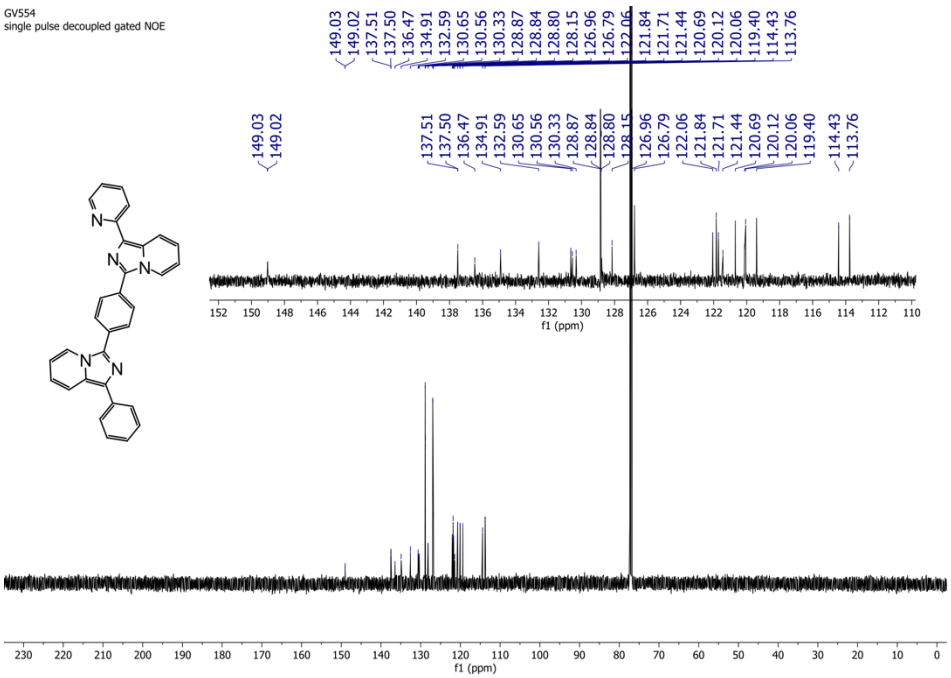

Figure S114. ^{13}C-NMR spectrum of 200 in $CDCl_3$.

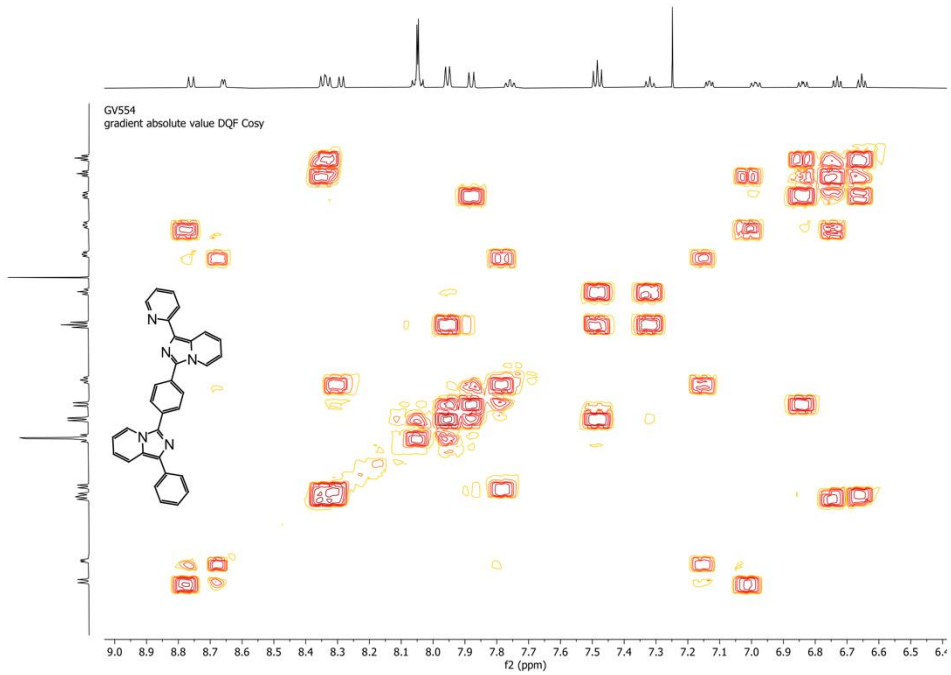

Figure S115. H,H COSY-NMR spectrum of 200 in $CDCl_3$.

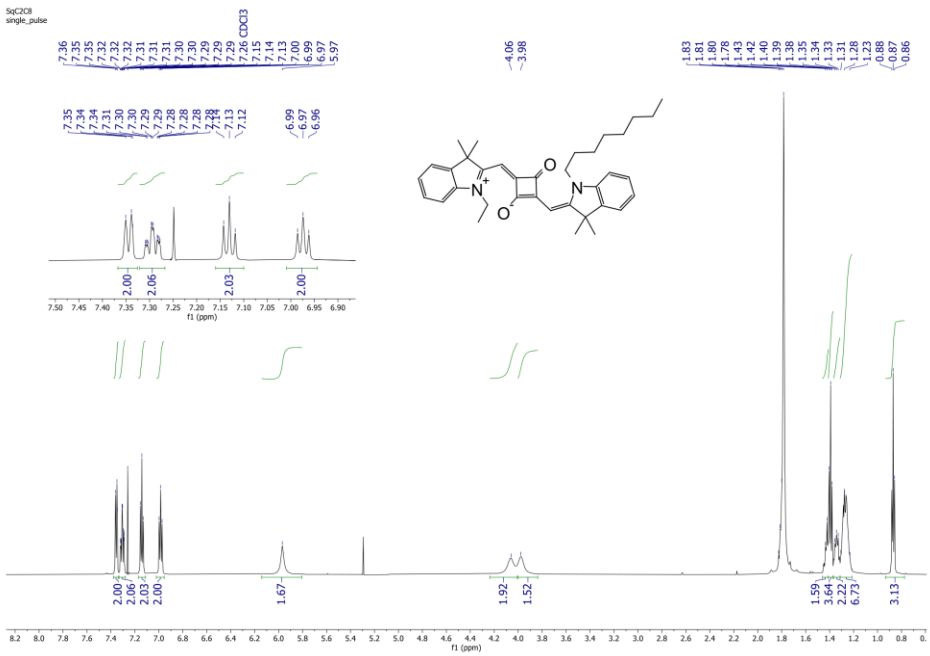

Figure S116. ^{1}H-NMR spectrum of 216 in $CDCl_3$.

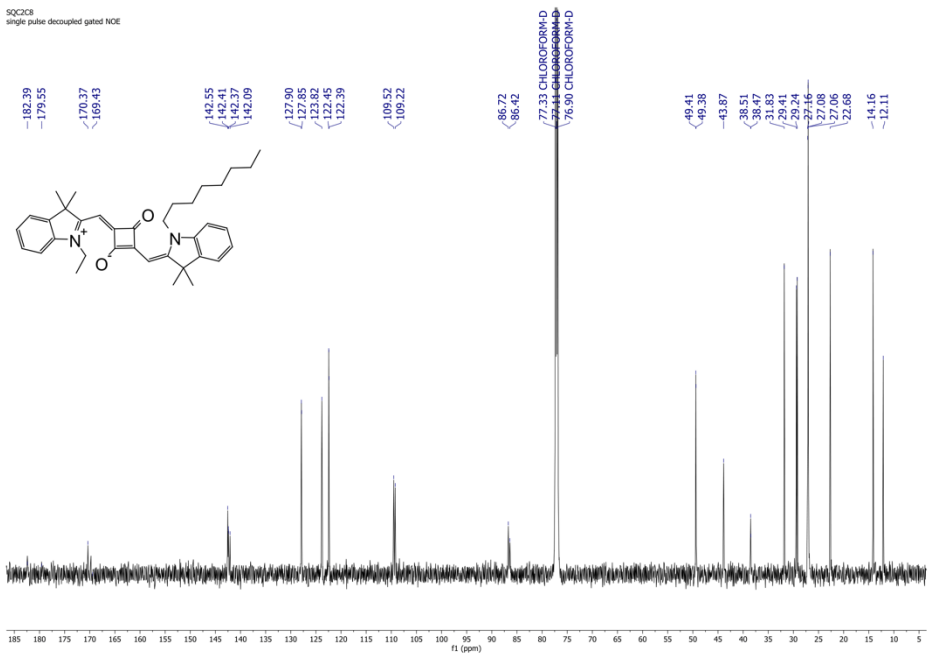

Figure S117. ^{13}C-NMR spectrum of 216 in $CDCl_3$.

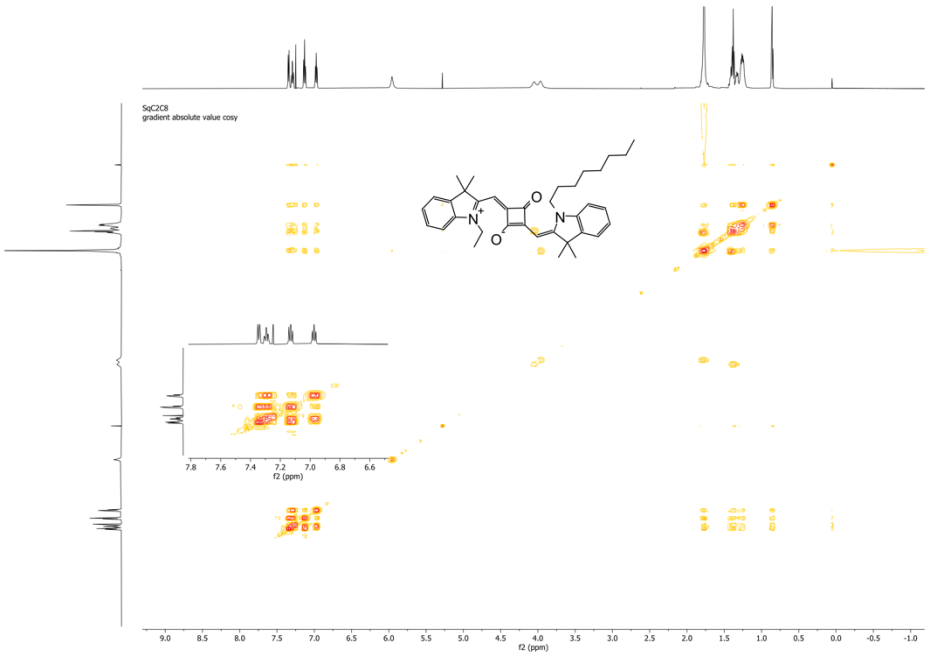

Figure S118. H,H COSY -NMR spectrum of 216 in $CDCl_3$.

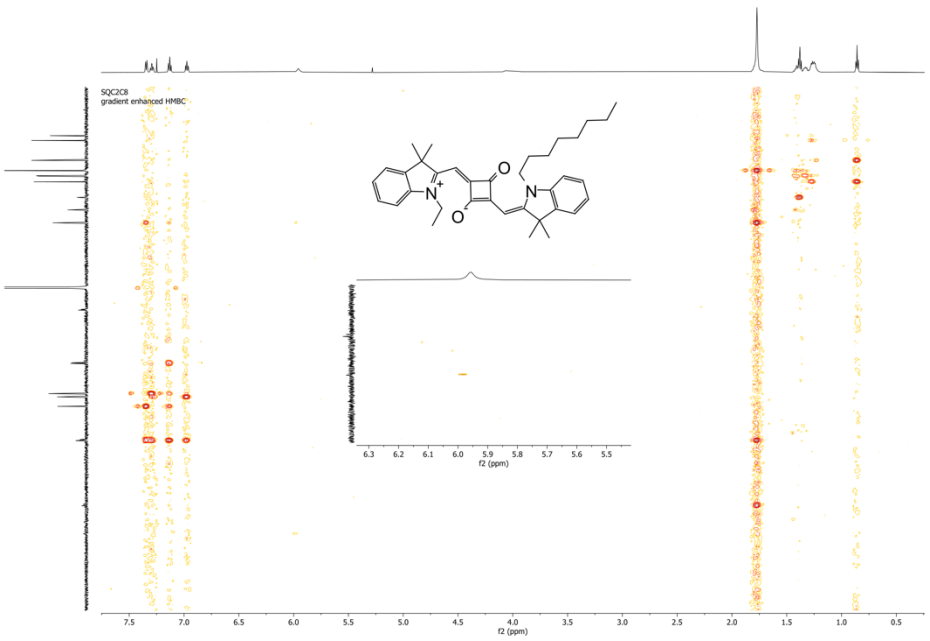

Figure S119. HMBC-NMR spectrum of 216 in $CDCl_3$.

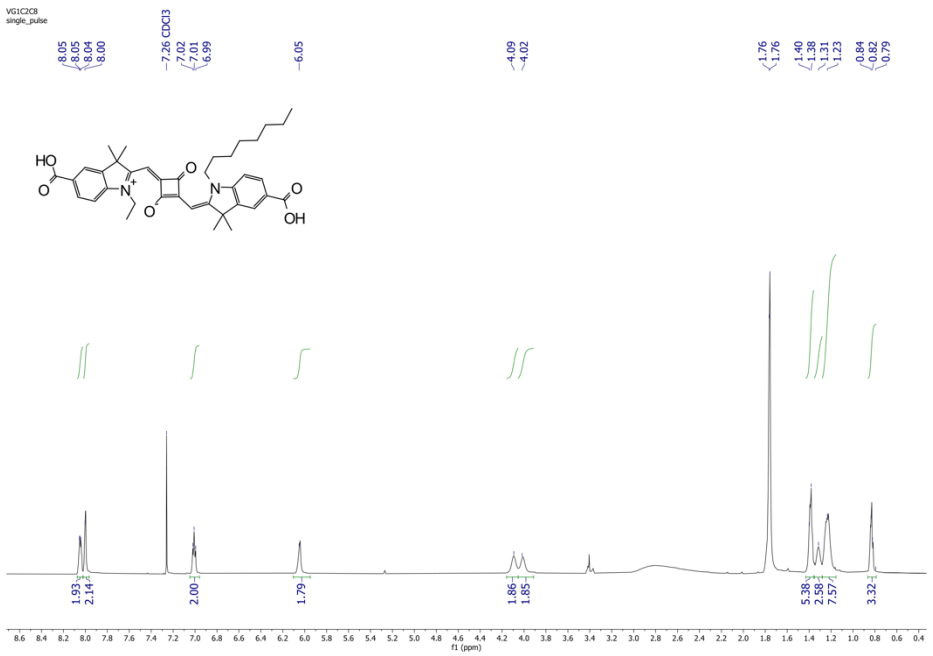

Figure S120. ^{1}H-NMR spectrum of 217 in $CDCl_3$.

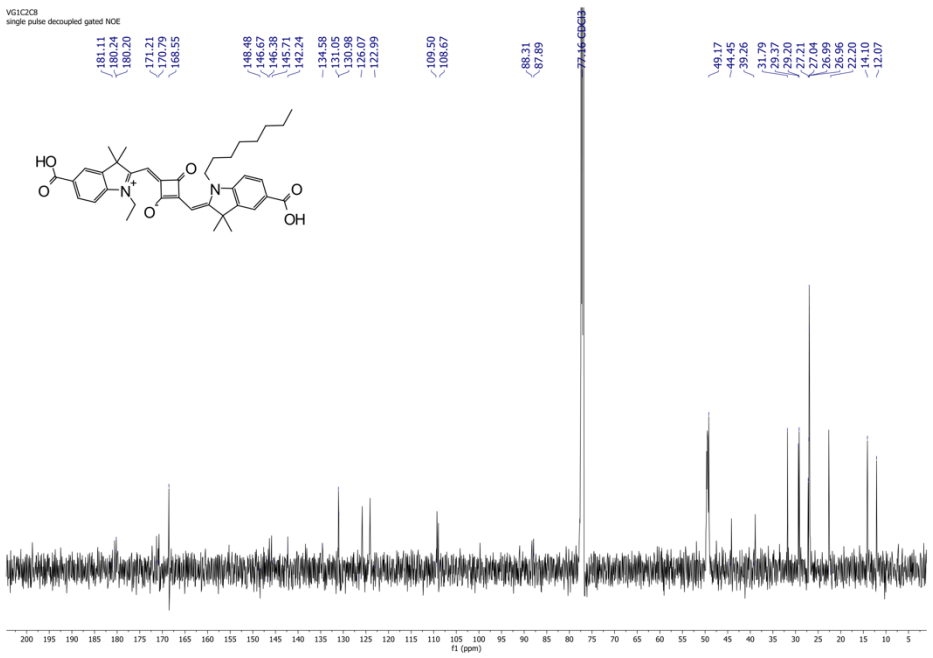

Figure S121. ^{13}C-NMR spectrum of 217 in $CDCl_3$.

Figure S122. H,H COSY -NMR spectrum of 217 in $CDCl_3$.

Figure S123. ^{1}H-NMR spectrum of 218 in $CDCl_3$.

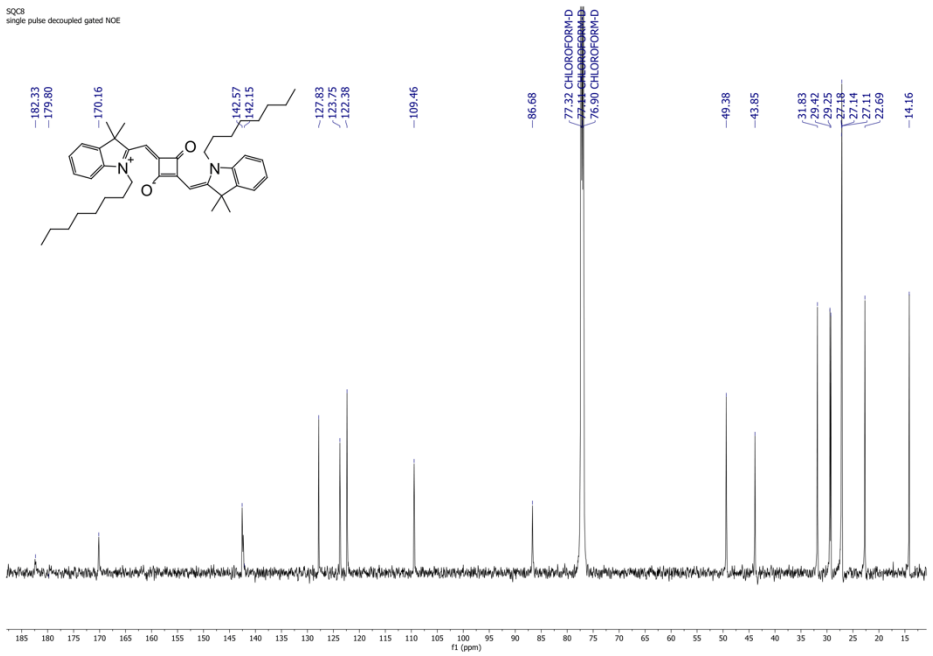

Figure S124. ^{13}C-NMR spectrum of 218 in $CDCl_3$.

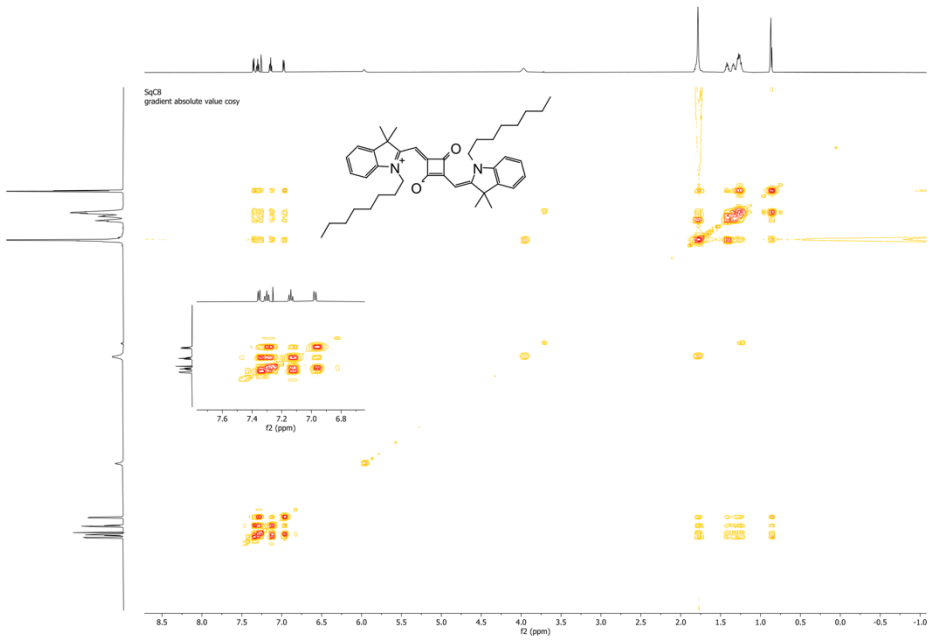

Figure S125. H,H COSY -NMR spectrum of 218 in $CDCl_3$.

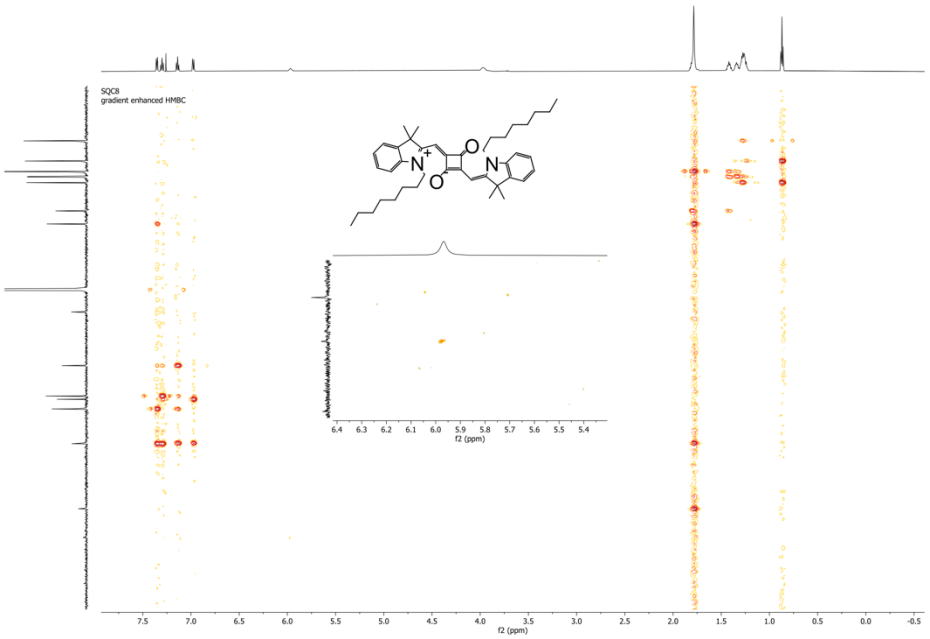

Figure S126. HMBC -NMR spectrum of 218 in $CDCl_3$.

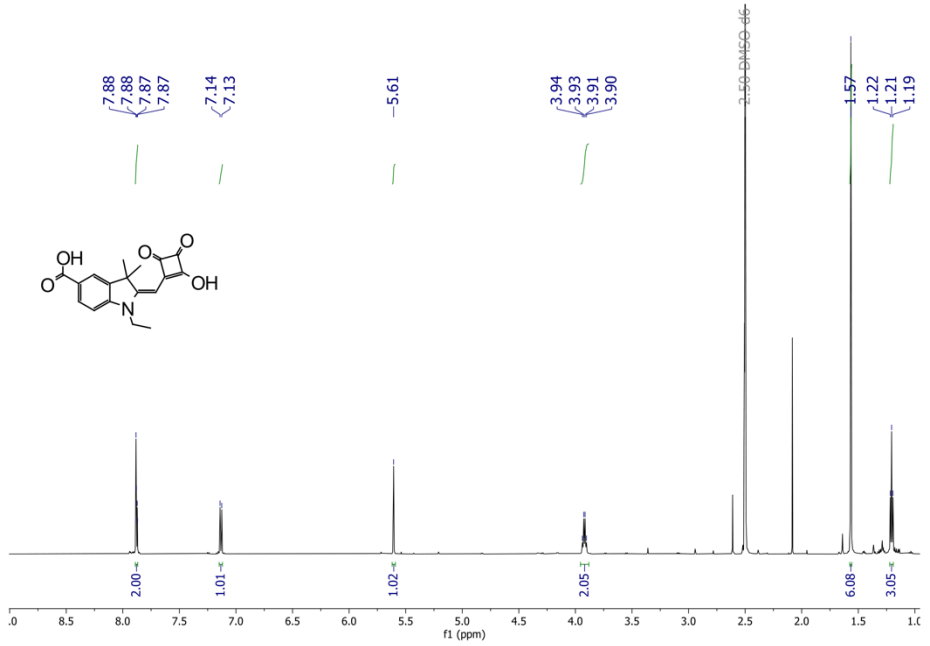

Figure S127. ^{1}H-NMR spectrum of 221 in $CDCl_3$.

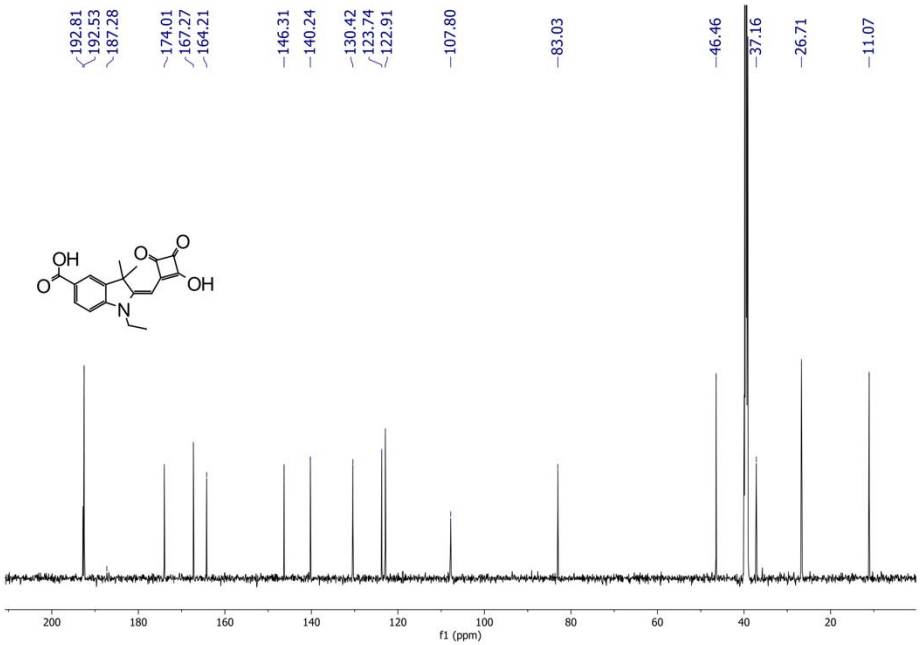

Figure S128. ^{13}C-NMR spectrum of 221 in $CDCl_3$.

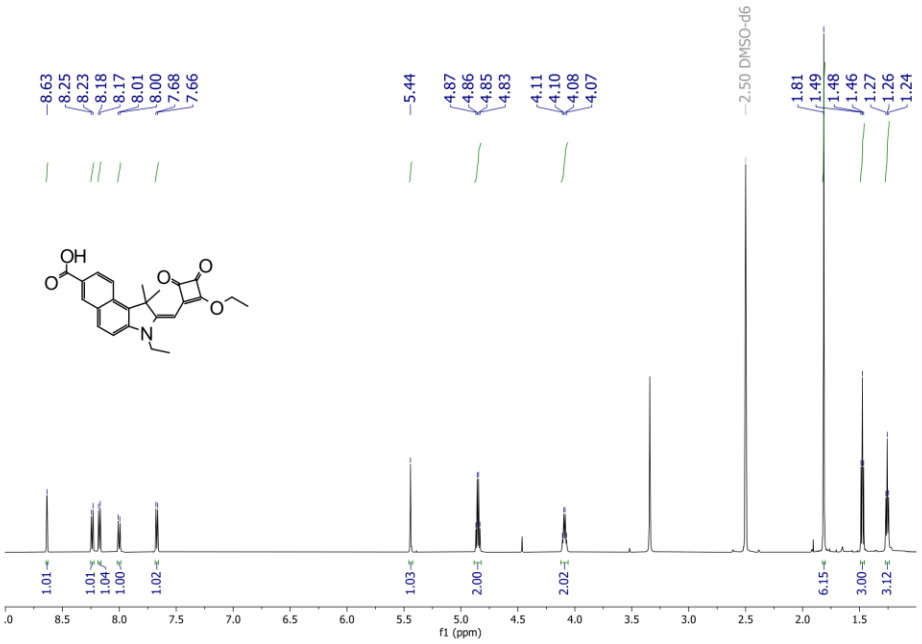

Figure S129. ^{1}H-NMR spectrum of 223 in $CDCl_3$.

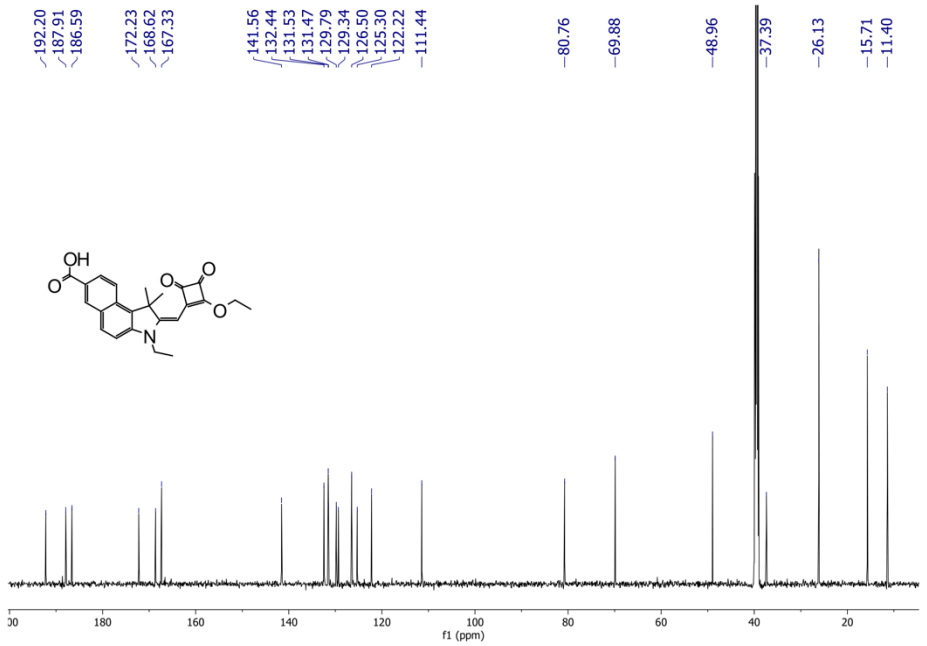

Figure S130. ^{13}C-NMR spectrum of 223 in $CDCl_3$.

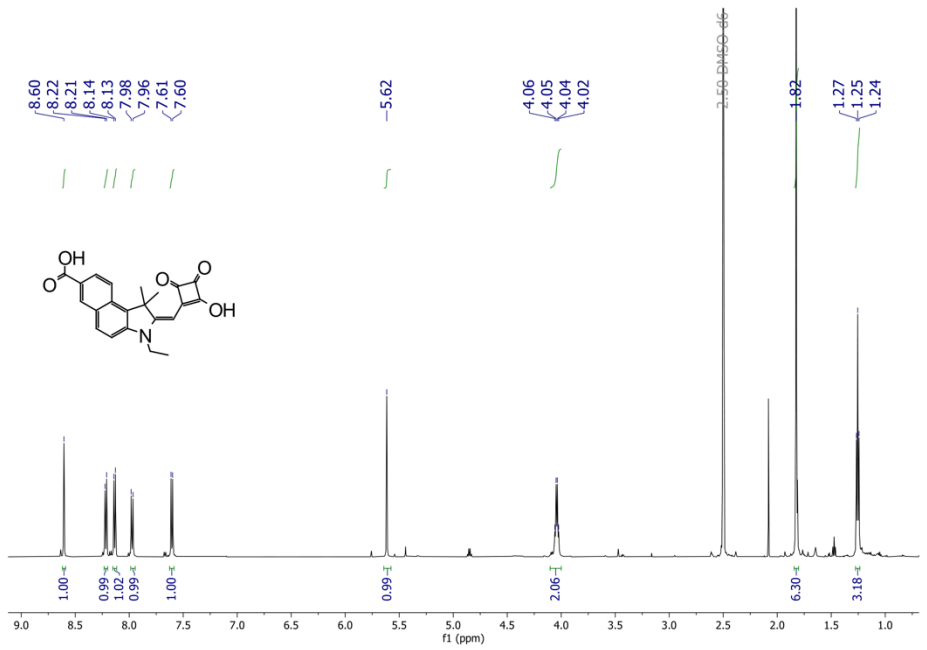

Figure S131. ^{1}H-NMR spectrum of 224 in $CDCl_3$.

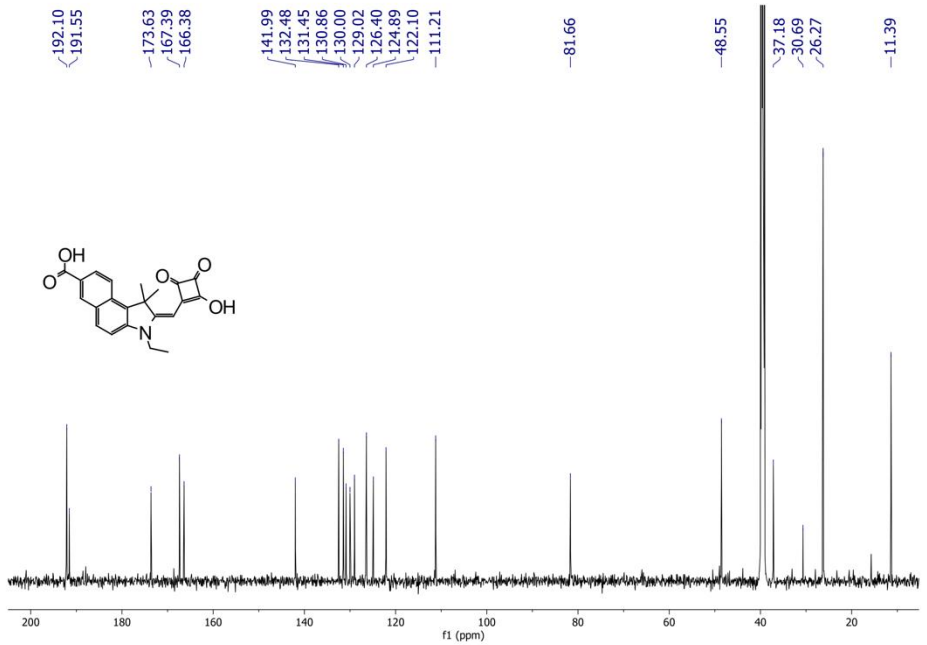

Figure S132. ^{13}C-NMR spectrum of 224 in $CDCl_3$.

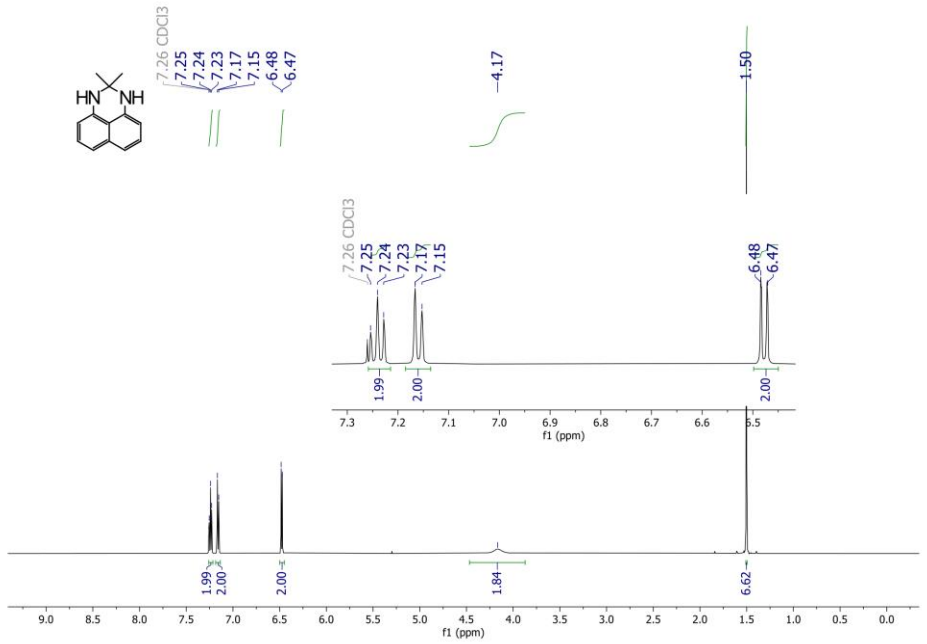

Figure S133. ^{1}H-NMR spectrum of 226a in $CDCl_3$.

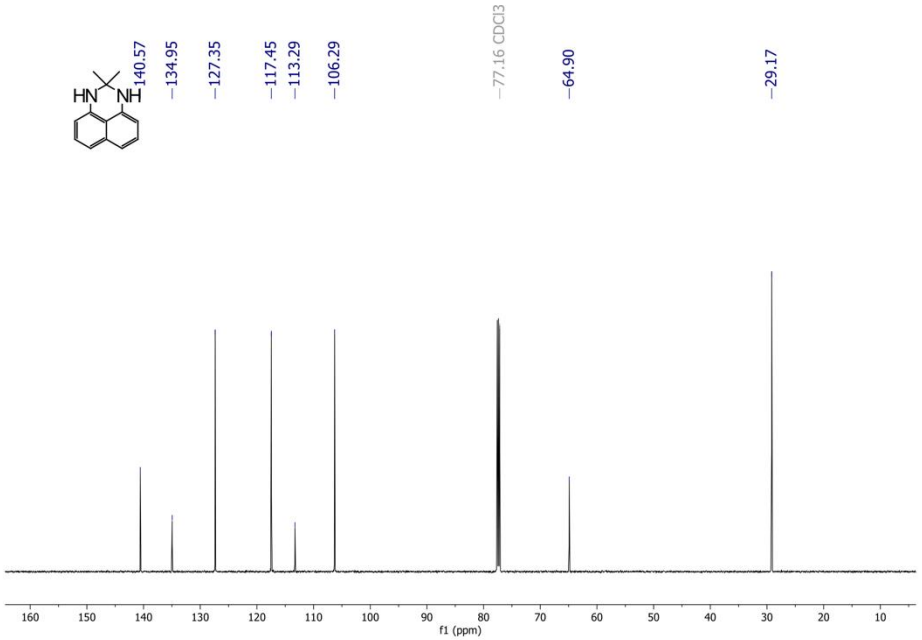

Figure S134. ^{13}C-NMR spectrum of 226a in $CDCl_3$.

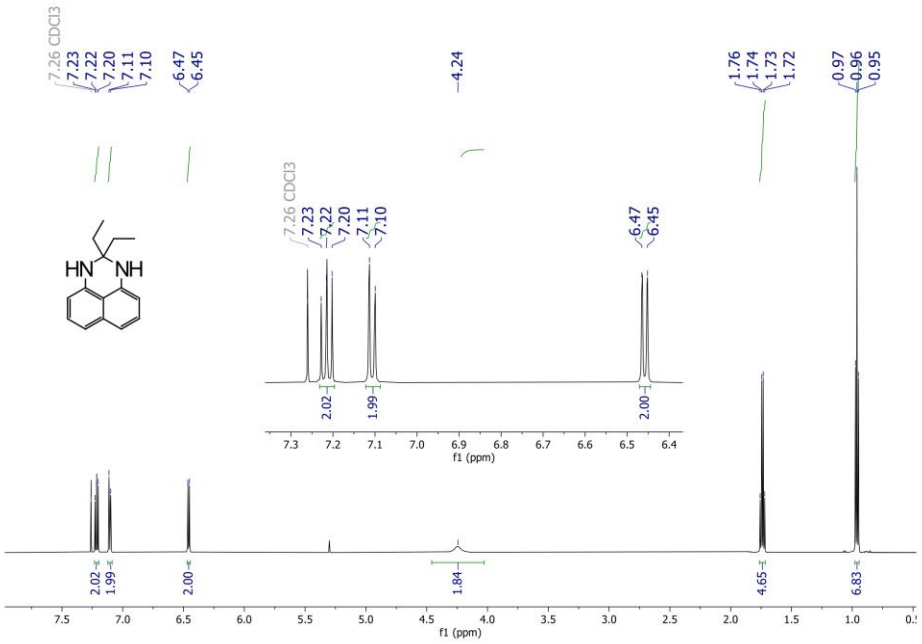

Figure S135. ^{1}H-NMR spectrum of 226b in $CDCl_3$.

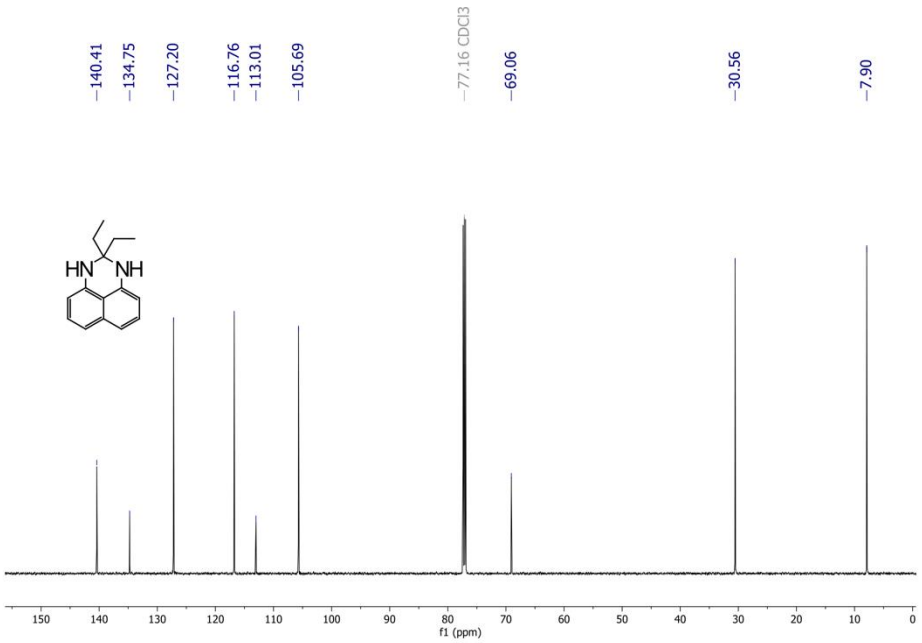

Figure S136. ^{13}C-NMR spectrum of 226b in $CDCl_3$.

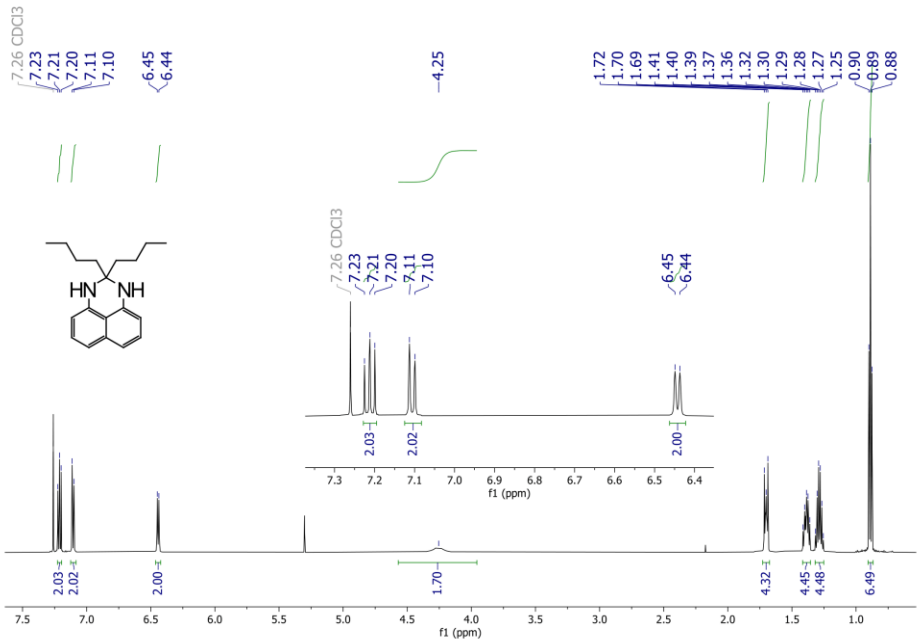

Figure S137. ^{1}H-NMR spectrum of 226c in $CDCl_3$.

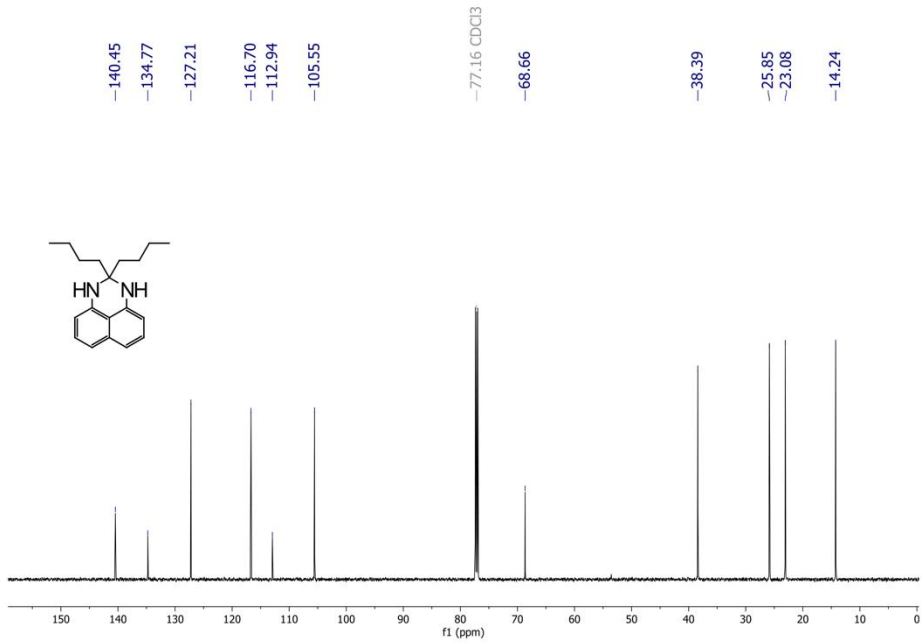

Figure S138. ^{13}C-NMR spectrum of 226c in $CDCl_3$.

Figure S139. ^{1}H-NMR spectrum of 226d in $CDCl_3$.

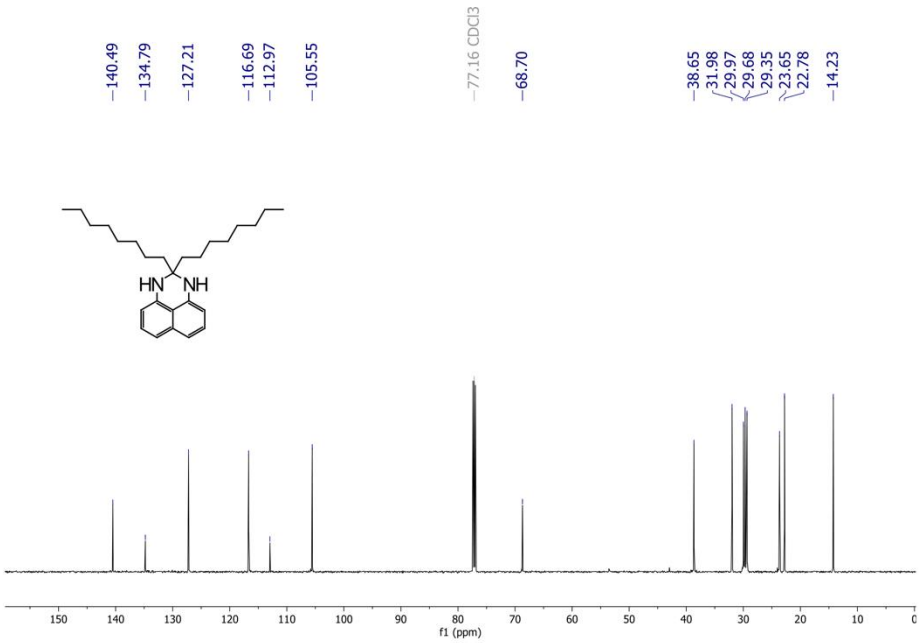

Figure S140. ^{13}C-NMR spectrum of 226d in $CDCl_3$.

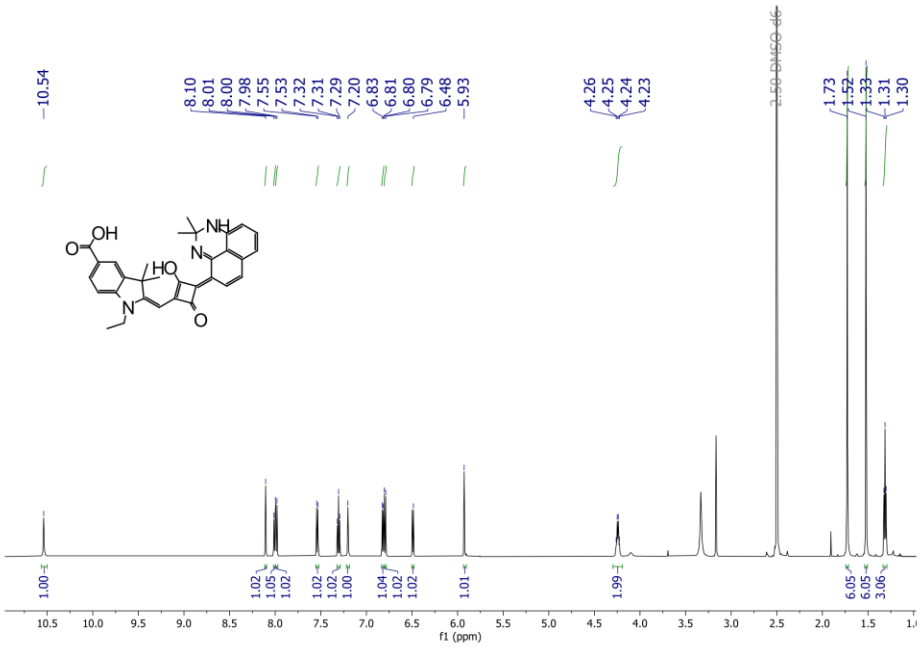

Figure S141. ^{1}H-NMR spectrum of 227 in $CDCl_3$.

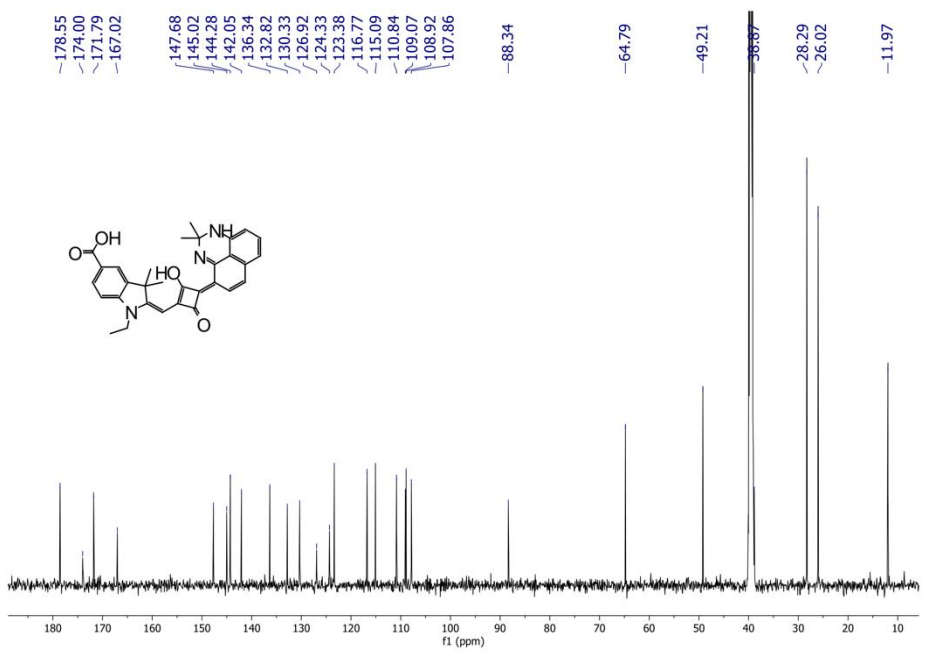

Figure S142. ^{13}C-NMR spectrum of 227 in $CDCl_3$.

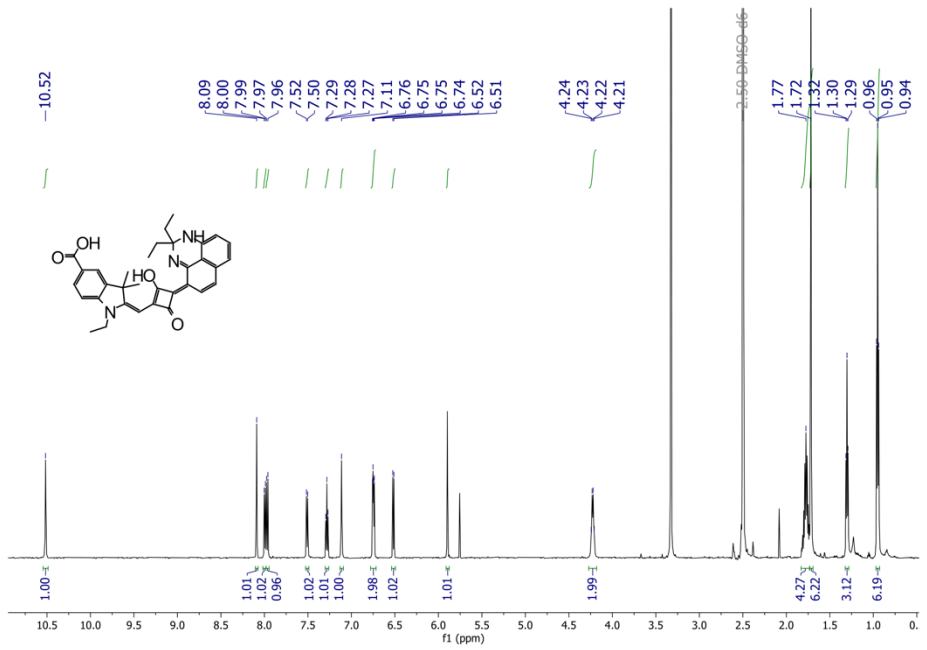

Figure S143. ^{1}H-NMR spectrum of 228 in $CDCl_3$.

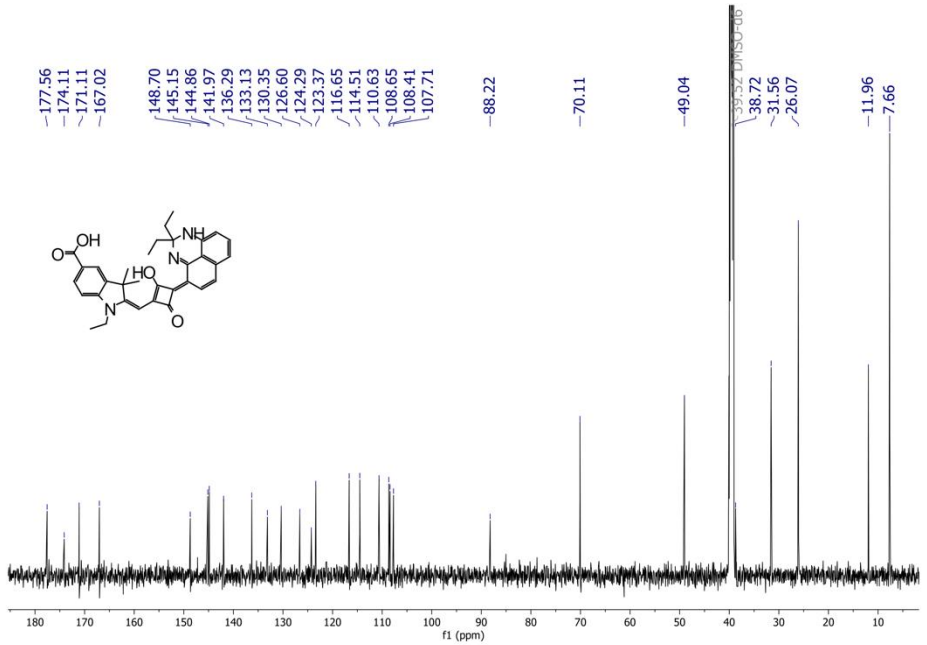

Figure S144. ^{13}C-NMR spectrum of 228 in $CDCl_3$.

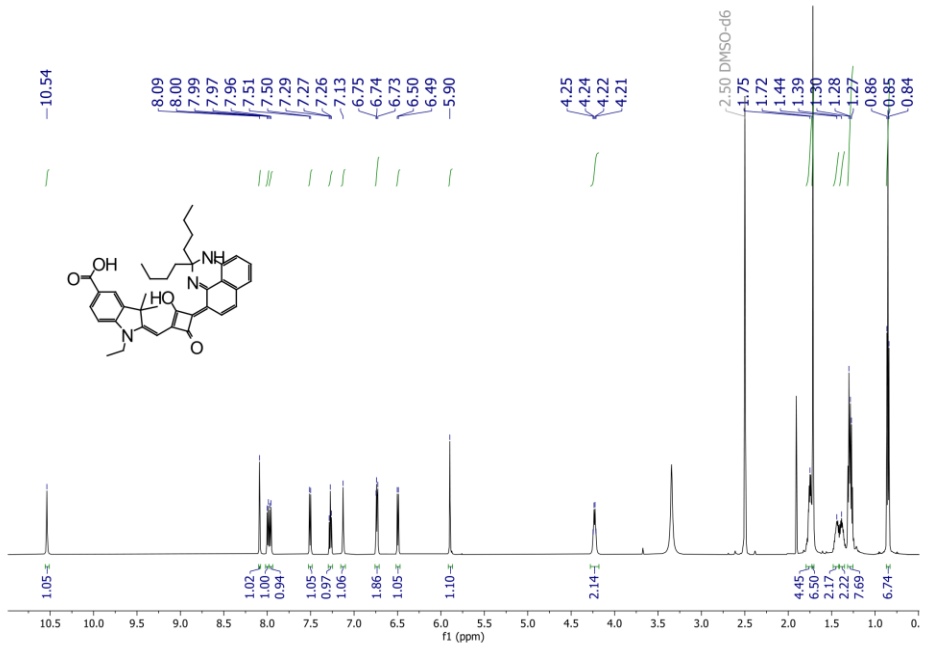

Figure S145. ^{1}H-NMR spectrum of 229 in $CDCl_3$.

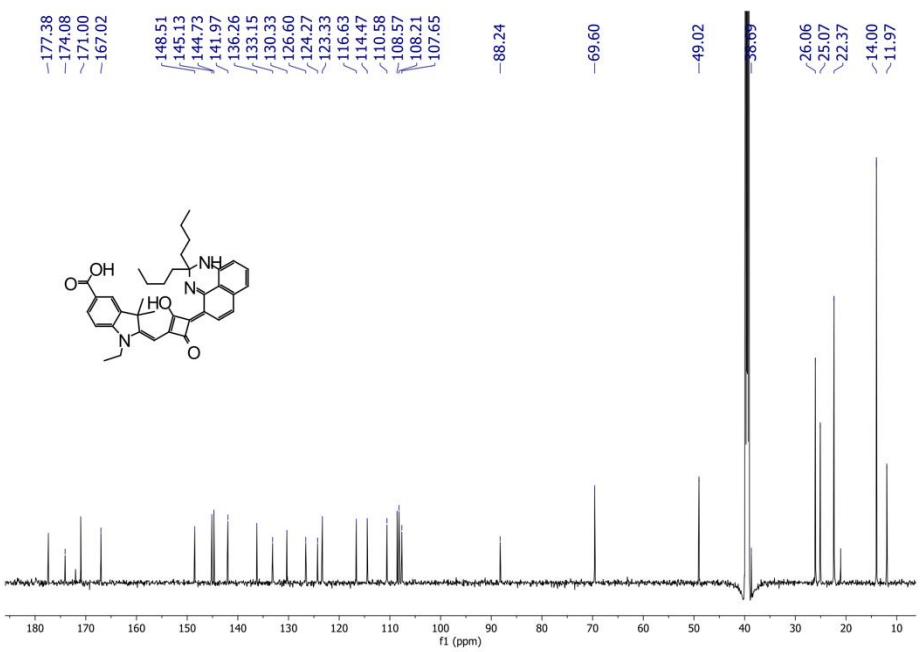

Figure S146. ^{13}C-NMR spectrum of 229 in $CDCl_3$.

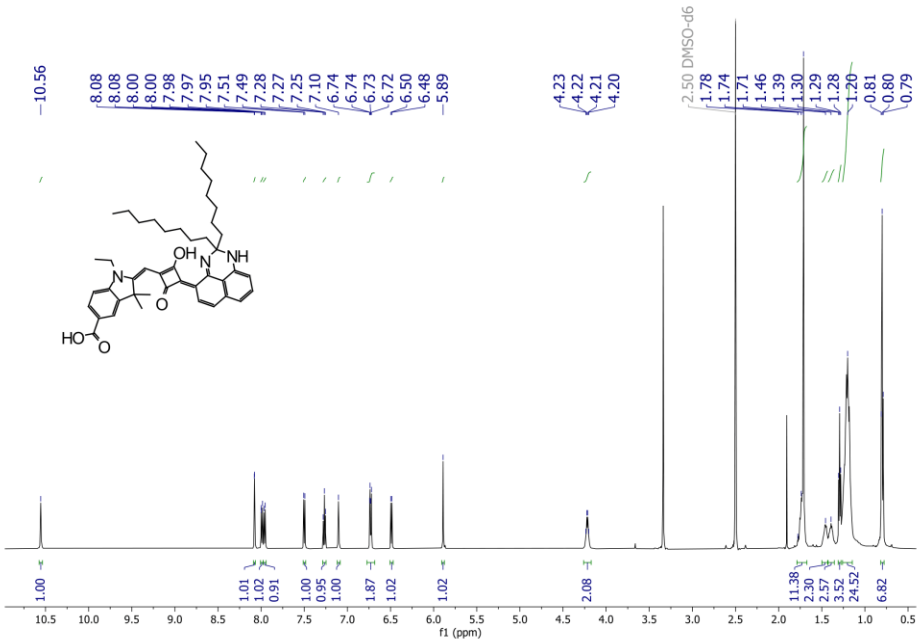

Figure S147. ^{1}H-NMR spectrum of 230 in $CDCl_3$.

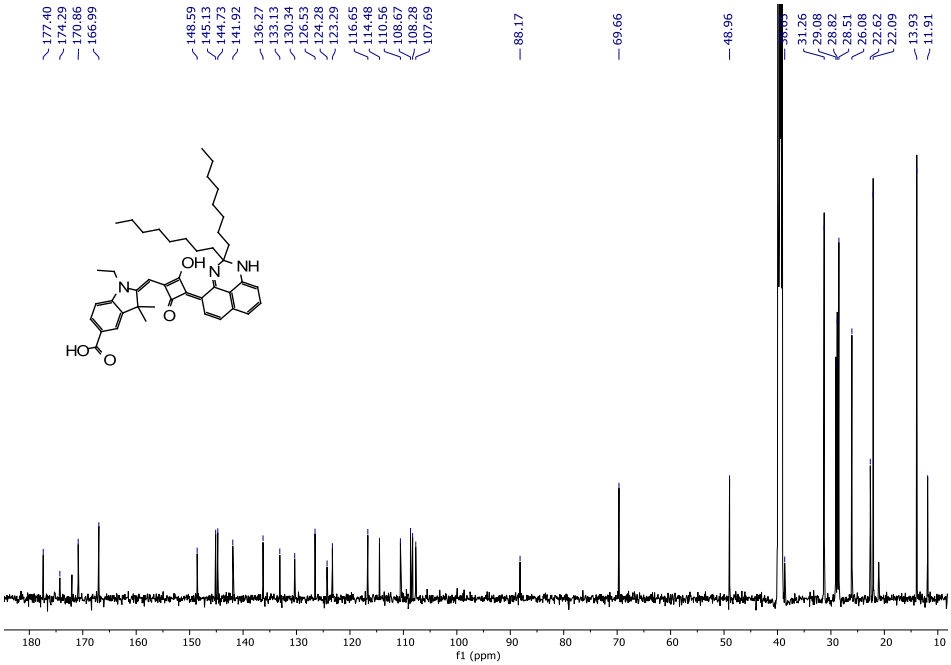

Figure S148. ^{13}C-NMR spectrum of 230 in $CDCl_3$.

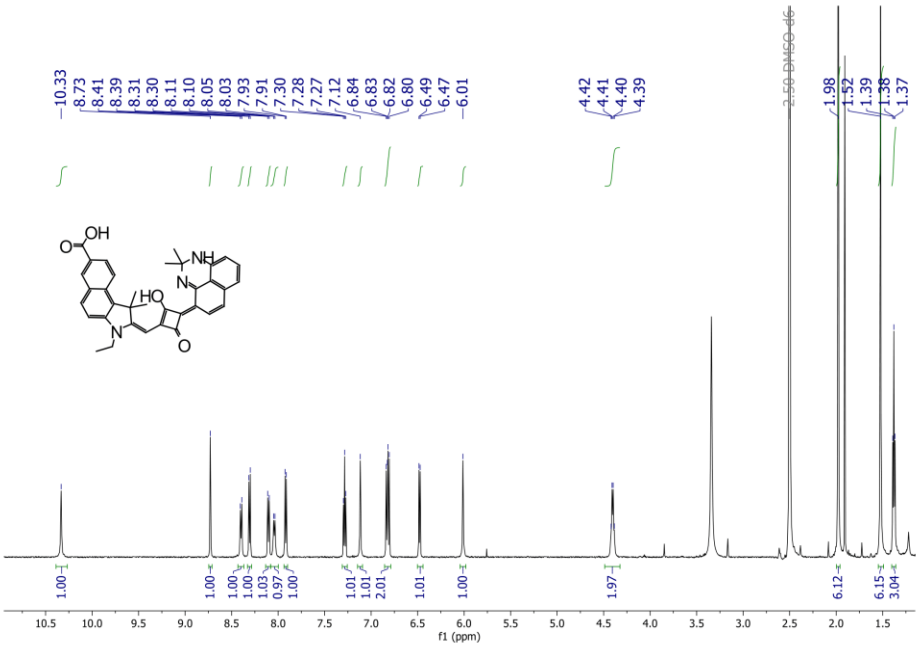

Figure S149. ^{1}H-NMR spectrum of 231 in $CDCl_3$.

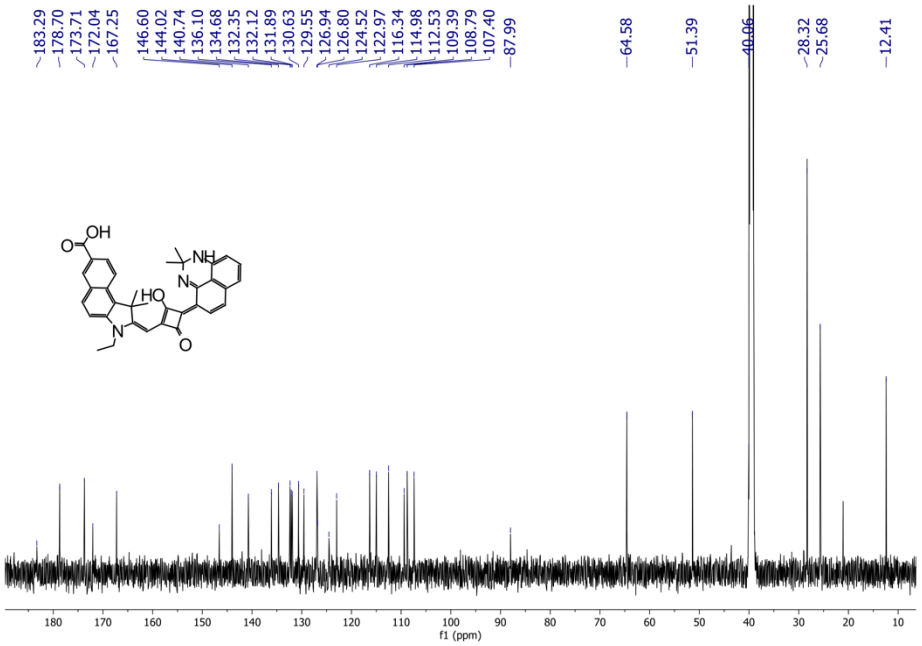

Figure S150. ^{13}C-NMR spectrum of 231 in $CDCl_3$.

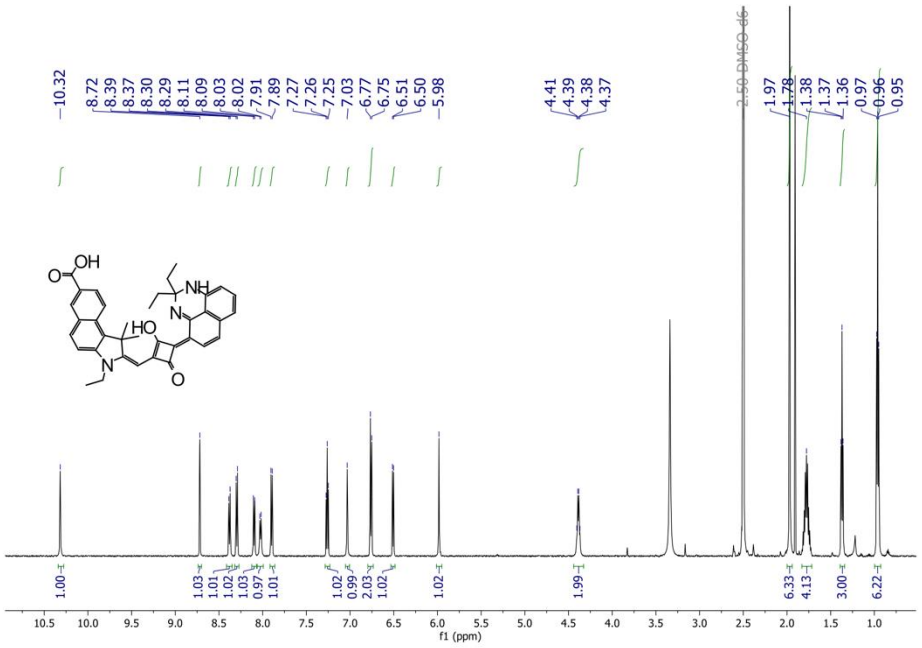

Figure S151. ^{1}H-NMR spectrum of 232 in $CDCl_3$.

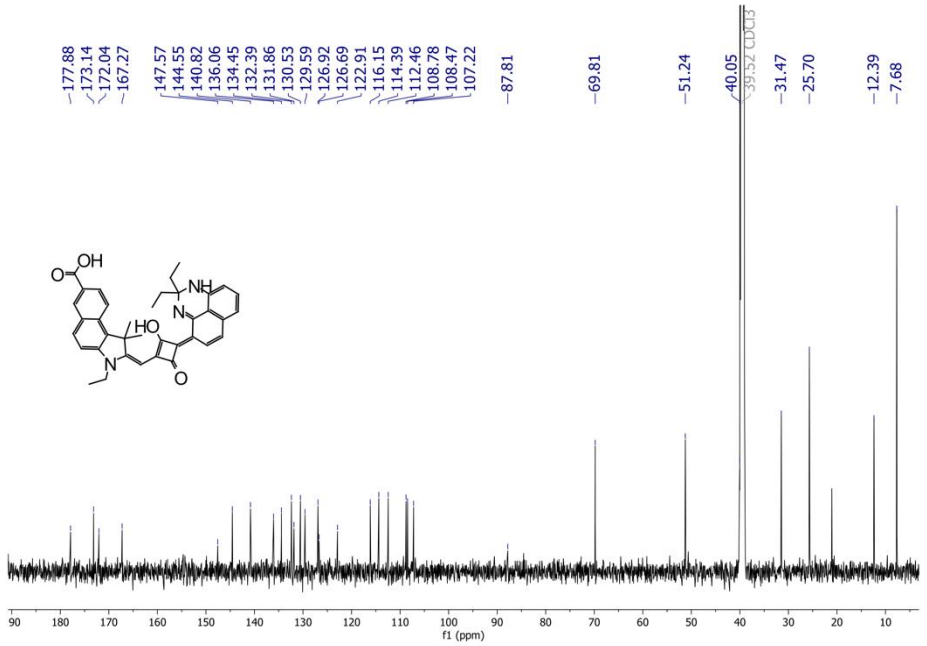

Figure S152. ^{13}C-NMR spectrum of 232 in $CDCl_3$.

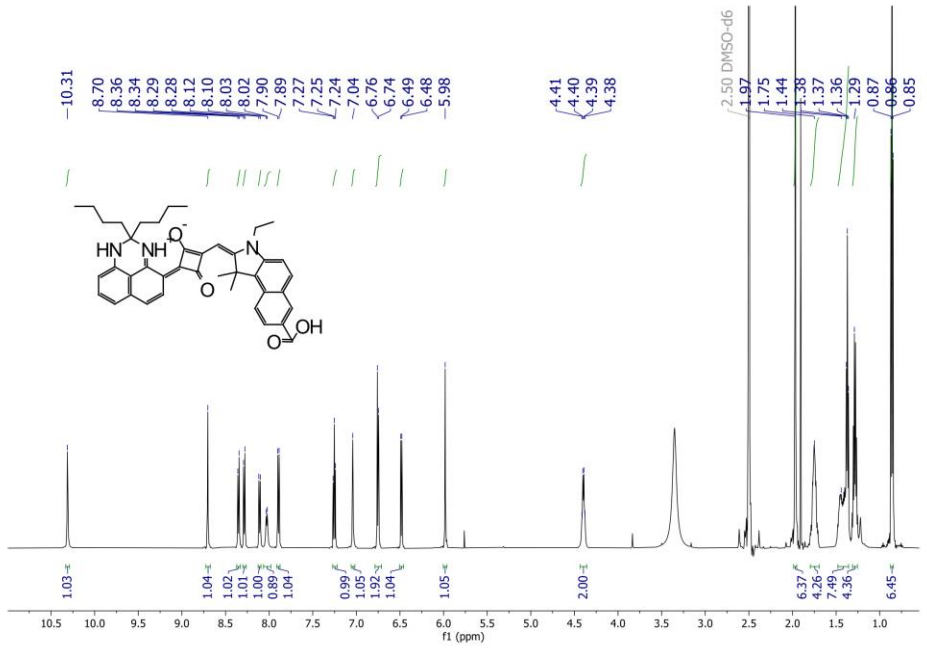

Figure S153. ^{1}H-NMR spectrum of 233 in $CDCl_3$.

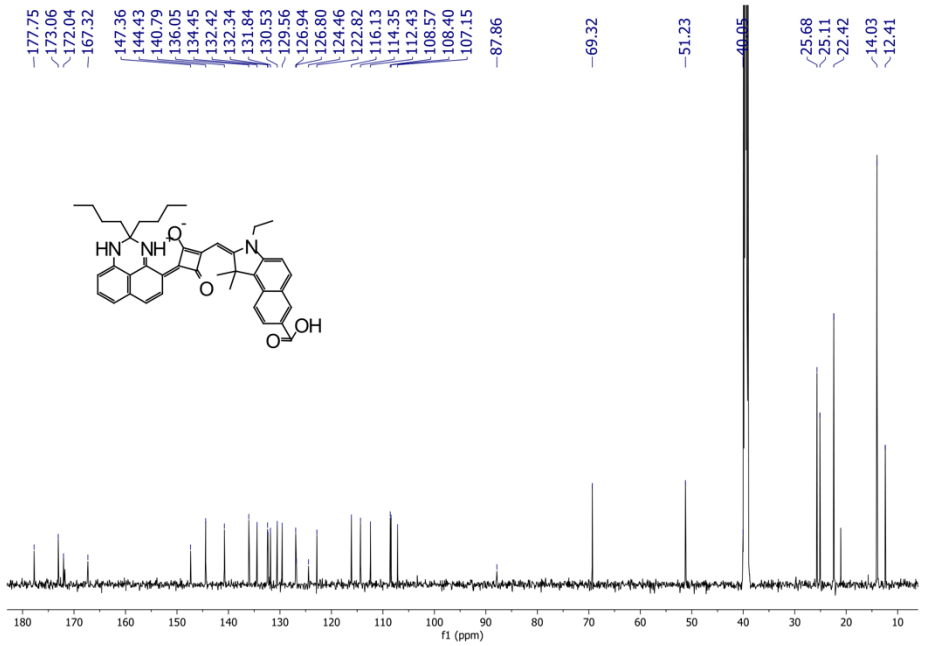

Figure S154. ^{13}C-NMR spectrum of 233 in $CDCl_3$.

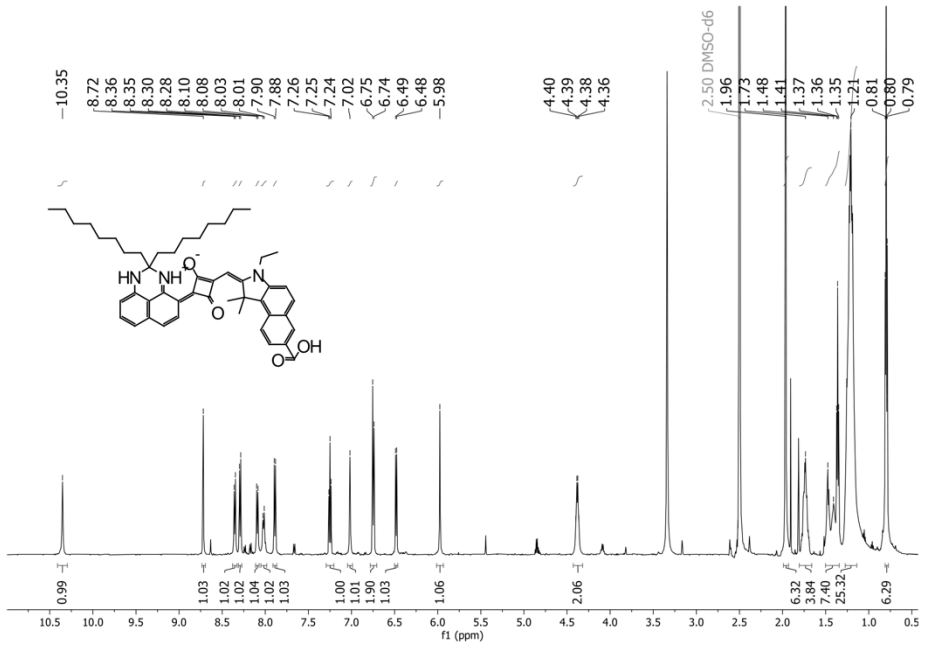

Figure S155. ^{1}H-NMR spectrum of 234 in $CDCl_3$.

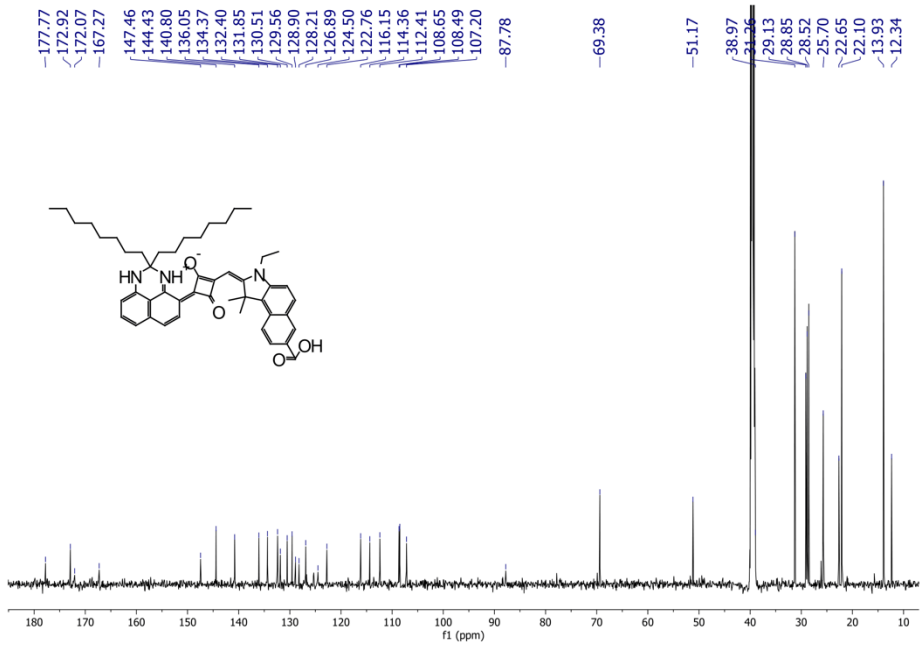

Figure S156. ^{13}C-NMR spectrum of 234 in $CDCl_3$.

REFERENCES

[1] https://commission.europa.eu/news/11th-citizens-energy-forum-empowering-consumers-clean-energy-transition-2019-09-12_en, .

[2] Y. You, Y. He, P. E. Burrows, S. R. Forrest, N. A. Petasis, M. E. Thompson, *Adv. Mater.* **2000**, *12*, 1678.

[3] S. H. Yun, S. J. J. Kwok, *Nat. Biomed. Eng.* **2017**, *1*, 8.

[4] J. R. Lakowicz, *Principe of Fluorescence Spectroscopy - 3rd Edition*, Springer, New York, **2006**.

[5] C. Buehler, J. Dreessen, K. Mueller, P. T. C. So, A. Schilb, U. Hassiepen, K. A. Stoeckli, M. Auer, *Assay Drug Dev. Technol.* **2005**, *3*, 155.

[6] J. K. A. Kamal, L. Zhao, A. H. Zewail, *Proc. Natl. Acad. Sci.* **2004**, *101*, 13411.

[7] J. R. Lakowicz, *Photochem. Photobiol.* **2000**, *72*, 421.

[8] A. T. Krueger, B. Imperiali, *ChemBioChem* **2013**, *14*, 788.

[9] G. Loving, B. Imperiali, *J. Am. Chem. Soc.* **2008**, *130*, 13630.

[10] G. Weber, F. J. Farris, *Biochemistry* **1979**, *18*, 3075.

[11] M. E. Vázquez, M. Nitz, J. Stehn, M. B. Yaffe, B. Imperiali, *J. Am. Chem. Soc.* **2003**, *125*, 10150.

[12] M. Nitz, A. R. Mezo, M. H. Ali, B. Imperiali, *Chem. Commun.* **2002**, 1912.

[13] K. Rittinger, J. Budman, J. Xu, S. Volinia, L. C. Cantley, S. J. Smerdon, S. J. Gamblin, M. B. Yaffe, *Mol. Cell* **1999**, *4*, 153.

[14] M. Eugenio Vázquez, D. M. Rothman, B. Imperiali, *Org. Biomol. Chem.* **2004**, *2*, 1965.

[15] M. E. Vázquez, J. B. Blanco, B. Imperiali, *J. Am. Chem. Soc.* **2005**, *127*, 1300.

[16] G. S. Loving, M. Sainlos, B. Imperiali, *Trends Biotechnol.* **2010**, *28*, 73.

[17] A. V Strizhak, V. Y. Postupalenko, V. V Shvadchak, N. Morellet, E. Guittet, V. G. Pivovarenko, A. S. Klymchenko, Y. Mély, *Bioconjug. Chem.* **2012**, *23*, 2434.

[18] K. E. Sapsford, L. Berti, I. L. Medintz, *Wiley Encycl. Chem. Biol.* **2008**, 1.

[19] T. D. Craggs, *Chem. Soc. Rev.* **2009**, *38*, 2865.

[20] S. Habuchi, R. Ando, P. Dedecker, W. Verheijen, H. Mizuno, A. Miyawaki, J. Hofkens, *Proc. Natl. Acad. Sci.* **2005**, *102*, 9511.

[21] V. Sample, R. H. Newman, J. Zhang, *Chem. Soc. Rev.* **2009**, *38*, 2852.

[22] S. H. Back, J. H. Park, C. Cui, D. J. Ahn, *Nat. Commun.* **2016**, *7*,

10234.
[23] A. J. Steckl, *Nat. Photonics* **2007**, *1*, 3.
[24] Y. Kawabe, L. Wang, S. Horinouchi, N. Ogata, *Adv. Mater.* **2000**, *12*, 1281.
[25] G. S. He, Q. Zheng, P. N. Prasad, J. G. Grote, F. K. Hopkins, *Opt. Lett.* **2006**, *31*, 359.
[26] H. J. Round, *Electr. World* **1907**, *49*.
[27] H. Wellker, *Semiconductor devices and methods of their manufacture*, **1957**.
[28] G. A. Wolff, R. A. Hebert, J. D. Broder, *Phys. Rev.* **1955**, *100*, 1144.
[29] O. G. Folberth, *Zeitschrift für Naturforsch. A* **1955**, *10a*, 502.
[30] G. Rostky, *http://www.datamath.org/Display/Monsanto.html*, **1997**.
[31] H. Rupprecht, J. M. Woodall, K. Konnerth, D. G. Pettit, *Appl. Phys. Lett.* **1966**, *9*, 221.
[32] J. M. Woodall, R. M. Potemski, S. E. Blum, R. Lynch, *Appl. Phys. Lett.* **1972**, *20*, 375.
[33] J. I. Pankove, E. A. Miller, D. Richman, J. E. Berkeyheiser, *J. Lumin.* **1971**, *4*, 63.
[34] https://www.nobelprize.org/prizes/physics/2014/press-release/, **2014**.
[35] J. W. Stinson, *US Patent 4*, **1991**, pp. 992, 704.
[36] J. Cho, J. H. Park, J. K. Kim, E. F. Schubert, *Laser Photon. Rev.* **2017**, *11*, 1600147.
[37] R. M. Potter, P. Pike, S. V. Galginaitis, *Light-emitting phosphor-diode combination, US Patent 3*, **3AD**, pp. 529, 200.
[38] S. Tabuchi, *Light emitting semiconductor apparatus, Japanese Utility Model Patent Application Publication No. S50-79379*, **1973**.
[39] D. A. Stevenson, W. C. Rhines, H. P. Maruska, *Gallium nitride metal-semiconductor junction light emitting diode, US Patent 3*, **1974**, pp. 819, 974.
[40] H. Tokailin, C. Hosokawa, *Electroluminescent element, US Patent 5*, **1992**, pp. 126, 214.
[41] Y. Shimizu, *Planar light source, Japanese Patent Application Publication H08-7614*, **1996**.
[42] B. Baretz, M. A. Tischler, *Solid-state white light emitter and display using the same, US Patent 6*, **2003**, pp. 600, 175.
[43] U. Reeh, K. Höhn, N. Stath, G. Waitl, P. Schlotter, J. Schneider, R. Schmidt, *Light-radiating semiconductor component with luminescence conversion element, US patent 7*, **1996**, p. 078,732.
[44] Y. Shimizu, K. Sakano, Y. Noguchi, T. Moriguchi, *Light-emitting device having a nitride compound semiconductor and a phosphor containing a garnet fluorescent material, US Patent 5*, **1999**, pp. 998, 925.
[45] R. Haitz, F. Kish, J. Tsao, J. Nelson, R. K. Haitz F. Tsao, J. Nelson,

J, *Optoelectron. Ind. Dev. Assoc. forum* **2000**, 1.
[46] E. F. Schubert, *Light-Emitting Diodes*, 2nd ed., Cambridge University Press, **2006**.
[47] http://hyperphysics.phy-astr.gsu.edu/hbase/wien.html, .
[48] H. A. Olanrewaju, W. W. Miller, W. R. Maslin, S. D. Collier, J. L. Purswell, S. L. Branton, *Poult. Sci.* **2016**, *95*, 727.
[49] G. Tosini, I. Ferguson, K. Tsubota, *Mol. Vis.* **2016**, *22*, 61.
[50] S. Wahl, M. Engelhardt, P. Schaupp, C. Lappe, I. V Ivanov, *J. Biophotonics* **2019**, *12*, e201900102.
[51] X. Min, Z. Huang, M. Fang, Y.-G. Liu, C. Tang, X. Wu, *Inorg. Chem.* **2014**, *53*, 6060.
[52] X.-H. He, N. Lian, J.-H. Sun, M.-Y. Guan, *J. Mater. Sci.* **2009**, *44*, 4763.
[53] H. Yu, W. W. Zi, S. Lan, H. F. Zou, S. C. Gan, X. C. Xu, G. Y. Hong, *Mater. Res. Innov.* **2012**, *16*, 298.
[54] V. Tucureanu, A. Matei, A. M. Avram, **2015**, *23*, 239.
[55] C.-C. Chiang, M.-S. Tsai, M.-H. Hon, *J. Electrochem. Soc.* **2008**, *155*, B517.
[56] M. Pattison, M. Hansen, N. Bardsley, G. Thomson, K. Gordon, A. Wilkerson, K. Lee, V. Nubbe, S. Donnelly, 2022,.
[57] E. Commission, I. Directorate-General for Internal Market Entrepreneurship and SMEs, *Study on the review of the list of critical raw materials: final report*, Publications Office, **2017**.
[58] U. S. Department of the Interior, *Fed. Regist.* **2018**, *83*, 23295.
[59] S. Ahonen, N. Arvanitidis, A. Auer, E. Baillet, N. Bellato, K. Binnemans, G. A. Blengini, D. Bonato, E. Brouwer, S. Brower, M. Buchert, R. Bütikofer, H. C. Viegas, J. P. Cescutti, A. Chmielarz, P. Christmann, C. Claessen, G. Cozigou, D. de Oliveira, É. A. Deady, R. Denis, F. Pulido, M. Edvardsson, D. Fontana, C. Forsgren, J.-C. P. Gabriel, R. Gauss, M. Gernuks, A. J. Gibbon, M. Gislev, J. R. J. Goddin, M. Gómez, M. Gonçalves, K. M. Goodenough, T. Graupner, M. Grohol, O. Gutfleisch, J. Gutzmer, H. Hejny, H. L. O. Holmstrom, S. Hredzák, E. Jernström, A. Jha, P. Kalvig, R. Kefferputz, D. Kennedy, J. Kooroshy, F. La Marca, O. Larcher, M. Leijd, H. B. M. Lenting, F. D. Lindner, E. Loois, P. L. Vicente, P. A. J. Lusty, T. Makanyire, P. Millet, A. Morales, Z. Németh, A. Ocera, E. J. Offerman, K. D. Papavasileiou, I. Paspaliaris, D. P. Peck, M. Pellegrini, S. Pellet-Rostaing, U. A. Peuker, M. Quix, M. L. Räisänen, E. V. Redondo, X. Revest, A. Rollat, J. Salminen, S. Sanchez-Segad, I. Santavaara, G. Schmidt, R. S. Sheridan, A. S. L. Sjöqvist, S. V \vSolar, M. Sundgren, C. Tattam, M. Taxiarchou, M. Taylor, G. Tiess, A. Tukker, C. van der Eijk, A. Van Maercke, J. van Veen, S. Vecchione, K. C. Vrancken, H. Le Vu, A. Walton, E. Westin, A. Wittenberg, H. Wotruba, G. Ye, S. Zaleski,

Strengthening the European rare earths supply-chain. Challenges and policy options, **2015**.
[60] S.-H. Shin, H.-O. Kim, K.-T. Rim, *Saf. Health Work* **2019**, *10*, 409.
[61] M. Edahbi, B. Plante, M. Benzaazoua, *J. Clean. Prod.* **2019**, *212*, 1232.
[62] Y. Kanazawa, M. Kamitani, *J. Alloys Compd.* **2006**, *408–412*, 1339.
[63] J. R. Tuenge, B. J. Hollomon, H. E. Dillon, L. J. Snowden-Swan, *Life-Cycle Assessment of Energy and Environmental Impacts of LED Lighting Products, Part 3: LED Environmental Testing*, **2013**.
[64] P. Gaffuri, E. Stolyarova, D. Llerena, E. Appert, M. Consonni, S. Robin, V. Consonni, *Renew. Sustain. Energy Rev.* **2021**, *143*, 110869.
[65] McKinsey Global Institute, *Manufacturing the future: The next era of global growth and innovation*, **2018**.
[66] H. Lu, Z. Huang, M. S. Martinez, J. C. Johnson, J. M. Luther, M. C. Beard, *Energy Environ. Sci.* **2020**, *13*, 1347.
[67] Y. Xu, X. Wang, W. L. Zhang, F. Lv, S. Guo, *Chem. Soc. Rev.* **2018**, *47*, 586.
[68] B. Li, M. Lu, J. Feng, J. Zhang, P. M. Smowton, J. I. Sohn, I.-K. Park, H. Zhong, B. Hou, *J. Mater. Chem. C* **2020**, *8*, 10676.
[69] T. VanWie, E. Wysocki, J. R. McBride, S. J. Rosenthal, *Chem. Mater.* **2019**, *31*, 8558.
[70] X. Wang, Y. Guo, Z. Li, W. Ying, D. Chen, Z. Deng, X. Peng, *RSC Adv.* **2019**, *9*, 9777.
[71] H. Zhang, H. Zhang, A. Pan, B. Yang, L. He, Y. Wu, *Adv. Mater. Technol.* **2021**, *6*, 1.
[72] N. Le, M. Zhang, K. Kim, *Quantum Dots and Their Interaction with Biological Systems*, Vol. 23, **2022**.
[73] http://data.europa.eu/eli/dir_del/2017/1975/oj, .
[74] O. Karatum, H. B. Jalali, S. Sadeghi, R. Melikov, S. B. Srivastava, S. Nizamoglu, *ACS Photonics* **2019**, *6*, 939.
[75] M. Bidikoudi, E. Fresta, R. D. Costa, *Chem. Commun.* **2018**, *54*, 8150.
[76] H. Huang, A. S. Susha, S. V Kershaw, T. F. Hung, A. L. Rogach, *Adv. Sci.* **2015**, *2*, 1500194.
[77] X. Li, F. Cao, D. Yu, J. Chen, Z. Sun, Y. Shen, Y. Zhu, L. Wang, Y. Wei, Y. Wu, H. Zeng, *Small* **2017**, *13*, 1603996.
[78] S. Pathak, N. Sakai, F. Wisnivesky Rocca Rivarola, S. D. Stranks, J. Liu, G. E. Eperon, C. Ducati, K. Wojciechowski, J. T. Griffiths, A. A. Haghighirad, A. Pellaroque, R. H. Friend, H. J. Snaith, *Chem. Mater.* **2015**, *27*, 8066.
[79] K. Bi, D. Wang, P. Wang, B. Duan, T. Zhang, Y. Wang, H. Zhang, Y. Zhang, *J. Nanoparticle Res.* **2017**, *19*, 174.
[80] H. C. Yoon, H. Kang, S. Lee, J. H. Oh, H. Yang, Y. R. Do, *ACS*

Appl. Mater. Interfaces **2016**, *8*, 18189.
[81] C. Sun, Y. Zhang, C. Ruan, C. Yin, X. Wang, Y. Wang, W. W. Yu, *Adv. Mater.* **2016**, *28*, 10088.
[82] J. Li, J. Yan, D. Wen, W. U. Khan, J. Shi, M. Wu, Q. Su, P. A. Tanner, *J. Mater. Chem. C* **2016**, *4*, 8611.
[83] H. F. Sijbom, R. Verstraete, J. J. Joos, D. Poelman, P. F. Smet, *Opt. Mater. Express* **2017**, *7*, 3332.
[84] P. Dorenbos, *J. Phys. Condens. Matter* **2005**, *17*, 8103.
[85] P. Arunkumar, Y. H. Kim, H. J. Kim, S. Unithrattil, W. Bin Im, *ACS Appl. Mater. Interfaces* **2017**, *9*, 7232.
[86] R. Verstraete, H. F. Sijbom, J. J. Joos, K. Korthout, D. Poelman, C. Detavernier, P. F. Smet, *ACS Appl. Mater. Interfaces* **2018**, *10*, 18845.
[87] R. Verstraete, G. Rampelberg, H. Rijckaert, I. Van Driessche, E. Coetsee, M.-M. Duvenhage, P. F. Smet, C. Detavernier, H. Swart, D. Poelman, *Chem. Mater.* **2019**, *31*, 7192.
[88] H.-D. Nguyen, C. C. Lin, R.-S. Liu, *Angew. Chemie Int. Ed.* **2015**, *54*, 10862.
[89] G. Heliotis, P. N. Stavrinou, D. D. C. Bradley, E. Gu, C. Griffin, C. W. Jeon, M. D. Dawson, *Appl. Phys. Lett.* **2005**, *87*, 103505.
[90] I. O. Huyal, U. Koldemir, T. Ozel, H. V. Demir, D. Tuncel, *J. Mater. Chem.* **2008**, *18*, 3568.
[91] E. Gu, H. X. Zhang, H. D. Sun, M. D. Dawson, A. R. Mackintosh, A. J. C. Kuehne, R. A. Pethrick, C. Belton, D. D. C. Bradley, *Appl. Phys. Lett.* **2007**, *90*, 31116.
[92] C.-Y. Sun, X.-L. Wang, X. Zhang, C. Qin, P. Li, Z.-M. Su, D.-X. Zhu, G.-G. Shan, K.-Z. Shao, H. Wu, J. Li, *Nat. Commun.* **2013**, *4*, 2717.
[93] Q. Gong, Z. Hu, B. J. Deibert, T. J. Emge, S. J. Teat, D. Banerjee, B. Mussman, N. D. Rudd, J. Li, *J. Am. Chem. Soc.* **2014**, *136*, 16724.
[94] H. Tetsuka, A. Nagoya, R. Asahi, *J. Mater. Chem. C* **2015**, *3*, 3536.
[95] D. Zhou, H. Zou, M. Liu, K. Zhang, Y. Sheng, J. Cui, H. Zhang, B. Yang, *ACS Appl. Mater. Interfaces* **2015**, *7*, 15830.
[96] L. Niklaus, H. Dakhil, M. Kostrzewa, P. B. Coto, U. Sonnewald, A. Wierschem, R. D. Costa, *Mater. Horiz.* **2016**, *3*, 340.
[97] O. N. Ermakov, M. G. Kaplunov, O. N. Efimov, I. K. Yakushchenko, M. Y. Belov, M. F. Budyka, *Microelectron. Eng.* **2003**, *69*, 208.
[98] H.-F. Xiang, S.-C. Yu, C.-M. Che, P. T. Lai, *Appl. Phys. Lett.* **2003**, *83*, 1518.
[99] D. Di Martino, L. Beverina, M. Sassi, S. Brovelli, R. Tubino, F. Meinardi, *Sci. Rep.* **2014**, *4*, 4400.
[100] S. Guha, R. A. Haight, N. A. Bojarczuk, D. W. Kisker, *J. Appl. Phys.* **1997**, *82*, 4126.
[101] N. J. Findlay, J. Bruckbauer, A. R. Inigo, B. Breig, S. Arumugam,

D. J. Wallis, R. W. Martin, P. J. Skabara, *Adv. Mater.* **2014**, *26*, 7290.
[102] J. He, S. Yang, K. Zheng, Y. Zhang, J. Song, J. Qu, *Green Chem.* **2018**, *20*, 3557.
[103] C.-F. Lai, C.-J. Chang, C.-L. Hsieh, Y.-L. Chen, C.-S. Tuan, *Opt. Lett.* **2013**, *38*, 4082.
[104] N. J. Findlay, C. Orofino-Peña, J. Bruckbauer, S. E. T. Elmasly, S. Arumugam, A. R. Inigo, A. L. Kanibolotsky, R. W. Martin, P. J. Skabara, *J. Mater. Chem. C* **2013**, *1*, 2249.
[105] S. Nizamoglu, *Journal* **2016**, *20*, 490.
[106] R. Y. Tsien, *Annu. Rev. Biochem.* **1998**, *67*, 509.
[107] L. Niklaus, S. Tansaz, H. Dakhil, K. T. Weber, M. Pröschel, M. Lang, M. Kostrzewa, P. B. Coto, R. Detsch, U. Sonnewald, A. Wierschem, A. R. Boccaccini, R. D. Costa, *Adv. Funct. Mater.* **2017**, *27*, 1.
[108] V. Fernández-Luna, D. Sánchez-de Alcázar, J. P. Fernández-Blázquez, A. L. Cortajarena, P. B. Coto, R. D. Costa, *Adv. Funct. Mater.* **2019**, *29*, 1904356.
[109] D. M. Chudakov, M. V Matz, S. Lukyanov, K. A. Lukyanov, *Physiol. Rev.* **2010**, *90*, 1103.
[110] V. Fernández-Luna, P. B. Coto, R. D. Costa, *Angew. Chemie Int. Ed.* **2018**, *57*, 8826.
[111] E. A. Rodriguez, R. E. Campbell, J. Y. Lin, M. Z. Lin, A. Miyawaki, A. E. Palmer, X. Shu, J. Zhang, R. Y. Tsien, *Trends Biochem. Sci.* **2017**, *42*, 111.
[112] M. D. Weber, L. Niklaus, M. Pröschel, P. B. Coto, U. Sonnewald, R. D. Costa, *Adv. Mater.* **2015**, *27*, 5493.
[113] L. D. Lavis, R. T. Raines, *ACS Chem. Biol.* **2008**, *3*, 142.
[114] H. Kobayashi, M. Ogawa, R. Alford, P. L. Choyke, Y. Urano, *Chem. Rev.* **2010**, *110*, 2620.
[115] D. M. Chudakov, S. Lukyanov, K. A. Lukyanov, *Trends Biotechnol.* **2005**, *23*, 605.
[116] T. Ueno, T. Nagano, *Nat. Methods* **2011**, *8*, 642.
[117] G. L. Nicolson, *Biochim. Biophys. Acta - Biomembr.* **2014**, *1838*, 1451.
[118] D. Lingwood, K. Simons, *Science (80-.).* **2010**, *327*, 46.
[119] M. C. Rodrigo-Brenni, R. S. Hegde, *Dev. Cell* **2012**, *23*, 896.
[120] X. Cheng, J. C. Smith, *Chem. Rev.* **2019**, *119*, 5849.
[121] G. van Meer, D. R. Voelker, G. W. Feigenson, *Nat. Rev. Mol. Cell Biol.* **2008**, *9*, 112.
[122] M. J. Arends, A. H. Wyllie, In *Molecular Cell Pathology* (Eds.: Richter, G. W.; Solez, K. B. T.-I. R. of E. P.), Academic Press, **1991**, pp. 223–254.
[123] A. S. Klymchenko, *Acc. Chem. Res.* **2017**, *50*, 366.

[124] M. Collot, S. Pfister, A. S. Klymchenko, *Curr. Opin. Chem. Biol.* **2022**, *69*, 102161.
[125] A. S. Klymchenko, R. Kreder, *Chem. Biol.* **2014**, *21*, 97.
[126] Y. Niko, A. S. Klymchenko, *J. Biochem.* **2021**, *170*, 163.
[127] J. R. Lakowicz, D. R. Bevan, B. P. Maliwal, H. Cherek, A. Balter, *Biochemistry* **1983**, *22*, 5714.
[128] M. A. Haidekker, T. P. Brady, D. Lichlyter, E. A. Theodorakis, *Bioorg. Chem.* **2005**, *33*, 415.
[129] R. A. Badley, W. G. Martin, H. Schneider, *Biochemistry* **1973**, *12*, 268.
[130] B. R. Lentz, Y. Barenholz, T. E. Thompson, *Biochemistry* **1976**, *15*, 4521.
[131] M. M. Lapinski, G. J. Blanchard, *Chem. Phys. Lipids* **2007**, *150*, 12.
[132] A. S. Waggoner, L. Stryer, *Proc. Natl. Acad. Sci.* **1970**, *67*, 579.
[133] J.-P. Starck, Y. Nakatani, G. Ourisson, *Tetrahedron* **1995**, *51*, 2629.
[134] M. E. Jones, B. R. Lentz, *Biochemistry* **1986**, *25*, 567.
[135] A. H. Ashoka, P. Ashokkumar, Y. P. Kovtun, A. S. Klymchenko, *J. Phys. Chem. Lett.* **2019**, *10*, 2414.
[136] J. García-Calvo, J. López-Andarias, J. Maillard, V. Mercier, C. Roffay, A. Roux, A. Fürstenberg, N. Sakai, S. Matile, *Chem. Sci.* **2022**, *13*, 2086.
[137] J. Valanciunaite, E. Kempf, H. Seki, D. I. Danylchuk, N. Peyriéras, Y. Niko, A. S. Klymchenko, *Anal. Chem.* **2020**, *92*, 6512.
[138] A. P. Demchenko, Y. Mély, G. Duportail, A. S. Klymchenko, *Biophys. J.* **2009**, *96*, 3461.
[139] J. M. Kwiatek, D. M. Owen, A. Abu-Siniyeh, P. Yan, L. M. Loew, K. Gaus, *PLoS One* **2013**, *8*, e52960.
[140] D. M. Owen, C. Rentero, A. Magenau, A. Abu-Siniyeh, K. Gaus, *Nat. Protoc.* **2011**, *7*, 24.
[141] K. Simons, E. Ikonen, *Nature* **1997**, *387*, 569.
[142] D. A. Brown, E. London, *J. Biol. Chem.* **2000**, *275*, 17221.
[143] K. Simons, D. Toomre, *Nat. Rev. Mol. Cell Biol.* **2000**, *1*, 31.
[144] O. A. Kucherak, P. Didier, Y. Mély, A. S. Klymchenko, *J. Phys. Chem. Lett.* **2010**, *1*, 616.
[145] J. Shaya, M. Collot, F. Bénailly, N. Mahmoud, Y. Mély, B. Y. Michel, A. S. Klymchenko, A. Burger, *ACS Chem. Biol.* **2017**, *12*, 3022.
[146] J. Shaya, F. Fontaine-Vive, B. Y. Michel, A. Burger, *Chem. – A Eur. J.* **2016**, *22*, 10627.
[147] R. Saxena, S. Shrivastava, S. Haldar, A. S. Klymchenko, A. Chattopadhyay, *Chem. Phys. Lipids* **2014**, *183*, 1.
[148] O. A. Kucherak, S. Oncul, Z. Darwich, D. A. Yushchenko, Y. Arntz, P. Didier, Y. Mély, A. S. Klymchenko, *J. Am. Chem. Soc.* **2010**, *132*, 4907.

[149] Z. Darwich, A. S. Klymchenko, O. A. Kucherak, L. Richert, Y. Mély, *Biochim. Biophys. Acta - Biomembr.* **2012**, *1818*, 3048.
[150] P. Neuberg, A. Perino, E. Morin-Picardat, N. Anton, Z. Darwich, D. Weltin, Y. Mely, A. S. Klymchenko, J.-S. Remy, A. Wagner, *Chem. Commun.* **2015**, *51*, 11595.
[151] R. Saxena, S. Shrivastava, A. Chattopadhyay, *Biochim. Biophys. Acta* **2015**, *1848*, 1699.
[152] D. I. Danylchuk, P.-H. Jouard, A. S. Klymchenko, *J. Am. Chem. Soc.* **2021**, *143*, 912.
[153] D. I. Danylchuk, S. Moon, K. Xu, A. S. Klymchenko, *Angew. Chemie Int. Ed.* **2019**, *58*, 14920.
[154] T. Miteva, L. Palmer, L. Kloppenburg, D. Neher, U. H. F. Bunz, *Macromolecules* **2000**, *33*, 652.
[155] C. Shang, G. Wang, K. Liu, Q. Jiang, F. Liu, P.-T. Chou, Y. Fang, *Angew. Chemie Int. Ed.* **2020**, *59*, 8579.
[156] D. Raithel, L. Simine, S. Pickel, K. Schötz, F. Panzer, S. Baderschneider, D. Schiefer, R. Lohwasser, J. Köhler, M. Thelakkat, M. Sommer, A. Köhler, P. J. Rossky, R. Hildner, *Proc. Natl. Acad. Sci.* **2018**, *115*, 2699.
[157] Z. Sun, Q. Zang, Q. Luo, C. Lv, F. Cao, Q. Song, R. Zhao, Y. Zhang, W.-Y. Wong, *Chem. Commun.* **2019**, *55*, 4735.
[158] Y. Zang, E.-D. Fung, T. Fu, S. Ray, M. H. Garner, A. Borges, M. L. Steigerwald, S. Patil, G. Solomon, L. Venkataraman, *Nano Lett.* **2021**, *21*, 673.
[159] B.-K. An, J. Gierschner, S. Y. Park, *Acc. Chem. Res.* **2012**, *45*, 544.
[160] J.-S. Yang, S.-Y. Chiou, K.-L. Liau, *J. Am. Chem. Soc.* **2002**, *124*, 2518.
[161] A. Fin, A. Vargas Jentzsch, N. Sakai, S. Matile, *Angew. Chemie Int. Ed.* **2012**, *51*, 12736.
[162] P. D. Kiser, M. Golczak, K. Palczewski, *Chem. Rev.* **2014**, *114*, 194.
[163] M. Sheves, K. Nakanishi, B. Honig, *J. Am. Chem. Soc.* **1979**, *101*, 7086.
[164] D. Alonso Doval, S. Matile, *Org. Biomol. Chem.* **2013**, *11*, 7467.
[165] A. Goujon, A. Colom, K. Straková, V. Mercier, D. Mahecic, S. Manley, N. Sakai, A. Roux, S. Matile, *J. Am. Chem. Soc.* **2019**, *141*, 3380.
[166] M. Dal Molin, Q. Verolet, S. Soleimanpour, S. Matile, *Chemistry* **2015**, *21*, 6012.
[167] K. Strakova, L. Assies, A. Goujon, F. Piazzolla, H. V Humeniuk, S. Matile, *Chem. Rev.* **2019**, *119*, 10977.
[168] L. Assies, J. García-Calvo, F. Piazzolla, S. Sanchez, T. Kato, L. Reymond, A. Goujon, A. Colom, J. López-Andarias, K. Straková, D. Mahecic, V. Mercier, M. Riggi, N. Jiménez-Rojo, C. Roffay, G.

Licari, M. Tsemperouli, F. Neuhaus, A. Fürstenberg, E. Vauthey, S. Hoogendoorn, M. Gonzalez-Gaitan, A. Zumbuehl, K. Sugihara, J. Gruenberg, H. Riezman, R. Loewith, S. Manley, A. Roux, N. Winssinger, N. Sakai, S. Pitsch, S. Matile, *Chimia (Aarau).* **2021**, *75*, 1004.
[169] D. A. Doval, M. D. Molin, S. Ward, A. Fin, N. Sakai, S. Matile, *Chem. Sci.* **2014**, *5*, 2819.
[170] M. Dal Molin, Q. Verolet, A. Colom, R. Letrun, E. Derivery, M. Gonzalez-Gaitan, E. Vauthey, A. Roux, N. Sakai, S. Matile, *J. Am. Chem. Soc.* **2015**, *137*, 568.
[171] Q. Verolet, S. Soleimanpour, K. Fujisawa, M. Dal Molin, N. Sakai, S. Matile, *ChemistryOpen* **2015**, *4*, 264.
[172] Q. Verolet, M. Dal Molin, A. Colom, A. Roux, L. Guénée, N. Sakai, S. Matile, *Helv. Chim. Acta* **2017**, *100*.
[173] Q. Verolet, A. Rosspeintner, S. Soleimanpour, N. Sakai, E. Vauthey, S. Matile, *J. Am. Chem. Soc.* **2015**, *137*, 15644.
[174] X. Zhang, N. Sakai, S. Matile, *ChemistryOpen* **2020**, *9*, 18.
[175] J. García-Calvo, J. López-Andarias, N. Sakai, S. Matile, *Chem. Commun.* **2021**, *57*, 3913.
[176] J. García-Calvo, J. Maillard, I. Fureraj, K. Strakova, A. Colom, V. Mercier, A. Roux, E. Vauthey, N. Sakai, A. Fürstenberg, S. Matile, *J. Am. Chem. Soc.* **2020**, *142*, 12034.
[177] M. A. Haidekker, E. A. Theodorakis, *J. Biol. Eng.* **2010**, *4*, 11.
[178] K. Y. Law, *Chem. Phys. Lett.* **1980**, *75*, 545.
[179] M. A. Haidekker, N. L'Heureux, J. A. Frangos, *Am. J. Physiol. Heart Circ. Physiol.* **2000**, *278*, H1401.
[180] M. K. Kuimova, *Phys. Chem. Chem. Phys.* **2012**, *14*, 12671.
[181] M. E. Nipper, M. Dakanali, E. Theodorakis, M. A. Haidekker, *Biochimie* **2011**, *93*, 988.
[182] M. Dakanali, T. H. Do, A. Horn, A. Chongchivivat, T. Jarusreni, D. Lichlyter, G. Guizzunti, M. A. Haidekker, E. A. Theodorakis, *Bioorg. Med. Chem.* **2012**, *20*, 4443.
[183] F. Liu, T. Wu, J. Cao, S. Cui, Z. Yang, X. Qiang, S. Sun, F. Song, J. Fan, J. Wang, X. Peng, *Chem. – A Eur. J.* **2013**, *19*, 1548.
[184] X. Peng, Z. Yang, J. Wang, J. Fan, Y. He, F. Song, B. Wang, S. Sun, J. Qu, J. Qi, M. Yan, *J. Am. Chem. Soc.* **2011**, *133*, 6626.
[185] A. Polita, S. Toliautas, R. Žvirblis, A. Vyšniauskas, *Phys. Chem. Chem. Phys.* **2020**, *22*, 8296.
[186] T. J. Lambert, *Nat. Methods* **2019**, *16*, 277.
[187] M. D. Weber, L. Niklaus, M. Pröschel, P. B. Coto, U. Sonnewald, R. D. Costa, *Adv. Mater.* **2015**, *27*, 5493.
[188] R. N. Day, M. W. Davidson, *Chem. Soc. Rev.* **2009**, *38*, 2887.
[189] U. K. Sukumar, A. Natarajan, T. F. Massoud, R. Paulmurugan, *Top. Med. Chem.* **2019**, *34*, 149.

[190] S. H. Mejías, G. Roelfes, W. R. Browne, *Phys. Chem. Chem. Phys.* **2020**, *22*, 12228.
[191] N. Barbero, C. Magistris, J. Park, D. Saccone, P. Quagliotto, R. Buscaino, C. Medana, C. Barolo, G. Viscardi, *Org. Lett.* **2015**, *17*, 3306.
[192] Y. Xu, Z. Li, A. Malkovskiy, S. Sun, Y. Pang, *J. Phys. Chem. B* **2010**, *114*, 8574.
[193] G. M. Paternò, L. Moretti, A. J. Barker, C. D'Andrea, A. Luzio, N. Barbero, S. Galliano, C. Barolo, G. Lanzani, F. Scotognella, *J. Mater. Chem. C* **2017**, *5*, 7732.
[194] E. Haldon, C. M. Nicasio, P. J. Pérez, *Org. Biomol. Chem.* **2015**, *13*, 9528.
[195] M. Meldal, C. W. Tornoe, *Chem. Rev.* **2008**, *108*, 2952.
[196] J. M. J. M. Ravasco, H. Faustino, A. Trindade, P. M. P. Gois, *Chem. – A Eur. J.* **2019**, *25*, 43.
[197] H. Vollmann, H. Becker, M. Coyell, H. Streeck, *Justus Liebigs Ann. Chem.* **1937**, *531*, 1.
[198] F. Würthner, S. Ahmed, C. Thalacker, T. Debaerdemaeker, *Chem. - A Eur. J.* **2002**, *8*, 4742.
[199] S.-L. Suraru, F. Wurthner, *Angew. Chemie - Int. Ed.* **2014**, *53*, 7428.
[200] F. N. Miros, S. Matile, *ChemistryOpen* **2016**, *5*, 219.
[201] F. Chaignon, M. Falkenström, S. Karlsson, E. Blart, F. Odobel, L. Hammarström, *Chem. Commun.* **2007**, 64.
[202] F. Doria, M. Di Antonio, M. Benotti, D. Verga, M. Freccero, *J. Org. Chem.* **2009**, *74*, 8616.
[203] S. V. Bhosale, S. V. Bhosale, M. B. Kalyankar, S. J. Langford, *Org. Lett.* **2009**, *11*, 5418.
[204] A. Nowak-Król, K. Shoyama, M. Stolte, F. Würthner, *Chem. Commun.* **2018**, *54*, 13763.
[205] Y. Zhao, Y. Domoto, E. Orentas, C. Beuchat, D. Emery, J. Mareda, N. Sakai, S. Matile, *Angew. Chemie - Int. Ed.* **2013**, *52*, 9940.
[206] R. E. Dawson, A. Hennig, D. P. Weimann, D. Emery, V. Ravikumar, J. Montenegro, T. Takeuchi, S. Gabutti, M. Mayor, J. Mareda, C. A. Schalley, S. Matile, *Nat. Chem.* **2010**, *2*, 533.
[207] N. Sakai, J. Mareda, E. Vauthey, S. Matile, *Chem. Commun.* **2010**, *46*, 4225.
[208] N. Sakai, J. Mareda, S. Matile, *Chem. Commun.* **2010**, *46*, 4225.
[209] R. S. K. Kishore, V. Ravikumar, G. Bernardinelli, N. Sakai, S. Matile, *J. Org. Chem.* **2008**, *73*, 738.
[210] A. Fin, I. Petkova, D. A. Doval, N. Sakai, E. Vauthey, S. Matile, *Org. Biomol. Chem.* **2011**, *9*, 8246.
[211] A. A. Berezin, A. Sciutto, N. Demitri, D. Bonifazi, *Org. Lett.* **2015**, *17*, 1870.

[212] T. Kim, C. Lin, J. D. Schultz, R. M. Young, M. R. Wasielewski, *J. Am. Chem. Soc.* **2022**.
[213] S. Ghosh, X.-Q. Li, V. Stepanenko, F. Würthner, *Chemistry (Easton).* **2008**, *36*, 11343.
[214] S. Yagai, T. Seki, T. Karatsu, A. Kitamura, F. Würthner, *Angew. Chemie Int. Ed.* **2008**, *47*, 3367.
[215] S. Erten, S. Alp, S. Icli, *J. Photochem. Photobiol. A Chem.* **2005**, *175*, 214.
[216] G. Sathiyan, R. Ranjan, S. Ranjan, A. Garg, R. K. Gupta, A. Singh, *ACS Appl. Energy Mater.* **2019**, *2*, 7609.
[217] A. Dessì, M. Calamante, A. Sinicropi, M. L. Parisi, L. Vesce, P. Mariani, B. Taheri, M. Ciocca, A. Di Carlo, L. Zani, A. Mordini, G. Reginato, *Sustain. Energy Fuels* **2020**, *4*, 2309.
[218] Y. Wang, H. Liu, Q. Pan, N. Ding, C. Yang, Z. Zhang, C. Jia, Z. Li, J. Liu, Y. Zhao, *ACS Appl. Mater. Interfaces* **2020**, *12*, 46483.
[219] Z. Zhang, Y.-A. Chen, W.-Y. Hung, W.-F. Tang, Y.-H. Hsu, C.-L. Chen, F.-Y. Meng, P.-T. Chou, *Chem. Mater.* **2016**, *28*, 8815.
[220] J. Y. Jung, S. J. Han, J. Chun, C. Lee, J. Yoon, *Dye. Pigment.* **2012**, *94*, 423.
[221] Z. Dikmen, O. Turhan, M. Yaman, V. Bütün, *J. Photochem. Photobiol. A Chem.* **2021**, *419*, 113456.
[222] N. A. Sayresmith, A. Saminathan, J. K. Sailer, S. M. Patberg, K. Sandor, Y. Krishnan, M. G. Walter, *J. Am. Chem. Soc.* **2019**, *141*, 18780.
[223] A. Dessì, M. Calamante, A. Mordini, L. Zani, M. Taddei, G. Reginato, *RSC Adv.* **2014**, *4*, 1322.
[224] M. Li, C. An, W. Pisula, K. Müllen, *Acc. Chem. Res.* **2018**, *51*, 1196.
[225] Q. Nie, A. Tang, Q. Guo, E. Zhou, *Nano Energy* **2021**, *87*, 106174.
[226] J. Du, M. C. Biewer, M. C. Stefan, *J. Mater. Chem. A* **2016**, *4*, 15771.
[227] B. A. D. Neto, J. R. Correa, J. Spencer, *Chem. – A Eur. J.* **2022**, *28*, e202103262.
[228] C. Ruan, X. Bai, C. Sun, H. Chen, C. Wu, X. Chen, H. Chen, V. L. Colvin, W. W. Yu, *RSC Adv.* **2016**, *6*, 106225.
[229] W.-C. Geng, Y.-C. Liu, Y.-Y. Wang, Z. Xu, Z. Zheng, C.-B. Yang, D.-S. Guo, *Chem. Commun.* **2017**, *53*, 392.
[230] Z. Zhao, J. Geng, Z. Chang, S. Chen, C. Deng, T. Jiang, W. Qin, J. W. Y. Lam, H. S. Kwok, H. Qiu, B. Liu, B. Z. Tang, *J. Mater. Chem.* **2012**, *22*, 11018.
[231] J. Huang, Y. Xu, Q. Hou, W. Yang, M. Yuan, Y. Cao, *Macromol. Rapid Commun.* **2002**, *23*, 709.
[232] A. A. El-Shehawy, N. I. Abdo, A. A. El-Barbary, J. Lee, *Alternating Copolymers Based on 2, 1, 3-Benzothiadiazole and Hexylthiophene: Positioning Effect of Hexyl Chains on the*

Photophysical and Electrochemical Properties, Wiley Online Library, **2011**.
[233] Z. Gao, Y. Hao, M. Zheng, Y. Chen, *RSC Adv.* **2017**, *7*, 7604.
[234] Y. Hao, Y. Chen, *Dye. Pigment.* **2016**, *129*, 186.
[235] H. Dong, H. Yang, J. Zhao, X. Liu, Y. Zheng, *J. Lumin.* **2021**, *231*, 117840.
[236] F. Würthner, S. Ahmed, C. Thalacker, T. Debaerdemaeker, *Chem. – A Eur. J.* **2002**, *8*, 4742.
[237] G. Volpi, R. Rabezzana, *New J. Chem.* **2021**, *45*, 5737.
[238] G. Colombo, G. Attilio Ardizzoia, S. Brenna, *Inorganica Chim. Acta* **2022**, *535*, 120849.
[239] E. Fresta, G. Volpi, C. Garino, C. Barolo, R. D. Costa, *Polyhedron* **2018**, *140*, 129.
[240] F. Shibahara, E. Yamaguchi, A. Kitagawa, A. Imai, T. Murai, *Tetrahedron* **2009**, *65*, 5062.
[241] H. Wang, W. Xu, Z. Wang, L. Yu, K. Xu, *J. Org. Chem.* **2015**, *80*, 2431.
[242] J. Wang, L. Dyers, R. Mason, P. Amoyaw, X. R. Bu, *J. Org. Chem.* **2005**, *70*, 2353.
[243] G. Volpi, *Asian J. Org. Chem.* **2022**, *11*, e202200171.
[244] S. Priyanga, T. Khamrang, M. Velusamy, S. Karthi, B. Ashokkumar, R. Mayilmurugan, *Dalt. Trans.* **2019**, *48*, 1489.
[245] M. Roy, B. V. S. K. Chakravarthi, C. Jayabaskaran, A. A. Karande, A. R. Chakravarty, *Dalt. Trans.* **2011**, *40*, 4855.
[246] G. Volpi, E. Priola, C. Garino, A. Daolio, R. Rabezzana, P. Benzi, A. Giordana, E. Diana, R. Gobetto, *Inorganica Chim. Acta* **2020**, *509*, 119662.
[247] A. L. Guckian, M. Doering, M. Ciesielski, O. Walter, J. Hjelm, N. M. O'Boyle, W. Henry, W. R. Browne, J. J. McGarvey, J. G. Vos, *Dalt. Trans.* **2004**, 3943.
[248] Z. Xu, Z. Chen, A. Liu, R. Ji, X. Cao, Y. Ge, *RSC Adv.* **2019**, *9*, 8943.
[249] Y. Ren, L. Zhang, Z. Zhou, S. Wang, Y. Xu, Y. Gu, X. Zha, *New J. Chem.* **2018**, *42*, 13884.
[250] E. Fresta, G. Volpi, M. Milanesio, C. Garino, C. Barolo, R. D. Costa, *Inorg. Chem.* **2018**, *57*, 10469.
[251] E. Sitarska, A. Diz-Muñoz, *Curr. Opin. Cell Biol.* **2020**, *66*, 11.
[252] R. J. Leiphart, D. Chen, A. P. Peredo, A. E. Loneker, P. A. Janmey, *Langmuir* **2019**, *35*, 7509.
[253] J. Wang, R. Mason, D. VanDerveer, K. Feng, X. R. Bu, *J. Org. Chem.* **2003**, *68*, 5415.
[254] G. Volpi, C. Garino, E. Priola, C. Magistris, M. R. Chierotti, C. Barolo, *Dye. Pigment.* **2019**, *171*, 107713.
[255] G. Volpi, G. Magnano, I. Benesperi, D. Saccone, E. Priola, V.

Gianotti, M. Milanesio, E. Conterosito, C. Barolo, G. Viscardi, *Dye. Pigment.* **2017**, *137*, 152.
[256] G. Volpi, C. Garino, E. Priola, E. Diana, R. Gobetto, R. Buscaino, G. Viscardi, C. Barolo, *Dye. Pigment.* **2017**, *143*, 284.
[257] G. Volpi, C. Garino, E. Conterosito, C. Barolo, R. Gobetto, G. Viscardi, *Dye. Pigment.* **2016**, *128*, 96.
[258] G. Volpi, S. Galliano, R. Buscaino, G. Viscardi, C. Barolo, *J. Lumin.* **2022**, *242*, 118529.
[259] R. Koynova, M. Caffrey, *Biochim. Biophys. Acta - Rev. Biomembr.* **1998**, *1376*, 91.
[260] G. Albrecht, C. Rössiger, J. M. Herr, H. Locke, H. Yanagi, R. Göttlich, D. Schlettwein, *Phys. status solidi* **2020**, *257*, 1900677.
[261] Z. Huang, R. P. Haugland, *Biochem. Biophys. Res. Commun.* **1991**, *181*, 166.
[262] J. Wu, Z. Shi, L. Zhu, J. Li, X. Han, M. Xu, S. Hao, Y. Fan, T. Shao, H. Bai, B. Peng, W. Hu, X. Liu, C. Yao, L. Li, W. Huang, *Adv. Opt. Mater.* **2022**, *10*, 2102514.
[263] I. A. Karpenko, M. Collot, L. Richert, C. Valencia, P. Villa, Y. Mély, M. Hibert, D. Bonnet, A. S. Klymchenko, *J. Am. Chem. Soc.* **2015**, *137*, 405.
[264] T. Mukherjee, R. J. Martinez-Sanchez, K. T. Fam, S. Bou, L. Richert, D. Garnier, Y. Mély, S. Kanvah, A. S. Klymchenko, M. Collot, *Mater. Chem. Front.* **2021**, *5*, 2459.
[265] M. Collot, P. Ashokkumar, H. Anton, E. Boutant, O. Faklaris, T. Galli, Y. Mély, L. Danglot, A. S. Klymchenko, *Cell Chem. Biol.* **2019**, *26*, 600.
[266] J. Karpenko, A. S. Klymchenko, S. Gioria, R. Kreder, I. Shulov, P. Villa, Y. Mély, M. Hibert, D. Bonnet, *Chem. Commun.* **2015**, *51*, 2960.
[267] M. Collot, R. Kreder, A. L. Tatarets, L. D. Patsenker, Y. Mely, A. S. Klymchenko, *Chem. Commun.* **2015**, *51*, 17136.
[268] G. Xia, H. Wang, *J. Photochem. Photobiol. C Photochem. Rev.* **2017**, *31*, 84.
[269] A. Ajayaghosh, *Acc. Chem. Res.* **2005**, *38*, 449.
[270] K. Ilina, W. M. MacCuaig, M. Laramie, J. N. Jeouty, L. R. McNally, M. Henary, *Bioconjug. Chem.* **2020**, *31*, 194.
[271] A. Treibs, K. Jacob, *Angew. Chemie Int. Ed. English* **1965**, *4*, 694.
[272] E. Terpetschnig, J. R. Lakowicz, *Dye. Pigment.* **1993**, *21*, 227.
[273] L. Beverina, P. Salice, *European J. Org. Chem.* **2010**, *2010*, 1207.
[274] S. Kim, G. K. Mor, M. Paulose, O. K. Varghese, C. Baik, C. A. Grimes, *Langmuir* **2010**, *26*, 13486.
[275] Y. Fujita, Y. Murakami, A. Noda, S. Miyoshi, *Bioconjug. Chem.* **2017**, *28*, 642.
[276] H. S. Mehr, N. C. Romano, R. Altamimi, J. M. Modarelli, D. A.

Modarelli, *Dalt. Trans.* **2015**, *44*, 3176.
[277] M. Soethoudt, S. C. Stolze, M. V Westphal, L. Van Stralen, A. Martella, E. J. Van Rooden, W. Guba, Z. V Varga, H. Deng, S. I. Van Kasteren, *J. Am. Chem. Soc.* **2018**, *140*, 6067.
[278] K. M. Bonger, R. J. van den Berg, L. H. Heitman, A. P. IJzerman, J. Oosterom, C. M. Timmers, H. S. Overkleeft, G. A. van der Marel, *Bioorg. Med. Chem.* **2007**, *15*, 4841.
[279] C. Zheng, S. Pu, J. Xu, M. Luo, D. Huang, L. Shen, *Tetrahedron* **2007**, *63*, 5437.
[280] F. Yang, X.-L. Xu, Y.-H. Gong, W.-W. Qiu, Z.-R. Sun, J.-W. Zhou, P. Audebert, J. Tang, *Tetrahedron* **2007**, *63*, 9188.
[281] S. Deprets, G. Kirsch, *European J. Org. Chem.* **2000**, *2000*, 1353.
[282] M. R. Michaelides, Y. Hong, S. DiDomenico, E. K. Bayburt, K. E. Asin, D. R. Britton, C. W. Lin, K. Shiosaki, *J. Med. Chem.* **1997**, *40*, 1585.
[283] J. Park, N. Barbero, J. Yoon, E. Dell'Orto, S. Galliano, R. Borrelli, J.-H. Yum, D. Di Censo, M. Grätzel, M. K. Nazeeruddin, *Phys. Chem. Chem. Phys.* **2014**, *16*, 24173.
[284] R. Bisht, V. Sudhakar, M. F. Mele Kavungathodi, N. Karjule, J. Nithyanandhan, *ACS Appl. Mater. Interfaces* **2018**, *10*, 26335.

APPENDIX

PUBLICATIONS

- De Rossi, F., **Renno, G.**, Taheri, B., Nia, N. Y., Ilieva, V., Fin, A., Di Carlo, A., Bonomo, M., Barolo, C., Brunetti, F. Modified P3HT materials as hole transport layers for flexible perovskite solar cells, *J. Power Sources,* **2021**, 494, 229735 *[equal contribution of Dr. F. De Rossi and Mr. G. Renno]*
- Giordano, M., **Renno, G.**, Quagliotto, P., Barolo, C., Cravotto, G., Fin, A., Viscardi, G. Solid-Phase Synthesis of Asymmetric Cyanine Dyes*, Current Organic Chemistry*, **2021**, 25, 1739 – 1754
- De Rossi, F., Taheri, B., Bonomo, M., Gupta, V., **Renno, G.**, Yaghoobi Nia, N., Rech, P., Frost, C., Cazzaniga, C., Quagliotto, P., Di Carlo, A., Barolo, C., Ottavi, M., Brunetti, F. Neutron irradiated perovskite films and solar cells on PET substrates, *Nano Energy*, **2022**, 93.
- Ferrara, S., Mejias, S.H., Liutkus, M., **Renno, G.**, Stella, F., Kociolek, I., Fuenzalida-Werner, J.P., Barolo, C., Coto, P.B., Cortajarena, A.L., Costa, R.D. Designing Artificial Fluorescent Proteins: Squaraine-LmrR Biophosphors for High Performance Deep-Red Biohybrid Light-Emitting Diodes, *Adv. Funct. Materials*, **2022**, 32, 2111381.
- Pelliccioli, V., Cardano, F., **Renno, G.**, Vasile, F., Graiff, C., Mazzeo, G., Fin, A., Longhi, G., Abbate, S., Rosetti, A., Villani, C., Viscardi, G., Licandro, E., Cauteruccio, S. Synthesis, Stereochemical and Photophysical Properties of Functionalized Thiahelicenes, *Catalysts*, **2022**, 12, 366.
- **Renno, G.**, Cardano, F., Volpi, G., Barolo, C., Viscardi, G., Fin, A. Imidazo[1,5-a]pyridine-Based Fluorescent Probes: A Photophysical Investigation in Liposome Models, *Molecules*, **2022**, 27, 3856.

- **Renno, G.**, Cardano, F., Ilieva, V., Viscardi, G., Fin, A. Near-Infrared squaraine dyes as bright fluorescent probes: a structure-activity photophysical investigation in liposomes, *Eur. J. Org. Chem.* **2022**, e202200833.

POSTER

- **Renno G.**, Ilieva, V., Nia Y. N., Bonomo M., Di Carlo A., Quagliotto P., Brunetti F., Viscardi G., Barolo C. "Synthesis and characterization of conducting polymers based on 3-hexylthiophene". Poster presented at: *OrBitaly 2019*. Naples, Italy. 2019, 21st-23rd October.
- **Renno, G.,** Cardano, F., Barolo, C., Viscardi, G., Cravotto, G., Fin, A. "Structure to function investigation in NIR dyes for bilayer membrane imaging". Poster presented on Twitter at: 1st Virtual Symposium for Young Organic Chemists – SCI, 2020, November 3rd-6th
- **Renno, G**., Cardano, F., Barolo, C., Viscardi, G., Cravotto, G., Fin, A. "NIR dyes for bilayer membrane imaging: a structure-function investigation". Poster presented on Twitter at: RSC Poster Twitter Conference, 2021, March 2nd
- **Renno, G.,** Giordano, M., Barbero, N., Quagliotto, P., Cravotto, G., Viscardi, G., Fin, A. "NIR squaraine dyes for cell bilayer bioimaging: a structure-activity investigation". Poster will be presented at: XXVII Congresso Nazionale della Società Chimica Italiana. 2021, September 14th-23rd.
- **Renno, G.,** Giordano, M., Barbero, N., Cravotto, G., Quagliotto, P., Viscardi, G., Barolo, C., Fin, A. Perimidine-based NIR squaraine dyes as cell membrane probes: a structure-to-function investigation in liposomes." Poster will be presented at: Giornate Italiane di Fotochimica 2021. 2021, September 23rd-24th**.**

- **Renno, G.,** Giordano, M., Barbero, N., Cravotto, G., Quagliotto, P., Viscardi, G., Barolo, C., Fin, A.Novel squaraine dyes as cell membrane probes: a structure to function investigation. RSC Poster Twitter Conference. March 1st, 2022.
- **Renno, G.,** Ferrara, S., Nejrotti, S., Bokan, M., Cardano, F., Moran Plata, M. J., Barbero, N., Fin, A., Costa, D. R., Barolo, C. Naphthalene diimides organic emitters for artificial fluorescent proteins: a sustainable approach toward white bio-hybrid LEDs. Poster presented at: Congresso Nazionale di Fotochimica 2021. Turin, Italy. 2021, December 16th – 18th.
- Giordano, M. **Renno, G.,** M., Barbero, N., Cravotto, G., Quagliotto, P., Barolo, C., Viscardi, G., Fin, A. Novel perimidine-based squaraine dyes as cell membrane probes: a structure to function investigation in liposomes. Poster presented at: Congresso Nazionale di Fotochimica 2021. Turin, Italy. 2021, December 16th – 18th.

SEMINARS

- *"1st Virtual Symposium – ChemBioChem"*. May 28th 2020. Virtual event.
- *"Bioconjugation in Polymer Chemistry - ACS"*. August 6th 2020. Virtual event.
- *Synthetic Organic Electrochemistry: Basic Concepts and Scale-up*; Scientific Update. 16th September 2020. Virtual Event.
- *EurJOC Virtual Symposium* - Special Edition: Journeé DCO – EurJOC, 30th September 2020. Virtual Event.
- *New Frontiers in Synthetic Chemistry* 2020, RSC, 11th – 12th November 2020. Virtual Event.

CONGRESSES, CONFERENCES

- *SCI – ViSYOChem 2020*, 3rd-6th November 2020. Virtual Event.
- *SCI – XXVII Congresso Nazionale*, 14th – 23rd September 2021. Virtual Event.
- *GIF – Giornate Italiane di Fotochimica*, 23rd-24th September 2021. Virtual Event.
- *GIF – Congresso Nazionale di Fotochimica 2021*. Turin, Italy. 2021, December 16th – 18th.

SCHOOLS

- AEBIN *Photochemistry School 2020*. Online. September 7th 2020 – September 9th 2020.
- ISOS 2021 - *XLV "A. Corbella" International Summer School on Organic Synthesis*. Virtual event. 14th-17th June 2021.
- IX Ciamician Photochemistry School, Bologna, IT (6th-9th June 2022).

ATTENDED Ph.D. COURSES

- *Solid State – NMR.* Prof. R. Gobetto, Prof. M. R. Chierotti. Chemistry Department, University of Turin. 2020.
- *Electrochemical Energy Storage and Conversion Systems* Prof. M. Sgroi. Chemistry Department, University of Turin. 2020.
- *Chemical Sensors for Scientific Research and Everyday Life.* Prof. O. Abollino. Chemistry Department, University of Turin. 2020.
- *The vitreous state.* Prof. L. Battezzati. Chemistry Department, University of Turin. 2020.
- Carbanion Chemistry in Organic Synthesis. Prof. V. Pace. Chemistry Department, University of Turin. 2020.

- Organic Chemistry for Chemical Biology and Biomedical Applications, Prof. A. Fin. Chemistry Department, University of Turin. 2021.
- Organic and Hybrid Materials for Biochemical Applications. Prof. N. Barbero, Chemistry Department, University of Turin. 2021.
- Materials in optoelectronic applications for energy generation. Prof. J. Yum, Dott. M. Bonomo. Chemistry Department, University of Turin. 2022